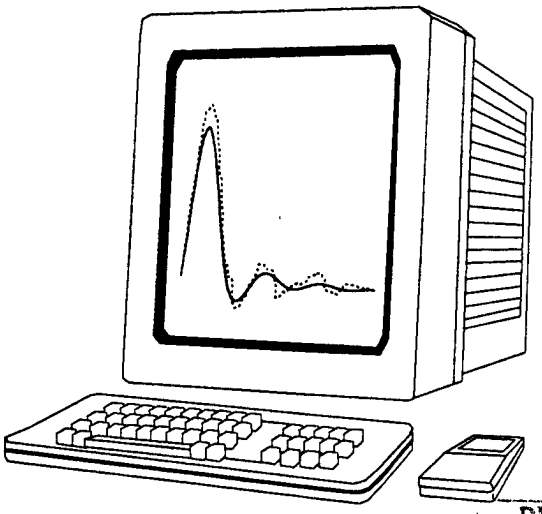
LA-UR-93-3839
Issued: November 1993

Proceedings of the Numerical Modeling for Underground Nuclear Test Monitoring Symposium

Durango, Colorado March 23–25, 1993

Editors:
Steven R. Taylor
James R. Kamm



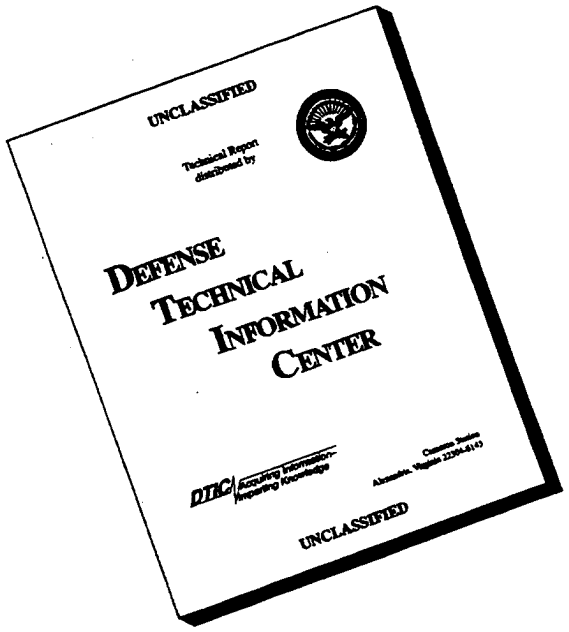
DISTRIBUTION STATEMENT A
Approved for public release;
Distribution Unlimited

This symposium was sponsored by Office of Arms Control and Nonproliferation of the United States Department of Energy and hosted by the Source Region Program of Los Alamos National Laboratory. The Laboratory is operated by the University of California for the United States Department of Energy under Contract W-7405-ENG-36.

19960925 150

DTIC QUALITY INSPECTED 1

DISCLAIMER NOTICE



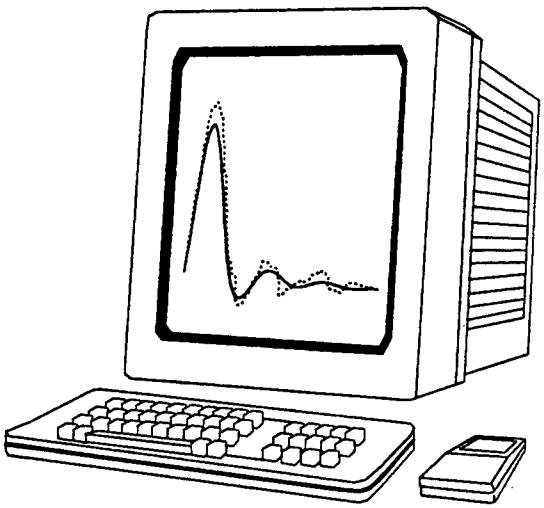
THIS DOCUMENT IS BEST QUALITY AVAILABLE. THE COPY FURNISHED TO DTIC CONTAINED A SIGNIFICANT NUMBER OF PAGES WHICH DO NOT REPRODUCE LEGIBLY.

LA-UR-93-3839
Issued: November 1993

Proceedings of the Numerical Modeling for Underground Nuclear Test Monitoring Symposium

Durango, Colorado March 23–25, 1993

Editors:
Steven R. Taylor
James R. Kamm



This symposium was sponsored by Office of Arms Control and Nonproliferation of the United States Department of Energy and hosted by the Source Region Program of Los Alamos National Laboratory. The Laboratory is operated by the University of California for the United States Department of Energy under Contract W-7405-ENG-36.

THIS PAGE INTENTIONALLY LEFT BLANK.

Contents

Summary of the NMUNTM Symposium 1
Steven R. Taylor and James R. Kamm

Explosion Source Phenomenology

Numerical Modeling and the Physical Basis of Seismic Discriminants 11
Marvin D. Denny

Modeling the Explosion-Source Region: An Overview 17
Lewis A. Glenn

Material Response Modeling

Rock Strength Under Explosive Loading 25
Norton Rimer and William Proffer

A Semi-Empirical Two Phase Model for Rocks 31
Martin B. Fogel

It's Material Strength, Not a Negative Grüneisen Gamma 37
Kurt H. P. H. Sinz and William C. Moss

The Effect of Dilatancy on the Unloading Behavior of Mt. Helen Tuff 49
Armand V. Attia and M. B. Rubin

Statistical Crack Mechanics 57
John K. Dienes

Incorporating Damage Mechanics into Explosion Simulation Models 65
Charles G. Sammis

Planar Impact Experiments for EOS Measurements 93
Michael D. Furnish

Large Scale Hugoniot Material Properties for Danby Marble 99
Eric J. Rinehart

Experimental and Theoretical Studies of Spectral Alteration in Ultrasonic Waves Resulting from Nonlinear Elastic Response in Rock 107
Paul A. Johnson, Katherine R. McCall, and George D. Meegan, Jr.

Fundamental Observations Concerning Hysteresis in the Deformation of Intact and Jointed Rock with Applications to Nonlinear Attenuation in the Near Source Region 121
Greg N. Boitnott

Nonlinear Hysteresis in an Endochronic Solid 135
Steven M. Day, Jean-Bernard Minster, Michael Tryon, and Lois Yu

Analyzing Lagrange Gauge Measurements of Spherical, Cylindrical, or Plane Waves 149
John B. Aidun

Numerical Simulations

Influence of Equation of State and Constitutive Behavior on Seismic Coupling 157
Thomas N. Dey

Sensitivity of the Close-In Seismic Source Function to Rock Properties 169
Fred N. App

Yield Estimation Based on Calculated Comparisons to Particle Velocity Data Recorded at Low Stress 183
John Rambo

Simulation of Seimic Signals from Asymmetric LANL Hydrocode Calculations 205
Jeffrey L. Stevens, Norton Rimer, Eldon J. Halda, Terrance G. Barker, Cecil G. Davis, and W. E. Johnson

Ground Motion Analysis of OSSY 217
Robert P. Swift and Charles M. Snell

Explosive Shielding by Weak Layers 227
William L. Fourney, Richard D. Dick, and Thomas A. Weaver

Atmospheric Signals Produced by Cavity Rebound 237
Eric M. Jones, Fred N. App, and Rodney W. Whitaker

Modelling of Nuclear Explosions in Hard Rock Sites 247
Wendee M. Brunish and Fred N. App

Effects of Explosions in Hard Rocks 259
François E. Heuze, O. R. Walton, D. M. Maddix, R. J. Shaffer, and T. R. Butkovich

Modeling Underground Explosions in Porous Limestone 267
John W. White

Using Neural Networks to Infer the Hydrodynamic Yield of Aspherical Sources 275
Bill Moran and Lewis A. Glenn

Comments on Statistical Issues in Numerical Modeling for Underground Nuclear Test Monitoring 285
Wesley L. Nicholson and Kevin K. Anderson

Seismic Source

Constraints on Equivalent Elastic Source Models from Near-Source Data 291
Brian Stump

2-D and 3-D Numerical Modeling of Seismic Waves from Explosion Sources 299
Keith L. McLaughlin, Jeffrey L. Stevens, Terrance G. Barker, Steven M. Day, and B. Shkoller

Directional Excitation of R_g due to Ripple-Fired Explosions: Two-Dimensional Finite-Difference Simulations 311
Rong-Song Jih

Equivalent Elastic Treatment of Near Source Propagation 319
Lane R. Johnson

Seismic Waveform Modeling of Explosions at Distances of 10–100 km 327
Robert Herrman, Ghassan Al-Eqabi, and Kevin Hutchensen

Modeling of Tamped and Decoupled Explosions in Salt 341
Peter Goldstein and Lewis A. Glenn

Coupling of an Overdriven Cavity 349
H. Douglas Garbin

Simulating High-Frequency Seismograms in Complicated Media: A Spectral Approach 357
Jeffrey L. Orrey and Charles B. Archambeau

Modeling Seismic and Atmospheric Wave Fields Generated by Near Surface Sources 367
Charles B. Archambeau, John B. Davies, and Jeffrey L. Orrey

Analysis of Near-Field Data from a Soviet Decoupling Experiment 375
Chandan Saikia, James P. McLaren, and Donald V. Helmberger

Free-Field Ground Motion Measurements in the Nonlinear-to-Elastic Transition Region 397
Kenneth H. Olsen and Anthony L. Peratt

THIS PAGE INTENTIONALLY LEFT BLANK.

SUMMARY OF NUMERICAL MODELING FOR UNDERGROUND NUCLEAR TEST MONITORING SYMPOSIUM

Steven R. Taylor and James R. Kamm
Geophysics Group, Los Alamos National Laboratory
Los Alamos, NM 87545

The symposium for Numerical Modeling for Underground Nuclear Test Monitoring was held March 23–25, 1993 in Durango, Colorado. The meeting was funded by the DOE Office of Arms Control and Nonproliferation and hosted by the Source Region Program at Los Alamos National Laboratory (LANL). The topic for this meeting came about through discussions with Marv Denny, who was on assignment at DOE Headquarters from Lawrence Livermore National Laboratory (LLNL). An open question raised during these conversations was how numerical modeling techniques are being used to understand the effects of explosion-source phenomenology on test ban treaty monitoring. Numerical studies are becoming increasingly important in the evaluation of capabilities for proliferation monitoring; this trend has accelerated with the curtailment of the nuclear testing program. During these discussions, the issue of the uniqueness and limitations of numerical models arose. It was decided to address these questions by convening a group of experts to present and discuss the problems associated with modeling of close-in data from explosions. Thus, the purpose of the meeting was to discuss the state-of-the-art in numerical simulations of nuclear explosion phenomenology with applications to test ban monitoring. In particular, we wished to focus on the uniqueness of model fits to data, the measurement and characterization of material response models, advanced modeling techniques, and applications of modeling to monitoring problems.

The second goal of the symposium was to establish a dialogue between seismologists and explosion-source code calculators. Seismologists are faced with numerous problems associated with the monitoring of test ban treaties and, more recently, with the detection of nuclear tests in a proliferation environment. These problems involve detecting nuclear explosions and discriminating them from numerous other types of seismic sources (e.g., earthquakes, chemical explosions, mine seismicity). Seismologists are trained in linear wave propagation at very small strains, a field that is in stark contrast to the strongly nonlinear phenomena modeled by the code calculators. Thus, it is useful for the calculators to be exposed to some of the issues that seismologists deal with in monitoring nuclear explosions and modeling seismic data. It is also beneficial for the seismologists to see

some of the numerous complexities associated with the computation of shock wave propagation through highly nonlinear media, so that they (the seismologists) may recognize the limitations of the simple linear models that they often employ. The third goal of the meeting was to aid in defining future directions of research in the effects of source-region phenomenology on nuclear test monitoring.

The meeting was divided into five main sessions: Explosion Source Phenomenology, Material Response Modeling, Numerical Simulations, The Seismic Source, and Phenomenology from Near Source to Far Field. Lew Glenn (LLNL) gave the keynote address entitled "Modeling the Explosion-Source Region: An Overview." Invited presentations were also given by Norton Rimer (S-Cubed): "Rock Strength Under Explosive Loading," Tom Dey (LANL): "Influence of Equation of State and Constitutive Behavior on Seismic Coupling," Steve Day (SDSU): "Seismic Source Models for Explosions: Insights from Numerical Simulations," Marv Denny (DOE/OACN): "Numerical Modeling of the Physical Basis of Seismic Discriminants," and Jim Lewkowicz (Phillips Lab): "Seismic Verification Research: Who Does It and Why They Do It." Following the sessions, summary presentations were given by Fred App (LANL), Bob Bass (SNLA), Art Cox (LANL), and Brian Stump (SMU). We asked the summarizers to give their views on what they heard during the meeting, what they considered the important technical problems to be, and to suggest future directions of research. We also asked them to discuss how they thought this type of research could address issues in proliferation monitoring. The summary session was followed by an open discussion.

We feel that the symposium achieved many of its intended goals. First, a dialogue was established between those performing close-in calculations and seismologists. As discussed by Fred App, the models employed are not to be used in a predictive mode, but to act as a tool for understanding the various processes involved in shaping the waveforms that radiate from the near-source region. As was clear from the presentations, most of our experience relates to materials found at NTS, which is a very limited geological environment. In order to improve monitoring capabilities in a proliferation environment, however, it is imperative that we develop the ability to understand and model a wide variety of materials. In proliferation monitoring, seismologists are faced with the challenge of detecting and identifying clandestine nuclear explosions from the plethora of events recorded worldwide. To further complicate the matter, many suspect events are recorded on only a few stations and originate from regions about which we have little geophysical information. This particular aspect of proliferation monitoring was wonderfully illustrated in the summary presentation of Brian Stump, in which he discussed the challenges associated with identifying the December 31, 1992, event from Novaya Zemlya.

The Novaya Zemlya event gives some perspective to the view that seismology is a data-driven science; however, it is clear that an understanding of phenomenology obtained through modeling efforts does aid in the interpretation of such events. Marv Denny highlighted the connection between modeling and seismic observations in his discussion of the physical basis of discriminants. An improved understanding through modeling is desirable, since observations alone are insufficient to adequately understand the factors controlling discrimination performance.

The modeling capabilities developed over the last decades are truly impressive. Nonetheless, large gaps remain in our ability to accurately represent geologic materials (even those with which we have much experience) as well as our understanding of the salient physics that governs their dynamic response. Through presentations and subsequent discussions at this meeting, the number and magnitude of the complexities associated with close-in modeling was evident. Foremost among these issues appears to be the measurement and representation of dynamic material properties in the near-source region. It is important to develop techniques that adequately measure and represent *in situ* material response characteristics. Microphysical models are also important because of the flexibility they offer in representing different types of materials under varying conditions, as well as the insights they may provide into highly nonlinear and strongly anisotropic effects.

As pointed out by Bob Bass in his summary talk, it appears to be easier to represent material response in the very close-in region. The data begin to show more scatter when stresses are at a level such that material strength becomes important. Fred App also emphasized that material response in the inelastic region affects waveform characteristics that are important for discrimination. Much discussion was also given to coupling of the close-in calculations with seismic wave propagation codes. These efforts, spearheaded by researchers affiliated with S-Cubed, will contribute significantly to the improvement of our understanding of monitoring capabilities in different geologic environments. Finally, the calculations need to be benchmarked against data. With the imminent demise of the U.S. nuclear test program, chemical explosion experiments take on renewed importance in understanding explosion-source phenomenology in different geologic environments. This shift of experimental priorities has implications for the importance of the Non-Proliferation Experiment in determining the scaling relations between nuclear and chemical explosions.

In the following, we have attempted to represent the comments of the summarizers, based on their view foils and our notes. All insights contained herein are attributable solely

to the summarizers; we accept responsibility and apologize for any omissions or misrepresentations.

Fred App (LANL): In the containment community, calculations are used primarily to develop understanding of the processes important to containment; predictive modeling capabilities, while desirable, are not possible with current modeling techniques, and, indeed, may never improve significantly. The manner in which modeling is used in containment, and how modeling should be used in verification, is captured in the words of Starfield and Cundall [1]:

Models - how and why we build them and use them

> The world is too complex for our understanding—it does not help if we build models that also are too complex. There often is a tendency for modelers to concentrate on detail and build models that are too complex and unwieldy. It is futile ever to expect to have sufficient data to model rock masses in the same manner used for some other applications such as structural analysis/response predictions. We are working in an inherently data-limited environment. A model should be a simplification of reality rather than an imitation of reality. The purpose of modeling in a data-limited environment should be to gain understanding and to explore potential trade-offs and alternatives, rather than to make absolute predictions. One should design or borrow the simplest model that will allow the important mechanisms to occur, and can serve as a laboratory for the experiments one has in mind. The model becomes a laboratory for those who build it. A model can provide some specific examples that serve to keep our imaginations within realistic bounds. It is often tempting, once a modelling process is complete and new understanding has been acquired, to point out that the mechanisms revealed are "obvious" and that the modelling was not really necessary. A model is an aid to thought, rather that a substitute for thinking.

It is clear from this meeting that seismologists believe material property differences in the source region do make a difference in the far-field observations, despite the effects of the earth filtering and path complexities involved in further shaping of the seismic signal. It may be that gas-filled porosity ("easy" to measure) and shear strength ("difficult" to measure) are the two key physical properties that affect the far field source function. Microphysical models may put the important issues of shear strength and damage on a stronger physical foundation; waveform matching is another important way of determining *in situ* shear strength.

Seismologists have discussed how the effect of hysteresis loops and harmonic distortions that can modify the waveform in the elastic regime, and have shown how spall, geologic layering, and topography are incorporated into the models. The link-up between

close-in codes and seismic codes using the representation theorem is a very important effort, showing remarkably good agreement between theoretical and observed results.

There is much good work going on at both ends—the close in and far field—but the question remains, as Peter Goldstein put it: How do we "bridge the gap?" This symposium is the start of that process. The number one problem for the close-in modelers is to determine which of the close-in properties are important to the seismologist. We must determine how well materials must be characterized to suit the purposes of verification. An issue that must be resolved is that values calculated for the close-in seismic source function [2] do not always agree with far-field observations. For example, a plot of corner frequency versus yield for various rock types shows no separation between rock types at teleseismic distances. Similarly, Brian Stump stated that overshoot (rebound) generally is not observed in the far field, yet there is abundant evidence it exists in the close-in region. Marv Denny mentioned that corner frequency is important, but corner frequency is influenced by overshoot, which, in turn, is influenced by shear strength. Are the difficulties in reconciling close-in with far-field observations due to earth filtering or inadequate characterization of the geologic media?

Some specific proposals related to modeling of the close-in field are:

- Develop a better understanding of hydrodynamic coupling (i.e., coupling of source energy to the surrounding medium) by using modeling together with CORRTEX and radiochemical analysis, in an attempt to quantify the relation of such coupling to field measurable quantities (e.g., gas porosity, density, etc.).
- Investigate the effects of phase changes and hysteretic effects in the high pressure EOS to determine what role such mechanisms play in shaping the close-in waveform.
- Perform calculations using more physically-based mechanical models (e.g., effective stress models, microphysical fracture models) to determine if they substantially improve material descriptions over the more phenomenologically-based models.
- Compare calculated close-in source function properties with source functions derived from experimentally measured data at regional and teleseismic ranges.
- Link stress-wave codes with seismic codes to investigate the relationships between close-in waveforms and distant seismic source functions.

Bob Bass (SNLA): Figure 1, which shows scaled range versus scaled displacement from several underground nuclear tests, highlights a key issue at the heart of the modeling process. As shown in this plot, close to the source (i.e., at stresses above, say, 100 kbar), there is not much scatter in the data; the modeling community can do a good job simulating these results as long as good EOS data are available (such a feat was not possible 30 years ago). Further from the source (i.e., at lower stresses), however, the scatter in the experimental data becomes appreciable and the applicability of laboratory material characterization to the numerical modeling process becomes problematic. This

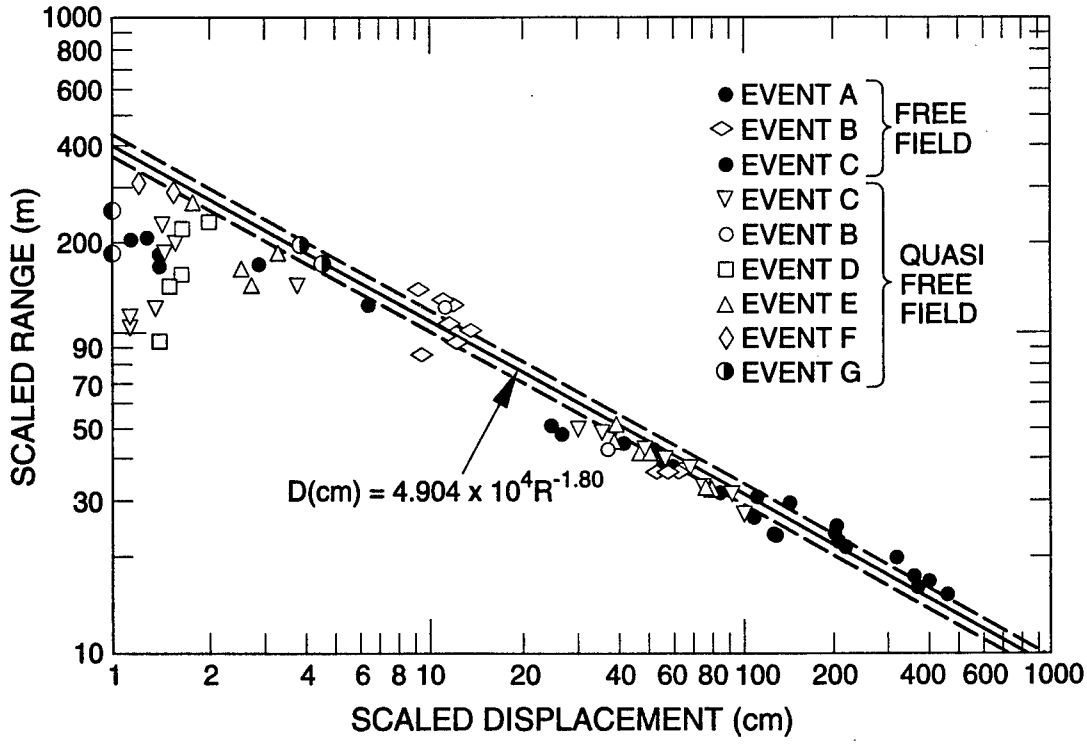


Figure 1. Scaled range vs. scaled displacement for several underground nuclear tests. At greater ranges, the scatter in these experimental data becomes appreciable and the ability to model ground motion remains problematic.

issue is evidenced by comparison of Mike Furnish's small-scale and Eric Rinehart's large-scale experiments: the laboratory samples used to derive material properties are too small to be representative of the *in situ* rock; field-determined EOSs and release paths are required. Furthermore, perhaps one should intentionally use "poor quality," not "high quality," large-scale samples. The important question of the relationship of the small-strain lab data to the large-strain field data must be addressed.

Further important modeling issues include the effects of gas-filled porosity, cracks, and loading paths on model results. In addition, Norton Rimer presented a good damage model that is applicable at ranges at which the pressures are comparable to the rock strength. The scatter in the data at scaled ranges greater than about 100 m/kt$^{1/3}$ suggests strong, complicated effects at seismic ranges, i.e., at and beyond the range at which peak stresses are comparable to the rock strength. What are we to make of measurements in which the non-radial motions are greater than the radial motions? Are we in deep trouble since we cannot model these correctly? MISSION CYBER and DISCO ELM present such a problem: velocities, accelerations, and stresses for MISSION CYBER were anomalously low compared to those recorded for the similar DISCO ELM event. The work of Bill Fourney, Richard Dick, and Tom Weaver on these events is interesting in that they

question the measurements. The results from the Non-Proliferation Experiment, when compared with previous HE and nuclear shots, will be interesting and aid in the investigation of the nuclear/chemical explosion equivalence issue.

Art Cox (LANL): Jargon is rife in this field and everyone uses it. Some examples:

Seismic Moment	- that time when the earthquake hits and things shake
Block Motions	- offensive football line activities to prevent quarterback sack
Evasion	- the art of answering questions on Sunday morning talk shows
Microscopic failure	- a matter that was not very important anyway
Radial stress	- a physical situation when the waist belt is too tight
Corner frequency	- the police car siren stopping a driver in the next block
Working point	- the place where we go every day to earn our paychecks
Representation theorem	- the principle of free elections for our government
Far field	- a subject very remote from well understood stellar astrophysics
Shear strength	- the quality that sustains us in coping with politicians
Free field	- a garden that has already had all the tomatoes picked
Overburden	- excessive government taxes
Source function	- the job of providing things, such as groceries
Cavity radius	- hopefully the same size as the dentist's filling
Scaling	- preparing fish for the banquet
Regression analysis	- an unpleasant report from the doctor
Session chairman	- an intelligent person with one eye on the clock
Conference organizer	- a very patient scientist

(And remember that 1 GPa = 10 kbar.)

Important problems and future research areas related to modeling efforts:

- Characterization of material response on release from the Hugoniot; specifically, what is the effect of the Grüneisen gamma on material response?
- What mechanisms influence coupling and decoupling? The SALMON and STERLING events provided real evidence of coupling, as did MISTY ECHO. The work of Tom Dey and Lew Glenn & Peter Goldstein highlighted modeling approaches to this question.
- What are the effects of island and mountain geometries on transmitted signals?.
- The interrelated topics of strength, joints, cracks, dilatancy, porosity, etc., must be characterized and standardized.
- What is the effect of cavity collapse on RDP overshoot?
- It would be worthwhile to further investigated the properties of limestone with ice.
- More numerical seismic simulations are needed to obtain a better understanding of seismic discrimination.

Important problems and future research areas related to proliferation and monitoring:

- Continued funding of the important issues we have discussed and identified is necessary.
- Permit scientists choose what technical problems are the most important, and monitor their efforts by requiring frequent presentations in conferences similar to this one.

- If possible, detailed studies of possible proliferant sites should be made and made available to the modeling community.

Brian Stump (SMU): *Where have we been?* Although we have learned a lot at this meeting about material effects, particularly of NTS materials, the transition to elastic behavior at intermediate-to-low stresses is still a topic that needs further investigation. For example, what are the mechanisms responsible for nonlinear behavior at low stresses? Simple approaches such as those presented by Lane Johnson may be a good first-order approach for many materials. Although nonlinear modeling can be used to quantify important phenomenology, the predictive capabilities remain modest. The seismic community has developed good experience and capability for 1-D and 2-D seismic wave propagation (e.g., Don Helmberger). We are beginning to couple nonlinear stress wave calculations to seismic wave propagation codes using the representation theorem, as discussed by Steve Day and Jeff Stevens; this effort is useful in the investigation of the critical physics. We have begun to study similarities and differences between chemical and nuclear explosions, as mentioned by Lew Glenn. Decoupling has been modeled and is supported by a few observations.

Where are we going? Questions remain concerning the use of equivalent elastic source functions for explosions. For example, what is the physical basis for the properties of the RDP? What are the effects of heterogeneous geology on our inferences? There are many different source types that have not been investigated by the calculators. For example, it would be useful to apply the tools and techniques that have been applied to nuclear explosions to chemical explosions (how do they compare to nuclear explosions?), mining explosions (how do arrays of sources, distributed in space and time, couple energy?), rock bursts, underground mine collapses, and earthquakes. How do source-generated body waves and surface waves propagate to regional distances (~200–2000 km)? We need to develop a physical understanding of discriminants such as M_s/m_b (surface wave magnitude/body wave magnitude) and spectral differences. We need experimental programs to answer well-posed questions, so that basic phenomenology and physics can be resolved, and their implications on regional waveforms determined. The use of moderate-sized chemical explosions may aid in this cause, in which different materials (different regions of the world?) could be investigated in a controlled manner, and the link between near-source and regional wave propagation could be investigated.

The bottom line of this entire effort is ***discrimination****, i.e., event identification.* To perform this task, limits must be set as to how small a source is to be identified; e.g., a 10 kt decoupled explosion has m_b ~ 3.0–3.5, while a 1 kt decoupled shot has m_b ~ 2.5.

Mining blasts (of which there are more than 10^4/yr) are perhaps the most problematic in terms of classification. To obtain the information required for discrimination, regional monitoring (~200 km–2000 km from source) will be necessary. Further understanding of evasion scenarios (e.g., decoupling, masking) will be needed, as will the development of a physical understanding of useful discriminants. The key issue of discrimination is highlighted in the view foils provided by Alan Ryall of DARPA, which illustrate the difficulties associated with identifying the source of the December 31, 1992, event originating from Novaya Zemlya.

As is clear by the comments of the summarizers, many open questions and research opportunities remain in the field of numerical modeling for underground nuclear test monitoring. We feel that a high priority for the close-in modeling community is the problem of accurately describing material response from limited laboratory data, while the seismologists must continue their work on the all-important problem of event identification. We hope these proceedings will provide some guidance to our colleagues in this field, and foster future dialogue among those involved in this diverse research area.

We thank the presenters for their research and contributions to this volume, and the summarizers for their perspectives on these issues. We kindly acknowledge the assistance and cooperation of the session chairmen in running the symposium. We thank Fran DiMarco and Kim Nguyen of the LANL Protocol Office, and Marie Kaye of the LANL Nuclear Test Containment Office for their assistance in organizing and running the meeting.

Steven R. Taylor James R. Kamm
Los Alamos, NM
July, 1993

REFERENCES

1. A. M. Starfield and P. A. Cundall, Toward a Methodology for Rock Mechanics Modelling, *Int. J. Rock Mech. Min. Sci. & Geomech. Abstr.* **25** (3) pp. 99–106 (1988).

2. M. D. Denny and L. R. Johnson, The Explosion Seismic Source Function: Models and Scaling Laws Reviewed, in *Explosion Source Phenomenology*, Geophysical Monograph 65, S. R. Taylor, H. J. Patton, and P. G. Richards, eds., American Geophysical Union, Washington, DC, 1991.

THIS PAGE INTENTIONALLY LEFT BLANK.

Numerical Modeling and the Physical Basis of Seismic Discriminants

Marvin D. Denny
U.S. Department of Energy, Office of Arms Control

Abstract

Accurate seismic event discrimination is critical to detection of nuclear explosions. Numerical modeling applied to seismic event discrimination can lead to increased reliability of proliferation detection. It is particularly applicable to error budgeting and to understanding explosion and earthquake phenomenologies. There also is a need for minimum requirements to validate the models used in numerical modeling.

1. Introduction

Numerical modelers may need an introduction to the seismic monitoring problem in the context of proliferation detection. With that, I'm quite sure that they will see many ways in which to make useful contributions.

For the longest time, our emphasis was on monitoring the Russian Federation's test program. Shortly after Reagan's election, I attended a Defense Advanced Research Projects Agency (DARPA) meeting where someone said very clearly: "Pay attention, guys, the problem is yield estimation, not discrimination." Verification of the Comprehensive Test Ban (CTB) Treaty had been the primary concern under the Carter administration and that meant, and still does mean, discriminating earthquakes and quarry blasts from underground nuclear explosions. But times have changed again. Interest is once more focused on a CTB with the added dimension of proliferation detection.

Monitoring for the first test of a potential proliferator, whether clandestine or not, is a more difficult task than monitoring to verify a CTB. Under a CTB, the other party has a known nuclear capability and infrastructure that can be monitored by other means. Furthermore, some mechanism would probably be negotiated to resolve false alarms. On the other hand, with a potential proliferator, no such knowledge of nuclear capability or infrastructure may exist, and false alarms will be a big problem. In fact, if efforts to detect the tell-tale signs of production capability have failed, there may be some segments of our own government with strong motives to not believe any evidence of a test.

Since there might not be a mechanism to resolve false alarms, some elements of the government may not want to act even if the evidence is clear. Something similar to this occurred during the infamous South Atlantic event that Seymour Hersh, in his book, *The Sampson Option*, called the third of three Israeli nuclear tests. It was simply a problem the administration of the time did not want to deal with.

In some future case we may need to be able to assert with a very high degree of certainty that an event was a nuclear test, and that will not be easy. On the other hand, in some cases, maybe even the weakest evidence will do. Regardless, it seems to me that a better theoretical understanding of the basis of the seismic discriminants would raise our community's credibility significantly with those who might need to act on the evidence.

2. How can Numerical Modeling Help?

Numerical modeling can help in two ways. First is the error budget problem, and second is the basic phenomenology of explosions and earthquakes. To understand how these would help, let us start with a cursory look at seismic event identification. The chief discriminant, or means to identify an event as an earthquake, is depth. If a seismic event can be determined to be sufficiently deep, it can safely be considered an earthquake. However, when this criteria fails, other techniques must be used, such as an energy ratio in either the time or frequency domain.

I will give an example of both time and frequency domain discriminants, but first, a definition of the seismic source function is needed. In its simplest form, consistent with a permanent displacement, the source function is completely defined by four parameters, as shown in Figure 1. On the left is a frequency domain log-log plot of the source function, with a corresponding time-domain plot on the right.

The four parameters are illustrated on the left. They are the dc level M_0, called the seismic moment; the corner frequency f_c; the overshoot; and the high-frequency asymptote n, called the roll-off. In the time domain, the moment controls the overall amplitude; the corner frequency controls the period; the overshoot, or lack of it, controls the decay and whether or not a negative portion exists; and finally the roll-off controls the rise time: the faster the roll-off, the longer the rise time.

The most successful discriminant has been the

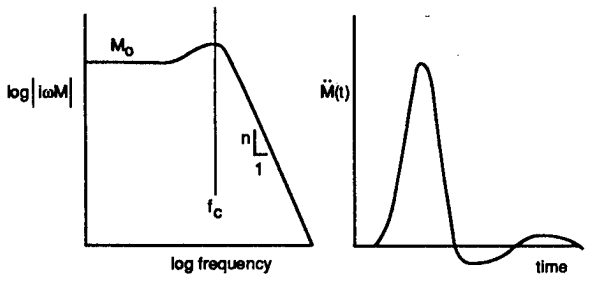


Figure 1. Schematic illustrating frequency domain and time-domain representation of the seismic source function.

M_S-m_b. It is a time-domain measurement originally made on teleseismic signals passed through two narrow-band filters that are separated by about a factor of about 40 in frequency. This choice of band passes has a long history and was somewhat hardware driven and arbitrary. Basically, the low-frequency band was chosen to record surface waves, while the other was chosen to record body waves.

I'm not sure who first noticed that earthquakes and explosions tend to form two groups when body-wave magnitudes are plotted against surface-wave magnitudes. It may have been Willis et al. in 1963.[1] Figure 2, illustrating the M_S-m_b discriminant, is from Douglas, 1981.[2] The body-wave magnitude is on the vertical axis while the surface-wave magnitude is on the horizontal axis. The scale is the same in both frames, and the solid line is the same.

Some questions immediately arose, such as: "What is the physical basis for the difference?" and "Do the populations merge at low magnitude as it appears here?" It also had its share of criticism, primarily that its usefulness is limited to the high detection threshold of surface waves relative to body waves.

On the question of the physical basis, Douglas et al., 1971[3] and 1972,[4] were among the first to go on record arguing that differences in the source mechanism are sufficient to discriminate between explosions and earthquakes. That is, an earthquake is a shear wave source, whereas an explosion is a compressional wave source.

Aki, Bouchon, and Reasenberg followed in 1974.[5] They concluded that the overshoot accounted for the M_S-m_b success and that it would not work below an m_b of about 3 because of the way the spectrum scales.

In the same year, Peppin and McEvilly[6] compared western United States earthquakes with Nevada Test Site (NTS) explosions and their aftershocks and collapses, as shown in Figure 3. The comparisons were done at each of four stations. The explosions consistently separate from the other types of events down to m_b ≈3.3 and do not appear to merge at low magnitude. Peppin and McEvilly concluded that the focal depth and spatial source dimension seemed unlikely to be prime factors in the discriminant's success; that the focal mechanism was a possibility, but that the source time function seemed to be the most likely causal parameter. Thus, nearly 20 years ago the difference in the source spectra had some, but not unanimous support as the physical basis for the success of the M_S-m_b discriminant. If this were true, then one of

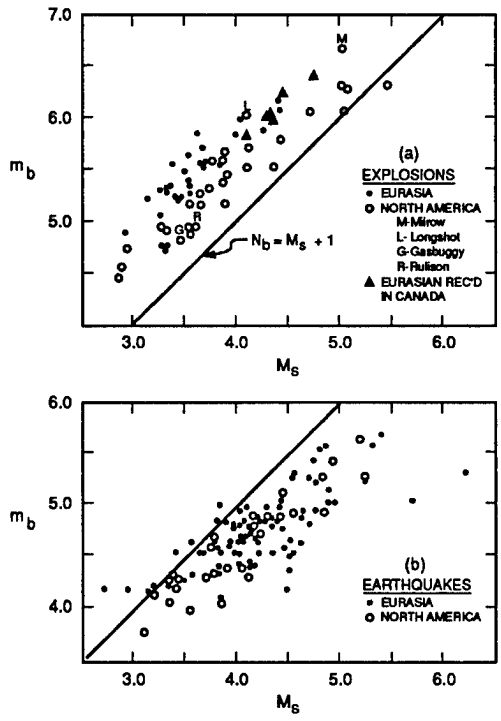


Figure 2. M_S-m_b seismic discriminants (from Douglas et al., 1981).[2]

the two possibilities shown in Figure 4 must also be true. In this figure, the vertical lines marked M_S and m_b indicate the centers of the two passbands. If you look carefully at this figure, you'll see that one consequence of this assumption is that the two populations must merge as the events become smaller. To visualize this, just imagine that the passbands are held fixed at the vertical lines, but that the spectra are moved down in amplitude and to higher frequency as the events get smaller. Eventually, both passbands will be operating on the flat portion of the spectra. When this happens, there can be no separations.

Also in 1974, a new discriminant was developed based on the premise that there is a significant source spectral difference that contributes to the success of the M_S-m_b discriminant. Let's take a look at Archambeau's variable frequency magni-

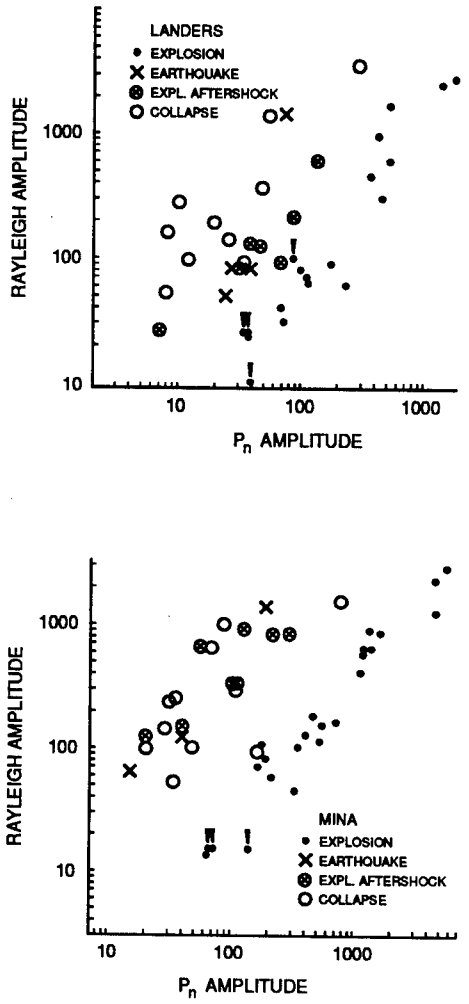


Figure 3. Regional Rayleigh-wave amplitude vs P_n amplitude at LLNL station Landers (top) and Mina (bottom) for different source types (from Peppin and McEvilly).[6]

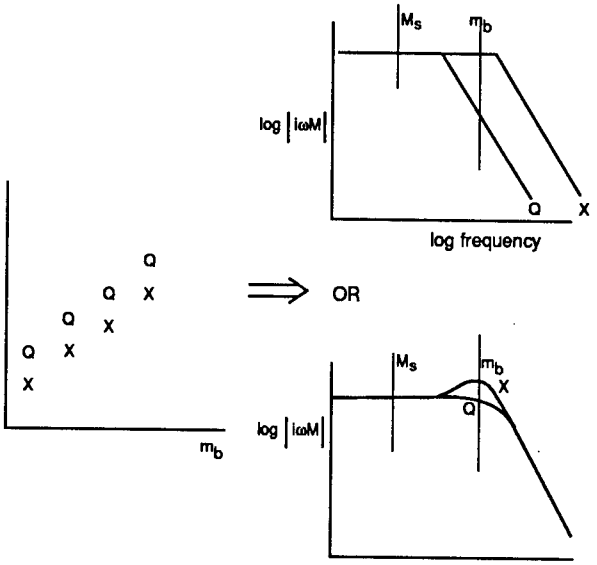


Figure 4. Schematic showing potential effects of the seismic source time function on the M_S-m_b discriminant.

tude discriminant.[7] Its real beauty is that it could, in principle, be applied to any body phase and so could be used on even the smallest event, provided a signal of some sort could be obtained.

Savino et al.[7] in 1980 applied this technique to Eurasian events as shown in Figure 5 with good results. But if you apply the same visualization exercise to the spectral sketch on the right-hand side of the figure as we did on the last figure, you'll observe that at some small magnitude, the separation should again disappear. The vertical lines indicate frequencies that should be held fixed. In fact, the separation in the data does appear to narrow at the bottom. The authors, however, attributed this to the decrease in signal-to-noise ratio for smaller events.

For both the M_S-m_b and variable frequency

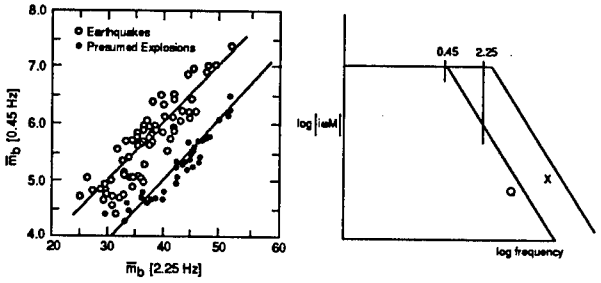


Figure 5. Variable frequency magnitude discrimination results for Eurasian earthquakes and explosions recorded at the LASA array (from Savino et al.).[7]

magnitude, we have seen that if the differences in the source spectra are a significant contributor to the discriminants, then the two populations should merge at low magnitude. There is some further evidence that they, in fact, do. Figure 6 is from Taylor et al.[8] where the M_S-m_b discriminant has been applied to regional data. It is consistent with

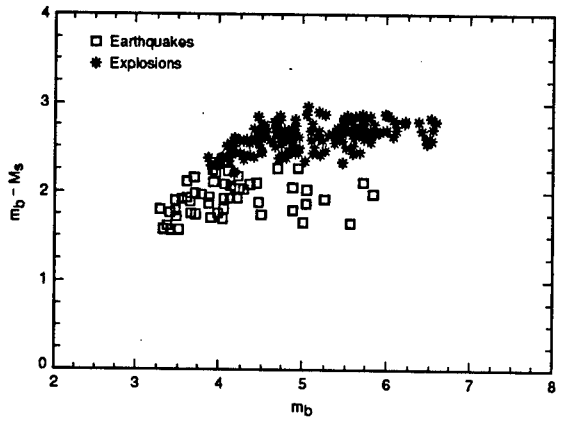


Figure 6. Regional M_S-m_b for NTS explosions and western United States earthquakes (from Taylor et al., 1988).[8]

Figure 2 from Douglas,[2] but the merging is clearer and the separation is not as great.

Taylor et al.[9] also applied a spectral ratio discriminant, similar to the variable frequency magnitude discriminant, to several regional phases as shown in Figure 7. The individual plots show some overlap that appears to be greatest for the lower magnitudes. Thus the regional data support the hypothesis of a convergence of the discriminants at lower magnitudes. However, there is a problem. The variable-frequency magnitude discriminant and both the regional and teleseismic M_S-m_b discriminants imply explosions have more high-frequency content for the same moment than do earthquakes. The data from Figure 7 imply the opposite.

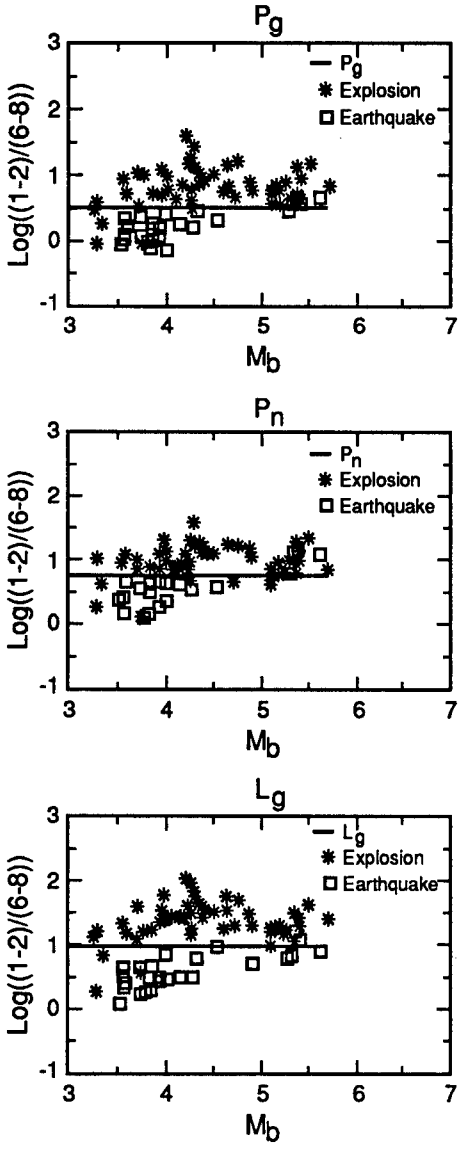


Figure 7. Spectral ratio discriminant for NTS explosions and western United States earthquakes for regional phases P_g, P_n, and L_g (from Taylor et al.).[9]

A possible explanation for the difference between the data in Figure 5 and Figure 7 is differences in the source materials at the two test sites. Taylor and I published a paper[9] attributing the differences to the roll-off to be expected in the different source materials. But I don't think that is true anymore. It does not explain the regional data of Figure 6. More likely to be the case is that the corner frequency is dependent on the material properties in the source region and these are just simply different for the two sets of explosions.

What is really going on? There are two papers that set the standard for analyzing the error budget. The first of these is Stevens and Day's 1985 paper,[10] and the other is by Patton and Walter.[11] What Stevens and Day did was to analytically account for the differences between the M_S-m_b for earthquakes and explosions and then evaluated them with finite difference simulations. Patton and Walter did something similar, but for the seismic moment and the P_n magnitude. They also assessed the differences only for a few special cases.

As seen in Table 1, there are three terms in the analytic solution, not counting the secondary contributions due to the free surface. The important thing to note is that M_S is measured from the flat part of the spectrum and should, therefore, be simply proportional to it. Both studies indicate that differences in the source region material properties and in the source spectra contribute more on the average than do the focal mechanism and its resultant radiation pattern. The major contribution of the focal mechanism, as shown by Stevens and Day, is that it can account for a significant amount of the scatter in the earthquake data. Stevens and Day's M_S-m_b simulations indicate that the two populations merge at low magnitude.

Table 1.
Effects of Source Properties on Seismic Discrimination

	Patton & Walter	Stevens & Day
Difference Source	log M_o - m_b	M_S - m_b
Radiation (focal mechanism)	.25	.35 ± .5
Material Properties	.51	.7
Spectrum	.71	.5

There seems to be plenty of evidence that spectral differences make a significant contribution and that the two populations should merge at low magnitude. But there are also studies that don't show merging. I frankly don't know what they mean. I

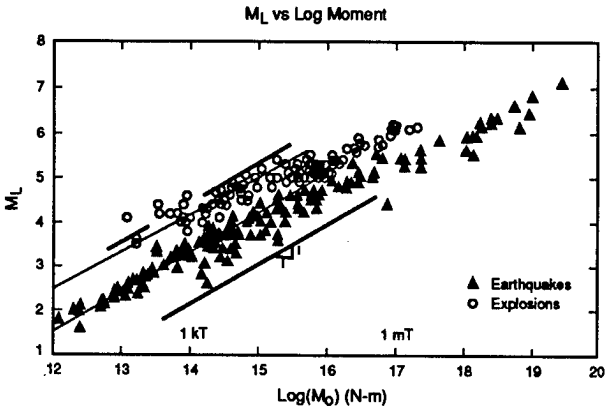


Figure 8. M_L vs M_0 for 173 earthquakes and 128 explosions (from Woods and Helmberger).[12]

don't doubt the data, but I don't understand it either, and we really need to. This could be an important result.

Figure 8 was recently published by Woods and Helmberger.[12] Does this mean that there are no differences in the source spectra? If this is true, then the main differences must come from source material properties and the focal mechanism. If the material property differences are only a result of local structure, then a shallow earthquake (i.e., one at a depth comparable to an explosion) could be expected to discriminate only on the basis of its focal mechanism. Therefore, it would seem that successful discrimination is not too likely, and shallow earthquakes will probably be false alarms.

One thing seismologists could do, that they are not accustomed to doing, is to collect data on corner frequency. This hasn't been done routinely because the narrow-band systems commonly in use make this a difficult, if not an impossible, task. There are also lots of questions about the path's contribution to the signal and how to treat it. Nevertheless, there have been special studies using broad-band instruments where corner frequencies have been estimated and it seems to me that more are in order.

This is the kind of error budgeting, or physical accounting, that I think we have to get much better at in the future if we are to do a credible job of identifying events. It is also one way numerical modeling can help. I can't believe very many false alarms will be tolerated. A few too many and this community will simply be ignored. It will not be good enough to simply use statistics drawn from two populations like these. For one thing, the explosion populations only exist for a few well-known test sites. We need to become much more confident in identifying the differences so that realistic limits can be evaluated for regions where we have no previous explosion data.

The other way numerical modeling can help is in the identification of critical mechanisms in explosion and earthquake phenomenology. For example, an early explanation of the corner frequency for explosions was that it is determined by the range at which tensile cracks no longer form. But this was just an arm-waving explanation based on erroneous estimates of the elastic radius. All the data taken in the free field that I've ever seen, indicate that the corner frequency is created very close to the cavity. The pulse shape simply does not change throughout the entire nonlinear region. A better explanation was recently suggested by Lew Glenn, namely, that the corner frequency simply is the result of the end of the cavity growth. It's these kind of fundamentals that have yet be accurately and fully explained that could help significantly.

Using numerical simulation to account for differences in seismic discriminants would be very helpful. However, these simulations are entirely dependent on the physical mechanisms modeled. How do we judge the value of a simulation? Some standards are required.

Any model of a physical mechanism to be used in a simulation should have supporting laboratory data, and in the case of explosions, the results should be consistent with three well-documented empirical quantities of cavity size, seismic moment, and corner frequency. Any discrepancies should be fully and carefully explained.

I don't know how many times I've seen a report when the author claimed to have matched some free-field data. Usually what is meant is that something close to the peak particle velocity at one or more ranges has been produced. But such a simple measure of success falls far short of putting the result into a meaningful content. To me this means computing the cavity size, the seismic moment, and the corner frequency and comparing the calculated values with the empirical observations.

I'm less sure of what requirements should be placed on earthquake simulations, but clearly we need more empirical information on corner frequency.

To answer the question of how to assess the value of a simulation we will have to call on our statistician friends. We had them look at the hydrodynamic yield methodology, and the things that they turned up were simply amazing. It would be most useful to have them get involved. Perhaps they could develop some kind of figure of merit for how well a given model reproduces the known results.

Finally, if we are going to make real progress

in modeling for the error budget, it is important to have an active test program. Expert opinion won't do. But, I don't mean the existing weapons test program. The trouble with it is that the weapons developers performed nearly the same experiment over and over again. The only things that they ever varied, and then only inadvertently, were the gas-filled porosity of the emplacement medium and the yields. No, I mean one that we have control of so that relevant experiments can be designed.

To be useful, a test program has to include materials other than alluvium, tuff, and rhyolite. A very useful program could be constructed around intermediate-size chemical explosions of about 1 ton. If these were done in combination with a laboratory program to test core samples taken from the emplacement medium, we could learn by leaps and bounds.

Completion of the Non-Proliferation Experiment is important. Much smaller chemical explosions seem to have shown that there is little if any difference in the seismic signals between chemical and nuclear explosions when both are fully contained. The Non-Proliferation Experiment is located in the midst of many previous, well-instrumented nuclear experiments so that the differences, if any, should be well defined. I am hopeful that the Non-Proliferation Experiment will lay the foundation for a future seismic discrimination experimental program. I consider such a program essential to make real progress in understanding and modeling the physical basis of seismic discrimination.

The views expressed in this paper are those of the author only and do not reflect those of the Office of Arms Control.

References

1. Willis, D. E., J. DeNoyer, and J. T. Wilson, "Differentiation of Earthquakes and Underground Nuclear Explosions on the Basis of Amplitude Characteristics," *Bull. Seism. Soc. Am.*, **53**, 979-987 (1963).
2. Douglas, A, "Seismic Source Identification: A Review of Past and Present Research Efforts," NATO Advanced Study Institutes, *Series C*, **74**, D. Reidel Publishing Co., Durdrecht, Holland (1981).
3. Douglas, A., J. A. Hudson, and V. K. Kembhavi, "The Relative Excitation of Seismic Surface and Body Waves by Point Sources," *Geophys. J. R. Astr. Soc.*, **23**, 451-460 (1971).
4. Douglas, A., J. A. Hudson, and V. K. Kembhavi, "A Quantitative Evaluation of Seismic Signals of Teleseismic Distances–III, Computed P and Rayleigh Wave Seismograms," *Geophys. J. R. Astr. Soc.*, **28**, 385-410 (1972).
5. Aki, K., M. Bouchon, and P. Reasenberg, "Seismic Source Function for an Underground Nuclear Explosion," *Bull. Seism. Soc. Am.*, **64**, 131-148 (1974).
6. Peppin, W.A. and T. V. McEvilly, "Discrimination among Small Magnitude Events on Nevada Test Site", *Geophys. J.*, **37**, 227-243 (1974).
7. Savino, J. M., C. B. Archambeau, and J. F. Masso, "VFM Discrimination Results from a Ten Station Network," *Systems, Science, and Software*, VSC-TR-81-29, La Jolla, CA (1980).
8. Taylor, S. R., M. D. Denny, E. S. Vergino, and R. E. Glaser, "Regional Discrimination between NTS Explosions and Western U.S. Earthquakes," *Bull. Seis. Soc. Am.*, **79**, 1142-1172 (1989).
9. Taylor, S. R., N. W. Sherman, and M. D. Denny, "Spectral Discrimination between NTS Explosions and Western U.S. Earthquakes at Regional Distances," *Bull. Seism. Soc. Am.*, **79**, 1142-1172 (1989).
10. Stevens, J. L. and S. M. Day, "The Physical Basis of M_b:M_S and Variable Frequency Magnitude Methods for Earthquake/Explosion Discrimination," *J. Geophys. Res.*, **90**, 3009-3020 (1985).
11. Patton, H. J. and W. R. Walker, "Regional Moment: Magnitude Relations for Earthquakes and Explosions," *Geophys. Res. Lett.*, **20**, 277-280 (1993).
12. Woods, B. B. and D. V. Helmberger, "A New Seismic Discriminant for Earthquakes and Explosions," *Trans. Am. Geophys. Un.*, 74-91, (1993).

MODELING THE EXPLOSION–SOURCE REGION: AN OVERVIEW*

L. A. Glenn
University of California
Lawrence Livermore National Laboratory
Earth Sciences Department, Shock Physics Group
P.O. Box 808, MS L-200, Livermore, CA 94550

Introduction

The explosion-source region is defined as the region surrounding an underground explosion that cannot be described by elastic or anelastic theory. This region extends typically to ranges up to 1 km/(kt)$^{1/3}$ but for some purposes, such as yield estimation via hydrodynamic means (CORRTEX and HYDRO PLUS), the maximum range of interest is less by an order of magnitude. For the simulation or analysis of seismic signals, however, what is required is the time resolved motion and stress state at the inelastic boundary. Various analytic approximations have been made for these boundary conditions, but since they rely on near–field empirical data they cannot be expected to reliably extrapolate to different explosion sites. More important, without some knowledge of the initial energy density and the characteristics of the medium immediately surrounding the explosion, these simplified models are unable to distinguish chemical from nuclear explosions, identify cavity decoupling, or account for such phenomena as anomalous dissipation via pore collapse.

Our purpose here is to present an overview of the physics involved in simulating underground nuclear explosions. In what follows, we first describe the fundamental equations involved, discuss solution methods, coordinate frames and dimensionality. Then we identify the factors that most influence the seismic response. Taking appropriate rock samples, measuring the rock properties, and developing realistic constitutive models are subjects important enough to warrant two other keynote presentations. Here we emphasize the coupling between the rock properties and the characteristics of the explosion cavity and exemplify this coupling by briefly reviewing the important subjects of cavity decoupling and nuclear/chemical source equivalence. We conclude with a brief discussion of the main problems in obtaining accurate prediction of source-region response, i.e., material inhomogeneities and imprecise knowledge of material properties.

* Work performed under the auspices of the U. S. Department of Energy by Lawrence Livermore National Laboratory under contract #W-7405-Eng-48

Fundamental Equations

In divergence form, the equations describing the conservation of mass, momentum, and total energy respectively are:

$$\frac{1}{\rho}\frac{D\rho}{dt} = -\nabla \cdot \mathbf{u} \tag{1}$$

$$\rho \frac{D\mathbf{u}}{dt} = -\nabla (p + p_R) + \nabla \cdot \sigma + \mathbf{f} \tag{2}$$

$$\rho \frac{De}{dt} = -\nabla \cdot [\mathbf{u}(p + p_R)] + \nabla \cdot (\mathbf{u} \cdot \sigma) + \nabla \cdot [(\kappa + \kappa_R)\nabla T] + \mathrm{Q} \tag{3}$$

ρ is the mass density, $\mathbf{u}$ the particle velocity vector, p the material pressure, σ the deviatoric stress tensor, and $\mathbf{f}$ the body-force per unit volume (gravity) vector. $p_R = a_R T^4/3$ is the radiation pressure, where a_R is the radiation density constant (7.563×10^{-15} erg/cm^3/(°K)^4) and T is the temperature. $e = e_m(\rho, T) + (1/2)\,\mathbf{u}\cdot\mathbf{u} + a_R T^4/\rho$ is the total specific energy. The first term in the latter expression, e_m, represents the material specific internal energy, the second term the specific kinetic energy, and the last term the specific energy associated with the radiation field. κ is the linear coefficient of thermal conductivity and $\kappa_R = 4D_R a_R T^3$, where D_R is the Rosseland radiation diffusion coefficient. Q is the rate at which energy is generated by the device per unit volume.

It should be noted that the equations (1) – (3) are not closed until an equation of state, $p = p(\rho, T, ...)$ and a constitutive model $\sigma = \sigma(\rho, T, \epsilon, ...)$ are defined. Here ϵ is the strain tensor and the continuation inside the parentheses is meant to imply that path dependence, porosity, and rate effects may be also be involved.

Explosion Phases

Simulating the explosion can be divided into 3 phases, since not all the terms in the above equations are significant at the same time. This allows operator splitting to be employed which can simplify the calculations; for multidimensional problems, different codes are often employed for each phase. The first phase we call the radiation–coupled hydrodynamic phase, the duration of which is typically $0 < t < 10$ μs. In this period the pressure is so large that strength and overburden effects can be ignored, deleting the last 2 terms on the right-hand-side (RHS) of equation (2) and the 2nd term on the RHS of equation (3). We note that radiation transport is normally significant only when aspherical sources are employed and hydrodynamic yield estimation is required or when large (decoupling) cavities are employed; in the latter case the radiation diffuses ahead of the shock front and thereby mitigates the

hydrodynamic impulse delivered to the wall. The diffusion approximation for the radiation transport is valid so long as the medium is optically thick. When photon mean free paths become comparable to characteristic structural lengths, such as the cavity radius, a flux limiter is employed to restrict the energy transport to physically allowable values.

The hydrodynamics phase occurs in the interval 10 μs $< t <$ 1 ms/kt$^{1/3}$. In this interval, not only are strength and overburden negligible, but all radiation effects are as well. The pressure is determined strictly by the material equation of state.

The final phase, in which $t >$ 1 ms/kt$^{1/3}$, we identify as strength–coupled hydrodynamics. By this point, the peak pressure has decreased typically below 10 GPa. The equation of state and the overall constitutive model may be quite complex. The pressure may exhibit strain–path and / or porosity dependence and the *in situ* yield strength is determined by the (overburden) pressure, porosity, and the degree of water saturation. The subsequent yield strength (on loading and unloading) may be enhanced by pressure and strain hardening, or degraded by damage and thermal softening. Morover, the initial overburden state may deviate significantly from lithostatic, an important consideration when explosions take place in large cavities.

Coordinate Frames

The usual procedure for solving source–region problems is to difference equations (1) – (3) directly in the time domain. Explicit time differencing, where state variables are updated strictly from their values at earlier time, is normally employed because of the ease of implementation and computational speed. An exception is made when considering the radiation diffusion term in equation (3), where (unconditionally stable) fully implicit schemes are the rule. The reason is that the Courant time step required for stable solution of the explicit radiation operator is many orders of magnitude less than for the coupled hydrodynamic system.

The mesh or grid employed for spatial differencing can be either structured, with fixed connectivity, or unstructured. Three kinds of structured grids have been used extensively. To briefly review them, consider the convective operator

$$\frac{D}{dt} \equiv \frac{\partial}{\partial t} + \mathbf{w} \cdot \nabla \tag{4}$$

where $\mathbf{w} \equiv \mathbf{u} - \mathbf{s}$; $\mathbf{u}$ is the particle velocity vector and $\mathbf{s}$ is the local coordinate frame velocity vector. If $\mathbf{u}$ is everywhere $= \mathbf{s}$, $\mathbf{w} = \mathbf{0}$ and we have a Lagrangian coordinate frame, in which the advection operator is eliminated altogether. Although this simplifies the solution,

Lagrangian frames normally cannot be used throughout because of mesh tangling problems and because the time step required for stable solution may become infinitesimal. When this occurs, a *rezoning* or *dezoning* operation is required, which amounts to overlaying a new grid on the old and interpolating the field variables thereon.

Alternately, if $\mathbf{s}$ is everywhere $= 0$, $\mathbf{w} = \mathbf{u}$, and we have an Eulerian frame in which the mesh is stationary. In practice, this is usually accomplished in 2 steps. First the Lagrangian operator is employed to compute the motion in the material frame; the grid points are then moved back to their original position and the advection operator is used to remap the field quantities. Eulerian frames permit accurate spatial differences to be computed and are the easiest to visualize. Their disadvantage is that they require interpolation to define moving interfaces and tend to diffuse information across these interfaces. Moreover, they are inefficient in that the resolution of moving fronts, such as shock waves, requires the mesh density to be fine everywhere since the direction of wave motion is not normally known in advance. This problem can sometimes be alleviated by employing a multigrid scheme, in which all wave fronts are tracked, and fine grids are superimposed only at the fronts.

In the most general case, $\mathbf{s}$ and $\mathbf{w}$ can be adapted to the problem at hand; in this case the scheme is called ALE (arbitrary Lagrangian-Eulerian). ALE schemes allow interfaces to remain Lagrangian while the mesh is continuously deformed elsewhere. Various algorithms have been employed for optimizing the mesh motion.

Methods that use unstructured grids can theoretically eliminate mesh tangling problems without introducing excessive diffusion. They fall into two categories, distinguished primarily by the means employed for calculating the spatial derivatives. In the Free Lagrange formulation, nearest neighbor clustering of mass points is used to obtain standard finite difference approximations for the gradient and divergence of state variables. In the Smoothed Particle Hydrodynamics scheme, Monte Carlo theory is applied to the discrete representation of mass points in order to obtain a continuous representation of the state variables; analytical differentiation then gives the required spatial derivatives. Both methods require fairly complex rules for associating points and, at least to date, are fairly slow compared with conventional structured formulations.

Dimensionality

Most source–region problems that generate boundary conditions for seismic propagation can be solved in 1 dimension, and assuming spherical symmetry. Typically, from 10^2 to 10^4 nodes are employed, depending on the required spatial resolution and the simulations can be carried out on a workstation in a few minutes to a few hours. When complicated

topography or stratification is important, say for accurate spectral representation, or to simulate interfacial effects such as spall, $2D$ or even $3D$ codes are required. $2D$ problems are normally calculated with axial symmetry although plane strain and plane stress solutions are also possible. Typical simulations employ from 10^4 to 10^6 nodes and require from a few hours on a workstation to a few days on a supercomputer. Fully $3D$ simulations that employ of the order of 10^7 nodes or less can be carried out on a supercomputer, and a few problems of this size have been run on massively parallel machines, however high-resolution $3D$ problems are still mostly beyond the state-of-the-art.

Factors that Influence the Seismic Response

The factors that most affect explosion-source region simulations can be divided into two main categories: properties of the rock media and characteristics of the explosion cavity. The most important of the rock properties is the strength (both in shear and in tension). Moreover, it is not sufficient to know the failure envelope; the behavior during and after initial failure is equally important. For example, the morphology might be altered by tensile cracking which, in turn, could markedly reduce the subsequent resistance to shear. Alternately, as exemplified by the behavior of certain salt rocks, plastic strain can cause an increase in shear strength via a hardening mechanism. Still greater plastic strain dissipates sufficient energy to melt the salt with attendant loss of all strength. The strength of the rock is also strongly influenced by the porosity and degree of water saturation; strength degradation due to pore pressure effects is well known.

Other rock features that affect the seismic response include the elastic moduli, the response to shock loading and release (as determined by the high–pressure equation of state), the overburden state (as determined by the depth of burial and amount of damage surrounding the initial excavated cavity), and the topography and stratification.

The most important characteristic of the explosion cavity is the initial energy density, i.e., the device energy per unit volume before the cavity walls begin to move. The maximum pressure in the cavity, p_{cmx}, is directly proportional to this quantity. For tamped explosions, p_{cmx} is large compared with any elastic modulus and virtually all the energy is delivered to the rock (via radiative transfer and $p\,dV$ work). On the other hand, for explosions in very large excavated cavities, p_{cmx} can be significantly less than the modulus and only a small fraction of the explosive energy goes into work on the walls. This is the basis of the cavity decoupling concept.

The high–pressure equation of state of the rock significantly affects the seismic response

when p_{cmx} is sufficiently high; its influence is much reduced when the yield-scaled size of the explosion cavity is increased beyond a certain point because p_{cmx} is then at or below the elastic limit and the release isentrope is virtually the same as the shock Hugoniot. Similarly, the overburden stress state can have important influence on the seismic amplitude when the explosion takes place in a large cavity, where the p_{cmx} is of the same order as the shear stress near the cavity wall, but is much less important for well–tamped explosions because, in the latter case, the shear stress in this region is negligible compared with p_{cmx}.

Other aspects of the cavity that may affect the seismic response are the initial mass density (the sum of the device mass, including inert material, and that of the surrounding air, if any, per unit volume before the cavity walls begin to move) and the thermodynamic characteristics of the cavity contents. For example, a tamped chemical explosion differs from a tamped nuclear explosion not only in the initial energy density, but also in the temperature and composition of the explosion products.

Cavity Decoupling

The fundamental assumption underlying the estimate of explosive yield from an underground explosion by seismic means is that the seismic amplitude (ϕ_∞) is a unique function of the yield. That this is not the case for an explosion conducted in a large enough cavity is understood to mean that, in this case, a fraction of the yield is not delivered to the rock medium surrounding the cavity, i.e., the explosion is decoupled. For a fully tamped explosion, however, virtually all the energy in the device goes into the rock. It can be shown[1] that even though this occurs, ϕ_∞ may not be a unique function of the yield. In the limiting case of a perfectly elastic–plastic medium, for example, the seismic amplitude vanishes altogether as the energy density grows arbitrarily large (increasing yield in a fixed hole or decreasing the hole size with fixed yield). The reason for this is that the energy delivered to the rock, in this case, is entirely in thermal form and a Hooke's Law medium only produces pressure when compressed; thermal energy has no effect. Of course, real rocks do not behave in this fashion, but the effect persists, to some extent, even with more realistic materials. Regardless of the material model, as the initial energy density in the cavity is increased, the fraction that ends up in the rock in thermal form increases. For initial cavity radii greater than roughly 1 m/kt$^{1/3}$, the thermal component of the pressure in the rock is a relatively small fraction of the total. As a consequence, it is in this regime that increasing the initial energy density in the cavity normally produces decreasing seismic amplitude. But it is also in this regime that the total energy coupled to the wall diminishes with increasing cavity size. These two competing effects typically produce a maximum amplitude somewhere in

the range $1 < r_0 W^{-1/3} < 10$ m/kt$^{1/3}$.

For nearly fully decoupled cavities the seismic amplitude is especially sensitive to the ambient atmosphere inside the cavity and to the overburden state. Large, air-filled cavities promote pressure spikes on the walls which increase damage, thereby weakening the rock and increasing ϕ_∞. These same spikes enhance the high frequency content of the seismic–source spectrum and hence reduce the decoupling factor at high frequency. Since the impulse delivered to the rock face varies as the square–root of the cavity–gas mass, evacuating the cavity, at least in part, reduces the damage. The same effect can be had by substituting hydrogen or helium for the air. Either of these measures will extend the radiation phase of the fireball growth, allowing less energy to go into shock motion. In this way, the pressure on the wall can be made to approach a step function, with no spikes.

Distinguishing Between Chemical and Nuclear Explosions

Chemical and nuclear explosives are fundamentally different in three ways. In the fully tamped condition, the energy density of nuclear explosives can be varied over several orders of magnitude whereas the value for chemical explosives is fixed. For example, $r_0 W^{-1/3} = 5.22$ m/kt$^{1/3}$ for tamped TNT, whereas the value for nuclear explosives can be as low as 0.1 m/kt$^{1/3}$, or even less. Second, due to thermodynamic source characteristics, the pressure (at the same energy density) is significantly higher for chemical explosives. And third, dynamic effects on the cavity wall are much more pronounced with chemical than nuclear explosives. Since the impulse delivered to the rock face varies as the square-root of the explosive mass, and the latter is typically 3 orders of magnitude higher with chemical explosives, the prompt damage to the walls is normally greater in this case.

The net effect is to expect higher seismic amplitudes for the same explosive yield with chemical explosives. Calculations of explosions in salt, for example, indicate that the asymptotic value of the reduced displacement potential is more than 50% higher for a tamped TNT explosion than was observed in the SALMON event (a tamped nuclear explosion in the Tatum salt dome).[2] The use of a lower energy chemical explosive (like pelletol or anfo) would reduce the difference somewhat but, to obtain equal amplitudes, the chemical explosion would have to be carried out in a slightly untamped configuration, i.e., in a cavity roughly twice as large as the charge. Although other factors, such as charge shape and differences in overburden may also influence the comparison, these conclusions have clear implications to calibration and evasion issues.

Concluding Remarks

The implementation of computer codes to solve the source region problem has advanced significantly over the past 25 years. Very good agreement can be obtained between calculation and experiment when **enough** information is available. Accurate simulations can usually be performed by skilled modelers but, while simulation is relatively easy, prediction is much more difficult. Part of the reason is that laboratory measurements on core-sized rock samples may not be representative of the mechanical behavior of the extant rock mass from which the samples derive. The cores are invariably of dimension small compared with the calculational elements so that local inhomogeneities, often quite large, must be averaged to obtain representative values for the material models. Most important, simulation of explosions at unidentified (clandestine) locations implies an imperfect knowledge of the *in situ* material properties and emplacement geometry. The main task of the modeler is to derive plausible models and to estimate the error under these conditions.

References

1. Glenn, L. A., Energy-density effects on seismic decoupling, *J. Geophys. Res.*, **98**, no. B2, Feb. 10, 1993.

2. Glenn, L. A., Differences in coupling between chemical and nuclear explosions, *Proceedings of the DOE/LLNL Verification Symposium on Technologies for Monitoring Nuclear Tests Related to Weapons Proliferation*, Las Vegas, NV, May 6-7, 1992.

ROCK STRENGTH UNDER EXPLOSIVE LOADING

Norton Rimer and William Proffer, S-Cubed

This presentation emphasizes the importance of a detailed description of the nonlinear deviatoric (strength) response of the surrounding rock in the numerical simulation of underground nuclear explosion phenomenology to the late times needed for test ban monitoring applications. We will show how numerical simulations which match ground motion measurements in volcanic tuffs and in granite use the strength values obtained from laboratory measurements on small core samples of these rocks but also require much lower strength values after the ground motion has interacted with the rock. The underlying physical mechanisms for the implied strength reduction are not yet well understood, and in fact may depend on the particular rock type. However, constitutive models for shock damage and/or effective stress have been used successfully at S-Cubed in both the Geophysics Program (primarily for DARPA) and the Containment Support Program (for DNA) to simulate late time ground motions measured at NTS in many different rock types.

The DNA has supported extensive constitutive modeling efforts at S-Cubed and elsewhere in a continuing effort to understand UGT phenomenology. Of current interest to DNA is the measurement and numerical simulation of the compressive residual stresses hypothesized to surround the explosive cavity at late times (approximately one second to many minutes) and thus prevent radioactive cavity gases from escaping through the surrounding rock. The extensive data obtained by the DNA in support of their testing program in the tunnels beneath Rainier Mesa provide a unique source of constitutive modeling information for zeolitized, saturated tuff. This information includes quasi-static laboratory material properties testing on core samples of tuff along a number of relevant strain paths and characterization of the tuff microstructure conducted by Terra Tek, explosive tests on one foot diameter tuff cylinders in the SRI laboratory, *in situ* pre- and post-shot geophysical and geological investigations, and nuclear and high explosive ground motion measurements.

Using this extensive information, S-Cubed has developed two somewhat different computational shock damage models for tuff which simulate the existing ground motion measurements equally well yet give different residual stresses and far field signals. The following summary of this model development effort will be directed towards the closely related modeling validation issues important to the Underground Test Monitoring Effort. The discussion of competing models leads naturally to considerations regarding the validation of individual models, the problem of uniqueness in the models, and the data needed to resolve this issue. Volumetric rock response models, *i.e.* the high pressure equation of state and the hysteretic crushup of gas porosity so important in simulating the peak stress and particle velocity attenuations with radial range near the explosion, are discussed briefly in the context of explaining the limitations of present models to predict ground motions.

Material Properties Tests

Laboratory quasi-static uniaxial strain load/unload tests on cylindrical core samples of tuff are performed to peak confining pressures of 4 kbar to obtain values for the tuff gas void content (one to two percent on average), material moduli to represent the porous crush response, and stress differences which are used in defining the failure surface of the virgin tuff. (Stress differences from more standard triaxial compression (TX) tests on these soft tuffs were earlier found to be within 10 percent of the uniaxial strain results.) The uniaxial strain (UX) loading, in which lateral (radial) strain is prohibited through continual adjustments in the lateral (confining) pressure, best represents in the laboratory the path of *in situ* shock loading. However, the UX unloading path does not represent well the calculated unloading path (Rimer, Ref. 1) in which the sample is stretched laterally as it is pushed radially outward from the explosion.

Laboratory UX tests on cores which had experienced multi-kilobar stress levels from an earlier event (Butters and LaComb, Ref. 2) showed substantially reduced stress differences, particularly at high confining pressures, when compared with the stress differences measured on tuff samples taken before this event. Underground measurements of seismic velocities near the event produced cavity also showed considerable reduction in the shear wave velocity. These measured shear velocities increased in magnitude with range from the working point.

As a result of a substantial research effort to approximate these results, involving laboratory tests on different strain paths, Terra Tek at present "damages" virgin material in the laboratory by subjecting virgin core samples to a UX load to 4 kbar followed by an unload along a "biaxial strain" (BX) path. This BX unload path holds the axial strain constant at its maximum value (reached at 4 kbar), while reducing the lateral confinement to allow the sample to stretch laterally. To document the effect of this "labo-

ratory damage" strain path on the material, the sample is then reloaded in triaxial compression to determine a stress difference at some confining pressure. These damage experiments show reduction in tuff strength on the order of a factor of two at low confining pressures, but little reduction at confining stresses of 2 kbar or greater.

More recently, laboratory UX load and TX load tests on cores recovered from near the working point of other shots showed that *in situ* shock damage was considerably greater than implied by the above laboratory damage tests, particularly at high confining pressures. Scanning Electron Microscopy (SEM) techniques at Terra Tek also showed that the samples recovered postshot had suffered much more severe damage to their skeletal structure than had the laboratory damaged samples. Further investigation of the loading paths calculated by Rimer (Ref. 1) to occur during spherically divergent explosive ground motions showed that the material experienced much greater shear strains (in this geometry, equivalent to radial minus lateral strain) on unloading from the same peak stress levels than are recorded in the laboratory during UX load followed by BX unload. In the *in situ* free field case, the axial (radial) strain increases in compression on unload as the material displaces outward, while the lateral strain increases dramatically in tension. Due to the enormous distortions along this path, the tuff must be continually failing in shear.

Subsequently, Terra Tek (Ref. 3) conducted a number of laboratory material properties tests along strain paths suggested by Rimer which approximated the calculated *in situ* paths by a UX load, followed by two distinct unload segments; an unload at constant shear strain of the elastic volumetric strain built up during the loading, followed by a large increase in shear strain at virtually constant volumetric strain. Strain gauge data obtained from these laboratory tests along the last unload segment are, however, highly suspect due to severe nonuniform distortions of these test samples. The accompanying stress measurements indicate that the distortions probably begin once the failure surface of the sample is encountered during the unload (and rapid shear failure begins). Unlike the *in situ* case, where a tuff element is constrained by adjoining tuff elements due to the spherical symmetry, the laboratory sample in the testing machine is not well constrained laterally and the effects of the end caps on the sample are not well understood. Thus, we were unable to obtain reliable material properties data along the strain paths relevant to an underground explosion.

Strength Reduction Models

The impetus behind the development of continuum damage mechanics for the non-ductile response of rocks and other brittle materials is a general acceptance that the theory of plasticity is not adequate to cover the nonlinear response of this class of materials. Although numerous models based on phenomenology and micromechanics have been developed to describe constitutive behavior for rock and rock-like materials, the practical application of these theoretical models in the framework of existing calculational capabilities is so far lacking. Most of the models are either calculationally intractable, require the measurement and use of unobtainable material parameters, or ignore the ductile characteristics of the behavior which are equally important for our purposes.

Therefore, we have chosen to continue using plasticity theory (since it has been shown to adequately model some of the behavior of tuffs), and to modify the description of the yielding and failure of the tuff to include a damage parameter (to represent the brittle processes) which is based on the calculated strains rather than micromechanical parameters. A two failure surface elastic-plastic formulation is used to represent the virgin and damaged states, with the "damage parameter" controlling at any time exactly where the failure envelope is in relation to these two bounding surfaces. The use of available laboratory and *in situ* material properties data for tuff (discussed above) in defining both the virgin and damaged failure surface provides practical limits to the choice of this damage parameter.

Damage models of this type were developed by Rimer and Lie (Ref 4) and Fogel and Patch (Ref. 5) in order to simulate the particle velocity records from the SRI small scale laboratory explosive experiments in rock-matching grout. Subsequently, the ONE TON TNT explosive test was conducted by SNL for the DNA in order to provide ground motion data in Rainier Mesa tuff for these modelers. Numerical predictions made using the tuff damage models described in Ref. 6 and 7 agreed well both with the ground motion data from ONE TON and with the particle velocity records from additional SRI experiments in cores of this tuff. For these simulations, the maximum volumetric strain seen by the tuff element was used as the damage parameter in interpolating between the virgin and damaged failure surfaces during unload. Data for the damaged failure surface and for the volumetric strains at which damage occurs were obtained from "laboratory damage" tests on virgin cores samples similar to those described above. In this presentation, this type of damage model will be referred to as the "old" damage model.

It is noted here, in passing, that dilatant behavior, in which the volume of the sample actually increases during triaxial compression, is commonly seen in laboratory testing of tuff and other geologic materials and is usually the result of the formation and extension of open microcracks within

the sample before macroscopic failure. Dilatancy, in the form of additional volumetric increases (beyond elastic response), is also seen during the BX unload. Our current models of material behavior do not include this effect, primarily because available ground motion data is matched better when dilatancy is excluded from the models.

As described in references 4 and 6, the ground motion data in both grout and tuff have been simulated equally as well using an effective stress model originally applied to the numerical simulation of the particle velocity records from the PILEDRIVER event in granite (See Rimer, *et al.*, Ref 8 for details of this ad hoc effective stress model). Since damage occurs only to the skeleton of the tuff and not to the interstitual fluid, the concept of effective stress could be used to better model the effects of pore fluid interaction with the material skeleton. However, application to zeolitized tuff is complicated by the difficulty of obtaining experimental data on pore pressure or drained strength in this very low permeability material. For the simulations described in Reference 6, we determined the needed drained strength data from earlier numerical simulations of ground motions in very similar tuffs. For the purpose of the study described here, we will assume that damage acts on the entire material and not just the skeleton.

The New Damage Model

In the absence of reliable laboratory data on the desired strain paths, we have used the very low strengths obtained from post-shot core samples to define the "*in situ* damaged" failure surface for our new model. This lower failure surface will be assumed to be a consequence of the large shear strains calculated to occur as a result of the spherically divergent geometry of *in situ* explosions. Thus, the maximum shear strain (strain difference) will be used as the damage parameter to interpolate between the virgin and damaged failure surfaces during both loading and unloading of the tuff element.

Significant skeletal damage is hypothesized here to begin to occur during uniaxial strain loading to mean stresses of 1-2 kbar. Because damage modeling is initiated on loading, this model, unlike the older model, results in a continuous description of the failure surface during the interpolation. Note, however, that the "upper" or "virgin" failure surface may no longer be interpreted as the UX response of the material once damage is initiated on loading. This UX loading response beyond the initiation of damage is always some combination of the upper failure surface and the much lower damaged surface. Since the actual shape of the interpolated surface is dependent upon the loading path, the upper surface is not explicitly known from the laboratory data. Rather we use simulations of the load-unload paths from a peak pressure of 4 kbar from the "laboratory damage" tests to define the upper surface. Thus, the new model is made consistent with both the "*in situ* damage" material properties data and the laboratory damage material properties data along the UX load/BX unload strain path.

For our interpolation, we define two parameters, ei, the shear strain required to initiate damage, and ef, the shear strain required for complete transition to a specified damaged failure surface. No data exists which fully defines these shear strains. Although the value of ei is assumed (in the absence of data) to correspond to a specified mean stress level from UX load tests, damage would also be initiated in the model at lower stress levels during any unload (from a lower peak stress) which exceeds this shear strain. Results of laboratory strain path tests, in conjunction with SEM views of the samples before and after testing, could possibly be used to better determine this parameter.

The parameter ef is much more difficult to quantify. The choice of this parameter should always be made in conjunction with the choice of a damaged failure surface. Since the required large shear strains are difficult to achieve in the laboratory without catastrophic failure of the test sample, values of ef are, for now, best determined from the maximum shear strains obtained from free field ground motion calculations at the ranges at which strength measurements are available from post-shot cores. Measurements from core samples at a number of ranges, in conjunction with the calculations, would ideally give both the fully damaged surface (and ef) and a relationship between damage and shear strain which could define the form of the interpolating function. In practice, core may not be retrievable at ranges of interest, and the resulting strength measurements on retrievable cores are likely to show significant scatter with range both due to pre-shot inhomogeneities in the tuff and to block motions as a result of the event. Thus, relevant laboratory tests would be useful to define the strain parameters.

Rather than embarking upon a detailed parameter study using the new model, we decided to perform a few scoping calculations to see whether the calculated phenomenology of interest to containment (residual stress fields, ground motions, cavity motion), were significantly different from earlier calculations made using the old damage model, described briefly above. A complete description of the parameters used in both damage models and the results of these scoping calculations may be found in Proffer and Rimer (Ref 9). Five calculations were made with the new model. Model parameters for the first four calculations consisted of a single set of shear strain parameters, ei and

ef, and a range of damaged strengths varying from "mush" to approximately one-half of the virgin strength.

For these calculations ei was chosen to be 2%, which corresponds to a peak mean stress of 1.3 kbar to initiate damage during uniaxial strain loading (for the particular volumetric response appropriate to the tuff of interest). A value of 10%, considerably greater than seen during biaxially strain unloads from 4 kbar, was used for ef. Figure 1 shows the damaged failure surfaces and upper or "virgin" surfaces used for the five ground motion calculations with the new damage models (labeled Runs 55-59). Also shown are the virgin and damaged failure surfaces for Run 29, for the current or old damage model.

The damaged surfaces for Runs 55 and 56 were obtained from actual data from the post-shot core samples at different pre-shot ranges (Run 58 also damages the shear modulus but has failure surfaces identical to Run 56). Run 57 used a damaged failure surface which was more consistent at low pressures with the laboratory-induced damage of Run 29 than with the data on post-shot samples. Based on ground motion calculations which show maximum shear strains of 20-60%, it was felt that the 10% shear strain was not consistent with the lowest damaged failure surface. Run 59, the fifth calculation, was made using an ef of 30% for this "mush". (ei was also changed to 2.5% to better fit the data).

Comparisons were made between Run 29, for the old damage model, and the new model Runs 55-59 along the

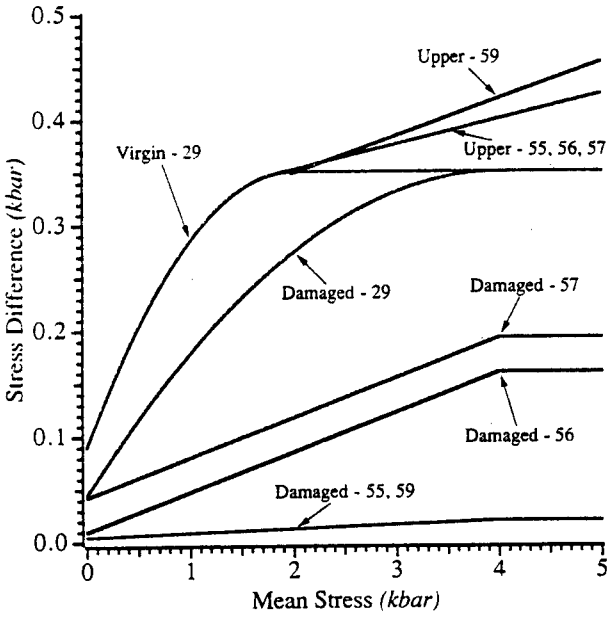


Figure 1. Failure surfaces for scoping calculations with both current (29) and new damage models.

UX load/BX unload path. Unloads from 4 kbar peak stress agreed well for all of the parameter sets. However, the BX unload response of the old and new models diverge substantially from peak stresses of 8 kbar, with the new model giving much lower strengths as the larger shear strains cause the interpolation to more heavily weight the damaged failure surfaces, and eventually exceed the ef of 10%. The combination of lowest damaged failure surface and lowest ef gives the greatest disparity with the results of the old damage model. The large difference in the magnitudes of the strength reduction will be reflected even more strongly in the ground motion results which follow.

Ground Motion Results

The inclusion of a strength reduction model in the calculations effects the ground motions as follows:

- Final cavity radius is increased slightly by the inclusion of damage. (Therefore, cavity pressure is decreased slightly.) Little difference is seen between the results with either the old or new damage model. Calculated cavity radius remains in good agreement with measurements.
- Cavity overshoot, the maximum cavity radius seen during the calculation minus the final cavity radius, is increased using damage. This overshoot is a factor of 2.4 to 4 times larger in the new model runs than calculated using the old model. The enhanced overshoot is a measure of the reduced resistance of the damaged rock core near the cavity to the elastic rebound of the rock further from the cavity.
- Peak radial stress (above the one-half kbar level) and peak particle velocity are virtually unaffected by the introduction of damage. The match to measurements is usually quite good.
- The onset of rebound is significantly delayed so that peak displacements are calculated to be larger. The new damage model gives broader positive velocity pulses, substantially higher peak displacements, but only slightly larger final displacements due to an increase in both the negative velocity pulse amplitude and duration. Measurements of particle velocity pulses to long enough duration and close enough to the source are not available to validate the models.
- Yield radius and elastic radius (void crushup) are moved further out from the cavity by the damage models with the largest yield radius corresponding to the greatest strength reduction.
- Peak residual stresses are diminished with increased damage, and their locations move outward from the cavity as shown in Figure 2 for the calculations of this study. The magnitude of the hoop stresses relative to the cavity pressure (approximately 95 bars) gives an indication of the potential for a gas-driven fracture to breach the containment stress field. Thus, the results

using the newer damage formulation imply that cavity gases could be expected to propagate further from the cavity without significant resistance from the stress field.

Conclusions

The results of the calculations with the new damage model do not require any new interpretation of the ground motion phenomenology. Damage, occurring due to the passage of the shock wave and subsequent lateral distortion of the rock behind it, is hypothesized to result in a central core of rock surrounding the event-produced cavity which cannot support as large stress differences. This core region has reduced resistance to either the outward push of the cavity, or the elastic rebound of the surrounding rock, resulting in an enhanced cavity overshoot. Since the central core cannot support as large stress differences, the cavity pressure must be resisted primarily by material further from the cavity. The use of the laboratory measurements on post-shot cores simply reduces the strength of the core region while the new shear strain-based damage parameter extends this core to larger radial positions.

It should be emphasized again that the model parameters chosen for these scoping calculations were fitted to give essentially the same results along laboratory uniaxial strain loads to 4 kbar followed by biaxial strain unload as did the old damage model. Thus, these models are not sufficiently constrained by the types of laboratory measurements presently being made. Since the newer shear strain-dependent model parameters have the additional feature of approximating laboratory test data on post-shot tuff samples which have been damaged by the event itself, our conclusion at this time is that the new model, with realistic material properties such as used for Run 56 or 59, probably has greater validity than the old damage model currently in use.

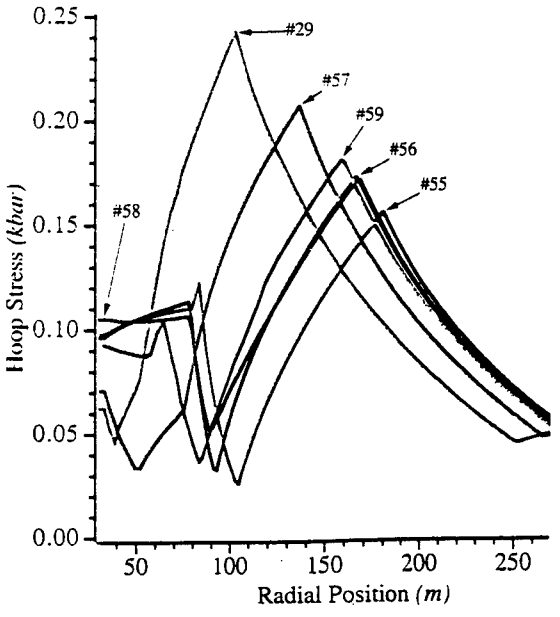


Figure 2. Residual hoop stress *versus* radial positions. For these plots the vertical axis has been placed at the final cavity radius, not at the working point position.

The primary need is to generate material properties data that better constrain the calculational model. Since laboratory core samples fail catastrophically when driven along the strain paths calculated for the divergent ground motions, other techniques should be investigated which are not limited by the inadequacy of the physical constraints on a core sample in the testing machines. *In situ* rock is confined by similar rock undergoing the same strain paths. Perhaps the SEM techniques, which clearly show the additional *in situ* damage, in conjunction with new laboratory tests, might be used to define the model parameters.

The computational damage models are, of course, phenomenological or empirical rather than based on first-principles micromechanical or continuum damage concepts and presume that the tuff behaves as a statistically homogeneous continuum with no fault or other block motion. Both damage models give reasonable agreement with measurements of stress and velocity *versus* time on a nuclear event. Late time stress measurements on a nuclear or large HE event, which are presently being attempted under DNA funding, could be used to choose between the proposed models or could suggest yet another modeling approach. However, smaller scale explosive experiments are not recommended due to rate-dependent strength effects which are probably unimportant on the nuclear scale.

Implications for Seismic Monitoring

At similar ranges beyond the elastic radius, the scoping calculations with the new damage model for tuff give final displacements and therefore static RDP's which are at most 10-15% larger than calculated using the older damage model, and 25% larger than calculated without any damage at all. Yet, due to the calculated large central core of damaged tuff, confirmed by actual material properties tests on post-shot core samples, the calculated peak displacements increase greatly with increased damage. Peak and final displacements differ by more than a factor of two at the yield radius and by more than a factor of three at the elastic radius, thus implying a strong frequency dependence in the RVP transform. This suggests that it may be misleading in some cases to characterize the seismic source simply by use of the calculated low frequency RDP.

Numerical simulations of the PILEDRIVER event in granitic rock, for example, have shown that some strength reduction mechanism (from the large strengths measured on granite cores) is also required to match the measured long duration particle velocities. Use of the laboratory strength alone gives very narrow positive and negative velocity pulses, and thus too small displacements and spectra. Inclusion of dilatancy in the calculation improves the agreement with velocity pulse widths only slightly but gives a factor of five larger amplitude spectra. Calculations made using an effective stress model (Rimer *et al.*, Ref. 8) to provide the strength reduction after shock passage, needed to match the velocity records, gave extremely peaked spectra. Calculations made without any strength reduction mechanism, but using much lower strengths (200 bars) in the virgin rock, can be made to match the positive velocity pulses, but give much shorter duration negative velocities (and much less peaked spectra). Figure 3 compares the spectra from these four calculations. Detailed comparisons between these calculations (and others) and velocities and displacements from PILEDRIVER may be found in Ref. 10, along with a theoretical discussion by S.M. Day of the relation between the weakened core and the overshoot of the spectra.

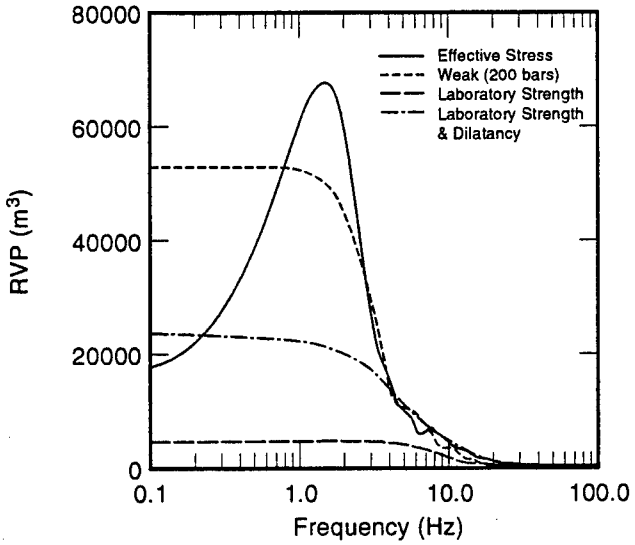


Figure 3. Calculated PILEDRIVER spectra for four granite strength models.

Other continuum strength reduction models, such as damage or "joint loosening" are possible. For hard rocks, some combination of mechanisms, for example, applying either damage or effective stress concepts to the weaker joint fill material (clay gouge for PILEDRIVER) while using the laboratory strength for the intact rock, may be more physically appropriate, but certainly will be more difficult computationally. Our experience suggests however that more complicated models will require additional material properties data, which will be difficult or impossible to obtain. Therefore, we recommend the use of relatively simple phenomenological models for strength reduction which incorporate the available laboratory data and have been validated by comparisons with late time ground motion measurements in the nonlinear near source region for similar rock types.

Acknowledgement

This work was supported by DNA under Contract DNA001-92-C-0074.

References

1. Rimer, N., "The Effects of Strain Paths Calculated for Spherically Symmetric Explosions on Measured Damage in Tuff," S-Cubed Report SSS-R-88-8988, SEPTEMBER 1987.

2. Butters, S.W., and J.W. LaComb, "Effect of Shock Loading on Rock Properties and In Situ States," Terra Tek Report DNA 5380T, June 1980.

3. Torres, G., R. Johnson, and W. Martin, Strain Path Tests on Tuff from Drill Hole U12n.11 UG-1 and UG-2," Terra Tek Report TR 89-79, February 1989.

4. Rimer, N., and K. Lie, "Numerical Simulation of the Velocity Records from the SRI Grout Spheres Experiment" S-Cubed Report DNA-TR-82-54, September 1982.

5. Fogel, M.B., and D.F. Patch, "Deviatoric Response Models and Residual Stress Field Calculations for SRI Grout," PacTech Report PT-U83-0591, January 1983.

6. Rimer, N., and K. Lie, "Numerical Predictions of the Ground Motion from a ONE TON In Situ High Explosive Event in Nevada Test Site Tuff," S-Cubed Report SSS-R-84-6493, January 1984.

7. Fogel, M.B., and D.F. Patch, "Material Response Models and Ground Motion Calculations for High Explosive Tests in G-Tunnel Tuff," PacTech Report DNA-TR-84-124, January 1984.

8. Rimer, N., H.E. Read, S.K. Garg, S. Peyton, S.M. Day, AND G.A. Hegemier, "Effects of Pore Fluid Pressure on Explosive Ground Motions in Low Porosity Brittle Rocks," S-Cubed Report DNA-TR-85-245, 1984.

9. Proffer, W., and N. Rimer, "Another Computational Damage Model for Tuff," S-Cubed Report SSS-DTR-90-11961, October 1990.

10. Rimer, N., J.L. Stevens, and S.M. Day, "Effect of Pore Pressure, Fractures, and Dilatancy on Ground Motion in Granite," S-Cubed Final Report AFGL-TR-87-0136, April 1987.

A SEMI-EMPIRICAL TWO PHASE MODEL FOR ROCKS

Martin B. Fogel
SAIC,10260 Campus Pt Dr., Mail Stop C-2, San Diego, CA 92121

This model uses a simple description for both the high and low pressure phases of the material. The specific heat at constant volume, α, and the Gruneisen parameter, Γ are assumed constant. We further assume that on the $T=0$ °K isotherm the pressure as a function of specific volume has the Murnahagn form. Given these assumptions, the free energy per unit mass has the form,

$$f = \alpha(T - T_0) + \frac{c_0^2}{x}\left\{\frac{1}{x-1}\left[\left(\frac{v_0}{v}\right)^{x-1} - \left(\frac{v_0}{v_a}\right)^{x-1}\right] + \left(\frac{v}{v_0} - \frac{v_a}{v_0}\right)\right\}$$
$$+ e_0 - Ts_0 - \alpha T \ln\left\{\left(\frac{T}{T_0}\right)\left(\frac{v}{v_a}\right)^{\Gamma}\right\}, \qquad (1)$$

at $T=T_0$ and $v=v_a$, $s=s_0$, and $e=e_0$. The cold volume, v_0, and ambient volume, v_a, are defined via the pressure which is given by

$$P = -\left(\frac{\partial f}{\partial v}\right)_T = \frac{c_0^2}{x v_0}\left[\left(\frac{v_0}{v}\right)^x - 1\right] + \frac{\Gamma \alpha T}{v}, \qquad (2)$$

At v_0 and $T=0$ the pressure is zero. The ambient volume, v_a, is defined such that at $T=T_0$, the pressure is 0.1 MPa.

The construction of a single phase model requires the specification of eight parameters, e_0, s_0, α, Γ, v_0, c_0, T_0 and x. The ambient values, T_0, e_0, and s_0 have little impact on the response of a single phase. They are used to define the equilibrium phase boundary between the two phases. Moreover, it is only the differences between the values for the two phases that matter. So of the sixteen parameters, only fourteen have physical significance.

An equilibrium multi-phase model is constructed by specifying the parameters for each phase. The equilibrium phase boundary is defined as the set of pressure-temperature pairs for which the Gibbs potential of the two phases are equal. The volume change across the transition is determined from the individual phase models by imposing pressure and temperature equilibrium for each P-T pair along the phase boundary.

Our approach to modeling the measured response of tuff is to assume that the Hugoniot tracks a phase boundary. Each phase is described using the above single phase free energy. The Gibbs potential is not used to determine this phase boundary, though, the measured Hugoniot is. This boundary is therefore, not an equilibrium phase boundary, and the Clausius-Clapyron equation does not hold. The mass fraction of each phase at a point on this boundary is determined as in the equilibrium model, i.e., from the specific volumes of the individual phases and the measured specific volume on the Hugoniot.

Hugoniot data and the assumptions of pressure and temperature equilibrium between the two phases provides sufficient constraints to determine the phase boundary. There are four unknowns; temperature, specific volumes of the two phases and the mass fraction y. The Hugoniot data provides pressure, the specific volume and energy of the mixed phase. Mass and energy conservation provide the additional constraints required to close the system.

On unload the high pressure phase mass fraction remains unchanged until the pressure drops sufficiently far below the peak pressure attained by the material. This behavior is incorporated in the model by postulating a transition between the two phases that takes place at low pressure and that satisfies the Gibbs phase rule. This boundary lies below the one defined using the Hugoniot data. Once this phase boundary line is crossed all the high pressure phase is converted back to the low pressure phase.

The two "phase boundaries" that this model uses can be thought of as bounding lines of a metastable region. On load the low pressure phase persists until the Hugoniot based phase boundary is reached at which point some high pressure phase is produced. During unload this high pressure phase persists to a much lower stress which is determined by its regime of metastability as represented by the lower phase line.

This model was used to fit some tuff data measured by Sandia[1] and KTech[2]. Comparisons of the response of the model, denoted as HT-073192, with this data are shown in Figure 1. The first two figures of this set are Hugoniot comparisons, and include shock velocity versus particle velocity and pressure versus compression. The second two show release adiabat comparisons plotted as pressure versus compression. We chose to use compression rather than specific volume in order to eliminate the difference caused by variations in the initial density of the samples. The model response is in good agreement with the data. Both the Hugoniot and the release paths are well matched.

We constructed a second model, called GT-090292, with steeper releases to illustrate the effect release paths have on the computed attenuation. Given the form of our model, it is not possible to change the release adiabats without also modifying the Hugoniot. The new model's Hugoniot is close to the old one and

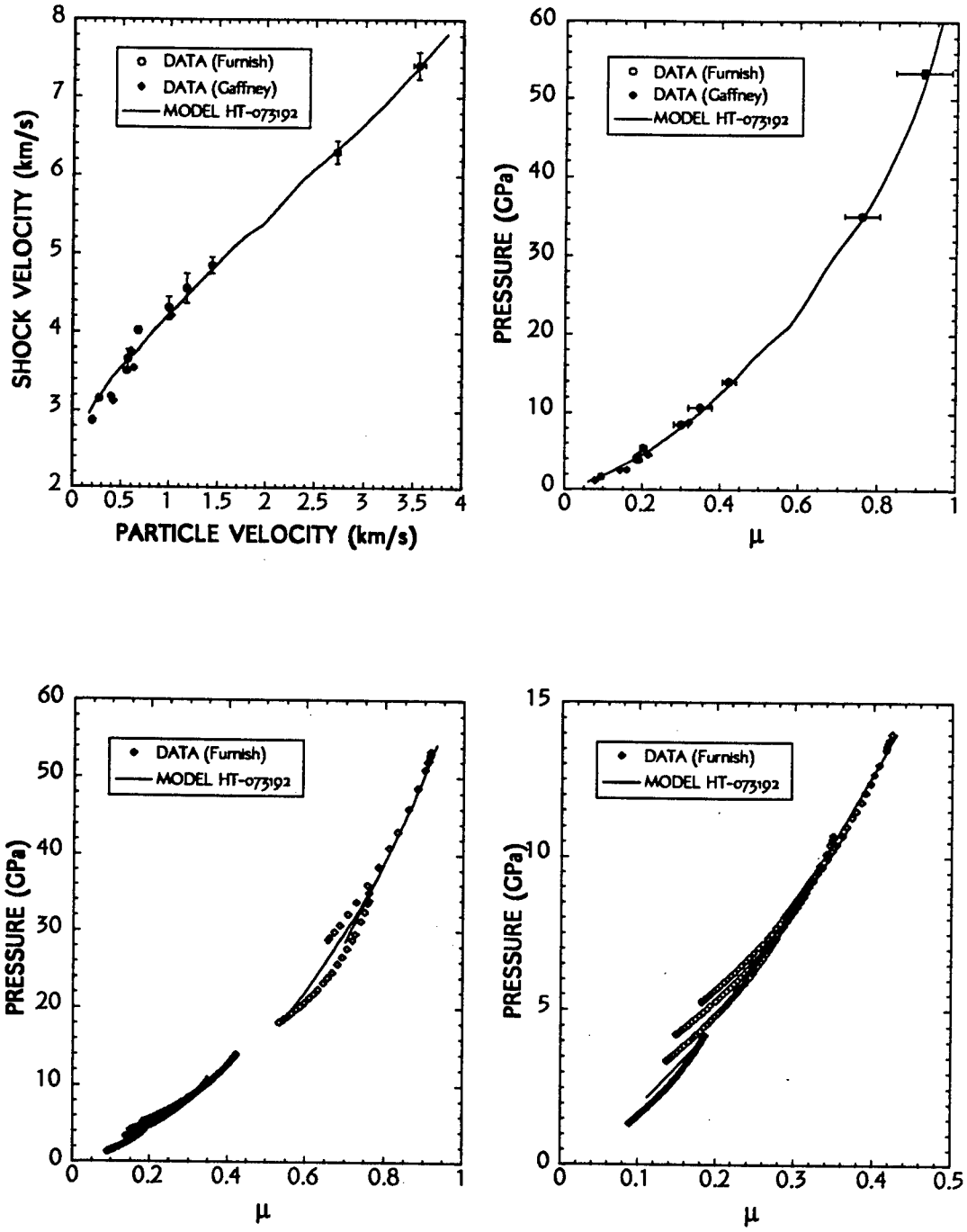


Figure 1. Comparison of model HT-073192 response with gas gun data.

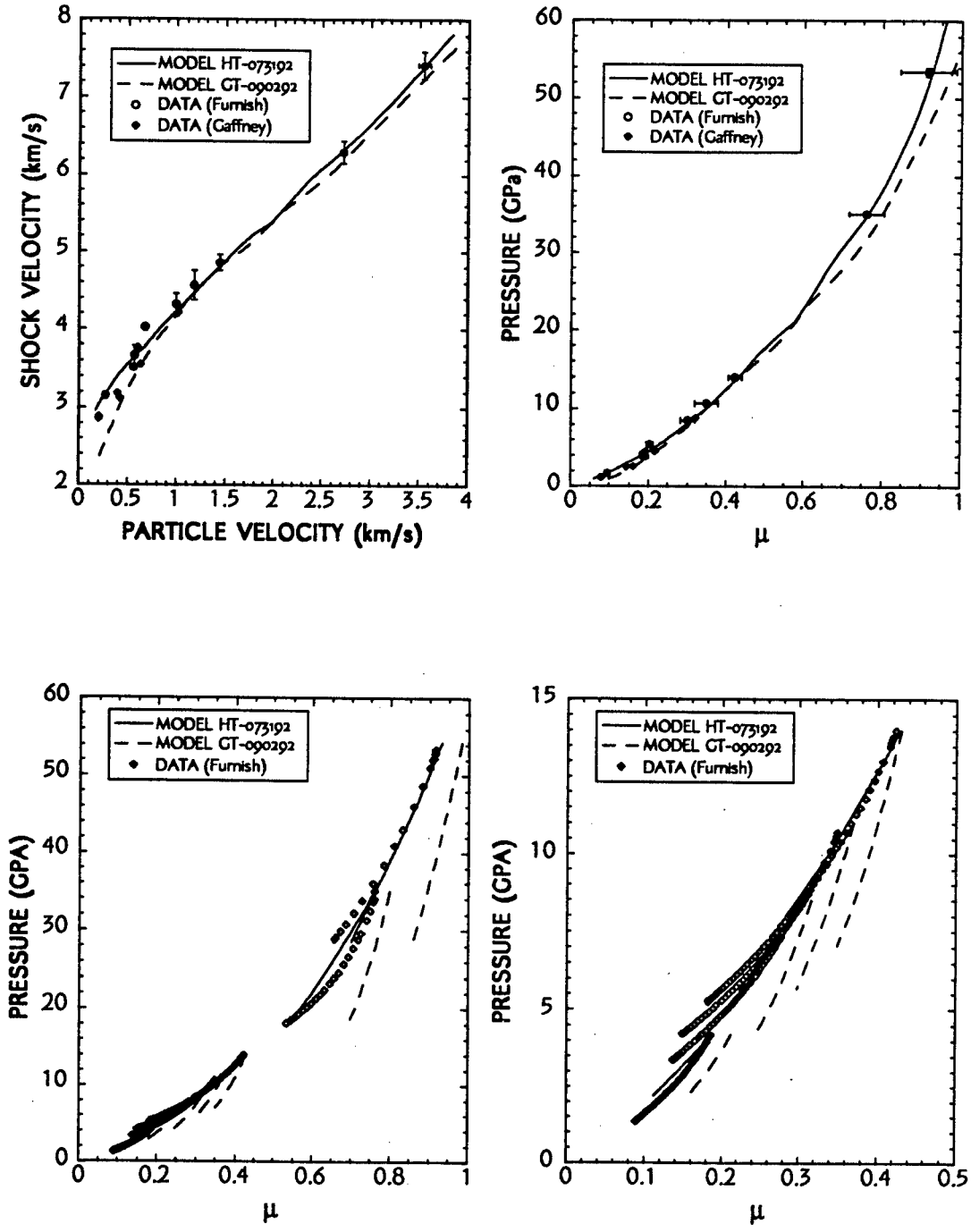


Figure 2. Comparison of models HT-073192 and GT-090292 response with gas gun data.

matches the data fairly well. Comparison of the two model's response with the data is shown in Figure 2.

Model GT-090292 is softer at stresses below 7 GPa and above 25 GPa. Between those bounds the two models have very similar behavior. Both are within the scatter of the Hugoniot data, though model HT-073192 is a better fit to the data. Comparisons of the release adiabats in Figure 2 show that the new model is more hysteretic than the old model and the laboratory data.

These models were used in spherically symmetric simulation of a 1 KT fully tamped nuclear burst. The cavity region was chosen to be 90 cm in radius and a constant $\Gamma=4/3$ gas was used to describe the cavity material. Outside this region was tuff. The tuff region extended to 12 m and was zoned with uniform cells 1.5 cm wide. Comparison of the computed peak stress and velocity versus scaled range and that measured on several recent tuff events is shown in Figure 3.

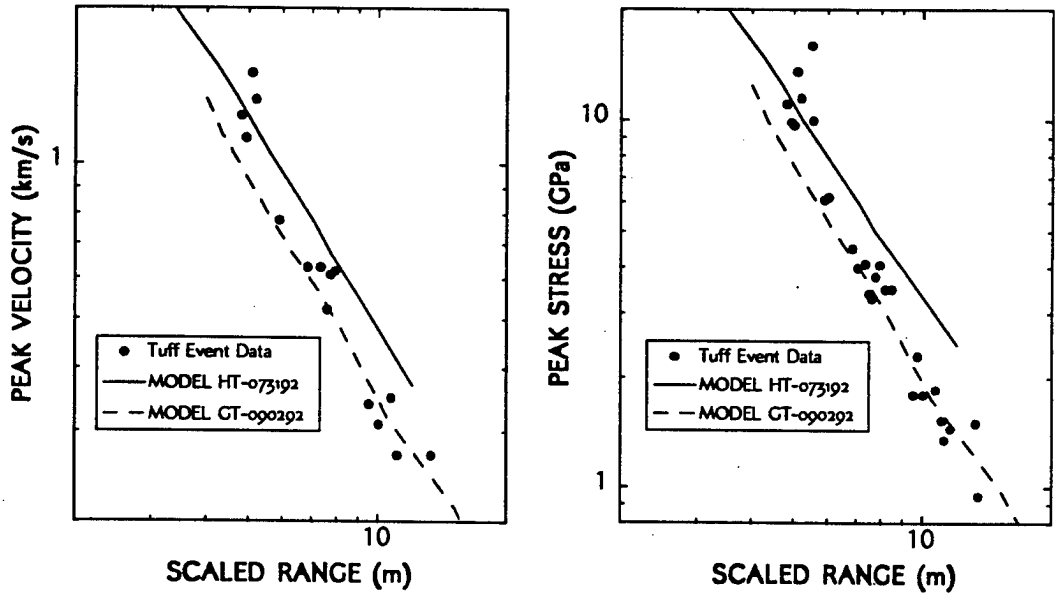


Figure 3. Peak velocity and stress versus range comparison.

We made no correction to the measured data for bore hole inclusion effects. Our understanding has been that for these events such a correction is small, definitely within the scatter in the data. Reported event yields were used to scale the range of the gauge packages. Only data that can be considered as arising from a spherically symmetric shock has been included in the plot.

Model GT-090292 agrees well with the data. The attenuation rate for both models is nearly the same. The second one, however, produces peaks that are uniformly lower. This is caused by the additional hysteresis incorporated into the second model. The computed attenuation rates are less than the least squares fit line to all the data. This disagreement may imply that the gas gun data is not representative of the response of the material in the field.

In conclusion we found that a simulation of a nuclear burst using a model that matches the laboratory response data for tuff did not agree well with the field data There are two possible reasons for this disagreement. The equation of state for the vaporized material or of the tuff at very high pressures (above 300 GPa) could be wrong. Errors in this regime of the EOS could lead to increased coupling efficiency and thereby higher peaks. The other possibility is that the material in the field does not behave as one would expect based on gas gun data in the 10-100 GPa pressure range. Both the Hugoniot and the release adiabat data are suspect. It is not possible to decide among these choices without additional data.

ACKNOWLEDGEMENTS

This work was funded in part by OSIA through contract number OSIA01-91-C-0016 and by DNA through contract number DNA001-92-C-0045. The author would like to thank Dr. Eric Rinehart, OSIA Contract Technical Monitor, whose support and gentle prodding made this work possible. The author would also like to thank Dr. Byron Ristvet, DNA Contract Technical Monitor, whose support made the presentation of this paper possible.

REFERENCES

[1] Furnish, Michael D., private communication to Audrey Martinez July 15 1992.

[2] Smith, Eric, private communication to Audrey Martinez July 17 1992

It's Material Strength, Not a Negative Grüneisen Gamma

Kurt H. P. H. Sinz, William C. Moss

Lawrence Livermore National Laboratory, February 1993

ABSTRACT

Hydrocode simulations of CORRTEX data (shock position as a function of time) require a model for the material properties of the medium in which the explosion occurs. Prior to the BULLION underground nuclear test, Furnish performed gun experiments on core samples that were taken from a satellite hole near the working point. We have analyzed some of these data and constructed a constitutive model that is consistent with the gun data. The model consists of a Mie-Grüneisen equation of state that is parameterized using the Hugoniot, a Grüneisen gamma that is only volume dependent, and a pressure dependent strength model. Previous analyses of these particular experiments have ignored material strength, because of its lack of influence on numerical simulations of the CORRTEX data. However, if strength is excluded, negative gammas are required to fit Furnish's data, but these negative gammas give an extremely poor fit to the CORRTEX field data.

Our simple model, which includes strength, has a positive volume dependent gamma. The model fits Furnish's laboratory data and the measured experimental CORRTEX data. What is remarkable about the model is that all of the parameters in it can be obtained from the gun data, indicating that laboratory experiments of this type (and perhaps others) on core samples are potentially more useful than believed previously.

INTRODUCTION

Typical simulations of field experiments such as COntinuous Reflectometry of Radius versus Time EXperiments (CORRTEX) require the material properties of the field geology. In this type of experiment the time dependence of the position of the shock due to an underground nuclear explosion is measured and this data is used to infer the magnitude, i.e. the yield, of the explosion. The ability to estimate yields is important for the verification of treaty imposed yield limits of underground nuclear tests.

There frequently are concerns whether dynamic, one-dimensional, planar laboratory testing of local soil samples can provide enough constitutive information about the material to construct a model that can simulate the CORRTEX data. These concerns are justified because accurate simulations of CORRTEX data are essential for reliably estimating yields.

*Work performed under the auspices of the U.S. Department of Energy by the Lawrence Livermore National Laboratory under contract number W-7405-ENG-48.

In the BULLION experiment, soil samples were taken prior to the nuclear event and tested in the laboratory by Furnish [1]. Past efforts to construct a material model from Furnish's data have focused on obtaining the Hugoniot, the effects of Grüneisen gamma and possible phase transitions [2,3]. Models that use only the Hugoniot and the Grüneisen gamma have been unsuccessful in consistently simulating both the laboratory and field experiments. Here we show that the addition of a strength model to a basic Mie-Grüneisen description of the material can simulate both the laboratory data and the field data.

FURNISH DATA

Figure 1 shows Furnish's experimental set-up. The experimental assembly containing the sample to be tested is traveling at high velocity towards an aluminum buffer that is backed by a LiF window. The experimental data are the impact velocity of the sample assembly and the velocity time history data assembly velocity time history data assembly obtained by using a VISAR [4] (velocity interferometer) at the interface between the aluminum buffer and the LiF window. We emphasize that this is not the particle velocity in the sample but we attempt to infer the properties of the sample from this data. Figure 2 shows a schematic sample of the interface velocity vs. time. While some of the detailed sensitivities indicated in this figure will be discussed later, the identity of the main features of this trace can be readily verified by following the signal paths shown in Figure 1. The short plateau level ending at time t_A (Fig. 2) contains the Hugoniot information pertaining to the aluminum while the long extended plateau between times t_A and t_R contains the Hugoniot information of the sample. The main release of the shock into the backing foam results in the fall-off beginning at time t_R in the velocity profile of the aluminum LiF interface.

The material model combines the Mie-Grüneisen model with a strength of materials model [5]. Grüneisen gamma, the shear modulus and the yield strength are functions of the volume. No provision is made for pore crush or other hysteretical effects.

The pressure is given by:

$$P(V,E) = -\frac{2}{3}Y_H(V) + \sigma_H(V)\left[1 - \frac{\Gamma(V)}{2}\mu\right] + \Gamma(V)\frac{E}{V}$$

where Y_H is the yield strength, σ_H is the Hugoniot stress, Γ is the Grüneisen gamma and V is the specific volume. μ is given by $\mu = \frac{\rho}{\rho_0} - 1$ where ρ is the density and ρ_0 is the reference density. The Hugoniot stress, σ_H, is given by

$$\sigma_H(V) = \rho_0 c_0^2 \frac{\mu(1+\mu)}{(1-(S-1)\mu)^2}$$

where S is the slope of the Hugoniot in shock-velocity vs. particle-velocity space. c_0 is the axis intercept in this space. The yield strength on the Hugoniot is assumed to be the same as off the Hugoniot.

The stress deviators, S_{ij} , the shear modules, G, and the strain deviators, de_{ij}, are related by

$$S_{ij} = 2G(V)de_{ij}$$

This completes the description of our material model.

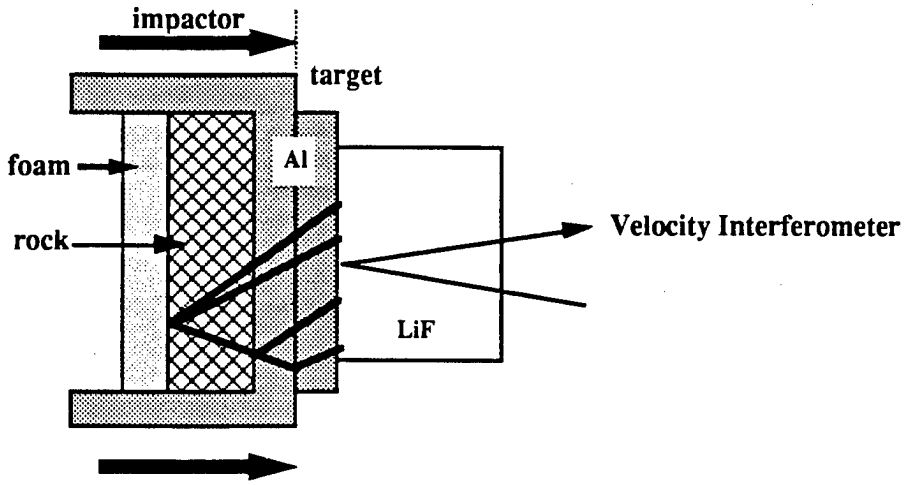


Fig. 1 Sketch of Furnish's reverse ballistic experiment. The signal paths are shown and start with the shocks generated by the collision of the aluminum cup containing the sample with the stationary aluminum target plate. The release of the shock from the sample into the foam is indicated by two paths since it occurs over an extended period of time. A sample velocity trace obtained by interferometry along with the interpretation of the main features is shown in Figure 2.

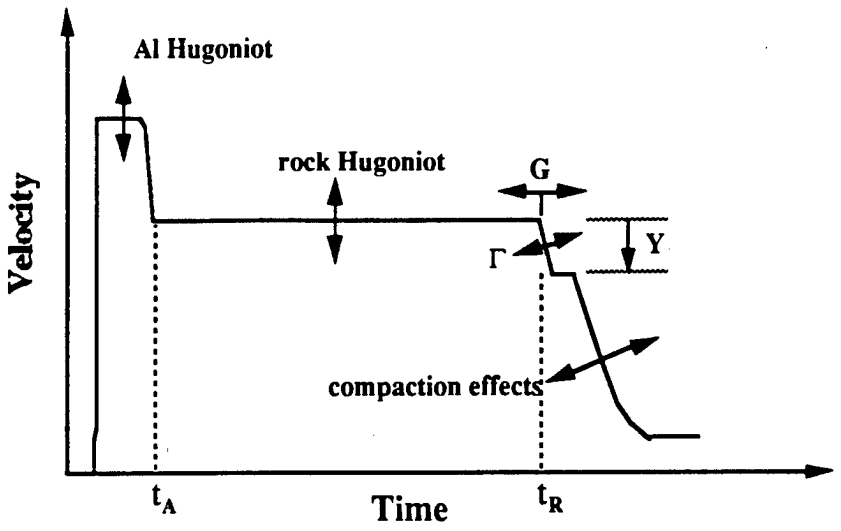


Fig. 2 Sketch showing the main sensitivities of velocity trace data to the components of the material model. These sensitivities are determined from numerical simulation of the laboratory shock data of Furnish.

FITTING THE DATA

We analyze four of Furnish's experiments. The labeling of these experiments follows Reference 1 and is BUL-2, BUL-3, BUL-4, and BUL-5. These data are shown in Figure 3. Peculiarities in the data traces shown in Figure 3 are easily visible. They include the deep "notch" between the aluminum feature and the long plateau. It has been suggested that this notch is caused by a preexisting gap in the sample assembly [6]. We ignore this feature in our analysis.

Several traces such as BUL-5 in Fig. 3 display a "bump" before the long "roll-off." Scoping calculations show that a layer of greater density between the sample and the backing foam could cause such a bump. Speculation as to the origin of such a layer might include a relationship to water which could be exuded from the sample during gun firing of the sample assembly. However, the detailed origin is unknown. For our purposes we ignore this "bump" feature in our analysis of the data.

Furnish used a 1-d hydrocode to extract one Hugoniot point for each rock sample by averaging the plateau data to a single value. The data structure in this region has been attributed to sample inhomogeneities [6]. His results are shown in Figure 4 along with the fit that we use to define the Hugoniot. The shock pressures associated with the experiments that we analyze in detail range from 22 kb to 460 kb.

The main sensitivities of the model to the data traces are illustrated in Figure 2. We assume that we know the equation-of-state and the constitutive parameters for the LiF and the aluminum, so we look for changes in the

calculated traces as a function of variations in the parameters for our rock model. The simulations show that the timing of the initial release (roll-off) from the long plateau is dominated by the shear modulus.

A small ledge, which is identifiable in several of the data traces, is most strongly affected by the yield strength. Too low a yield strength causes this ledge to be absorbed in the plateau while too high a yield strength causes it to disappear into the asymptotic release. The detailed path of getting from the onset of the release to this ledge depends mostly on the Grüneisen gamma. The long-term release from the plateau is probably affected by the hysteretical properties of the shock-compacted material but is not discussed here.

The Grüneisen gamma which we obtain from fits to the data, is shown in Figure 5. The lower end of the curve results from an estimate based on mixture theory [7] while the upper end is simply the asymptotic limit of gamma. Two curves are shown for compressions between 1 and 2.3. The dashed curve was obtained by fitting experiments BUL-3, BUL-4 and BUL-5 with each experiment yielding one point as indicated. Linearly interpolating between these values results in a continuous curve. BUL-2 is not affected by Grüneisen gamma. When using this set of values in the calculation of the

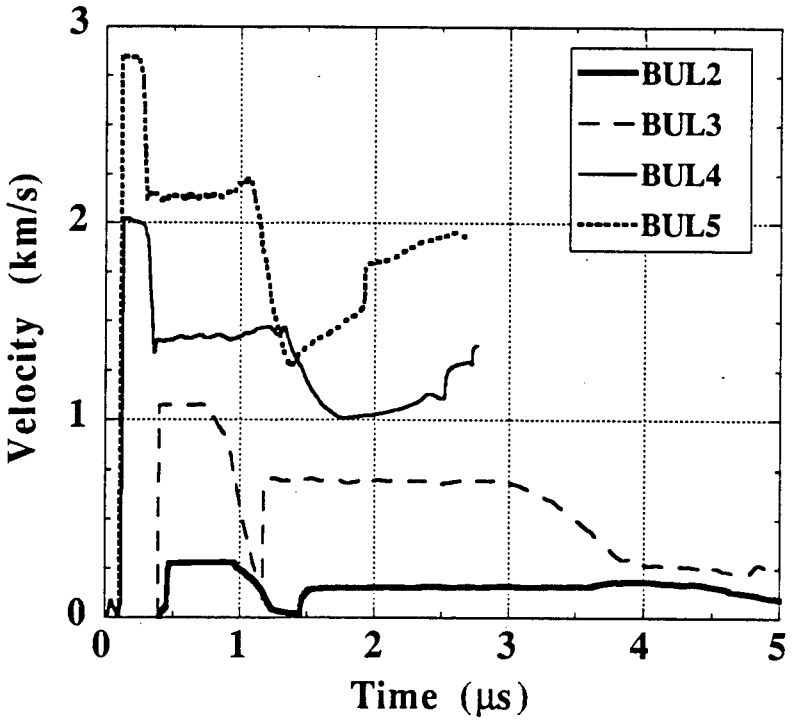


Fig. 3 Velocity traces of four of Furnish's experiments: BUL-2, BUL-3, BUL-4, BUL-5.

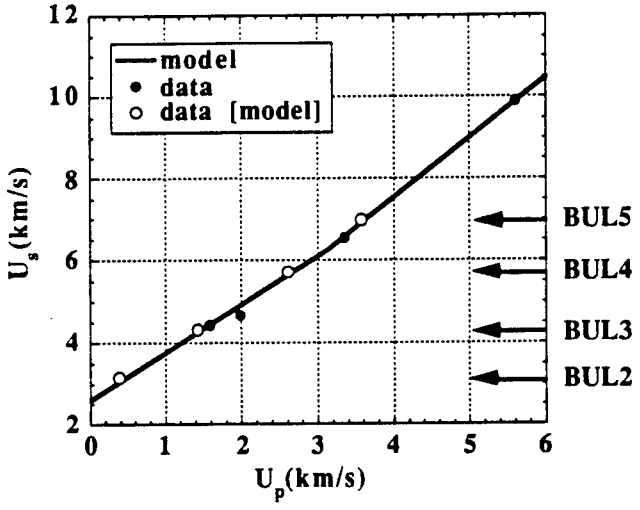


Fig. 4 Hugoniot points for Furnish's experiments. The experiments which we analyze are shown as open circles. The lines are the fit that we use to represent the Hugoniot.

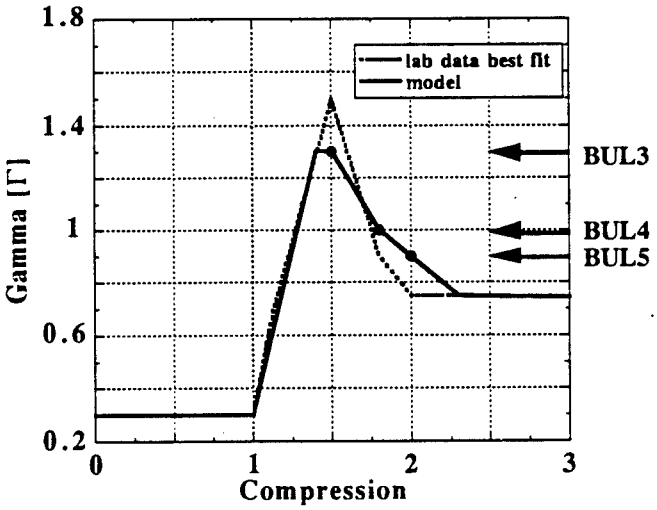


Fig. 5 Grüneisen gamma vs. compression. The dotted curve represents the best fit to experiments BUL-3, BUL-4 and BUL-5. BUL-2 is insensitive to the value of Grüneisen gamma. The low end is obtained from mixture theory and the high end approaches the asymptotic value of gamma. The actual gamma used in our calculations is also shown and is explained in the test.

field experiment, nearly all of equation-of-state space is accessed while for the calculation of Furnish data only a small slice of this space is relevant for each experiment. This caused numerical problems for the simulation of the field data, that are linked to the Grüneisen equation of state and are known to us from past work [8]. The simplest way of dealing with these problems was to avoid them by using the solid curve for gamma instead. The latter curve joins the asymptotic region of the dashed curve by linear extrapolation.

Figure 6 shows the strength parameters. At pressures corresponding to BUL-5 strength effects cease to be important probably because of complete material failure. This is represented by letting the shear modulus and the yield strength vanish. BUL-3 serves as an example of the fit obtained with our model in Figure 7 which also illustrates the sensitivity of the fit to the value of gamma. Both the experimental trace and the model fit are shown. The model value of gamma for this experiment (compression 1.5) is 1.3. Also shown are two curves which were obtained by turning strength off, i.e. the yield strength is set to zero. One curve uses the model value of gamma (1.3 for this experiment) and the other curve uses gamma = 0. It is apparent that without strength the roll-off is late and that a negative gamma is required to match the timing of the roll-off. The match of the latter two, no-strength curves to the detailed shape of the experimental roll-off is poor. Figure 8 shows a close-up of the early roll-off. Figure 9 shows another close-up of the early roll-off and illustrates the gamma sensitivity of our model when strength is employed. Differences in the value of gamma ranging from 1.0 to 1.5 result in fits to the data of distinctly different quality with a value of 1.5 being the preferred one.

The same plot shows a step in the calculated traces during the very early roll-off from the plateau. There appears to be a corresponding step in the experimental trace. The calculated step is the result of the detailed elastic properties of the aluminum which are not represented in the simple aluminum model given by Furnish that we used. Use of a full aluminum model does, however, present us with the following beneficial possibility: this aluminum feature in the experimental traces could be used as an index to locate the plateau levels for the Hugoniot fits. Such a strategy could help to get around the problem of averaging the data which defines the main plateau to obtain a fit while enhancing the quality of the calculated fits. Irrespective of this possible improvement, we were able to obtain fits for the BUL-2, BUL-4, and BUL-5 experiments of a quality comparable to that illustrated for BUL-3.

CALCULATION OF FIELD EXPERIMENT

A check of the drill logs [9] for the BULLION experiment showed that Furnish's test samples were taken from the proximal of two satellite holes which were drilled for the emplacement of CORRTEX cables. The model which was developed to fit Furnish's laboratory data as described above was used to calculate the R-t data obtained also from the proximal hole in the field

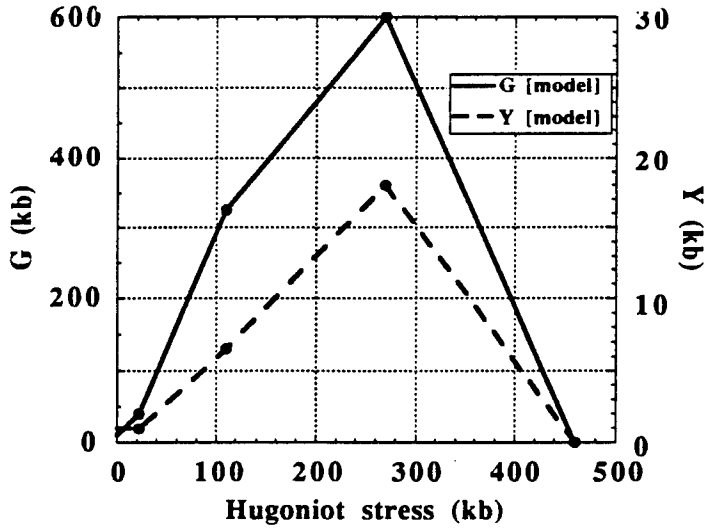


Fig. 6 Shear modulus and yield strength for BULLION tuff vs. Hugoniot stress as obtained from our simulations. The values for BUL-2, BUL-3, and BUL-4 are represented by the dots from left to right respectively. For BUL-5 the material appears to undergo complete failure and the values of Y = 0 and G = 0 are assigned.

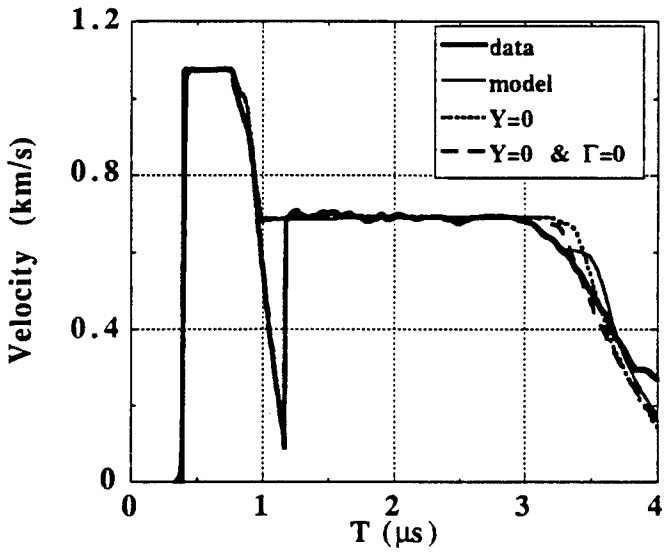


Fig. 7 Experimental trace and model fit for BUL-3. Fits that vary the Grüneisen gamma in the absence of strength are also shown. A close-up of the early roll-off is shown in Figure 8.

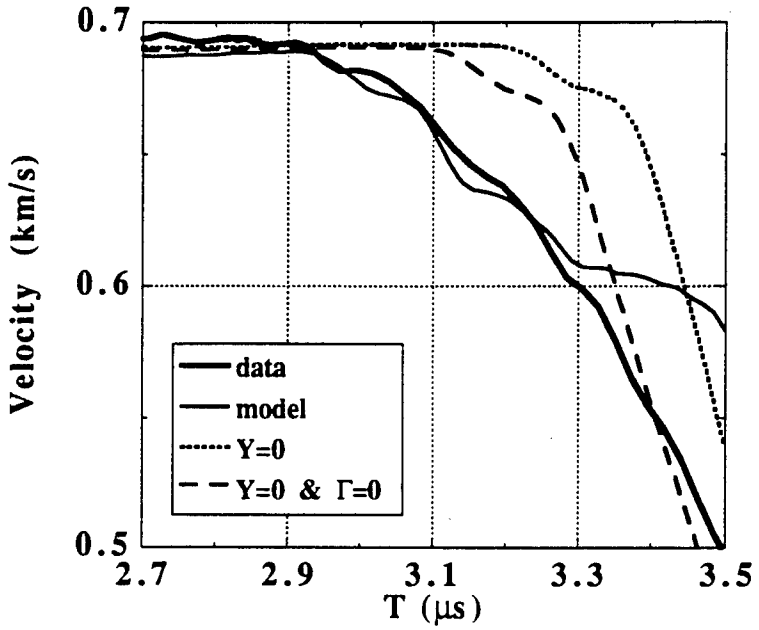


Fig. 8 Close-up of early roll-off in Figure 7.

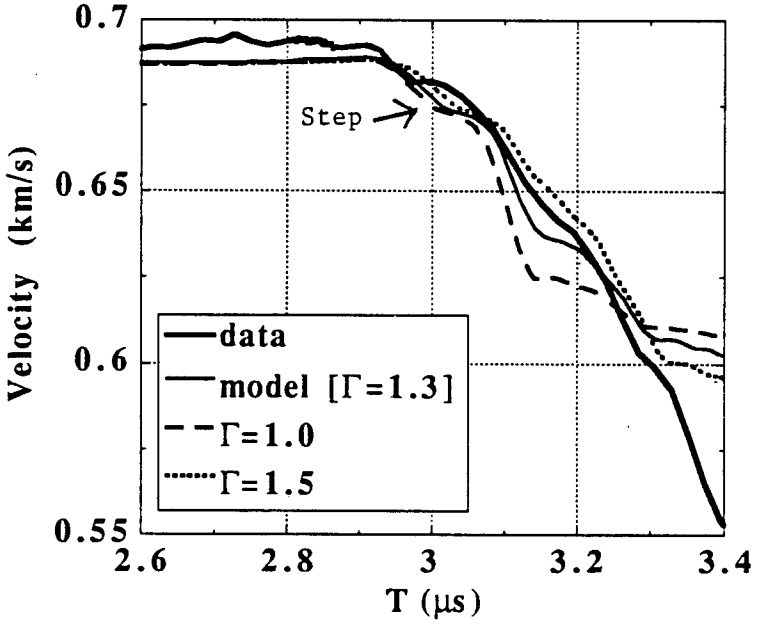


Fig. 9 Close-up of early roll-off for BUL-3. The solid line is the experimental trace. The calculated traces are obtained using the model values for the strength parameters but the values of Grüneisen gamma are varied as indicated.

experiment. The calculation was performed with an assumed yield and the resulting R-t curve was compared to field data. Using the method of simulated explosion scaling [10] the yield of the BULLION experiment was inferred within 10%. The normalized yield is shown in Figure 10 as a function of time. A constant value of 1 would correspond to on exact fit. This result completes the bridging of the gap between laboratory data, which characterizes the medium and, the field data. It should be noted that the scaling algorithm depends on the cube of the radius so that a 10% error in the estimated yield requires the calculation of R to an accuracy within 3%. This fit was achieved without any consideration of differences in the strain paths between the laboratory and the field experiments.

We found that the numerical simulation of the field data was in fact insensitive to the strength properties of the soil but it was very sensitive to the values of the Grüneisen gamma. In the case of the laboratory experiment, however, we were unable to obtain a satisfactory fit to the Furnish data unless we also included a strength model. It was this fit which permitted the extraction from Furnish's laboratory data of positive values of Grüneisen gamma which were used in the successful simulation of the field experiment.

CONCLUSIONS AND RECOMMENDATIONS

We have shown that a single material model can be constructed which fits both Furnish's laboratory data as well as a CORRTEX field experiment. Our model consists of a basic, strength corrected Mie-Grüneisen equation of state with a volume dependent gamma. It appears that the detailed features in the data traces which are associated with the release of the shock pressure in the sample are physically meaningful. A more complete analysis of Furnish data is warranted with a model that includes hysteretical behavior of the elastic properties of the samples. Such effects become evident during the time-asymptotic release from a shock-compacted state. It is likely that this type of approach would lead to a more detailed understanding of the behavior of soil in the dynamic high pressure regime and would reduce the remaining error in the calculated R-t data.

This work further demonstrates that laboratory experiments such as the reverse ballistic experiments done by Furnish can be used to determine the Hugoniot, the Grüneisen gamma and the strength parameters of a material in the dynamic, high-pressure regime. The quality of the laboratory data and the resulting constitutive information is sufficiently good to permit the accurate calculation of more general field experiments. It is, therefore, suggested that laboratory experiments may be far more valuable in the prediction of field experiments than previously believed. The main limitation in establishing this connection may, in fact, be the lack of a proper material model and the incomplete analysis of the laboratory data. In our study the laboratory data is the sole source of the parameters for the material model that successfully simulated the field data.

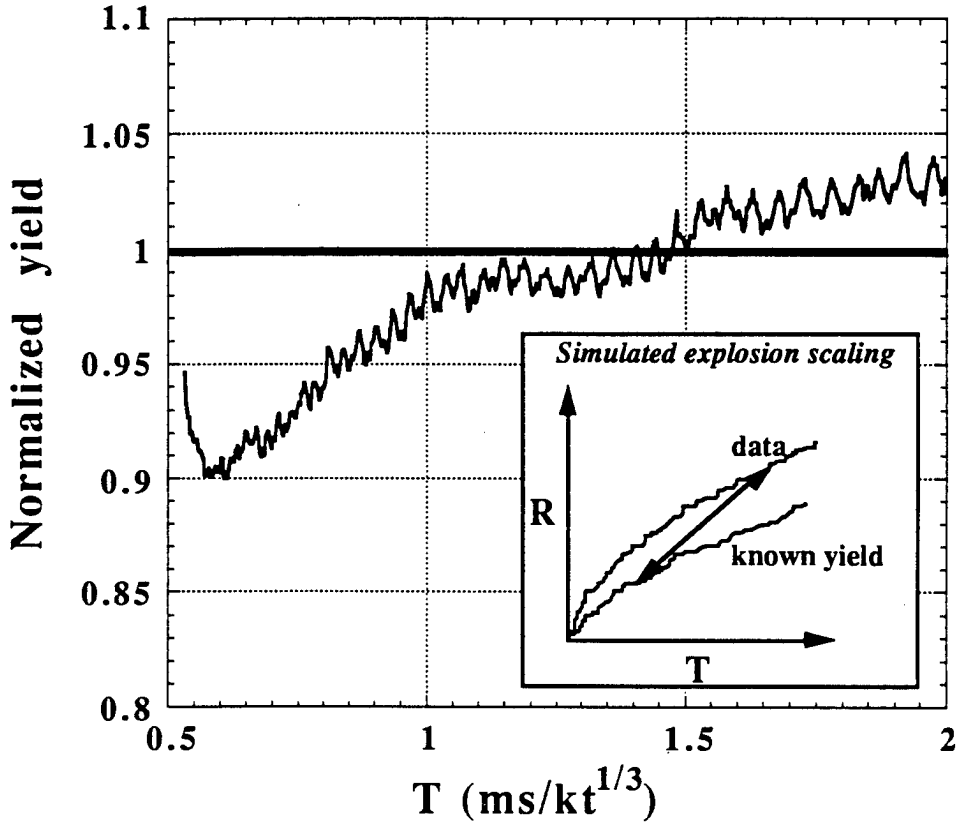


Fig. 10 Calculated normalized yield of field experiment (BULLION) vs. time. A normalized yield of one corresponds to the radiochemical yield.

REFERENCES

1. Michael Furnish, "Measuring the Dynamic Compression and Release Behavior of Rocks and Grouts Associated with Hydro-Plus," *SAND92-0984*, 1993.

2. Kurt H. P. H. Sinz, unpublished.

3. Shel Schuster, "High Pressure EOS for Bullion Tuff," *California Research and Technology*, September 12, 1990.

4. L. M. Barker, R. E. Hollenbach, "Laser Interferometry for Measuring High Velocity of any Reflecting Surface", *J. Appl. Phys.*, vol. 43, 4669 (1972).

5. William C. Moss, "The Effect of Material Strength on Determining Pressures "on" and "off" the Hugoniot," *J. Appl. Phys.*, vol. 55 (7), April 1, 1984.

6. Michael Furnish, private communication.

7. David Young, private communications.

8. Kurt H. P. H. Sinz, "Anomalous Branch of the Hugoniot in the Grüneisen Equation of State," July 1991, unpublished.

9. Bill Mc Kinnis, NTS, private communication, Feb. 1993.

10. Bass, R. C., Larson, G. E., "Shock Propagation in Several Geologic Materials of Interest in Hydrodynamic Yield Determinations," Sandia National Laboratory, *Rep. SAND77-0402*, March, 1977.

THE EFFECT OF DILATANCY ON THE UNLOADING BEHAVIOR OF MT. HELEN TUFF *

A. V. Attia

Earth Sciences Department
Lawrence Livermore National Laboratory
P.O. Box 808, Livermore, California 94550

M. B. Rubin

Faculty of Mechanical Engineering
Technion - Israel Institute of Technology
32000 Haifa, ISRAEL

ABSTRACT

In order to understand the role of rock dilatancy in modeling the response of partially saturated rock formations to underground nuclear explosions, we have developed a thermodynamically consistent model for a porous material, partially saturated with fluid. This model gives good predictions of the unloading behavior of dry, partially saturated, and fully saturated Mt. Helen tuff, as measured by Heard.[1]

We define dilatancy as an increase in porosity and compaction as a decrease in porosity. Analysis by Bhatt[2] et al of laboratory data[1] of this dry porous tuff indicated that pore dilation can occur when the pressure is positive but decreasing. Indeed, when we ignored dilatancy in our model, we obtained significant discrepancy between the predicted and the observed unloading pressure-volume path.

For the simplest existing model, it can be shown that dilatancy at positive pressure violates the second law of thermodynamics. We therefore generalized a simple model to include the possibility of dilatancy at positive pressure. This was accomplished by diminishing the Helmholtz energy by a function of porosity, with parameters determined by laboratory dilation and compaction data using dilation and compaction surfaces.

In constructing a dilation surface, we noticed that the data suggests that pore dilation may begin either immediately upon unloading, or soon after. To model dilation immediately upon unloading, we take the dilation surface to coincide with the compaction surface. We interpret the resulting deviations of such a prediction from the data as an indication of hardening of the dilation surface.

Hardening equations for dilatancy with accompanying softening during compaction were therefore added with parameters adjusted to fit the unloading dry response from the highest measured pressure (3.9 GPa).

Using the model parameters derived from the dry response, we obtained good predictions of partially saturated and fully saturated response.

Spherical explosion simulations in dry tuff show that dilatancy markedly increases peak particle velocity, at locations sufficiently far away from the source. This effect can be explained by observing that an *elastic* unloading wave can propagate *quickly in non-dilatant* material to clip peak response more than a *plastic* wave which propagates *slowly in dilatant* material.

* *Work performed under the auspices of the U.S. Department of Energy by Lawrence Livermore National Laboratory under contract #W-7405-Eng-48*

INTRODUCTION

We are interested in assessing the role of rock dilatancy in calculating the seismic coupling[3] between an underground nuclear explosion and the region far from the source. In this paper, we will describe the role of dilatancy in modeling the unloading behavior of Mt. Helen tuff, and we will examine the effects of dilatancy on particle velocity time-histories predicted by spherical explosion simulations. A complete, detailed model formulation will be given in Reference 4, to be submitted for publication in the near future. We will limit the model description here to simple notions of a porous model and to the main ideas driving the model development.

We define dilatancy as an increase in porosity and compaction as a decrease in porosity. In particular, we are concerned with *inelastic* changes in porosity, associated with the dissipative processes occurring during pore crushing and partial pore recovery. To build our model, we begin by assessing the importance of dilatancy on the prediction of the pressure-volume path during unloading of dry porous tuff. By using a non-dilatant model as a test bed and building block, we show that dilatancy cannot be ignored.

However, in order to model dilatancy and satisfy the second law of thermodynamics, we diminish the Helmholtz free energy with a new function of porosity, constructed from laboratory compaction/dilation data. We thus define compaction and dilation constraints on the pressure.

Furthermore, in order to follow the observed unloading behavior, we find it necessary for the dilation constraint to exhibit hardening during unloading and softening during reloading.

Material constants of the modified model are determined by matching loading and unloading response of dry Mt. Helen tuff. Then we use these same material constants to predict saturated and partially saturated response.

Finally, we discuss the effect of dilatancy on simulations of spherical explosions in dry tuff, and we summarize our results.

BASIC MODEL

Kinematics

We consider a simple model of a porous material, modeled as a continuum representing a solid (matrix) material that occupies a three-dimensional multiply-connected region of space. With reference to the present configuration, an elemental volume dv of porous material is assumed to be composed of solid volume dv_s and pore volume dv_p such that

$$dV = dV_s + dV_p \qquad (1a)$$

$$dv = dv_s + dv_p \qquad (1b)$$

where dV, dV_s, dV_p are the values of dv, dv_s, dv_p respectively, in a fixed reference configuration. The porosity ϕ and its reference value Φ are then defined by

$$\Phi = \frac{dV_p}{dV} \qquad (2a)$$

$$\phi = \frac{dv_p}{dv} \qquad (2b)$$

When the porous material is compressed or expanded, the solid volume, pore volume and porosity may change. For our present purposes, we define pore compaction as a process which causes a decrease in porosity ($\dot{\phi}<0$) and pore dilation as a process which causes an increase in porosity ($\dot{\phi}>0$). Furthermore, the relative volume is defined as the ratio of current volume to reference volume such that:

$$J = \frac{dv}{dV} \qquad (3a)$$

$$J_s = \frac{dv_s}{dV_s} = \frac{1-\phi}{1-\Phi} J \qquad (3b)$$

$$J_p = \frac{dv_p}{dV_p} = \frac{\phi}{\Phi} J \qquad (3c)$$

$$J_f = \frac{dv_f}{dV_f} = \frac{\phi}{S\Phi} J \qquad (3d)$$

where J, J_s, J_p, and J_f are the total, solid, pore, and fluid relative volumes, respectively, and where the saturation S in the reference configuration is given by:

$$S = \frac{dV_f}{dV_p} \qquad (4)$$

Constitutive Relations

Axioms of constitutive theory together with principles of conservation of mass, balance of momenta, conservation of energy, and the balance of entropy require that the stresses in the material be derivable from a thermodynamic potential, namely the Helmholtz free energy . We assume that the total free energy is the sum of the free energy of the dry porous solid and the free energy of the fluid partially or fully filling the pores. Furthermore, we diminish the total free energy by a function of porosity $F(\phi)$. This function allows us to model pore dilation during unloading at positive pressure. Pressures in the solid $p_s(J_s)$ and the fluid $p_f(J_f)$, obtained from the corresponding free energies, form the total pressure p, given by:

$$p = (1 - \phi)\, p_s + \phi\, p_f \qquad (5)$$

Also, the *effective pressure* is defined by:

$$p_e = p - p_f \qquad (6)$$

Thermodynamic Restrictions and Dilatancy

In Reference 4, we show that, for this model, the second law requires that:

$$-\bar{p}_e \dot{\phi} \geq 0, \qquad \bar{p}_e = p_e - \frac{f(\phi)}{J_s} \qquad (7a,b)$$

where, the function $f(\phi)$ is determined by $F(\phi)$ and the current porosity , $\bar{p}_e$ is a modified effective pressure, and a superposed dot denotes material time differentiation. Note that when $F(\phi)$ vanishes, the function $f(\phi)$ also vanishes and (7) reduces to:

$$-p_e \dot{\phi} \geq 0 \qquad (8)$$

This means that in order for porous compaction and dilation to be dissipative, the effective pressure p_e must be positive during compaction and negative during dilation. However, the experimental data in Figure 1 for a dry material with $p_e = p$ ($p_f = 0$) indicates that dilation occurs during unloading at positive effective pressure p_e, which violates the thermodynamic restriction (8). On the other hand, when $f(\phi)$ does not vanish, then the modified effective pressure $\bar{p}_e$ can remain negative during dilation at positive effective pressure p_e, thus satisfying the restriction (7a).

In the present work, we are motivated by the notion of yield surfaces in plasticity theory to introduce a compaction surface g_c and a dilation surface g_d by

$$g_c = \bar{p}_e - \kappa_c \leq 0, \qquad (9a)$$

$$g_d = -\bar{p}_e + \kappa_d \leq 0, \qquad (9b)$$

where g_c vanishes during compaction and g_d vanishes during dilation. The parameters κ_c and κ_d are hardening parameters which in general are determined by evolution equations for their rates.

Given the laboratory pressure-volume data (J*,p*) at each point along a hydrostatic loading-unloading curve, the solid and fluid equations of state, the initial value of porosity Φ, the kinematic relations (3b), (3d), and the kinetic relation (5), we calculate the porosity ϕ at

each point. Then this data can be used to determine parameters in the presumed forms for $F(\phi)$ and the evolution equations for κ_c and κ_d.

For a given volume change, we first find the response assuming no change in porosity. If $g_c > 0$, then the compaction constraint has been violated, so we reduce the porosity iteratively until g_c vanishes. On the other hand, if $g_d > 0$, then the dilation constraint has been violated, so we increase porosity iteratively until g_d vanishes.

Hardening and softening of dilation surface

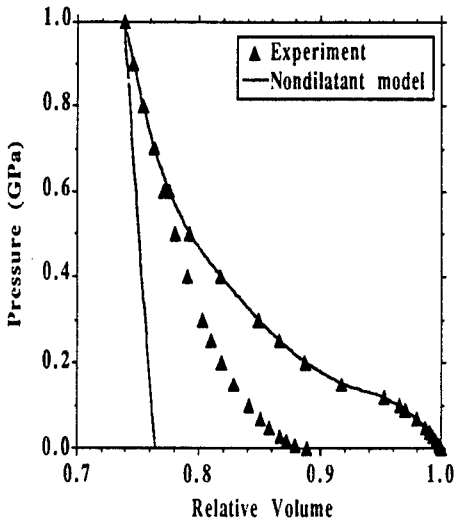


Figure 1: Effect of not modeling dilatancy

Experimental data, as shown in Figures 1 and 2, indicates that porosity increases immediately upon unloading from peak pressures of 1 GPa and 3.9 GPa, respectively. In order to model this feature, we consider the compaction and dilation constraints to nearly coincide at the onset of unloading from peak compaction. As we unload, we *harden* the dilation surface away from the compaction constraint. Conversely, as we reload, we need to *soften* the dilation surface toward the compaction constraint.

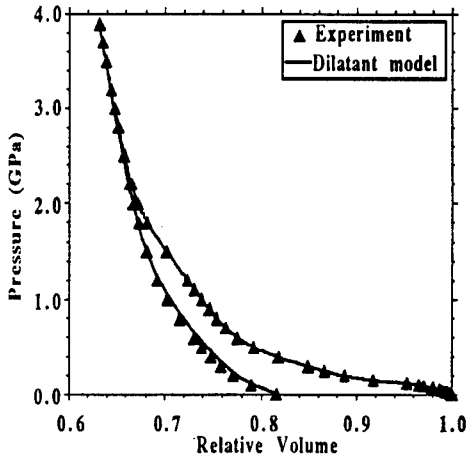


Figure 2: Effect of modeling dilatancy

To model hardening and softening of the dilation surface, without violating the second law, we use the parameter κ_d, introduced in the previous section. Evolution equations for softening during compaction and hardening during dilation are described in Reference 4.
Figure 2 shows that we can now reproduce the observed unloading, when we use dilatancy with hardening.

CALCULATIONS

Wet response

Figure 3 shows loading and unloading predictions for nearly fully saturated Mt Helen tuff. These predictions used the

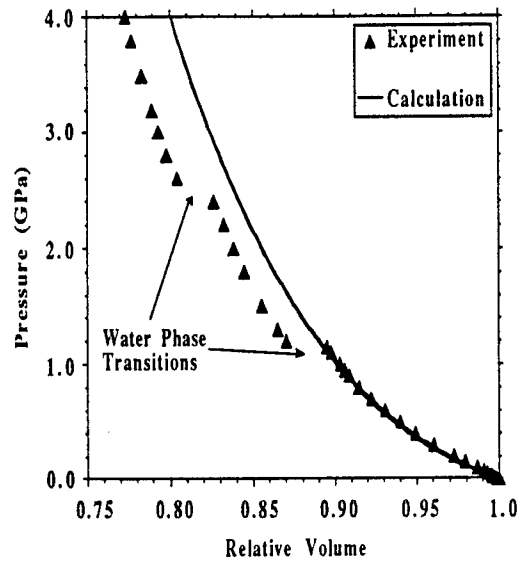


Figure 3: Fully saturated response.

model parameters calibrated from the dry data for unloading from 3.9 GPa and equations of states for the solid and water. The prediction shows excellent agreement with the laboratory data up to about 1.2 GPa. Above this pressure, water is known to undergo phase transitions[1] , which were not modeled.

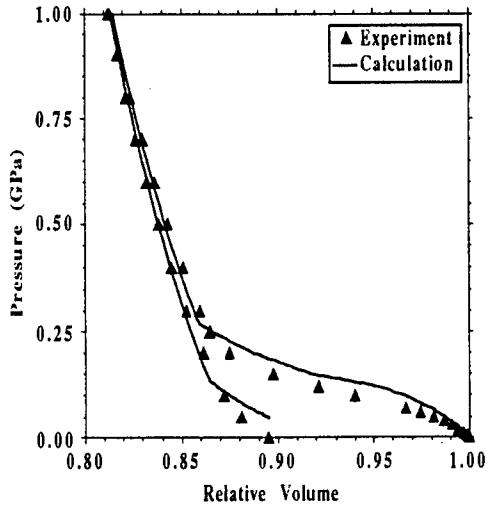


Figure 4: Partially saturated response.

Figure 4 shows predictions for loading and unloading for partially saturated tuff. The nominal saturation level was 50%. However, we used 64.1% , based on matching the onset of nonzero fluid pressure, as noted by the sharp increase in slope in the loading curve. The loading prediction lies slightly above the data, because it is known that partially saturated tuff is weaker than dry tuff, due to chemical water-rock interaction[1].

Spherical explosion simulation

In order to evaluate the effect of dilatancy on tuff response to spherical explosions, an HE spherical explosion was simulated in dry Mt. Helen tuff, with and without dilatant behavior during unloading. The HE source simulation is identical to the one used by White[5], in modeling PETN, which was used in SRI[6] experiments on limestone. A 0.45 cm radius ball of decompressed PETN explosive (with a 0.05 cm thick outer plastic shell) was ignited at the center of the limestone sphere, 13.5 cm in outer radius.

In our simulations, the limestone was replaced by dry Mt. Helen tuff. The dilatancy and hardening model parameters were developed above for fitting measured loading and unloading pressure-volume states for dry tuff. For comparison purposes (see Figures 5 and 6), we also developed a modified set of parameters to model non-dilatant behavior during unloading; i.e., maintaining porosity constant while pressure decreases from a positive value at peak compacted state.

Poisson's ratio was 0.16, based on ultrasonic measurements[1] of shear and compressional velocities in dry tuff. Tensile strength was taken as zero. Heard[1] gives only one point for dry shear strength. Consequently, a dry shear strength curve was constructed using the following three (p,Y) points, where p is the pressure and Y is the maximum stress difference in uniaxial strain:

(a) p=0.66 GPa, Y=0.48 GPa, from Heard[Table 4][1] et al .

(b) p=0, Y=0, for consistency with zero tensile strength

(c) p=0.1 GPa, Y=0.2 GPa, an arbitrary choice for pressure and a value of strength chosen below the tensile

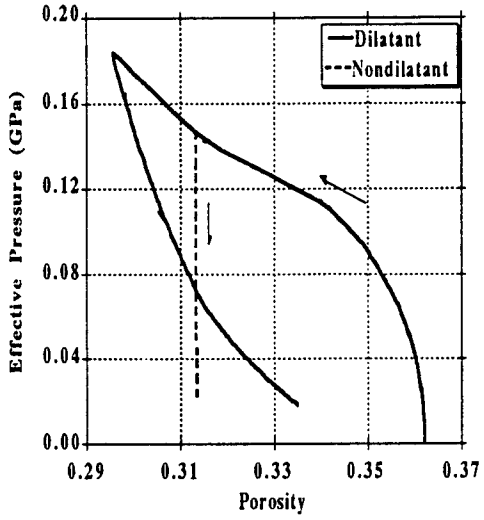


Figure 5: Effect of dilatancy on pressure response.

fracture limit (Y= 0.3 GPa) for zero tensile strength.
These three points were fitted to a form developed by Butkovich[7] for Y as a function of mean stress p:

$$Y(p)=\frac{2p}{a+bp} \qquad (10)$$

with a=0.6875 and b=3.125 GPa^{-1}.

Figure 5 shows pressure-volume paths during loading and unloading, 1.0 cm from the center of the explosive source. Notice that for the dilatant material, the unloading behavior is primarily plastic, with a soft modulus. On the other hand, for the non-dilatant material, the unloading behavior is primarily elastic, with a stiff modulus.

At the same location, Figure 6 shows particle velocity as a function of time. Notice that the peak velocity is smaller for the non-dilatant material than for the dilatant material. Notice also the steeper decay in particle velocity for the more dilatant material.

These results show that an unloading wave travels more slowly in dilatant material than in non-dilatant material, because of the softer unloading evidenced by dilatant material. This behavior, in turn, causes a *delay in attenuation* of particle velocity, showing a higher peak and steeper decay in the more dilatant material.

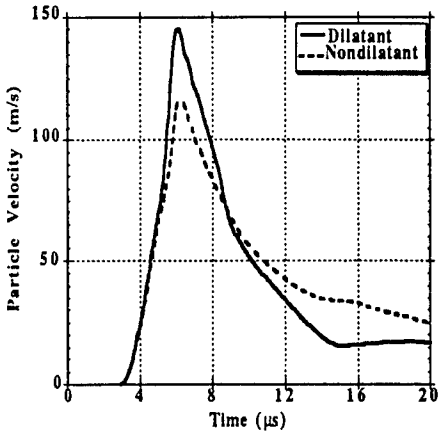


Figure 6: Effect of dilatancy on attenuation.

SUMMARY

In order to model the observed dilatant unloading of Mt. Helen tuff and satisfy the second law, we diminished the Helmholtz free energy by a function $F(\phi)$ of porosity. When we applied this model to simulate a spherical explosion in this tuff, we found that dilatant unloading caused a *delay in attenuation* of particle velocity, showing a higher peak and steeper decay in the more dilatant material.

Further work is needed to compare this model with other effective stress models (such as that of Drumheller[8]) and to explore the influence of nonzero fluid pressure. Also, it is desirable to extend the model to allow treatment of melting and vaporization of rock.

REFERENCES

1. H.C. Heard, B.P. Bonner , A. G. Duba, R.N. Schock, and D.R. Stephens (1973), "High Pressure Mechanical Properties of Mt. Helen, Nevada Tuff",

Lawrence Livermore National Laboratory report UCID-16261.

2. J.J. Bhatt, M.M. Carroll, and J.F. Schatz (1975), "A Spherical Model Calculation for Volumetric Response of Porous Rocks". ASME J. Appl. Mech. V. 42 n 2, pp 363-368.

3. L. A. Glenn (1992), "Energy-Density Effects on Seismic Decoupling", Lawrence Livermore National Laboratory report UCRL-JC-109393.

4. M. B. Rubin and A.V. Attia, "Analysis of Material Dissipation Due to Porous Compaction and Dilation in an Effective Stress Theory" (to be submitted for publication).

5. J. W. White (1993), "Computer Modeling of Low Pressure Laboratory Experiments on Indiana Limestone and Sierra White Granite and the Implications for Yield Estimation", Lawrence Livermore National Laboratory report UCRL-ID-112449.

6. S. A. Miller and A. L. Florence (1992), "Laboratory Particle Velocity Measurements on Indiana Limestone and Sierra White Granite". GL-TR-91-000.

7. T. R. Butkovich (1973), "A Technique for Generating Pressure-Volume Relationships and Failure Envelopes for Rocks", Lawrence Livermore National Laboratory report UCRL 51441

8. D. S. Drumheller (1987), "A Theory for Dynamic Compaction of Wet Porous Solids", Int. J. Solids Structures, Vol. 23, No. 2, pp. 211-237.

THIS PAGE INTENTIONALLY LEFT BLANK.

STATISTICAL CRACK MECHANICS

John K. Dienes, Theoretical Division, Los Alamos

Though it is sometimes possible to simulate the ground blast from a single explosive shot with a simple computer algorithm and appropriate constants, the modelling methods in common use cannot account for major changes in geology or shot energy because the fault structure, microcracking, tectonic stresses, brittle-ductile transition, water content and many other mechanical features are not represented in significant detail. Another problem with simple computer models is that anisotropic effects resulting from preferred joint orientation, layering, and crack coalescence are not accounted for. An alternative approach called Statistical Crack Mechanics (SCM), which was developed as part of the oil-shale program in the seventies, accounts for crack opening, shear, growth, and coalescence. The importance of shear cracks is not often recognized in modelling, and their existence is even questioned by some, but the ubiquity of visible faults in the earth testifies to their importance, and the paper of Howe et al. (1985) clearly shows both their existence and importance. That paper deals with the behavior of TNT, and in such a reactive material the role of shear cracks is clarified by blackened and melted regions. A recent paper by Kalthoff and Winkler (1987) shows that wings develop in shear cracks at low strain rates, but in high-speed processes cracks tend to grow in their own planes. This effect is discussed in another context by Horii and Nemat-Nasser (1986) who are concerned with Dugdale's kind of behavior at crack tips. The growth of cracks in their own planes makes possible the statistical treatment that is the core of SCM. Without this premise, the statistics would be intractable. Numerous photographs and micrographs show that shocked materials tend to involve arrays of planar cracks.

The analysis of crack coalescence was treated with a theory for the statistical distribution of both isolated and connected cracks. The original statistical theory was based on an analytic solution to a linear Liouville equation derived for this purpose assuming constant crack size (Dienes,1978). A more sophisticated theory that accounts for the decreasing mean free path that develops in the later stages of fragmentation has also been developed (Dienes,1985). A method for determining the permeability of rock based on these results and in addition, some concepts from

percolation theory has been reported (Dienes,1982) and discussed by Gueguen et al (1986) and Gueguen and Dienes (1989).

Though much research has been devoted to brittle and ductile behavior and to the brittle-ductile transition, we are far from having a proven constitutive law that accounts for behavior in the brittle regime and for the transition. Calculations in the ductile regime can be expected to be fairly reliable, since successful cratering calculations were reported as early as 1968 (Dienes and Evans). However, many effects such as melting, thermal softening, strain-rate sensitivity, and solid-state phase changes are still not included in most standard codes. A framework for a unified brittle-ductile theory has been developed in SCM. The approach generalizes Reuss's 1930 hypothesis concerning superposition of elastic and plastic strain rates for small deformations. In SCM the concept of superposition is proven to apply to arbitrarily large strains and to combined elastic, plastic and fracture behavior. A computer algorithm representing the theory has recently been incorporated into the PRONTO code, allowing for the calculation of very complex geometries. An extension of these concepts that leads to predictions of dilatancy is under development.

The current approach differs considerably from the use of flow laws, whereby an attempt is made to account for the behavior of brittle materials by modifying plasticity theory as discussed, for example, by Sandler and Baron (1985). That approach fails, however, to account for microscopic behavior, instabilities, or for the strain-rate and size effects observed in brittle materials such as rock, glass, ceramics and grains of explosive. These effects come from crack growth. An early attempt by Drucker and Prager (1952) to account for dilatancy by relating it to the pressure dependence of the flow stress has been shown to be in conflict with experimental evidence by Spitzig and Richmond (1984) and by Sandler and Baron (op. cit.). The premise for the flow-law approaches is that materials are microscopically *stable* and that strain due to cracking is analogous to strain due to plastic flow. It is clear that such approaches represent only a first attempt to develop constitutive relations — they ignore the evidence for *unstable* behavior given by crack bursting, acoustic emission, stepping of stress-strain curves (Savart-Masson effect, Bell, 1973), strain-softening and many other kinds of erratic behavior that are observed in the brittle and brittle-ductile regimes. In order to make flow laws tractable, isotropy is usually assumed, though it is well-known that this approximation is

appropriate only during initial loading and is not even roughly valid during unloading or reloading with complex stress paths. In particular, isotropic hardening fails to account for the hysteretic behavior observed in cyclic plastic flow.

Whereas the flow-law approach modifies the treatment of plastic strain rate to account for failure, the SCM approach considers fracture to reduce the elastic moduli and adds a strain rate due to crack growth. Thus, the stretching **D** (the symmetric part of the velocity gradient) can be represented by the superposition principle

$$\mathbf{D} = \mathbf{D}^e + \mathbf{D}^p + \mathbf{D}^g + \mathbf{D}^R + \mathbf{D}^{nl}$$

where $\mathbf{D}^e$ represents the stretching due to elastic behavior, including the reduced compliance due to cracks; $\mathbf{D}^p$, the stretching due to plastic flow; $\mathbf{D}^g$, the stretching due to crack growth; $\mathbf{D}^R$, the stretching due to material rotation (Dienes,1979,1987); and $\mathbf{D}^{nl}$, the stretching due to nonlinear contributions from the equation of state. To convert this into a useful computational scheme, constitutive laws relating the stretching to the stress and other state variables and their rates are required for each of the terms. This is discussed in parts II and III of the Theory of Deformation, (Dienes 1989, part III in preparation). The final result can be expressed as

$$\overset{\bullet}{\sigma} = F(\sigma, \mathbf{D}, \alpha)$$

where the time derivative must be taken and the variables computed in appropriate rotating (polar) axes. Kinematic hardening is accounted for with a back stress α. Its rate and other rates are defined using the theory of polar decomposition in which the deformation gradient can be represented as a product of a positive-definite part and a rotational part, so that $\mathbf{F} = \mathbf{VR}$ (Chadwick,1976, Dienes,1987). It is particularly important to account for rotation accurately when dealing with highly anisotropic materials, a subject recently addressed by Zheng (1992).

The SCM approach is sometimes criticized for using more computer time and being too complex, but the increase in computer time is only twofold, and the complexity is not significantly greater than in damage theories. For this investment we get a

representation of the physical behavior at the microscopic level that can account for phenomena such as permeability, fragmentation, shear banding, and hot-spot formation in explosives. It cannot be claimed that the treatment of microscopic behavior in the current article is especially realistic, since there are many simplifying assumptions. However, the theory is capable of generalization in many different ways as the need arises. Some of the generalizations that are in progress are discussed in the penultimate paragraph.

The approach described here provides a way to account for microstructure and, hence, for phenomena that are not accessible to macroscopic calculations, such as permeability and explosive hot spots. Analysis of dynamic geophysical processes such as explosions, earthquakes, volcanoes, asteroid fragmentation, impact cratering, and avalanches provide other applications of the theory. A drawback of the method is that many of the constants required are not normally known for specific materials. At SRI a parallel effort by Seaman, Curran and Murri (1985) and many others has involved experiments capable of generating the data necessary for their modelling effort. Ideally, theory, numerical calculations, material characterization, and dynamic experiments should go together, but most studies have been too fragmented to allow this kind of modelling to reach a useful level of sophistication. The urgency of the cold war was frequently used to justify the absence of long-term planning. Perhaps the new world situation (1993) will allow for a more coherent expenditure of research funds.

The treatment of a number of nonlinear processes is under development in SCM, but some additional study and coding will be required before they are ready for general use. Seven examples are cited here. (1) Dilatancy needs to be investigated. This process, originally observed by Bridgman (1949), is thought to depend on the microscopic generation of voids under shear (Zoback and Byerlee, 1975). It has eluded detailed theoretical description, though some progress is being made, as discussed by Fischer and Patterson (1989). A new theoretical approach to dilatancy is based on a theory of T-cracks, which shows that they can open under pure shear, and turns out to yield surprisingly simple results (Dienes, 1993). The results can be incorporated into SCM as part of a statistical treatment in the same way that plane cracks have been previously treated. (2) Strain-rate effects due to the finite speed of crack growth are predicted by the approach in this article, but better data are needed and the results should be tested. (3) Size effects are

well-known to civil engineers but have been inadequately characterized in constitutive modelling. Much data is based on tests of very small samples so that the effect of large defects is ignored. (4) Phase changes and other high-pressure effects need to be accounted for. (5) The coalescence model described here assumes a constant mean free path, but it seems clear that in many situations the mean free path will decrease in the course of fragmentation as crack size increases. A theoretical approach to this process has been described by Dienes (1985) but has not been implemented in any computer code. (6) Many practical materials are composites, and failure of such materials has not been sufficiently characterized. (7) The brittle-ductile transition depends on a variety of state variables such as temperature, pressure, and strain rate. A general theoretical treatment is not yet available though the main features are known (Evans, Fredrich and Wong, 1990). Those authors include an intermediate semibrittle regime in their analysis of the data.

Rather than pursuing and attempting to verify the SCM approach in general, we are applying the method in special projects where there is enough interest to establish the required material properties. They can be determined from stress-strain curves and other standard tests, or back-fitted by comparison with macrocopic experiments (exploding-wire, impact, etc.), or estimated by analogy with similar materials. It needs to be emphasized that the properties of interest are standard in mechanics, and can often be estimated from handbook data. For many projects we do not require all the parameters since in many cases only a few dominate the process. For fragmentation studies we do not normally require a high standard of prediction — all that is required is an understanding of the main effects — still a considerable challenge. The general approach presented here is useful in allowing analysts to put various processes into a single context. What is needed now is to implement the improved theory in the SCM computer algorithm, better numerical modelling, and detailed material properties. The success of the theory will depend on its usefulness in a variety of case histories. It is unlikely that any single theory of materials can predict all possible kinds of failure, but a unified approach helps us to relate and interpret many observations that are otherwise disconnected. In addition, the current approach allows us to understand better the variability of material properties that results from variability in defects. This is probably the most important application.

REFERENCES

Bell, F.J. (1973) ,"The Experimental Foundations of Solid Mechanics," Handbuch der Physik, VIa/1, Springer-Verlag

Bridgman, P. W. (1949), "Volume changes in the plastic stages of simple compression," J. Appl. Phys. 20, pp1241-1251

Chadwick, P. (1976), Continuum Mechanics , George Allen and Unwin Ltd., London

Dienes, J.K., and M.W.Evans (1968), "Cratering Calculations with a Hydrodynamic Strength Code," Behavior of Dense Media Under High Dynamic Pressures, Gordon and Breach

Dienes, J. K. (1978), "A Statistical Theory of Fragmentation," in: Y. S. Kim, ed. Proc. 19th U.S. Rock Mechanics Symposium, Stateline, Nev.

Dienes, J. K. (1979), "On the Analysis of Rotation and Stress Rate in Deforming Bodies," Acta Mechanica, vol. 32, pp. 217-232.

Dienes, J. K., and L. G. Margolin (1980), "A Computational Approach to Rock Fragmentation," in D. A. Summers, Ed., The State of the Art in Rock Mechanics, Proc. 21st U.S. National Symposium on Rock Mechanics, Rolla, Mo.

Dienes, J. K. (1981), "On the Effect of Anisotropy in Explosive Fragmentation," in H. H. Einstein, ed., Rock Mechanics from Research to Application, Proc. 22nd U. S. Symposium on Rock Mechanics, M.I.T., Cambridge, Mass.

Dienes, J. K. (1982), "Permeability, Percolation and Statistical Crack Mechanics," in R. E. Goodman and F. E. Heuze, Issues in Rock Mechanics, Proc. 23rd Symposium on Rock Mechanics, Berkeley, Cal.

Dienes, J. K. (1983), "Statistical Crack Mechanics," in J.-P. Boehler, Ed., Failure Criteria of Structured Media, Proc. Colloque International du CNRS no. 351, Villard-de-Lans, France

Dienes, J.K. (1985), "A Statistical Theory of Fragmentation Processes, " Mechanics of Materials, 4, No. 3, pp. 325-335.

Dienes, J.K. (1987), "Theory of Deformation, Part I, Kinematics," Los Alamos National Laboratory Report, LA-11063-MS, Vol. I

Dienes, J.K. (1989), "Theory of Deformation, Part II, Physical Theory," Los Alamos Report, LA-11063-MS, Vol. II

Dienes, J.K. "Theory of Deformation, Part III, The SCRAM code," In Preparation.

Dienes, J. K. (1993), "Unified Theory of Flow and Fragmentation," to appear in Numerical Modelling of Dynamic Flow, Failure, and Fragmentation, Springer-Verlag

Dienes, J.K., "Shearing of T-Cracks and a Mechanism of Dilatancy," to be submitted to Acta Mechanica

Drucker, D.C. and W. Prager (1952), "Soil Mechanics and Plastic Analysis or Limit Design, " Quart. Appl. Math. 10 (2)

Evans, B., J.T.Fredrich and T.-F.Fong (1990), "The Brittle-Ductile Transition in Rocks: Recent Theoretical and Experimental Progress," Geophysical Monographs 56

Fischer, G. J. and M.S. Paterson (1989), "Dilatancy During Rock Deformation at High Temperatures and Pressures," JGR 94, No. B12, pp 17,607-17,617

Gueguen, Y, C. David and M. Darot (1986), "Models and Time Constants for Permeability Evolution," Geophysical Research Letters, 13, pp 460-463

Gueguen, Y, and J. Dienes (1989), "Transport Properties of Rocks from Statistics and Percolation," Mathematical Geology, 21, 1

Howe, P.M., G. Gibbons Jr., and P.E Webber (1985), "An Experimental Investigation of the Role of Shear in Initiation of Detonation by Impact," Proc. Eighth Symposium (International) on Detonation, Albuquerque, NM

Kalthoff, J.F. and S. Winkler (1987), "Failure Mode Transition at High Rates of Shear Loading in Impact Loading and Dynamic Behavior of Materials," Vol. I, C.Y. Chiem, H.D. Kunze and L.W. Meyer, Eds., Informationsgesellschaft Verlag

Nemat-Nasser, S. (1982), "On Finite Deformation Elasto-Plasticity," Int. J. Solids Structures, Vol. 18, No. 10, pp. 857-872

Nemat-Nasser, S. and H. Horii (1982), "Compression-Induced Nonplanar Crack Extension with Application to Splitting, Exfoliation and Rockburst," J. Geophys. Res., 87, No. B8, pp. 6805-6821

Reuss, A. (1930), "Berucksichtigung der elastischen Formanderung in der plastizitats Theorie," Zeits. ang. Math. Mech., 10, pp. 266-269

Sandler, I. and M. Baron (1985), Numerical Models for Dynamic Loading, in Mechanics of Geomaterials, Ed. by Z. Bazant, John Wiley and Sons, Ltd.

Seaman, L., D.R. Curran and W.J. Murri (1985), "A Continuum Model for Dynamic Tensile Microfracture and Fragmentation," JAM 52, p. 593

Spitzig, W.A. and O. Richmond (1984), "The Effect of Pressure on the Flow Stress of Metals", Acta Metall., 32, No. 3, pp.457-463

Zheng, Q.S. (1992), "On the generalization of constitutive laws from their arotational forms," Acta Mechanica 91, pp. 97-105

Zoback, M.D. and J.D.Byerlee (1975),"The Effect of Cyclic Differential Stress on Dilatancy in Westerly Granite Under Uniaxial and Triaxial Conditions," JGR 80, 11, pp 1526-1530

INCORPORATING DAMAGE MECHANICS INTO EXPLOSION SIMULATION MODELS

Charles G. Sammis

Department of Geological Sciences

University of Southern California

Los Angeles, CA 90089-0740

ABSTRACT

The source region of an underground explosion is commonly modeled as a nested series of shells. In the innermost "hydrodynamic regime" pressures and temperatures are sufficiently high that the rock deforms as a fluid and may be described using a PVT equation of state. Just beyond the hydrodynamic regime, is the "non-linear regime" in which the rock has shear strength but the deformation is nonlinear. This regime extends out to the "elastic radius" beyond which the deformation is linear. In this paper we develop a model for the non-linear regime in crystalline source rock where the nonlinearity is mostly due to fractures. We divide the non-linear regime into a "damage regime" in which the stresses are sufficiently high to nucleate new fractures from preexisting ones and a "crack-sliding" regime where motion on preexisting cracks produces amplitude dependent attenuation and other non-linear effects, but no new cracks are nucleated. The boundary between these two regimes is called the "damage radius".

The micromechanical damage mechanics recently developed by Ashby and Sammis (1990) is used to write an analytic expression for the damage radius in terms of the initial fracture spectrum of the source rock, and to develop an algorithm which may be used to incorporate damage mechanics into computer source models for the damage regime. Effects of water saturation and loading rate are also discussed.

INTRODUCTION

Recent advances in seismic discrimination and yield estimate of underground nuclear explosions have been based largely on high-frequency local phases such as L_g and higher-mode surface waves. This shift in focus to higher frequencies has stimulated new interest in understanding the non-linear seismic coupling near the source, and in the mechanics of near-surface spallation which is observed for most large explosions. While current numerical source models give an adequate representation of coupling and spall for sources buried in alluvium, significant discrepancies have been observed between model predictions and observed ground motions near explosions emplaced in hard rock like tuff and granite. These discrepancies usually involve the observation of a much broader pulse than predicted by the simulation (Rimer et al., 1987), and significantly lower displacement amplitudes (App and Brunish, 1992). App (1993) has recently identified the shear strength as the most important property of near-source rocks in shaping the seismic source function.

The problem appears to be that the numerical programs, which do a good job of modeling the compaction processes which dominate non-linear coupling in sediments, do not adequately describe the processes of crack growth and fragmentation which dominate non-linear coupling in hard rock. Crack growth is poorly modeled by current simulation programs for two reasons. First, the strength of a cracked rock is scale dependent --strength decreases as the square root of crack length. The strength of granite measured in the laboratory is significantly larger than the strength of a granitic mass in the field simply because the length of preexisting cracks are limited by the size of the lab specimen. Hence laboratory mechanical data can not be used directly in the simulation programs. Also, the strength of the rock decreases as cracks grow

during loading. A second problem has to do with the fact that, where compaction is a strengthening process which leads to a homogenization of the strain field, crack growth is a weakening process which leads to shear localization.

These same scaling problems may also explain why numerical simulations of spallation in hard rock do not seem to be as successful as those in sediments (App and Brunish, 1992). Whereas a local tensile failure criterion may work for sediments, size effects inherent in the fracture controlled tensile strength of hard rock become important.

What is needed for a more accurate numerical simulation of explosions in hard rock is a rheology which explicitly accounts for the effects of nucleation, growth, and interaction of fractures on elasticity and strength. Such rheologies are generally categorized as being "damage-mechanics" based, where "damage" is a measure of the size and density of fractures. Damage mechanics rheologies can be roughly divided into two groups: empirical formulations which are based on fracture mechanics but which have many adjustable parameters (Costin, 1983, 1985), and those which are based on a micromechanical modeling of the nucleation, growth, and interaction of fractures growing from preexisting cracks in the rock (Ashby and Sammis, 1990). The advantage of model-based damage mechanics is that it explicitly accounts for the initial fracture spectrum in the source rock, and thus deals with the scaling problem discussed above. In Ashby and Sammis (1990), we have shown that our model gives a good description of the failure surface for a wide range of rock types with no unphysical adjustable parameters. The current challenge is to cast the damage mechanics into a form which can be incorporated into numerical codes which simulate underground explosions. In this paper we discuss one algorithm which can be used to

incorporate model-based damage mechanics into a spherically symmetric "one dimensional" code.

However, as summarized in the next section, our current damage mechanics formulation has several limitations which also need to be addressed. First, it assumes all the preexisting flaws are the same size. Second, it does not explicityly include the effects of water saturation. Third, it assumes static elastic fracture mechanics and ignores dynamic effects on the stress intensity factor which may be important in the explosion application (see e.g.. Rubin and Ahrens, 1992: Grady and Kipp, 1979). Finally, it does not give a good representation of the post-failure regime where the material is strain weakening. Possible solutions to these problems are also discussed.

DAMAGE MECHANICS

There have been several recent attempts to model the nucleation, growth, and interaction of microcracks both numerically (Horii and Nemat-Nasser, 1985) and analytically (Ashby and Hallam, 1986; Sammis and Ashby, 1986, Horii and Nemat-Nasser, 1986). The results, which have been tested using two and three dimensional models of flaws in brittle plastic and glass, are expressed as a stress intensity factor of the form:

$$K_I = F(l, \sigma_3)\,\sigma_1\sqrt{\pi a} \qquad (1)$$

where σ_1 and σ_3 are, respectively, the maximum and minimum principal stresses, 2a is the dimension of the starter flaws, and l is the extension of the "wing cracks" (as we shall call the out-of-plane extensions of the starter flaws which grow parallel to σ_1; these are illustrated in Figure 1). Analytic expressions of the function F in eqn. (1) for the nucleation and growth of fractures before

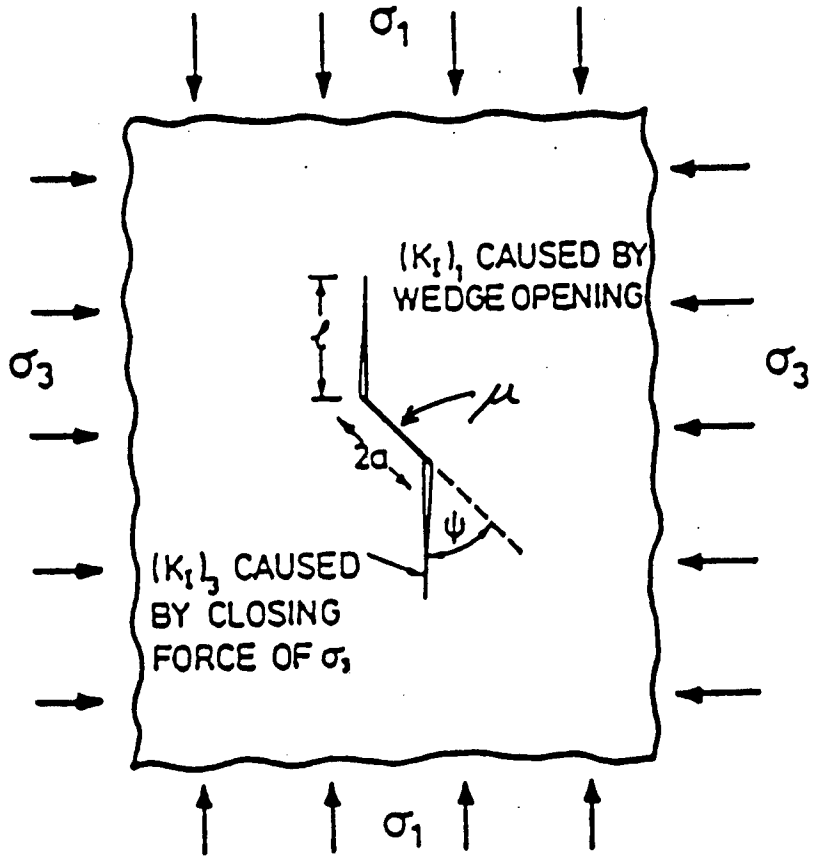


Figure 1. Geometry of flaws modeled in the Ashby and Sammis (1990) damage mechanics. Mode II sliding on the starter flaws of length 2a nucleates and drives tensile "wing cracks" of length ℓ Sliding on the starter flaw is controlled by a coefficient of friction μ..

interaction becomes important may be found in Sammis and Ashby (1986) when the starter flaws are pores, and in Ashby and Hallam (1986) when they are inclined cracks. For a given state of stress, (σ_1, σ_3), the wing cracks will extend until K_I falls to K_{Ic} where K_{Ic} is the critical stress intensity factor, a material property. Equation (1) may be rewritten in terms of a dimensionless stress, s_1, defined as

$$s_1 = \frac{\sigma_1 \sqrt{\pi a}}{K_{Ic}} \tag{2}$$

Ashby and Sammis (1990) have developed a model for the interaction between growing tensile microcracks when all starter flaws are the same size, 2a. For their model, the stress intensity factor at the tip of the wing crack is

$$K_I = \frac{\sigma_1 \sqrt{\pi a}}{C_2 \left((D/D_0)^{1/3} - 1 + \beta/\alpha\right)^{3/2}} \left\{ (1 - C_1 \lambda) \left[1 + 2 \left((D/D_0)^{1/3} - 1\right)^2 \left(\frac{D_0^{2/3}}{1 - D^{2/3}} \right) \right] \right. \tag{3}$$

$$\left. - \lambda C_4 \left((D/D_0)^{1/3} - 1\right)^2 \right\}$$

where

$$\lambda = \frac{\sigma_3}{\sigma_1}$$

$$C_1 = \frac{\left(1 + \mu^2\right)^{1/2} + \mu}{\left(1 + \mu^2\right)^{1/2} - \mu} \tag{4}$$

$$C_2 = \pi \alpha \sqrt{\frac{3\alpha}{\beta}} \left(\left(1 + \mu^2\right)^{1/2} - \mu \right)^{-1}$$

$$C_4 = 2\pi\alpha^2\sqrt{\frac{3}{\beta}}\left(\left(1+\mu^2\right)^{1/2}-\mu\right)^{-1}$$

In these expressions, μ is the coefficient of friction on the starter flaws and α and β are geometrical factors near 1. Note that this expression for C_4 corrects an error in eqn. (29) of Ashby and Sammis (1990).

The initial damage, D_0, and the current damage, D, are defined as

$$D_0 = \frac{4}{3}\pi\left(\alpha a\right)^3 N_v \qquad (5)$$

$$D = \frac{4}{3}\pi\left(1+\alpha a\right)^3 N_v$$

where N_v is the number of cracks per unit volume.

The first term in curly brackets in eqn. (3) is the wedging force opening the cracks plus the crack-crack interaction and the second is the effect of the confining stress resisting this opening. Assuming the cracks propagate until K_I falls to K_{Ic}, amalgamating the constants, and using the definition of s_1 given in (2), eqn. (3) can be written as

$$s_1 = \frac{C_2\left(\left(\frac{D}{D_0}\right)^{1/3} - 1+\frac{\beta}{\alpha}\right)^{3/2} + s_3\left[C_1\left(1+\left(\frac{C_3 D_0^{2/3}}{1-D^{2/3}}\right)\left(\left(\frac{D}{D_0}\right)^{1/3}-1\right)^2\right)+C_4\left(\left(\frac{D}{D_0}\right)^{1/3}-1\right)^2\right]}{1+C_3\frac{D_0^{2/3}}{\left(1-D^{2/3}\right)}\left(\left(\frac{D}{D_0}\right)^{1/3}-1\right)^2} \qquad (6)$$

where $s_3 = \frac{\sigma_3\sqrt{\pi a}}{K_{Ic}}$ and $C_3 = 2$. Note that in Ashby and Sammis (1990) tensile stress was defined as positive whereas here compression is positive.

In Fig. 2, eqn. (6) has been used to calculate the stress s_1 necessary to produce damage D, for a coefficient of friction $\mu = 0.6$ and for several values of

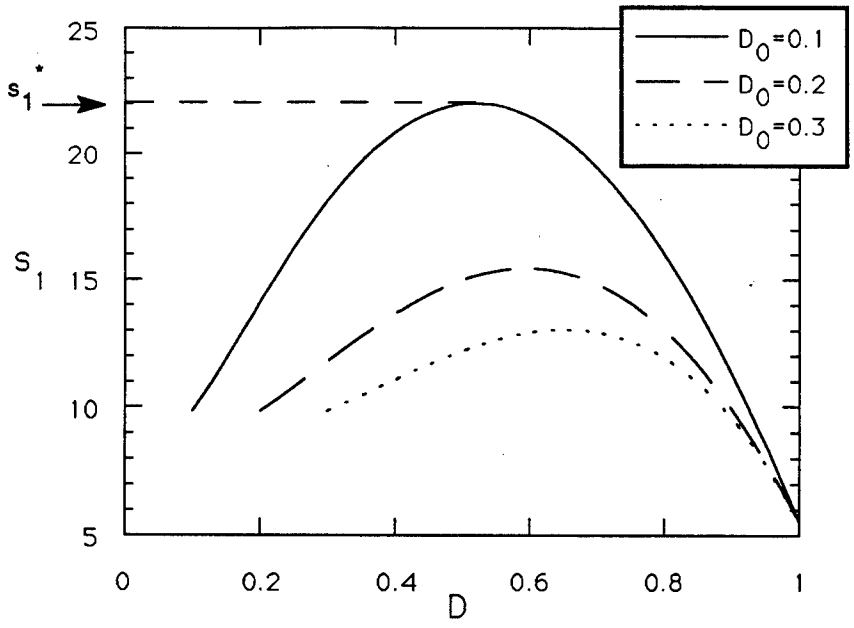


Figure 2. Dimensionless stress, s_1, as a function of damage, D, for three different values of the initial damage, D_0. The curves reach a maximum which is defined as the failure stress, s_1^*. Beyond this stress, a weakening rheology causes shear localization, the details of which are not predicted by the model. Note that the higher the initial damage, the lower the failure stress.

the initial damage D_0. For values of D near D_0, an increase in s_1 is required to increase the damage. However, s_1 is observed to reach a maximum, beyond which an increase in damage can be produced by a reduced stress. For levels of damage past the maximum in s_1, a weakening rheology causes shear localization, the details of which are not predicted by the model. The maximum value of s_1 is identified as the failure stress. Ashby and Sammis (1990) have shown that this model gives a good representation of the failure surface for a wide range of rocks without the introduction of any arbitrary "unphysical" constants.

APPLICATIONS TO UNDERGROUND EXPLOSIONS

Seismic Coupling

The question of seismic coupling is central to the use of seismic waves for discrimination and yield estimate. The effects of rock type and water saturation on seismic coupling are usually studied by forward modeling using numerical simulation. As discussed above, recent discrepancies between simulated and observed ground motions for sources in hard rock suggest that crack growth must be important in these environments. The micromechanically based damage mechanics outlined in the previous section suggests that the size and density of fractures in hard rock may be more important parameters in controlling coupling than the actual rock type.

To help focus the discussion, consider the schematic diagram of a buried explosive source shown in Fig. 3. Three non-linear regimes can be identified: the "hydrodynamic regime" in which rock flows, at extremely high pressures and temperatures, the "damage regime" in which the rock behaves as a solid but stresses are large enough to extend existing cracks, and the non-linear "crack-sliding" attenuation regime in which stresses are large enough to produce amplitude dependent attenuation but not sufficiently large to cause additional

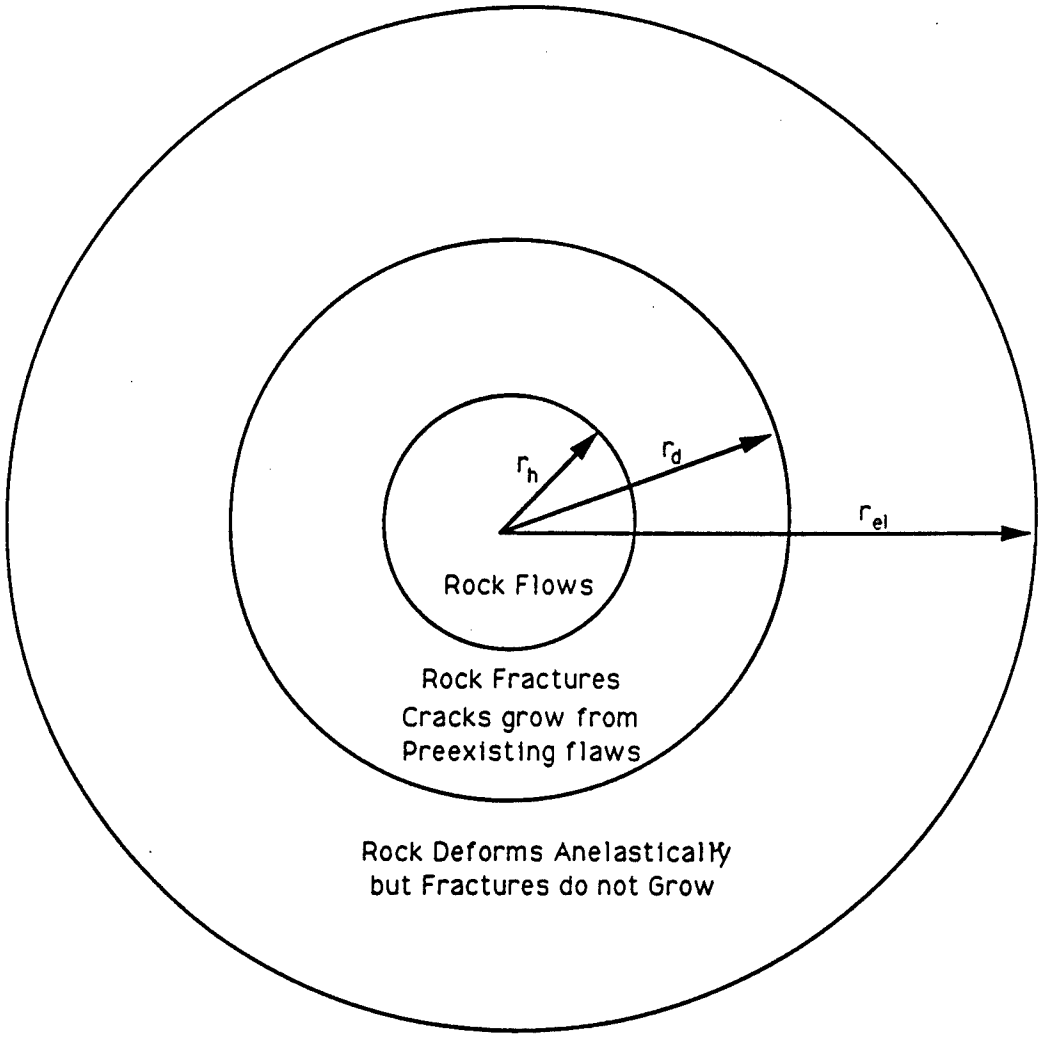


Figure 3. Schematic diagram of a buried explosive source showing the three deformation regimes discussed in the text.

fracture. The hydrodynamic radius, r_h, depends on the equation of state of the emplacement medium and is the subject of high pressure shock wave studies. The damage radius, r_d, is defined by the condition that the peak radial stress has fallen to a level just sufficient to nucleate fractures from initial flaws in the emplacement medium. The damage mechanics developed by Ashby and Sammis (1990) allows a quantitative evaluation of r_d. The equation for the radial stress σ_r required to initiate flaws when the hoop stress is σ_θ is

$$\sigma_r = \sigma_o + c_1\sigma_\theta \qquad (7)$$

where c_1 depends on the coefficient of friction μ on the starter flaws

$$c_1 = \frac{\sqrt{1+\mu^2} + \mu}{\sqrt{1+\mu^2} - \mu}$$

The other constant σ_0 is defined as

$$\sigma_o = \frac{\sqrt{3}}{\sqrt{1+\mu^2} - \mu}\left(\frac{K_{1c}}{\sqrt{\pi a}}\right)$$

where, as above, K_{1c} is the critical stress intensity factor for tensile failure and 2a is the length of the initial flaws in the emplacement medium.

It is important to note that the damage radius is not simply a function of rock-type. In fact, the parameters K_{1c} and μ are almost independent of rock type. Rather, r_d is most sensitive to the size, 2a, of the largest flaws in the emplacement medium. One of the effects of ground water saturation is to reduce the effective μ on pre-existing cracks which can make r_d significantly larger.

The elastic radius r_{el} is more difficult to define because there is no physical cutoff to the non-linear attenuation. However, if amplitude dependent attenuation is due to motion on pre-existing flaws, then r_{el} can be expected to scale with flaw-size in a similar way as the damage radius since a smaller stress is required to produce motion on a larger fracture. In fact, if the source

emplacement medium is heavily jointed, the elastic radius could be very large indeed. The effect of water saturation on the elastic radius is not so obvious since a reduction in the coefficient of friction allows cracks to move out to a larger distance but, at the same time, reduces the non-linearity of this slip.

The Mechanics of Spall in Hard Rock

Most underground nuclear explosions are accompanied by spallation of the ground surface. Spall is defined as a parting of near surface layers which were originally in contact in response to the stress waves produced by a contained underground explosion (Eisler and Chilton, 1964; Day et al., 1983). Upon reflection at the free surface, the stress becomes tensile, and spall is produced when these tensile stresses exceed the tensile strength of the near surface geological materials. The near-surface material is observed to first accelerate upward in response to the stress impulse, then to decelerate under the action of gravity, and finally to "slap down" closing the tensile gap.

The spall phenomenon has been shown to have observable seismic consequences. While Day et al. (1983) showed that spall does not contribute to surface waves with periods in excess of about 10 sec., several studies suggest that it can make a significant contribution to short-period seismic waves (Patton 1988, McLaughlin et al., 1988; Taylor and Randall, 1989). Based on numerical simulations of nuclear explosions conducted in hard rock, App and Brunish (1992) estimate that the kinetic energy associated with spall, and potentially available as a secondary source of seismic waves, is about one fourth that available for seismic waves radiating out from the point source explosion.

Since recent advances in explosion discrimination and yield estimate are based largely on short period regional phases such as Lg and higher mode Rayleigh waves, there has been a renewed interest in understanding the spall

phenomenon and in its proper representation in source models. Day and McLaughlin (1991) have further developed the point-force representation of spall introduced by Day et al. (1983). Their derivation is based on a horizontal tension crack model, the parameters of which are constrained by observed motions near ground zero.

There is, however, evidence that the geometry and physical process of spallation may be more complex than the propagation of a single horizontal tensile crack. Stump (1985) found evidence from subsurface acceleration measurements for variations in the depth of spall associated with a buried chemical explosion. Numerical simulations (Walton and Heuze, 1989; App and Brunish, 1992) predict that spallation occurs over a roughly conical region which is deepest beneath ground zero.

App and Brunish (1992) investigated the physical processes which govern spallation by numerically modeling motion at the free surface above events which span a wide range of test environments: MERLIN in desert alluvium, HEARTS in tuff beneath the water table at Yucca Flat, TOWANDA in tuff beneath the water table on Pahute Mesa, and HOUSTON above the water table in very dense rock on Pahute Mesa. Based on their modeling, they made the following important observations:

(1) The less than 1g "spall" accelerations often observed for low yield events in alluvium may not be true spall. Rather, they may be due to near surface Coulomb shear failure of the near-surface alluvium.

(2) For the events in detonated in tuff, the spall motions observed at surface ground zero are very sensitive to the thickness of the surface alluvial cover, but were also observed to depend on rock properties at the source point.

(3) For the two events on Pahute Mesa (TOWANDA and HOUSTON), differences in observed surface motions were primarily due to differences in

saturation and rock strength within a few cavity radii of the explosion. For TOWANDA a near-surface low velocity layer appears to have significantly influenced the spall depth.

It is interesting that they had the least success in modeling surface motions for HOUSTON - the event detonated in the hardest rock. Characterizing the calculations for this event as "largely unfruitful to this point in the study", they speculate what the problem may be: "we suspect that our modeling of subsurface spall is incorrect." In their model, subsurface spall occurs in all model elements where tensile stresses are developed. While this may be a good approximation for cohesionless alluvium (and appears to give a good simulation of observed ground motion) it can be questioned for crystalline rock. The tensile strength of crystalline rock should depend on the spectrum of preexisting fractures and reflect stress concentrations associated with growing cracks.

Stump and Weaver (1992) present further evidence that our current understanding of the spall phenomenon is not complete. They analyzed nuclear explosions detonated above the water table at Pahute Mesa, comparing spall zone velocities, displacements, and dwell times for consistency with a simple ballistic gravitational model. They found that the observed displacements may be as much as a factor of two to four timed greater than predicted by the observed velocities and dwell times, and speculate that this discrepancy may reflect the continuous nature of the spall process and/or the role of material strength in these phenomena.

INCORPORATING DAMAGE MECHANICS INTO A SPHERICALLY SYMMETRIC SOURCE SIMULATION

In the standard algorithms used to calculate the stress and strain paths in the source region of an underground explosion, the initial stresses are used in the equations of motion to find the displacements. These displacements are used to calculate the strains which are then used, with the elastic constants, to find the stress. The new stresses are then used in the equation of motion to find the displacements in the next time step, and so on. The incorporation of damage mechanics into this algorithm requires the introduction of a new variable, the damage defined in eqn. (5). As discussed above, damage is a measure of the fracture density in each material element of the model. In general damage is a tensor which reflects the distribution of fracture size and orientations at each location within the rock. However, for the simple spherically symmetric source, crack growth can be assumed to be radial.

The flow diagram for a computer algorithm which can be used to include damage in a spherical source is shown schematically in Figure 4. Each boxed procedure has been numbered and will now be discussed in turn.

Procedure 1: The Equations of Motion

Assume that we are beginning the i^{th} time step of the calculation. The stresses from the pervious time step, $\sigma_{\alpha\beta}^{i-1}$, are used to find the current displacements u_{α}^{i} , which, in turn, are used to compute the new strains, $\varepsilon_{\alpha\beta}^{i}$. This step is exactly as in the normal algorithm and is not affected by the incorporation of damage mechanics.

Procedures 2 & 3: The Elastic Constants and Stresses

The elastic constants are used to compute the new stresses $\sigma_{\alpha\beta}^{i}$ from the strains $\varepsilon_{\alpha\beta}^{i}$ found in Procedure 1 above. The elastic constants are a function of

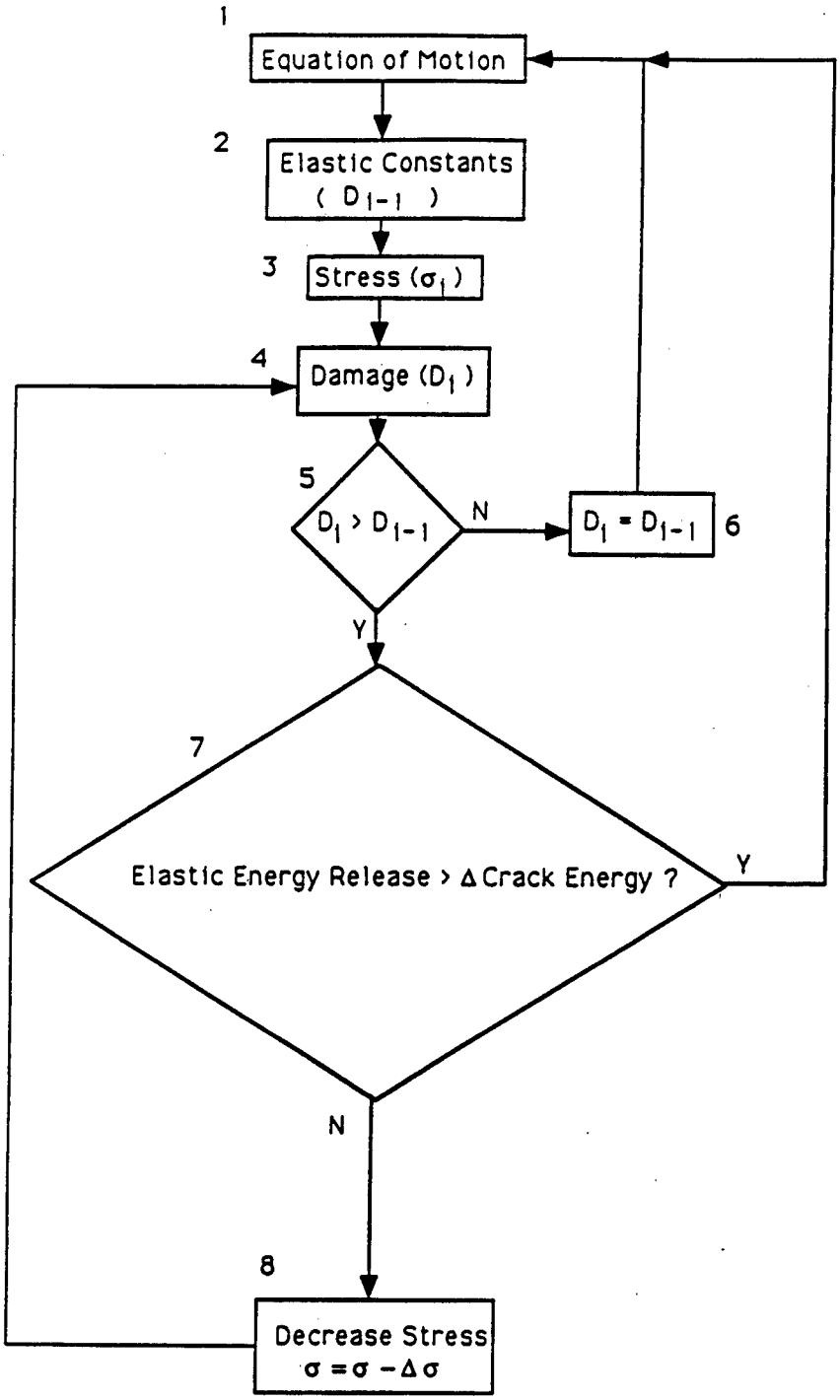


Figure 4. Flow diagram for a computer algorithm which may be used to incorporate damage mechanics into a spherically symmetric explosion source model.

the damage, and, they also depend on whether new damage is being done during the time step. Consider, for example, the stress-strain curve in Fig. 5. In this figure, the stress has been increased over the path labeled (1), decreased over path (2), and then increased again over paths (3) and (4). Note that the effective Young's modulus, $E = d\sigma_{11} / d\varepsilon_{11}$, is significantly lower over paths (1) and (4) where damage is increasing than it is over paths (2) and (3) where the stress is below that corresponding to the existing damage so that no new damage is being created. The hysteresis on the paths (2) and (3) is caused by frictional slip on the starter flaws (see Fig. 1), but the crack extension ℓ is constant over these paths.

For paths (2) and (3), where the cracks are not extending, the results of Budianski and O'Connell (1976) can be used to find the elastic constants as a function of the crack density. As shown in Fig. 6 (from O'Connell and Budianski, 1974), the elastic moduli decrease as the crack density increases. The crack density in their model is $\varepsilon = N_v \langle a^3 \rangle$, which may be expressed in terms of damage as (see equation (5))

$$D = \tfrac{4}{3}\pi\varepsilon \tag{8}$$

In Figs. 7 and 8 the Young's modulus and Poison's ratio predicted by the Budianski and O'Connell model are plotted as a function of the damage. They are both roughly linear and may be closely approximated by

$$E = E_o(1 - 0.425D) \tag{9}$$

$$\nu = \nu_o - 0.10D \tag{10}$$

where E_o and ν_o are the moduli of the uncracked solid.

In Procedure 2 of the algorithm in Fig. 4, the isotropic elastic moduli are calculated using the damage from the previous time step D^{i-1} in equations (9) and (10). These moduli are then used, with the current strains, $\varepsilon^i_{\alpha\beta}$, found in Procedure 1, to calculate the new stresses $\sigma^i_{\alpha\beta}$.

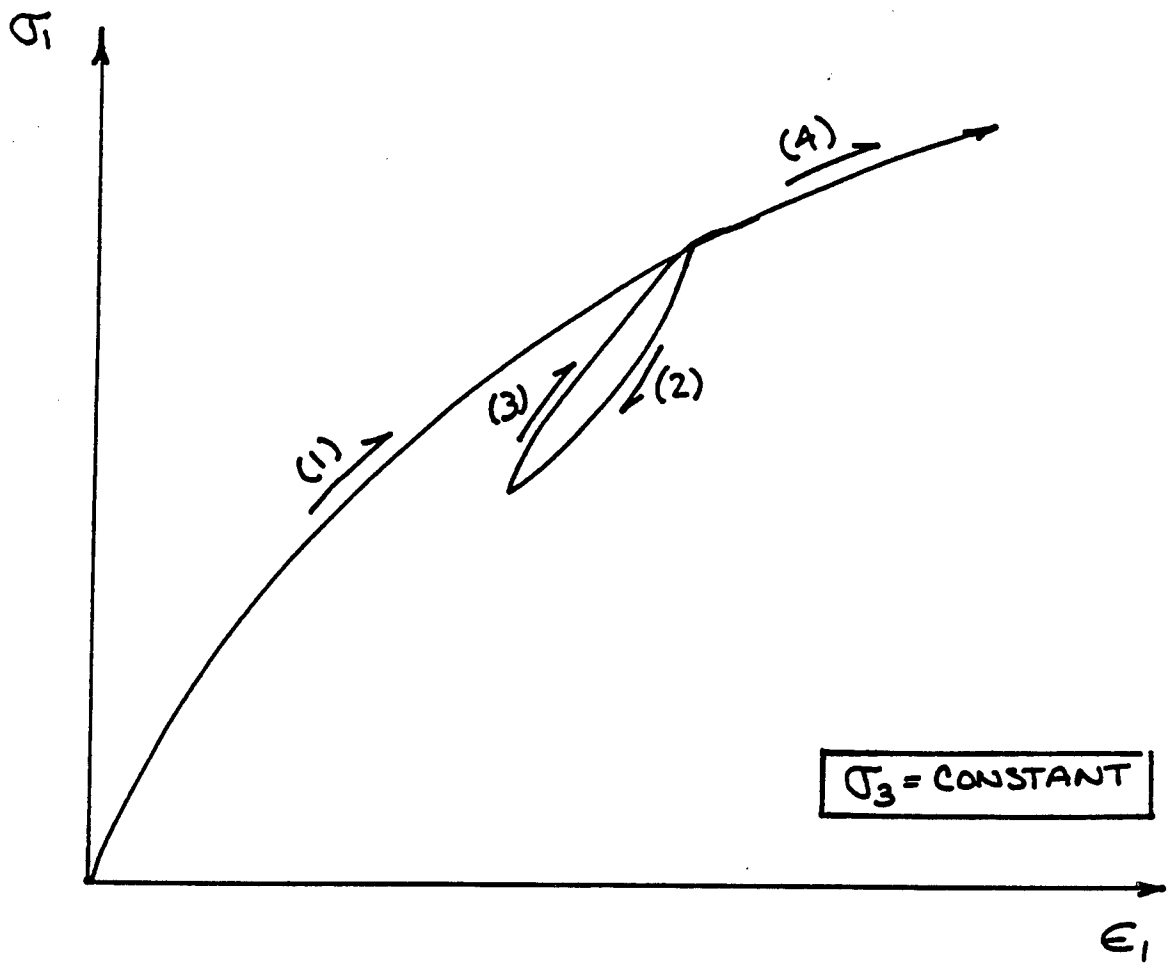


Figure 5. Schematic stress-strain curve illustrating the lower effective elastic modulus over paths (1) and (4) where crack growth is increasing the damage.

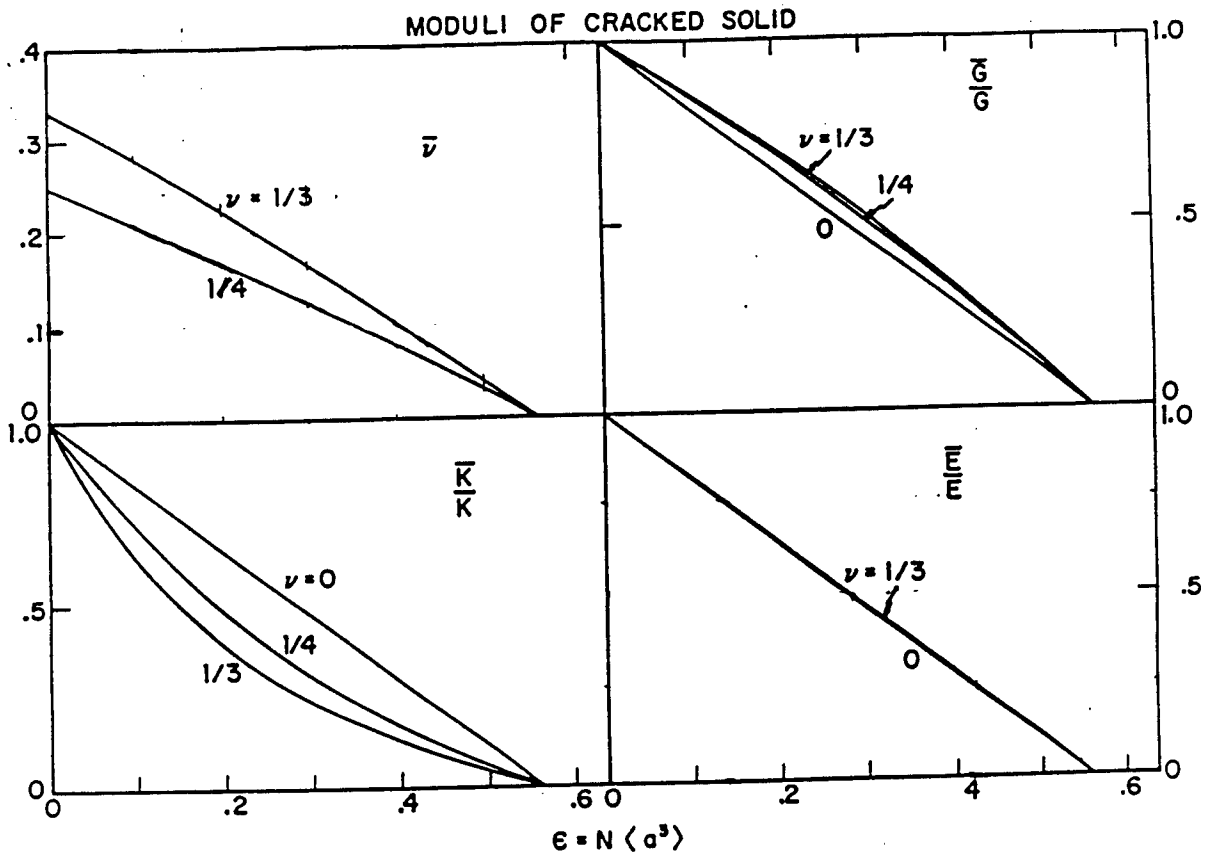


Figure 6. Decrease in the elastic moduli with increasing crack density (from O'Connell and Budianski, 1974).

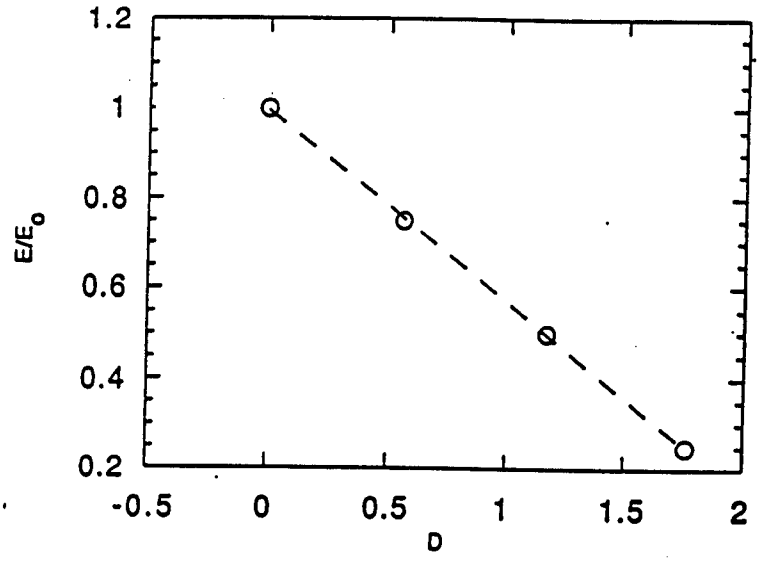


Figure 7 Young's modulus as a function of damage.

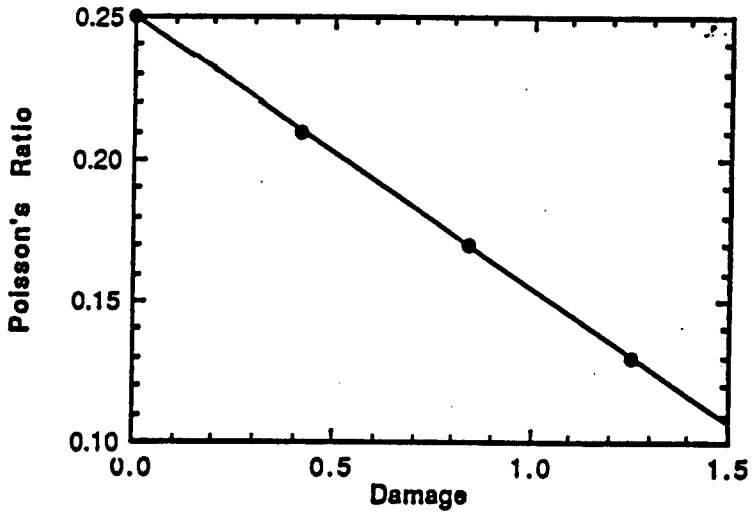


Figure 8 Poison's ratio as a function of damage.

Procedure 4: Calculating the Equilibrium Damage

The equilibrium damage D^i appropriate to the new stress state $\sigma^i_{\alpha\beta}$ is found using a table of damage as a function of the dimensionless pressure p and maximum dimensionless shear stress, τ. These dimensionless stresses are defined in terms of the dimensionless stresses $s_{\alpha\beta}$ as

$$\begin{aligned} p &= \tfrac{1}{3}(s_{11} + s_{22} + s_{33}) \\ &= \tfrac{1}{3}(s_{11} + 2s_{33}) \qquad \text{when } s_{22} = s_{33} \end{aligned} \tag{11}$$

$$\tau = \tfrac{1}{2}(s_{11} - s_{33}) \tag{12}$$

and K_{1c} is the critical stress intensity factor for mode I (tension) fracture.

Since Ashby and Sammis (1990) assume uniform deformation, the model is inadequate for the post-failure regime which is dominated by shear localization. We assume that D remains fixed beyond failure at its peak value, and that τ falls to its frictional value, τ_f, given by

$$\tau_f = \left(\frac{\mu}{\sqrt{1+\mu^2} - \frac{\mu}{3}} \right) p \tag{13}$$

Finally, the shear stress can never rise above the yield stress, σ_y, which is given by

$$\begin{aligned} \sigma_y{}^2 &= \tfrac{1}{2}\left[(\sigma_1 - \sigma_2)^2 + (\sigma_2 - \sigma_3)^2 + (\sigma_3 - \sigma_1)^2\right] \\ &= (\sigma_1 - \sigma_3)^2 \qquad \text{when } \sigma_2 = \sigma_3 \end{aligned} \tag{14}$$

The yield strength σ_y can be derived from the hardness, H, data since σ_y=H/3. At higher values of τ, strain is accommodated by plastic mechanisms which do not involve crack damage. It is thus possible that, at very high values of p, the material could yield while the damage remains at Do.

Procedure 5: Has the damage increased during the i^{th} time step?

If the damage D^i appropriate to $\sigma^i_{\alpha\beta}$ found in the previous step is less than or equal to D^{i-1} in the preceding time step, then it was correct to use the Budianski and O'Connell (1976) elastic constants given by Equations (9) and (10). As indicated in the flow chart (Figure 4) the $\sigma^i_{\alpha\beta}$ just determined in the i^{th} time step can then be used in the equation of motion (Procedure 1) to begin the i+1 time step.

However, if $D^i > D^{i-1}$, then the damage has increased during the i^{th} time step and the effective elastic constant should be less than that given by equations (9) and (10). In the following procedure we develop an algorithm to find the appropriate stress and damage for the strain $\varepsilon^i_{\alpha\beta}$.

Procedure 6: If the Damage Has Not Increased During the i^{th} Time Step

If the equilibrium damage associated with the new stress state $\sigma^i_{\alpha\beta}$ is less than the current damage (from the previous time step) D^{i-1}, then the damage remains unchanged and we set $D^i=D^{i-1}$.

Procedure 7: Adjusting the Stress and Damage if the Damage Has Increased During the i^{th} Time Step

If the equilibrium damage associated with the new stress state $\sigma^i_{\alpha\beta}$ is greater than the current damage (i.e., if $D^i>D^{i-1}$) then we must recalculate the stress. This is because the elastic constants used to find $\sigma^i_{\alpha\beta}$ from $\varepsilon^i_{\alpha\beta}$ are too large (since they assume no increase in crack density). We do this by relaxing $\sigma^i_{\alpha\beta}$ until the elastic energy released during the i^{th} time step is equal to the increased crack energy associated with the increase in damage

For clarity, we begin our analysis with the special case of uniaxial compression. We will then extend the results to 3-D. Consider an increment of

strain $d\varepsilon_{11}$ which is caused by the stress σ_{11}. The work done per unit volume is then

$$\sigma_{11} d\varepsilon_{11} = \sigma_{11} d\varepsilon_{11}^{e} + dW_c \tag{15}$$

The first term on the right is the work done over the elastic strain increment $d\varepsilon_{11}^{e}$; the second is the work done to extend the wing cracks. For $d\varepsilon_{11}^{e}$ we write

$$d\varepsilon_{11}^{e} = \frac{d\sigma_{11}}{E_o} \tag{16}$$

The work required to extend the wing cracks from ℓ to $\ell + \delta\ell$ is

$$dW_c = 2N_v \left(2\int_A^{A+\delta A} \frac{[K_I(\sigma_{11}, \ell)]^2}{E} dA \right)$$

$$\approx 4N_v \frac{K_{Ic}^{\,2}}{E} \delta A \tag{17}$$

In this expression A is the area per crack at the beginning of the i^{th} time step while δA is the increase in this area during the i^{th} time step. E is the effective Young's modulus appropriate for D^{i-1} (equation 9). K_I can be replaced with K_{Ic} since the cracks grow at the critical stress intensity. We can express A and δA in terms of the damage as

$$A = \frac{\pi(\alpha a)^2}{D_o^{\frac{2}{3}}} \left[D^{i-1}\right]^{\frac{2}{3}} \tag{18}$$

$$\delta A = \frac{\pi(\alpha a)^2}{D_o^{\frac{2}{3}}} \left\{ \left[D^{i}\right]^{\frac{2}{3}} - \left[D^{i-1}\right]^{\frac{2}{3}} \right\} \tag{19}$$

for N_V we write

$$N_v = \frac{3}{4\pi}\left(\frac{1}{\alpha a}\right)^3 D_o \tag{20}$$

Hence the crack energy becomes

$$dWc = \frac{3D_o^{\frac{1}{3}}}{\alpha a}\frac{K_{Ic}^{\,2}}{E}\left\{\left[D^i\right]^{\frac{2}{3}} - \left[D^{i-1}\right]^{\frac{2}{3}}\right\} \tag{21}$$

With these substitutions, equation (15) may be written

$$\sigma_{11}^i d\varepsilon_{11}^i \geq \frac{\sigma_{11}^i\left[\sigma_{11}^i - \sigma_{11}^{i-1}\right]}{E_o} + \frac{3D_o^{\frac{1}{3}}}{\alpha a}\frac{K_{Ic}^{\,2}}{E}\left\{\left[D^i\right]^{\frac{2}{3}} - \left[D^{i-1}\right]^{\frac{2}{3}}\right\} \tag{22}$$

As indicated in the flow diagram (Fig. 4), $\sigma_{11}{}^i$ is incrementally reduced, a new D^i calculated, and equation (22) reevaluated until it is satisfied. The relaxed $\sigma_{11}{}^i$ is then used in procedure 1 to begin the i+1 time step.

Now consider the case of interest: triaxial compression in which $\sigma_{11} > \sigma_{22} = \sigma_{33}$. In this case equation (15) becomes

$$\sigma_{11}d\varepsilon_{11} + 2\sigma_{33}d\varepsilon_{33} = \sigma_{11}d\varepsilon_{11}{}^e + 2\sigma_{33}d\varepsilon_{33}{}^e + dW_c \tag{23}$$

Writing $d\varepsilon_{33} = -\nu d\varepsilon_{11}$ we have

$$(\sigma_{11} - 2\nu\sigma_{33})d\varepsilon_{11} = (\sigma_{11} - 2\nu_o\sigma_{33})d\varepsilon_{11}{}^e + dW_c \tag{24}$$

If we again use eqn. (16) for $d\varepsilon_{11}^{e}$ and equation (21) for dW_c, eqn. (24) can be written:

$$(\sigma_{11}^{i} - 2\nu\sigma_{33}^{i})d\varepsilon_{11}^{i} \geq \frac{(\sigma_{11}^{i} - 2\nu\sigma_{33}^{i})\left[\sigma_{11}^{i} - \sigma_{11}^{i-1}\right]}{E_o} + \frac{3D_o^{\frac{1}{3}}}{\alpha a}\frac{K_{Ic}^{2}}{E}\left\{\left[D^{i}\right]^{\frac{2}{3}} - \left[D^{i-1}\right]^{\frac{2}{3}}\right\} \quad (25)$$

As in the uniaxial case, we relax σ_{11}^{i} and σ_{33}^{i} from their values predicted by the Budianski and O'Connell theory (equations (9) and (10)). For each incremental reduction we recalculate the equilibrium damage D^i and then reevaluated equation (25). The stresses and corresponding damage are adjusted until (25) is satisfied. These stresses are then used in Procedure 1 to begin the i+1 step.

This triaxial case presents one problem that has not been discussed. Both σ_{11}^{i} and σ_{33}^{i} (σ_{rr} and $\sigma_{\theta\theta}$ for the spherical source) may be relaxed, and it is not clear how to do this in a non-arbitrary way. This problem, however, is not unique to the damage formulation and must be faced in any model which has a failure surface. One of two approaches is usually used: radial return or normal return. In the radial return scheme, each stress is reduced an amount proportional to its size. The stress is thus reduced along a radius in p - τ space until the energy equation (25) is satisfied. In the normal return scheme, each stress is reduced in such a way that the return is normal to the failure surface and thus the reduction is along the shortest path in p-τ space. The radial return is usually chosen since it is easier to implement and no physical argument has been made for either scheme.

DISCUSSION

The algorithm developed in the preceding section should allow the model-based damage mechanics formulated by Ashby and Sammis (1990) to be incorporated into current numerical source simulation codes. The approach

taken in this paper has the advantages that it accounts for the size and density of preexisting fractures in the source rock in a physical way and allows the first-order effects of water saturation (i.e.. the reduction of sliding friction on preexisting fractures) to be investigated. However, as presently formulated, the damage mechanics we use is somewhat limited in that it assumes all fractures are the same size and it is based on equilibrium elastic fracture mechanics and thus ignores the effects of high loading rates on the stress intensity factor (Grady and Kipp, 1979; Rubin and Ahrens, 1992). The inclusion of these effects is conceptually straightforward and will simply add to the complexity of the algorithm.

Acknowledgments

This work was supported by Air Force Office of Scientific Research contract #F49620-93-1-0284 and by a subcontract from Lawrence Livermore National Laboratory's DOE contract #W-7405-ENG-48.

REFERENCES

App, F.N., Sensitivity of the close-in seismic source function to rock properties, Los Alamos National Laboratory Report LAUR-93-1884, May, 1993.

App, F.N., and W.M. Brunish, Modeling surface motion and spall at the Nevada test site, Los Alamos National Laboratory Report LAUR-92-400, January, 1992.

Ashby, M.F. and S.D. Hallam, The failure of brittle solids containing small cracks under compressive stress states, Acta metall., 34, 497-510, 1986.

Ashby, M.F., and C.G. Sammis, The damage mechanics of brittle solids in compression, PAGEOPH, 133, 489-521, 1990.

Budianski, B., and R.J. O'Connell, Elastic moduli of a cracked solid, Int. J. Solids struct., 12, 81-97, 1976.

Costin, L.S., A microcrack model for the deformation and failure of brittle rock, J. Geophys. Res., 88,9485-9492, 1983.

Costin, L.S., Damage mechanics in the post failure regime, Mechanics of Materials, 4, 149-160, 1985.

Day, S.M., N. Rimer, and J.T. Cherry, Surface waves from underground explosions with spall analysis of elastic and nonlinear source models, Bull. Seism. Soc. Am., 73, 247-264, 1983.

Day, S.M., and K.L. McLaughlin, Seismic source representation for spall, Bull. Seism. Soc. Am., 81, 191-201, 1991.

Dick, R.D., and W.L. Fourney, Effects of rock properties on explosive source modeling: preliminary results, Los Alamos National Laboratory Report LAUR-92-3277, September, 1992.

Eisler, J.D., and F. Chilton, Spalling of the Earth's surface by underground explosions, J. Geophys. Res., 69, 5285-5293, 1964.

Grady, D.E., and M.E. Kipp, The micromechanics of impact fracture of rock, Int. J. Rock Mech. and Mining Sci. Abst., 16, 293-302, 1979.

Horii, H., and S. Nemat-Nasser, Compression-induced microcrack growth in brittle solids: axial splitting and shear failure, J. Geophys. Res., 90, 3105-3125, 1985.

Horii, H., and S. Nemat-Nasser, Brittle failure in compression: splitting, faulting and brittle-ductile transition, Phil. Trans. R. Soc. Lond., A319, 337-374, 1986.

McLaughlin, K.L., T.G. Barker, S.M. Day, B. Shkoller, and J.L. Stevens, Effects of depth of burial on explosion and earthquake regional seismograms: regional discrimination and yield estimation, S-CUBED report SSS-R-88-9844, La Jolla, Ca., 1988.

Patton, H.J., Source models of the Harzer explosion from regional observations of fundamental-mode and higher mode surface waves, Bull. Seism. Soc. Am., 78, 1133-1157, 1988.

Rimer, N., J.L. Stevens, and S.M. Day, Effect of pore pressure, fractures, and dilatancy on ground motion in granite, S-Cubed Report SSS-R-87-8670, 1987.

Rubin, A.M., and T.J. Ahrens, Impact-induced tensional failure in rock, J. Geophys. Res., in press, 1992.

Sammis, C.G., and M.F. Ashby, The failure of brittle porous solids under compressive stress states, Acta metall., 34, 511-526, 1986.

Sammis, C.G., The formulation of a spherically symmetric source model based on a damage mechanics rheology, Proceedings of 12th DARPA/GL Seismic research Symposium, Key West Florida, 347-352, 1990.

Stump, B.W., Constraints on explosive sources with spall from near-source waveforms, Bull. Seism. Soc. Am., 75, 361-377, 1985.

Stump, B.W., and T.A. Weaver, Physical models of spall zone ground motions and the determination of spatial decay rates, Los Alamos National Laboratory Report LAUR-92-451, January, 1992.

Taylor, S.R., and G.E. Randall, The effects of spall on regional seismograms, Geophys. Res. Lett., 16, 211-214, 1989.

Walton, O.R., and F.E. Heuze, Discrete element modeling of explosions in jointed rocks, in Proc. DOE/LLNL Symp. Explosion-Source phenomenology, H.J. Patton and S.R. Taylor (Editors), Lawrence Livermore National Laboratory Report No. CONF-890398, 1989.

Planar Impact Experiments for EOS Measurements[1]

Michael D. Furnish, Sandia National Laboratories

Introduction

The community concerned with the numerical modeling of groundshock produced by underground nuclear tests must have access to materials data to benchmark models of rock behavior. Historically the primary source of these data has been planar impact experiments. These experiments have involved gun, explosive and electrical launchers. Other methods of introducing planar shocks include shock driving by in-contact explosives or laser bursts. This paper briefly describes gun launcher-based planar impact methods used to characterize geological materials at Sandia National Laboratories.

A very important part of these studies is the use of time-resolved interferometry techniques[1] for measuring shock wave structures. In addition to Hugoniot data, it has become possible[2] to obtain information about yield strengths, shock viscosity, release trajectories, multiwave structures, spall properties and the strength of materials in the shocked state. Techniques have been developed to determine the dynamic material properties at strain rates of 10^5 to 10^{10} sec^{-1} at stresses ranging from less than 1 GPa to about 250 GPa. In particular, rate-dependent effects and release hystereses can be characterized[3]. These sets of data are crucial in evaluating strain-rate-dependent viscoplastic or viscoelastic material models.

Impact Studies of Geological Materials

Groundshock studies generally involve geological materials, which pose special challenges for impact experiments. Most importantly, samples are likely to contain heterogeneities (mm or larger scale). These affect experiments in several ways. Often a buffer must be used between the sample and the diagnostic to protect the diagnostic from the effects of an uneven shock, as well as to average a signal passed through the heterogeneous sample. Samples must be selected with an eye toward having results represent the bulk of the available material, but at the same time the samples must be uniform enough to allow a meaningful experiment (restrictions which may be difficult to simultaneously satisfy). Sample selection generally favors the most homogeneous and competent samples, and as such may bias the results of any dynamic study of these materials.

The effects of heterogeneities are more important at lower pressures. This is true in laboratory-scale experiments where small-scale inhomogeneities such as selectively altered crystals may have a more marked effect on results at lower pressures than at higher pressures. It is also true in the field; as interest shifts from groundshock behavior close-in to an event ($\sigma > 100$ kb) to groundshock behavior in the stress region only slightly above the elastic limit ($\sigma \sim 1$ kbar), large-scale inhomogeneities such as joint systems become important.

Often water is an important component of the material of interest. When it is, the experiment may need to isolate the sample from vacuum, and possibly from gauges or reflective films as well. The sample may need to be machined without being allowed to dry. If the sample location is above the

1. This work performed at Sandia National Laboratories supported by the U.S. DOE (and partially by the Defense Nuclear Agency) under contract #DE-AC04-76DP00789.

water table, the sample may be partially saturated. Such partial saturations are extremely difficult to maintain, and the only practical avenue may be to choose an end-member saturation (dried or fully saturated) for the tests.

Other important experimental considerations for natural samples may include a need to preserve volatiles content (especially water), friability of a specimen rendering difficult its fabrication into a usable gas-gun sample, and whether the sample can withstand the kilogravity to megagravity environment of a gun launch without damage.

Experimental Configurations of Interest

The most generally usable configuration for gas-gun testing has a sample in the target, and is shown below. It is especially appropriate for measuring loading wave profiles, Hugoniot states and

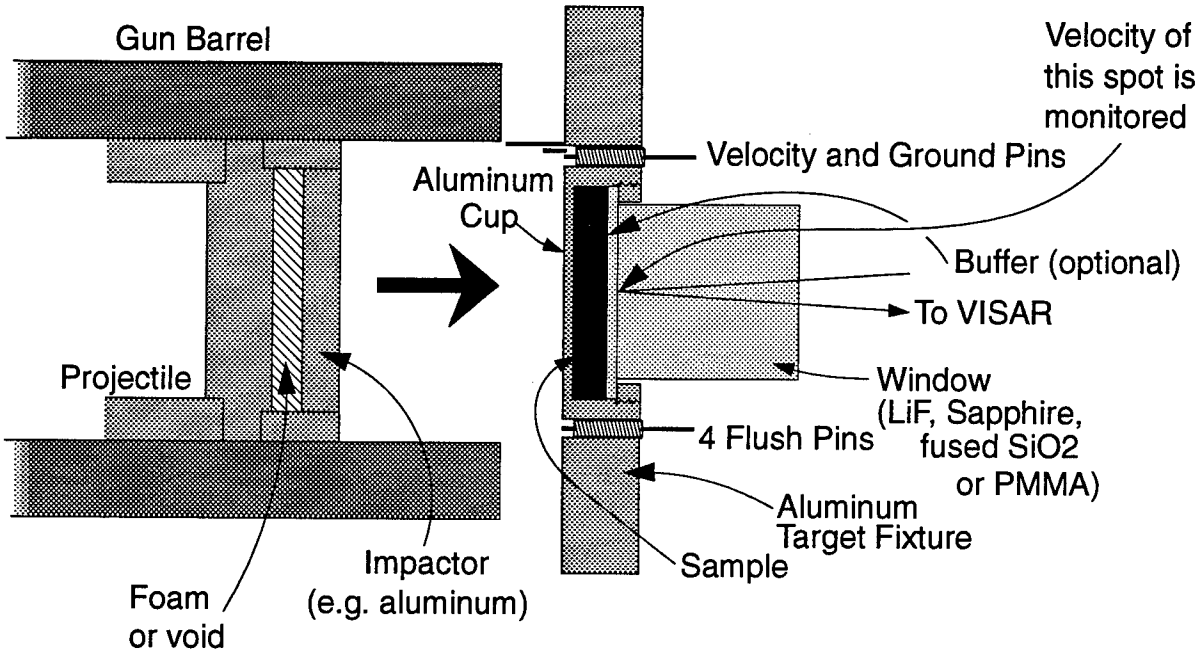


Figure 1. Forward Ballistic Configuration

strength properties (Hugoniot Elastic Limit for loading, the strength at the Hugoniot state, and the tensile or spall strength). If a window material can be chosen which is an approximate shock impedance match for the sample (such as Z-cut sapphire for iron, or lithium fluoride for slate or granite), a continuous release path may be measured; otherwise the pressure and particle velocity of a single point on the release (or reshock) of the sample may be determined. If the shock impedance of the window is chosen as much lower than that of the sample, spall properties of the sample may be measured as well as Hugoniot properties.

Analysis of the velocity profile from such a test consists of determining the precursor and Hugoniot states from the transit time across the sample (hence velocity of the observed waves), then extracting available release or spall information[4]. If the window is a fairly close impedance match to the sample and the waveforms entering and leaving the sample are known (easiest if no buffer is used), Lagrangian integration of the wave velocities yields a table relating stress, strain, time, shock velocity and wave velocity[3]. For many materials, the strain rate during loading varies approximately as the fourth power of the Hugoniot stress[5]. If buffers are used, wavecode modeling of the experiment to match the observed waveform may yield the pressure-volume path, although this procedure is somewhat more laborious[6]. If the window is a poor impedance match for the sample, the

average amplitude of the waveform "plateau" may be used with the Hugoniot of the window to calculate a single partial release or reshock state of the sample. Finally, if the sample has spalled, the amplitude of the pull-back signal may yield the spall strength of the sample[7].

For conditions where a window matching the shock impedance of the sample cannot be found, Hugoniot and continuous release paths may be measured using the geometry shown in Figure 2[4]. This configuration, called "reverse-ballistic,", has been used extensively for measuring Hugoniot and release properties of rocks and grouts. It may be used with water-saturated samples (as may the forward-ballistic configuration). Hugoniot states are derived by impedance matching, while release properties are extracted by modeling the experiment in a wavecode with an adjustable release description. This method does not give any direct information about loading characteristics, such as precursors and material strength, and in fact may give misleading results if incorrect assumptions about these quantities are made[4]. For example, if an unanticipated precursor is present, an impedance match calculation of the Hugoniot state will give correct values of pressure and particle velocity, but the shock velocity and density calculated from these under the steady-wave assumption will not be correct. Under certain conditions, however, a family of such tests can be used to determine precursor conditions. It is normally most useful if the dynamic strength of the material is small compared to the Hugoniot stress.

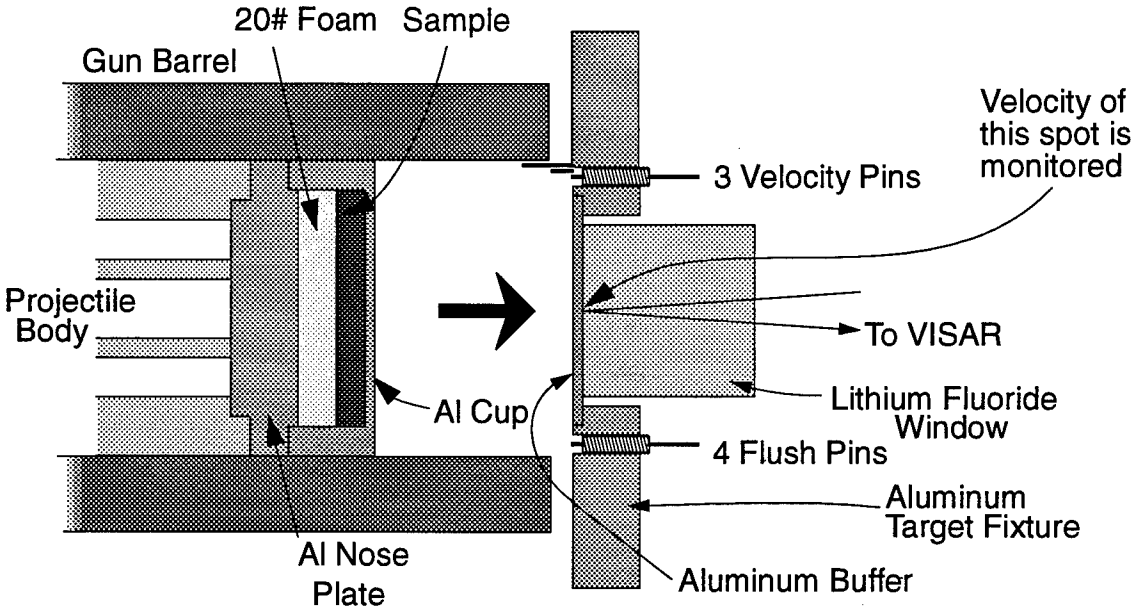


Figure 2. Reverse Ballistic Configuration

Strengths and Limitations of Gun Impact Tests for EOS Measurements

Let us make several general comments about gas-gun tests (where the term "gas gun" here includes powder guns and 2-stage light gas guns as well as compressed-gas guns). Fundamentally these tests are uniaxial strain tests of hand-specimen-sized samples. As such, they cannot readily assess large-scale properties of heterogeneous bodies, nor can they directly assess the effects of wave divergence (such as the role of hoop stresses in reducing mean stress and causing pullback). Various studies have been performed to assess the roles of heterogeneities, generally aimed to model or observe a system with one or a few simple structures, although the behavior of families of these features under high strain rates remains unclear (but of considerable importance for stresses near the elastic limit of these materials).

Wave divergence effects may be assessed with actual divergent wave environments. While such environments can be produced from impact experiments (e.g. propagating a shock along a rod), the more traditional divergent wave experiments (exploding wire or point charge) may allow a more straightforward relation to physical systems of interest.

On the other hand, gas-gun tests conducted to separate shear and longitudinal properties may be better experiments for benchmarking individual parameters in material models for calculating non-planar wave behavior. These tests normally require generating a plane shear wave by a tilt-impact or anisotropic shock-processing material (e.g. Y-cut quartz), then coupling this wave into the sample and out at the other side. For geologic materials, this coupling is more difficult to ensure than with more uniform solids. When such experiments can be made to work, they can constrain a large set of physical parameters describing the dynamic behavior of the material. They are able, as well to separate volume effects (such as phase transitions) from strength- and Poisson's ratio- effects such as the Hugoniot elastic limit and strength effects upon release. These effects generally cannot be separated in a simple longitudinal wave impact experiment.

Stresses are limited by the ability of window materials to remain transparent. The most common window materials in use, and their useful stress limits, are lithium fluoride (160 GPa +)[8], Z-cut sapphire (elastic to 14 GPa; may recover transparency above 50 - 60 GPa)[9], PMMA (20 GPa; has viscoelastic behavior)[10], and fused silica (8 GPa; produces ramp wave below 3 GPa)[9]. At low stress ranges (1 - 3 GPa), lithium fluoride is slightly affected by its elastic-plastic transition.

Within these constraints, gas gun tests are able to produce a wide range of materials properties data for materials undergoing high strain-rate deformation.

In summary, the following waveform illustrates representative properties which can be obtained for metallic or stony geological materials (represented here for a forward-ballistic test):

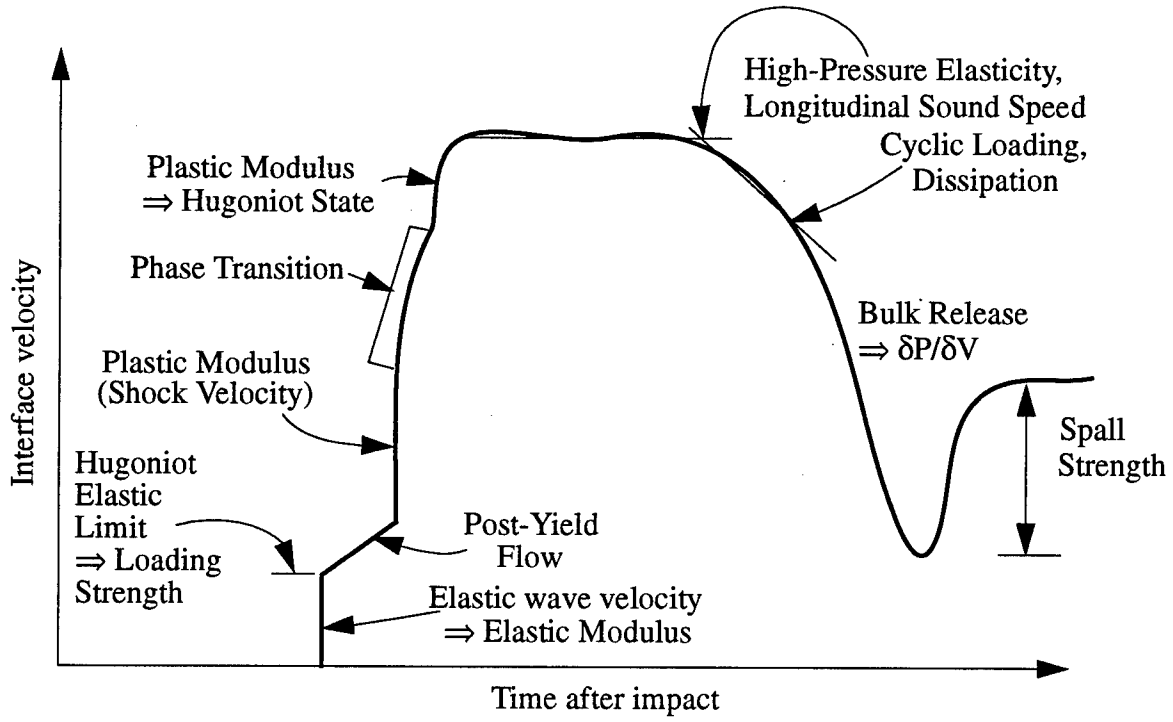


Figure 3. Correspondence Between Wave Features and Physical Properties

Acknowledgments

I am very happy to acknowledge the Defense Nuclear Agency (Experimental Shock Physics Office) for support for many of the impact tests I have been able to conduct, and the chance to learn from those tests. I especially thank Audrey Martinez and Eric Rinehart at DNA. I also happily acknowledge the tireless work of Ron McIntosh in heading up the actual operating of the guns and assembly of the tests for much of this work.

References

1. For a general description, see L. C. Chhabildas, Survey of diagnostic tools used in hypervelocity impact studies, Int. J. Impact Engng, 5, 205-220, 1987. The original reference is L. M. Barker and R. E. Hollenbach, Laser interferometer for measuring high velocities of any reflecting surface, J. Appl. Phys, 43, 4669-4675, 1972.

2. L. Davison and R. A. Graham, Shock compression of solids, Physics Reports 55, 255, 1979.

3. M. D. Furnish, L. C. Chhabildas, D. J. Steinberg and G. T. Gray III, Dynamic material properties of refractory materials: Molybdenum, pp. 229 - 240 in High Strain Rate Behavior of Refractory Metals and Alloys, R. Asfahani, E. Chen and A. Crowson (eds.), The Minerals, Metals and Materials Society, 1992.

4. M. D. Furnish, Recent advances in methods for measuring the dynamic response of geological materials to 100 GPa, Int. J. Impact Engng, (proceedings of 1992 Hypervelocity Impact Symposium), in press

5. J. W. Swegle and D. E. Grady, Shock viscosity and the prediction of shock wave rise times, J. Appl. Phys., 58, 692, 1985.

6. M. D. Furnish, Measuring the dynamic compression and release behavior of rocks and grouts associated with Hydro-Plus, Sandia National Laboratories report, SAND92-0984, in press.

7. L. C. Chhabildas, L. M. Barker, J. R. Asay and T. G. Trucano, Spall strength measurements on shock-loaded refractory metals, pp. 429-432 in Shock Compression of Condensed Matter - 1989, S. C. Schmidt, J. N. Johnson and L. W. Davison (eds.), Elsevier Science Publishers, 1990.

8. J. L. Wise and L. C. Chhabildas, Laser interferometer measurements of refractive index in shock-compressed materials, pp. 441-454 in Shock Waves in Condensed Matter, Y. M. Gupta (ed), Plenum, 1985.

9. L. M. Barker and R. E. Hollenbach, Shock-wave studies of PMMA, fused silica, and sapphire, J. Appl. Phys., 41, 4208-4226, 1970.

10. K. W. Schuler and J. W. Nunziato, The dynamic behavior of polymethyl methacrylate, Rheol. Acta, 13, 265-273, 1974.

THIS PAGE INTENTIONALLY LEFT BLANK.

LARGE SCALE HUGONIOT MATERIAL PROPERTIES FOR DANBY MARBLE

Eric J. Rinehart

Experimental Shock Physics
Defense Nuclear Agency
Kirtland AFB, MN 87115

OBJECTIVES:

HYDROPLUS, which is the methodology for nuclear underground testing yield verifications of non-standard tests, requires accurate stress and particle velocity measurements. The methodology (Reference 1) also requires material properties and equation-of-state (EOS) measurements of geologic materials. EOS measurements are to be obtained from laboratory sample, gas gun testing.

The objective the DISTANT MOUNTAIN test series was to demonstrate the accuracy of stress and velocity measurements in hard, low porosity rocks. The tests also provided a comparison of large size (almost in-situ) material properties with those obtained from laboratory testing of the same material and of materials considered to be nearly identical. Finally, this test series addressed the problems posed by a material having a clear precursor wave preceding the main shock wave.

A requirement for this test was to provide a large scale high explosive (HE) test bed. The experiment should have planar loading so that a clear comparison of stress, particle velocity, and shock velocity could be made. The material used in the test should have a well known phase transition or H_{el} so that a predictable precursor was established. Finally, the material should not be dependent upon what filled the air voids so a low porosity rock was needed. Saturating the rock could not be easily done in the field.

The test series consisted of three individual tests. The first test, DM1, established the material properties of the marble. The second two tests looked at stress and velocity gage errors obtained when gages were placed in bore holes and grouted. Each test was identical and gages used in the last two tests that were placed in contact with the rock (not in the bore hole) could also be used to look at consistency of gages in different, but material from the same quarry, that is similar material.

This paper only reports on the material properties gained and the errors that may be associated with stress and velocity measurement.

EXPERIMENT DESIGN:

To meet testing requirements, low grade, commercially available Danby Marble was chosen. Physical property testing indicated homogeneity, low voids and a dry material. Previous small scale testing had been done to high pressures so that an initial EOS was known for test design.

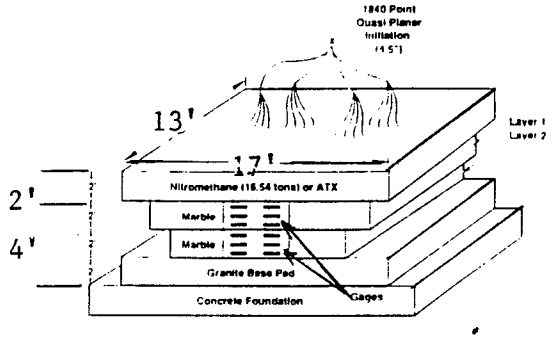


Figure 1. Test bed layout.

The test design concept is shown in Figure 1. The test bed size was chosen to allow full scale in-material gages in the test bed. Since linear dimensions scale as the cubed root of the charge size doubling or halving of the charge does not really make a substantial difference. About 20 T was considered the need. Two dimensional lateral (relief effects) were considered. Lateral dimensions were calculated such that 50 μsec of 1-D plane strain could be assured at a depth of 3.5 feet. Consideration was also given to the propagation of the precursor.

Blocks of the marble were designed and fabricated so that gage elements could be placed "in the rocks" and for convenience of test construction. Calculations indicated that spaces between blocks should be kept less than 0.01". For voids greater than that, the precursor might be lost or shock attenuation might be unacceptable. The blocks were to be level because liquid explosive was to be placed in direct contact with the marble.

Approximately 20 T of nitromethane was chosen as the driver. A 24" thickness provided sufficient shock durations and an attenuation rate with respect to depth such that gages recorded stresses in the 100 to 50 Kbar range. Bottom initiation of the nitromethane would provide a square topped wave-form, but shock arrival jitter developed from firing the pool at once could not be tolerated. Thus, top initiation was decided upon. Calculations of the dimensions of a hexagonal booster pattern clearly showed that (to $\pm 2\%$) a planar wave in both amplitude and arrival would be established with a 4½ inch spacing. Each booster contained 100 g of C-4 explosive.

Testing results showed that the explosive performed exceptionally well. Time differences across the test bed did not exceed 1.6μs (s.d.). No jitter was noted in the stress or velocity measurements.

INSTRUMENTATION:

Measurement of the shock wave was made at 6" intervals. Estimates of particle velocity (U_p) and stress (P)[1] were made. The types of gages and the geometry used allowed redundancy checks of U_s and P, if U_p was also measured. The two primary gages used were flat packs for stress and the KRATZ gage for particle velocity (Figure 2). Time-of arrival (TOA) at the stress gages and at elements in the KRATZ gages provided U_s. Details of the electronics, etc., are beyond the scope of this paper.

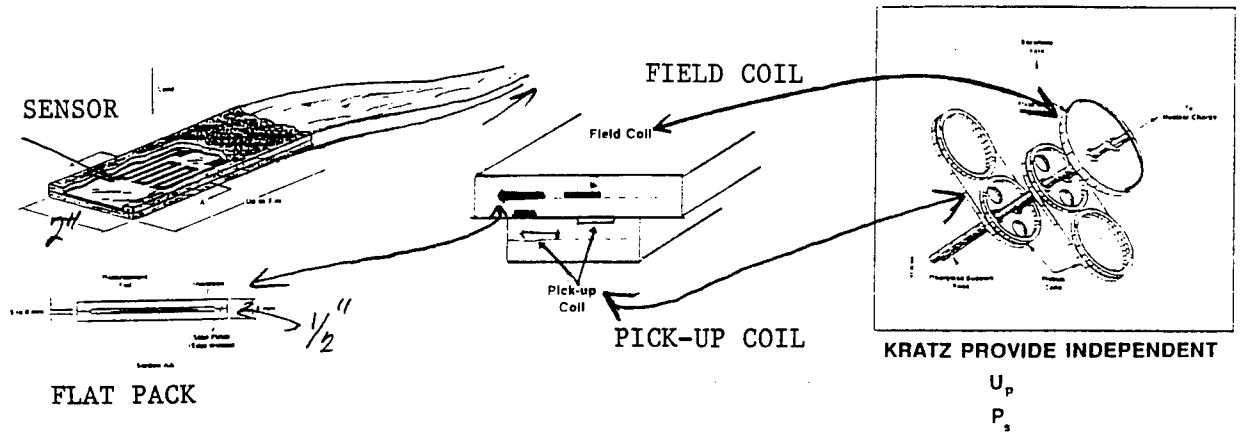


Figure 2. Showing the two primary gages used in these tests.

Stress flat packs consist of piezoresistive sensitive material sandwiched between insulators and hardened steel plates. Because of the mismatch of the marble, the steel, insulators, and sensing element, a ring-up period of a few microseconds was necessary before free field measurement of stress was assured. The stress flat packs were epoxied in grooves machined into the limestone blocks. Strain sensors, a part of the flat pack, indicated arrivals of non-1-D effects. The stress flat packs were identical to those being fielded on HYDROPLUS.

Particle velocity and shock velocity, at a point, were measured with KRATZ gages. The KRATZ gage consists of one field coil and up to three pick-up coils. The pick-up coils sense the movement of the field coil and report, up to shock arrival at the pick-up coil, the particle velocity of the field coil which is the same as the free field. Knowing the distance between the field coils and pick-up coils, along with the shock destruction time of the pick-up coil, gives an independent measure of shock velocity. Thus, the $P = \rho_o U_p U_s$ plane wave equations-of-motion gives an independent measure of pressure. Individual field and pick-up coils were epoxied into machined grooves in the rocks. Gage details are given in Reference 1.

TEST RESULTS:

One set of stress time histories are shown in Figure 3. (Additional stress measurements were made on all three events.) Things to note are: 1) high peak due to gage/rock impedance mismatches[2], 2) precursor, 3) long durations, and 4) consistent stress attenuation with respect to depth. Peak stresses were obtained by intersecting the rise to peak with a line drawn along the smooth time decay. Because the gages are placed directly in the rock, no bore

---

[1] It is recognized that vertical stress was measured. Since measured strengths of only 5 kbar were noted, it is convenient to use P for pressure.

[2] That this is clearly true was shown by using a thin stress gage with no armor. Although the gage failed early, the high peak did not exist. Calculations also imply that the peak is real, but due to gage/rock mismatches.

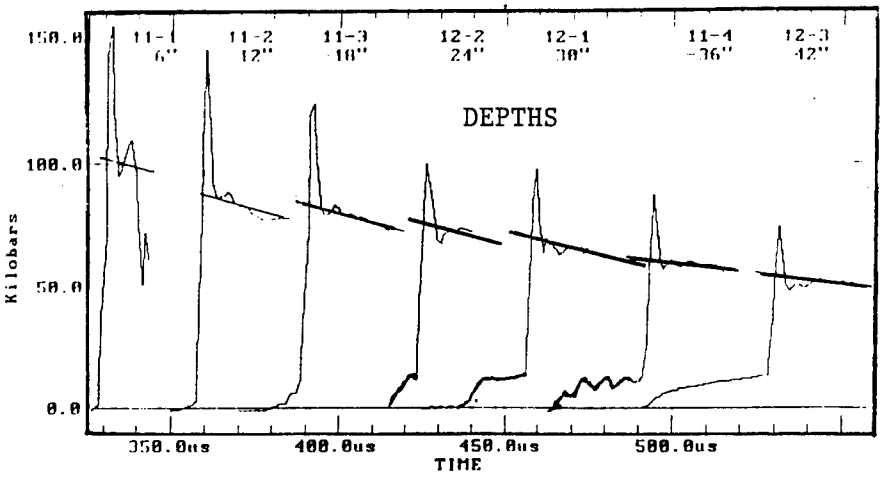


FIGURE 3. Stress time histories for DM-1.

hole interactions are expected. Three stress measurements from the three different tests, but at identical levels, show the consistency of data (Figure 4). Stress measurements are reported to within 10% of each other using

$$\text{Error} = \frac{1}{n}\left(\left(P_m^2 - P_a^2\right) / P_a^2\right)^{1/2}$$

where P is pressure, m is measurement, and a is average. One set of pick-up KRATZ velocity measurements for a field coil placed at 2 ft is shown in Figure 5. Note: the precursor, the reproducibility, and the duration. (In HYDROPLUS the duration of velocity measurements is not expected to last beyond the transmission of the shock across the bore hole. The plane strain in this test probably increase survival times.) Also, note that the arrival of the precursor at the middle of the first pick-up coil causing a detectible reduction in apparent velocity. This reduction is not to be confused with true release of the material but is only an artifact of the type of gage used. Estimates of particle velocity errors are in the 10% range although the number of gages was not as great as stress gages so that a detailed error analysis could not be done.

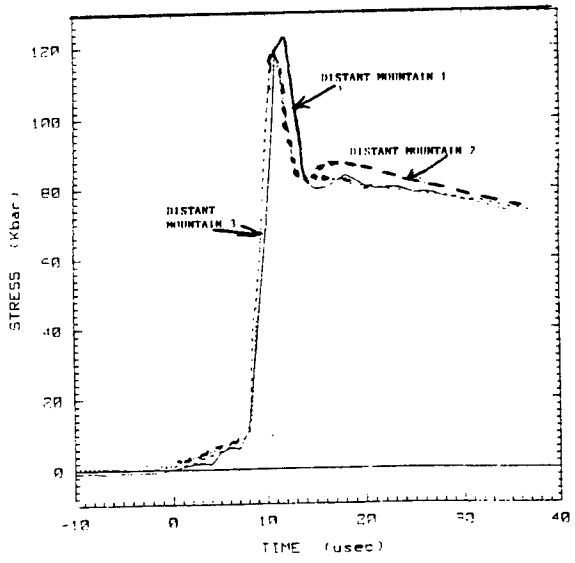


Figure 4. Stress history comparison for three field experiments. Peak stress in the free field is 82 kbar.

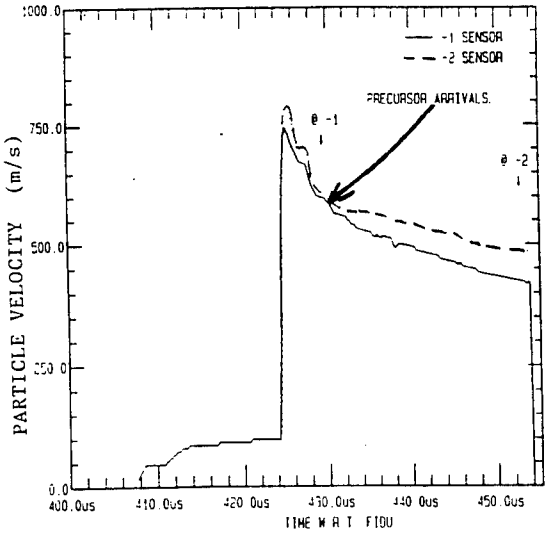


Figure 5. Comparison of two KRATZ pick-up coils. Note decay is due to arrival of precursor.

A direct comparison of stress and particle velocity for a depth of 2' was possible in test 1 (Figure 6). Velocity is read along the right axis and stress along the left. Conversion of stress to velocity has not been done. Note, the differences in arrival times of the initial precursor created by strength limits; note the identical arrival times of the main shock. These data clearly show that initial TOA, even when taken from gages carefully machined in rock material do not appear consistent. The material must fail and close around the gage ($P > H_{el}$) before any consistent TOA can be estimated. Details of the precursor suggest strength limits of approximately 6.7 Kbar and phase transitions from Calcite I to Calcite II at 11.3 Kbar, for large samples (Figure 7).

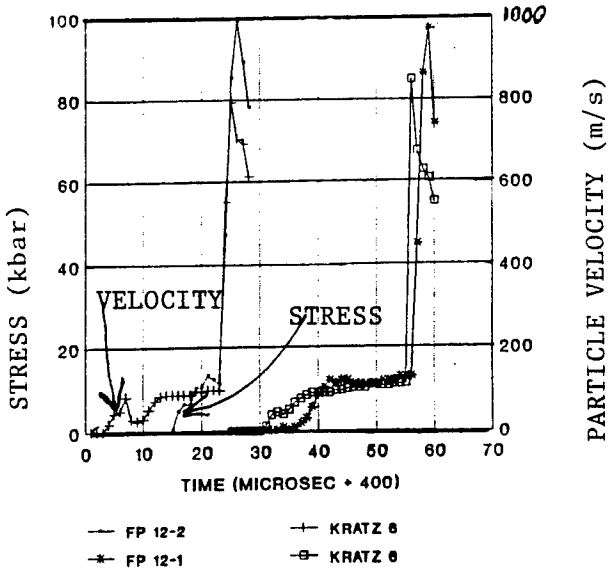


Figure 6. Comparison of stress and particle velocity histories.

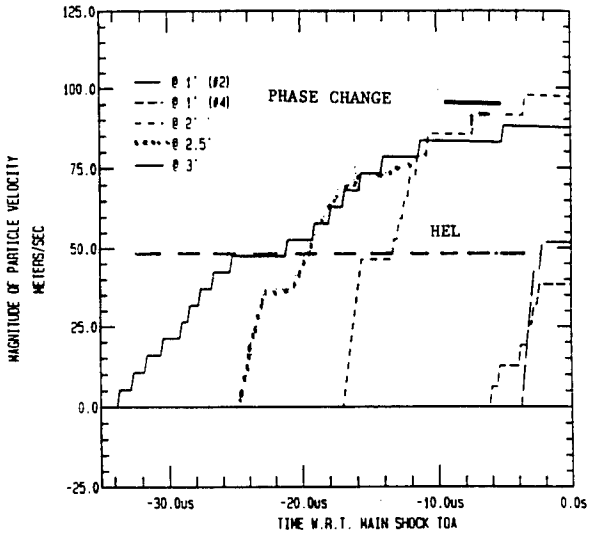


Figure 7. Close-up of presursor velocity wave form. Note strength and phase changes.

Arrival times, peak stresses from flat pack and KRATZ gages, and particle velocities from KRATZ gages are shown plotted with respect to range in Figure 8. Data from three field tests were used where the measurements were taken in the rock. (No bore hole measurements were used in this analysis.) Linear fits to the data were found applying least squares criteria. Other statistical models were tried, but the errors attributed to randomness were not substantially lowered so a linear statistical model was used.

The fits are:

$$\text{Range} = 1.72 - 0.0157P$$

$$\text{Range} = 1.73 - 0.0189U_p$$

$$\text{Range} = 3.80 - 6.89\ E - 4\ U_s$$

for pressures $50 < P < 100$ kbar..

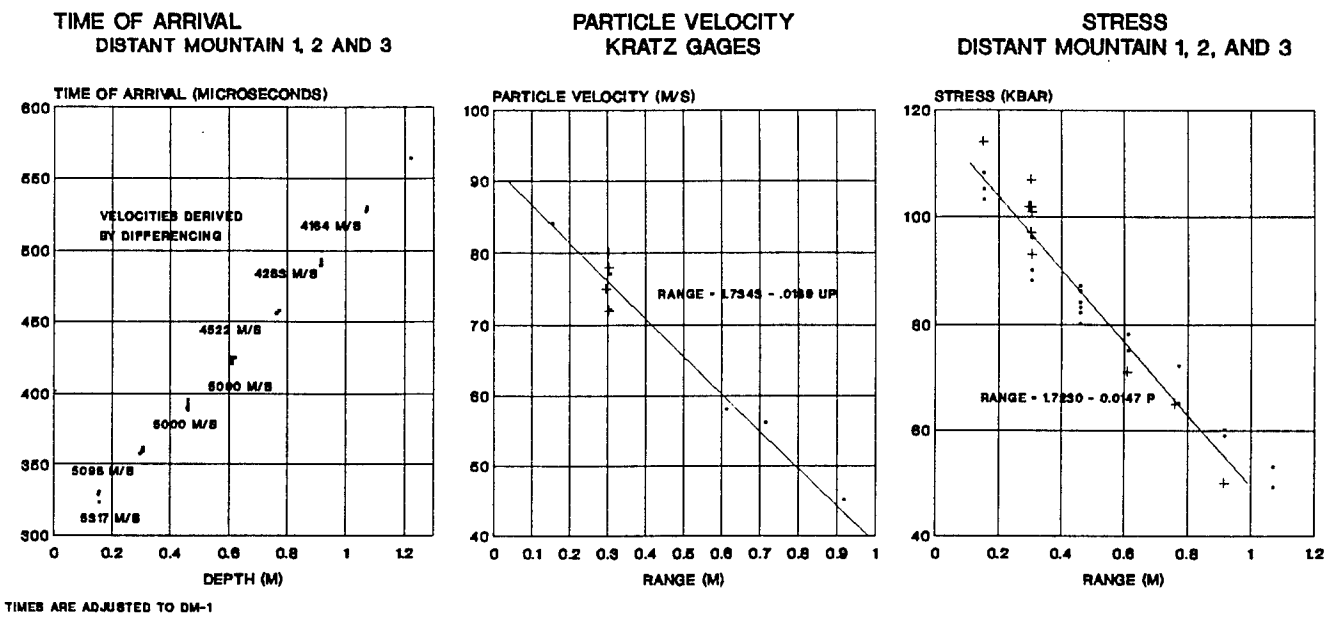


FIGURE 8. Data from all three DM Tests. Linear fits found using least squares method. Alternative statistical models were not warrented.

Combining the fits and setting ranges equal, we have

$$P = -0.68 + 1.29\ U_p \qquad \text{for } 50 < P < 100 \text{ Kbar}$$

$$U_s = 3004 + 27.4\ U_p$$

$$C = 5979 \text{ m/s at } P = 11 \text{ Kbar}$$

Where P is in Kbar, U_s and U_p are in m/s, and C is the elastic wave speed of the precursor due to the strength limit. These equations are the best least squares fitting estimates of U_p vs U_s and P vs U_p for the field (not point by point) assuming a linear statistical model.

EQUATION-OF-STATE:

Figure 9 contains all dry calcite, limestone, and marble data contained in the DNA data base. Overlain on these data are the best fit P vs U_p equations and data taken individually from the KRATZ gage. Also shown are data obtained from gas gun, small sample estimates.

The large DM test data is consistent with gas gun data. The overall error of the large sample data is approximately the same as laboratory data. The marble data is different from data obtained from small scale, calcite, single crystal data.

CONCLUSION:

1. Precursors can propagate in large block samples. The precursors can interfere with knowing accurate arrival times of the main shock and stress corresponding to strength limits and phase changes.

2. Errors in stresses and velocity measurements do not exceed 10% for well planned field tests. This error was intra-test and inter-test. But these errors do not include physical problems in grouting gages in bore holes.

3. Materials known to have precursors will measure a constant shock and particle velocity with respect to range until the strength or phase changes occur. The constant particle velocity was used on following test as a velocity gage validation method--one knows what the velocity really is.

4. Large sample EOS data are consistent with gas gun data.

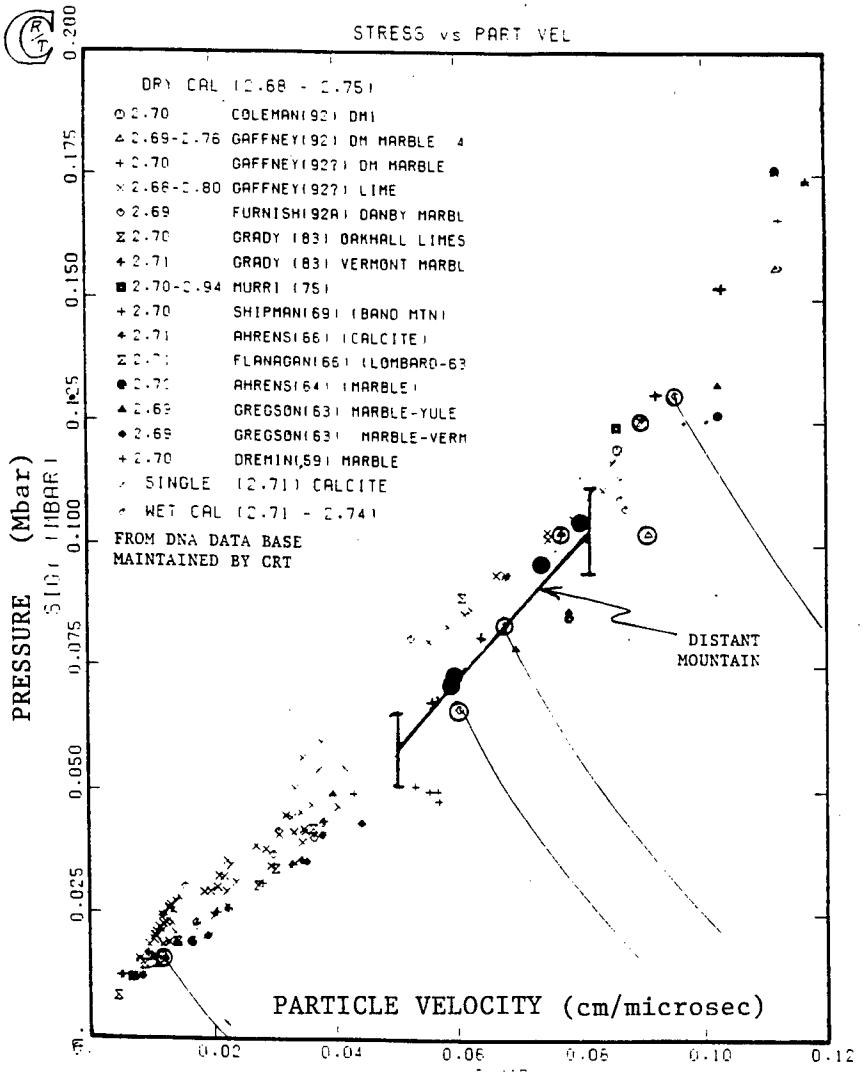


FIGURE 9. Pressure versus particle velocity for DM.

ACKNOWLEDGEMENTS:

Any large scale field test includes numbers of players. SRI International (D. Keough and P. DeCarli) integrated the field test and provided the stress gages and rock quality control. I often wonder if P. DeCarli was just jesting when he suggest these tests over a beer. S-CUBED (P. Coleman) made and fielded the KRATZ particle velocity gages. New Mexico Engineering Research Inst. (N. Baum) designed and placed the explosives .

REFERENCE:

Defense Nuclear Agency, HYDRO PLUS Applications Handbook, Draft, March 21, 1991.

Experimental and Theoretical Studies of Spectral Alteration in Ultrasonic Waves Resulting From Nonlinear Elastic Response in Rock

P. A. Johnson, K. R. McCall, and G. D. Meegan, Jr.

Earth and Environmental Sciences Division, MS D443, Los Alamos National Laboratory,
Los Alamos, New Mexico 87545, USA

Experiments in rock show a large nonlinear elastic wave response, far greater than that of gases, liquids and most other solids. The large response is attributed to structural defects in rock including microcracks and grain boundaries. In the earth, a large nonlinear response may be responsible for significant spectral alteration at amplitudes and distances currently considered to be well within the linear elastic regime.

Recordings of seismic waves at various distances from the source are used to estimate the magnitude of the source, characterize high frequency roll-off and model source parameters. It is generally assumed that beyond a few source radii, seismic waves propagating outward from the source reside in an elastically linear material, i.e., in a material that has a linear relationship between stress and strain. A nonlinear relationship between stress and strain (nonlinear elasticity) implies wave multiplication leading to the creation of sum and difference frequency waves, i.e., the failure of wave superposition. Thus, if seismic waves propagate at sufficient strains in a suitably large volume for nonlinear elastic effects to be important, then important features in a seismogram will be modified by elastic nonlinearity. Estimates of magnitude, assessment of roll-off, and models of source parameters should be consistent with nonlinear elastic behavior.

Several laboratory studies of nonlinear elastic behavior in solids already exist[1]. These studies show that spectrum alteration in the form of harmonics increases with wave propagation distance. However, study of nonlinear elastic behavior in rock is relatively new[2-9]. In contrast to most solids, rock is strikingly heterogeneous on scales from millimeters to tens of meters due in part to structural defects in the form of microcracks, grain boundaries and fractures. These structural defects cause a large compliance and therefore a large nonlinear elastic response in rock. As a result, the cubic anharmonicity (the first order nonlinear elastic contribution) in rock is typically many orders of magnitude greater than in other solids[2,7,10].

Our goal in this work is to examine the extent to which source frequency content is altered during nonlinear seismic wave propagation. To this end, we have conducted ultrasonic experiments to study the spectral changes that take place along the wave propagation path. For a

plane wave propagating in an elastic material with cubic anharmonicity, the amplitude of the 2ω harmonic is proportional to xk^2U^2, where x is the propagation distance, $k = \omega/c$ is the wave vector, and U is the displacement amplitude of the source at frequency ω. Our initial experiments focused on confirming this result. We confirmed that the amplitude of the 2ω harmonic scaled with x. At fixed x, the amplitude of the 2ω harmonic scaled as frequency squared (k^2) and as source amplitude squared (U^2). Thus the fundamental prediction for the behavior of the 2ω harmonic in rock was confirmed. The compressional nonlinear modulus β was measured to be $-7000 \pm 25\%$ ($|\beta|$ is less than 10 for most solids[1,10]). We also observed the strong growth of odd harmonics 3ω and 5ω, suggesting that a higher order term in the stress-strain relationship (quartic anharmonicity) may be necessary to give a complete theoretical description of nonlinear elastic behavior in rock. We argue, based on our observations at ultrasonic frequencies, that the effect of nonlinear elasticity on seismic wave propagation may be large, and should be considered in modeling.

Theory

The equation of motion for a homogeneous elastic solid, to second order in the displacement (cubic anharmonicity in the elastic moduli), is derived in several texts[11,12,13]. The inclusion of linear attenuation leads to a straightforward modification of this equation[14,15,16]. For a longitudinal plane wave propagating in the x-direction, the equation of motion in the absence of attenuation is[16]

$$\frac{\partial^2 u(x,t)}{\partial x^2} - \frac{1}{c^2}\frac{\partial^2 u(x,t)}{\partial t^2} = -\beta \frac{\partial}{\partial x}\left(\frac{\partial u(x,t)}{\partial x}\right)^2, \qquad (1)$$

where β is the nonlinear coefficient defined as

$$\beta = \frac{3(\lambda+2\mu)+2(l+2m)}{2(\lambda+2\mu)},$$

$u(x,t)$ is the displacement, c is the compressional velocity, λ and μ are second order elastic moduli (Lame coefficients), and l and m are third order elastic moduli (Murnaghan coefficients).

The term on the right hand side of Eq. (1), the (nonlinear) interaction of the displacement with itself, causes the creation of sum and difference frequency waves. Equation (1) can be solved analytically, for example, by an iterative Green function technique[15]. Solution to this equation for a source at the origin of frequency ω and amplitude U is, to first order in the nonlinearity,

$$u(x,t) = u_0(x,t) + u_1(x,t) = Ue^{i(kx-\omega t)} + \frac{\beta U^2 k^2 x}{2} e^{i(2kx-2\omega t)}, \qquad (2)$$

where $u_0(x,t)$ is the displacement solution to the linearized equation of motion and $u_1(x,t)$ is the first order correction to $u_0(x,t)$ due to the nonlinear interaction. Note that a source at the origin of frequency ω and initial displacement amplitude U generates a plane wave at frequency ω with amplitude U and a second plane wave at frequency 2ω whose amplitude grows linearly with the distance of propagation x, the square of the fundamental wavevector k and the square of the fundamental amplitude U. In our experiment, we test for these signatures of a 2ω harmonic due to cubic anharmonicity.

Experimental Apparatus

The apparatus used in the experiments is shown in Figure 1. A 2 m long by 6 cm diameter rod of Berea sandstone was used for the experiments. One end of the sample was tapered in order to minimize reflections. To accommodate the detectors (pin transducers), 11 small holes were drilled into the rod at 5 cm intervals, up to a distance of 58 cm from the source transducer.

A self-monitoring drive transducer composed of a piezoelectric crystal with a backload and capable of direct displacement measurement was constructed for use as the source[9]. A small diameter hole was drilled through the center of the backload and transducer and a fiber optic probe was positioned in the hole to directly measure the rock displacement at the source. This probe is sensitive to 10^{-9} m over a frequency range of 0–200 kHz.

The source transducer was amplified and driven with a single frequency, amplitude modulated N cycle wave train; N ranged from 8 to 24. Frequencies of 8 to 24 kHz were used and care was taken to assure that the measured signals were not contaminated by reflections from the opposite end of the sample. Detected signals were output to a 16 bit waveform analyzer. Source displacements ranged from 10^{-9}–10^{-6} m. Strain levels at the source were measured to be $6–60\times10^{-6}$, and, at the limit of the measurement range (58 cm), strain levels were $0.6–9\times10^{-6}$.

Experimental Observations

The most fundamental experimental observation providing evidence for nonlinear elastic behavior in the sample is shown in Figs. 2 and 3. Fig. 2 shows the frequency spectrum measured at the source for a drive frequency $\omega/2\pi$ of 13.75 kHz. The five different curves correspond to five amplitudes of the source transducer varying over a factor of approximately 50. The source displacement spectrum is relatively monochromatic containing only a small fraction of 2ω at large drive levels (from electronic distortion). Fig. 3 shows the displacement frequency spectrum at 58 cm, also at increasing drive level. For detected displacements at the fundamental

frequency as small as 10^{-8} m, the composition of the displacement frequency spectrum at 58 cm is extremely rich in harmonics not present at the source, out to at least 6ω. Further, these higher harmonic displacement fields have amplitudes that are a sensitive function of the drive amplitude. Similar results were obtained for 30 frequencies in the range 8–24 kHz.

In order to emphasize how little wave distortion is required to produce the harmonics shown in Fig. 3, Fig. 4 shows a portion of the time signal at large input drive level collected at 58 cm (large amplitude solid line) in relation to a pure sine wave of equal amplitude (dashed line). The difference between the two signals is the low amplitude solid line.

The amplitude of the displacement field at 2ω was found to increase linearly with source-receiver distance x. A representative result is shown in Fig. 5, where the relative amplitude R of the 2ω harmonic is plotted as a function of distance from the source transducer for a 13.75 kHz drive. R is the ratio of the amplitude u_1 at 2ω (source frequency of ω) to the amplitude u_0 at 2ω (source frequency of 2ω). This ratio was taken in order to correct for detector site effects and intrinsic attenuation. According to Eq. (2), this ratio is proportional to the propagation distance:

$$R = \frac{|u_1(x,2\omega)|}{|u_0(x,2\omega)|} \propto x \, . \tag{3}$$

The results in Fig. 5 confirm this prediction. Measurements throughout the frequency range 8–24 kHz showed similar results. [The fluctuations about the fit line in Fig. 5 are attributed to positional and frequency dependent elastic scattering from the periodic array of detectors. Periodic scatterers cause rapid spatial fluctuations in wave amplitude along the length of the rod and produce an effective increase in absorption in the rod[9]] .

The two other predictions for 2ω harmonic behavior in rock with cubic anharmonicity, described at the end of the theory section, were also confirmed: at fixed x, u_1 scaled as frequency squared (k^2) and as source amplitude squared (U^2)[9]. As a consequence of the agreement between the behavior of the observed 2ω harmonic amplitude and Eq. (2), we are confident that a significant portion of the observed response is due to cubic anharmonicity in the elastic response of the rock.

The compressional nonlinear parameter β was calculated from Eq. (2),

$$\beta = -\frac{2\, c^2\, |u_1(x,2\omega)|}{\omega^2\, x\, |u_0(x,\omega)|^2} \, , \tag{4}$$

where u_1 is the amplitude at 2ω and u_0 is the amplitude at ω when the source frequency is ω, $c = 2600 \pm 50$ m/s, $\omega/2\pi = 13.75 \pm 0.002$ kHz, and $x = 3.0 \pm 0.1$ cm. We find that $\beta = -7000 \pm 25\%$ for our sandstone sample.

We have used the simplest form of the theory, Eq. (2), to discuss and analyze the data, neglecting the effects of attenuation and higher order terms in the solution to Eq. (1). We have available the results of a complete treatment of the theoretical problem including attenuation[16] and a full set of experimental studies of the linear response of our sample. Numbers derived from experimental results are used in the theory to provide a guide to the conduct of the experiment. Values of β obtained by others are consistent with the above value [2,7]. The value of β is also similar to that obtained for other extremely nonlinear media such as a liquid containing gas bubbles[17,18].

The results in Figs. 2 and 3 show spectral growth at harmonics higher than 2ω. In particular, we find that the 3ω harmonic amplitude grows proportionally with U^3, a result which is in agreement with a second order correction to Eq. (2)[16]. We also observe strong growth in amplitude of other odd harmonics and, when the source is excited at two frequencies ω_1 and ω_2, intermodulation terms such as $2\omega_2-\omega_1$ are observed to grow strongly in amplitude. This suggests that higher order terms (i.e., quartic anharmonicity) in the stress strain relationship may be necessary to give a complete description of nonlinear elastic behavior in rock.

Discussion

What do our observations imply for seismic wave propagation in the earth? In order to answer this question, we examine some important considerations affecting nonlinear elastic behavior in seismic waves.

How does the nonlinear response of rock vary as a function of depth in the earth? It is known from laboratory experiments[19] that the dependence of velocity on applied stress in rock is very large due to structural defects such as grain boundaries and cracks which act to make the material compliant. At pressures of order 0.5–1.0 kbar, depending on the degree or type of structural defect, velocity becomes relatively independent of applied pressure, as is the case for materials such as metals or single crystals. Therefore, if the nonlinear response is similar at seismic frequencies we expect that the strongest nonlinear response due to structural defects in the earth will occur to depths of several kilometers. At deep crustal and upper mantle depths, the question of the presence of defects in the form of open cracks and fractures, which could cause a large nonlinear response, is under discussion[20,21,22,23]. Evidence suggesting the existence of open cracks at deep crustal and upper mantle depths is based on larger than expected (from laboratory experiments) electrical conductivity measurements[20,21,22,23], deep borehole observations of open cracks and fractures[24,25], inferences from metamorphic processes where chemically bound water is forced into defects [26], direct observation of cracks in upper mantle xenoliths[27], seismic source inferences requiring large fluid pressures[28], and anisotropy in wave propagation attributed to aligned cracks and fractures[29]. Based on the above evidence, it is

possible that a large nonlinear response is present as deep as the base of the crust and upper mantle due to the existence of structural defects that act to make the material more compliant.

Are strains large enough to produce a significant nonlinear response at large distances from a seismic source, and will the ω^2 dependence of the nonlinear response, Eq. (2), make nonlinear effects at seismic frequencies negligible? We have numerically modelled the propagation of a plane wave produced by a broadband source (Blackman-Harris window) at seismic frequencies including nonlinear elasticity and attenuation[16]. We chose $\beta = -10^3$, and specific dissipation Q (equivalent to energy loss per cycle) for an active tectonic region of order 10^2. The initial source displacement amplitude was chosen to be consistent with a typical displacement from a magnitude 5.5 source[30,31]. In Fig. 6, we show the evolution of the displacement frequency spectrum at 1, 10, and 100 km including the nonlinear response to first order. Note especially the change in corner frequency with propagation distance. Clearly, the effect of nonlinear elasticity on the displacement frequency spectrum with distance is significant, especially at low frequency and in the high frequency roll-off portion of the spectrum.

In conclusion, our results indicate that the progressive effect of nonlinear response in rock on the frequency spectra of seismic waves may be significant for waves propagating in the earth's crust and upper mantle. Remote observations of seismic frequency spectra may be substantially different from the originating source frequency spectrum. Further studies of nonlinear elastic response in rock as a function of pressure, fluid saturation, structural defect, and dimension are forthcoming.

Stress - Strain Hysteresis

We have also studied the relationship between applied stress and the resulting strain as a function of time for the case of a continuous sine wave source. The following has application to modeling of hysteresis observed in static stress-strain data in addition to illustrating another manner of viewing the nonlinear response for transient or continuous waves. For this example the external stress applied at the origin is

$$\sigma = 2(\lambda + 2\mu)U \left[\chi(\omega_0)A(\omega_0)e^{-i\omega_0 t} - \chi(-\omega_0)A(-\omega_0)e^{-i\omega_0 t}\right]. \quad (5)$$

Here,

$$\chi(\omega) = 1 - \frac{\Delta}{1 - (\pm)\, i|\omega\tau|},$$

Δ can be thought of as the fractional amount of the displacement derivative that is retarded in time, τ is the characteristic damping time, and the $\pm$ always refers to the sign of the angular frequency[15].

By making the assumption that τ and Δ are the same for all displacement components, we are assuming that Q is the same for both compressional and shear waves, and that both types of waves experience the same velocity shift from low to high frequencies. In the absence of attenuation Eq. (5) becomes,

$$\sigma = 2(\lambda + 2\mu)Uk_0 \cos(\omega_0 t). \tag{6}$$

We have taken measured strain to be the linear strain defined by $\varepsilon_L = \frac{\partial u}{\partial x}$. In Fig. 7, we show the time trace of strain as a function of applied stress. The stress is applied at $x = 0$ and the strain is calculated one wavelength away ($\lambda = 200$ m). Fig. 7a is a plot of strain as a function of stress in the absence of attenuation. Fig. 7b is a plot of strain as a function of stress when attenuation is present. The input parameters for the calculation were $\omega_0/2\pi = 30$ Hz, $U = 10^{-3}$ m, $c = 6000$ m/s, $\beta = -10^3$, $\delta = -10^6$ (second order nonlinear coefficient)[32], $\tau = 0.01$ s, $\Delta = 0.1$, $x = 200$ m, and $\lambda + 2\mu = 10^5$ MPa. Note that in Fig. 7a, the first order nonlinear contribution to the strain consists of symmetric lobes about the origin, while the second order nonlinear contribution is asymmetric, causing the total strain to roll over toward an asymptote. The direction of the roll over of the second order term depends on the sign of the nonlinear coefficient δ which is always negative for rock in our experience. In Fig. 7b we see that attenuation adds hysteresis to the linear strain. At these levels of attenuation, the first order nonlinear contribution is changed very little from its contribution in the absence of attenuation.

Acknowledgements

This work was performed under the auspices of the U.S. Department of Energy Office of Arms Control and Nonproliferation (code number GC010109) and the Office of Basic Energy Science (Contract # W-7405-ENG-36) with the University of California. A review by R. A. Guyer, and discussions with T. J. Shankland, R. J. O'Connell, S. R. Taylor, L. Hirsch, and B. P. Bonner are gratefully acknowledged.

References

1. Zarembo, L. K. & Krasil'nikov, V. A., *Sov. Phys. Uspekhi* **13**, 778-797 (1971).
2. Bakulin,V.N. & Protosenya, A.G., *Trans. (Doklady) USSR Acad. Sci., Earth Sci. Sec.* **263,** 314-316 (1981).
3. Johnson, P.A., Shankland, T.J., O'Connell, R.J. & Albright, J.N., *J. Geophys. Res.* **92,** 3597-3602 (1987).
4. Johnson, P. A. & Shankland, T. J., *J. Geophys. Res.* **94,** 729-733 (1989).

5. Beresnev, I. A. & Nikolaev, A. V., *Phys. of the Earth and Planetary Int.* **50**, 83-87 (1988).
6. Johnson, P. A., Hopson, T. M. & Shankland, T. J., *J. Acoust. Soc. Am.* **92**, 2842-2850.
7. Zinov'yeva, G.P., Nesterov, I.I., Zdhakhin, Y.L., Artma, E.E. & Gorbunov, Y.V., *Trans. (Doklady) USSR Acad. Sci., Earth Sci. Sec.* **307**, 337-341 (1989).
8. Bonner, B. P. & Wanamaker, B. J., in *Review of progress in quantitative NDE,* (ed. Thompson, D. O. & Chimenti, D. E.) **10B**, 1861-1867 (Plenum, New York, 1991)
9. Meegan, G. D., Johnson, P. A. & McCall, K. R., accepted *J. Acoust. Soc. Am.* (1993).
10. Ostrovsky, L.A., *J. Acoust. Soc. Am.* **90**, 3332-3337 (1991).
11. Landau, L. D. & Lifshitz, E. M.,*Theory of elasticity, 3rd edition* (Pergamon Press, Oxford, 1986).
12. Murnaghan, F. D., *Finite Deformation of an elastic solid* (Wiley, New York, 1951).
13. Green, R. E.Jr., *Treatise on materials science and technology, Vol. 3, Ultrasonic investigation of mechanical properties* (Academic Press, New York, 1973).
14. Gol'dberg, Z. A., *Sov. Phys. - Acoustics* **6**, 307-310 (1959).
15. Polyakova, A. L., *Sov. Phys. - Solid State* **6**, 50-54 (1964).
16. McCall, K. R., manuscript submitted to *J. Geophys. Res.* (1993).
17. Hamilton, M.F., in *Nonlinear wave propagation in mechanics -- AMD-* **77** 1-27 (The American Society of Mechanical Engineers, New York, 1986).
18. Wu, J. & Zhu, Z., *Acustica* **76, suppl. 4**, 83 (1992).
19. Birch, F., in *Handbook of Physical Constants* (ed. Clark, S. P. , Jr.) 97-174 (Geol. Soc. Am. Press, Connecticut).
20. Shankland, T. J. & Ander, M. E., *J. Geophys. Res.* **88**, 9475-9484, (1982).
21. Vanyan, L. L., Shilovsky, A. P., Okulessky, B. A., Semenov, V. Yu. & Sidelnikova, T. A., *Phys. Earth Planet. Int.* **54**, 163-168 (1989).
22. Bailey, R. C., Craven, J. A., Macnae, J. C. & Polzer, B. D., *Nature* **340**, 136-138, (1989).
23. Swartz, G., *Surveys in Geophys.* **11**, 133-161 (1990).
24. Kozlowski, Ye. A., *Sci. American* **251**, 106-112 (1984).
25. Emmermann, R. & Giese, P., *KTB Report 90-4,* Hannover, Germany (1990).
26. Winkler, F. G. F., *Petrology of Metamorphic Rocks,* (Springer Verlaag, 1974).
27. Anderson, T., O'Reilly, S. Y., & Griffin, W. L., *Contrib. Min. Pet.* **88**, 72-85 (1984).
28. Zoback, M. L.,Zoback, M. D. & Bonjer, K.-P., *EOS Trans. Am. Geophys. Union* **72**, 512, (1991).
29. Crampin, S., Chesnokov, E. M., & Hipkin, R. G., *Geophys. J. R. ast. Soc.* **76**, 1-16 (1984).
30. App, F. N. & Brunish, W. M., Los Alamos National Laboratory LAUR 92-500, 1-62, (1992).
31. Denny, M. D., Taylor, S. R., & Vergino, E. S., *Bull. Seism. Soc. Am.* **77**, 987-995, (1987).

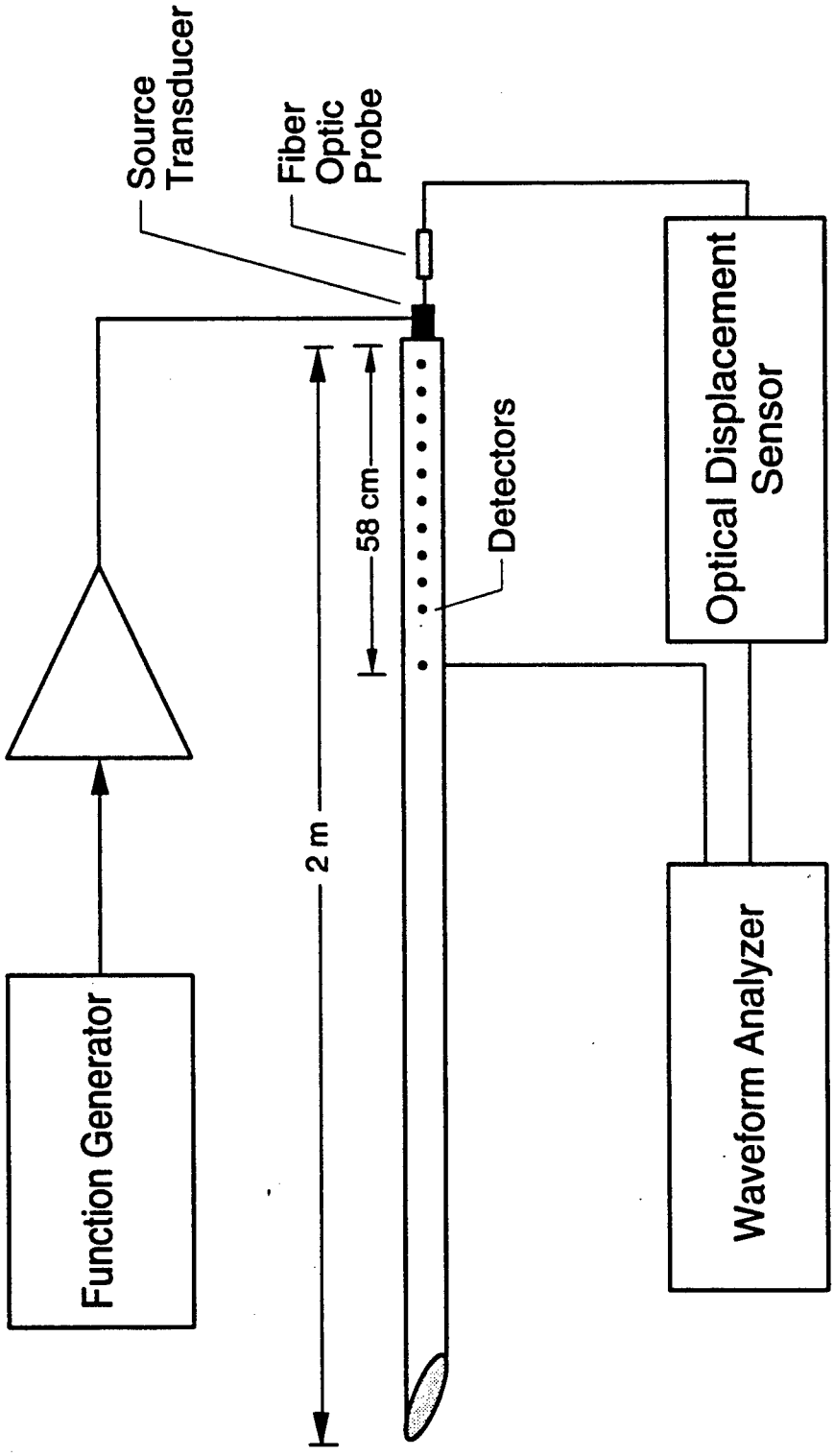


Figure 1. Experimental configuration.

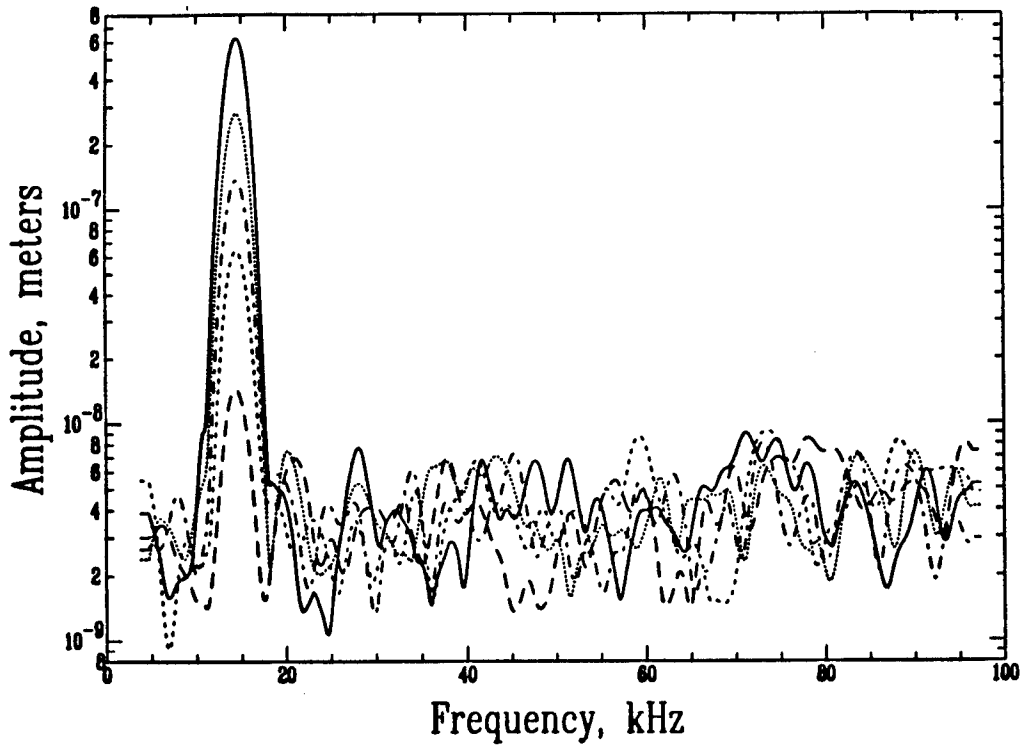


Figure 2. Source displacement spectrum at increasing applied voltages as shown by the different line types. Drive is at 13.75 kHz.

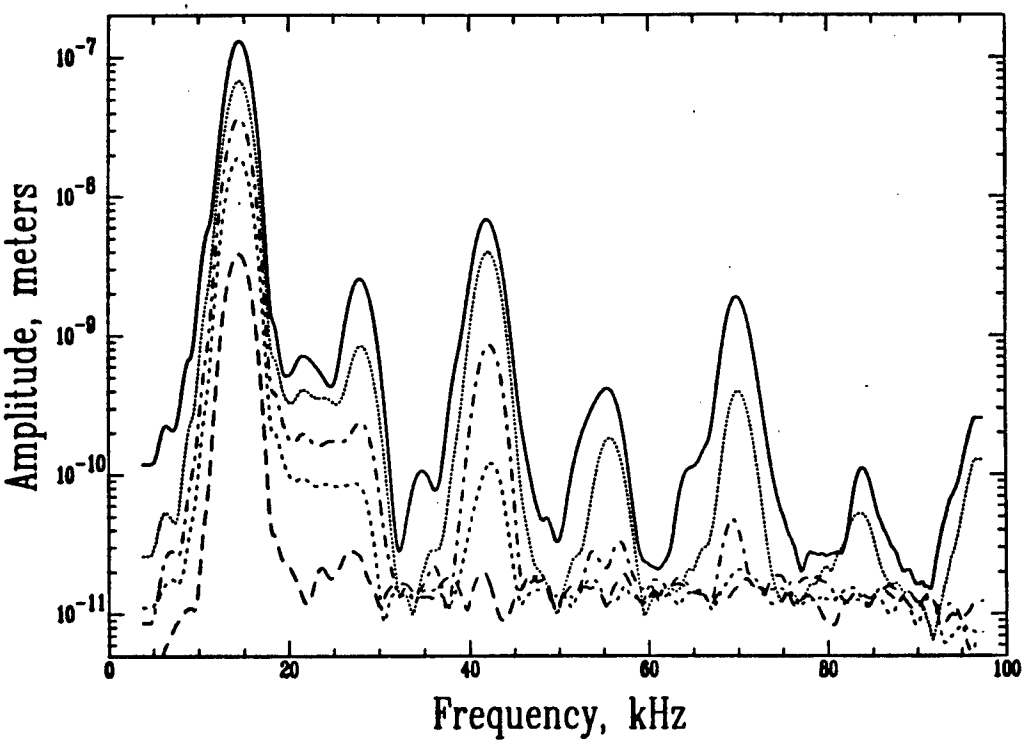


Figure 3. Displacement spectrum 58 cm from source at increasing applied voltages corresponding to Figure 2. Note the richness of the spectrum created by nonlinear elasticity in the rock during wave propagation. Drive is at 13.75 kHz.

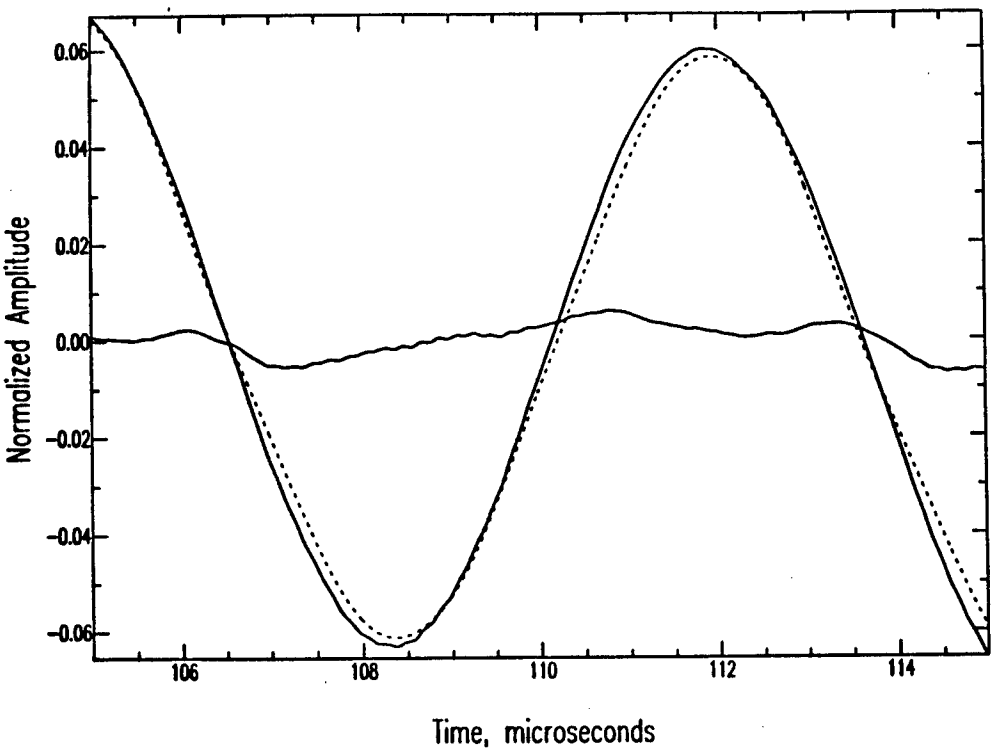


Figure 4. Time series showing distorted wave at 58 cm from source (large amplitude solid line) versus pure sine wave (dashed line). The difference between the two signals is the low amplitude solid line.

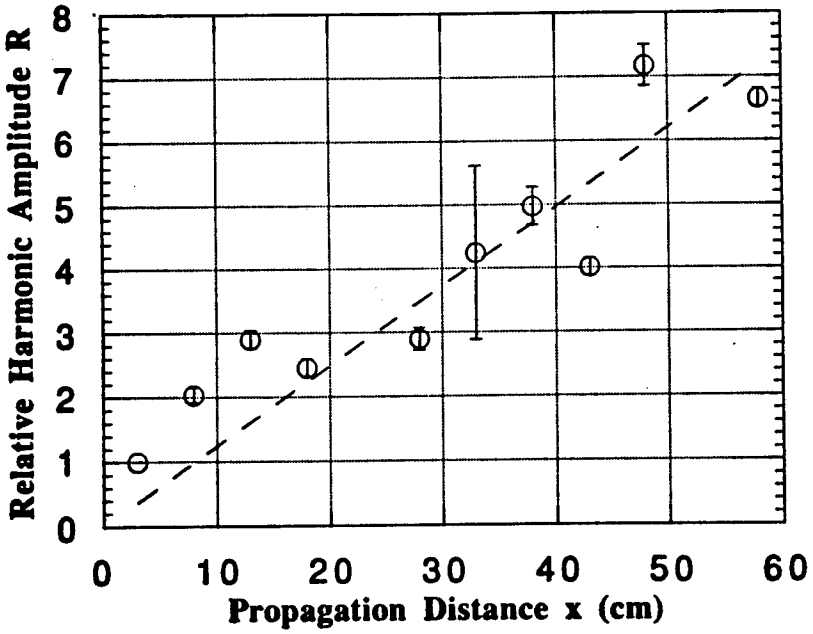


Figure 5. Dependence of harmonic amplitude on propagation distance ($R = u_1/u_0 \propto x$) for drive at 13.75 kHz. The dashed line is a least squares linear fit to the data. The harmonic amplitude is normalized to unity at the position nearest the source.

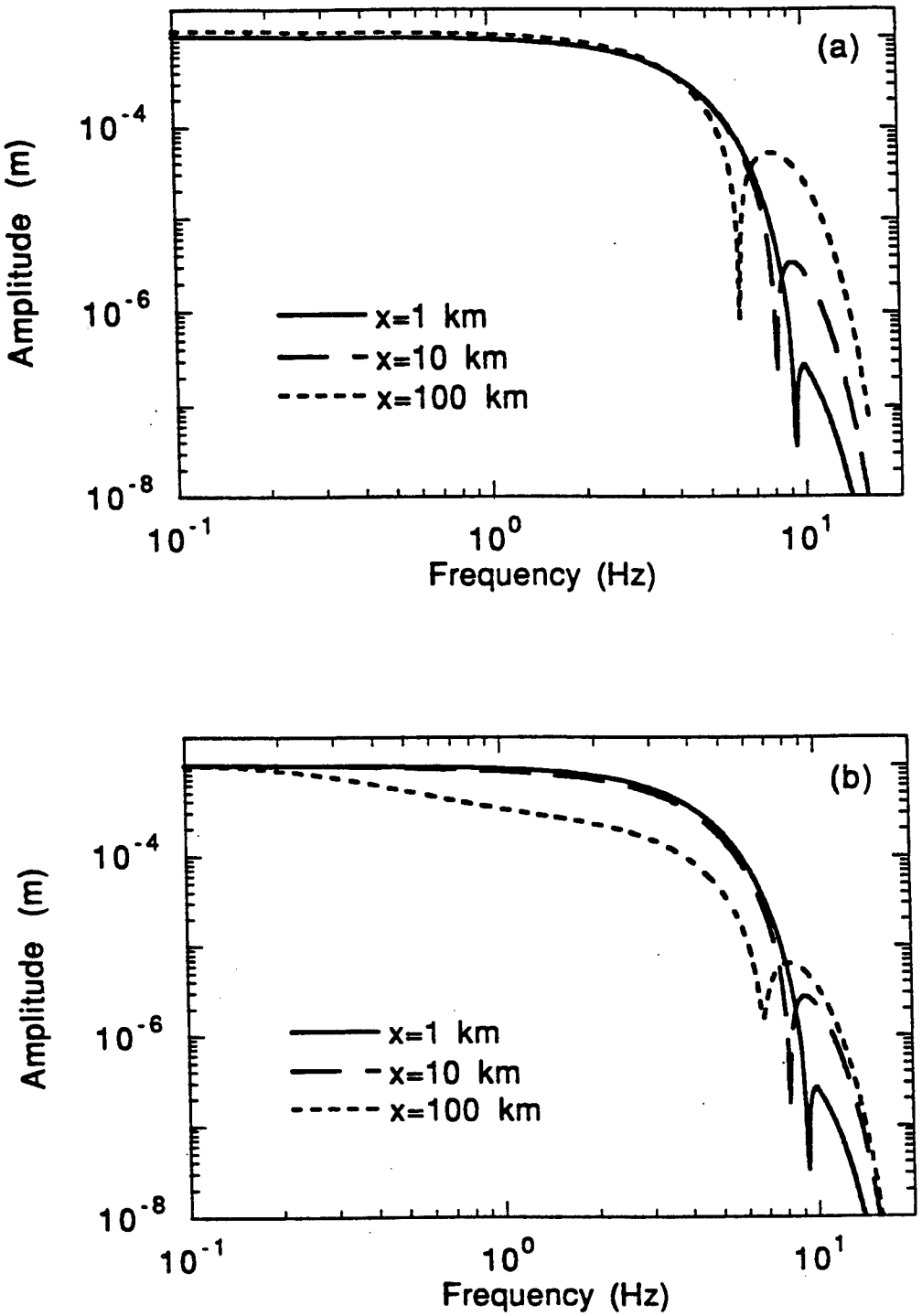


Figure 6. Model result showing evolution of the displacement spectrum with distance for a broad-band source at seismic frequencies. The source function was a Blackman-Harris window. The pulse propagates to x=1 km, 10 km and 100 km, respectively, producing sum and difference frequencies through a first order nonlinear interaction. (a) In the absence of attenuation. (b) Including attenuation. The initial displacement was chosen to correspond to a displacement from a magnitude 5.5 seismic source. The sharp drop in amplitude near 6, 8 and 9 Hz may be due to wave interference.

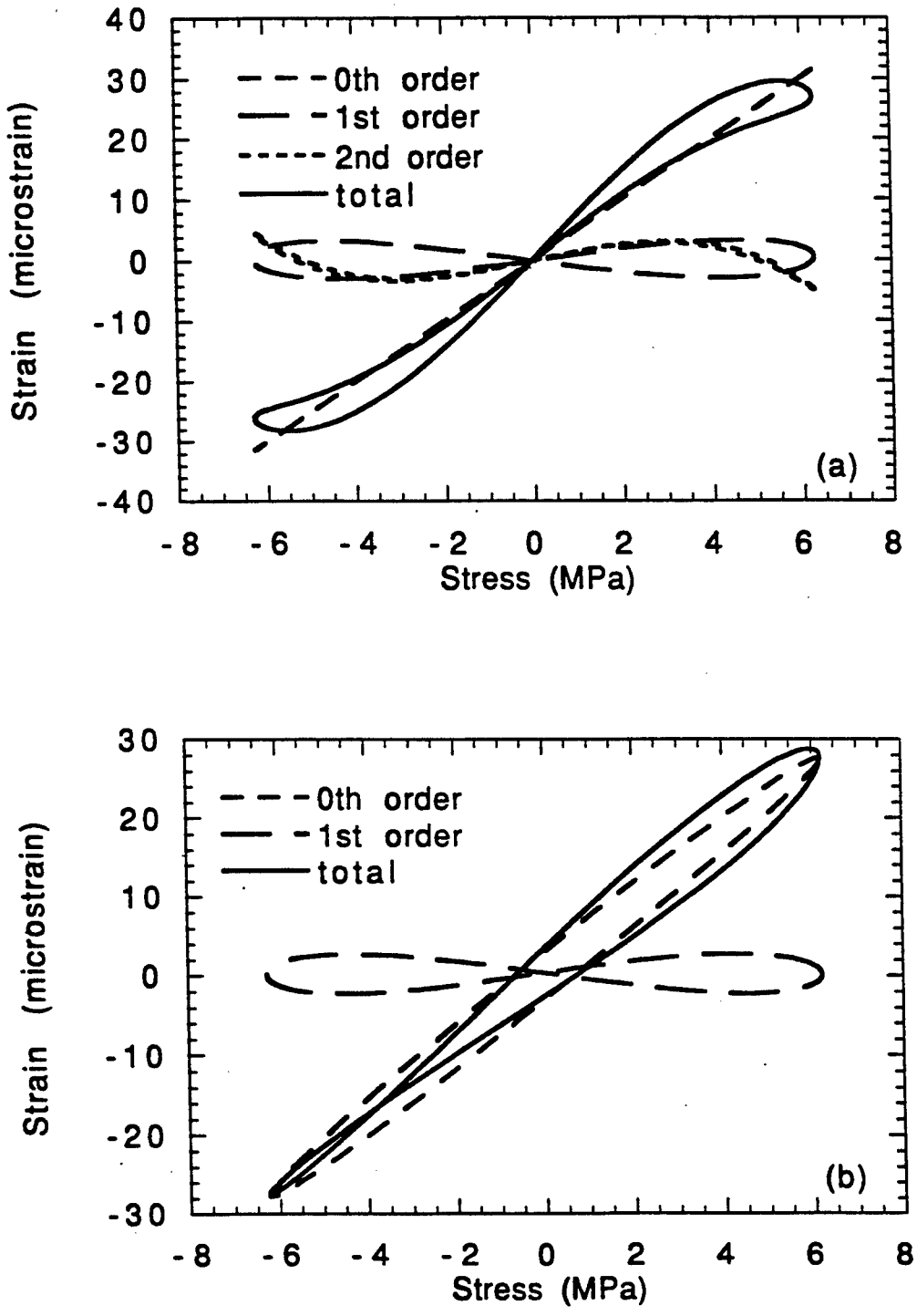


Figure 7. Stress-strain response over one cycle from a continuous sine wave source. The linear, first and second order nonlinear, and total strain response are shown. (a) In the absence of attenuation. (b) Including attenuation.

THIS PAGE INTENTIONALLY LEFT BLANK.

Fundamental Observations Concerning Hysteresis in the Deformation of Intact and Jointed Rock with Applications to Nonlinear Attenuation in the Near Source Region

G. N. BOITNOTT
New England Research, Inc.

Introduction

In order to estimate yields of large underground explosions, it is important that we have a clear understanding of the near source phenomena and their effects on regional and teleseismic signals. While it is generally accepted that a considerable amount of attenuation and resultant waveform distortion occurs due to nonlinear deformation near the source, an area that has received little attention is the broad enveloping region where moderate stress perturbations occur. In this region, where strain perturbation amplitudes range from microstrains to a few millistrains, the resulting deformation of rock is inelastic and nonlinear but little to no permanent deformation results. Owing to its great extent, the moderate strain regime has the potential to influence the entire frequency band of the regional and teleseismic signals and thus may be central to the problem of inferring source characteristics from far field signals (*Minster et al.,* 1991). Detailed rheological descriptions are required in order to understand the effects of the nonlinearities on the spectral content of regional and teleseismic signals (*Wortman and McCartor, 1991; Day et al.,* 1992).

Little quantitative information exists concerning the properties of rock in this moderate strain regime. Here we present experimental data concerning the fundamental aspects of the hysteresis in intact and jointed rocks in the moderate strain regime. Uniaxial stress tests on intact and jointed samples of Sierra White granite and Berea sandstone are used to illustrate the importance of mean stress and stress amplitude on the bulk properties of rock such as the effective $1/Q_E$ and average Youngs modulus. Fundamental observations concerning the loading path dependence of the deformation are outlined in the form of a phenomenological model for rock deformation which includes the amplitude and mean stress effects.

In addition to the results on intact rock, comparison of the results from fractured and intact samples provides insight into the relative importance of pre-existing rock joints in the moderate strain regime. Of particular interest is whether jointed rock will have characteristics which are fundamentally different from those of intact rock. If true, models based on laboratory data using intact rock will not be easily scalable to field situations without explicitly accounting for the properties of pre-existing rock joints. It is found that for the case of uniaxial compression, rock joints contribute surprisingly little to the total energy loss per loading cycle. However, the data suggests that the presence of rock joints may introduce strong nonlinearities in the effective elastic modulus which may be important for wave propagation in the moderate strain regime.

Experimental Procedure

A schematic diagram of the experimental set-up and an example of the loading history for a typical test is shown in Figure 1. The experiments are being conducted on a servo-controlled uniaxial apparatus operated in load feedback from a foil strain gage load cell mounted above the sample. Three spring loaded displacement transducers are mounted on rings which are attached directly to the sample. The gage length between the rings is 28.6 mm.

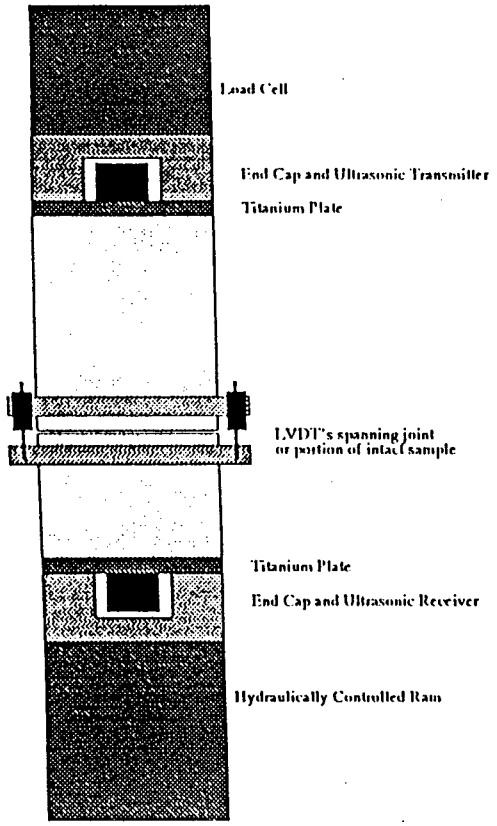
Right cylinders nominally 7.62 cm in diameter are used for the construction of the samples. For samples containing tension fractures, we start with a 7.62 cm diameter by 30.5 cm long core. A 30 degree flair carbide tool is used to score a 1.27 mm deep groove at the midpoint along the circumference of the core. The core is then supported at each end using two V blocks and loaded at the center point in a hydraulic press until fracture. This procedure produces a nominally flat tension fracture perpendicular to the core axis. After the fracture has been induced, the core is cut and the ends ground, producing a sample as shown schematically in Figure 1a.

An example of the loading history for a typical test is shown in Figure 1b. After an initial cycle to peak load, sinusoidal stress oscillations are performed having various amplitudes and centered at various mean stresses. For intact samples, this type of experiment is used to characterize bulk properties such as $1/Q_E$ and average Youngs modulus as a function of both the mean stress and the amplitude of the stress perturbation. For fractured samples, these experiments provide a measurement of joint stiffness as well as the energy loss per cycle due to the joint.

Intact Rock

An example of the stress-strain response for intact Berea sandstone is shown in Figure 2. Note that the stress-strain relation for each successive cycle overlay after the first quarter cycle. Thus the hysteresis loops are to first order closed and repeatable. This is found for both Berea sandstone and Sierra White granite. Average Youngs modulus <E> and the effective $1/Q_E$ versus the amplitude of the stress oscillation are shown in Figure 3. For Sierra White granite, <E> is a weak function of stress amplitude and mean stress, while for Berea sandstone, <E> is strongly influenced by both stress amplitude and mean stress. For Sierra White granite, $1/Q_E$ is a strong function of stress amplitude but a weak function of mean stress, while for Berea sandstone, $1/Q_E$ is strongly dependent on both stress amplitude and mean stress.

A number of features in the data indicate that the rheology in the moderate strain regime is highly nonlinear. First, the amplitude dependence of the attenuation and modulus is a clear indication of nonlinearity. In addition, the hysteresis loops are strongly cusped and to some extent asymmetric and curved (rather than elliptical as would be required by a linear rheology). Similar results have been found for the case of shear stress oscillations by *Bonner and Wanamaker,* (1990a,b). All of these features suggest that nonlinearities are prevalent in the moderate strain regime. The implications of these nonlinearities will only be understood through forward modeling based on realistic rheological models.



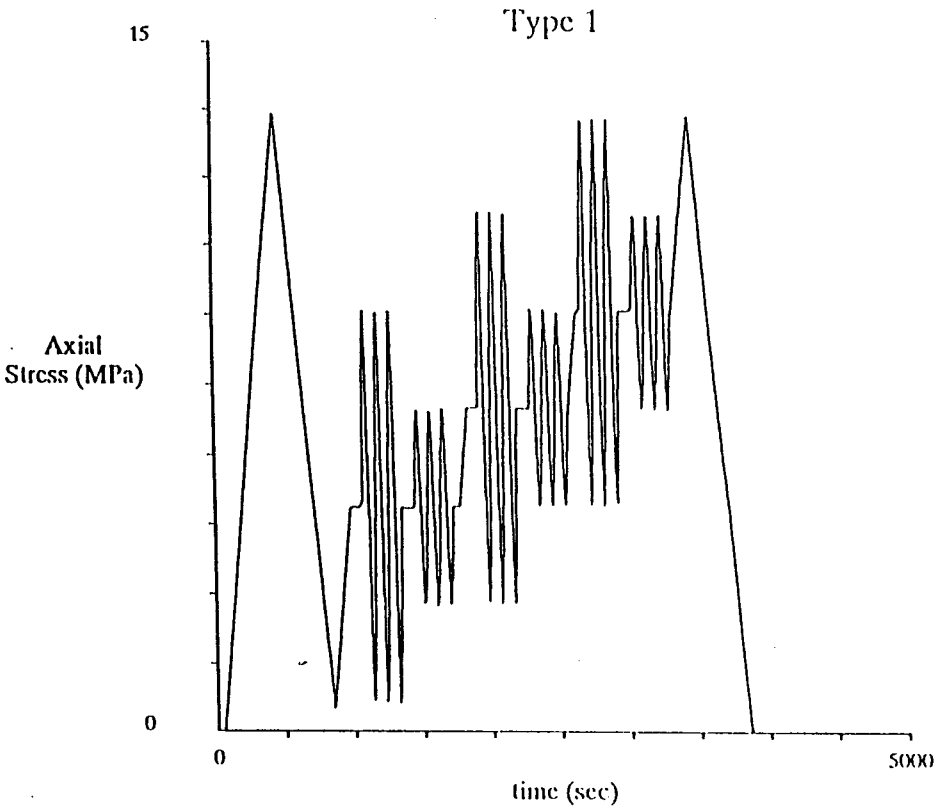


Fig. 1:

a) Schematic diagram of the experimental set-up used for characterizing the rheology of both jointed and intact rock subject to uniaxial stress.

b) Example of the time history of the axial stress for a typical experiment. After an initial cycle to peak load, sinusoidal stress oscillations are performed having various amplitudes and centered at various mean stresses. For intact samples, this type of experiment is used to characterize bulk properties such as 1/Q and Youngs modulus as a function of the mean stress and the amplitude of the stress perturbation. For fractured samples, these experiments provide measurement of joint stiffness energy loss per cycle due to the joint.

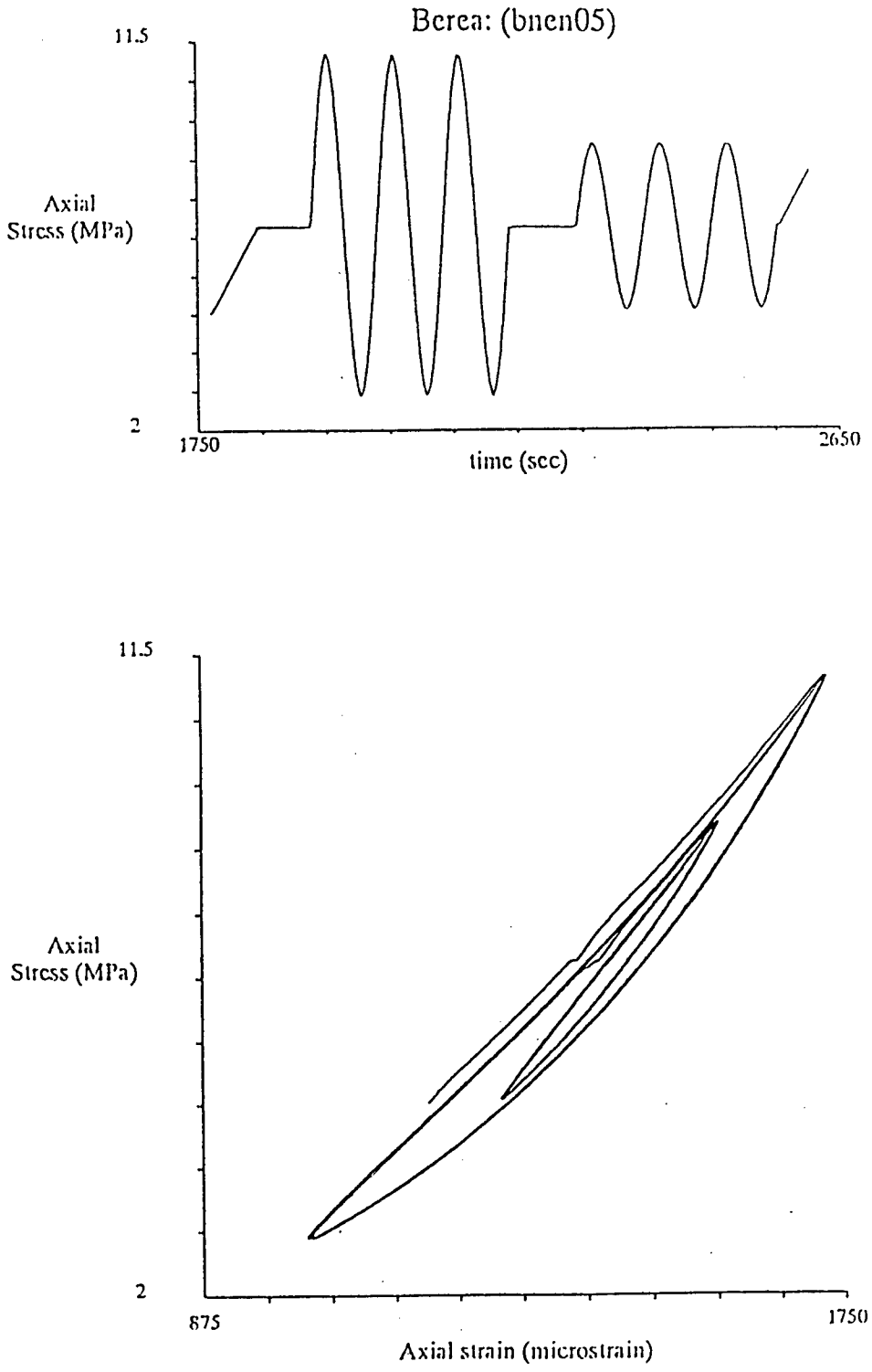


Fig. 2:

a) Time history of a portion of the experiment shown in Figure 1. Note each set of oscillations begins and ends at the zero-crossing of the perturbation.

b) Stress-Strain response for an intact sample of Berea sandstone during the portion of the loading history shown in (a). Note that the stress strain relation for each successive cycle overlay after the first quarter cycle. Thus the hysteresis loops are to first order closed and repeatable. This is found for both Berea sandstone and Sierra White granite.

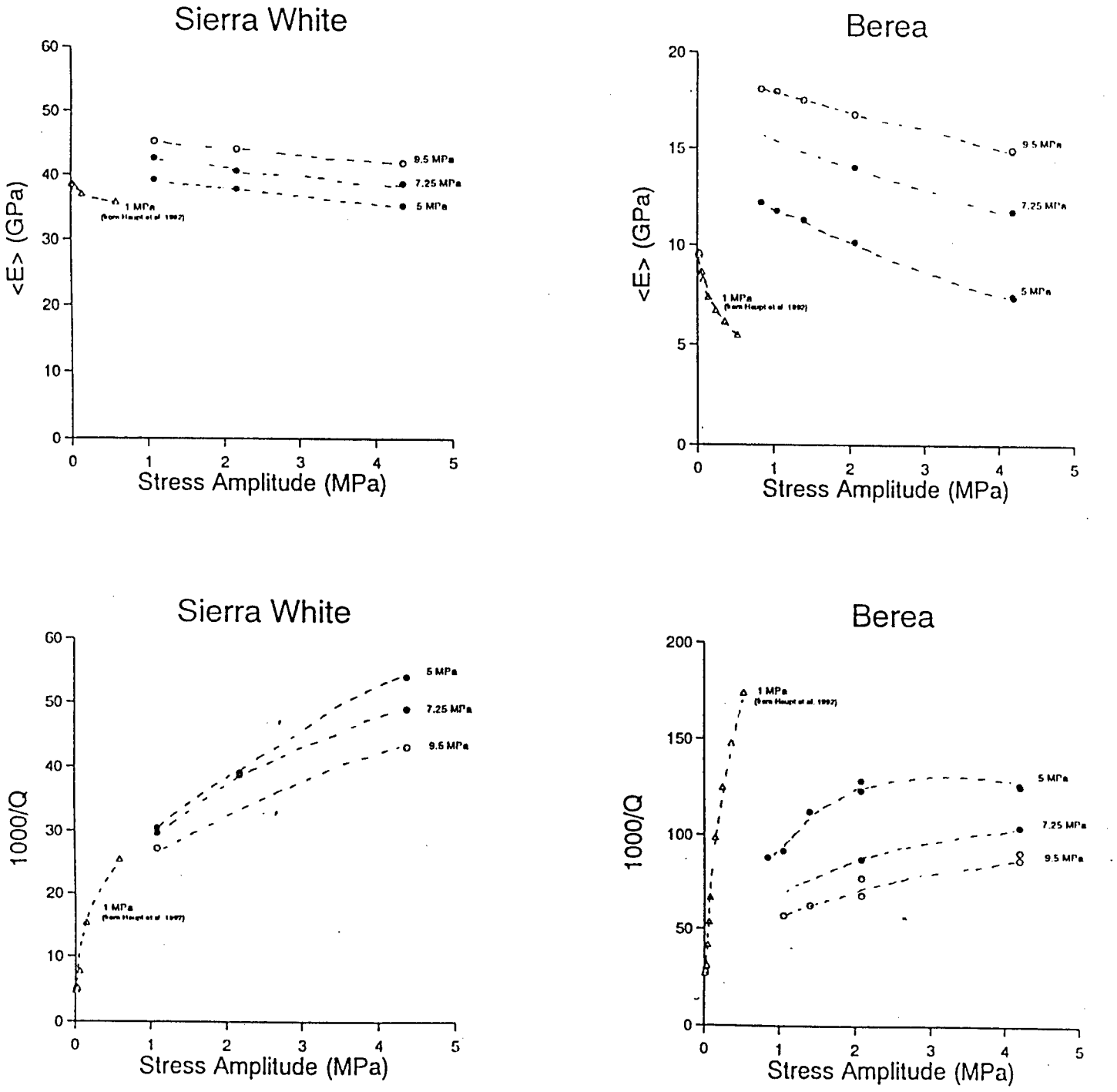


Fig. 3:

Effective bulk properties for intact Sierra White granite and Berea sandstone. Data are plotted at various mean stresses denoted by the different symbols. Note that for Sierra White granite, the average Youngs Modulus $<E>$ is a weak function of stress amplitude and mean stress, while for Berea sandstone, <E> is strongly influenced by both stress amplitude and mean stress. For Sierra White granite, $1/Q_E$ is a strong function of stress amplitude but a weak function of mean stress. In contrast, $1/Q_E$ is strongly dependent on both stress amplitude and mean stress for Berea sandstone. (Data at a mean stress of 1 MPa are from *Haupt et al.*, 1992.)

Constructing a General Rheology

The analysis of $<E>$ and $1/Q_E$ illustrates that rock type, mean load, and stress amplitude are all important variables which control the bulk properties thought to be important for wave propagation. However it is clear that knowing these bulk properties is not sufficient to model wave propagation in the moderate strain regime since they do not uniquely describe the underlying nonlinearities which may be important in wave propagation (*Day et al.,* 1992). Thus we are in need of rheological models which adequately reproduce the features observed in the laboratory in a way which is also suitable for forward modeling through numerical simulation.

Holcomb [1981] and *Scholz and Hickman* [1983] demonstrated that deformation of intact and jointed rock in the moderate strain regime exhibits end-point memory. In its simplist form, this means that when a sample is subjected to a stress cycle, the sample will return to a previous stress-strain state at the stress values of previous extrema. For complex loading, multiple reversal points can be "remembered" simultaneously. The notion that a rock will "remember" all extrema in the past loading history leads to a somewhat cumbersome chore for developing a general rheology. However, recent tests on Sierra White granite and Berea sandstone have produced further simplifications to the notion of "memory".

Figure 4 shows the results of an experiment designed to test the "memory" of a rock subject to changes in uniaxial stress. In this experiment, we were particularly interested in whether the local Young's modulus ($E = \partial\sigma/\partial\varepsilon$) during loading was a function of the previous local maximum in stress. Note that the Young's modulus during loading is independent of the previous local maximum. The modulus vs. load paths during the multiple loading segments all overlay, yet each segment was preceded by a different local stress maximum. Similar results are found for the case of unloading, where it is found that the modulus during unloading is independent of the previous minimum. Both Berea sandstone and Sierra White granite are found to exhibit this behavior. Thus, the modulus versus load relationship during both loading and unloading are to first order unique functions of the last load extremum and require no memory of previous extrema. This important result indicates that the rheology may not require long term memory of previous loading history prior to the previous local extremum in the stress-time history.

An additional experiment which illustrates some other important features of hysteresis in rock deformation is shown in Figure 5. In that figure, we illustrate a parameterization of the observed hysteresis which embodies the fundamental features of the deformation, including the effects of rock type, mean load, and load history. We note that there are a number of features of the modulus-stress relationship which can easily be taken advantage of in parameterizing the rheology. The developed parameterization can be briefly summarized as follows:

- Deformation exhibits end point memory and hysteresis loops are closed and reproducible.
- With the exception of some complications in the immediate vicinity of a reversal in load, the modulus-load relationship during both loading and unloading are well defined by simple linear functions of stress.

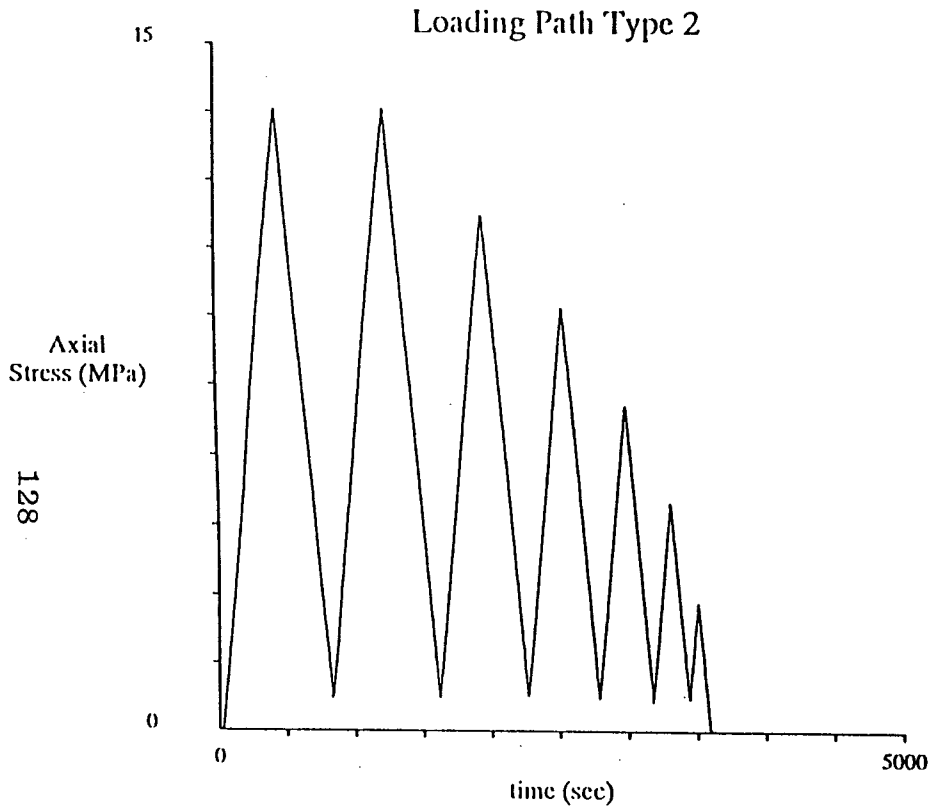
- The modulus E' defined graphically in Figure 5 is found to be a material property which defines the modulus upon load reversal in the absence of the ΔE effect.
- The parameter B which describes the decrease in modulus with decrease in stress is found to be a material property which is a simple function of the previous peak stress.
- Transient stiffening at reversals in load direction (defined graphically in Figure 5 as ΔE) is found to be proportional to the amplitude of the local stress perturbation and decays as a simple function of stress during loading or unloading.
- Once E', B, and ΔE have been constrained, the parameter b defined in Figure 5 is uniquely specified by the observation that loops must be closed (i.e. end point memory). Additionally, the parameters A and a are in effect arbitrary for the problem at hand and come out directly through integration.

Examples of predicted loops compared to measured stress-strain paths are shown in Figure 6. Here we see that the effects of both the mean stress and the amplitude of the stress perturbation on the hysteresis loops are well preserved by the rheological description. These figures serve as an illustration that a general rheology is tractable. Importantly, the same parameterization can be used for both Sierra White granite and Berea sandstone, two rocks with very different microstructural and mechanical properties. The rheology is formulated in a differential form which can be easily parameterized in terms of the stress history, and thus should be well suited for incorporation into numerical models of wave propagation.

Jointed Rock

A comparison of hysteresis loops for intact Sierra White granite and a tension fracture in Sierra White granite is shown in Figure 7. As in the case of the Berea sandstone shown in Figure 2, the intact sample exhibits a strongly cusped shaped hysteresis loop with a fairly "constant" Youngs modulus. In contrast, the tension fracture is characterized by cusped loops with a highly nonlinear stress-displacement relation, exhibiting a strong stiffening at higher loads. In figure 7b, the joint closure which is plotted is the deformation attributed to the presence of the joint - i.e. the deformation of the intact rock has been removed from the measured displacement.

As a first order model of the potential effect of fractures on the bulk properties of a rock mass, bulk linear strain for a fractured rock can be derived by summing the contributions of the strain in the intact rock with the strain which would result from the displacement due to the presence of joints. In Figures 7c and 7d we illustrate some example computations based on the data on Sierra White granite. Note that for the case of 1 joint per meter, the deformation of the joints contribute little to the bulk properties of the jointed mass. There is little noticeable difference between the intact results and those which include the additional deformation of the joints. In contrast, for the case of 10 joints per meter, the presence of the joints noticeably influences the bulk rheology (i.e. the character of the hysteresis loop). In this case, the strong load dependence on the stiffness of the joints is apparent by the curved nature of the inferred hysteresis loop.



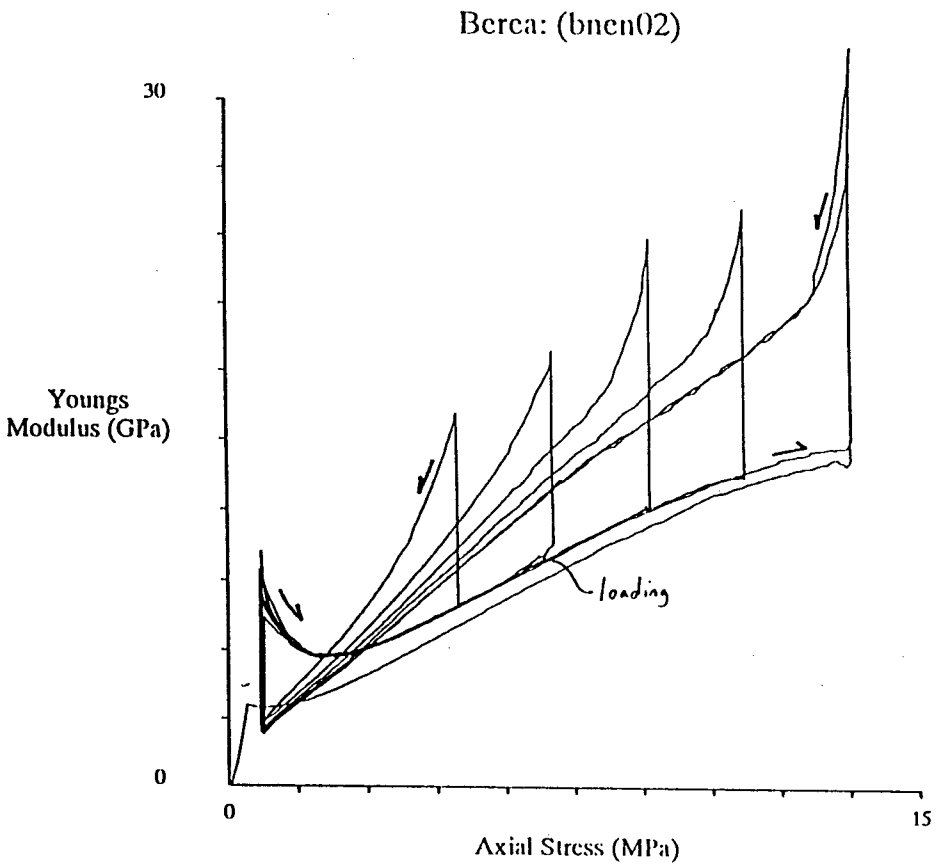


Fig. 4:

a) Stress history of an experiment designed to test the "memory" of a rock subject to uniaxial stress perturbations. In this experiment we were particularly interested in whether the modulus versus load relationship during loading was a function of the previous local maximum in stress.

b) Local Youngs modulus ($\partial\sigma/\partial\varepsilon$) versus axial stress for the experiment shown in (a) on an intact sample of Berea sandstone. Note that the Youngs modulus during loading is independent of the previous local maximum. This suggests that the rheology may be parameterized in a way which does not require long term memory of the loading history.

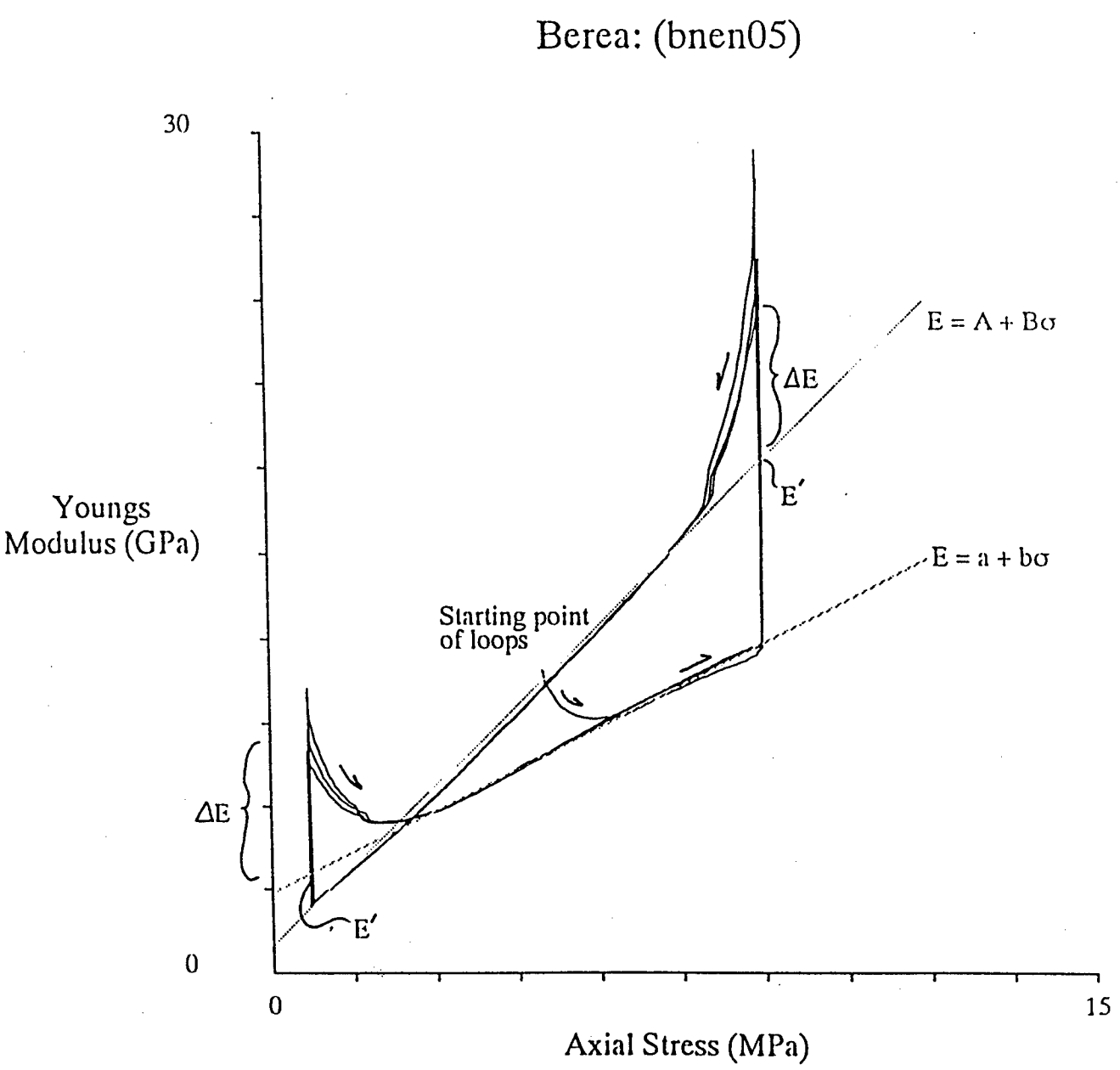


Fig.5:

Local Youngs modulus ($\partial\sigma/\partial\varepsilon$) versus axial stress for Berea sandstone during three consecutive 4.25 MPa amplitude cycles at a mean stress of about 5 MPa. The loading path and stress-strain response are similar to that for the first three cycles illustrated in Figure 2. At each reversal in the direction of loading, there is a rapid increase (discontinuity) in the local modulus. During the unloading portion of the cycles, the modulus versus load relationship is approximately linear ($E = A + B\sigma$). Similarly, during the loading portion a linear relationship is also seen. The modulus E', which is defined by extending the line ($E = A + B\sigma$) to the maximum and minimum stresses, appears to be a well defined material property, independent of the loading path used to define it. For both Berea sandstone and Sierra White granite, E' is found to be a unique function of axial stress. The extra stiffening ΔE near each reversal in stress direction is found to be a unique function of the amplitude of the local stress perturbation. The effect of this stiffening decreases during the first MPa or so of loading or unloading. The unloading parameter B is found to be a unique function of the local stress maximum. With these three parameters, we can generate a general rheology for cyclic loading which includes the effects of stress amplitude and mean stress.

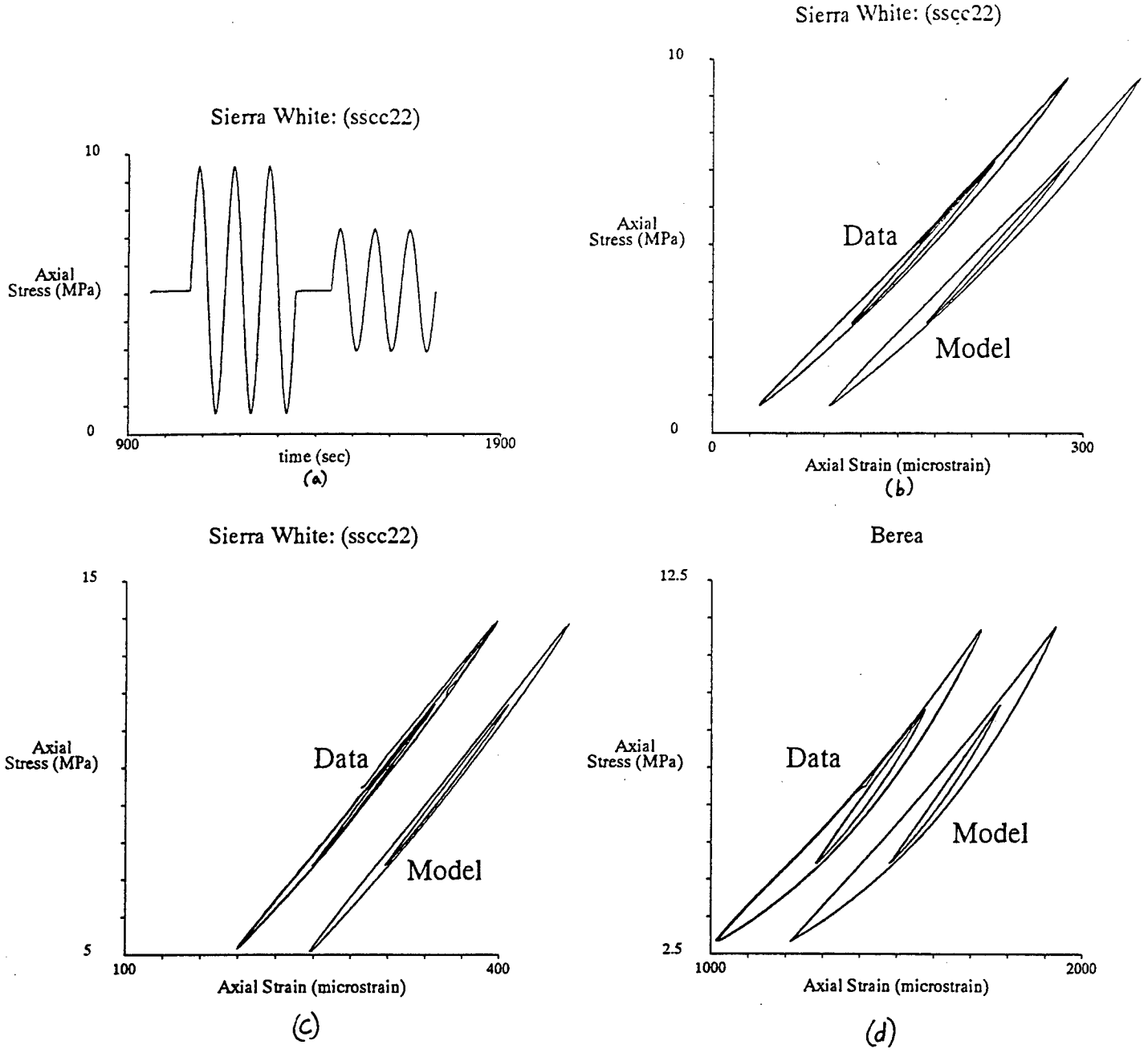


Fig. 6:

a) Portion of the loading path used for comparison between measured data and the model discussed in the text. In this case the mean stress was approximately 5 MPa.

b) Measured and modeled stress-strain path for Sierra White granite during the loading shown in (a). The model results have been offset for comparison. Note that the gross features of the deformation are well described by the model. Refinement of model parameters should improve the fit.

c) Results of a similar comparison as in (a) and (b) except this time the mean stress was approximately 9.5 MPa. The same values of model parameters were used in both (b) and (c), illustrating that the model includes the effect of both mean stress and stress amplitude.

d) Results of a similar comparison for Berea sandstone at a mean stress of approximately 7.25 MPa. The same parameterization is capable of modeling both Sierra White granite and Berea sandstone.

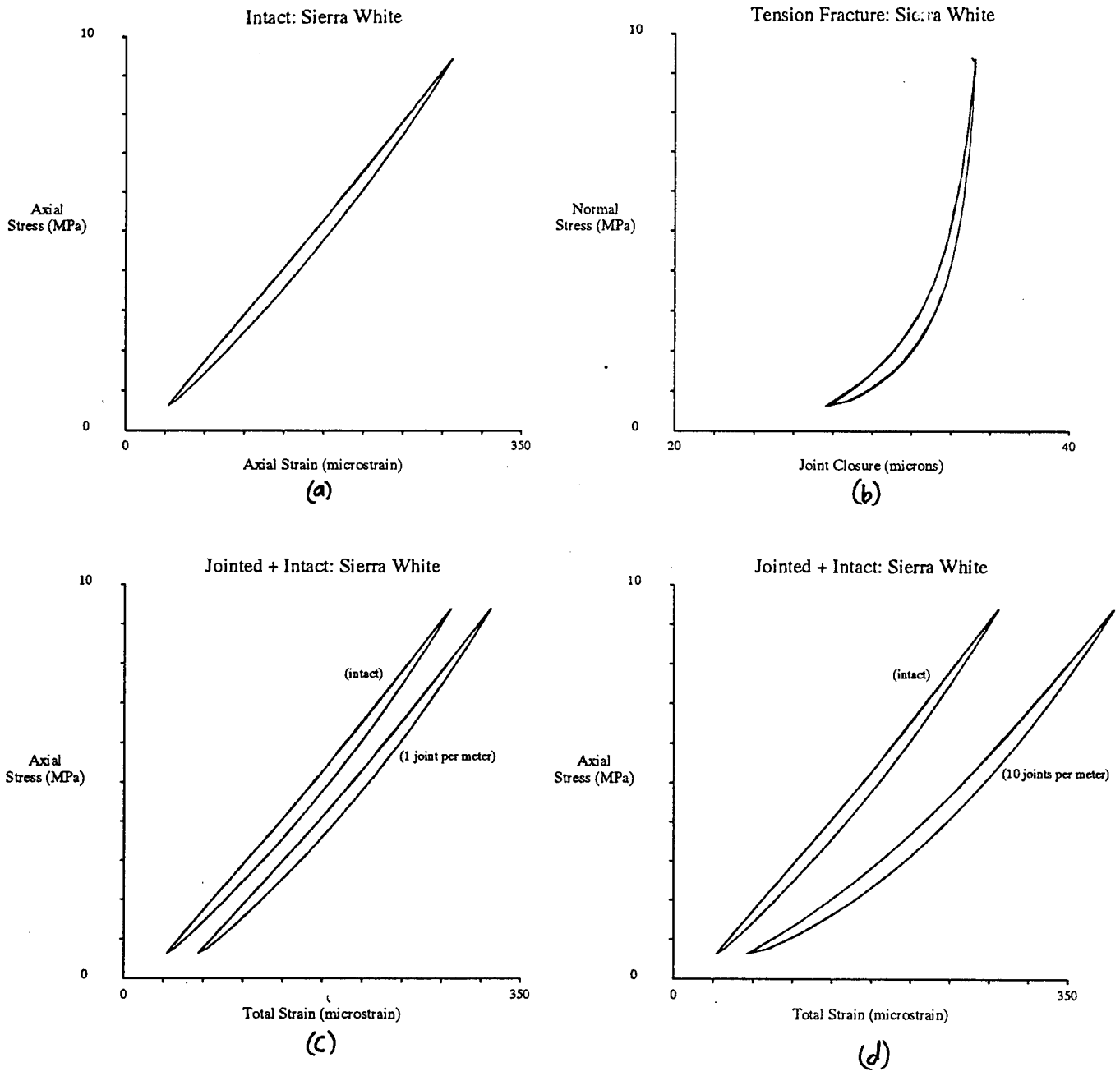


Fig. 7:

Comparison of hysteresis loops for intact Sierra White granite and a tension fracture in Sierra White granite.

a) The intact sample exhibits a strongly cusped shaped loop with a fairly constant average Youngs modulus.

b) In contrast, the tension fracture is characterized by cusped loops with highly non-linear stress-displacement relation, exhibiting a strong stiffening at higher loads. Here, the joint closure is defined as the deformation attributed to the presence of the joint (i.e. the measured displacements have been corrected for the deformation of the intact sample).

c) Bulk linear strain as a function of uniaxial stress derived by summing the contributions of the strain in the intact rock with the displacement due to the tension fracture. The response of the intact rock is shown for comparison. In this example the computations assume 1 joint per meter. Note that under these conditions the deformation of the joint contributes little to the bulk properties of the jointed mass.

d) Same as in (c) except computations are for a fracture density of 10 joints per meter. For these conditions the presence of the joints noticeably influences the bulk rheology. Note however that even with this relatively high fracture density, the energy loss per cycle is not greatly increased by the addition of the joints.

It is of interest to note that the additional deformation of the joints adds little to the total energy loss. For the example shown in Figure 7b, the energy loss per loading cycle per square meter of nominal surface area of the joint is found to be 4.1 J/m^2. For the intact rock, integration of the stress strain response in Figure 7a indicates that the sample dissipates 92 J/m^3. Thus for the case of 10 joints per meter, the ratio of the energy loss due to the joints to that of the intact rock is on the order of 0.4. Thus, even with this high fracture density, the energy loss per cycle is not greatly increased by the addition of the joints. The dominance of dissipation in the intact rock is even more dramatic in Berea sandstone, where the intact rock dissipates considerably more energy while the joint has similar properties to that of the joint in granite. The data indicates that for the case of uniaxial stress oscillations, high fracture densities are required to significantly increase energy dissipation by the bulk material. It is interesting that as the stress amplitude increases, the relative importance of joints decreases. This indicates that joints will be most important at low mean stress and for small stress oscillations.

Qualitatively, the dominant effect of joints appears to be on the modulus, were the strong dependence of joint stiffness on the normal load contrasts with the relatively weak dependence of modulus on load in rocks. In the examples of Figure 7, for the case of 10 joints per meter, the overall shape of the hysteresis loops becomes noticeably curved. Such an effect will add nonlinearities of the type studied by *Johnson et al.* (1987, 1991) were load dependence of the modulus results in nonlinear elastic effects.

Summary

Experiments have been performed on jointed and intact Berea sandstone and Sierra White granite to characterize the rheology for the case of uniaxial stress oscillations. For Sierra White granite, $1/Q_E$ is a strong function of the amplitude of the stress perturbation and is weakly dependent on the mean stress. The average Youngs modulus is equally effected by mean stress and stress amplitude over the range tested. For Berea sandstone, $1/Q_E$ is a strong function of both the amplitude of the stress perturbation and the mean stress. The average Youngs modulus is strongly effected by both the mean stress and stress amplitude. Similar measurements on samples containing tension fractures indicate that joints subject to normal load oscillations will contribute little to the bulk energy dissipation in fractured rock. The data suggest that joints will be more important in controlling the effective elastic moduli of jointed rock. Studies of the local Youngs modulus versus axial load during cyclic loading have led to a rheology for intact rock which appears to describe the effects of both the mean stress and stress amplitude on the character of the hysteresis loops for the case of uniaxial stress.

Acknowledgements

I would like to thank B. Bonner, S. Day, R. Guyer, P. Johnson, K. McCall, and J-B. Minster for helpful discussions during the course of this research.

References

Bonner, B. P., and B. J. Wanamaker, Nonlinear acoustic effects in rocks and soils, *Rev. Prog. in Quant. Nondest. Eval., 9,* 1709, 1990.

Bonner, B. P., and B. J. Wanamaker, Acoustic nonlinearities produced by a single macroscopic fracture in granite, *Rev. Prog. in Quant. Nondest. Eval.,*

10B, 1861, 1990.

Day, S. M., J. B. Minster, and L. Yu, Numerical simulation of non-linear attenuation using an endochronic formulation, *in* Proceedings of the 14th annual PL/DARPA Seismic Research Symposium, J. F. Lewkowicz and J. M. McPhetres eds., PL-TR-92-2210, September 16, 1992.

Haupt, R. W., R. J. Martin, III, X. M. Tang, and W. Dupree, Elastic moduli and seismic wave attenuation in dry and saturated rock: modulus dispersion and attenuation, Final Report PL-TR-92-2199(II), Phillips Laboratory, Air Force Material Command, Hanscom Air Force Base, MA., July, 1992.

Holcomb, D. J., Memory, relaxation, and microfracturing in dilatant rock, *J. Geophys, Res., 86,* 6235-6248, 1981.

Johnson, P. A., T. J. Shankland, R. J. O'Connel, and J. N. Albright, Nonlinear generation of elastic waves in crystalline rock, *J. Geophys. Res., 92,* 3597, 1987.

Johnson, P. A., A. Migliori, and T. J. Shankland, Continuous wave phase detection for probing nonlinear elastic wave interactions in rocks, *J. Acoust. Soc. Amer., 89,* 598, 1991.

Minster, J. B., S. M. Day, and P. M. Shearer, The transition to the elastic regime in the vicinity of an underground explosion, *in* Explosion Source Phenomenology, S. Taylor, H. Patton, P. Richards, eds., *Geophysical Monograph 65,* Amer. Goephys. Union, 1991.

Scholz, C. H., and S. H. Hickman, Hysteresis in the closure of a nominally flat crack, *J. Geophys. Res., 88,* 6501-6504, 1983.

Wortman, W. R., and G. D. McCartor, Review of attenuation in salt at moderate strains, *in* Explosion Source Phenomenology, S. Taylor, H. Patton, P. Richards, eds., *Geophysical Monograph 65,* Amer. Goephys. Union, 1991.

THIS PAGE INTENTIONALLY LEFT BLANK.

Nonlinear Hysteresis in an Endochronic Solid

Steven M. Day
San Diego State University, San Diego, CA

Jean-Bernard Minster, Michael Tryon, and Lois Yu
Scripps Institution of Oceanography, IGPP, La Jolla, CA 92093

1. OBJECTIVES

Propagation of seismic waves in the nearfield where rock rheology is demonstrably nonlinear raises unique difficulties. Nonlinearity arises primarily in two forms at intermediate to large strains: (1) nonlinear elasticity, and (2) amplitude-dependent attenuation, which is a well documented behavior at intermediate strains and low confining pressure. The proper representation of nonlinear constitutive equations for rocks in this regime is a potentially important ingredient of quantitative source models.

Stress wave propagation and attenuation, in rocks and soils, show evidence of significant nonlinearity at strain amplitudes as low as 10^{-6}, leading in particular to an amplitude dependence of the apparent Q, most likely associated with friction along microcracks and joints [e.g. *Boitnott*, 1992]. Recent quasistatic laboratory testing of rock at low strain has permitted detailed high-quality observations of cusped hysteresis loops in this regime. These issues have been recently reviewed by *Minster et al.* [1991] and summarized by *Martin and Minster* [1992]. Nonlinear wave propagation in geological materials has also been observed and modeled in a different context by *Bonner and Wannamaker* [1991], and by *Johnson et al.* [1991]. Our objective is to identify and validate a rheological model (constitutive equation) for rocks, valid at moderate strains, that explains satisfactorily these various observations, and is appropriate for incorporation in numerical source and wave propagation codes, and apply the rheological model to improve our understanding of seismic source physics.

We have shown in previous work that nonlinear one-dimensional wave propagation can result in spectral distortions at all wavelengths, but that this effect is strongly pulse-shape dependent, and therefore call for a 3-D capability [*Minster et al.*, 1991]. More recently, we have found that our use of an approximate description of the phenomenological behavior of rocks in the nonlinear regime is flawed insofar as it is not able to simulate new high-quality laboratory observations of hysteresis loops in both Sierra White granite and Berea sandstone [*Day et al.*, 1992]. Ultimately, a complete description of the rheology in terms of a thermodynamically valid constitutive equation is really what should be used in numerical simulations, if it can be developed and validated experimentally.

2. NONLINEAR WAVE PROPAGATION AND ATTENUATION

Our earlier numerical modeling of nonlinear attenuation in the intermediate strain regime used viscoelastic theory as its point of departure [*Minster and Day*, 1986; *Minster et al.* 1991]. We review that approach here, in order to highlight its analogies as well as its contrasts with the new approach proposed in Section 4. A further reason for reviewing the numerical approach to viscoelasticity is that, to be acceptable, a model for the nonlinear intermediate strain regime should be well behaved in the low strain limit. Thus, it will be desirable to develop a numerical wave propagation treatment which reduces to linear viscoelasticity in the small amplitude limit.

2.1 *Broad-band approximation of amplitude-dependent attenuating rheology*

Based on a suite of one-dimensional simulations of nonlinear wave propagation problems *Minster et al.* [1991] concluded that a simple model in which Q^{-1} is simply assumed to be proportional to strain amplitude can explain the shape distortion of Lorentz peaks observed in the laboratory at moderate strains, and the apparent superposability of simple pulses even in the nonlinear regime. They also concluded that, in contrast to linear Q models for which the spectrum of the "Q operator" tends to unity at low frequencies, a nonlinear rheology may lead to significant spectral distortions *at all frequencies*, and energy losses can be substantial even at wavelengths long compared to the propagation distance. Thus, even though nonlinear rheology is only relevant within a limited distance from a seismic source, this raises the possibility that the far field source spectrum can be affected to some degree at all frequencies, including those pertinent to regional phases and teleseismic body waves.

Those results were based on an attenuation model described by

$$Q^{-1} = Q_a^{-1} + \gamma\varepsilon \quad , \tag{2.1}$$

where ε is the strain amplitude, γ is a material constant, and Q_a^{-1} represents a linear anelastic term controlled by mechanisms that mask the nonlinear ones at low strain. This form of amplitude-dependence describes well the bulk of laboratory evidence accumulated to date. Nonlinear wave propagation simulations were conducted in two steps. First, we used the Padé approximant method of *Day and Minster* [1984] to convert the stress-strain relation of a linear, anelastic solid, with frequency-independent Q, into differential form. An absorption band, with Q nearly constant at Q_0, and with minimum and maximum relaxation times τ_1 and τ_2, respectively, yields the following relation between stress history, $\sigma(t)$ and strain history, $\varepsilon(t)$

$$\sigma(t) = \int_0^t M_u \left[1 - \frac{2}{\pi Q_0} \int_{\tau_1}^{\tau_2} \left(1 - e^{-(t-t')/\tau}\right) \frac{d\tau}{\tau} \right] d\varepsilon(t') \quad , \tag{2.2}$$

where M_u is the unrelaxed modulus. We showed that (2.2) can be approximated by

$$\sigma(t) = M_u \left[\varepsilon(t) - \sum_{i=1}^{n} \zeta_i(t) \right] \quad , \tag{2.3}$$

where the ζ_i 's are relaxation terms governed by the n linear equations

$$\frac{d\zeta_i}{dt} + \nu_i \zeta_i = \frac{\tau_1^{-1} - \tau_2^{-1}}{\pi} w_i Q_0^{-1} \varepsilon(t) \quad , \tag{2.4}$$

The constants ν_i and w_i which depend on the order of approximation, n, are given by *Day and Minster* [1984], who also show that the operator defined by (2.3) and (2.4) converges to the exact result (2.2) as n increases. The second step is to generalize (2.4) by introducing a linear dependence of Q_0 on strain amplitude according to (2.1):

$$\frac{d\zeta_i}{dt} + \nu_i \zeta_i = \frac{\tau_1^{-1} - \tau_2^{-1}}{\pi} w_i \left(Q_a^{-1} + \gamma |\varepsilon(t)| \right) \varepsilon(t) \quad . \tag{2.5}$$

Then, (2.3) and (2.5) constitute the stress-strain equations for our one-dimensional finite difference simulations.

All differential operators generated by this procedure can be guaranteed to be causal, stable, and dissipative. However, that the method performs rather poorly when the absorption band is much broader than the calculational pass band, that is, the interval between the maximum and minimum frequencies resolvable by the numerical method. For example, the finite difference method is limited to the frequency band from $1/n\delta t$ to roughly $1/m\delta t$, where δt is the time step, n is the total number of time steps computed, and m is the number of time steps associated with the minimum resolvable wavelength; m is typically of the order of 20, and n may be up to several thousand for large two-dimensional calculations. We have devised a simple extension of the method which renders it suitable for broad absorption bands, without compromising its analytical and numerical simplicity. Using the Laplace transform in s-multiplied form, we reduce the stress-strain relation to its operational form:

$$\bar{\sigma}(s) = \bar{M}(s)\,\bar{\varepsilon}(s) \tag{2.6}$$

Note that the operational modulus $\bar{M}$ has the same dimensions as the step response M. The unrelaxed modulus M_u, the relaxed modulus M_R, the modulus defect, δM, and the normalized relaxation function ϕ, are given by

$$M_u = M(0) = \bar{M}(\infty)\ , \tag{2.7}$$

$$M_R = M(\infty) = \bar{M}(0)\ , \tag{2.8}$$

$$\delta M = M_u - M_R\ , \tag{2.9}$$

$$M(t) = M_R + \delta M\,\phi(t) \tag{2.10}$$

We represent the relaxation function in terms of a relaxation spectrum Φ,

$$\phi(t) = \int_{-\infty}^{\infty} \Phi(ln\ \tau)\, exp(-t/\tau)\, d(ln\ \tau) \tag{2.11}$$

resulting in the following integral expression for the operational modulus:

$$\bar{M}(s) = M_u - \delta M \int_0^{\infty} \frac{\hat{\Phi}(p)\, dp}{s+p} \tag{2.12}$$

where $\hat{\Phi}(p) = \Phi(ln\ \tau^{-1})$. We may now partition of the p integral into 3 regimes, separated by low-frequency cutoff p_{min} and high-frequency cutoff p_{max})

$$\bar{M}(s) = M_u - \delta M\,(I_1 + I_2 + I_3)\ , \tag{2.13}$$

$$I_1 = \int_0^{p_{min}} \frac{\hat{\Phi}(p)\, dp}{s+p} \qquad I_2 = \int_{p_{min}}^{p_{max}} \frac{\hat{\Phi}(p)\, dp}{s+p} \qquad I_3 = \int_{p_{max}}^{\infty} \frac{\hat{\Phi}(p)\, dp}{s+p} \tag{2.14,15,16}$$

The interval (p_{min}, p_{max}) is prescribed to coincide with the calculational pass band. The middle partition, I_2, is replaced with an n^{th} order Padé approximant, as before, but with the support interval of interval of Φ, (τ_2^{-1}, τ_1^{-1}), replaced by the interval (p_{min}, p_{max}) Then I_1 and I_3 are approximated by Taylor series about ∞ and 0, respectively. Laplace inversion leads to a representation of total stress as a sum of $n+2$ internal variables, each of which satisfies a first order differential equation. This permits us to model broad absorption bands efficiently and with much better accuracy than before.

3. LABORATORY OBSERVATIONS OF HYSTERESIS LOOPS

In order to validate the nonlinear models described above, we have conducted simulations of hysteresis loops measured at several strain amplitudes in uniaxial tests on Sierra White granite and Berea sandstone. These data have been collected by New England Research Inc., and have been kindly made available to us by Drs. R. Martin, R. Haupt, and G. Boitnott. As reported by *Day et al.* [1992], these simulations brought to light a serious shortcoming of our approach, namely that it does not produce the correct loop shapes when the strain amplitude is increased into the nonlinear regime. Various modifications of our general approach all resulted in failure, pointing to the need for a completely different treatment of the rheology, dealing *intrinsically* with the nonlinearity.

Laboratory stress-strain curves under cyclic loading characteristically exhibit the following features which a successful model must emulate:

- Hysteresis occurs, implying energy loss, and the effective Q characterizing this dissipation is strain-amplitude dependent.
- The hysteresis loops are cusped at reversal points, rather than elliptical (as would typify linear anelastic behavior).
- No yield surface is evident in the loading curves, at least for strains up to about 10^{-4}.
- Upon reversal of strain path, the tangent modulus is roughly equal to the instantaneous elastic modulus.

Typical raw laboratory data in the form of stress and strain histories are often rather noisy, and require filtering. Simple low-pass filtering smoothes the cusps, thereby masking the onset of nonlinear behavior, and affecting the measurement of moduli at and near the cusps. We have therefore developed a technique to filter separately the loading and unloading portions of the loops. It relies on the construction of a longer time series out of a half-loop—that is a portion of stress-strain history between two reversals, in which both stress and strain are monotonic. This is done by extending it in both directions with versions of itself, rotated by $\pm\pi$ about its end points. The extended time series is then de-meaned, de-trended, and low-pass filtered using a phaseless filter to avoid introduction of a phase shift. The filtered version is truncated to the original length after restoring trend and mean, and the stress-strain path reconstructed by concatenation of filtered segments. The rotation by $\pm\pi$ of the extensions has the advantage of preserving the continuity of the time series and its derivative, thereby limiting undesirable end effects. It is important to avoid introducing cusps into hysteresis loops when they are not present, and to avoid smoothing through a cusp or changing its angle, when one is present. Too strong a filter will change the slope near the end points, and therefore introduce a fictitious cusp. Misapplication of the technique is detectable because this will create overlaps or gaps between successive segments. The technique gives very satisfactory results for noise levels as large as 10 percent as we have been able to verify using synthetic loops contaminated with additive noise. This approach facilitates considerably the estimation of the tangent modulus, particularly near the loop ends where noise contamination is most worrisome.

Several of the features described above are evident in Figures 1 and 2, which show selected sequences of hysteresis loops in Sierra White and in Berea Sandstone, respectively, uder uniaxial stress. In both instances, the strain and stress time histories are showin in the top frame, followed by the corresponding stress-strain paths ()hystereiss loops) on an expanded scale, after removal of the mean slope, in order to emphasise the key nonlinear characteristics; the bottom frame illustrates the dependence of the tangent modulus on strain. In the filtered data, the cusped nature of the reversal points is evident. Also evident is the near-equality of the initial loading and unloading slopes. The results illustrate clearly the non-elliptical (nonlinear) character of the hysteresis loops at such moderate strain levels, and also bring out clearly the strain hardening which causes the loops to show upward concavity.

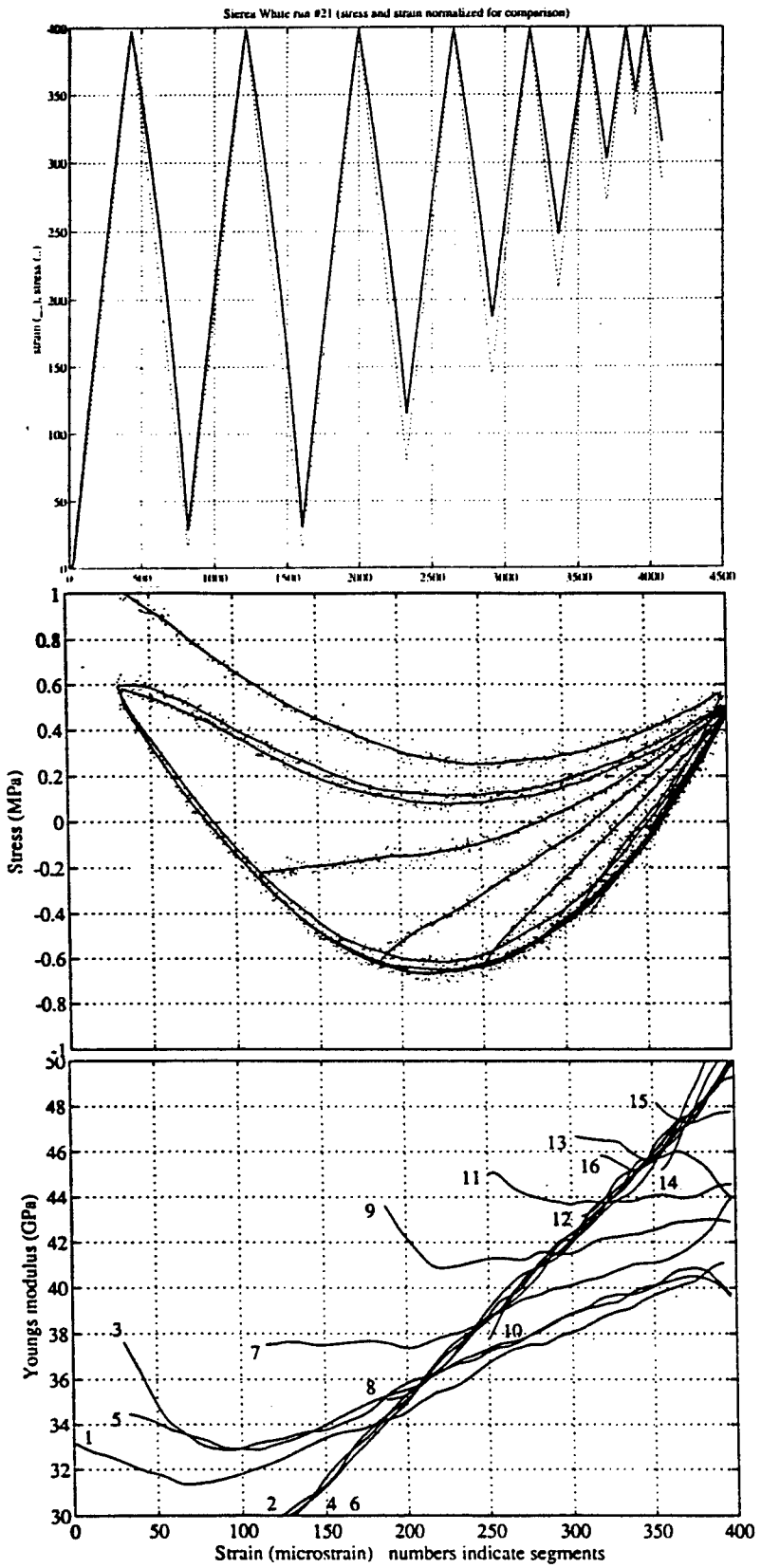


Figure 1: (a) Strain (solid line) and stress (dotted line) time histories for a uniaxial stress test on Sierra White granite. (b) corresponding stress and strain path, after smoothing; raw data are indicated by the dots, and the mean slope(modulus) of the hysteresis loops has been removed to emphasize the nonlinear characteristics. (c) Young's modulus dependence on strain for this test. Numbers indicate the various segments in the loading history, separated by path reversals.

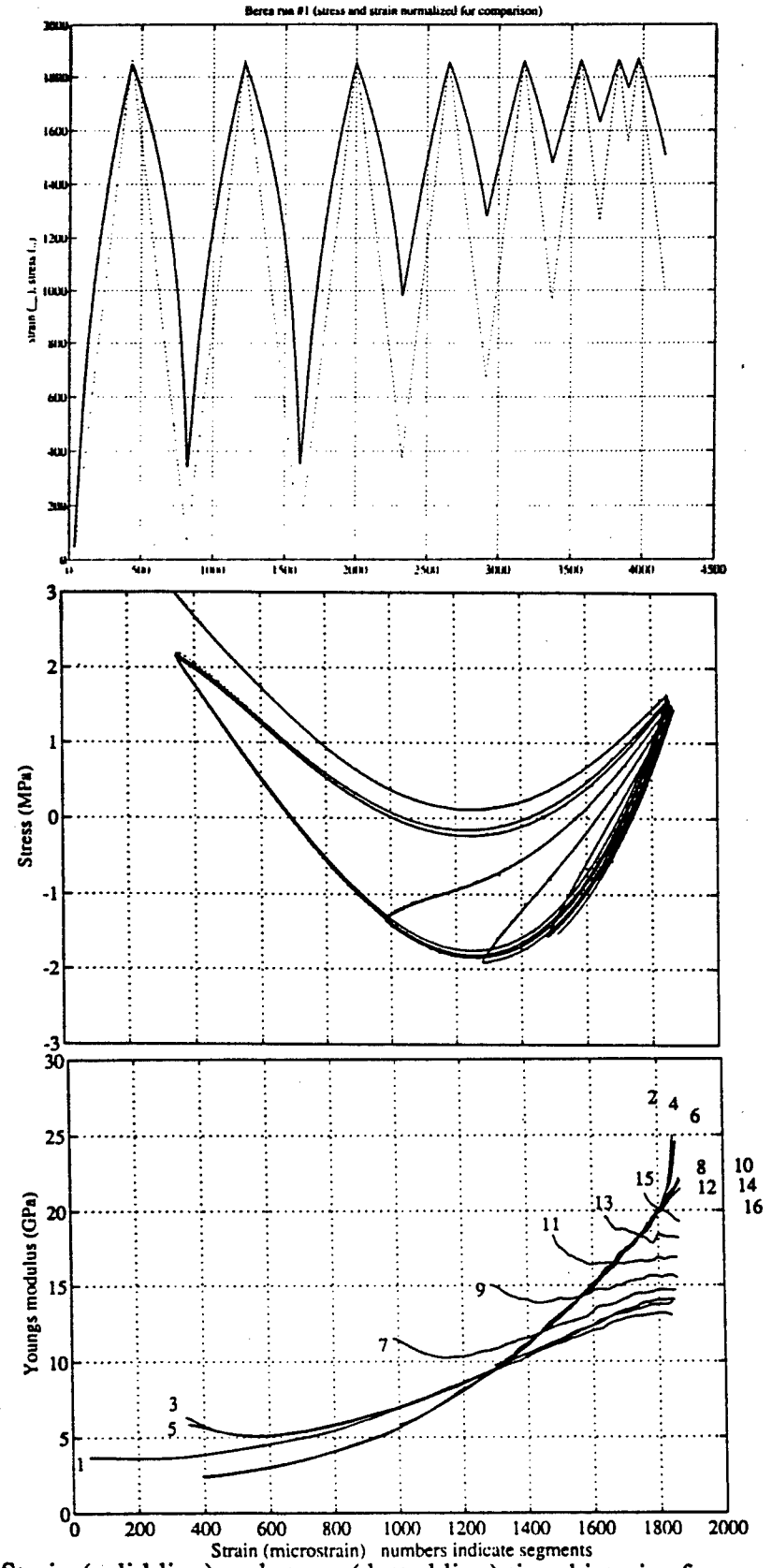


Figure 2: (a) Strain (solid line) and stress (dotted line) time histories for a uniaxial stress test on Berea Sandstone. (b) corresponding stress and strain path, after smoothing; raw data are indicated by the dots, and the mean slope(modulus) of the hysteresis loops has been removed to emphasize the nonlinear characteristics. (c) Young's modulus dependence on strain for this test. Numbers indicate the various segments in the loading history, separated by path reversals.

4. ENDOCHRONIC CONSTITUTIVE MODEL

4.1 Introduction

A successful rheological model should be capable of matching the features seen in Figures 1 and 2, which are often difficult to see in the raw data, but it should, as much as possible, avoid introducing a large number of additional model parameters for this purpose. The endochronic model described in this paper offers, we think, a very promising solution. In light of the observations outlined in the previous section, we have adopted an approach to modeling the moderate strain regime which departs sharply from viscoelastic models, yet retains much of the computational simplicity described in Section 2. We have introduced a phenomenological model for nonlinear attenuation, based on the endochronic framework of K. Valanis [e.g. *Valanis and Read*, 1979]. This model shows considerable success in replicating the main features of observed hysteresis loops in rock in the strain regime of interest. Equally important, the model is readily reduced to differential form, and we have demonstrated that the resulting differential equations can be readily solved numerically. Thus, this model is suitable for incorporation into finite difference and finite element stress wave codes. Note that numerical simplicity, efficiency, and stability are essential characteristics of a model which is to be of practical utility. For example, a single 2D numerical simulation may need to calculate the constitutive functional on the order of 10^9 times.

4.2 Background to the Endochronic Formulation

From the outset, we consider the class of constitutive models known as *simple materials*. With this restriction, the stress at a point depends only on the strain history at that point (not, for example, on strain gradients), i. e.,

$$\sigma(t) = F[e(t'),0\le t'\le t], \tag{4.1}$$

where F is a functional relating the stress σ to the strain history $e(t)$. For example: if F is linear and time invariant, equation (1) reduces to a convolution, and we have the usual formulation of viscoelasticity:

$$\sigma(t) = M(t) * e(t), \tag{4.2}$$

This restriction combined with rate independence constitute sufficient conditions to ensure preservation of cube root scaling. To specialize 4.1 for a rate-independent simple material, we express the strain history in terms of the strain path length ξ. Then

$$\sigma(t) = F[e(\xi),\dot{\xi},0\le\xi(t')\le\xi(t)], \tag{4.3}$$

The concept of rate-independence implies that there is no dependence of the rheology on the rate $\dot{\xi}$:

$$\sigma(t) = F[e(\xi),\ 0\le\xi(t')\le\xi(t)], \tag{4.4}$$

where

$$d\xi = (de{:}g{:}de)^{1/2}. \tag{4.5}$$

In other words, ξ is the strain path length, measured in terms of the metric g.

4.3 The Endochronic Material Model

Following *Valanis and Read* [1979], we consider the special case in which F is linear and shift-invariant in the *plastic* strain path length z

$$dz = (d\theta{:}g{:}d\theta)^{1/2} \tag{4.6}$$

where

$$d\theta = de - \frac{d\sigma}{2\mu} \tag{4.7}$$

is the plastic strain increment. The linear, shift-invariant assumption guarantees that we can write σ as a convolution over z; that is:

$$\sigma(t) = K(z) * \frac{d\theta}{dz} \tag{4.8}$$

If the kernel $K(z)$ is chosen to have an integrable singularity at $z = 0$, then all the features noted above are realized:

$$K(z) \propto z^{-\alpha}, 0 < \alpha < 1 \tag{4.9}$$

It is the singular behavior of the kernel that insures that loading and unloading at reversal points occurs with stress-strain slope equal to the elastic modulus. Furthermore, as demonstrated below, we have been able to show that the singular kernel ensures power law dependence of Q^{-1} on strain amplitude, in accordance with experimental observations cited previously.

4.4 Amplitude-Dependence of Q in the Endochronic Model

The power law amplitude dependence of Q^{-1} is derived by noting that

$$\sigma \propto \int_0^z (z-z')^{-\alpha} \frac{d\theta(z')}{dz'} dz' \; . \tag{4.10}$$

Restricting treatment to uniaxial loading,

$$\left|\frac{d\theta}{dz}\right| = 1 \tag{4.11}$$

so, in terms of the maximum plastic strain z_m,

$$\sigma \propto (z_m)^{1-\alpha} \; . \tag{4.12}$$

From the definition of Q^{-1} in terms of the area of the hysteresis loop, we obtain:

$$Q^{-1} \propto \frac{\sigma_m z_m}{\sigma_m^2} \; , \tag{4.13}$$

and from 4.13 and 4.14, we obtain

$$Q^{-1} \propto (\sigma_m)^{\alpha/(1-\alpha)} \; . \tag{4.14}$$

Note that for $\alpha = 1/2$, we have an approximately linear dependence on strain amplitude, in agreement with a large body of laboratory observations. The endochronic model thus appears capable of emulating laboratory observations of hysteretic behavior, as well as amplitude dependence of attenuation at moderate strain amplitudes.

4.5 Computational approach

To be useful for numerical simulations, the convolution form 4.8 must be converted to a differential constitutive equation. Since the endochronic model has a formal structure similar to linear viscoelasticity, we can carry out this conversion in a manner analogous to that used in Section 2. That is, we first Laplace transform 4.8,

$$\bar{\sigma}(s) = s\bar{K}(s)\bar{\theta}(s) \; . \tag{4.15}$$

We approximate $\overline{K}(s)$ by a rational function $\overline{K}_n(s)$, where n is the order of the denominator. Then, we develop $\overline{K}_n(s)$ as a partial fraction expansion

$$\overline{K}_n(s) = \sum_{j=1}^{n} \frac{\lambda_j}{s + \nu_j}, \tag{4.16}$$

where ν_j and λ_j are the poles and residues, respectively, of $\overline{K}_n(s)$.
Transformation back to the z domain yields the following system of differential equations for σ:

$$\sigma(z) = \sum_{j=1}^{n} \zeta_j$$
$$\frac{d\zeta_j(z)}{dz} + \nu_j \zeta_j(z) = \lambda_j \frac{d\theta}{dz} \tag{4.17}$$

Equations 4.6, 4.7, and 4.17 form the set of constitutive equations which are solved numerically. A convenient numerical scheme for the solution of such a system is given by *Murakami and Read* [1989], and we have successfully implemented that scheme to compute the numerical results shown in the next section.

5. APPLICATION TO LABORATORY AND FIELD DATA

To validate the use of the endochronic model, we have conducted simulations of hysteresis loops measured at several strain amplitudes in uniaxial tests on Sierra White granite and Berea sandstone data collected by New England Research Inc.

Figure 3 shows a comparison of such simulations with three observed loops in Sierra White, at stress levels of 3, 6, and 12 bars, respectively. The numerical simulations (which are symmetrical in stress and strain histories) match well the overall character of the observations; this includes in particular the increase in attenuation with increasing strain.

Figure 4 shows a similar comparison for Berea sandstone, for which the attenuation levels are much higher, as illustrated by the loop areas. With respect to attenuation and loop shape, the comparison is quite favorable. The theoretical loops simulate the amplitude dependence of Q and the non-elliptical loop shapes, including cusps at the ends. The mean slope decreases somewhat more rapidly with increasing strain amplitude for the experimental loops than it does for the theoretical loops. Further improvement of the model fit to the Berea Sandstone data can be obtained by introducing variations into the shape of the kernel function.

We have also calculated Q^{-1} as a function of strain amplitude for both the Sierra White Granite and Berea Sandstone models. The Berea model produces Q^{-1} nearly proportional to strain amplitude over the full range shown. The present Sierra White model also exhibits a strong amplitude dependence of Q^{-1}, although it departs slightly from the expected linear dependence of Q^{-1} on strain amplitude. This is probably as a result of approximations introduced in our current expansion of the singular kernel function.

The singular kernel endochronic model reproduces several key nonlinear phenomena associated with rock hysteresis at moderate strain. The approach represents a substantial improvement over earlier attempts to simulate amplitude-dependent attenuation using variants of viscoelasticity. Although purely phenomenological, the endochronic approach has the decided advantage that it readily reduces to a set of relatively simple differential equations which are easily solved numerically. All numerical results reported here were obtained by solving this system of differential equations numerically. Exactly the same algorithm can be applied to compute stress-strain behavior in numerical wave propagation codes.

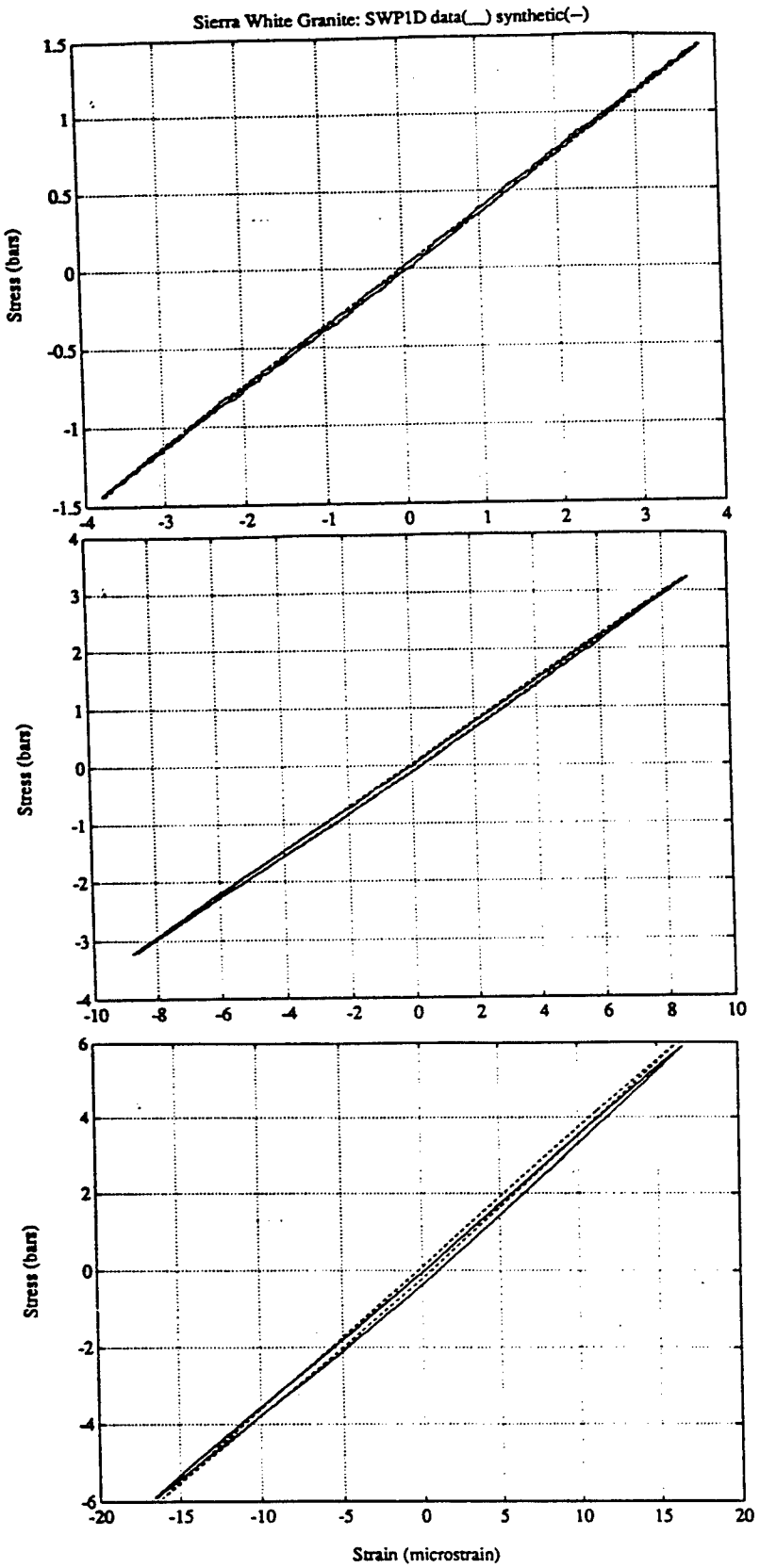


Figure 3: Comparison of endochronic simulations with three observed loops in Sierra White, at stress levels of 3, 6, and 12 bars, respectively. The numerical simulations (which are symmetrical in stress and strain histories) match well the overall character of the observations; this includes in particular the increase in attenuation with increasing strain. Additional simulations for larger stress amplitudes show that Q^{-1} continues to increase at large strain levels.

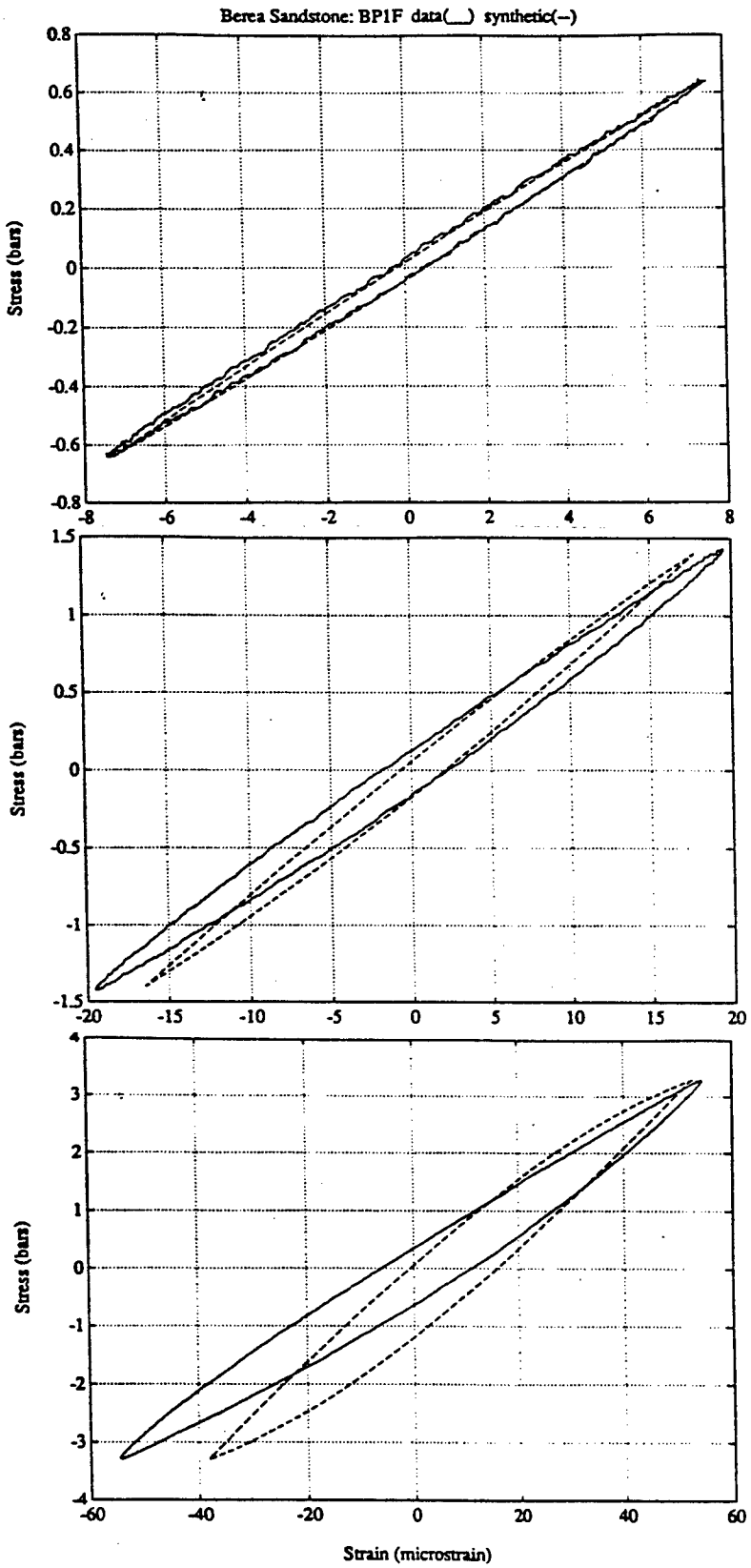


Figure 4: Similar comparison (see Figure 3) for Berea sandstone, for which the attenuation levels are much higher, as illustrated by the loop areas. Again, the comparison is quite favorable, including the amplitude dependence of Q, and the non elliptical loop shapes, with apparent cusps at the ends. It should be emphasized that, unlike many nonlinear models, the model used in these simulations depends only on a small number of parameters, once the kernel singularity is specified.

As stated before, a 1-D nonlinear numerical model is not easily generalized to 3-D. For stress wave propagation, there is much more to it than merely including geometrical spreading, because the rheology itself is amplitude-dependent. Applications of this class of algorithms to the interpretation of seismological data collected in the field require therefore development and validation of a full 3-D wave propagation capability. Intuition fails us, or is even misleading for nonlinear situations, so that it makes little sense to develop such a capability until the model has been fully verified on laboratory data in the 1-D situation. We will therefore defer such effort until later.

6. CONCLUSIONS

Existing theory for seismic wave propagation is almost exclusively linear, despite abundant experimental and observational evidence of nonlinear phenomena in earth materials for strain levels exceeding about 10^{-6}. Our long-term goal is to make a significant contribution to filling this gap in seismic theory. Our approach promises to provide a stable and efficient algorithm for numerical simulation of nonlinear wave propagation at intermediate strain levels, with computational requirements only modestly exceeding those of linear viscoelasticity. The method should enable numerical modeling to better account for near-source nonlinear phenomena, which in turn will improve our understanding of source physics for both earthquakes and buried explosions.

In particular, the importance of nonlinearity in the intermediate strain regime for detection, identification, and yield estimation of underground explosions remains a significant unresolved issue. Specific phenomena which should be considered include (1) the effects of nonlinear attenuation on surface reflections (e.g., "depth" phases such as pP and pS), both for sources sufficiently shallow, so that the nonlinear regime extends to the free surface, and for the case of strongly attenuating surface layers (soils); (2) effects of nonlinear attenuation on the efficiency of high frequency cavity decoupling; and (3) the effect of nonlinear attenuation on the spectral characteristics of regional seismic recordings from both shallow and overburied explosions. For example, *Taylor and Randall* [1989] have identified systematic spectral differences between regional seismograms from shallow explosions and overburied explosions at NTS. The spectra of regional phases play an important role in event identification in the context of a nonproliferation or even a CTBT treaty, and it is thus very important to establish the physical origin of such spectral differences. Our work is aimed ultimately at understanding such near-source effects.

This project is being undertaken in coordination with experimental work at New England Research Corporation (NER). Our modeling results will be used to help guide the design of subsequent NER experiments. Those model parameter which are found to be most critical in controlling the seismic signature of explosions should be identified and targeted for experimental study. Such collaboration has already been initiated, and all the data sets shown in this report have been made available as a result of it. Experiments conducted by NER to date have focused on uniaxial stress geometries. However, shear attenuation is most important in the Earth, so that future experiments in torsion are of particular importance, as well as experiments highlighting the effects of pore fluids and saturation, which are essential at low strains. We are particularly concerned with the ability of the endochronic model to accommodate such effects, in a phenomenological sense. In particular, we would prefer not to require a large number of additional parameters to achieve a reliable representation of the rheology in realistic circumstances. A carefully designed feedback between modeling and experimentation appears to be the appropriate strategy to achieve this goal.

Acknowledgments: This research was conducted under the auspices of the Department of Energy, Office of Research and Development, through the Lawrence Livermore National Laboratory, Project No. ST-364. Data used in this paper have been collected by New England Research Inc., and have been kindly made available to us by Drs. R. Martin, R. Haupt, and G. Boitnott. We thank Drs. B. Bonner of LLNL, P.A. Johnson and K.R. McCall of LANL for interesting and informative discussions.

7. REFERENCES

Boitnott, G. N., Nonlinear attenuation in the near-source region: characterization of hysteresis in the deformation of rock joints, *Proc. 14th DARPA/PL Seismic Res. Symposium,* 1992.

Bonner, B.P., and B.J. Wannamaker, Acoustic nonlinearities produced by a single macroscopic fracture in granite, *Rev. Prog. in Quant. Nondestructive Eval.* **10B,** 1861, 1991.

Day, S.M., J.B. Minster, and L. Yu, Numerical simulation of nonlinear attenuation using an endochronic formulation, *Proc. 14th DARPA/PL Seismic Res. Symposium,* 1992.

Day, S.M. and J.B. Minster, Numerical simulation of attenuated wavefields using a Padé approximant method, *Geophys. J. Roy. Astr. Soc.*, **78**, pp. 105-118, 1984.

Johnson P.A., A. Migliori and T.J. Shankland, Continuous wave phase detection for probing nonlinear elastic wave interactions in rocks, *J. Acoust. Soc. Amer.*, **89**, 598, 1991.

Martin R.J., and J.B. Minster, *Rheology of rocks at moderate strains with application to attenuation and source characterization*, NER conference report, Jan. 8, 1992.

Minster, J.B. and S.M. Day, Decay of wave fields near an explosive source due to high-strain, nonlinear attenuation, *J. Geophys. Res.*, **91**, pp. 2113-2122, 1986.

Minster, J.B., S.M. Day, S., and P.M. Shearer, The transition to the elastic regime in the vicinity of an underground explosion, *AGU monograph* XX (Proceedings of the 1989 DOE workshop on explosion seismic sources.), 229-238, 1991.

Murakami, H., and H. E. Read, A second-order numerical scheme for integrating the endochronic plasticity equations, *Computers and Structures, 31*, pp. 663, 1989.

Taylor, S.R. and G.E. Randall, The effects of spall on regional seismograms, *Geophys. Res. Lett.* , **16**, 211-214, 1989.

Valanis K.C., and H.E. Read, A new endochronic plasticity theory for soils, S-Cubed Rept. SSS-R-80-4294, 1979.

THIS PAGE INTENTIONALLY LEFT BLANK.

Analyzing Lagrange Gauge Measurements of Spherical, Cylindrical, or Plane Waves

John B. Aidun, T-1 MS B221
Los Alamos National Laboratory

NMUNTM Symposium, Durango CO, 24 March 1993

Material response characterizations that are very useful in constitutive model development can be obtained from careful analysis of in-material (embedded, Lagrangian) gauge measurements of stress and/or particle velocity histories at multiple locations. The requisite measurements and the analysis are feasible for both laboratory and field experiments. The final product of the analysis is a set of load paths (e.g., radial stress vs. radial strain, tangential vs. radial stress, tangential vs. radial strain, radial stress vs. particle velocity) and their possible variation with propagation distance. Material model development can be guided and constrained by this information, but extra information or assumptions are needed to first establish a parameterized representation of the material response.

A significant feature of the load paths is that variations with locations (besides peak amplitude attenuation) are indicative of rate-dependent material response. Hence, in-material gauge measurements present the possibility of characterizing rate-dependent behavior. However, it appears that exceedingly precise measurements are required to quantify rate-dependent response in geologic materials. One clear exception is noted.

The conservation relations for mass and momentum, which govern wave propagation, are presented next. The analysis of plane waves has been reported in detail previously (Aidun and Gupta, 1991) and is only briefly reviewed here. The steps for calculating the unmeasured dynamical variables in divergent waves are given and discussed. Finally, wave features that are indicative of rate-dependent material response are identified and two examples of rate-dependent response to plane-wave loading are given.

The governing equations for the three classes of waves can be expressed in the same form by introducing an index n. Setting n equal to (0, 1, 2) in the following equations yields the appropriate expression for (planar, cylindrical, spherical) waves, respectively. The variables are: time (t); Lagrangian position (h); Eulerian position (r); radial particle velocity (u_r); radial stress (σ_r); circumferential stress (σ_θ); density ($\rho = 1/v$). For plane waves, "radial" should be understood to designate the propagation direction.

The particle velocity is defined as

$$u_r = \left(\frac{\partial r}{\partial t}\right)_h . \qquad (1)$$

Conservation of mass is expressed by

$$\frac{\rho_o}{\rho} = \left(\frac{r}{h}\right)^n \left(\frac{\partial r}{\partial h}\right)_t . \tag{2}$$

An alternate form is obtained by taking the time derivative of Eq. (2),

$$\rho_o \left(\frac{\partial v}{\partial t}\right)_h = \frac{1}{h^n}\left[\frac{\partial (r^n u_r)}{\partial h}\right]_t . \tag{2a}$$

Taking normal stress to be positive in compression, momentum conservation is expressed by

$$-\rho_o \left(\frac{\partial u_r}{\partial t}\right)_h = \left(\frac{r}{h}\right)^n \left(\frac{\partial \sigma_r}{\partial h}\right)_t + \frac{n}{r}\frac{\rho_o}{\rho}(\sigma_r - \sigma_\theta) . \tag{3}$$

For plane waves, there are three equations and four unknowns: r, u_r, ρ, and σ_r. It is sufficient to measure one dynamical variable to determine the other three. Longitudinal particle velocity, stress, or impulse are routinely measured. Stress measurements tend to have lower precision owing to the difficulties of calibrating stress gauges. Precision of ±20% is respectable for a stress gauge measurements. Additionally, $(\partial^2\sigma_r/\partial h^2)$ typically must be evaluated from a few, sparsely located gauge records to calculate density. Together, these factors usually lead to very low precision density values.

The calibration of electromagnetic particle velocity gauges is absolute, following from Faraday's law of induction. Precision better than ±5% is routinely obtainable. However, a difficulty develops in calculating stress. Integrating Eq. (3) yields a constant time integral for stress,

$$\sigma(h,\tilde{t}) - \sigma(h_{bc},\tilde{t}) = -\rho_o \int_{h_{bc}}^{h} u_t(h',\tilde{t})\, dh' . \tag{4}$$

h_{bc} denotes a location at which the stress in known, without which only a stress difference is obtained. Typically, the wave front, where the stress is zero, must be used for h_{bc}. Consequently, for times later than the wave front arrival at the deepest gauge location, an extrapolation of the measured histories is needed. This can be avoided when two dynamical variables are measured. Forest (1992) discusses this with particular application to simultaneous measurement of longitudinal particle velocity and impulse.

For divergent waves there are five unknowns: r, u_r, ρ, σ_r, and σ_θ. Hence, two dynamical variables need to be measured, with radial particle velocity and stress being the most feasible choice. When these are measured at multiple ranges, h_i, the remaining quantities are calculated from the following integrated forms of the governing equations: Equation (1) provides a relation for constant $h = \tilde{h}$,

$$r(\tilde{h},t) = \tilde{h} + \int_{t_o}^{t} u_r(\tilde{h},t')\, dt' . \qquad (5)$$

Equation (2a) yields,

$$v(\tilde{h},t) = v(\tilde{h},t_o) + \frac{1}{\rho_o \tilde{h}^{\,n}} \int_{t_o}^{t} \left[\frac{\partial(r^n u_r)}{\partial h}\right]_t dt' . \qquad (6)$$

Equation (3) provides an expression for σ_θ at any specified (h,t) coordinate,

$$\sigma_\theta(h,t) = \sigma_r(h,t) + \rho \frac{r}{n}\left[\left(\frac{\partial u_r}{\partial t}\right)_h + \frac{1}{\rho_o}\left(\frac{r}{h}\right)^n \left(\frac{\partial \sigma_r}{\partial h}\right)_t \right]. \qquad (7)$$

Equations (5) - (7) are evaluated by first integrating the measured particle velocity histories along particle paths to determine $r(h_i,t)$. Second, surfaces must be fitted to the discretely-spaces histories of $r^n u_r$ and σ_r from which to determine the gradients and the particle acceleration. Equation (6) can then be integrated to obtain the specific volume v. The algebraic sum of the acceleration and the radial stress gradient in Eq. (7) provides the stress difference $\sigma_r - \sigma_\theta$.

Several points concerning the evaluation of Eqs. (5) - (7) should be noted. Foremost is that the determination of the needed gradients is the main difficulty of the analysis because measurements are typically made at only a few, widely spaced locations. The imprecision in the gradient values affects both v and σ_θ. The time integration in Eq. (6) does not ameliorate this. A related fundamental point is that the evaluation of numerical derivatives for the gradients and acceleration make the analysis equivalent to fitting the surfaces indicated above, notwithstanding the fact that many methods for determining numerical derivatives do not involve curve fitting explicitly. Directly fitting surfaces is encouraged because it permits easy, visual inspection of the goodness of the representation of the data. This extremely important, qualitative, initial check is the minimum evaluation of the fit that should be made.

In contrast to plane waves [see Eq. (4)], the analysis of divergent waves does not suffer from requiring extrapolation of the data; only integrations along particle paths are needed. A further convenience is that σ_θ is obtained without integration in Eq. (7), which decouples the uncertainties at different (h,t) coordinates. This is important because σ_θ may be highly imprecise when the acceleration and radial stress gradient are both large, as they usually have opposite signs. This imprecision is compounded by the imprecision in the stress gradient values, mentioned previously. The alternative of directly measuring σ_θ is under development, but, like measuring lateral stress in plane waves, it is very difficult to obtain reliable results.

Discussion of wave features that are indicative of rate-dependent

response requires classifying waves as simple or nonsimple. In simple waves any dynamical variable can be expressed as a function of another dynamical variable; there is no explicit time or space dependence. Examples include steady waves, centered waves, and dispersive waves in linear, anelastic media. Cowperthwaite and Williams (1971) showed that in simple, plane waves the contours of constant particle velocity, stress, and density, projected onto the h-t plane, are all straight lines. Equivalently, the contour slopes, which give the propagation speed for an increment of particle velocity, C_u, of stress, C_σ, or of density, C_v, are all equal. In nonsimple, plane waves the dynamical variables have explicit h and t dependencies, the contours are curved and the load paths vary with propagation distance. Hence, stress, for example, can be expressed as a function of u and t, but not u alone; the material response is rate-dependent. See Aidun and Gupta (1991) for a fuller discussion of this topic.

A practical determination of whether a plane wave is simple, and, hence, whether the material exhibited rate-dependent response, can be made by assessing the curvature of contours constructed from gauge data. Note, however, that rate-dependent response can produce simple waves (e.g. steady waves), and that an experiment can only reveal rate-dependence on the time scale of the measurement. Identifying contour curvature requires at least three gauge locations. Even so, with real data it can be difficult to judge whether the few discrete points defining each contour are colinear. In geologic materials, the curvature easily can be masked by the limited precision of the data. This observation indicates that the nonsimple contributions to the wave are comparatively small and that special care is needed to resolve and analyze them. There is one clear indication of contour curvature, and, hence, a nonsimple wave to make special note of; namely, a wave feature, besides the peak, that changes amplitude with propagation distance.

Conceptual guides in characterizing material response to plane wave loading are provided by the following wave decompositions into simple and nonsimple contributions.

$$\text{Define, at constant } t = \tilde{t},\ F(u,\tilde{t}) \equiv \int_{u_o}^{u} \left(\partial C_u(u',\tilde{t})/\partial t\right)_u \, du'. \tag{8}$$

Then stress in terms of particle velocity on constant $h = \tilde{h}$ is given by

$$\sigma(\tilde{h},t) - \sigma(\tilde{h},t_o) = \rho_o \int_{u(\tilde{h},t_o)}^{u(\tilde{h},t)} C_u(\tilde{h},u')\, du' + \rho_o \int_{t_o}^{t} F(\tilde{h},t')\, dt' . \tag{9}$$

The term involving F in Eq.(9) is the nonsimple contribution. Being related to contour curvature, F is expected to be small, making the nonsimple contribution small. However, the nonsimple contribution is definitely not negligible. Its

incremental magnitude relative to the simple contribution can be substantial, as in a flot-topped wave shown in the examples.

The preceding conclusions concerning simple and nonsimple, plane waves all follow from Cowperthwaite's (1971) derivation of the relation of C_σ to C_u. Because this derivation relies on the momentum conservation relation, Eqn. (3), the distinguishing features of nonsimple plane waves do not obtain for radial particle velocity and stress in divergent waves (Cowperthwaite, pers. comm.). Cowperthwaite's example of a Primakoff wave (Keough, et al., 1971) demonstrates that in simple divergent flow contours for one variable can be straight while those for another can be curved.

The two examples illustrate some distinctive features of stress and stain histories that can arise in nonsimple, plane wave propagations. The longitudinal particle velocity histories at three gauge depths shown in plot A of the first example are based on measurements in a plate impact experiment on a marble sample. The attenuation of the first rise with propagation distance makes this flow nonsimple. The simple form chosen to represent the particle velocity field permitted analytic solutions to be determined for the density compression and longitudinal stress fields. The particle velocity was taken to increase at a constant rate in each of two intervals and be constant thereafter. The first rise was taken to attenuate linearly with depth. The unloading response was not calculated.

In plot B, the density is constant when the particle velocity is spatially uniform, as required by mass conservation. However, this relation does not constrain the density gradient, and the denisty is observed to increase with depth in this nonsimple wave.

The stress in plot C increases much more slowly than the particle velocity during the second interval. When the particle velocity is constant and spatially uniform, the stress decreases at a steady rate. This stress relaxation is independent of depth, as required by momentum conservation. The finer, dashed lines in plot C result from retaining only the first term in Eq. (9). Their deviations from the bolder lines show that this simple-wave approximation is not reasonable for this wave. Not only are the magnitudes wrong, this result is unphysical: It shows a stress gradient existing while there is no particle acceleration, in violation of momentum conservation.

The stress-density paths at three depths, shown in plot D, diverge when the flow acquires the nonsimple feature after the first interval. The divergence occurs at lower stresses for greater depths. The stress relaxation that occurs when the particle velocity becomes constant produces the decrease in stress at constant density in plot D. The density gradient existing during this time causes the density at which the stress decrease occurs to vary with depth. The release-wave arrival at each depth, which follows the vertical decreases in stress on each path, does not coincide with the point of maximum stress. In the simple-wave approximation, the stress decrease at constant density would not be obtained, and the release wave arrival would correspond to the point of maximum stress on each particle path.

In plot A of the second example, the bold lines are particle velocity histories measured in another plate impact experiment on a marble sample. The dashed lines show several constant-depth slices through a piecewise-analytic surface that was fit to these histories up to the onset of unloading. The stress and density fields were computed by numerically integrating the conservation relations using partial derivative values taken from the fitted surface. The unloading response was calculated using the simple-wave approximation.

As in the previous example, a density gradient is obtained when the particle velocity is spatially uniform (plot B) and the simple-wave approximation yields a stress gradient when there are no particle accelerations (dotted lines in plot C). In contrast to the analytic example, the stress in plot C is observed to increase with time, independent of depth, while the particle velocity is constant and spatially uniform. The stress-strain paths in plot D are more complicated than for the analytic example and the nonsimple character is less pronounced.

In the higher amplitude experiments on marble samples, the error in the peak stress obtained from the simple-wave approximation decreased with increasing peak stress. This improvement appears to correspond to the decreasing relative contribution of the predominant nonsimple flow feature, the attenuating knee at 70 m/s particle velocity.

REFERENCES

Spherical Waves

Fowles, R, J. Appl. Phys. 41 (1970) 2740.

Grady, D. E., J. Geophys. Res. 78 (1973) 1299.

Keough, D. D., C. W. Smith, and M. Cowperthwaite, SRI International Interim Report, Project PYU 8567, Defense Atomic Support Agency DASA-2685, January 27, 1971.

Plane Waves

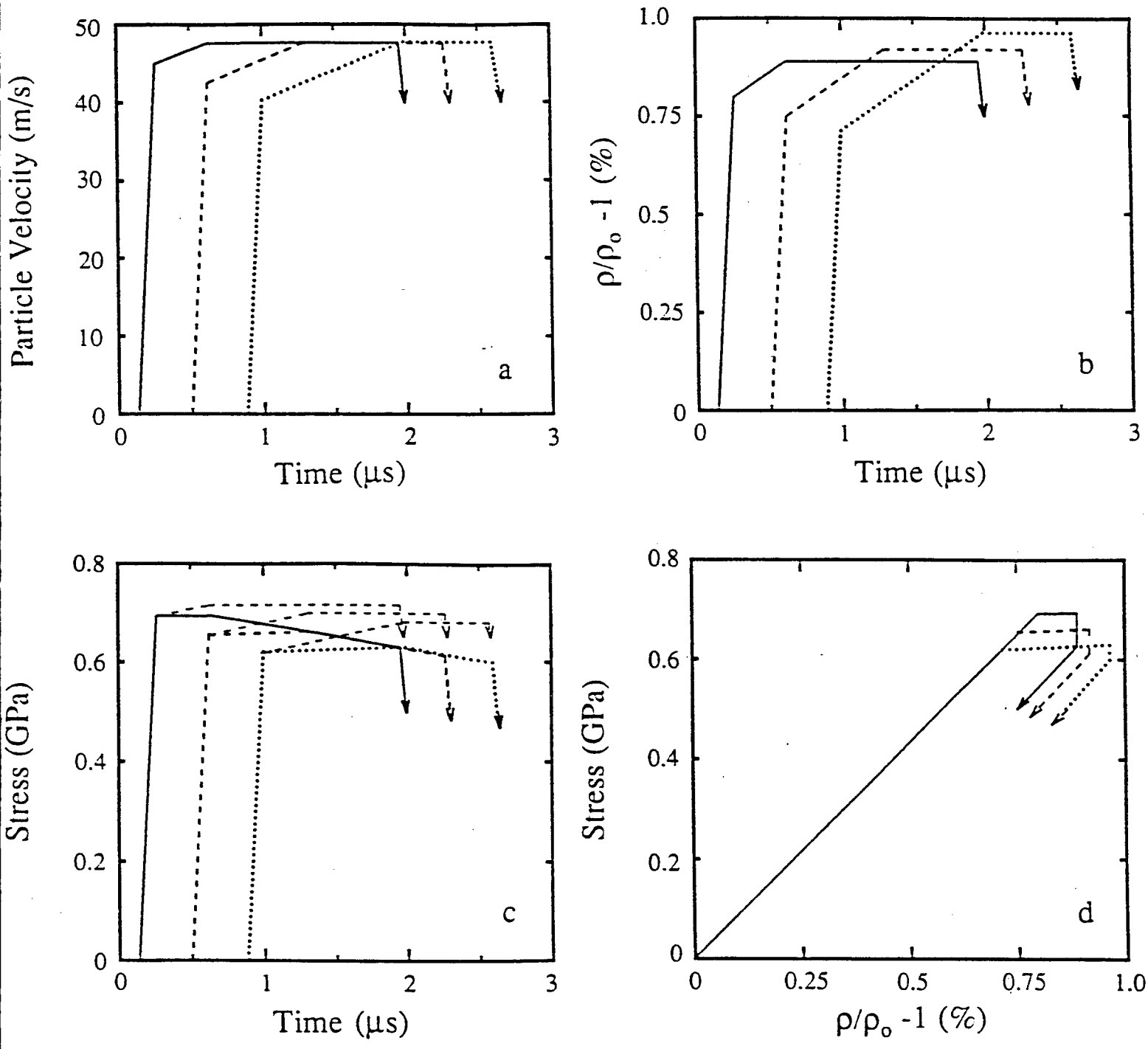
Aidun, J. B. & Y. M. Gupta, J. Appl. Phys. 69 (1991) 6998.

Cowperthwaite, M. and R. F. Williams, J. Appl. Phys. 42 (1971) 456.

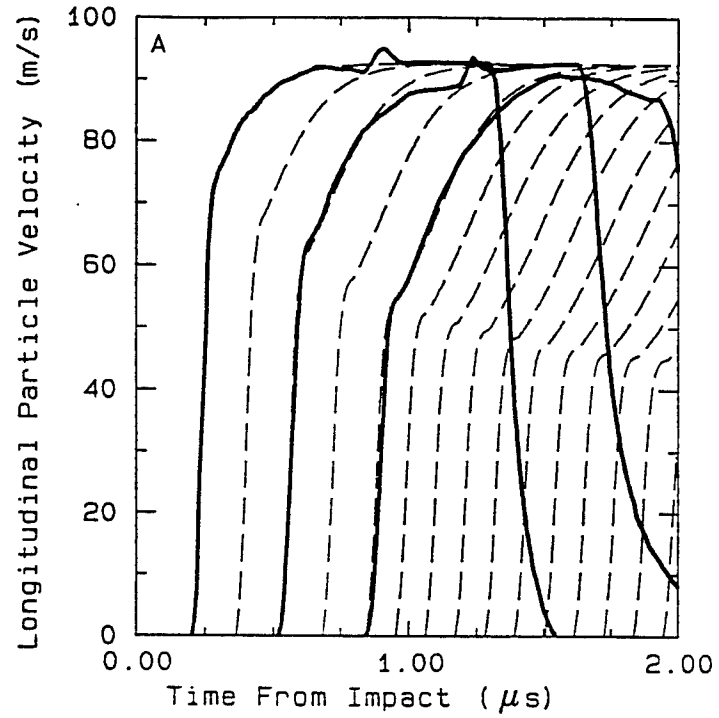
Cowperthwaite, M., p. 245 in *Shock Compression of Condensed Matter - 1991*, S. C. Schmidt, et al., eds. Elsevier Science (Amsterdam, 1992).

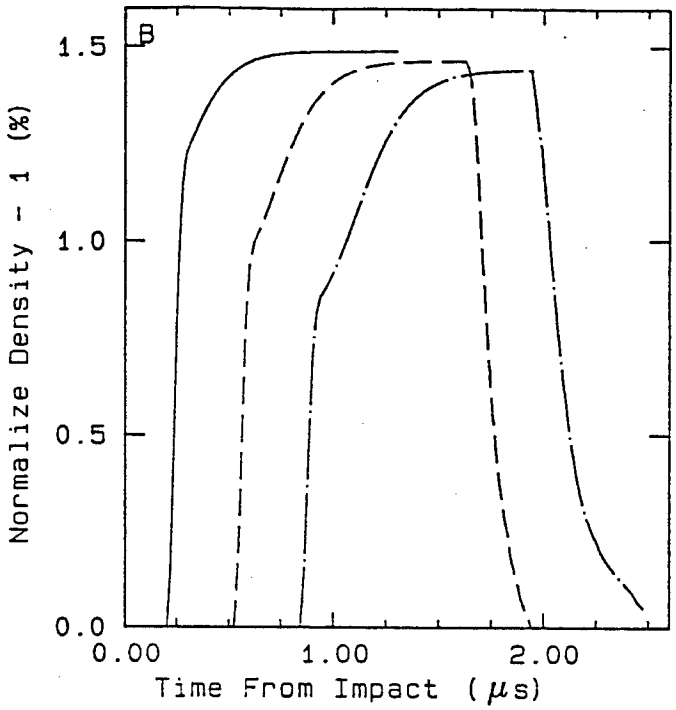
Forest, C. A., *ibid.* p. 317.

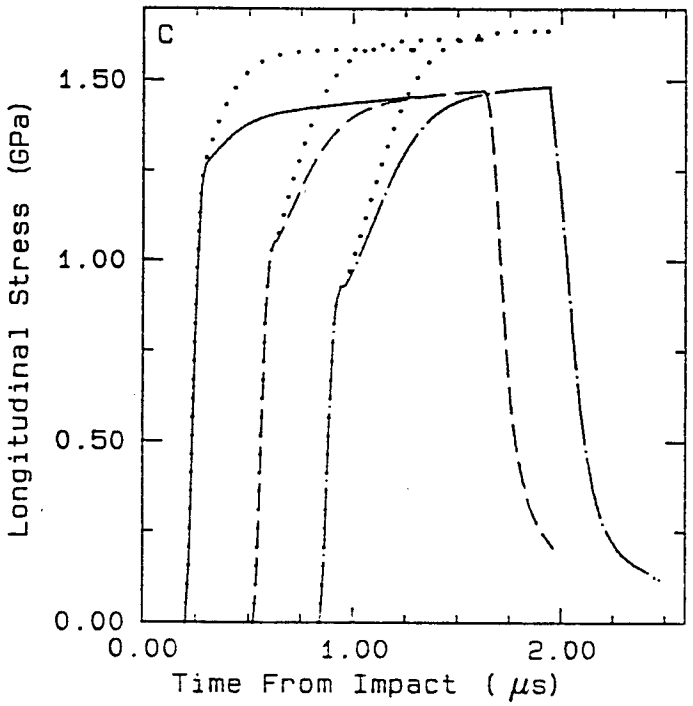
EXAMPLE 1

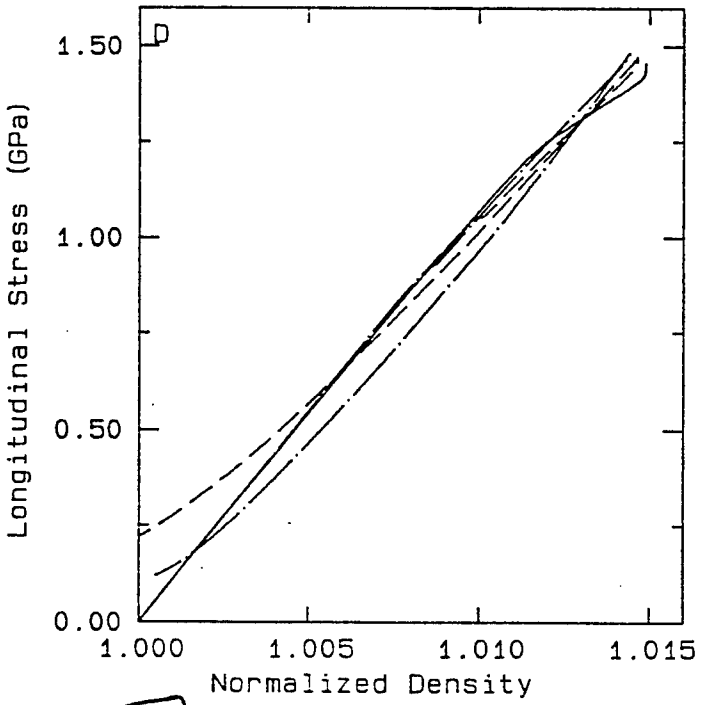

Particle Velocity (m/s)
50
40
30
20
10
0
0
1
2
3
Time (μs)
a
ρ/ρo -1 (%)
1.0
0.75
0.5
0.25
0
0
1
2
3
Time (μs)
b
Stress (GPa)
0.8
0.6
0.4
0.2
0
0
1
2
3
Time (μs)
c
Stress (GPa)
0.8
0.6
0.4
0.2
0
0
0.25
0.5
0.75
1.0
ρ/ρo -1 (%)
d

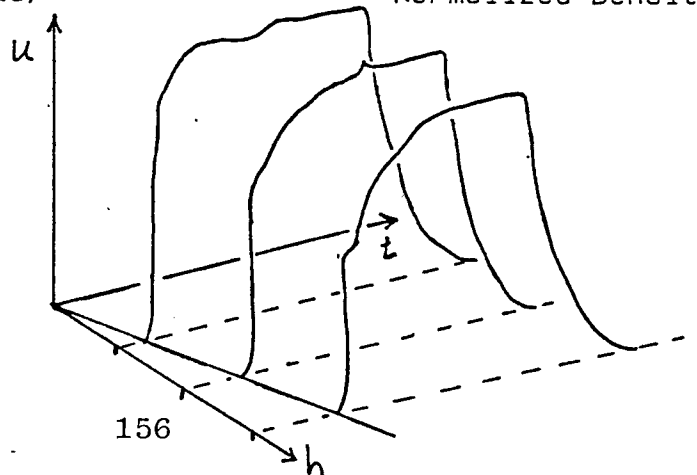
EXAMPLE 2


A
Longitudinal Particle Velocity (m/s)
100
80
60
40
20
0
0.00
1.00
2.00
Time From Impact (μs)


B
Normalize Density - 1 (%)
1.5
1.0
0.5
0.0
0.00
1.00
2.00
Time From Impact (μs)


C
Longitudinal Stress (GPa)
1.50
1.00
0.50
0.00
0.00
1.00
2.00
Time From Impact (μs)


D
Longitudinal Stress (GPa)
1.50
1.00
0.50
0.00
1.000
1.005
1.010
1.015
Normalized Density


u
t
156
h

INFLUENCE OF EQUATION OF STATE (EOS) AND CONSTITUTIVE BEHAVIOR ON SEISMIC COUPLING

T. N. Dey
Physics Division
Los Alamos National Laboratory
Los Alamos, NM 87545

ABSTRACT

A series of calculations, using a granite equation-of-state (EOS) illustrate the dependence on initial cavity size and on shear strength of parameters commonly used to describe the reduced velocity potential (RVP) and reduced displacement potential (RDP).

Calculations for explosions in cavities in granite support both the results of Terhune, et al. (1979) showing enhanced seismic coupling for initial cavities of a few scaled meters radii and the results of King, et al. (1989) showing no enhanced coupling in the hydrodynamic regime for the same initial cavity sizes.

Calculations of seismic coupling for tamped explosions with the same granite model except for variations in shear strength show the transition from a strength dominated regime to an overburden dominated regime. When the rock strength is insufficient to prevent a large cavity rebound driven by the overburden stresses, the coupling as measured by the asymptotic RDP value becomes independent of strength. The RDP overshoot parameter appears to be a good indicator of whether this is occurring. It may be a useful parameter to filter the database of seismic records from nuclear explosions when looking for correlations with rock properties.

INTRODUCTION

Two factors that influence the seismic waves produced by a nuclear explosion are decoupling produced by larger strengths and decoupling produced by detonating the explosion in a large cavity. A series of calculations, using a granite EOS illustrate the dependence on initial cavity size and on shear strength of parameters commonly used to describe the RVP and RDP.

Some of the work on decoupling by cavities shows apparently contradictory results. Work by Terhune, et al.on a deeply buried explosion in granite indicated the possibility of enhanced seismic coupling for cavities of about two scaled meters radii as compared with fully tamped configurations, while larger cavities would produce decoupling compared with the tamped configuration. On the other hand, work by King, et al. on coupling in the hydrodynamic regime (peak pressures greater than about 10 GPa) showed only decoupling for the range of cavity sizes studied, which was up to about five scaled meters radii. This study did show, however, that enhanced hydrodynamic coupling could be achieved if radiation pressure effects on the equations-of-state were omitted. King, et al. speculated that the enhancement demonstrated by Terhune, et al. for seismic coupling may be due to omitting this effect. One of the motivations for the work reported on here is to resolve this issue. This paper shows that decoupling in the hydrodynamic regime for cavities near two scaled meters radii occurs simultaneously with enhanced coupling in the seismic regime. The important consideration on where enhancement or decoupling is obtained is the comparison of the retained specific energy in the air in the cavity to that retained in the rock under similar pressure conditions.

The influence of shear strength in the rock mass on the coupling of explosion energy to the seismic field has received attention in many studies over the past few decades. The analytic studies typically show a strong dependence of the steady-state RDP on shear strength (e.g., Haskell 1961), while empirical studies (Denny and Johnson 1991) indicate that this dependence is not so clear in the data. The analytic studies have focused on the influence of strength, together with overburden stresses, in preventing cavity growth. This paper shows results for variations in shear strength of the same granite used in the cavity coupling calculations. The results of these calculations indicate that strength is also important in resisting cavity rebound, but that overburden stresses may overwhelm this effect. These results may help resolve some apparent conflicts between observations and theory.

COUPLING OF EXPLOSIONS IN CAVITIES

A series of calculations were carried out to try to resolve the differences in coupling for explosions in cavities in granite observed in calculations for the seismic regime by Terhune, et al. and for the hydrodynamic regime by King. et al. A model was developed that attempted to reproduce the material model and depth of burial used in the Terhune calculations. The pressure-volume and shear strength envelopes are copies of those in the Terhune report. The high pressure EOS used in the Terhune work could not be so readily duplicated, so the Sesame tabular EOS used by King et al. was substituted instead. Some adjustments in the pressure-volume curve of Terhune in the 5-10-GPa region were necessary to ensure a smooth transition from the low pressure to the high pressure EOS. The simulated depth of burial of 1000 m with an explosive yield of 1 kt used by Terhune was also used in these calculations, and the computational mesh was initialized with the linear elastic solution for stress concentration around an open spherical cavity. Radiation pressure effects on the EOS are included, but radiative energy transfer was not simulated.

Coupling in the hydrodynamic regime was estimated by comparing the ranges to peak stresses between 10 GPa and 100 GPa for calculations with a cavity compared with the baseline fully tamped calculation. The cube of the ratio of range to a specified peak stress for a cavity calculation

to the corresponding range in the baseline calculation gives an estimate of the apparent yield of the cavity calculation. The seismic coupling was estimated from the reduced displacement potential function computed at sufficiently large ranges, about 150 m, so that the material in the calculation was remaining in the linear elastic regime. The steady-state RDP value was used as a measure of the coupling.

Figure 1 shows results for coupling in the hydrodynamic regime as a function of cavity size. The results shown here confirm the results of King, et al. where only decoupling was observed in the hydrodynamic regime. Figure 2 shows results for coupling in the seismic regime. In contrast to the hydrodynamic regime, enhanced coupling is observed for cavities with radii of about 1 to 4 scaled meters. This confirms the results of Terhune, et al. The enhancement observed in the calculations reported here, about a factor of two at the peak, is actually larger than that seen in the Terhune calculations.

The results shown here should resolve the issue raised in King, et al. about the origin of the enhanced coupling in the seismic regime for certain cavity sizes. King, et al. speculated that the enhanced seismic coupling was due to the possible absence of radiation pressure effects in the Terhune high pressure EOS. The King, et al. position was that similar enhanced coupling or decoupling should occur in both the hydrodynamic and seismic regimes. The results displayed in Figures 1 and 2 show that this is not the case. Enhanced coupling or decoupling in the seismic regime is essentially independent of the same effects in the hydrodynamic regime. The causes for this behavior, and an explanation of the enhanced coupling region for the seismic regime for

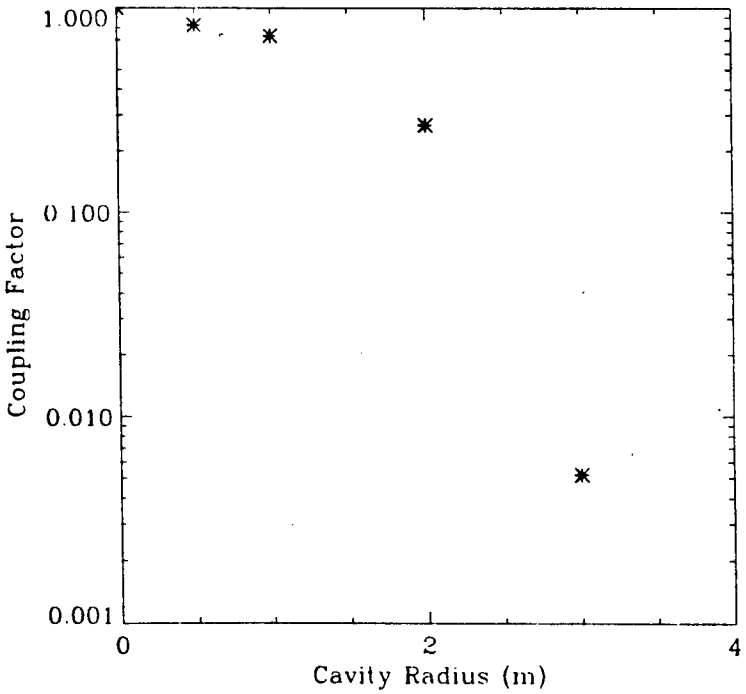


Fig. 1. Coupling in the hydrodynamic regime as a function of initial cavity radius.

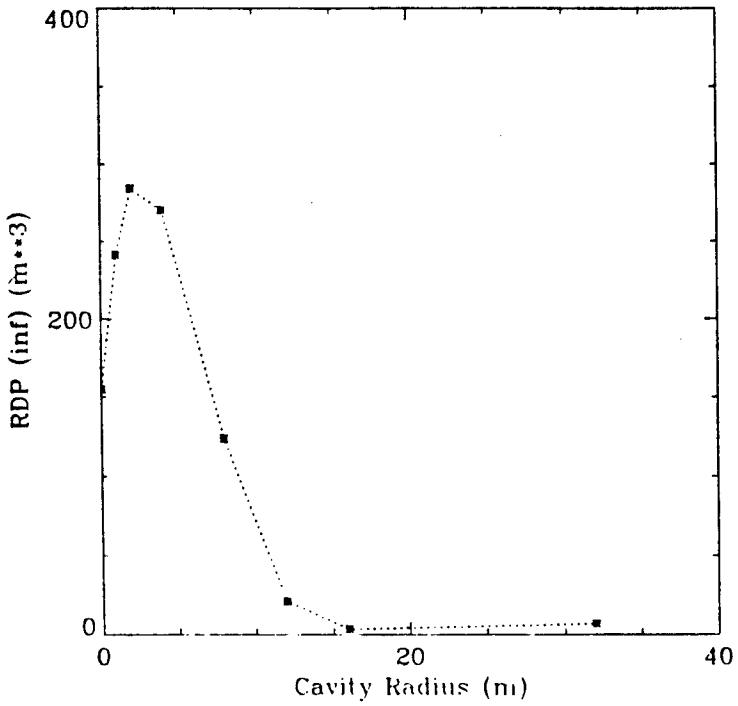


Fig. 2. Coupling, as shown by the steady-state RDP value, in the seismic regime as a function of the initial cavity radius.

granite, and the relative lack of such a region for tuff, have been traced to features of the release adiabatics for air and rock. These results will be discussed in a future paper.

STRENGTH EFFECTS ON COUPLING

An accurate assessment of the strength of a rock mass is difficult to obtain, while at the same time, strength may have important effects on coupling. Denny and Johnson review some of the work done on strength effects and coupling and note that the observations on coupling of events in strong rocks are not statistically distinguishable from those involving weak rocks. At the same time, theoretical investigations (i.e., Haskell) as well as near field measurements indicate that strength can have a significant effect on coupling.

A series of calculations was performed to study this issue. The baseline configuration is the tamped calculation used in the cavity decoupling study above. Calculations with the shear strength envelope multiplied or divided by various factors provide the variations.

The RDP functions and RVP spectra for these calculations are shown in Figures 3 and 4. Figure 5 shows results for the steady-state RDP as a function of the ratio of the strength envelope in the calculation in question to the baseline calculation. For strength ratios greater than about 0.4, the coupling as measured by this RDP value shows the expected trend with decreased coupling with increased strength. For strength ratios of 0.25 and less, the asymptotic RDP values are

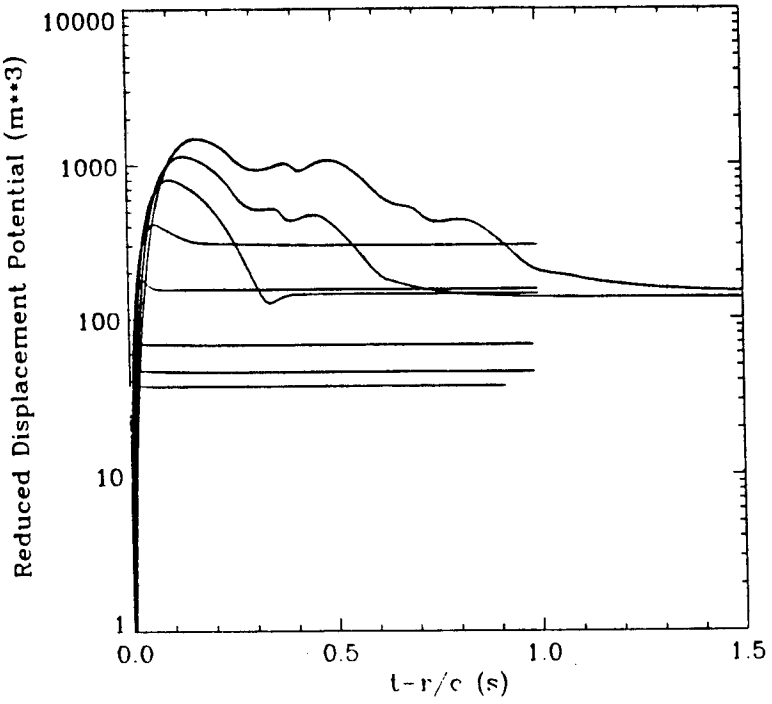


Fig. 3. RDP functions of various strength ratios. From top to bottom at 0.2 s, the lines correspond to strength ratios of 1/16, 1/8, 1/4, 1/2, 1, 2, 4, and 8.

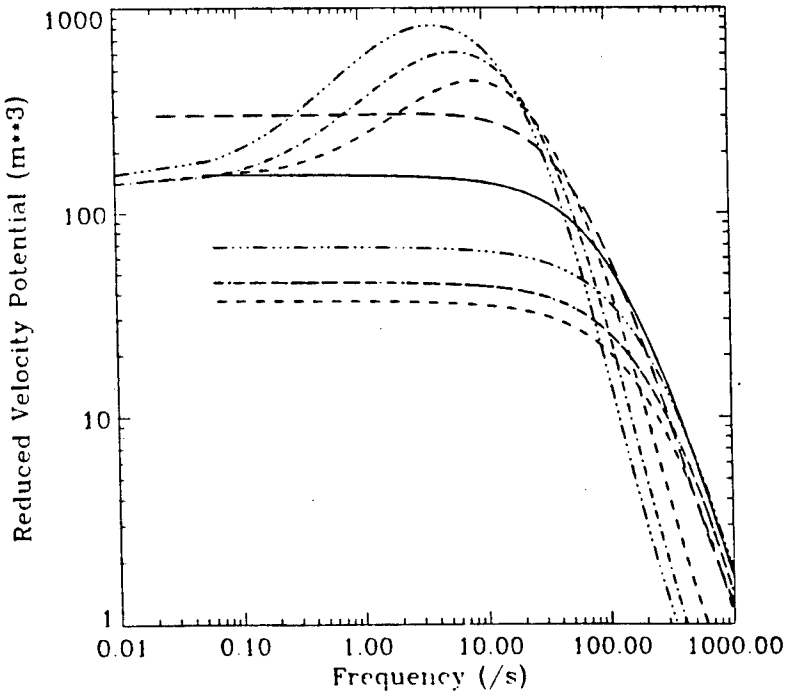


Fig. 4. RVD spectra for various strength ratios. From top to bottom at 5/s, the lines correspond to strength ratios of 1/16, 1/8, 1/4, 1/2, 1, 2, 4, and 8.

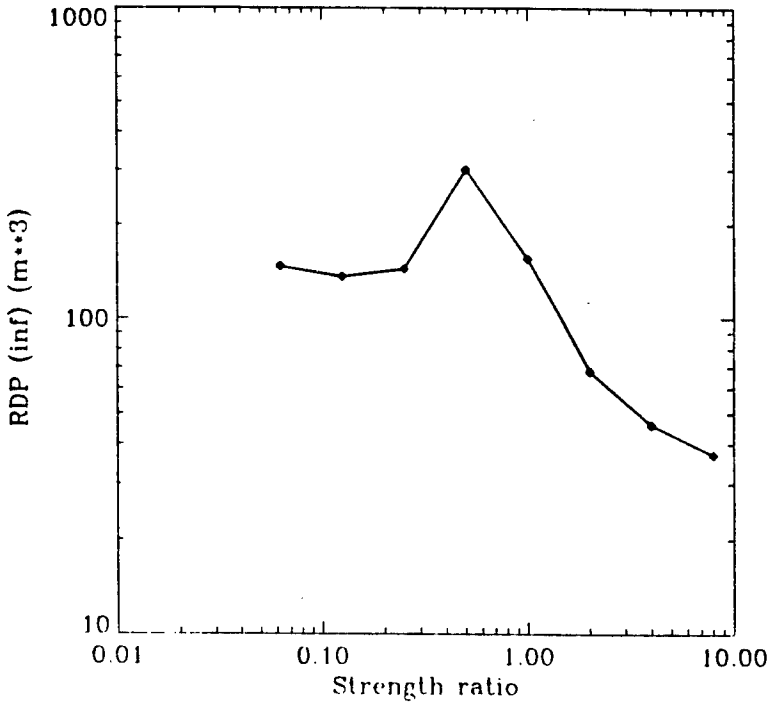


Fig. 5. Asymptotic value of the RDP as a function of the ratio of the strength envelope to that for the baseline case.

virtually independent of strength. The higher strength values follow the theoretical trends derived in the work of many investigators, while the lower strength behavior appears more consistent with the empirical results shown by Denny and Johnson.

Figure 6 gives more confidence in this result. This figure shows the asymptotic RDP value plotted as a function of the final cavity radius. The results from all the calculations, regardless of strength, fall on the same line. This line has the same slope, 3 on a log-log plot, as is theoretically expected, indicating that the asymptotic RDP values calculated are consistent with the displacements regardless of the strength used.

For all but the three smallest sets of strengths, the final cavity radius increases as strength decreased as is shown in Figure 7. For the three smallest sets of strengths, the trend changes. The final cavities are abruptly smaller than for moderately larger strengths, and the final cavity radius is approximately independent of the strength value. In contrast, the maximum transient cavity radius shows a monotonic trend of greater radius with lower strength in Figure 8.

For the four calculations with strength ratios of 1 or greater, the final cavity radius is only slightly smaller than the maximum transient cavity. The remaining four calculations, and particularly those three with the lowest strengths, have final cavities significantly smaller than the maximum transient cavity.

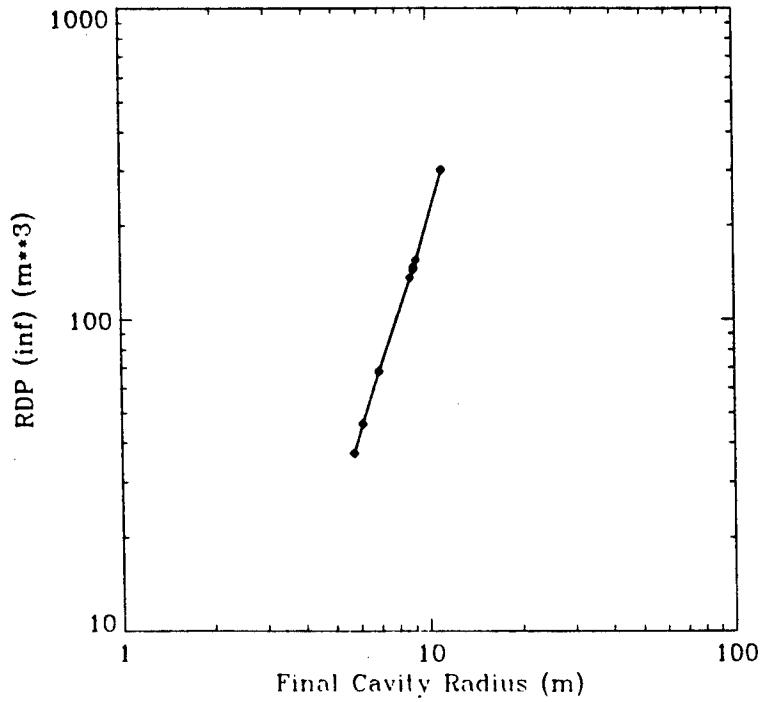


Fig. 6. Asymptotic value of the RDP as a function of the final cavity radius of the set of calculations.

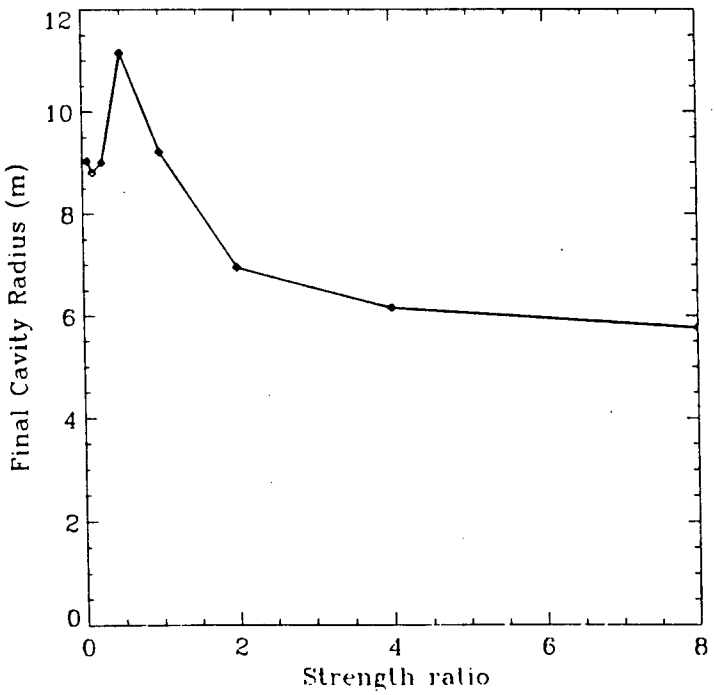


Fig. 7. Final cavity radius as a function of the ratio of the strength envelope to that for the baseline case.

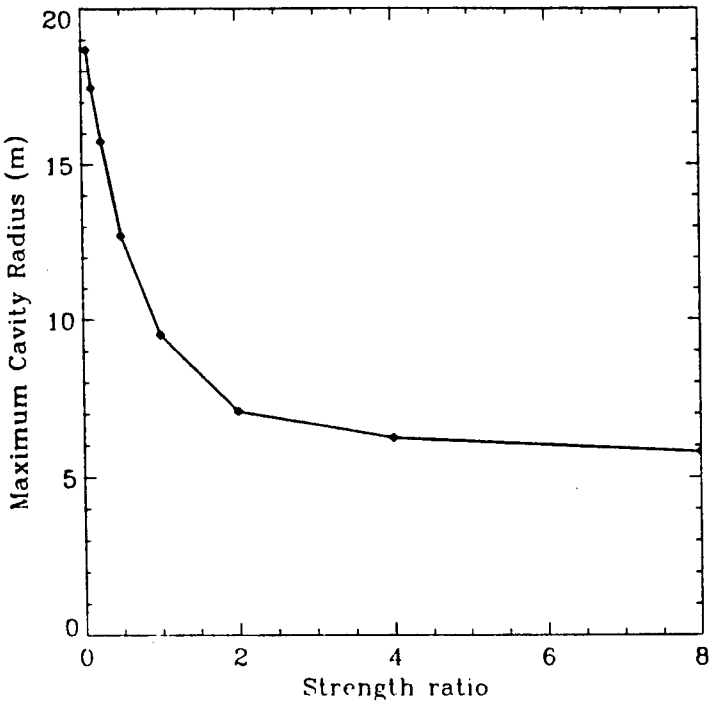


Fig. 8. Maximum transient cavity radius as a function of the ratio of the strength envelope to that for the baseline case.

Figure 9 shows the roll-off at high frequencies of the RVP spectra as a function of the strength ratio. Higher strength is accompanied by a steeper roll-off for strength ratios greater than about 1. At low strengths, however, the roll-off is also steep with a slope of about –2.45.

The changes in corner frequency with strength are illustrated in Figure 10. The corner frequency generally drops as strength decreases, although there is a discontinuity between the half and quarter strength calculations. This discontinuity occurs at the same strength ratio as the change from increasing to decreasing RDP with decreasing strength occurred. At high strengths, the results appear to be approaching a steady-state value of about 200/s. This frequency is of the right order of magnitude to accompany final cavity radii of about 6 m.

Overshoot in the RDP as a function of strength ratio is plotted in Figure 11. For all strength ratios of 1 or greater, the overshoot is only slightly greater than 1. For smaller strength ratios, the overshoot values increase dramatically as strength is decreased. This change in behavior also corresponds well with the change in trend of RDP as function of strength and the discontinuity in the corner frequency plot.

DISCUSSION

The large rebound from the maximum transient cavity size to the final cavity size for the lowest strength calculations indicates the source of the change in behavior from the higher strength calculations. During the early part of the problem, when the cavity is growing towards its

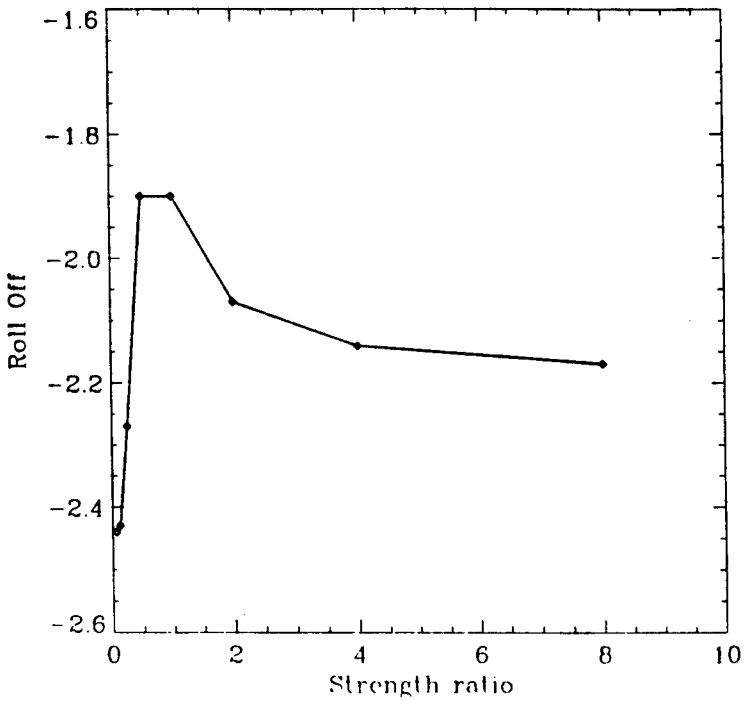


Fig. 9. Roll-off of the RVP spectrum as a function of the ratio of the strength envelope to that for the baseline case.

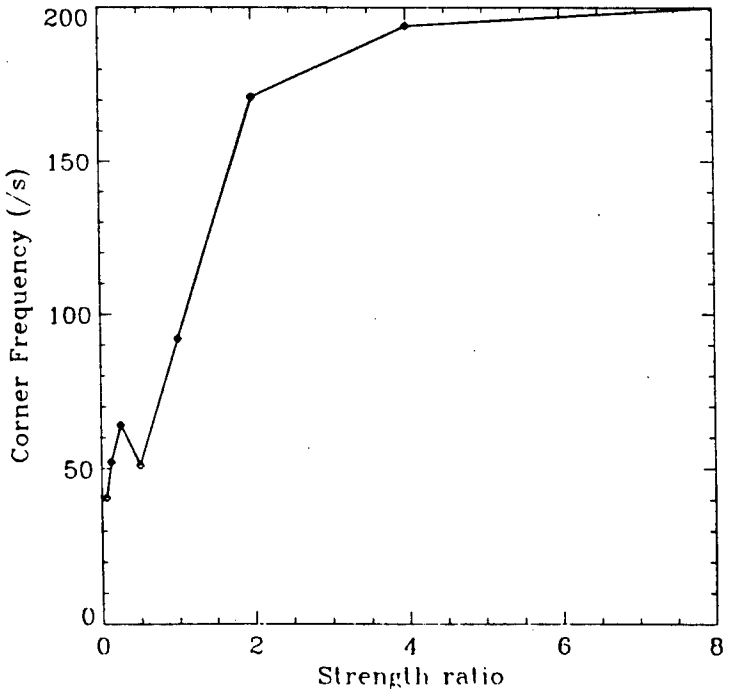


Fig. 10. Corner frequency of the RVP spectrum as a function of the ratio of the strength envelope to that for the baseline case.

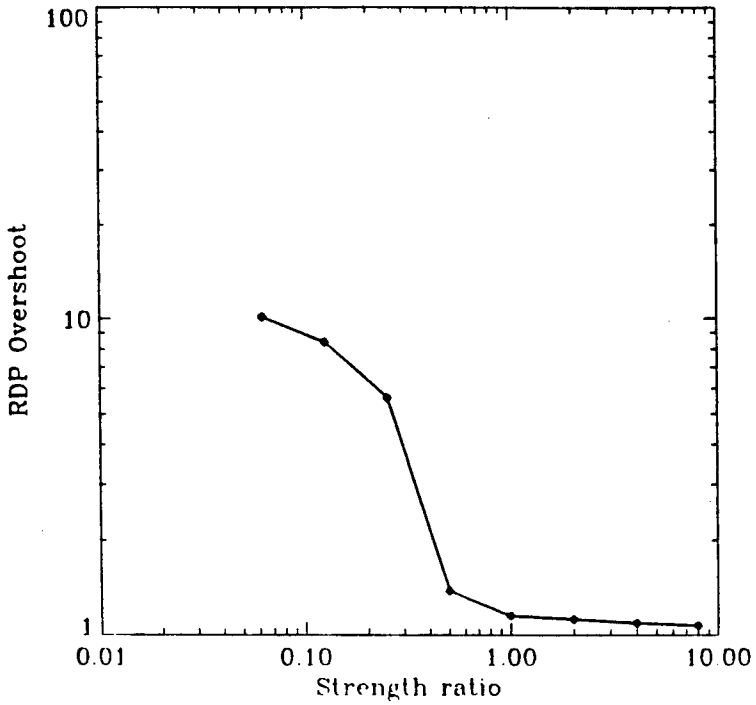


Fig. 11. Overshoot of the RDP as a function of the ratio of the strength envelope to that for the baseline case.

maximum transient size, both the overburden stresses and the rock strength are acting to resist the cavity growth. After the maximum size is reached, the overburden stress continues to try to shrink the cavity. Now, in addition to the resistance provided by the cavity pressure, the rock strength also resists the rebound of the cavity. For the cavity to rebound by more than a small amount, the rock must fail with a reverse sense of shear from that prevailing during the cavity growth phase. The calculations with the stronger failure envelopes have sufficient strength to prevent a large rebound. The low strength calculations do not have sufficient strength, and rebound continues until the cavity gases are sufficiently compressed so that the cavity pressure approximately balances the overburden pressure, a condition which leaves negligible shear stresses in the rock mass. Because this final state does not depend significantly on the rock strength, the seismic coupling as measured by the steady-state RDP value becomes independent of rock strength.

This condition, where the overburden pressure is more important than rock strength in determining the seismic coupling, is accompanied in these calculations by significant overshoot in the RDP curves, and, to a lesser extent, in changes in the roll-off of the RVP. This suggests that RDP overshoot may be a good indicator of the dominance of overburden pressure over rock strength in the seismic coupling process. Denny and Johnson remark on the lack of apparent significance of rock type to correlation of the steady-state RDP value with yield. The significance of rock type may be masked if the coupling of many of the events is dominated by the overburden pressure and not the rock strength. It might be a useful exercise to sort the seismic records from nuclear events according to whether there is significant RDP overshoot or not and then look for correlations of the steady-state RDP values with rock type.

CONCLUSIONS

Calculations for explosions in cavities in granite support both the results of Terhune, et al. showing enhanced seismic coupling for initial cavities of a few scaled meters radii and the results of King, et al. showing no enhanced coupling in the hydrodynamic regime for the same initial cavity sizes.

Calculations of seismic coupling for tamped explosions with the same granite model except for variations in shear strength show the transition from a strength dominated regime to an overburden dominated regime. When the rock strength is insufficient to prevent a large cavity rebound driven by the overburden stresses, the coupling as measured by the asymptotic RDP value becomes independent of strength. The RDP overshoot parameter appears to be a good indicator of whether this is occurring. It may be a useful parameter to filter the database of seismic records from nuclear explosions when looking for correlations with rock properties.

ACKNOWLEDGMENTS

Thanks to Fred App, Jim Kamm, Charles Snell, and Steve Taylor for helpful discussions on these results.

REFERENCES

Denny, M. D. and L. R. Johnson, "The explosion seismic source function: Models and scaling laws reviewed," in Explosion Source Phenomenology, S. R. Taylor, H. J. Patton, and P. G. Richards, eds., Am. Geophys. Union, pp. 1-24, 1991.

Haskell, N. A., "A static theory of the seismic coupling of a contained underground explosion," J. Geophy. Res., V. 66, pp. 2937-2944, 1961.

King, D. S., B. E. Freeman, D. D. Eilers, and J. D. Johnson, "The effective yield of a nuclear explosion in a small cavity in geologic material: Enhanced coupling revisited," J. Geophy. Res., V. 94, pp. 12375, 1989.

Terhune, R. W., C. M. Snell, and H. C. Rodean, "Enhanced coupling and decoupling of underground nuclear explosions," Lawrence Livermore National Laboratory report UCRL-52806, 1979.

THIS PAGE INTENTIONALLY LEFT BLANK.

Sensitivity of the Close-in Seismic Source Function to Rock Properties. (Condensed Version)

Fred N. App
Geophysics Group
Earth and Environmental Sciences Division
Los Alamos National Laboratory

A Condensed Version
Presented at the Symposium
"Numerical Modeling for Underground Nuclear Test Monitoring"
March 23-25, 1993, Durango, CO

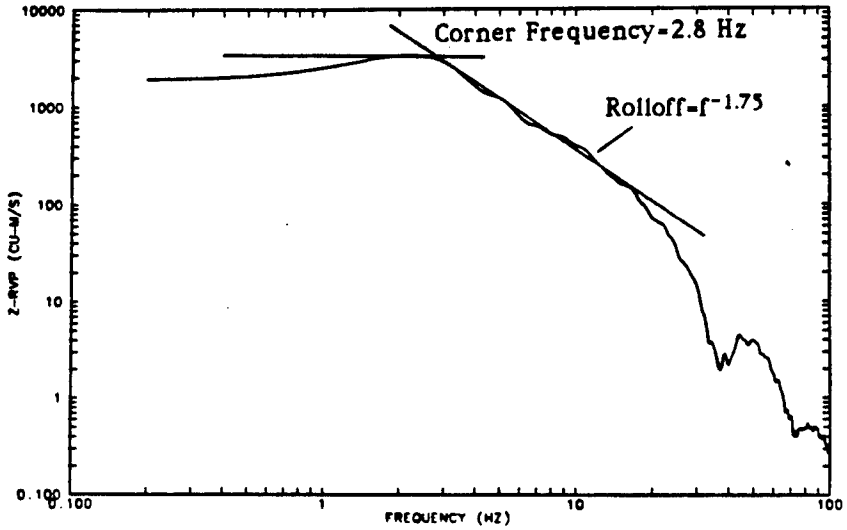
I. INTRODUCTION

The objective of this investigation is to determine and evaluate how rock properties near the origin of an explosion influence the close-in seismic source function. This is work in progress that represents one step in the systematic investigation of parameters important in the remote identification of underground nuclear tests. This is a condensed version of a full report of the same title (App, 1993). The reader is encouraged to reference that report for more details regarding material properties and cases examined. In the study, the "overshoot" and "steady state value" of the reduced displacement potential (RDP), and the "corner frequency" and "rolloff" of the reduced velocity potential (RVP) spectra are the properties of the source function used as principle measures of effect. These are illustrated in the example of Figure 1. A series of one-dimensional, spherically symmetric calculations are made with the computational mesh divided into six phenomenological regions. Figure 2 shows the geometry of the model. Material properties are modified in selected regions to evaluate source function sensitivities to properties in those regions. A calculation using a well characterized, nearly saturated tuff in all regions serves as a Baseline Case. Cases using other material properties are compared to the Baseline Case at a point located beyond the elastic radius at 300 m range (the edit point shown in Figure 2). For the Baseline Case, the peak stress at the edge of the hydrodynmaic region is about 1 GPa (10 kb). The peak stress at the outer edge of the cavity region is about 0.3 GPa (3 kb). Table I lists the cases discussed in this condensed report. Qualitative rather than quantitative differences are emphasized; i.e., scalar values for the source function properties are not listed.

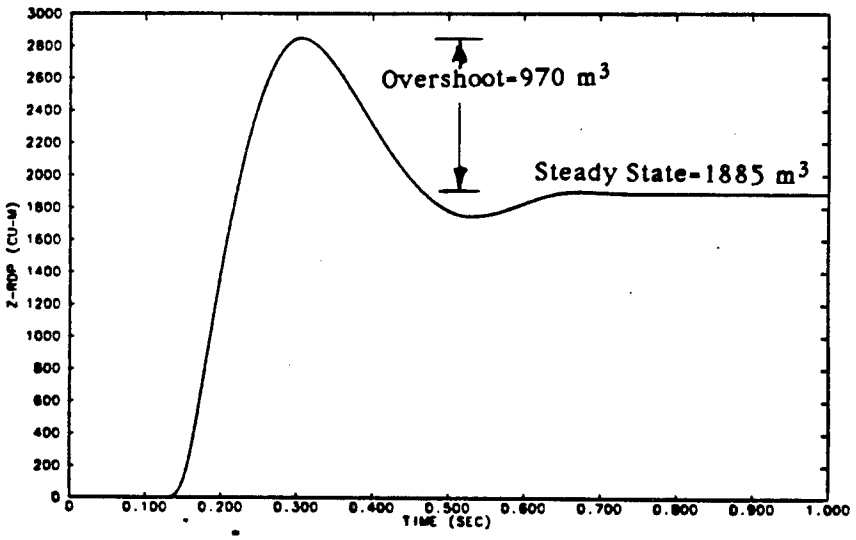
Some Relevant Properties of the Close-in Source Function

1. The "corner frequency" of the RVP spectra
2. The "rolloff" of the RVP at high frequencies
3. The "steady state value" of the RDP
4. The "overshoot" of the RDP

EXAMPLE



RVP SPECTRA



REDUCED DISPLACEMENT POTENTIAL

Figure 1. Example of four relevant properties of the source function RDP and RVP. These are the four properties selected for use as "measures of effect" for this study.

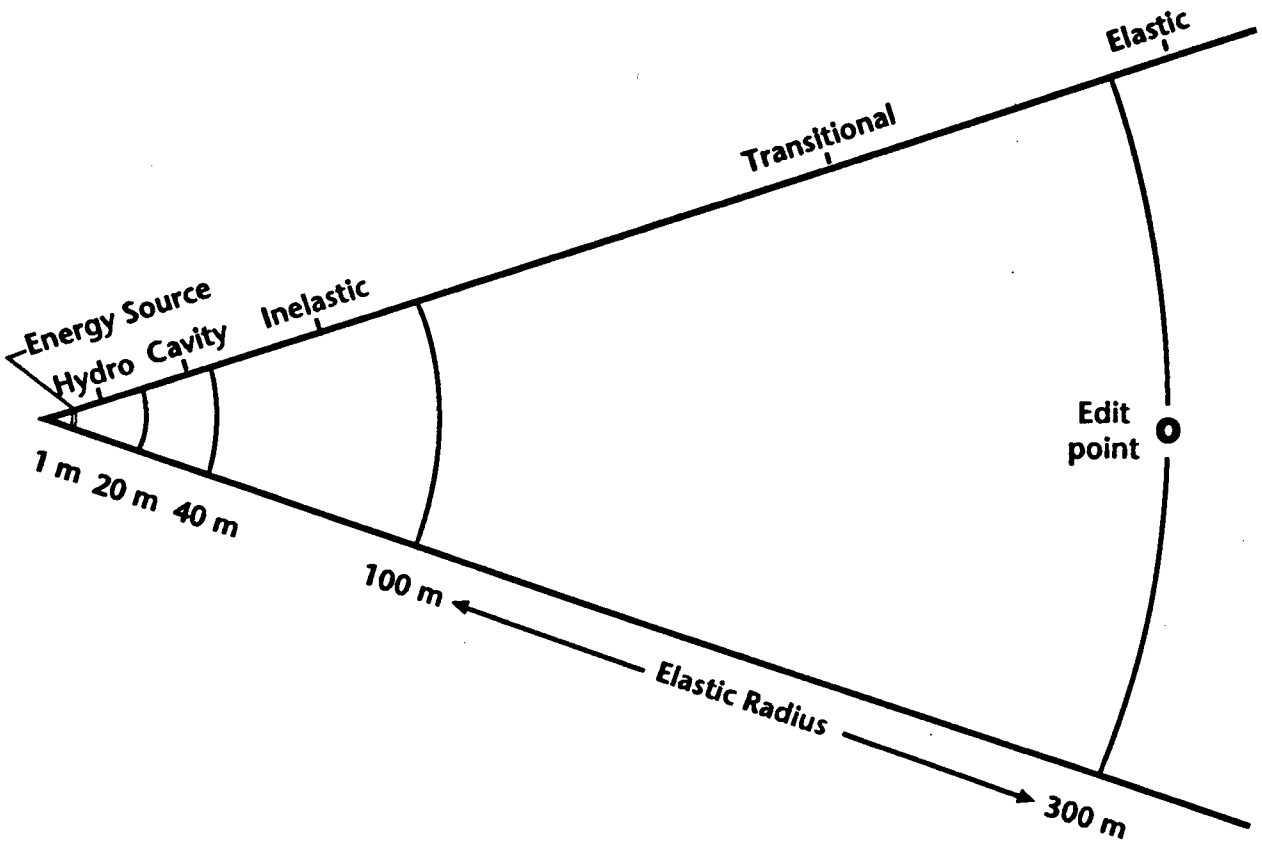


Figure 2. Geometry of the model. Spherical symmetry - indicated distances are from inner boundary of the energy source region, which is located 5 m from the center of the sphere. Case-by-case source function comparisons are made at the 300 m edit point.

TABLE I

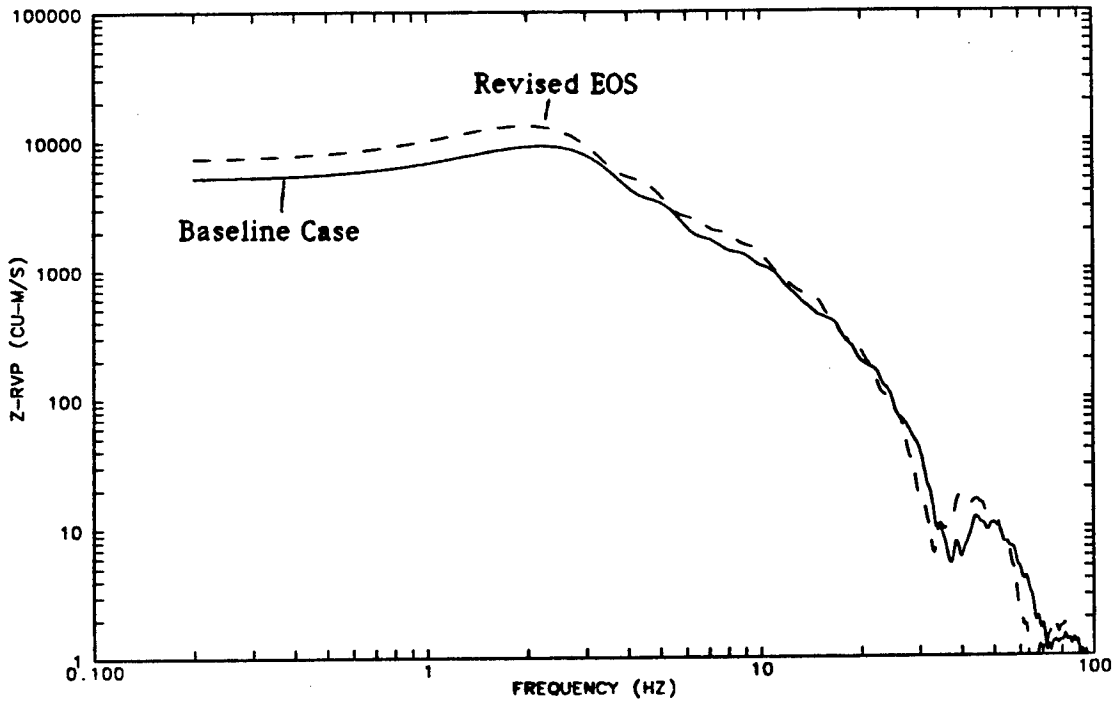
Case	Description
	Source Region - Energy Coupling.
1	Source Region - change cavity gas EOS by changing effective gamma for gamma law gas.
	Changes in Initial Bulk Density.
2a	Higher density rock to outer edge of hydro region.
2b	Higher density rock to outer edge of cavity region.
2c	Higher density rock in all regions.
3a	Lower density rock to outer edge of hydro region.
3b	Lower density rock to outer edge of cavity region.
3c	Lower density rock in all regions.
	Effects of Shear Strength.
4a	No damage to outer edge of hydro region.
4b	No damage to outer edge of cavity region.
4c	No damage for all regions.
	Changes in Rock Type.
5a	Granite to outer edge of hydro region.
5b	Granite to outer edge of cavity.
5c	Granite in all regions.
6a	Alluvium to outer edge of hydro region.
6b	Alluvium to outer edge of cavity region.
6c	Alluvium in all regions.

II. DISCUSSION

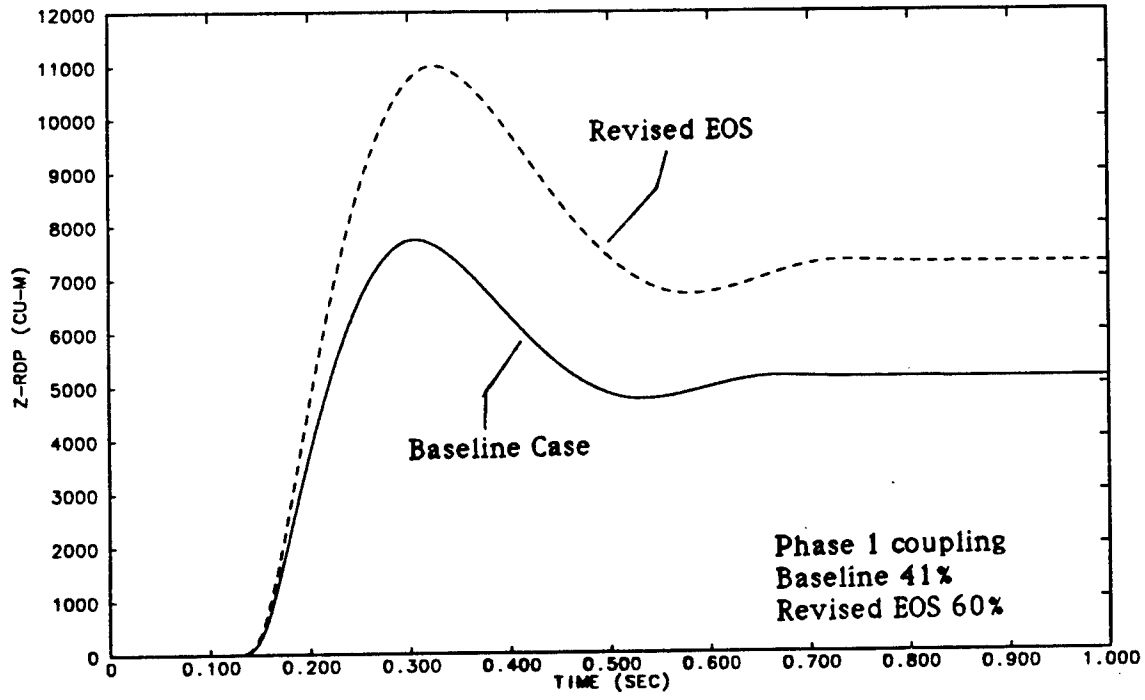
Energy coupling between a tamped explosion and the surrounding medium can be separated into two distinct phases. Phase 1 is the prompt coupling of energy into the shock wave. Vaporization, melt and the high pressure equation-of-state (EOS) play the dominant role in Phase 1 coupling, Phase 2 coupling is associated with coupling of energy from the shock wave into the elastic field, where energy losses to the medium due to compaction and other inelastic processes are important.

Case 1 specifically addresses the issue of Phase 1 coupling. It compares the Baseline Case with a calculation that uses a revised high pressure EOS. The input energies and the properties of the solid rock are identical for the two cases. For the revised EOS, the initial vapor pressure is 2.5 times greater than for the Baseline. As the shock wave develops and the cavity begins to form, the vapor pressures decrease and become very nearly equal by 0.3 ms problem time. There is no physical basis for the revised EOS - the point of the change is simply to demonstrate the sensitivity of the source function properties to variations and uncertainties in the high pressure regime (>20 GPa). Figure 3 compares the results of the two calculations. The amplitude of the RDP waveform is about 42% greater for the revised EOS than for the Baseline Case. Separate energy edits in the calculations show that 59% of the total energy remains behind in the cavity for the Baseline Case compared to only 40% for the revised EOS. This means there is considerably more energy available to the shock wave for the revised EOS. The higher RDP for the revised EOS case is due almost entirely to the increased Phase 1 coupling. This example shows that early time, high pressure cavity gas thermodynamics can affect coupling without affecting the shape of the waveform or spectral characteristics of the source function. In Figure 3, and in all subsequent figures dealing with the source function properties, the Phase 1 coupling is listed in the lower right-hand-corner.

The remainder of the cases deal primarily with Phase 2 coupling. Figure 4 shows the effect of substituting higher density material into selected regions of the model (Case 2). The in-situ bulk density is increased from its value of 1.85 Mg/m^3 for the Baseline tuff to 2.7 Mg/m^3. This is achieved by decreasing the total porosity from 41% by volume to nearly zero. Because of the decreased water to rock ratio, the loading reference curve of the high density rock is considerably stiffer than that of the Baseline tuff. The gas-filled-porosity (GFP) is unchanged between the two cases (about 1% GFP). Figure 4 shows that the changes in source function properties are quite small, even when all of the Baseline tuff is replaced by the higher density material. The source function obviously is insensitive to differences in the volumetric response characteristics of saturated or nearly saturated rocks at both high and low pressures.

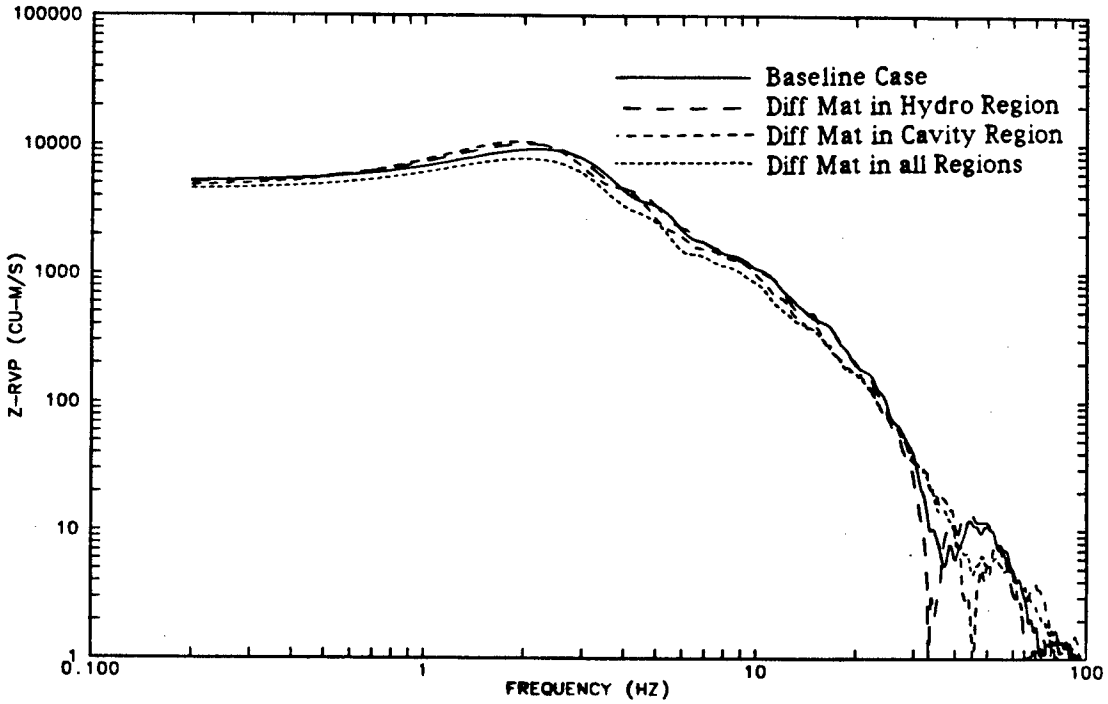


RVP SPECTRA

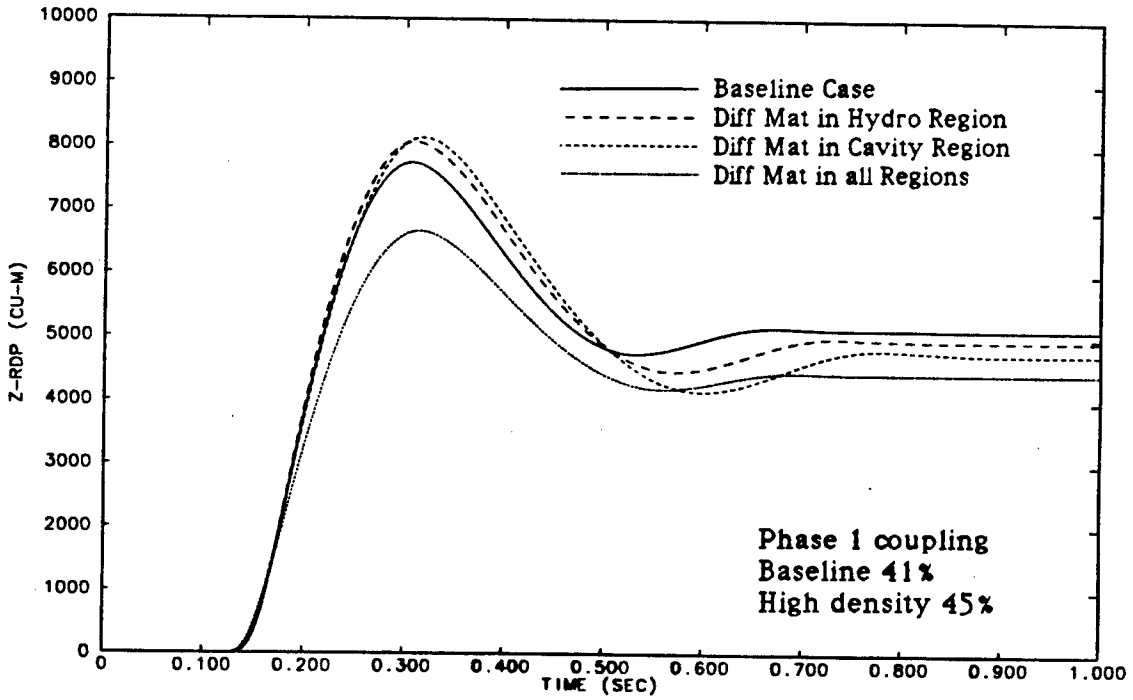


REDUCED DISPLACEMENT POTENTIAL

Figure 3. Case 1 - RVP spectra and RDP waveform comparisons at 300 m for two different cavity gas EOS treatments.



RVP SPECTRA



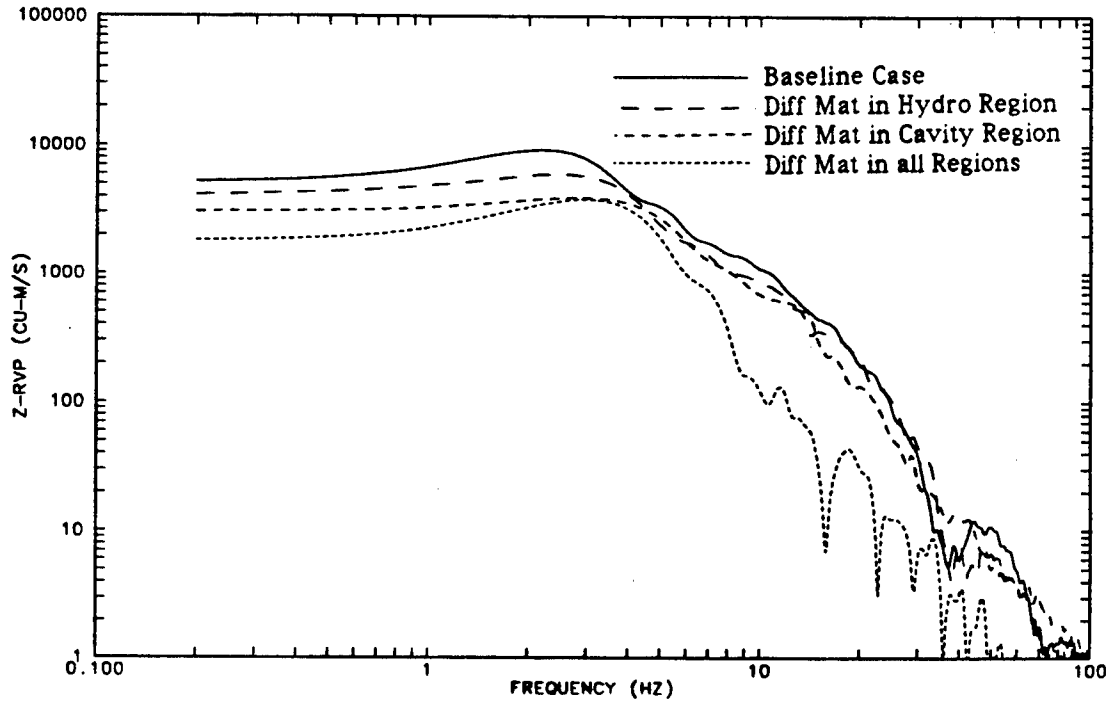
REDUCED DISPLACEMENT POTENTIAL

Figure 4. Case 2 - RVP spectra and RDP waveform comparisons at 300 m for substitution of higher density material into selected regions.

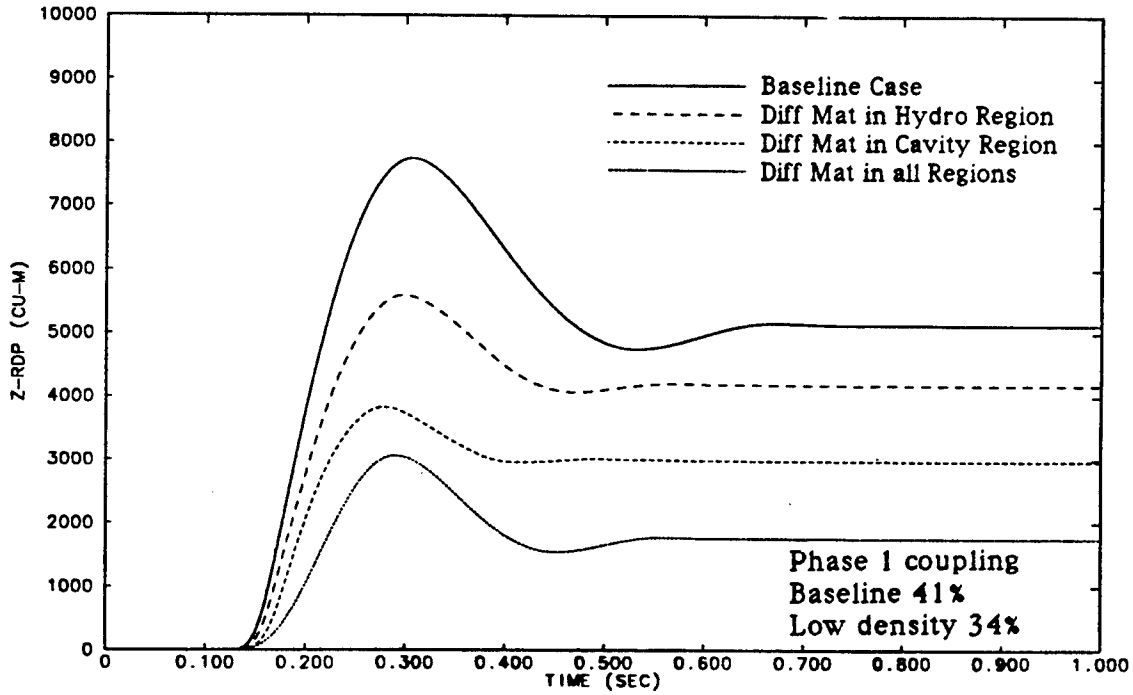
Figure 5 shows the effect of substituting lower density material into selected regions (Case 3). The reduced density is obtained by increasing the GFP from 1% to 20%. The rock to water ratio remains unchanged, therefore the loading reference curve for the solid component of the rock (rock plus water - no air) also is unchanged. The effects on the source function properties are significant. Both Phase 1 and Phase 2 coupling play a role here. The Phase 1 coupling efficiency is 34% for the lower density rock vs 41% for the Baseline tuff. With material substitution only into the hydrodynamic region, it appears that about all of the observed differences are due to the decrease in Phase 1 coupling. For substitution into the cavity region, about half is due to Phase 1 and half to Phase 2. Beyond the hydrodynamic region, differences in GFP have a strong effect on Phase 2 coupling and on both the amplitude and spectral characteristics of the source function

Figure 6 shows the effect of ground shock damage on the source function (Case 4). In this context, damage is defined as a reduction in the rock shear strength due to ground shock conditioning. Such weakening is known to occur in Tunnel Beds Tuff - the Baseline material. In this case, the substitute material is identical to the Baseline tuff except it is not allowed to damage. The effect is most noticeable on the overshoot and corner frequency, and then only when the replacement material is substituted into the cavity region and beyond. The effect is minimal for substitution only into the hydrodynamic region. For the case of material damage, the material is continually weakening as the cavity grows outward. When rebound occurs, the resistance to inward motion is considerably less than if the rock still possessed its original shear strength; thus there is more inward motion; i.e., more overshoot. The effect is not so much a damage effect per se as simply an effect of material shear strength. A material that is originally very weak would exhibit the same large overshoot behavior. In the particular example chosen here, the steady state value of the RDP is relatively unaffected.

Figure 7 shows the results for substitution of granite into the selected regions (Case 5). The main difference between granite and the earlier "high density" material is that the shear strength is increased to be representative of "good quality" dense rock. Also, in this case, the granite is not allowed to "damage". As shown in Figure 7, substitution into the hydrodynamic region has little influence on the source function characteristics. However, both the overshoot and corner frequency are strongly effected when granite is substituted into the cavity region. The steady state value of the RDP is most strongly effected in the "all granite" case, which is in marked contrast to the previous "all high density material" case (Figure 4). This implies that shear strength of material beyond the cavity has a dominant influence on the steady state value of the RDP.

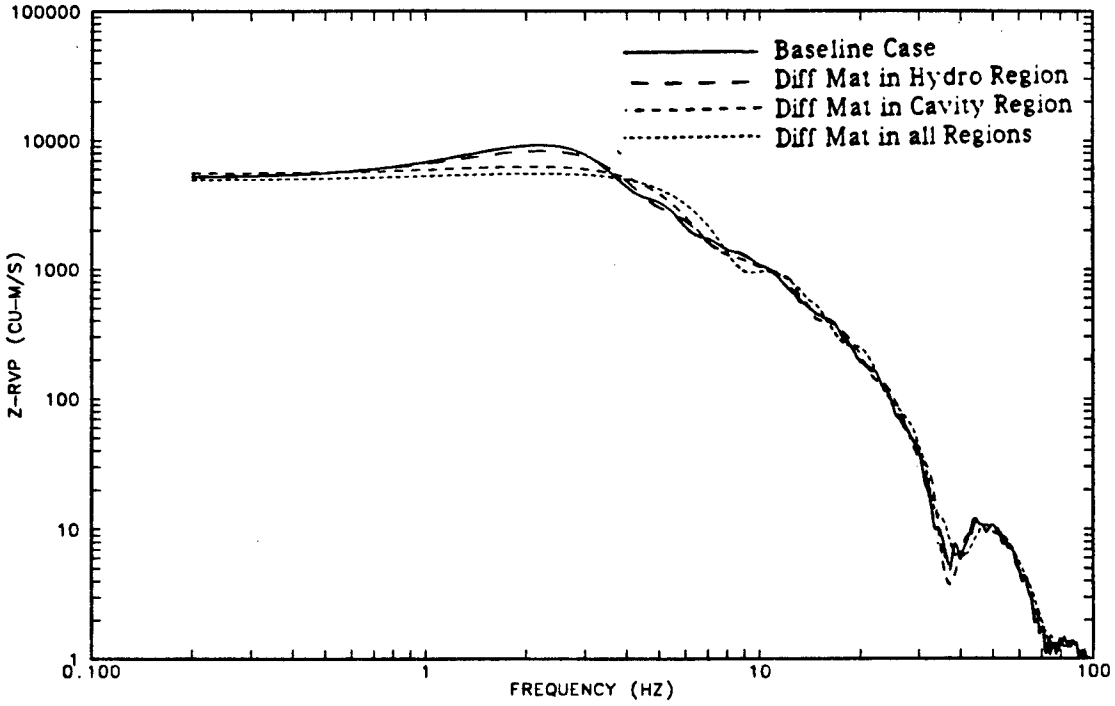


RVP SPECTRA

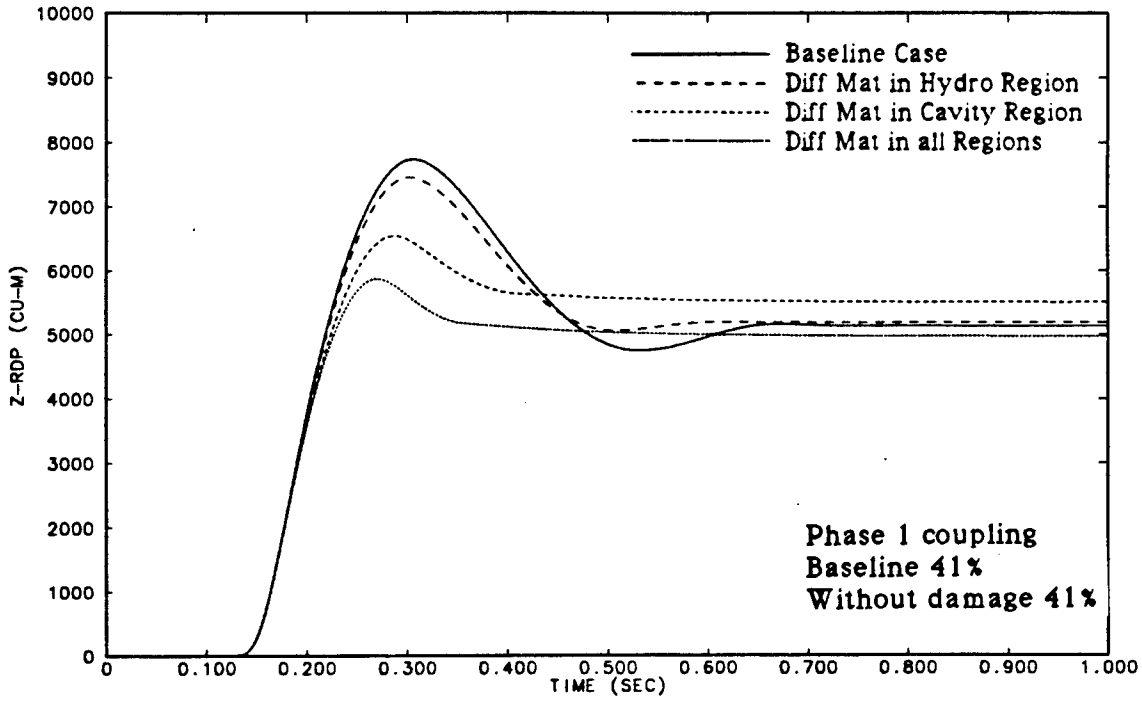


REDUCED DISPLACEMENT POTENTIAL

Figure 5. Case 3 - RVP spectra and RDP waveform comparisons at 300 m for substitution of lower density (higher gas-filled porosity) material into selected regions.

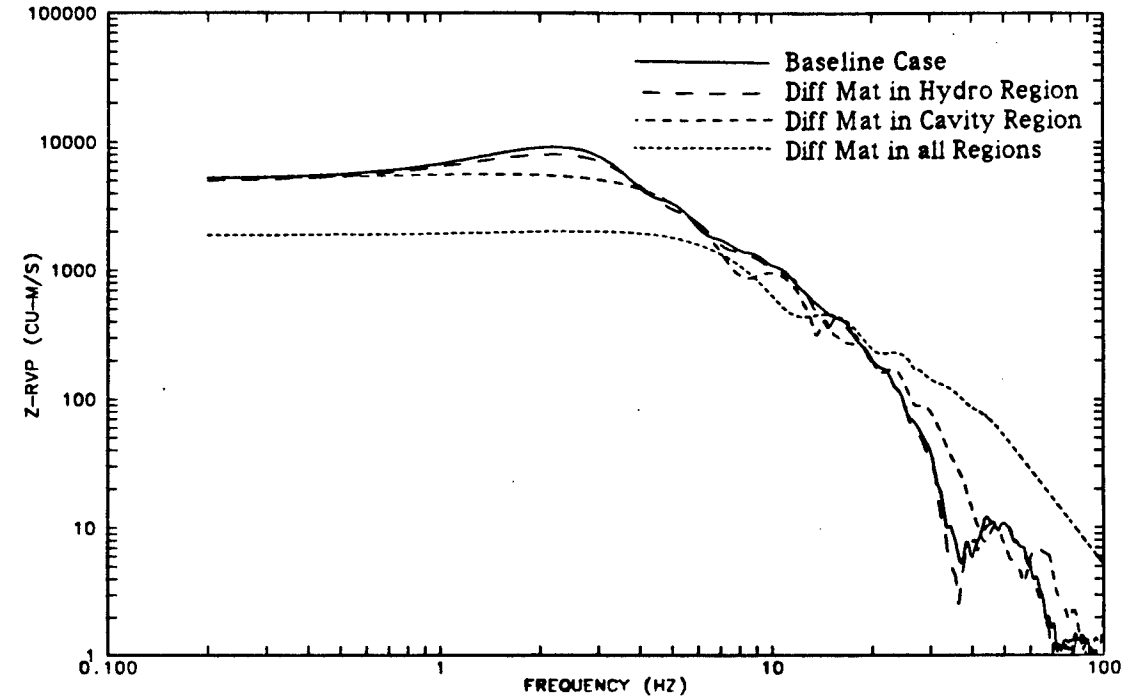


RVP SPECTRA

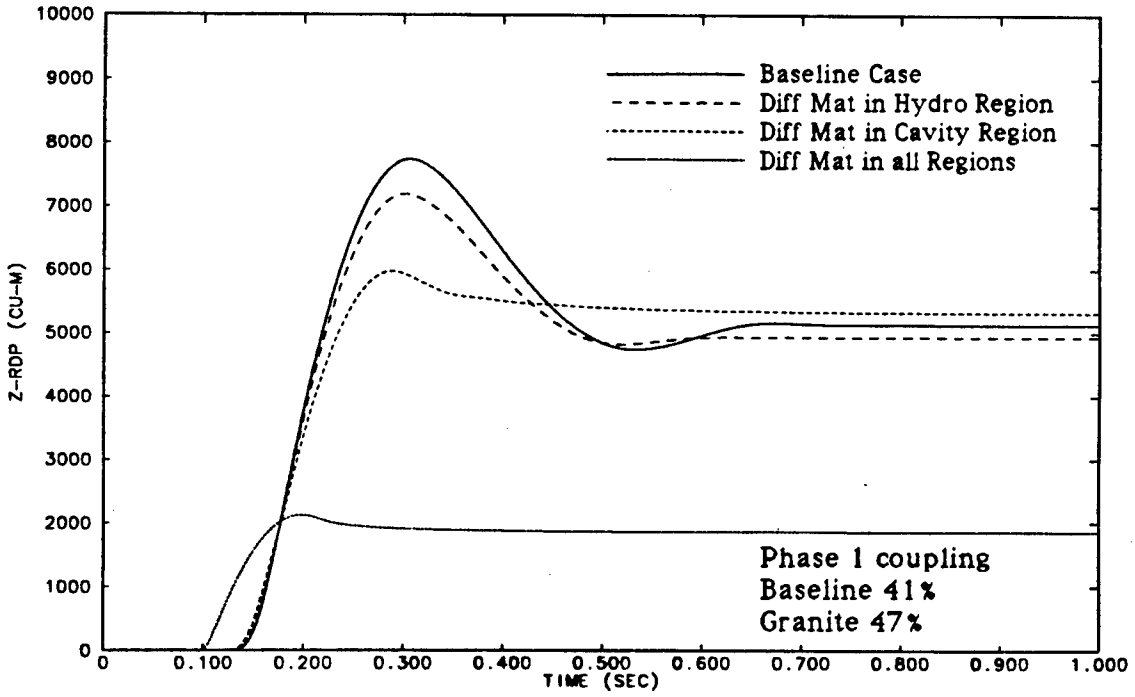


REDUCED DISPLACEMENT POTENTIAL

Figure 6. Case 4 - RVP spectra and RDP waveform comparisons at 300 m for substitution of "no-damage" material into selected regions.



RVP SPECTRA



REDUCED DISPLACEMENT POTENTIAL

Figure 7. Case 5 - RVP spectra and RDP waveform comparisons at 300 m for substitution of "good quality" granite into selected regions.

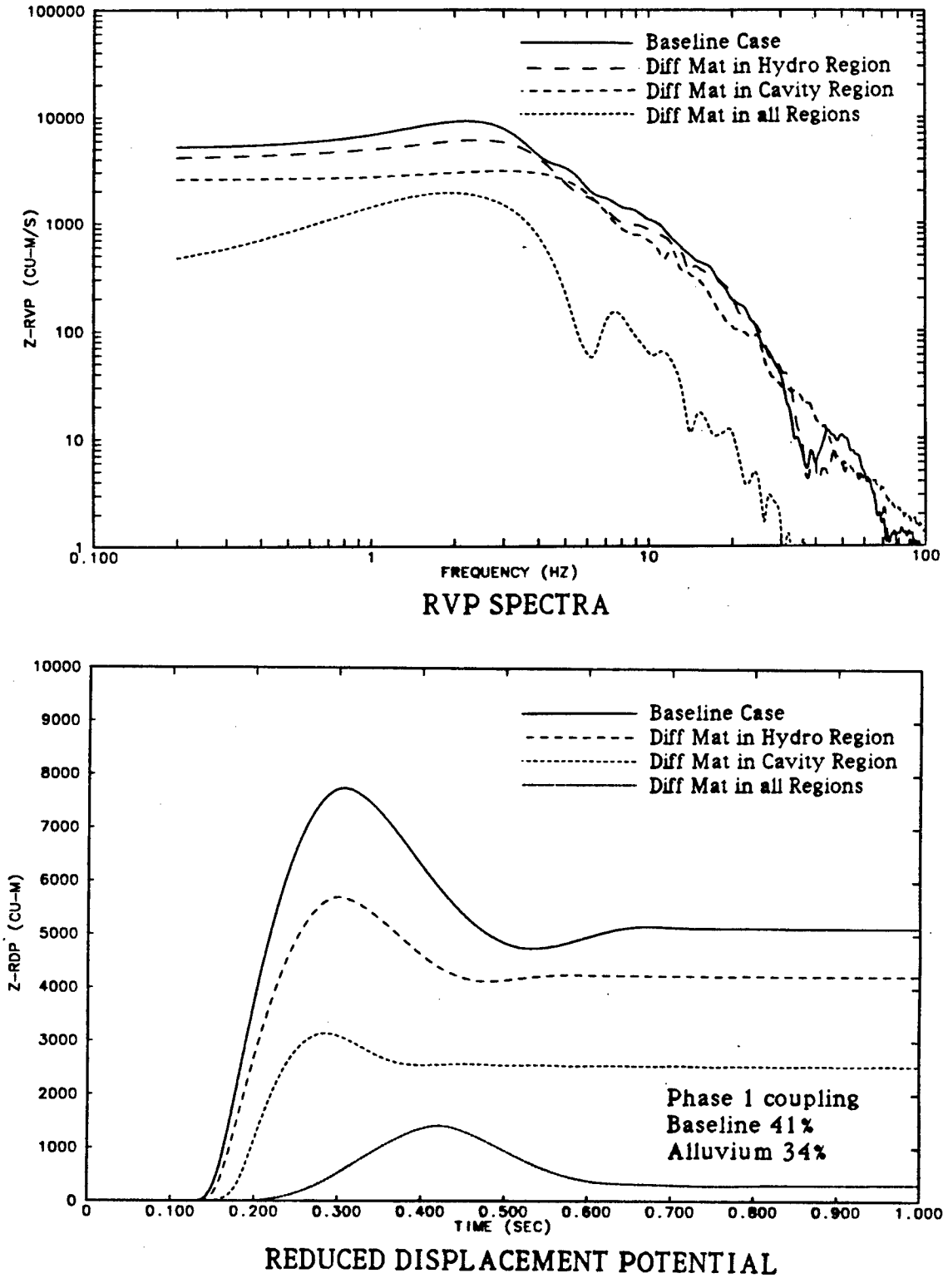


Figure 8. Case 6 - RVP spectra and RDP waveform comparisons at 300 m for substitution of Area 3 alluvium into selected regions.

Figure 8 shows the results for substitution of alluvium into the selected regions (Case 6). There are two significant differences between alluvium and the previously discussed "low density" material of Case 3. The alluvium has a much lower shear strength and it has a reduced resistance to pore crush. Similar to the results of the "low density" case (Figure 5), effects due to substitution into the hydrodynamic region are due almost entirely to decreased Phase 1 coupling. Substitution into the cavity region results in a substantial change in the steady state RDP, overshoot and corner frequency. The most pronounced effects on the source function properties occur in the "all alluvium" case, due to the combination of low pressure compaction of the gas porosity and low shear strength.

III. SUMMARY AND CONCLUSIONS

Following are some tentative conclusions. 1) The source function is insensitive to properties of the solid rock reference curve and Hugoniot above approximately 1 GPa (hydrodynamic region). 2) The source function may be sensitive to the cavity gas EOS at and above vaporization temperatures, but only in the sense that it makes the explosive yield appear larger or smaller than it actually is. 3) The source function is quite sensitive to the gas porosity outside the hydrodynamic region. 4) The source function is very sensitive to the material shear strength outside the cavity region. 5) There is a hint that each source function property has its own degree of sensitivity to the type of coupling and the types of materials present at a site.

There are some interesting implications. Since the very close-in material properties (within the cavity region) mainly affect coupling without affecting waveform or spectral characteristics, variations in rock response properties above 1 GPa are not likely to cause a problem in discriminating between intrinsically different types of events. Material properties in the inelastic region outside the cavity have a greater effect on waveforms and thus can affect both discrimination and yield estimation performance. The results of this study suggest the possibility that, at some level, the source function properties may be used to constrain the size and type of energy release without foreknowledge of the material properties at the origin.

IV. REFERENCE

App, F. N., "Sensitivity of the Close-in Seismic Source Function to Rock Properties", Los Alamos National Laboratory, In Preparation, 1993.

THIS PAGE INTENTIONALLY LEFT BLANK.

Yield Estimation Based on Calculated Comparisons to Particle Velocity Data Recorded at Low Stress*

John Rambo, Lawrence Livermore National Laboratory

ABSTRACT

This paper deals with the problem of optimizing the yield estimation process if some of the material properties are known from geophysical measurements and others are inferred from in-situ dynamic measurements. The material models and 2-D simulations of the event are combined to determine the yield. Other methods of yield determination from peak particle velocity data have mostly been based on comparisons of nearby events in similar media at NTS. These methods are largely empirical and are subject to additional error when a new event has different properties than the population being used for a basis of comparison. The effect of material variations can be examined using LLNL's KDYNA[1] computer code. The data from an NTS event provide an instructive example for simulation.

INTRODUCTION

Such calculations are used for containment analyses and they utilize a material model initially developed by Butkovich[2] which estimates strength and compressibility based on gas porosity, total porosity and water content determined from geophysical measurements. We used this model to determine yields for two nuclear detonations conducted in the same drill hole and separated in time by an amount that was sufficient to record separate ground motion features.

For the two devices, the peak particle velocity attenuations are different in regions traversed by both elastic waves and measured by the same particle velocity gages. The wave propagation from the lower device is enhanced by the water saturation and by effects attributed to wave focusing above the water table. These are features that should be and are simulated by 2-D calculations. The velocity gage data contain information

* Work performed under the auspices of the U.S. Department of Energy by the Lawrence Livermore National Laboratory under contract number W-7405-ENG-48.

independent of yield that can be related to the strength properties of the medium provided that there are more than two gages recording in the stress region of plastic deformation of the material. A modification to Butkovich's model incorporated approximate strengths derived from such data. Three calculations spanned the measured yield of each device by +-30% for a purely Butkovich type model and three calculations for a modified strength Butkovich model. The results of the calculations are discussed showing yield comparisons between the two strength models and suggestions are made for improving the technique.

PARTICLE VELOCITY OBSERVATIONS

The peak free surface velocities were unusual. The shot was composed of two devices. The lower event with depth-of-burial, DOB, of 689 m was detonated about 30 s before the upper event with DOB of 435 m. The upper event which was about 3 times the yield of the lower device and closer to the surface gave a lower peak surface velocity (1.01 m/s) than the lower placed event (1.43 m/s). Figure 1 shows a symbolic representation of the relationship.

Limited data were available for analysis of this event. There were few velocity gages and some areas of the satellite hole had no coverage[3,4] as shown in Figure 2. However, the available gages revealed important phenomena. The gages above the upper device recorded velocities from both events and the attenuations of the peak velocities were measured through the same medium. Geophysical logs (1972) were crude by todays standards. Review of recent events near the site show consistently higher grain density measurements . The methodology for this measurement has improved over the years and L. Mckague[8] has suggested using measured grain density values from one of the nearby recent events. Some strength and compressibility measurements on cores were performed for only a few locations[9]. They did not provide a complete representation of the geology and were not used in this analysis.

Time-of-arrival (TOA) of the outgoing waves are useful to evaluate material crushing caused by the lower event that could change the material properties for the upper event. Where the peak of the particle velocity is propagating at near the sound speed, we assume that elastic or almost elastic behavior is in effect and either purely elastic compression or minimal crush and/or damage to the material is occurring. The elastic onset (the time of the first positive detectable particle velocity) and the following time of the peak particle velocity arrival are shown for each event in Figure 3.

The slopes of the TOA values in Figure 3 translate to velocity of the wave between points. The onset velocities represent the elastic sound speed of the material between the measurement points. The slope of the peaks can be compared to the slope of the elastic onset to determine where the peaks are undergoing large amounts of plastic failure. Above the standing water level (SWL) where the gas porosity is high, the lower event peak velocities travel slowly indicating plastic failure. Further above the SWL the peak abruptly increases to a sound speed similar to the speed of the elastic onset. Some minor time spread of the two parts of the wave occurs upward to a location just below the upper device. Above the upper working point the onset and peak travel parallel (the same sound speed) until just below the surface where spall obscures the timing of the peak. The fact of the same sound speed for both onset and peak velocity indicates very little crush up of the material has occurred above the upper device. The peak wave velocity from the upper device shows a similar slow velocity for the pore-crush followed by a higher sound speed velocity to the surface. The onsets and peaks from both devices travel with about the same sound speed through the same upper region of the event site.

Attenuation of the peak particle velocity is usually material dependant. The most important factors are usually gas porosity and strength, where the peak of the wave is undergoing plastic failure. Where the wave is truly elastic, the attenuation should be R^{-1}. Particle velocity attenuations from calculations usually show an abrupt change in attenuation to R^{-1} when the stress falls below plastic failure into the elastic regime. This is accompanied by a sudden change to elastic sound speed at the same location. However, the data for the quasi-elastic attenuations do not follow the calculations in quite the same way.

A comparison of peak velocity vs range for both devices is shown in Figure 4. The log-log plots assume R=0 is at the depth-of-burial, DOB, of both devices and the attenuation is determined from a power fit to the data, $Up=aR^b$, where b is the attenuation exponent and Up is the peak particle velocity. The upper event attenuation, b, is about -2.9 and uses three data points above 9 m/s and one point almost in the spall zone (0.7 m/s). There is no information on the attenuation between 0.7 and 9 m/s. However, the attenuation of -2.9 compares well with a current event of CORNUCOPIA with the value[10] of -3.2. The upper event particle velocity values above 9 m/s were scaled to the particle velocities of CORNUCOPIA and resulted in a yield estimate very near the official yield.

INTERPRETATION OF THE DATA

From the scaling and the similarity in attenuations, the upper device data is interpreted as "normal" for an alluvium event and the material was not significantly changed by the lower device. The porous alluvial events experience strong energy attenuation because of the material failure and PdV work that accompany pore-crush. This dissipates the wave's kinetic energy in the source region and this decoupling is observed at seismic distances as well. The gas porosity in the source region is used to correct seismic yield estimations[11].

The lower device data show some unusual attenuations. Data from both devices have about the same particle velocity value at about 110 m range. Velocity (as a function of range) from the upper device attenuates steeply in porous material at a higher yield while the lower device velocities attenuate less steeply in a saturated material at a lower yield to get to about the same particle velocity at 110 m range. Above the 110 m range, the lower device data attenuation exponent is about -9.0 due to the gas porosity above the water table. The attenuation changes to -1.4 at about the place where sound speeds occur for the peak. An interesting observation is that the attenuations in the regions traversed at similar sound speeds are different for both peak velocity data sets as shown by the thickened lines of Figure 4. Since the upper data are normal and the material was not significantly changed by the lower event, then the lower device attenuation of -1.4 appears unusual. The first objective was to understand this unusual attenuation.

The second objective was to test scaling yield from event data to calculations based on limited knowledge of modeling parameters such as strength and compressibility. Suppose that good geophysical information is available. That is, assume information exists sufficient to provide continuous values with depth of total porosity, saturation, gas porosity, density, longitudinal velocity and possibly shear velocity. There is also some geological knowledge of the rock or soil type at the site of interest. The question posed is; how accurately can a calculation determine the yield with no knowledge from core measurements either of strength or of compressibility.

MODEL

A material model which was first developed by Butkovich, estimates compressibility based on density, water content, grain density, Poisson's ratio and longitudinal velocity. Strength in terms of the compressive elastic limit is estimated and the user can estimate shear strength from the

compressive elastic limit and Poisson's ratio if uniaxial strain is assumed. Additionally, strength can be estimated from particle velocity data where gage records are relatively close together and the peak velocities indicate plastic failure. Fortunately, both device data sets show plastic failure. Yield scalings were performed with calculations in two modes. One calculational set uses only the default strengths and the other set adds strength information derived from the particle velocity data. Each set of calculations was composed of three yields (+30%, actual yield, -30%) to test yield scaling. The +-30% yields are arbitrary. Three yields were calculated each for two strength cases and for both devices.

The calculational model consisted of several horizontal layers designed to capture some of the nuances of elastic properties and the gas porosity. Figure 5 shows some of the logging data to get material properties used in the model. The trace of the density, longitudinal velocity (DHAL)*, acoustic impedance and wt% of H_2O are shown next to the rock type. The units are mixed between English and SI because the original logs are in English units from an unpublished document . The depths of the layers are given in meters and the working points are shown in the left margin. The calculated value of gas porosity was derived from density, wt% H_2O, and grain density from nearby holes. The most significant modeling of gas porosity was the water table interface at 574 m depth. Above the interface the gas porosity is 13 vol% and it has a large influence on the wave attenuation. The default elastic limit strengths from Butkovich's model are shown, as well as the modified strengths derived from the particle velocity data. The modified strengths are considerably weaker than the default values and were used only in the layers for which the strengths could be estimated from the data.

DEFAULT STRENGTH CALCULATIONS

The default strength model did not produce velocities that scale well to either set of device data. The upper device data scales 60% high and the lower device is a factor of 2 low. The velocity data, except for the spall region, were scaled to each calculation of known yield and the average yields from each calculation were then averaged. The standard deviation for each of the three yield calculations did not accurately point to the actual yield calculation as the best fit This was primarily due to the systematic errors in the model from strengths that were too high.

Figure 6 shows the data and calculations for both devices. The upper device calculations show lower peaks for the particle velocities above

* Dry Hole Acoustic Log

9 m/s. The calculated values cross over and above the lower data. Both device calculations are symptomatic of strengths that are too high. High strengths near the cavity restrict outward displacement[13] and also the peak velocities. High strength, as the wave propagates outward to lower stresses causes the wave to propagate linear elastic at a position closer to the source. The calculated elastic attenuation rate tends to r^{-1}, a value much greater than the data ($r^{-2.9}$). Thus the calculation crosses above the data at lower stresses. The lower device calculations show reasonable agreement to the higher particle velocity data. These calculations tend to r^{-1} at the lower particle velocities and the calculations also cross above the data ($r^{-1.4}$). The interpretation of strength being too high for both calculations is aided by the knowledge of the yield being within +-30% and by strength estimates from the particle velocity data.

MODIFIED STRENGTH CALCULATIONS

The modified strength calculations are shown in Figure-7 and demonstrate a better fit to the data. The upper device calculations are still below most of the upper particle velocity data and the near surface modeling implies strengths that are still too strong. The lower device calculation scaled quite well to the data. The average of the standard deviations is about +-50% and is about as good a fit as can be expected with limited knowledge of the material strengths employed in this simple modeling approach to the scaling issue.

AGREEMENT OF CALCULATED PEAK SURFACE VELOCITY TO DATA

The agreement of the actual yield calculations to the peak free surface velocity data from both devices was good. The tables in Figure-8 show the agreement. However, considering the simplicity and approximations of the model, the very close agreement was fortuitous. The upper device data did not model the near surface spall region very well and wave forms in this region were not well matched. The data from the lower device showed much better agreement with wave forms.

FOCUSING ABOVE THE WATER TABLE

The calculations were useful for explaining the high surface velocity from the lower device. Shock waves usually travel slower in porous material and fast in the saturated material for plastic stresses less than 500-MPa. The slope of the compressibility relationship, P vs mu, is quite different for saturated and porous alluvium for the pressure ranges occurring near the water table. The shock wave travels at high velocity and low attenuation up to the water table interface and with slow velocity and high attenuation above. The effect of slowing down can be seen in

velocity contours of Figure 9. A circular contour line has been plotted over the second contour line to emphasize the shape difference below and above the water table (SWL). The wave is generally spherical in the calculation relative to the center of the explosion below SWL and has flattened considerably above.

The wave above the SWL is spherical as well but relative to a geometric center below the actual center as depicted schematically in Figure 10a. This is partially due to a Snell's Law effect at the SWL and has the analogy of focusing of light by a lens. The spherical divergence changes above the SWL as shown schematically with the solid radial lines from both geometric sources. Both 1-D and 2-D calculations have been compared using the same model parameters. The 1-D[14] calculations produce a spherical interface which eliminates the Snell's Law effect on the calculation. The attenuation effect of divergence above the SWL is shown in the schematic comparison of Figure 10b. The 2-D calculation agrees well with the 1-D calculation radially to the SWL. Above the SWL the 2-D calculation shows higher velocities and lower attenuations.

AXIAL PREFERENCE OF PORE COLLAPSE FLATTENS THE WAVE FRONT

There is a second effect that contributes to focusing. The path between the lower device and the water table is shortest in the axial direction. The stress at the water table is greatest at that point and diminishes horizontally along the water table as the wave takes longer paths (with more attenuation) to arrive. The highest stress, axial path at the SWL takes the longest porous crush-up time and distance to attenuate to elastic stress above the water table. The other paths take less crush up time and distance as shown in Figure 11. The crush up distance between the SWL and the curved line representing the location of elastic stress diminishes with horizontal distance. The decreasing time in the crush up has been observed from surface gages on the TYBO event[15]. The particle velocity vs time from locations along the ground surface showed greatest time separation between the elastic portion of the wave and the remnant of the plastic peak at surface ground zero (SGZ). Other observations on TYBO were very high SGZ surface velocity and a pronounced reduction of the peak surface velocities with horizontal distance.

SUMMARY

The surface velocities from both devices at first appeared anomalous. Comparisons with nearby alluvium event data indicate the upper device is a "normal" alluvium event and the velocity peak attenuation is similar. The sound speeds indicate that the alluvial material was not

significantly changed by the passage of the stress wave from the lower device prior to the detonation of the upper event. The lower event has high peak surface velocity because of lower peak attenuation in the saturated medium below the water table and the 2-D effect of wave focusing above the water table. The focussing is attributed to two effects; Snell's Law and the preference of the shock to run slow for a longer time during the pore-crush in the axial direction.

Calculations using Butkovich's model were used to test scaling the event data to the calculations of +-30% of the actual yield. The default strength model gave poor results and modified strength did better. The best yield estimates one could expect still contain errors of +-50% and in different geologies, severe systematic errors may dominate.

Significant improvements to the default modeling were due to well placed velocity gages from which strengths could be estimated. Future improvements for this event modeling are possible but most involve model changes based on the calculator's experience and are not easily justified without core measurements. There are measured strength data from core at some locations at the site which could be incorporated in simulations. This might resolve the issue of the importance of core samples. Other models developed for nearby events could be employed (such as a damage model)[16] to examine their sensitivity.

Improvements in the general process for a new event would require more velocity gages coupled with simulations to further develop material models. Perhaps analysis of Lagrangian measurements[17] (multiple velocity gages) could be employed to obtain better in-situ material properties. Core measurements at appropriate locations which include strength and compressibility would also be valuable.

ACKNOWLEDGEMENTS

I wish to thank John White for reviewing the paper and for general technical discussions. Discussions about the wave propagation above the water table were very useful. I also thank Ted Butkovich for his help with the computer calculations and post processing.

REFERENCES

1. Levatin, J. L., Attia, A. V., and Hallquist, J. O., "KDYNA USER'S MANUAL", Lawrence Livermore National Laboratory, Livermore, CA, UCRL-ID-106104, 1990.

2. Butkovich, T. R., "A Technique for Generation Pressure-Volume Relationships and Failure Envelopes for Rocks", Lawrence Livermore National Laboratory, Livermore, CA, UCRL-51441, Nov., 1973.
3. Wheeler, V. B., Lawrence Livermore National Laboratory, private communication, May, 1973.
4. Preston, R. G., Lawrence Livermore National Laboratory, private communication, May, 1973.
5. LLN-N Geology, "Geology of Emplacement Hole U2dj(FLAX)", Lawrence Livermore National Laboratory internal memorandum, GN-6-72, April, 28, 1972
6. Clarke, S. R., and L. McKague, "U2ge Site Characteristics Summary", CP 87-36, April, 1987
7. Howard, N., "U2fa Preliminary Site Characteristics Summary", AGTG 77-39, April 29, 1977
8. McKague, L., Lawrence Livermore National Laboratory, 1992, private communication, (Currently with Southwest Research Institute, San Antonio, Texas)
9. Brandt, H., and Chu, H., "Triaxial Tests of Alluvium, Final Report", University of California Department of Mechanical Engineering, Davis California, Contract Order Number 2100603, 1977
10. Hudson, B., Lawrence Livermore National Laboratory, private communication, Sept., 1992.
11. Vergino, E. S., and Mensing, R. W., "Yield Estimation Using Regional mb(Pn)", Bulletin of the Seismological Society of America, Vol. 80, No. 3, June 1990
12. Ramspott, L., "U2dj Site Characteristics Report", Lawrence Livermore National Laboratory, Internal Memorandum, Unpublished, March 30, 1972
13. Terhune, R. W., and Glenn, H. D., "Estimated Shear Strength of Earth Media at Nevada Test Site", Lawrence Livermore National Laboratory, Livermore, CA, UCRL-52358, 1977.
14. Snell, C. M. and Austin, M. G., "SOC Code: Lagrangian, Finite-Difference Calculational Technique in One-Dimensional Symmetry", Lawrence Livermore National Laboratory, Livermore, CA, UCID-18220, July, 1979.
15. Rambo, J. T., and Bryan, J. B., "Calculation of High Surface Velocity Due to Focusing in the TYBO Event", Proceeding of the Second Containment Symposium, Kirkland AFB, Albuquerque, NM, August 2-4, 1983.

16. Rimer, N., and Proffer,W., "Containment Phenomenology Using a New Shear-Strain-Based Computational Damage Model for Tuff", Proceeding of the Sixth Containment Symposium of Underground Nuclear Explosions, Reno, Nevada, September 24-27, 1991.
17. Aidun, J. B., and Gupta, Y. M., "Analysis of Lagrangian Gauge Measurements of Simple and Nonsimple Plane Waves", J. Appl. Phys. 69 (10), May 15, 1991.

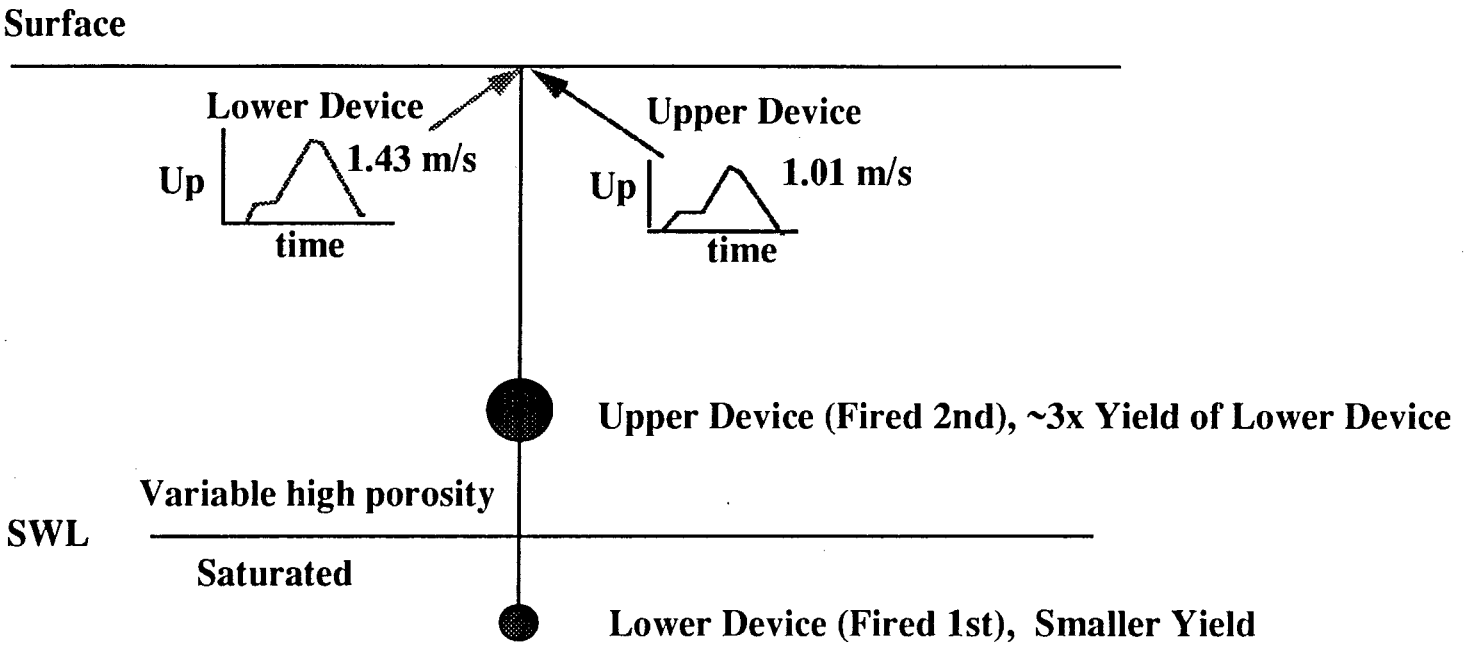


Figure 1. Schematic of device position and particle velocity results. Lower device is buried below the standing water level (SWL) and gives a higher peak surface velocity than the shallower, larger yield event.

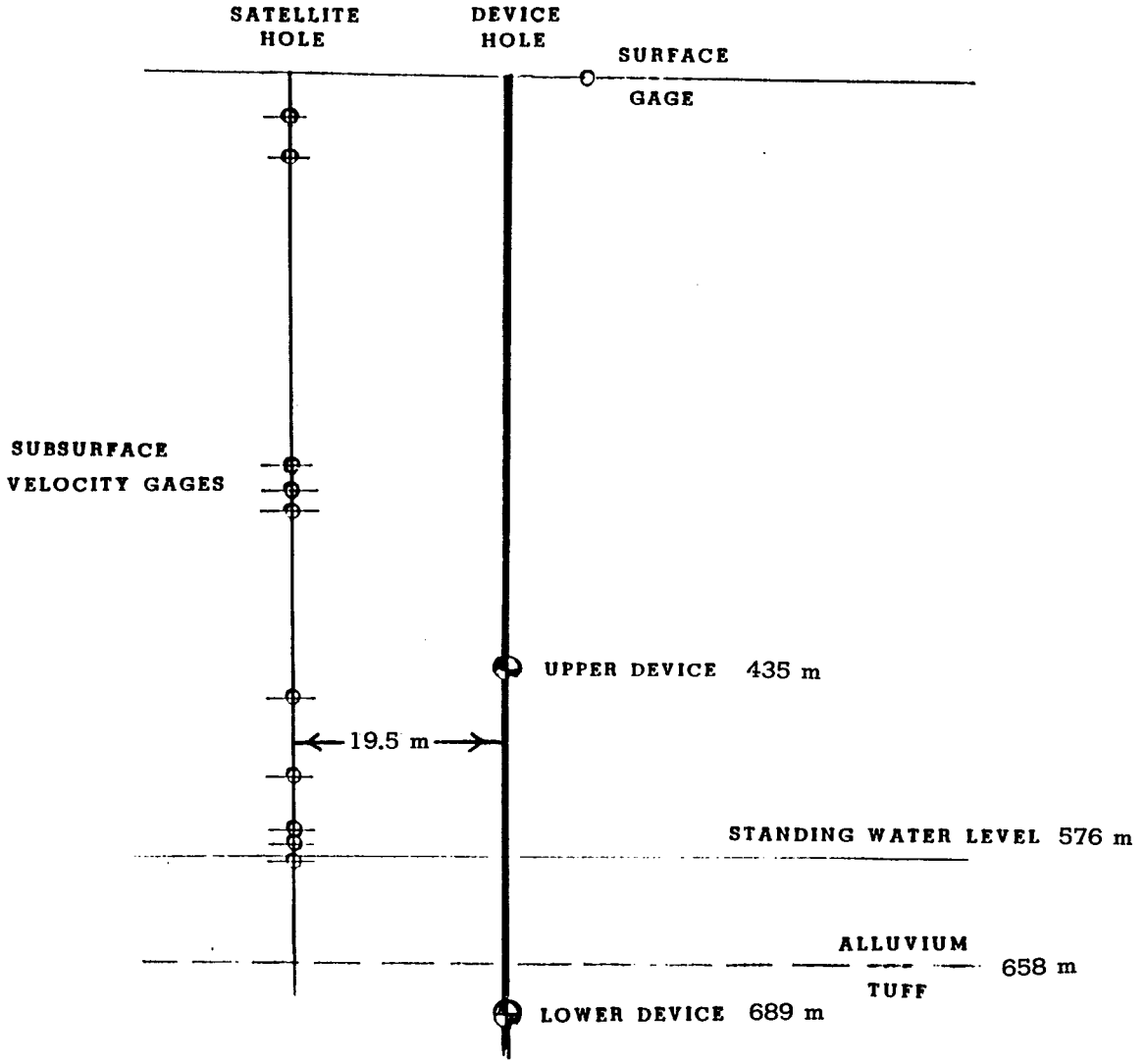


Figure 2. Schematic of gage locations relative to device locations. Gages above upper device recorded data from both devices.

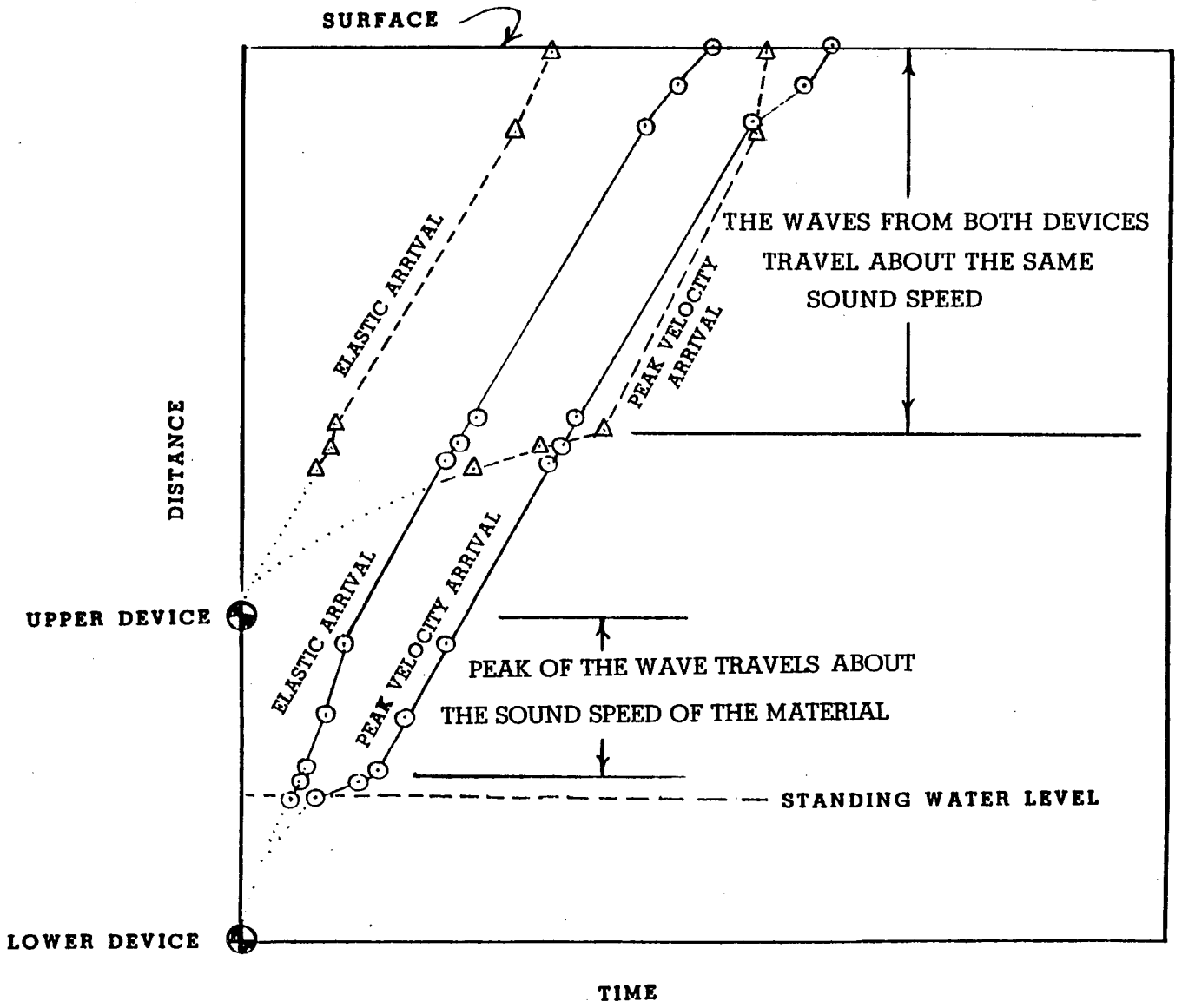


Figure 3. Time-of-arrival of elastic onset and the peak of the velocity wave from both devices. The peak velocity wave from the lower device (solid lines) travels at the sound speed before it passes the upper device. The peak particle velocity wave from the upper device (dashed lines) travels at about the same sound speed as does the lower one.

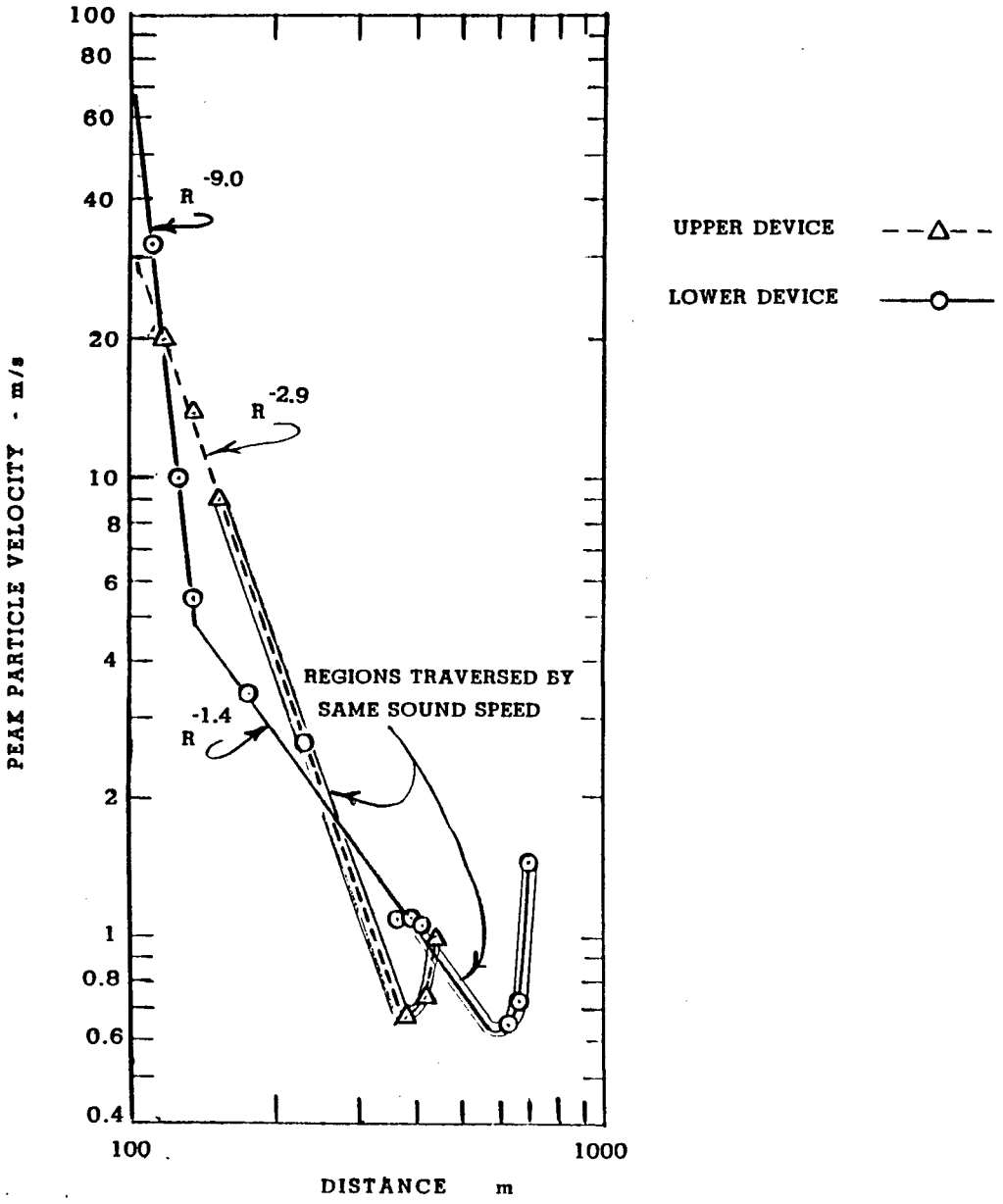


Figure 4. Peak particle velocity vs attenuation from both devices. Thick lines are areas traversed by waves from both devices at the same sound speed but both have different attenuation exponents.

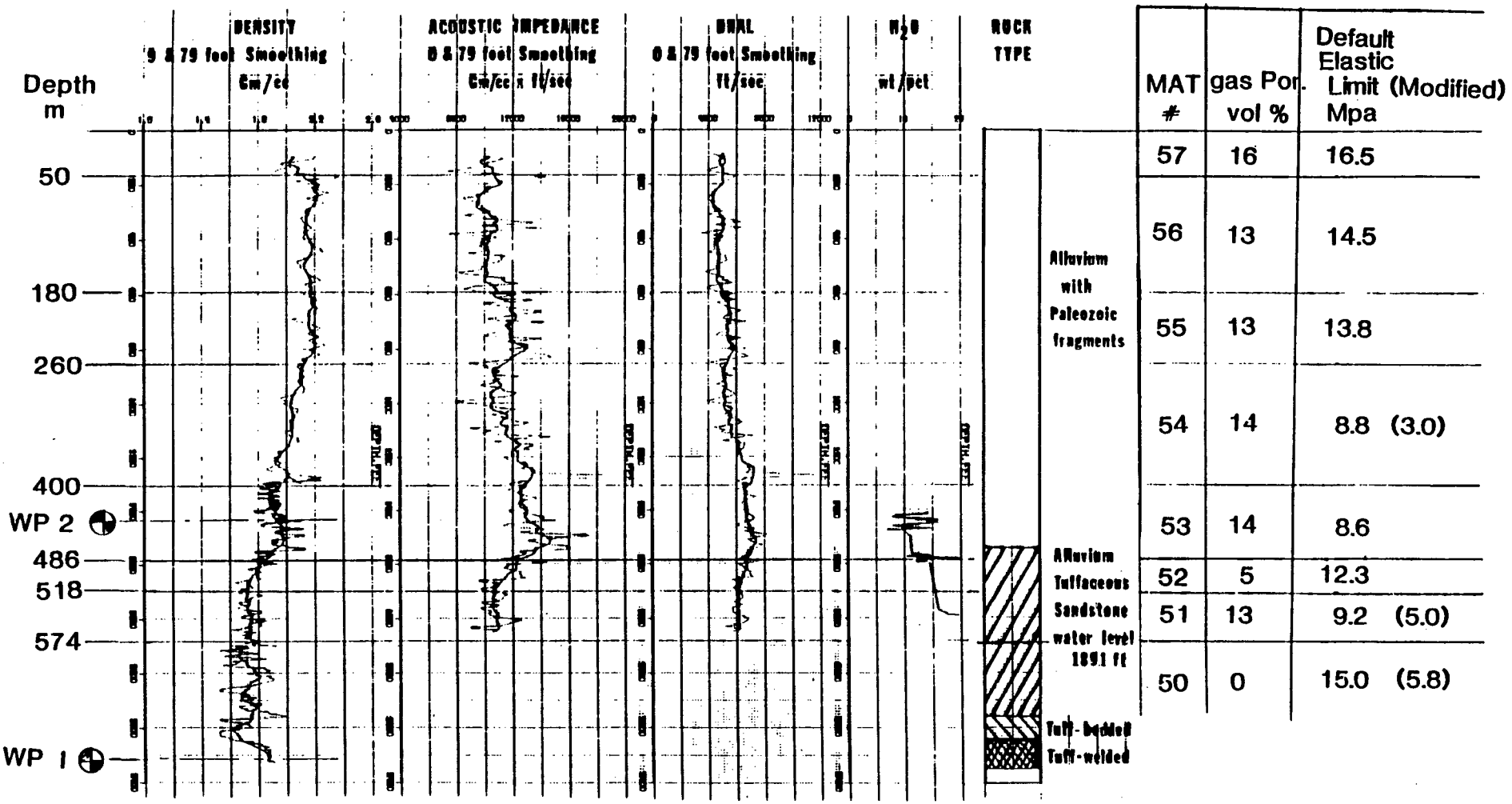
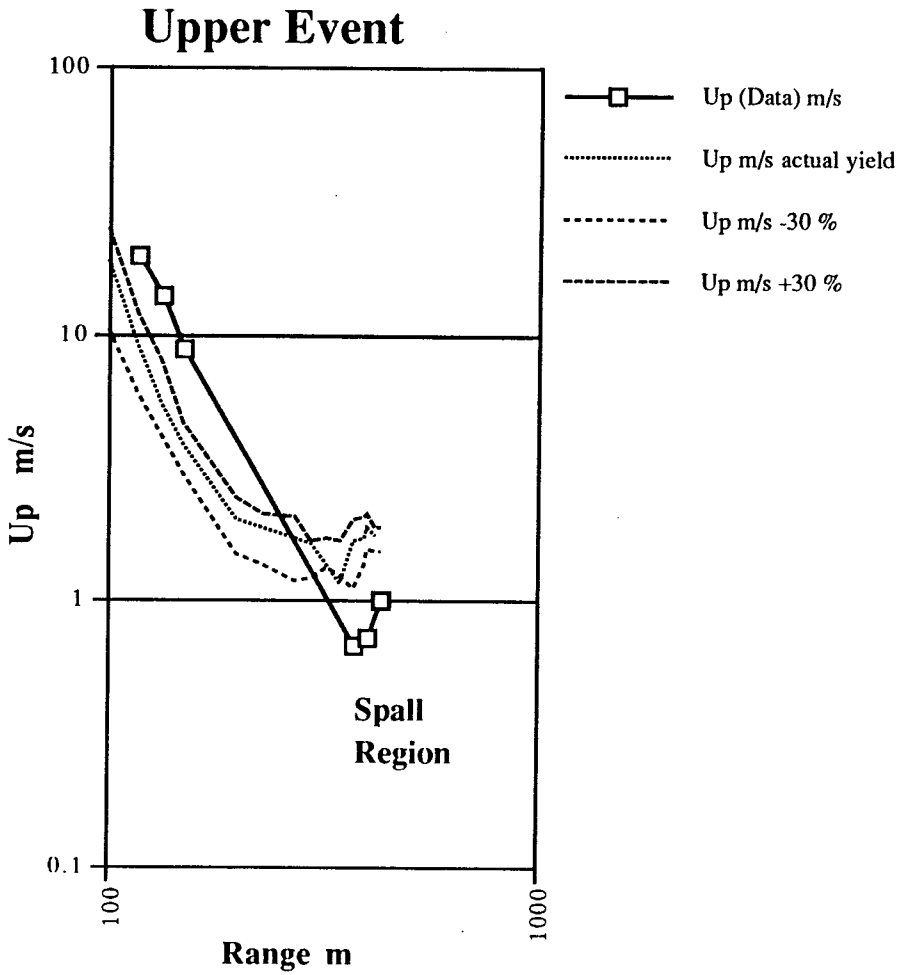
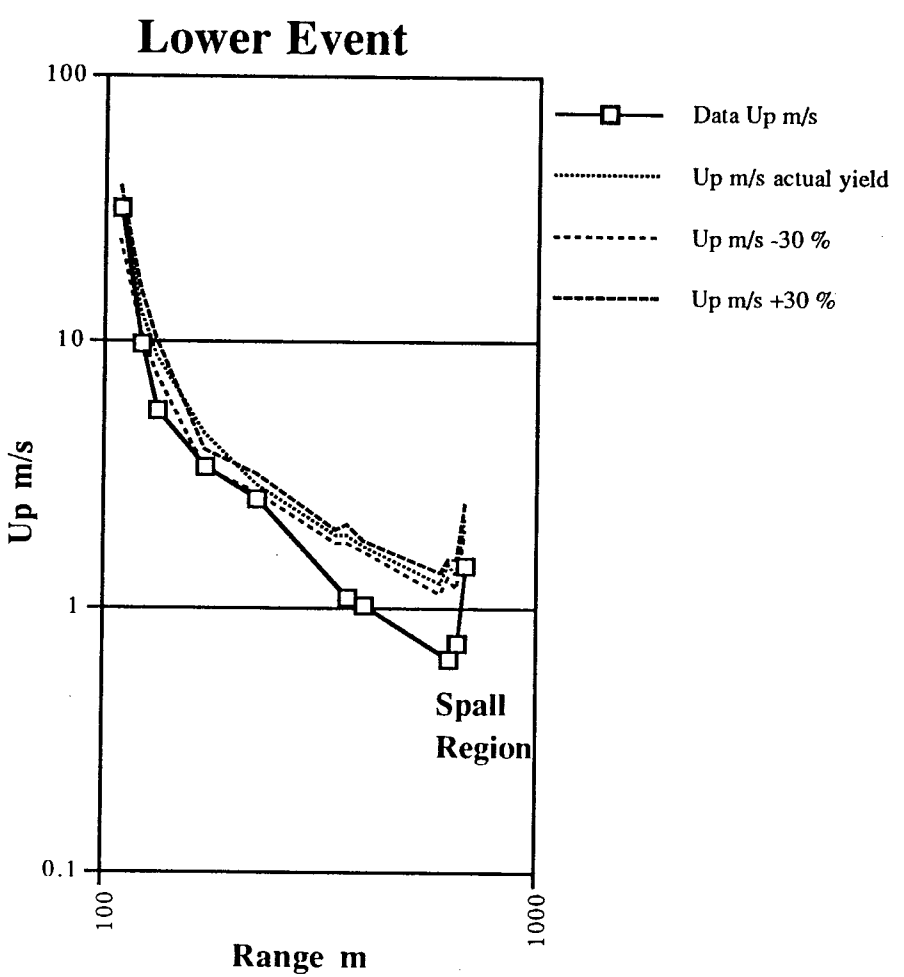


Figure 5. Geophysical model showing geophysical logs, selected layers, gas porosity, rock type and strength. Modified strengths are shown in parentheses. Gas porosity above water table (574 m depth) and strengths are the most important aspects of the model.



Average scaled yield 1.61

Std. dev. 0.45



Average scaled yield 0.47

Std. dev. 0.80

Figure 6. Comparison of default-strength calculations to data. Poor agreement is attributed to high default strength and causes the trace of the calculated peak velocities to pass above the data.

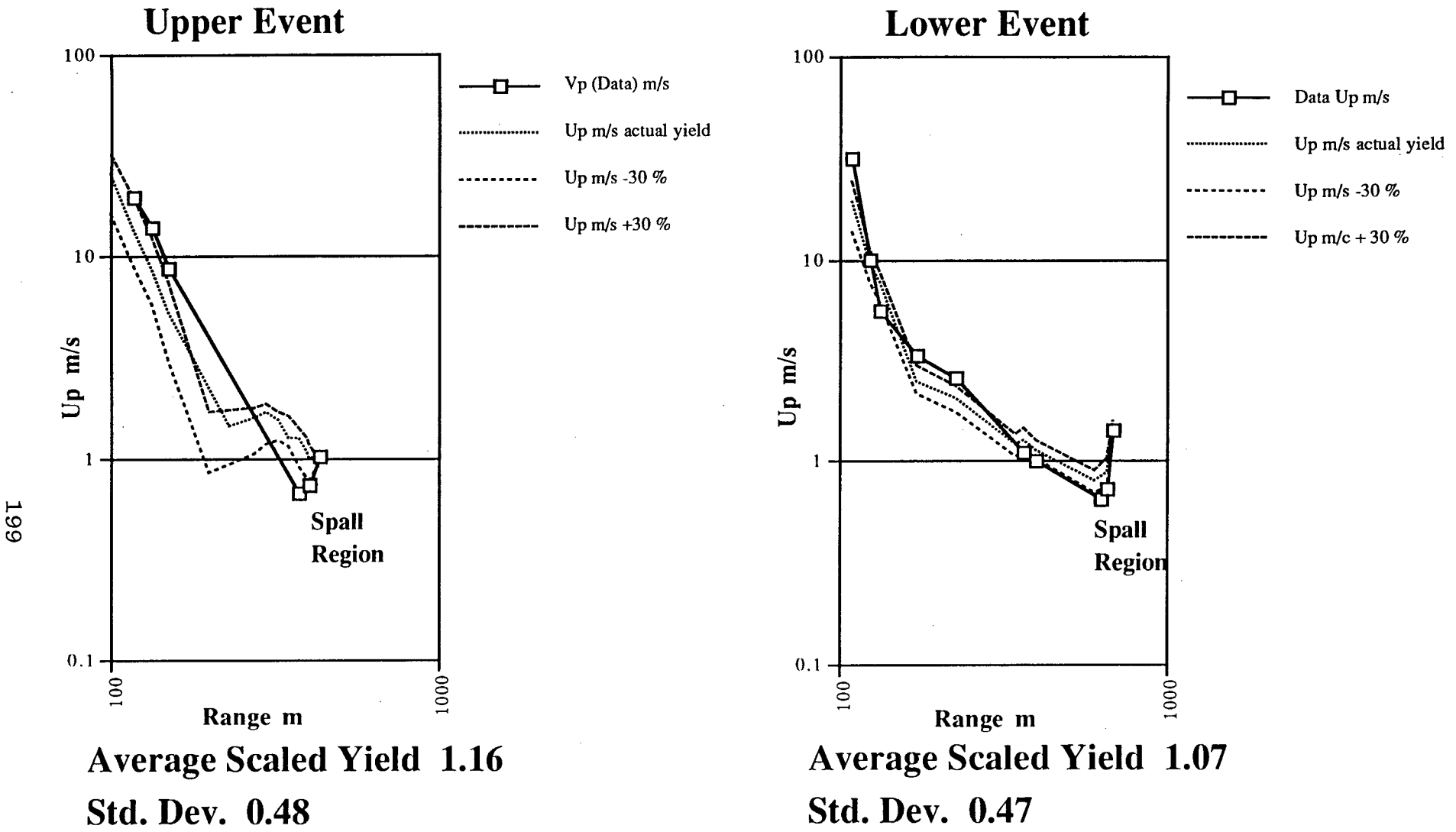


Figure 7. Comparison of modified-strength calculations to data. Better agreement is attributed to lower strength.

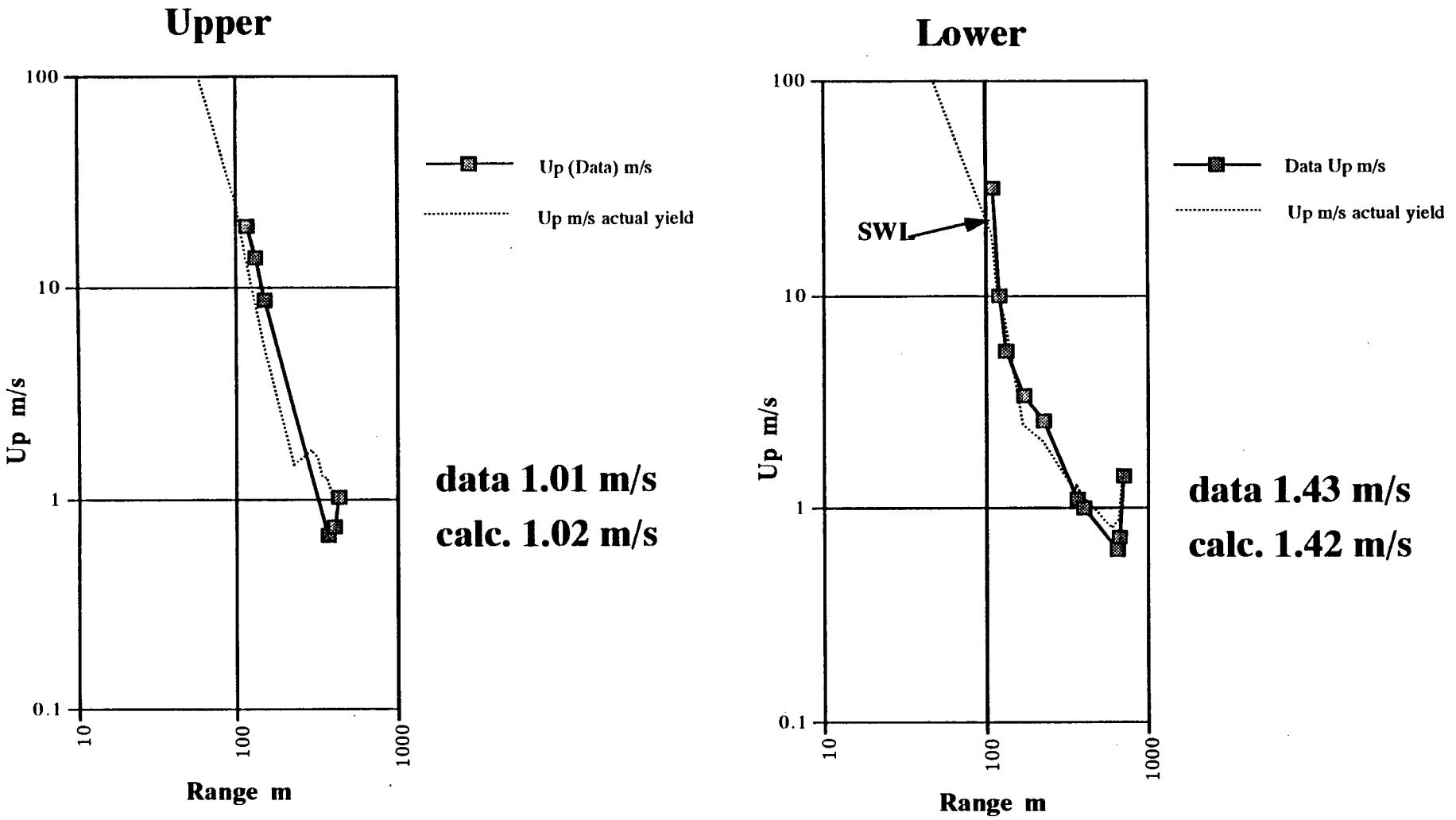


Figure 8. Free surface velocity has good agreement to modified-strength calculation run at actual yield. The upper event calculation shows poor agreement to the near surface data and the agreement at the surface may be fortuitous.

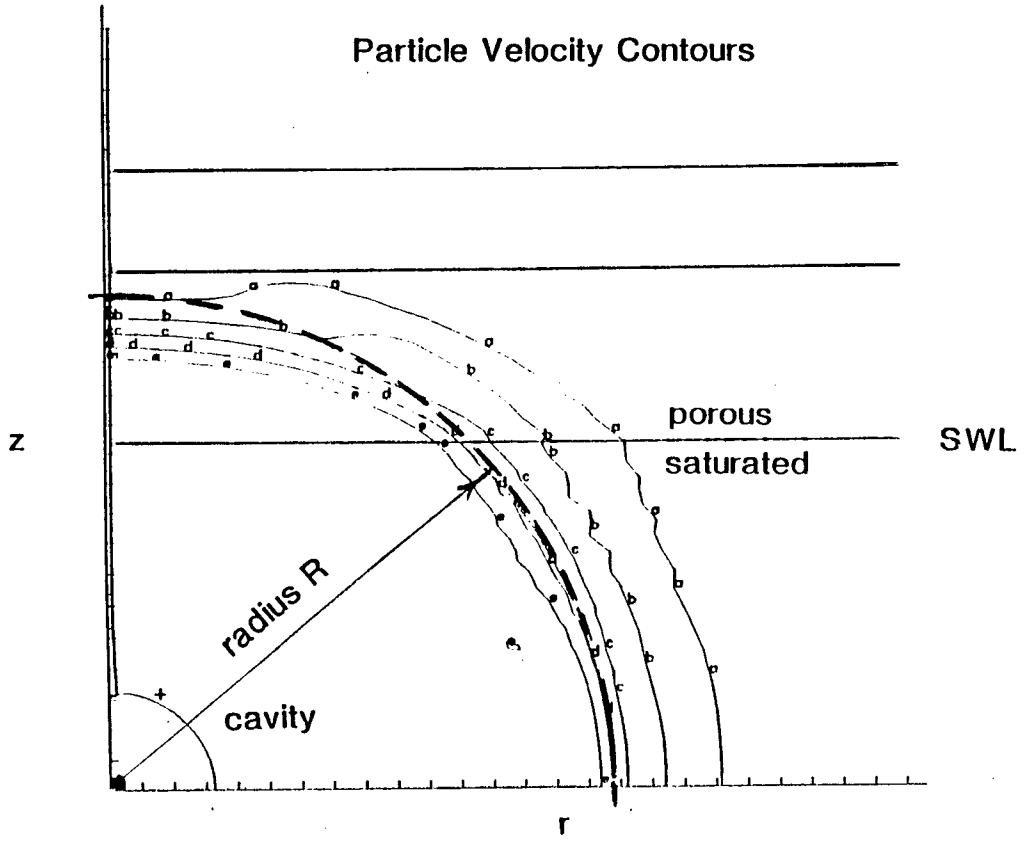


Figure 9. Flattening of the particle velocity wave above the water table is shown by comparison to a circular contour of radius R. Above the SWL the circular contour crosses over the velocity contours indicating a flatter wave front.

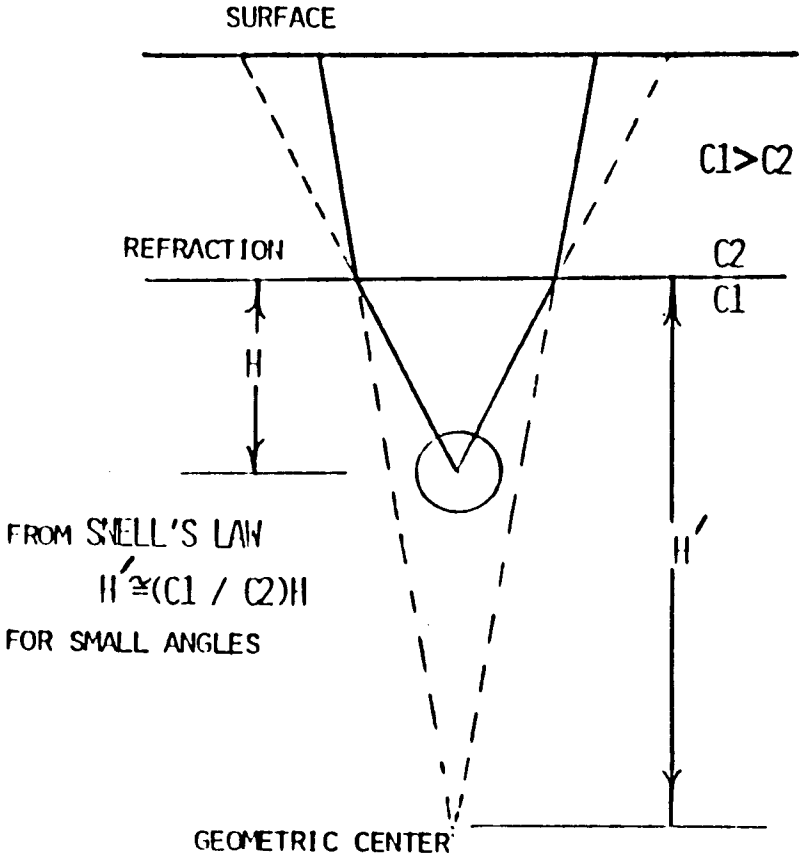


Figure 10 a. Schematic of Snell's law focussing. The solid line shows the change in radial divergence from the actual source center H below the SWL to an apparent source center H' above the SWL.

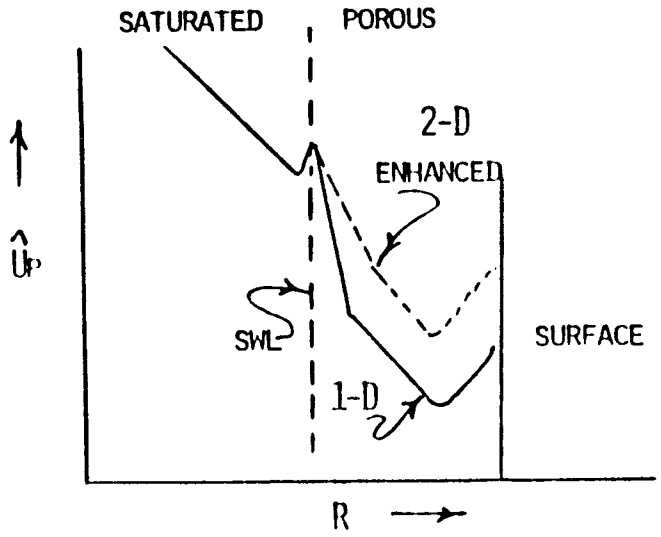


Figure 10 b. Schematic of attenuation difference between 1-D and 2-D calculations. Above the SWL the 2-D calculations show higher "enhanced" peak velocities due to the reduced radial divergence.

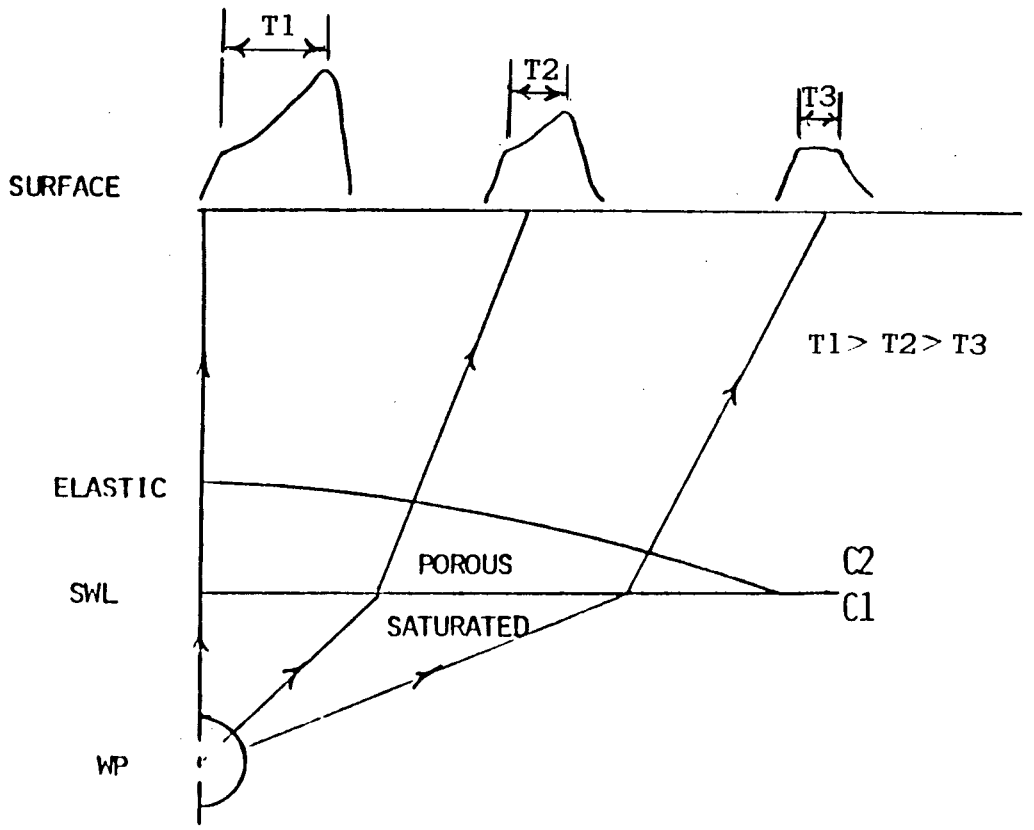


Figure 11. Schematic shows axial preference of porous crush and evidence found from surface velocity gages observed at he TYBO event. The peak of the wave travels slowly in the pore crush phase above the SWL and below the elastic curved line. Axially, the incident wave has the highest stress at the SWL than any other path. The axial stress takes longer and a greater distance for the peak to attenuate to elastic stress. Observations on TYBO showed wave forms along the surface which verified the diminishing time between elastic portions of the wave and the remnant of the plastic peak.

THIS PAGE INTENTIONALLY LEFT BLANK.

Simulation of Seismic Signals from Asymmetric LANL Hydrodynamic Calculations

Jeffry L. Stevens, Norton Rimer, Eldon J. Halda, Terrance G. Barker
S-CUBED, a Division of Maxwell Laboratories, La Jolla, CA
and
Cecil G. Davis, W. E. Johnson
Los Alamos National Laboratory, Los Alamos, NM.

Numerical Modeling for Underground Nuclear Test Monitoring Symposium

March 25, 1993

Summary

Hydrodynamic calculations of an asymmetric nuclear explosion source were propagated to teleseismic distances to investigate the effects of the asymmetric source on seismic signals. The source is an explosion in a 12 meter long canister with the device at one end of the canister and a metal plate adjacent to the explosion. This produces a strongly asymmetric two-lobed source in the hydrodynamic region. The hydrodynamic source is propagated to the far field using a three-step process. The Eulerian hydrodynamic code SOIL was used by LANL to calculate the material velocity, density, and internal energy up to a time of 8.9 milliseconds after the explosion. These quantities were then transferred to an initial grid for the Langrangian elastic/plastic finite difference code CRAM, which was used by S-CUBED to propagate the signal through the region of nonlinear deformation into the external elastic region. The cavity size and shape at the time of the overlay were determined by searching for a rapid density change in the SOIL grid, and this interior region was then rezoned into a single zone. The CRAM calculation includes material strength and gravity, and includes the effect of the free surface above the explosion. Finally, far field body waves were calculated by integrating over a closed surface in the elastic region and using the representation theorem. A second calculation was performed using an initially spherical source for comparison with the asymmetric calculation.

The results of this study show that the effect of an asymmetric explosion source of the type modeled in this study has no observable effect on the far field body waves from the explosion. Two factors are responsible for this effect: the initially asymmetric source becomes more symmetric as the shock propagates through the nonlinear region; and the dominant frequency of the far field body wave is low enough that it is insensitive to details of the explosion source.

Introduction

Under the Threshold Test Ban Treaty (TTBT), a nuclear explosion may be detonated in a canister that is limited to a length of no more than 12 meters and a radius of no more than 1.5 meters. The internal design of the canister is unrestricted, however, so it is permissible to arrange the device in ways that are designed to confuse hydrodynamic or seismic yield estimates. In this study, we investigate a case where the nuclear device is located at the upper end of the canister, and a heavy metal plate is located just beneath the device. Upon detonation, the plate vaporizes, absorbing some of the energy from the explosion, and impacts with the opposite end of the canister causing, in effect, a strong secondary source beneath the explosion. This results in an asymmetric source that complicates CORRTEX estimation of the explosion yield. In this study, we look at the effect of such a source on seismic yield estimates.

The asymmetric explosion source described above was modeled at LANL using the hydrodynamic code SOIL. In Figure 1, we show the density profile in the surrounding material at 0.1 msec after the explosion, and the pressure profile at 9 msec after the explosion. The density profile shows the highly asymmetric source that exists at early times. At later times, the source becomes more symmetric, but it is still quite asymmetric at 9 msec.

A total of three calculations were performed in order to evaluate the effect of the source asymmetry on the seismic signals. The first, denoted RHY1, is the propagation of the LANL calculation. The second, denoted RHY2 was a two-dimensional calculation of a tamped spherical source with the same yield in the same external medium. This calculation was performed for comparison with the RHY1 calculation. The third calculation was a one-dimensional calculation using the same initial cavity size and material properties as in the RHY2 calculation. This calculation was performed for comparison with the other calculations to assess the effect of the free surface interaction on the far-field body waves.

Propagation Method

Propagation from the hydrodynamic region to the far field is accomplished by using the ground motion from the Eulerian hydrodynamic calculation to drive a Lagrangian elastic/plastic finite difference code, carrying out the ground motion calculation to later times with material strength and gravity added, calculating the ground motion in the linear region surrounding the region of nonlinear deformation, and finally using the representation theorem to calculate the far field body waves.

S-CUBED has performed a number of studies using the representation theorem to propagate the results of nonlinear calculations (Stevens, *et al.*, 1991). Propagation of the hydrodynamic source adds several additional steps to this procedure. The first step is to determine the initial size and shape of the explosion-generated cavity at the end of the hydrodynamic calculation. The cavity is then rezoned into a single zone, and the ground motion in the external material is rezoned and overlayed onto the CRAM grid. This procedure must be performed carefully to avoid any artificial loss or gain of energy in the process. Also, since gravity is included in the CRAM calculation, care must be taken to ensure that the entire grid is in equilibrium after the overlay is performed. The S-CUBED hydrodynamic code STELLAR reads the output from the SOIL calculation, rezones it, and transforms it into input for CRAM. CRAM was modified to use the same equation of state as SOIL to ensure compatibility between the two runs.

Propagation to the far field (Figure 2) is based on the representation theorem (Aki and Richards, 1980) which is stated mathematically as:

$$u_n(\mathbf{x},t) = \int_{\Sigma} [u_i(\xi,t) * c_{ijpq}\, \nu_j\, \partial_q\, G_{np}(\mathbf{x},t;\xi) - G_{np}(\mathbf{x},t;\xi) * \nu_l \sigma_{ip}(\xi,t)\ ]\, d\Sigma \qquad (1)$$

This equation gives the far-field displacement $u_n(\mathbf{x},t)$ at the observer's position $\mathbf{x}$ in terms of spatial and temporal convolutions of the near-field displacements $u_i(\xi,t)$ and stresses $\sigma_{ip}(\xi,t)$ monitored at positions ξ on the surface Σ with propagation Green's functions $G_{np}(\mathbf{x},t;\xi)$. The Green's functions are the displacement responses in the n direction at $\mathbf{x}$ due to point forces in the p direction at ξ. In Equation (1), ν is the unit vector normal to the surface Σ and c_{ijkl} are the elastic coefficients. For the axisymmetric calculations presented in this report, the surface Σ is a cylinder whose axis is vertical. The Green's functions are appropriate to teleseismic body waves, calculated using the methods of Fuchs (1966).

In practice, the explosion simulations are saved on a cylindrical surface far enough removed from the source that the ground motions are linearly elastic. Equation (1) is evaluated numerically at the desired location $\mathbf{x}$, using analytic formulas for the Green's functions (Rodi, *et al.*, 1978; Bache, *et al.*,1982; and Day, *et al.*, 1983, 1986).

Overlay and CRAM Calculations

The overlay of the LANL calculation onto the RHY1 CRAM grid was performed at 8.9 msec after the start of the hydrodynamic calculation. The "cavity" size and shape were determined by searching for a rapid density change in the LANL grid, and this interior region was then rezoned into a single zone. The CRAM grid at the time of the overlay is shown in Figure 3. At this time the cavity has an irregular shape with an average radius of about 33 meters. The RHY2 calculation started with the source energy concentrated in a spherical cavity containing vaporized rock using an empirical vaporization radius of 10.1 meters (also shown in Figure 3 for comparison). A significant difference between the RHY1 and RHY2 calculations was the total mass of rock initially in the cavity. The equation-of-state used in the RHY1 calculation resulted in approximately twice the initial cavity rock mass of the RHY2 calculation. This resulted from an unrealistically high value for the adiabatic expansion constant, gamma (1.5), in the calculations, and led to a final cavity volume for RHY1 that was 50 percent larger than the RHY2 cavity volume. Due to the larger initial cavity in RHY1, displacements at the boundary of the CRAM grid were 20 percent higher in RHY1 than in RHY2. In both cases, however, the final cavity boundary was nearly spherical and the region of nonlinear deformation outside of the cavity was similar in shape and size. In Figure 4, we show the final grid, cavity size, and region of plastic yielding in the RHY1 and RH2 calculations.

Far Field P Waves

The explosion simulations were saved on a cylindrical surface far enough removed from the source that the ground motions are linearly elastic. In these calculations, the radius of the cylinder was about 1194 meters and the depth to the bottom of the cylinder was 1414 meters. The motions and stresses were propagated to observation locations below the calculation grid. Far field body waves calculated from the RHY1 calculation at three takeoff angles are shown in Figure 5, together with the body waves from the RHY2 calculation. For the reasons mentioned above, the body waves from the RHY1 calculation are about 10 percent larger than the body waves from the RHY2 calculation, however they are very similar in shape and duration, and there is no apparent increase in variation as a function of takeoff angle due to the initial asymmetric source. There are two reasons for this. First, although the initial source is asymmetric, most of these effects damp out as the shock propagates through the nonlinear region, and second, the dominant frequency of the far-field body wave is low enough that it is insensitive to details of the explosion source. In Figure 6 we show a comparison of the RHY1 body waves with those from a one-dimensional source and an

elastic free surface reflection. The differences between those two cases are quite pronounced indicating that nonlinear free surface effects substantially affect the body waves in contrast to small scale source variations which have minimal effect on far field body waves.

Conclusions

Near source asymmetries of the type modeled here have no observable effect on the far field body waves. Two factors are responsible for this effect:

1. The initially asymmetric source becomes more symmetric as the shock propagates through the nonlinear region;

2. The dominant frequency of the far field body wave is low enough that it is insensitive to details of the explosion source.

References

Aki, K. and P. G. Richards (1980), Quantitative Seismology -- Theory and Methods, W. H. Freeman and Company, San Francisco, California.

Bache, T.C., S.M. Day and H.J. Swanger (1982), "Rayleigh Wave Synthetic Seismograms from Multi-Dimensional Simulations of Underground Explosions", *Bull. Seism. Soc. Am., 1875-1888.*

Day, S. M., N. Rimer and J. T. Cherry (1983), "Surface Waves from Underground Nuclear Explosions with Spall: Analysis of Elastic and Nonlinear Source Models," *Bull. Seism. Soc. Am, 73*(54), pp. 247-264.

Day, S. M., N. Rimer, T. G. Barker, E. J. Halda and B. Shkoller (1986), ``Numerical Study of Depth of Burial Effects on the Seismic Signature of Underground Explosions," S-CUBED Report to the Defense Nuclear Agency, DNA-TR-86-114, SSS-R-86-7398, March.

Fuchs, K. (1966), "The Transfer Function for P-Waves for a System Consisting of a Point Source in a Layered Medium", *Bull. Seism. Soc. Am., 56(10)*, 75-108.

Rodi, W. L., J. M. Savino, T. G. Barker, S. M. Day and T. C. Bache, (1978), "Analysis of Explosion Generated Surface Waves in Africa, Results from the Discrimination Experiment and Summary of Current Research", Systems, Science and Software Quarterly Technical Report, SSS-R-78-3563.

Stevens, J. L., T. G. Barker, S. M. Day, K. L. McLaughlin, N. Rimer and B. Shkoller (1991), "Simulation of Teleseismic Body Waves, Regional Seismograms, and Rayleigh Wave Phase shifts Using Two-Dimensional Nonlinear Models of Explosion Sources," AGU Geophysical Monograph 65: Explosion Source Phenomenology, S. Taylor, H. Patton, P. Richards editors, ISBN 0-87590-031-3, pp. 239-252.

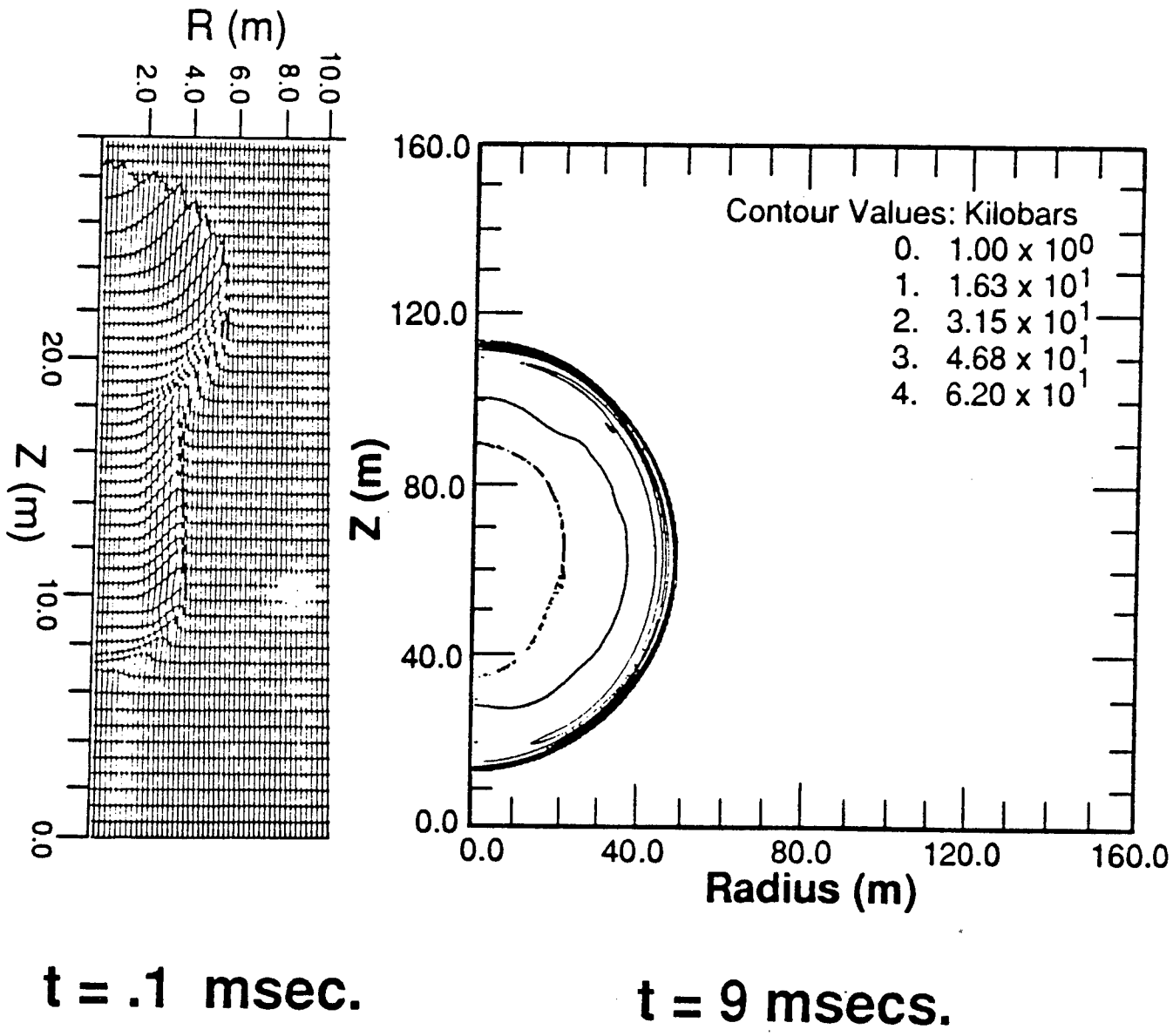


Figure 1. Density profiles at 0.1 msec and pressure profile at 9 msec from the SOIL calculation. The asymmetric source results from placing the explosion at the top end of the canister with a heavy steel plate beneath it.

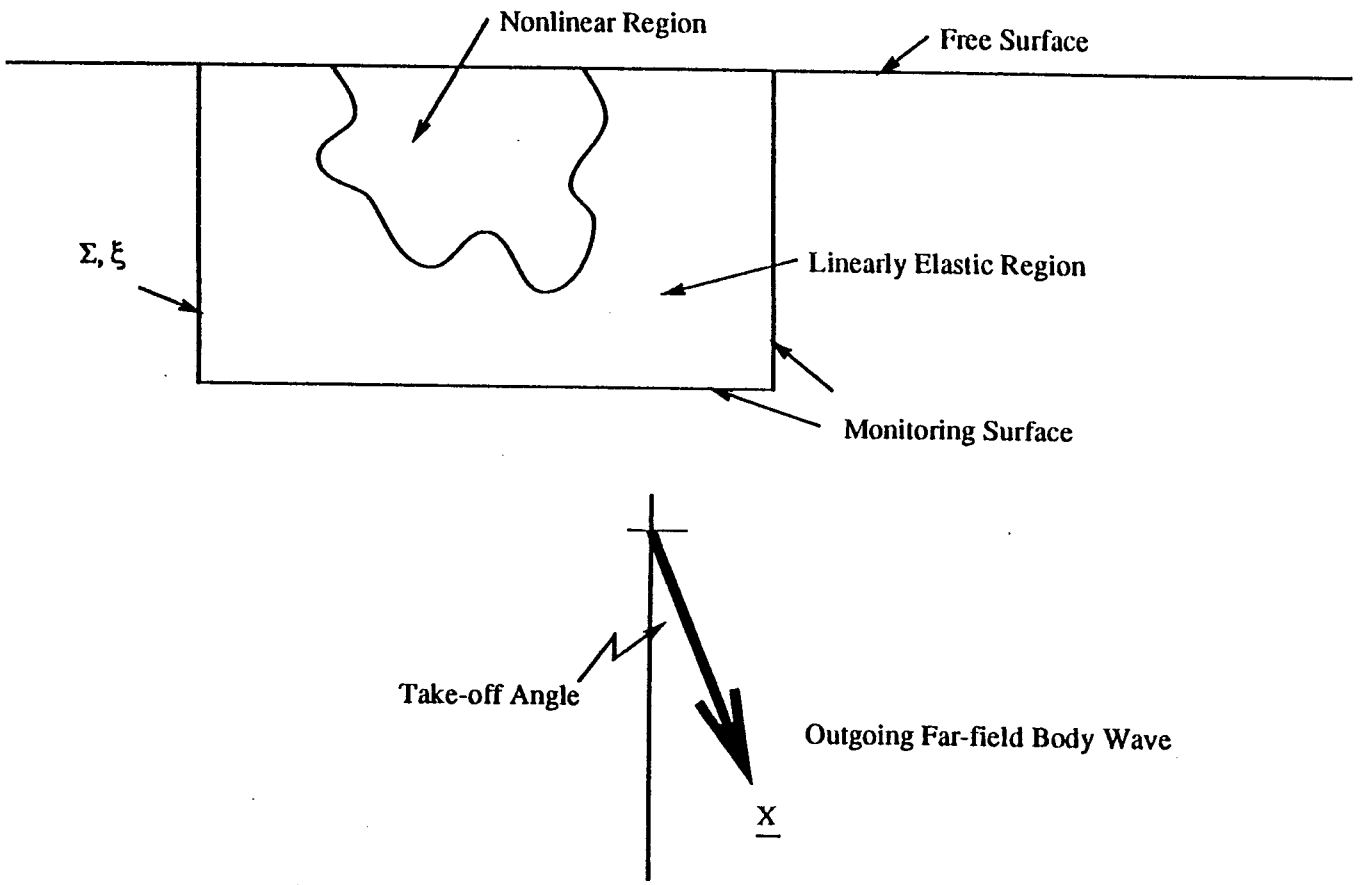


Figure 2. Schematic of the method used to propagate the numerical simulations into the far-field.

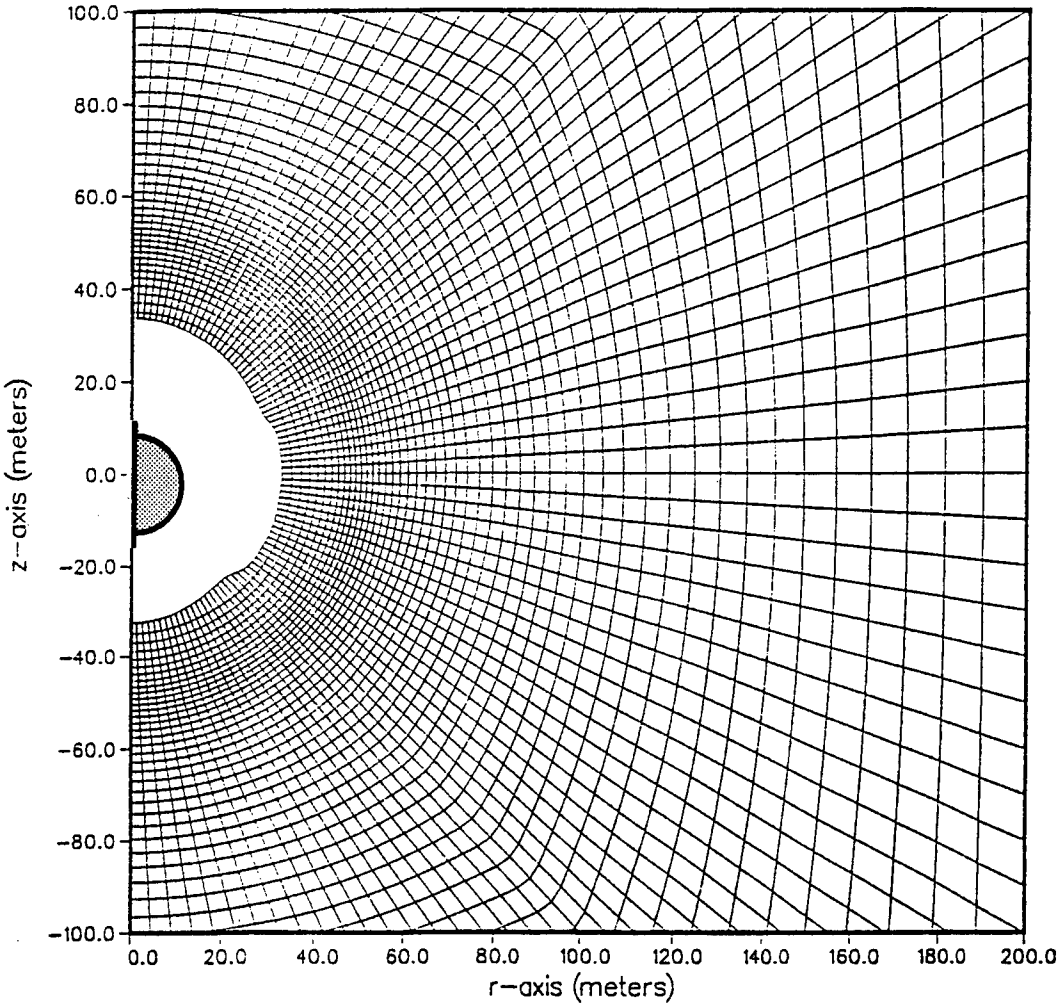


Figure 3. Initial grid for the RHY1 calculation at the time of the overlay from SOIL. Small central circle shows the starting radius for the spherically symmetric RHY2 problem.

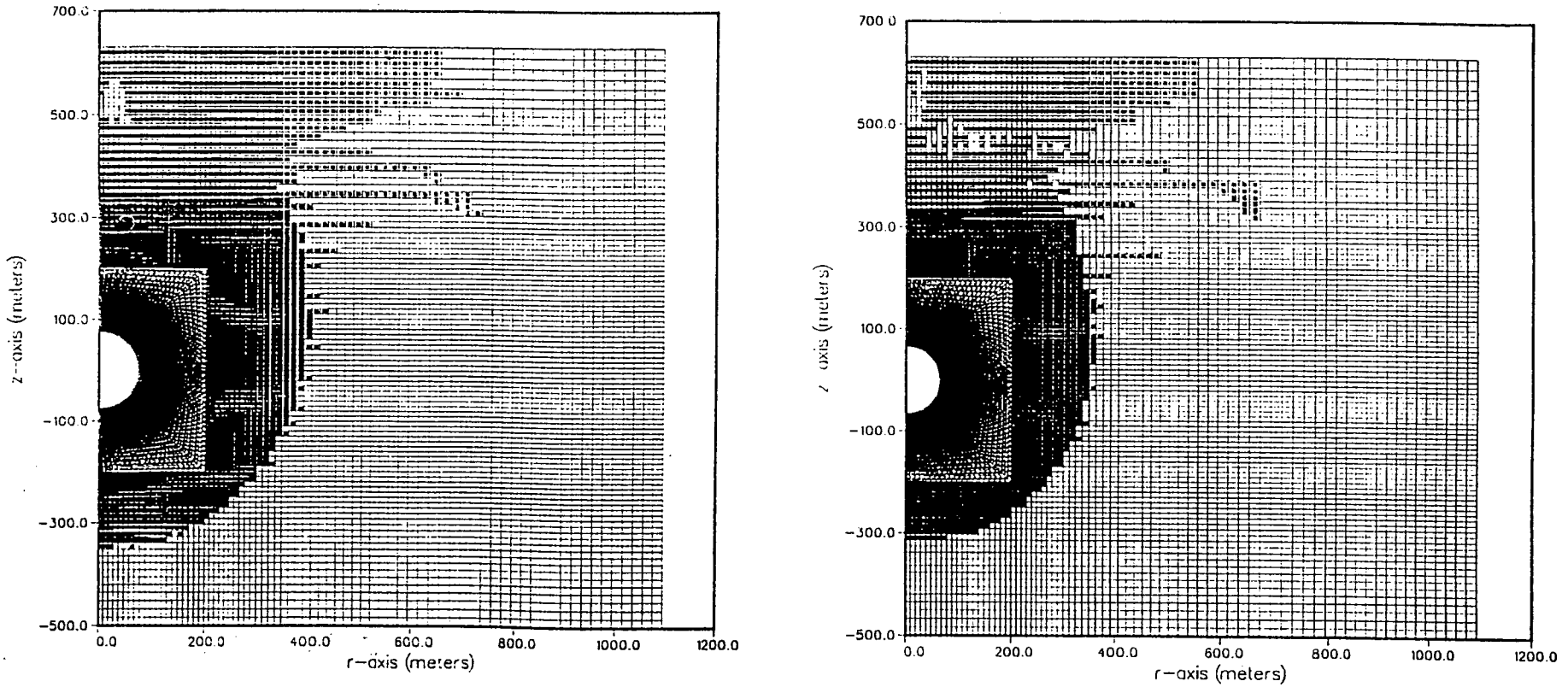


Figure 4. Final state of CRAM grid at the end of the calculation showing final cavity size and nonlinear region. SOIL overlay calculation (RHY1) on left; spherically symmetric source (RHY2) on right.

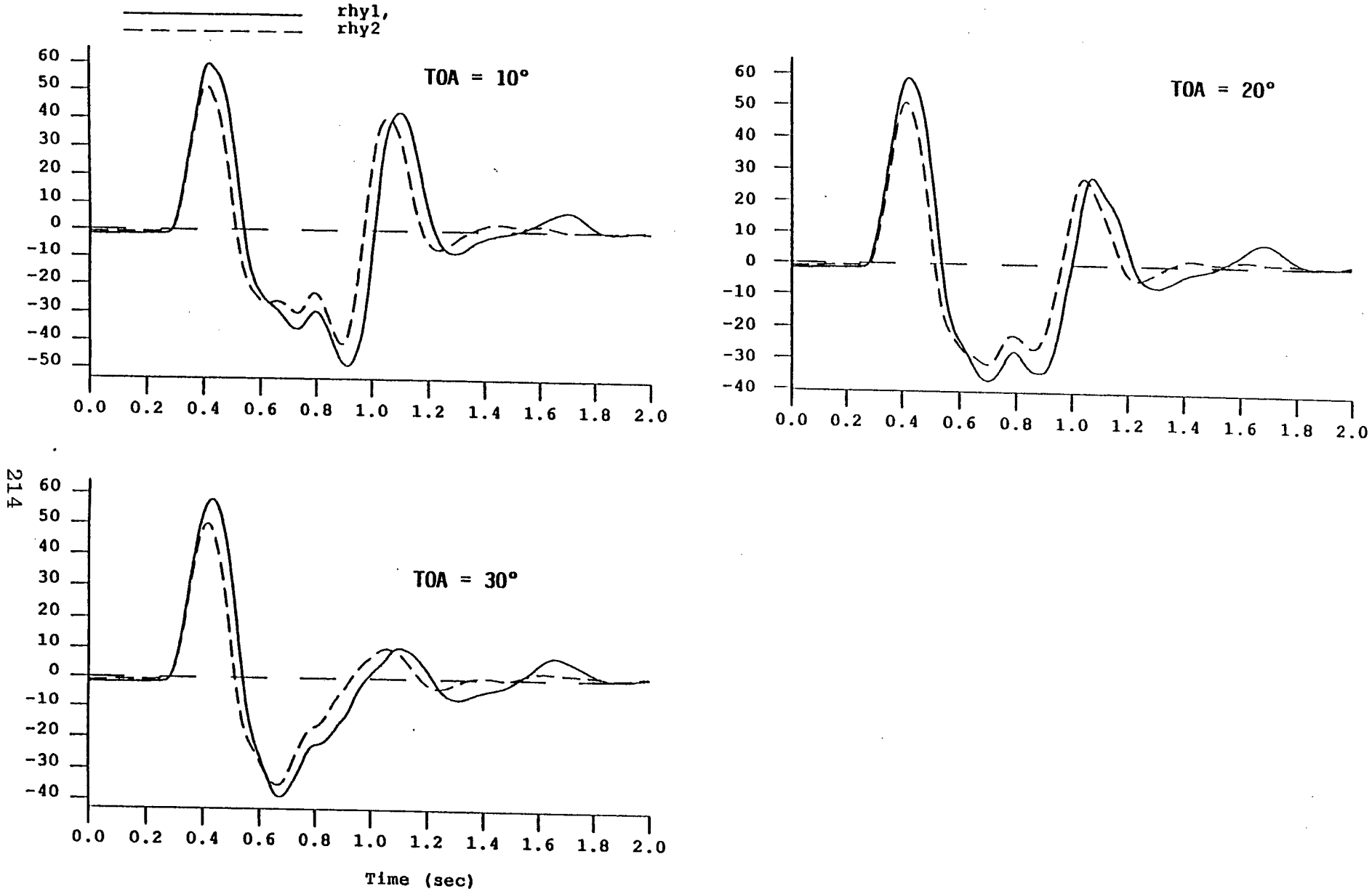


Figure 5. Comparison of the 2-D far-field P waves at three take-off angles for the RHY1 (solid lines) and RHY2 (dashed lines) calculations.

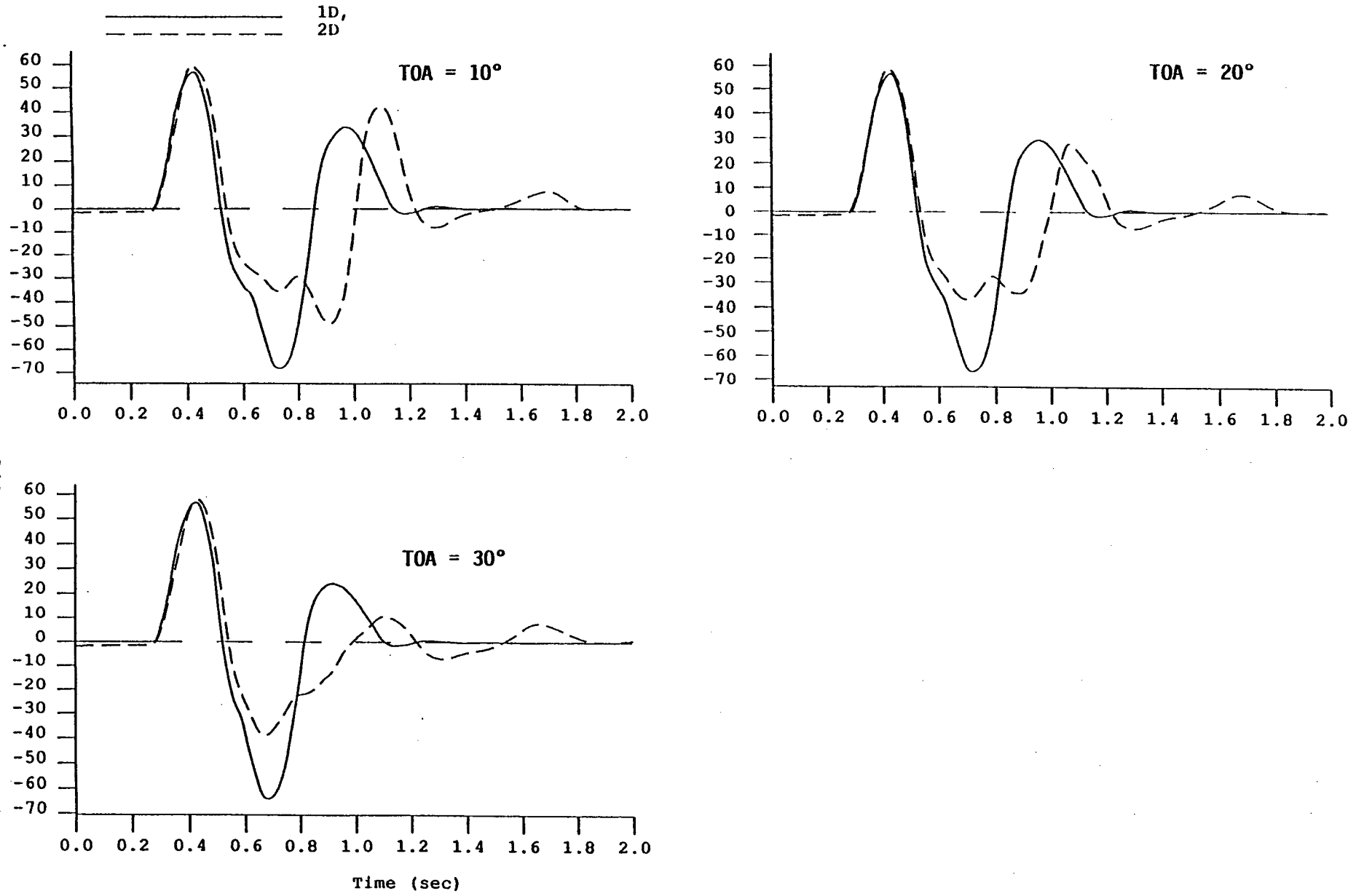


Figure 6. Comparison of the far-field P waves at three take-off angles for the 1-D (solid lines) and RHY1 (dashed lines) calculations.

THIS PAGE INTENTIONALLY LEFT BLANK.

Ground Motion Analysis of OSSY

Robert P. Swift
Charles M. Snell
Los Alamos National Laboratory, EES-5

Abstract

The On Site Seismic Yield experiment, OSSY, was performed to investigate the viability of a high-explosive technique to help estimate the yield of nuclear explosions. We have analyzed recorded data and conducted numerical simulations of the 100-pound OSSY experiments performed in hole UE-10 ITS #3 at the Nevada Test Site. Particle velocity wave forms from these experiments show a distinct dual-pulse structure in the close-in and far-field regions, with the amplitude of the second pulse being as large as or larger than the first pulse. To gain some insight into the cause of the dual-pulse feature, we examine how the explosion-induced close-in response is affected by (1) certain features of inelastic rock/soil constitutive models applied in the near-field region, (2) the large length-to-diameter charge ratio of 8, (3) the charge and gauge package emplacement, and (4) geology (e.g., layering) in the vicinity of the explosion. Our results from 1-D and 2-D simulations show the following: (a) The response, measured by accelerometers located above the charges, is significantly influenced by the charge length-to-diameter ratio out to a distance of 8 m. (b) The grout emplacement of the charge has very little effect on the response. (c) The geologic layering serves mainly to phase the arrival of the pulses. (d) The second pulse can be best accounted for by applying a dilatant feature that allows for pore recovery during unloading. Other material property variations do not provide any contribution to the formation of a second pulse.

Introduction

Reliable estimates of yield for underground nuclear explosions, based on seismic data, require knowledge of how close-in inelastic behavior can influence the characteristics of explosion-induced seismic waves. Small high explosive [HE] charges detonated in an emplacement hole provide a way to calibrate the seismic character of a particular site prior to a nuclear explosion. A technique, denoted as On Site Seismic Yield experiment [OSSY] Ref. 1, was developed to assess the use of small HE charges for the purpose of improving the seismic estimate of underground events. Using HE has an advantage over other seismic source generators, such as the airgun or vibroseis methods, in that it provides a calibration that includes nonlinear material behavior. During HE loading, a material region surrounding a charge is compacted irreversibly and fails in shear and/or tension in a manner similar to that for a nuclear explosion.

One set of OSSY experiments, conducted in September 1989 in hole UE-10 ITS #3, had four six-shot charge strings arrayed over a depth interval from 578 m up to 110 m. Each string consisted of three charge pairs of 100-pound and 10-pound C4 HE. Spacing between each charge pair was 40.3 m, with 8.7 m separation between the 10-pound and 100-pound charges. The charges on each string were detonated sequentially from the deepest to the shallowest. A discussion of surface data obtained on these experiments from three-component seismic receivers arrayed at various locations about the hole is given in Ref. 2. The data we are addressing here came from the two middle charge strings, shown in Figure 1, that had 14 accelerometer gauges spanning a distance of 11 m and starting 1.36 m above the top 100-pound charge. Particle velocity wave forms from these gauges showed a distinct dual-pulse structure, with the amplitude of the second

pulse being as large as or larger than the first pulse. The dual-pulse feature was also observed in the far-field surface measurements.

The objective of the present study is to determine a reason or reasons for the dual-pulse structure and to establish whether the feature is caused by constitutive behavior of the material, charge aspect ratio, grout emplacement influence, layering in the vicinity of the explosions, or a combination of some or all of the above. We accomplish this objective by a brief analysis of the OSSY down hole accelerometer data and by performing 1-D and 2-D numerical simulations. The results are summarized as follows: (1) The response for gauges closer than 8 m from the nearest 100-pound charge is significantly influenced by the charge length-to-diameter ratio. (2) The grout emplacement has only a minor effect on the response, with the exception of charge-string 3, whose response was greatly affected by borehole sloughing and an inadequate grout bonding of the gauge package to the borehole material. (3) Geologic layering does not contribute to the development of the second pulse but does play a role in phasing the arrival times of both the first and second pulses. (4) The second pulse can be best accounted for by applying a dilatant feature that allows for pore recovery during unloading. Other material property features do not provide any contribution to the formation of the second pulse.

OSSY Response

A schematic of the two middle OSSY charge strings 2 and 3 with down hole gauge arrays is shown in Figure 1. The lower string contained shots 7 through 12 and the upper

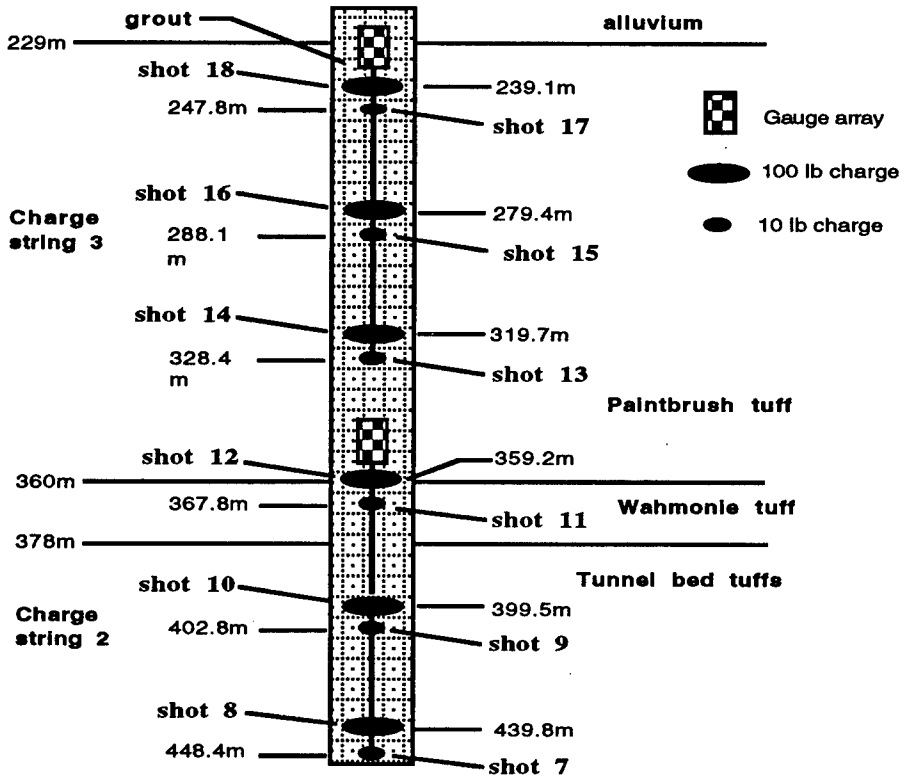


Figure 1. Schematic of OSSY charge strings 2 and 3 in hole UE-10 ITS #3

string contained shots 13 through 18. The even shot numbers correspond to the 100-pound charges and the odd numbers to the 10-pound charges. These shots were within the tuff units with the upper string gauge array being near an alluvium interface located at 229 m depth, where considerable sloughing of the borehole occurred in this region. A detailed analysis of the data for these two charge strings is given in Ref. 3. Briefly, wave form shapes for both strings are similar, but the amplitude and time-of-arrival [TOA] of the upper charge-string 3 responses are significantly affected by the sloughing of the borehole. Charges 17 and 18 closest to the gauge package were directly coupled to it via the excess grout poured in the sloughed region. However, the low amplitude response and late arrival time for charges 13 through 16 indicated that the gauge package was decoupled from the surrounding medium.

Because of the borehole sloughing problem, our modeling effort focuses on the lower charge string 2 data, and specifically, on the 100-pound shots 10 and 12. Some of the particle velocity wave forms recorded for these events are given in Figures 2 and 3.

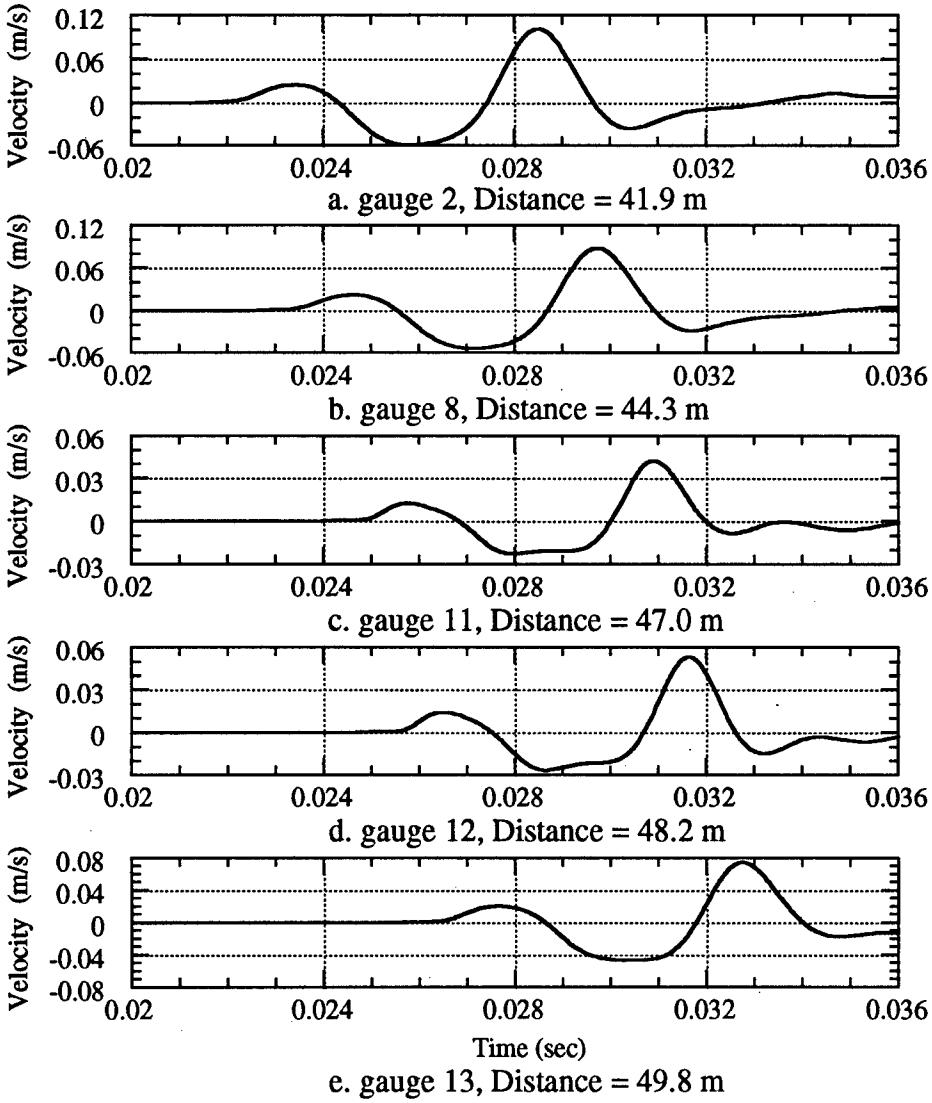


Figure 2. Particle velocity wave forms from OSSY shot 10.

The data obtained for the close-in gauges on shot 12, Figures 3a-c, are affected by their close proximity to the charge which has a length-to-diameter ratio of 8. Beyond 8 m in shot 12, Figures 3d-e, the evolving response is similar to the dual-pulse structure observed in shot 10, Figure 2, and in the other shots for this string.

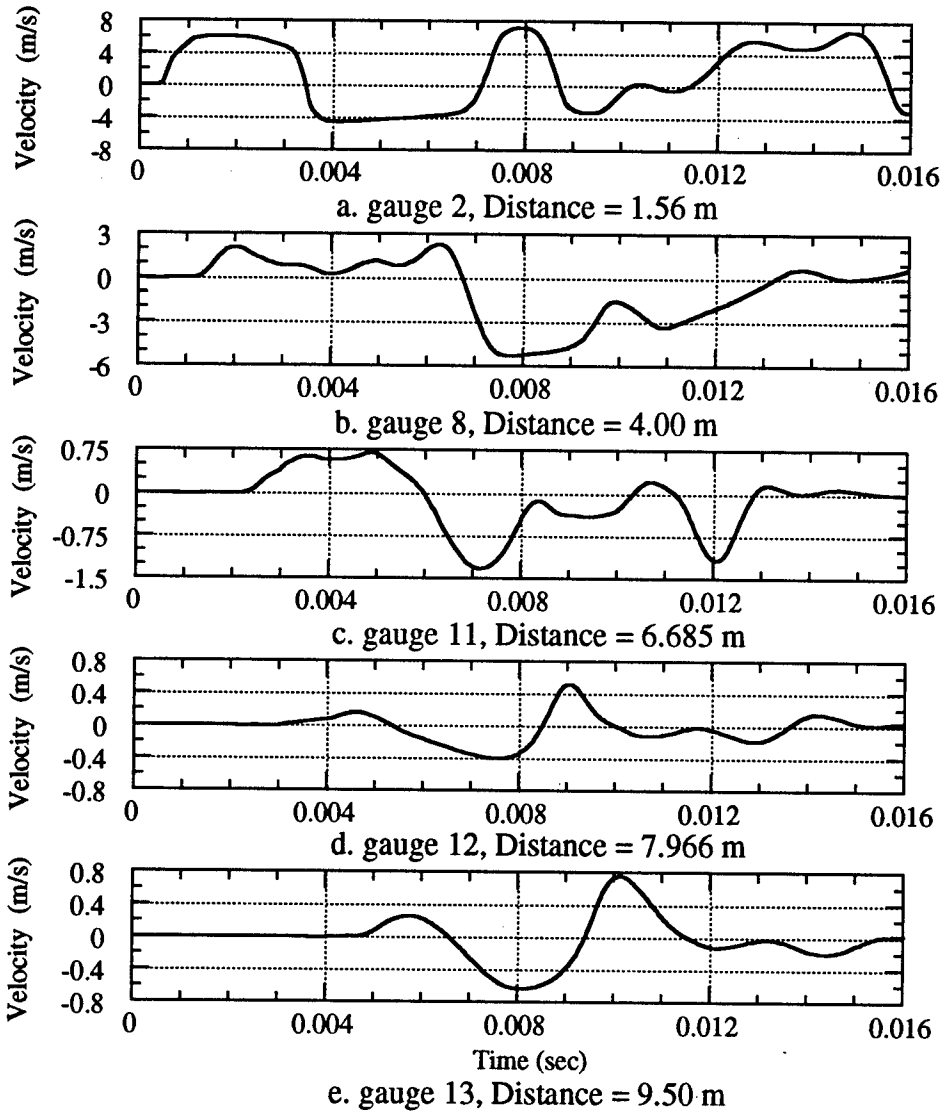


Figure 3. Particle velocity wave forms from OSSY shot 12.

Numerical Simulations

To investigate the cause of the dual-pulse structure observed on OSSY, we performed 1-D and 2-D finite-element simulations. Our goal was not to replicate the wave forms exactly, but simply to address the dual-pulse structure qualitatively by assessing material property effects for a simple constitutive model. The 1-D calculations ascertained what constitutive features could provide a representative dual-pulse response. The 2-D simulations addressed the charge aspect ratio, grout emplacement effects, and the influence of layering. Details of the constitutive models, simulation configuration, and a thorough discussion of the results are given in Ref. 3.

A constitutive feature that best accounts for the dual-pulse structure is dilatancy associated with partial recovery of compacted pore volume during unloading of the material. Specifically, we compare the calculated responses for the three different types of unloading behavior illustrated in Figure 4. One is unloading with constant porosity and the other two are unloading with different degrees of dilatant elastic pore recovery. The calculated 1-D responses are compared to data for shot 12 at 9.5 m in Figure 5.

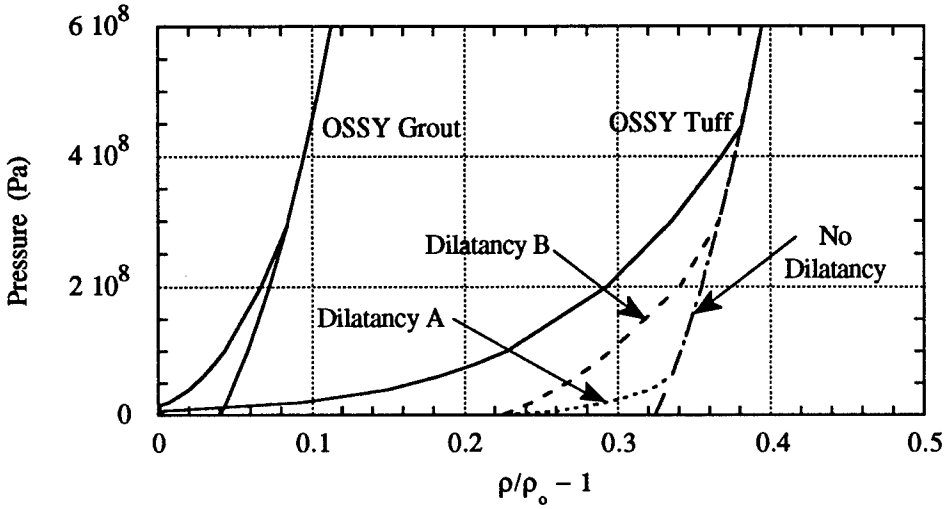


Figure 4. Pressure-excess compression models for OSSY.

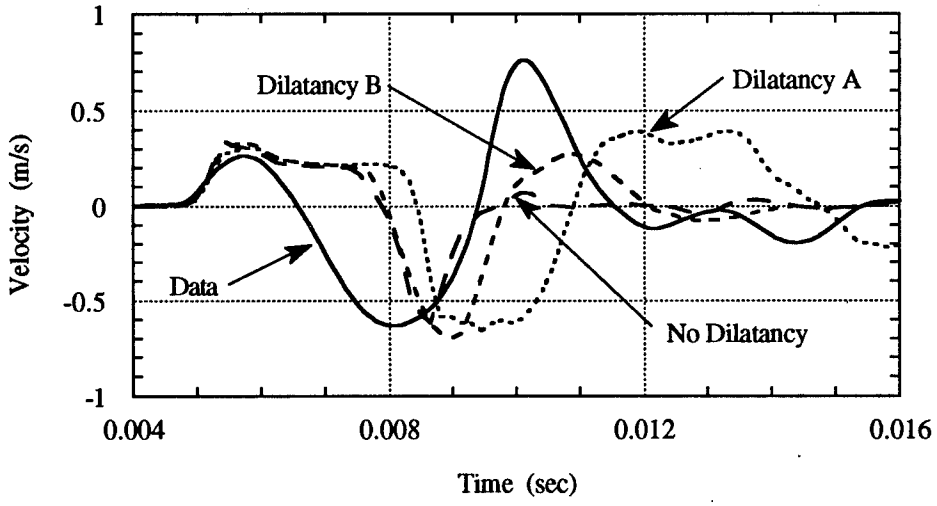


Figure 5. Comparison of data for shot 12 at 9.5 m with calculated response for different unloading conditions.

The constant porosity unloading (long dash line) does not induce a pronounced second pulse. The pore recovery feature for unloading does cause a significant second pulse, which is highly sensitive to the character of the dilatancy. The dilatant B condition gives better agreement to the data, and it along with the constant porosity condition will be examined in the 2-D simulations.

First, we define the extent of the region where the dilatancy B effect is important. Figure 6 compares the calculated response for the case where the region of dilatancy is restricted to the nonlinear portion of the problem (i.e., over 1 m to 2 m beyond the cavity) with the response when dilatancy acts over the entire grid, as in the above calculations.

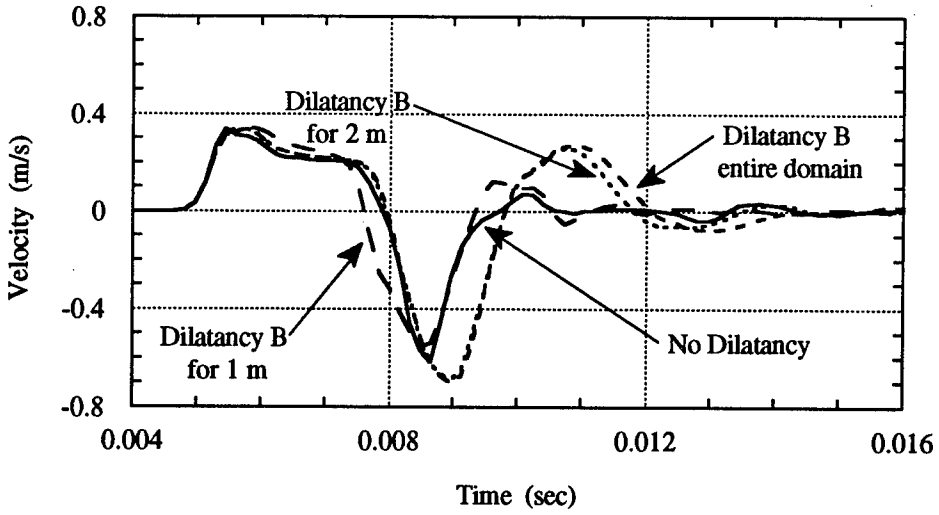


Figure 6. Effect of distance from charge over which dilatancy B acts on the calculated OSSY response at 9.5 m.

For a 1 m restriction, the first pulse is narrower and the second pulse is less pronounced in comparison to dilatancy acting over the entire region, but still more apparent than for no dilatancy. For a 2 m restriction, the response is very similar to that with dilatancy acting everywhere. The influence of dilatancy is confined to a region around the charge where sufficient compacting occurs to allow pore recovery. No other constitutive property has as much of an effect in generating a dual-pulse structure as does the dilatancy feature.

The effects of charge geometry, grout emplacement, and layering on the response are obtained with a 2-D axisymmetric configuration. The influence of the 8-to-1 charge length-to-diameter ratio is shown in Figure 7, which compares data to the calculated up-axis response (directly above the charge) and to the waist response (same distance horizontally and at the charge mid-point). The 1-D response for dilatancy B acting within 2 m of the charge is also superimposed. While the shape of the first pulse for the waist

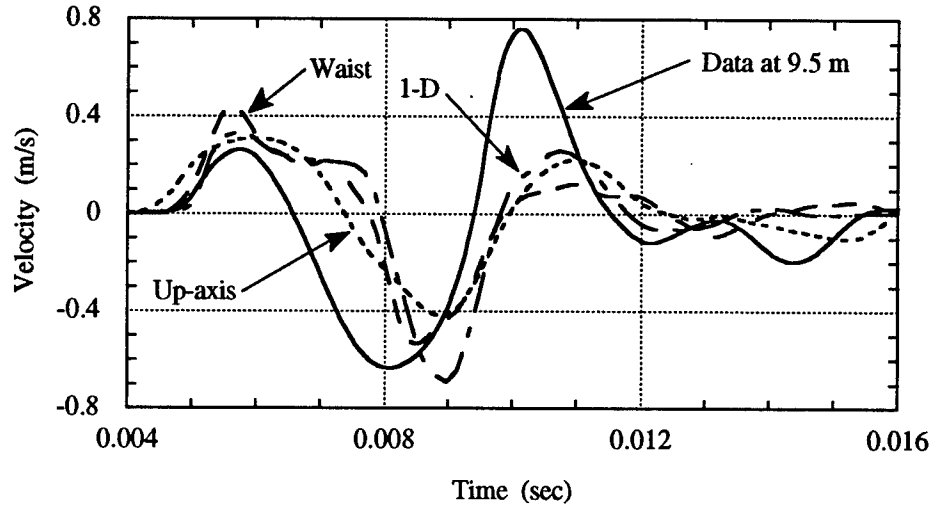


Figure 7. Comparison of 2-D response with charge aspect ratio of 8-to-1 to data at 9.5 m and 1-D response, for dilatancy B.

response is similar to the 1-D response, but with a higher peak, the second pulse is very different. The up-axis response, being sinusoidal, is more representative of the data, and is analogous to the 1-D response in the second pulse. Neither the waist nor the up-axis responses have the large negative peak that the data and the 1-D case exhibit. Phasing of the response is also poor. In contrast to these differences between the 1-D and 2-D calculated responses for a large aspect ratio, Figure 8 shows the similarity of the 1-D spherical response to the 2-D response for a cylindrical charge with an aspect ratio of one.

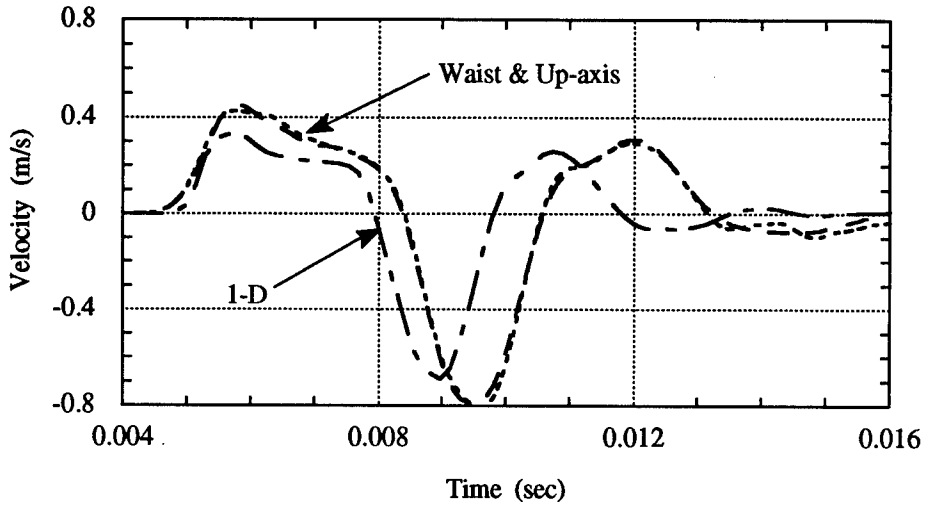
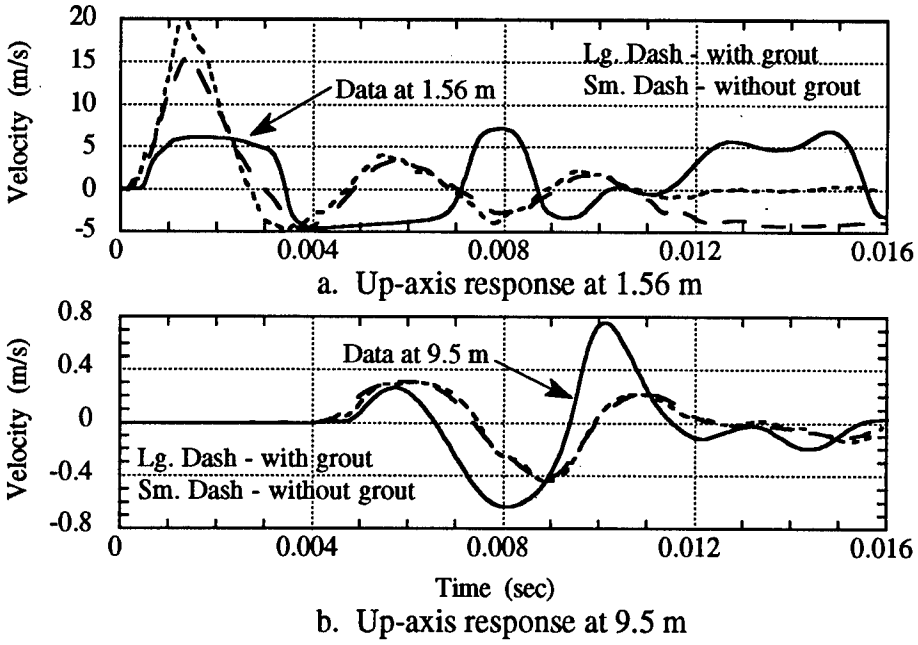


Figure 8. Comparison of 2-D up-axis and waist responses at 9.5 m for a charge aspect ratio of one to the 1-D response, for dilatancy B.

The calculated influence of the grout emplacement is shown in Figures 9a and b. The influence of the grout on the close-in response is apparent in Figure 9a, with the up-axis response having a higher peak when grout is omitted. At distances beyond about 4 m, the responses with and without grout, shown at 9.5 m in Figure 9b, are very close.



a. Up-axis response at 1.56 m

b. Up-axis response at 9.5 m

Figure 9. Calculated effect of grout emplacement compared to data.

The influence of layering examined in 2-D simulations included the 18 m thick Wahmonie tuff layer just below the gauge array and the shot 12 charge, see Fig. 1. This layer was modeled as being stronger and less compressible (see Ref. 3) than the Paintbrush and Tunnel bedded tuff units, which were assumed to have identical properties. Figure 10 compares the measured response at 9.5 m for shot 12 to the calculated responses for uniform and layered geology. A similar comparison is given in Figure 11 at 41.9 m for shot 10.

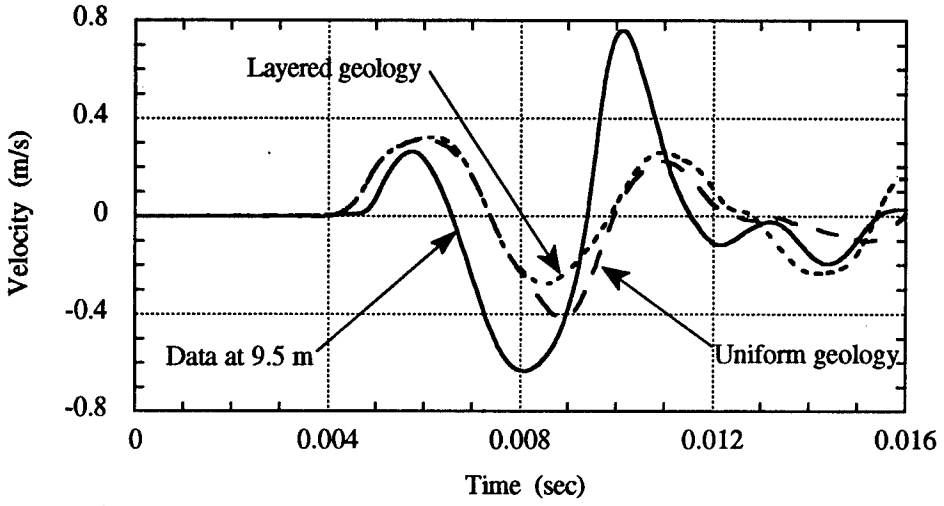


Figure 10. Comparison of data at 9.5 m for OSSY shot 12 with calculated responses for layered geology and uniform geology.

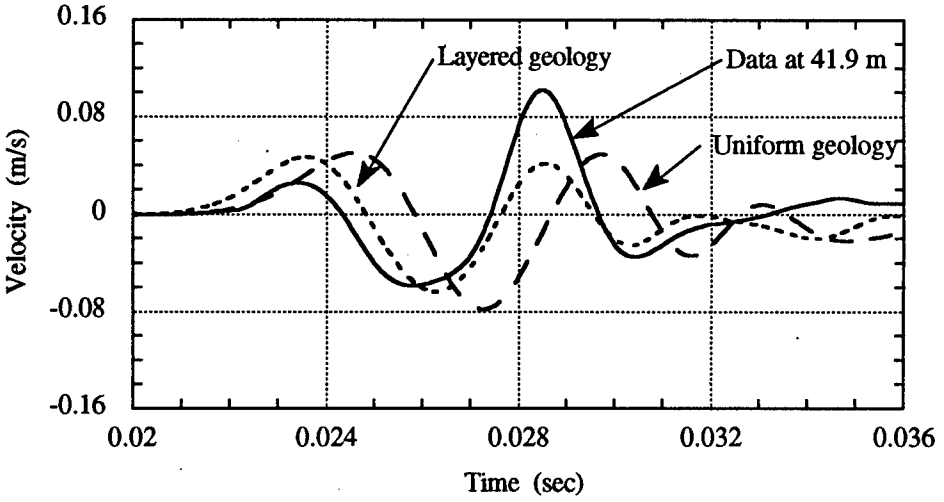


Figure 11. Comparison of data at 41.9 m for OSSY shot 10 with calculated responses for layered geology and uniform geology.

Very little difference is noted for the response at 9.5 m, with the exception that layering causes some modification to the negative phase and the second pulse. Also, the slightly earlier TOA noted in comparison to the 1-D calculation in Fig. 5 is due to coarser zoning for the 2-D case. The layering effect on the calculated response is more pronounced for shot 10, shown in Fig. 11, providing an improved TOA and phasing of the calculated wave forms to the data.

Conclusions

We have conducted analyses and numerical simulations of the OSSY experiment, that used HE charges in hole UE-10 ITS #3 containing different tuff layers. A large variation in the amplitude of the OSSY response from charge string 3 to that of charge string 2 is attributed to borehole sloughing in the vicinity of the gauge package for charge string 3 and a probable failure of the grout poured in this region to properly couple the gauge package to the surrounding medium. We find that the close-in OSSY response is significantly influenced by the large length-to-diameter charge ratio, but that the grout emplacement of the charge plays only a minor role in shaping the response. We find that the effect of layering on the response is more important for the shots below the Wahmonie layer and that the calculated phasing and TOA are greatly improved when the layering is accounted for. We find that the large second pulse in the dual-pulse feature of the response may be due to a dilatancy mechanism that allows for pore recovery during unloading. This feature appears to originate in the nonlinear compacting region close to the charge and is maintained out to the far field.

It is surmised that the spectral content from the measured close-in up-axis response will be affected by the charge configuration; however, it is doubtful that the effectiveness of OSSY as a seismic tool for calibrating an explosion site will be deterred. This is because the technique described in Ref. 1 uses a Green's function approach which removes the influence of the propagation path between the source and the seismic stations, i.e., the nuclear explosion is proportional, not to the absolute value of the seismic spectrum, but, to the ratio of the long-period spectral levels of the nuclear source to the HE source. Other uncertainties that may affect OSSY are local geology and the variability of source coupling. We have not addressed source coupling here, but we note, that decoupling of the gauge package in charge string 3 gave a response an order of magnitude less than that for charge string 2. A decoupled source could give a similar reduction in response amplitude. The dual-pulse feature could be important in understanding coupling and helpful in the discrimination of underground events. Hence, further study of its physical mechanisms and implications for event discrimination would be very beneficial.

Acknowledgments

Thanks to Marvin Denny for his helpful discussions with regard to this effort. This work has been supported, under the auspices of the U. S. Department of Energy, by the Los Alamos National Laboratory, under contract number W-7405-ENG-36.

References

1. M. D. Denny and S. R. Taylor, "On-Site Seismic Yield Estimation," Memorandum, SAG 89-9, Lawrence Livermore National Laboratory, April 27,1989.

2. L. R. Johnson and T. V. McEvilly, "OSSY Source Characterization-Summary Report," Department of Geology and Geophysics, University of California, and Center for Computational Seismology, Lawrence Berkeley Laboratory, September 1990.

3. R. P. Swift, "Ground Motion Analyses: OSSY (A High Explosive Experiment) and MERLIN (A Nuclear Event)," Lawrence Livermore National Laboratory Report, UCRL-ID-108616, October, 1991.

THIS PAGE INTENTIONALLY LEFT BLANK.

EXPLOSIVE SHIELDING BY WEAK LAYERS

W. L. Fourney, R. D. Dick, and T. A. Weaver
Group EES-3 Los Alamos National Laboratory

ABSTRACT This paper presents the results of a series of computations which were carried out to determine the effect that a layer of extremely weak rock embedded in an otherwise strong rock matrix would have on the displacements and velocities which result from the detonation of a nearby explosive source. The motivation for the study was the apparently different measurements obtained on the Mission Cyber Nuclear Event when compared to results obtained from other events of equal yield in similar geologic media.

INTRODUCTION While investigating various reasons which might be responsible for the apparent differences in the experimental results obtained by Sandia National Laboratories when measuring the close-in stresses and accelerations from nuclear events in P Tunnel at the Nevada Test Site it became apparent that there is an extremely large variation in the properties of tuff from the Rainer Mesa Area.

Figure 1 is a graph depicting relative strength of tuff obtained from a vertical core hole near the Mission Cyber Event. The values of strength shown were the authors estimation of what the strength might be based upon examination of the core from the surface to a depth of 1000 feet which was well below the working point for the Mission Cyber Event. Figure 2 presents a comparison of the relative strength values assigned by the authors with actual strength values as obtained in testing conducted by Terra Tek [1]. Terra Tek values for both unconfined strength and strength as determined from tri-axial tests are shown. The relative strengths from the Terra Tek data were determined by finding the numerical average of the strengths and assigning that strength a relative strength value of 5. This resulted in some values being greater than 10 but these values were plotted as a 10 in Figure 2. Note that where strength values are available that the relative strengths assigned do correlate well with those assigned by the authors - except in the area of the working point. Near the working point the strength values as determined by the authors are considerably higher than the results obtained by Terra Tek. Note also that there is a wide variation in the values of relative strength as assigned. The relative strengths go from very low values (less than 1.5) at the surface up to 7.5 at a depth of 140 feet and remain at that value until a depth of 440 feet is reached. There the strength begins to decrease and actually reaches a value of zero from 720 feet to 760 feet and then begins to increase. At the working point the relative strength was found to be quite high (7.5) but relative strength again drops to zero after that point is passed. Figure 3 shows photographs of the best and the worst of the core as determined from our examination of the vertical core. As can be seen from the photographs, the weakest core resembles a crumbly sand while the rock that was assigned a relative strength of 7.5 is competent rock with high unconfined strength and tri-

axial strength values. Figure 4 shows relative strength values determined from a horizontal core hole which was located near the Mission Cyber Event. In this case there is very little variation in the relative strength values assigned.

The large variations in strength were surprising and it was felt that such variations might provide a possible reason for the differences obtained from experimental measurements during the nuclear events. We therefore conducted a numerical study of the effect of weak layers such as those observed in the core library could have on the velocities and displacements resulting from the detonation of an explosive charge.

NUMERICAL STUDY The code that was used to predict the rock response was WONDY V, a one dimensional finite-difference wave propagation code developed and maintained by Sandia National Laboratories. The code integrates the one-dimensional Lagrangian differential equations of motion by use of finite difference analogs. We used the code in a spherical geometry and used an equation of state which was based on the P-alpha concept of void removal upon loading. This is the same equation of state utilized to predict response from nuclear events. The particular version that we used did not account for either strain rate effects or strength reduction due to damage caused by loading.

Figure 5 shows the model used in the computer code. In this particular case 3/8 gram of PETN covered with a thin jacket of PMMA makes up the explosive source. This is a geometry that had been used by Miller and Florence [2] at Stanford Research Institute to calibrate computer codes to predict the response of geologic material to explosive sources. We chose to run our computations in an Indiana Limestone material since this is one of the materials investigated by Miller and Florence [3]. Notice from Figure 5 that the weak layer is located 5 cm from the center of the model. For the case shown the thickness of the weak layer is 0.25 mm but in the study the layer thickness was varied from zero to 6 mm. The failure surfaces for both the weak and the strong layers are shown in Figure 6. Also shown in that figure are experimental results obtained for Indiana Limestone from static tests [3]. The three sets of experimental data are for dry, 50% saturated, and 100% saturated Indiana Limestone with the strongest rock being the dry limestone. The failure surface chosen represents the dry limestone but the failure values were increased to reflect the fact that the limestone is stronger than the static values at the high strain rates of the explosive tests. Notice that the strong rock has a strength of about 12 kbar for a confining (mean) stress value of 10 kbar. The weak rock on the other hand only has a yield of 2.2 kbar at a mean stress of 10 kbar. This is a reduction in yield strength of six. The other strength factors shown in Figure 6 are for the elastic pressure P_e and the crush pressure P_c. For the strong rock the elastic pressure was taken to be 0.6 kbar and for the weak rock 0.06 kbar. The crush pressure for the weak rock was also reduced

by a factor of 10 from 24 kbar to 2.4 kbar. The reduction in yield surface and in elastic and crush pressures are merely a best guess and may or may not be accurate representations of appropriate values.

RESULTS Figure 7 presents typical velocity values obtained from the calculations. In this case the radial particle velocities are shown for various thicknesses of weak rock layers located 50 mm from the charge center. When no weak layer was present the velocity at 65 mm from the charge center was 5 m/s. A layer of 0.5 mm thickness at 50 mm resulted in a decrease in velocity to a little more than 3 m/s while the thickest layer investigated (6 mm thick) reduced the velocity to about 1.7 m/s (or to about one third of the value if no weak layer were present). Figure 8 shows the loss in velocity as a function of weak layer thickness and Figure 9 shows the similar information for displacements. In this case the loss of velocity and displacement due to the presence of a weak layer are shown as a function of layer thickness. The presence of a layer of thickness 0.25 mm results in a loss of 1.2 m/s of velocity and 0.0006 mm of radial displacement. This is about 22 % of the velocity and 33.3 % of the displacement if no weak layer were present. As can be seen from Figures 8 and 9 the presence of a 6 mm thick layer results in a loss of about 67 % of the velocity and 60 % of the available displacement.

For the case being investigated the material at 50 mm from the charge center is under a state of elastic stress. In fact, an examination of the decay rate of the velocity with respect to distance from the charge center shows that the material between the charge center and out to about 25 mm undergoes large plastic deformation and the decay rates are large. From 25 mm outward the decay rate is much smaller and indicates elastic or low plastic loading. The above described computations were repeated with weak layers located at 35 mm from the charge center and at 10 mm from the charge center. The results for the weak layer at 35 mm were similar to those obtained when the weak layer was at the 50 mm location. At the 10 mm location the presence of the weak layers caused reductions in the magnitude of the velocity and unlike the results for the 50 mm and 35 mm locations the time duration of the velocity pulse increased significantly as the layer thickness increased. Figure 10 shows the velocities that are predicted at 25 mm from the charge center when the weak layer is located at 10 mm. Notice that there is very little difference between the no layer case and the case for the 1 mm thick weak layer. As the layer thickness increases, however, the pulse width increases greatly. For this case there were reductions in the displacements but they were not as severe as the reductions at greater distances from the charge center. Figures 11 and 12 give a summary of the results obtained in all three cases from the standpoint of velocities (Figure 11) and displacements (Figure 12). As can be seen from an examination of these figures when the layer is located at 50 mm the loss in displacement increases very rapidly up to a layer thickness of 1 mm and then continues to increase as layer

thickness increases - but not so rapidly as between 0 and 1 mm. The same is true for the case when the weak layer is located at 35 mm. For the case where the weak layer is located very near to the charge center (@ 10 mm) there is a rapid loss of displacement for layers up to 1 mm in thickness (20 % loss) and then little additional loss. This is because at that location the loading is severe enough to cause the rock to behave hydrostatically irrespective of the strength and the net effect of adding the weak layers is not as great as it is at greater distances from the charge. This unusual behavior at close in locations is also evident from observing Figure 11 where two different regimes seem to be represented by the velocity loss curve for the case where the weak layers are located 10 mm from the charge center. In the first regime (for thinner layers) the presence of the weak layers on velocity is very small. In the second regime (for thicker layers) the effect on velocities seem to agree more with the results from the two more distant locations for the weak layers.

When scaled to nuclear explosions the results are quite significant. Figure 13 shows the results scaled to a 1 kiloton device for the situation where the weak layer is located 68 meters from ground zero. As shown an 8 meter thick weak layer results in a loss in displacement of 58 %. Figure 14 shows similar results. In this case two displacement versus time curves are shown that would exist past the weak rock layer. Here the thickness of layer was only 1.33 meters but the loss in displacement was 41 %. From our examination of the core (in the vertical hole) it is not difficult to find the presence of weak rock layers significantly larger than 8 meters in thickness.

Figures 15 and 16 show the effects of the various input parameters when changed separately. For the study just described three parameters were all changed together -failure surface, elastic pressure, and crush pressure. In Figure 15 the failure surface is held constant and both the elastic and crush pressure are changed. There is very little difference between the first two cases in which the elastic pressure is 0.3 kbar and the crush pressure is 12 kbar versus the case where the elastic pressure is 0.6 kbar and the crush pressure is 24 kbar. For the last two cases shown in Figure 15 where the crush pressure is decreased to 2.4 kbar and the elastic pressure to 0 and .1 kbar the effect on velocity is quite dramatic. Figure 16 demonstrates that the most important input parameter with regard to shielding from an explosive source is the crush pressure. As shown in the figure for the same elastic pressure (0 kbar) a reduction in crush pressure from 12 to 2.4 kbar reduces the velocity by nearly a factor of two. Changes in the yield surface were found to affect the velocity and displacements but not nearly so much as the crush and elastic pressures.

CONCLUSIONS The study indicates that the presence of weak layers of reasonable thicknesses appear to have significant effects on velocities and displacements from an explosive source (and

presumably also on accelerations and stresses). The examination of the core from the Test Site also indicates that most of the weaker tuff is never tested (it is too weak to make specimens) and, therefore, is modeled with greater uncertainty in calculations of nuclear events. Furthermore our calculations seem to indicate that the presence of these weak layers should be included in the numerical calculations related to confinement and verification. We say this since a simple averaging technique to account for the presence of the weak layers would not provide a good estimate of the effects as determined from our calculations.

From our examinations of the core in the vicinity of Mission Cyber the apparent differences in the events in the P Tunnel Complex is not felt to be due to the presence of unaccounted for weak layers since if anything the tuff nearest to Mission Cyber was better than that observed near to the other events in P and N Tunnel - especially in the horizontal direction where the instruments were located.

For the future we are planning to conduct laboratory tests on the sand like tuff to determine more appropriate values to use for the elastic and crush pressures. We also will conduct explosive tests in models in which we have embedded a very weak layer between otherwise strong rock layers. These tests will aide us in better predicting the effects of weak layers on wave propagation from explosive sources. We also plan to run two dimensional calculations for similar geometries to determine if the transmission of the signals through the stronger layers above and below the weak layer prevent these large reductions in velocity and displacement. Additional details on the computations conducted can be obtained from [4].

ACKNOWLEDGEMENTS Many people have contributed to our study. We thank Fred App for his patience in getting us started using WONDY and helping us understand ground motion calculations and results. We acknowledge the assistance and technical expertise of Barbara Harris-West at DNA at the Nevada Test Site in providing access to the United States Geological Survey core library at NTS. Also we appreciate the work of the staff at the core library, namely Jerry Magner, Mark Tsatsa, Ron Martin, Dick Hurlbut, and Harry Covington. Finally, we appreciate the efforts of Susan Freeman (EES-3) in keeping our computers humming.

REFERENCES

[1] Torres, G., "Characterization of Material from the Nevada Test Site, Final Report for the Period January 1986 through March 1988 - Volumes I, II, and III", DNA-TR-88-278-V1, V2, V3, 1988.

[2] Miller, S. A. and A. L. Florence, "Laboratory Particle Velocity Experiments on Indiana Limestone and Sierra White Granite", SRI Final Report PL-TR-91-2277, Phillips Laboratory, Oct. 1991.

[3] Heard, H. C., Abey, A. E., and Bonner, B. E., "High Pressure Mechanical Properties of Indiana Limestone", Lawrence Livermore National Laboratory Report UCID-16501, June 11, 1974.
[4] Dick, R. D. and W. L. Fourney, "Effects of Rock Properties on Explosive Source Modeling - Preliminary Results", Los Alamos National Laboratory Report LAUR-92-3277, September 1992.

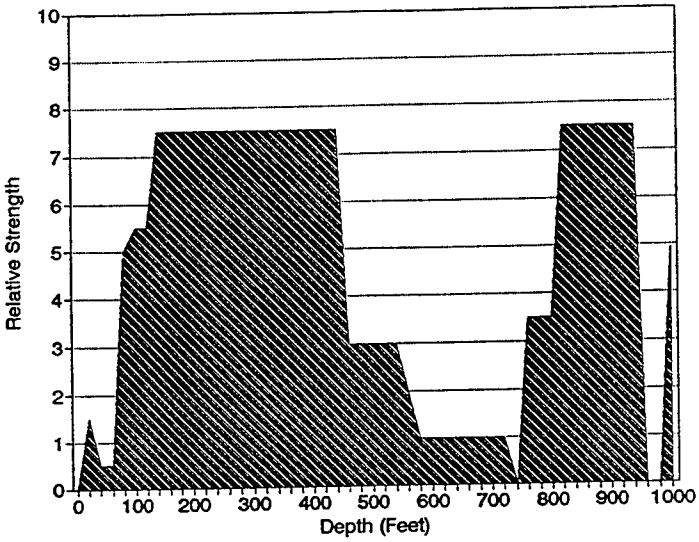


Figure 1. Relative strength versus depth for the vertical core from hole UE12P#4 near Mission Cyber.

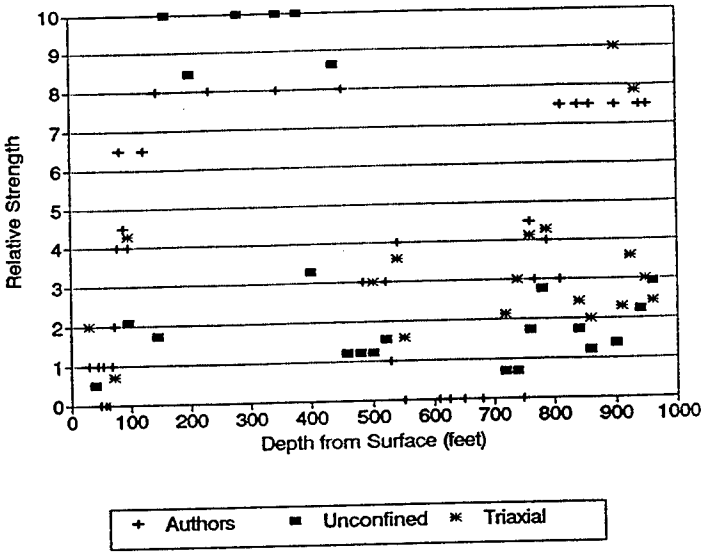


Figure 2. Comparison of relative strengths assigned by authors with strength data from testing conducted by TerraTek.

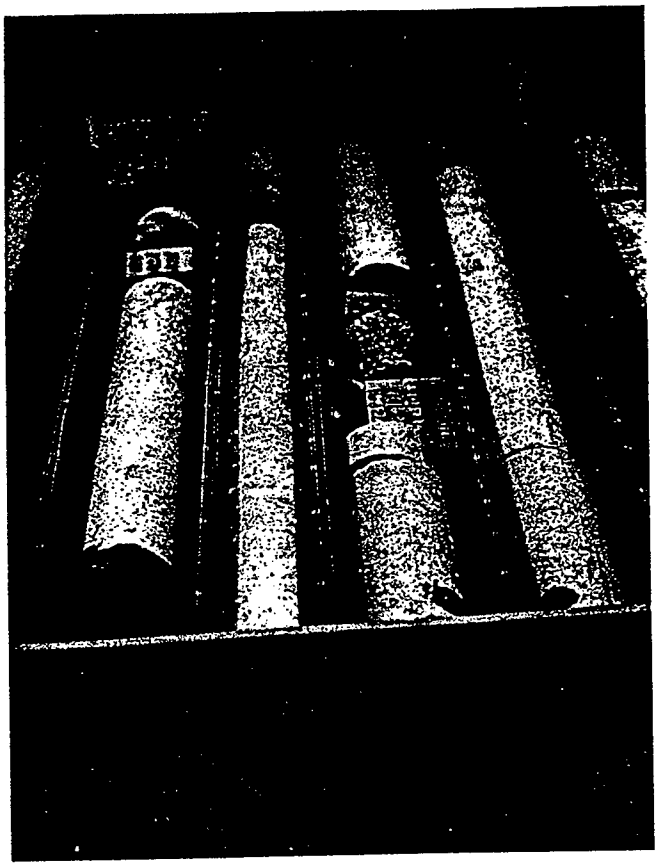


Figure 3a. Photograph of core from 822 feet (UE12P#4).

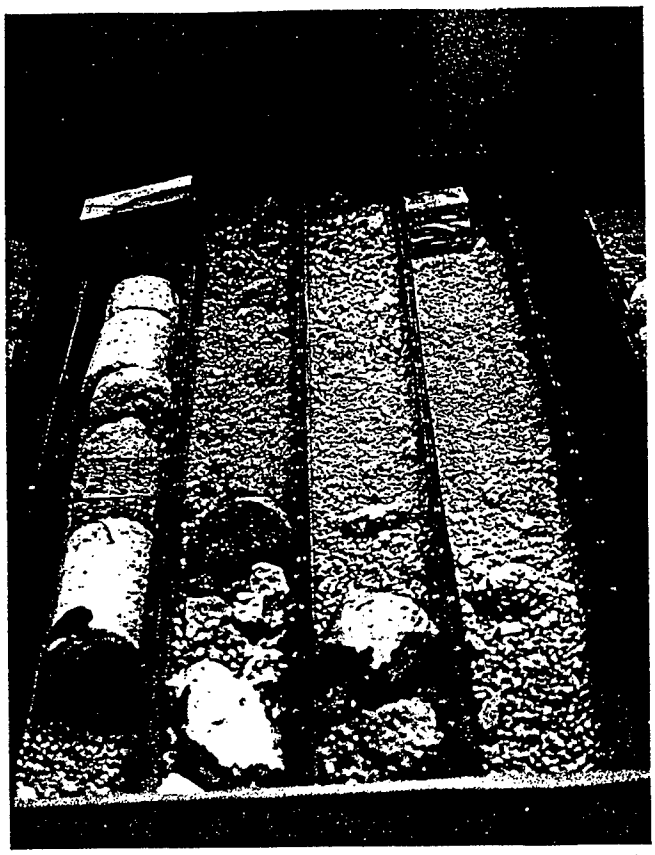


Figure 3b. Photograph of core from 680 feet (UE12P#4).

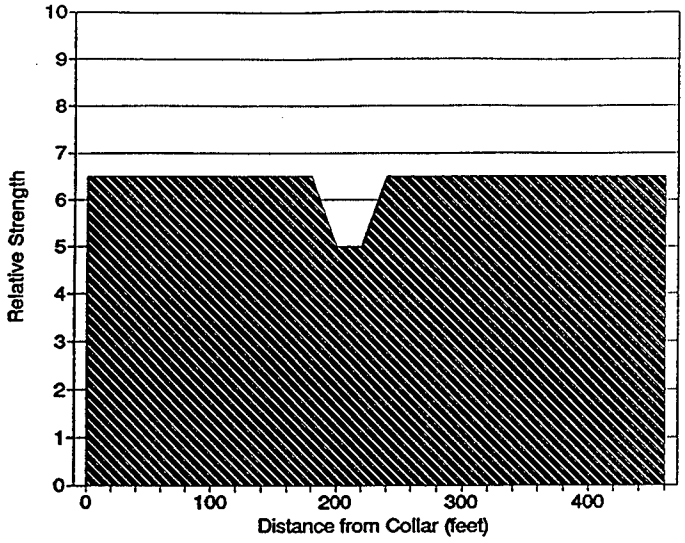


Figure 4. Relative strength versus depth for the horizontal core from hole U12P#02 IH-1 near Mission Cyber.

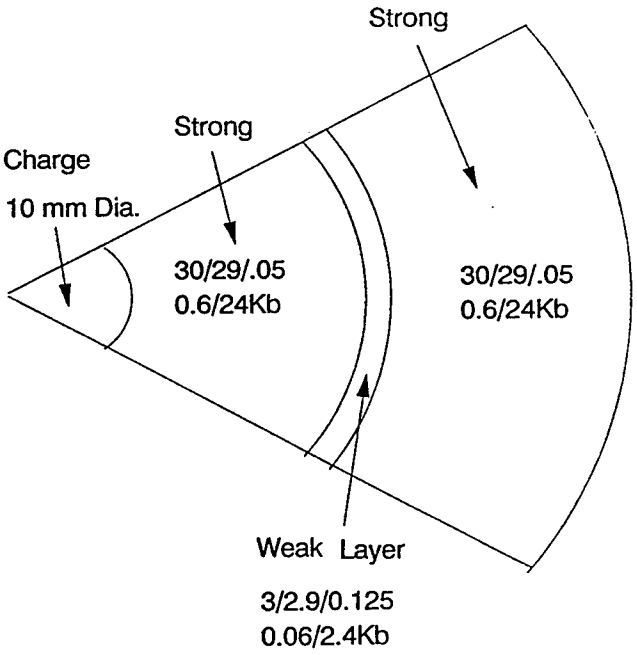
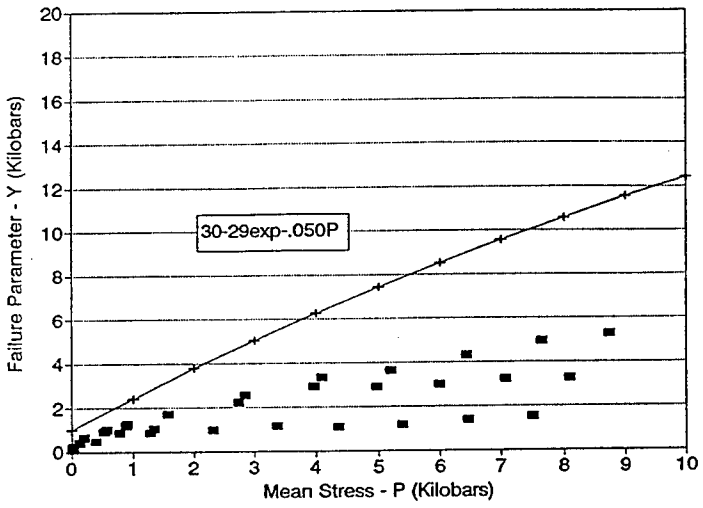


Figure 5. Geometry used in the study of effects of weak layers located at 50 mm from the charge center.



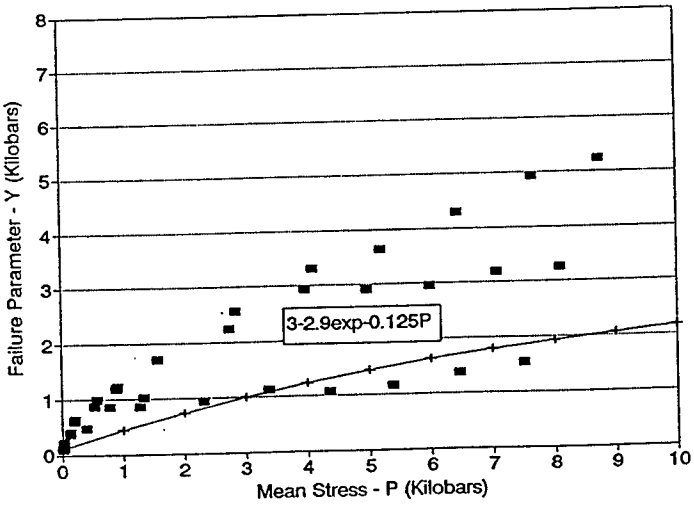


Figure 6. Comparison of failure surfaces for two selections of rock properties for a weak layer located at 10 mm.

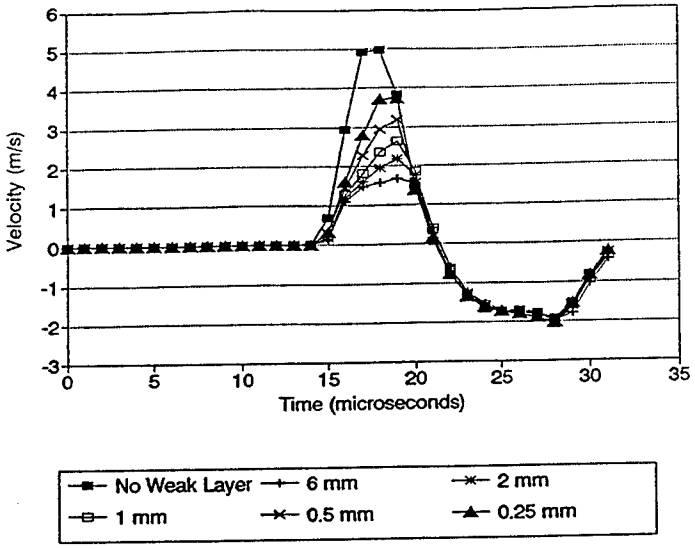


Figure 7. Velocities at 65 mm with weak layer located at 50 mm.

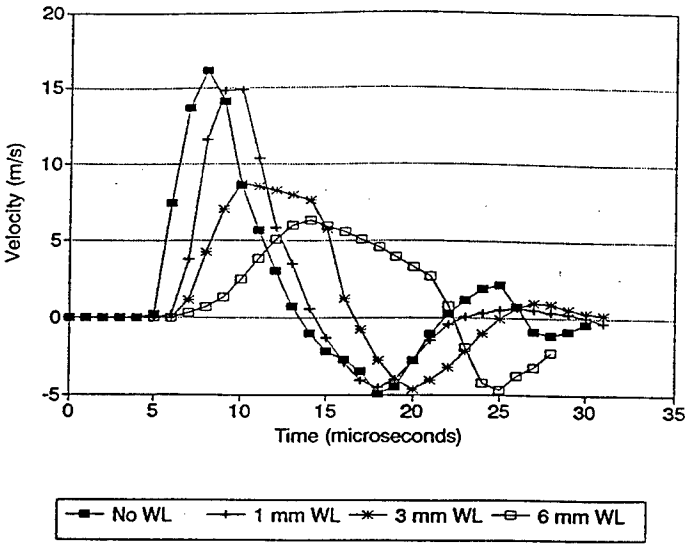


Figure 10. Velocities beyond weak layer - the weak layer at 10 mm.

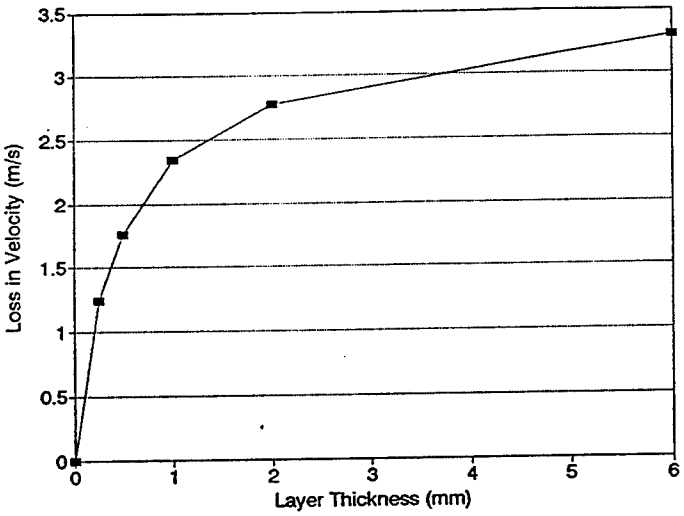


Figure 8. Loss of velocity across a weak layer as a function of weak layer thickness - layer at 50 mm.

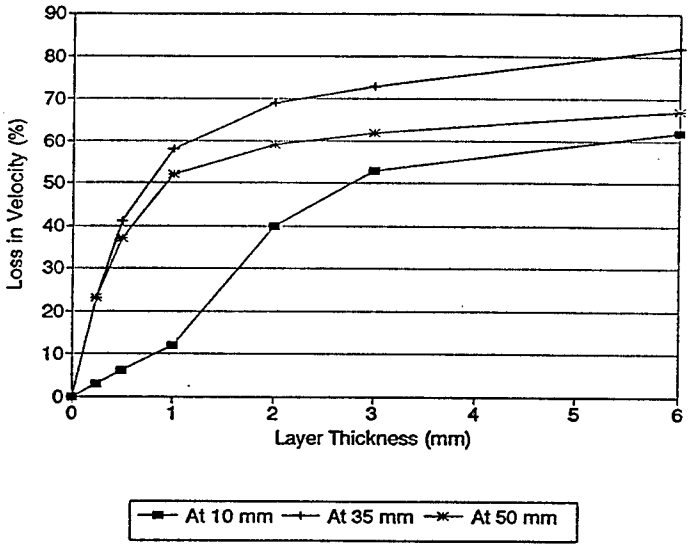


Figure 11. Loss of velocity versus layer thickness for layers located at 10, 35, and 50 mm.

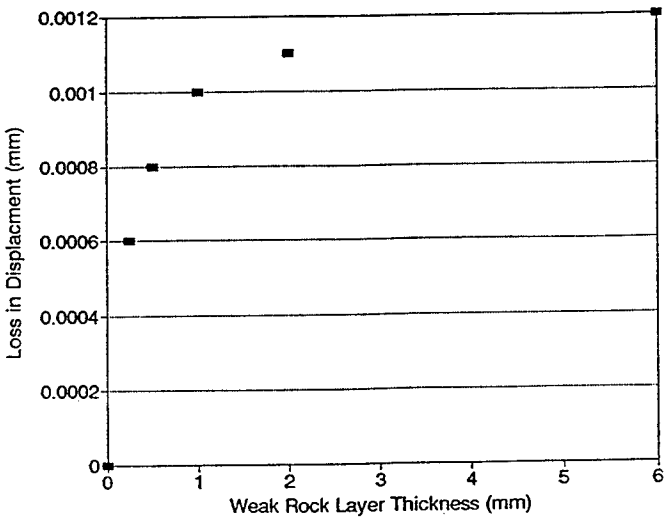


Figure 9. Loss of displacement across a weak layer as a function of weak layer thickness - layer at 50 mm..

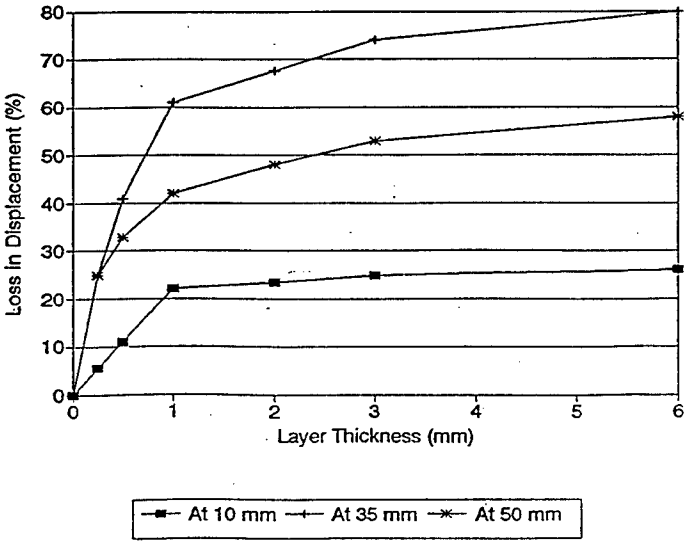


Figure 12. Loss of displacement versus layer thickness for layers located at 10, 35, and 50 mm from the source.

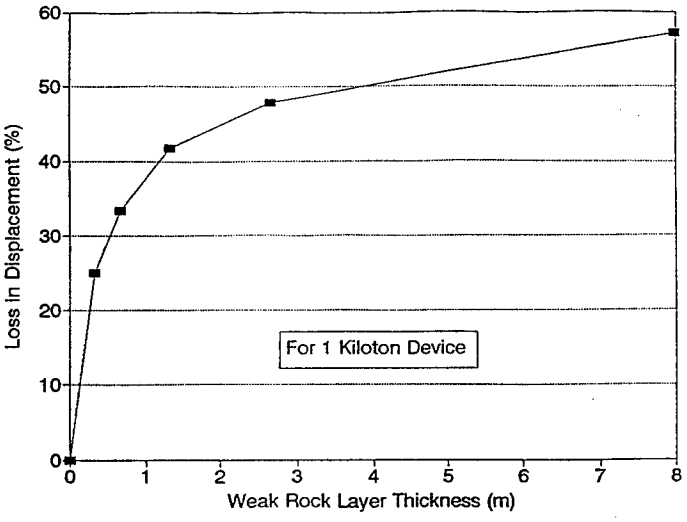


Figure 13. Prediction of loss of displacement from weak layers scaled to a one kiloton device.

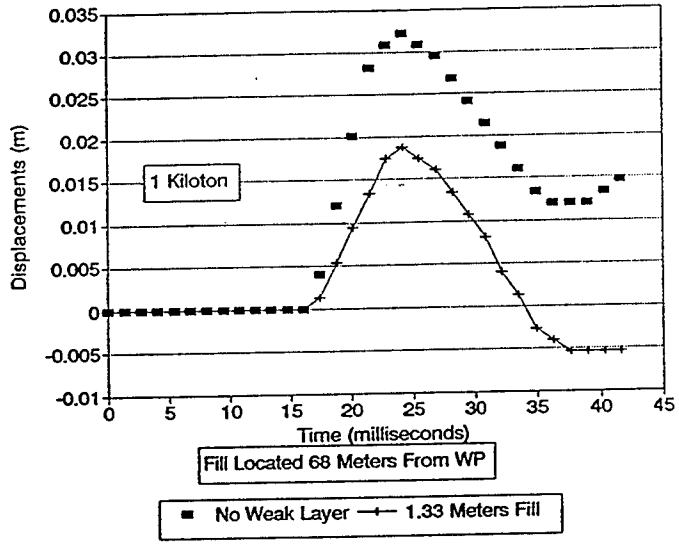


Figure 14. Loss of displacement at 70.7 meters for a 1.33 meter thick weak layer at 68 meters from a one kiloton device.

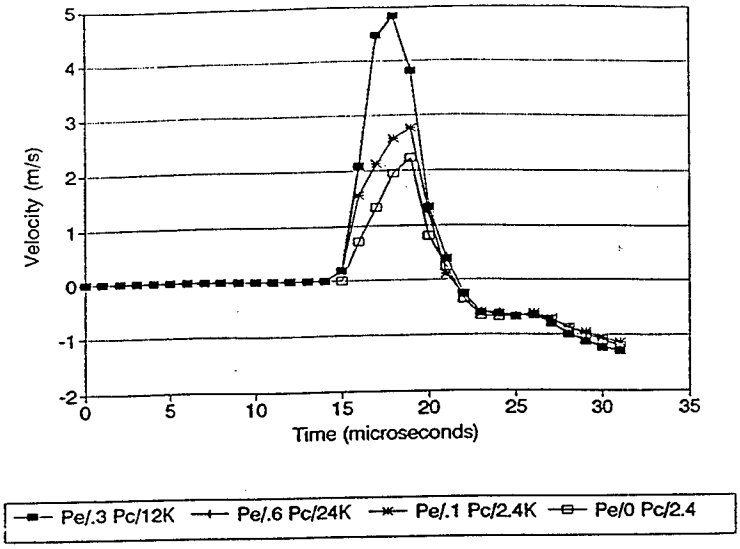


Figure 15. Comparisons of velocities at 65 mm when changes are made in elastic pressure and crush pressure with failure surface parameters held constant. Weak layer at 50 mm.

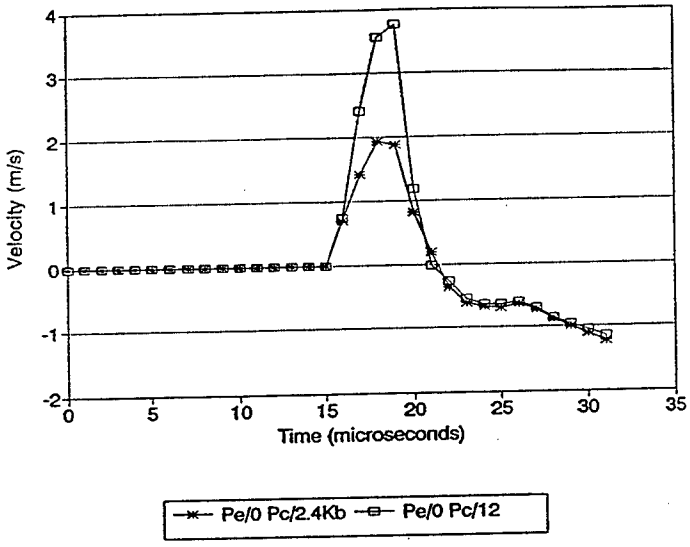


Figure 16. Comparisons of velocities at 65 mm when changes are made in crush pressure with failure surface and elastic pressure parameters held constant. Weak layer at 50 mm.

THIS PAGE INTENTIONALLY LEFT BLANK.

Atmospheric Signals Produced by Cavity Rebound

Eric M. Jones, Frederick N. App, and Rodney W. Whitaker
Earth and Environmental Science Division
Los Alamos National Laboratory

Presented by E. M. Jones at the Symposium
"Numerical Modeling for Underground Nuclear Test Monitoring"
March 23-25, 1993, Durango, CO

I. INTRODUCTION

An analysis of the atmospheric acoustic signals produced by a class of low-yield tests conducted just below the base of the alluvial cover in Yucca Flat of the Nevada Test Site (NTS), has revealed a clear manifestation of an elastic, cavity rebound signal. We use modeling as the basis for understanding the observed phenomena.

II. DISCUSSION

A typical underground nuclear test produces surface ground motions which, near surface ground zero (SGZ), are characterized by an initial period of positive accelerations followed, successively, by a period of purely ballistic motion (acceleration = -9.8 m/s^2) and a sharp, spall closure (slapdown) signal. A typical example is shown in Figure 1. A pressure gauge located at an altitude of 10 kilometers and a horizontal range of 15 kilometers would, in this typical case, detect an acoustic signal characterized by a broad, weak positive phase followed by a deep broad negative phase and, finally, a sharp positive pulse. The predicted pressure signal of an atmospheric acoustic wave for the case shown in Figure 1 is presented in Figure 2. An analysis of a set of such simulations has shown that the negative phase is produced by coherent arrivals of acoustic signals generated by the ballistic motion of the surface near ground zero and that the amplitude of this negative phase is proportional to the square of the peak particle velocity at SGZ (Jones et al, 1993). Similarly, the sharp positive phase is produced by slapdown motions in a region away from SGZ. The amplitude of this slapdown-related feature is proportional to the fourth power of the peak SGZ velocity.

Some of the acoustic energy that propagates outward at low elevation angles is refracted at altitudes of 40 to 50 kilometers and

can be detected with microphones at ground stations located a few hundred kilometers from the burst. Figure 3 presents the wind-corrected amplitudes measured at one such station for a selection of NTS tests plotted against the peak SGZ velocities measured on those same events. The solid line represents the results of an analytical model for the near-field negative phase, corrected for propagation effects. At high velocities, many of the points lie above the line and all show strong slapdown signals in the near field. At low velocities, most of the points also lie above the line but, for these tests, at least part of the explanation is the presence of a strong cavity rebound signal which adds energy to the acoustic signal.

Virtually all of the "low velocity" tests were conducted in the Ammonia Tanks Tuff geologic unit which, in Yucca Flat, underlies the alluvial valley fill and is located well above the water table. In Figure 4 we show the ground motion records for a typical shot of this type. The most noteworthy feature is the presence two intervals of ballistic - or nearly ballistic - motions separated by a relatively sharp, positive acceleration pulse. We note that, for the indicated peak velocity of about 0.7 m/s, a slapdown event would have been expected about 0.1 seconds later than the arrival of this "extra" pulse. In order to investigate the phenomenon, we performed a simulation of an event of this type. In Figure 5, we present a comparison of the measured and calculated surface motions. This comparison indicates that, although there are differences due to the preliminary nature of the material models used in the calculation, the overall character of the observed surface motions are reproduced. There is an initial spall, followed by spall closure, which is in turn is followed by an almost equally strong second spall phase. It is the double spall that is common to this type of event. Figure 6 is a representation of the subsurface conditions produced in the simulations at times of 400 ms and 520 ms. Spalled regions are shown on the left (stippled) and the direction and magnitude of motion, represented as vector fields, are shown on the right. By 400 ms, the initial explosion produced stress wave has reflected from the surface as a tensile rarefaction, resulting in the first spall. However, by this time a second pulse, indicated by the heavy, upward directed vectors just below the spall zone, is causing some recompaction to occur. By 520 ms, recompaction is complete and we observe the first slapdown signal at the surface. Not only is the second pulse the cause of premature closure, but it is strong enough to cause the surface material to enter a second spall phase immediately after the initial slapdown. In the simulation, the second pulse is due to an

elastic rebound of material in reaction to the initial outward push of the cavity, with some of it's motion directed upward toward the surface by the gradient of overburden pressure.

III. SUMMARY

A computer simulation has been instrumental in explaining the origin of a second spall observed at the free surface for a particular class of NTS events. Rebound following underground explosion is a well known phenomena, and it is considered an essential element in the creation of the compressive residual stress field that is so important in the containment of underground nuclear tests. But prior to this investigation, rebound had not been identified as the cause of the double spall signature at the ground surface. In previous ground motion simulations done in support of nuclear test containment, the timing and magnitude of rebound has been found to be sensitive to such factors as yield, depth-of-burial and material properties. Therefore, we would expect that the time at which the rebound associated second pulse arrives at the surface, and the pulse's amplitude, are influenced by these same factors. For the "low velocity" tests conducted in unsaturated tuff, the timing of the arrival of the rebound pulse appears to be near optimal for causing a second spall and increasing the total duration of spall, and this results in an enhanced atmospheric acoustic signal. The timing and magnitude of the rebound would be different for other classes of events (deeper, different yield, different materials), and thus the influence of the rebound pulse on spallation, and on the atmospheric signal, would also be different.

IV. REFERENCE

Jones, E. M., App, F. N. and Whitaker, R. W.,"Ground Motions and the Infrasound Signal: A New Model and the Discovery of a Significant Cavity Rebound Signal", Rept LAUR 93-861, Los Alamos National Laboratory, Los Alamos, NM, 1993

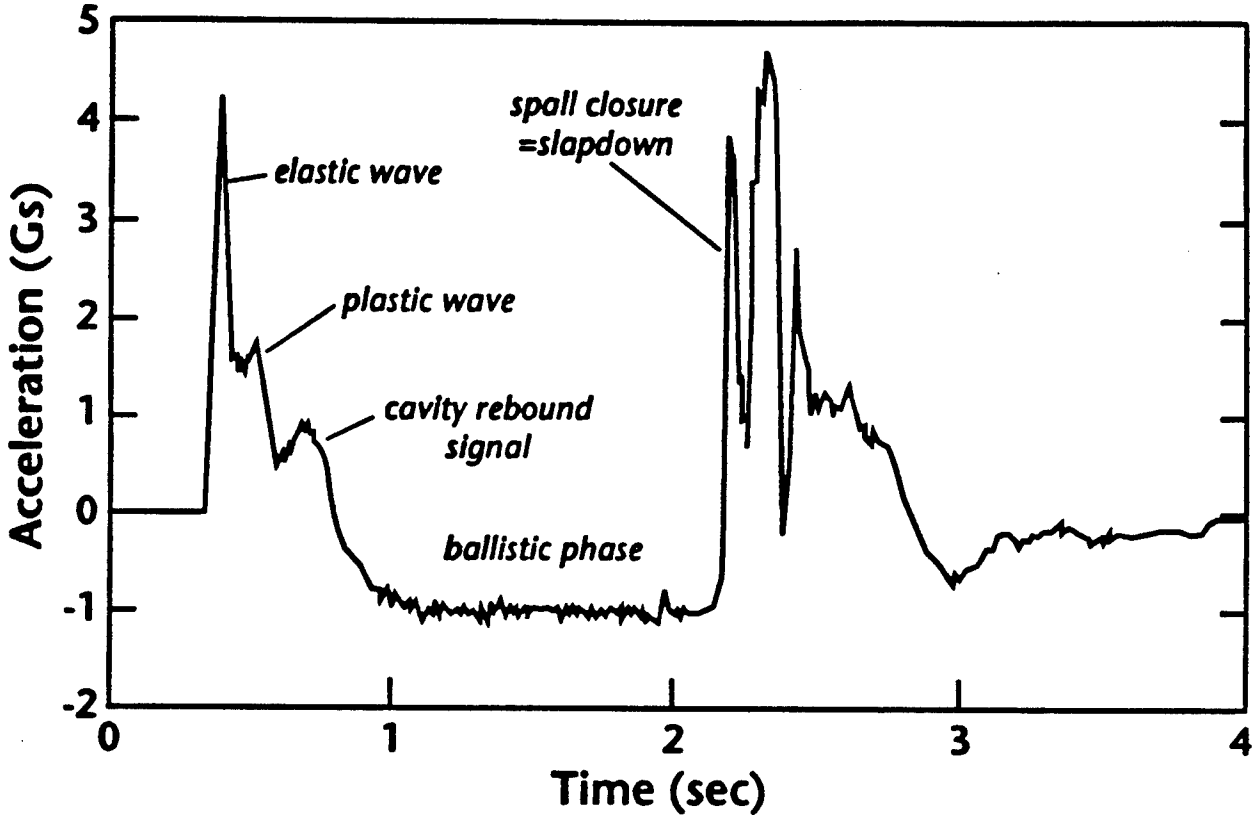


Figure 1. Ground motion accelerations measured at surface ground zero (SGZ) for an underground nuclear test with relatively high yield that was fired in saturated tuffs in Yucca Flat. The first pulse consists of three arrivals: an elastic wave, a plastic wave, and a cavity rebound signal. This positive phase is followed by an interval of ballistic motion and then by spall closure and slapdown. The peak positive particle velocity for this case is about 5.6 m/s and the peak upward displacement is about 3.7 m.

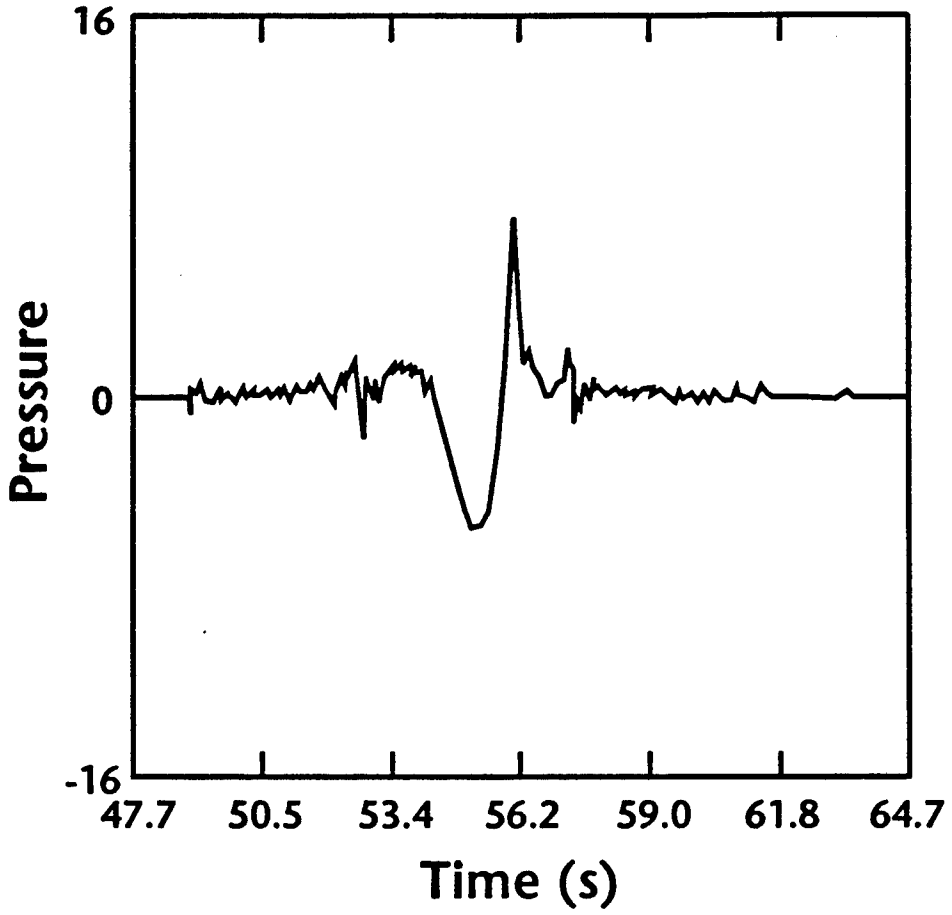


Figure 2. Near-field pressure history predicted for the case shown in Figure 1. This is the signal which is expected for an observer located 18 kilometers from SGZ at an elevation angle of 33 degrees. The broad negative phase is the result of coherent arrivals produced by ballistic motions in a region near SGZ while the sharp positive phase is the result of coherent arrivals produced by slapdown motions at locations removed from SGZ.

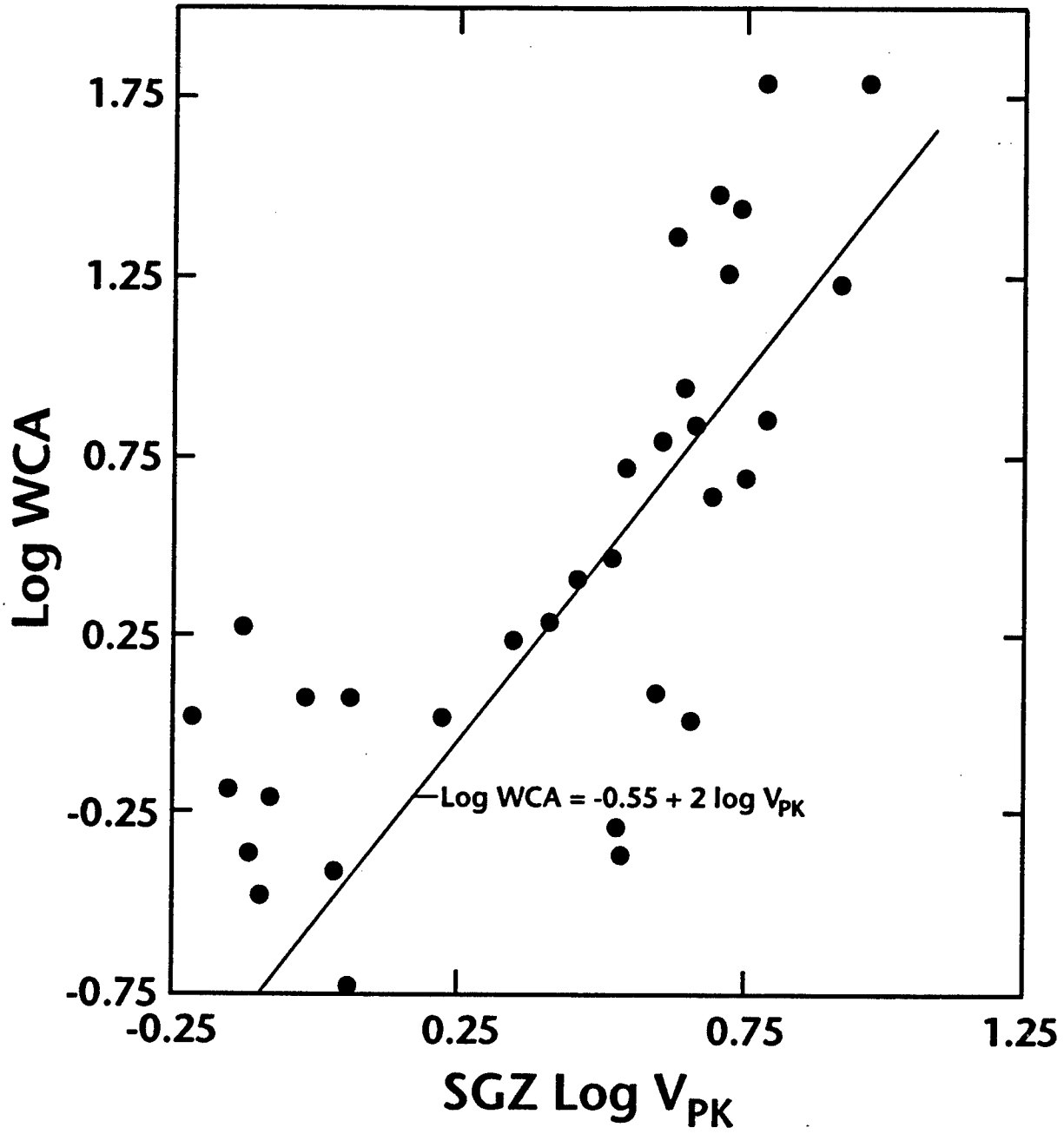


Figure 3. Measured infrasound wind-corrected amplitudes (WCAs) versus peak SGZ velocity. The solid curve is a representation of the ballistic model for the negative component of the near-field signal. At high peak velocities, WCAs tend to exceed the model predictions because of the positive phase associated with slapdown. At low peak velocities, the points also tend to lie above the model line, in part because of a cavity rebound signal described in this paper. Readers should note the four tests with log vpk between 0.5 and 0.7 which fall well below the model line. All four have well-defined ground motions with substantial intervals of ballistic motion. The reason why low values of WCA were measured for these shots is not understood.

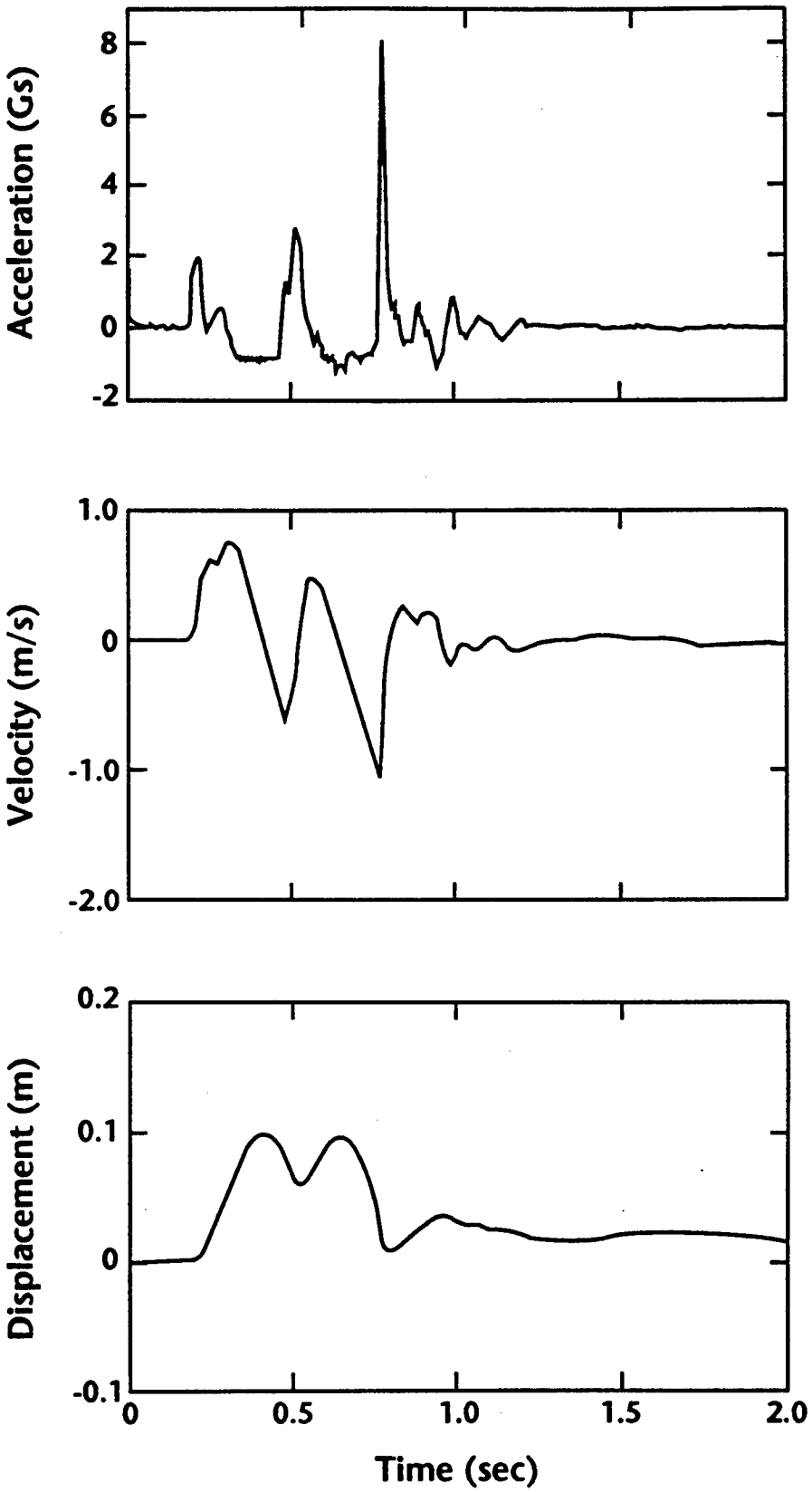


Figure 4. SGZ ground motions for a "low velocity" unsaturated tuff shot showing two intervals of ballistic motion separated by a signal resembling spall closure. Note, however, that this signal begins at a time when the surface displacement is still positive.

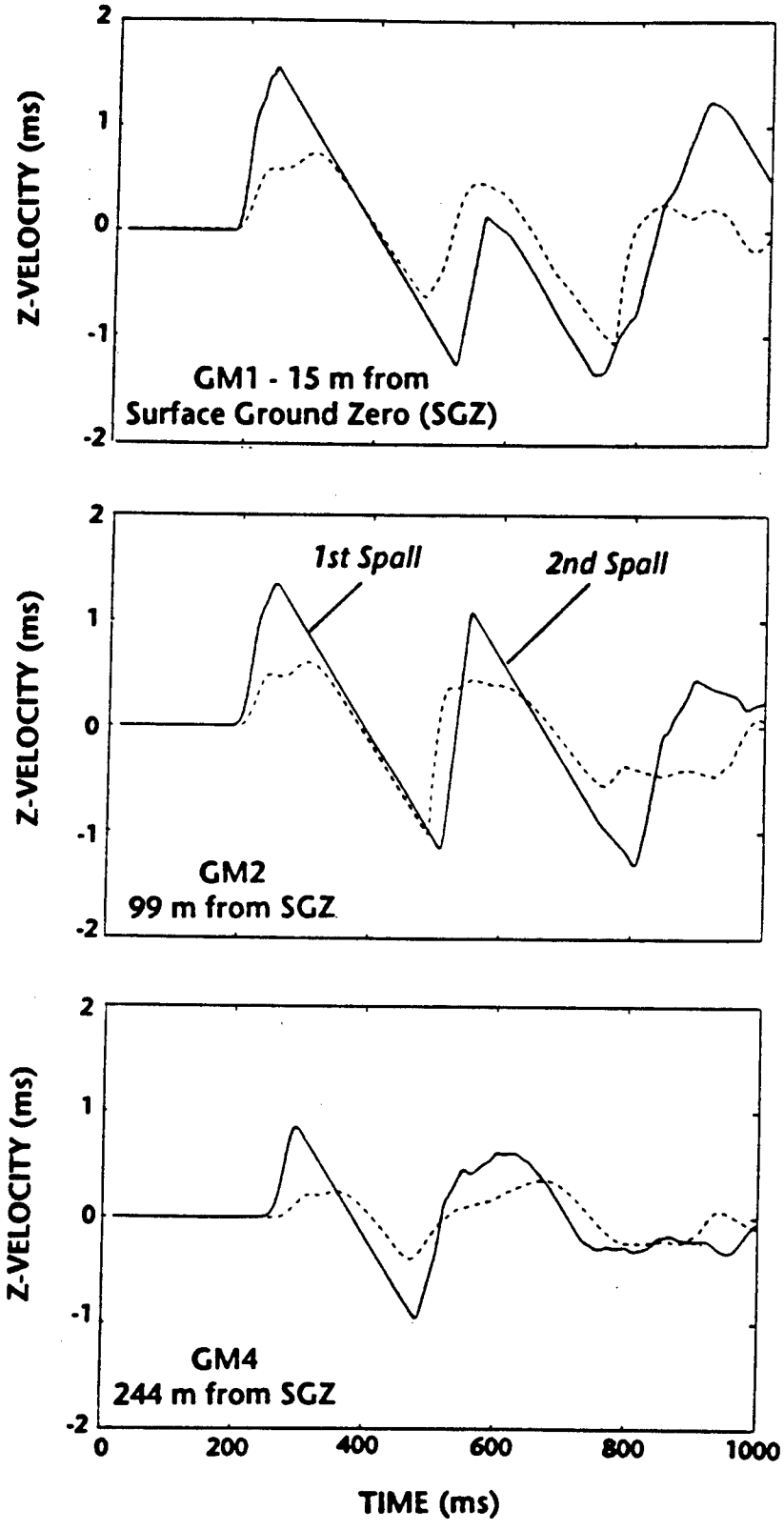


Figure 5. Calculated (solid) and measured (dashed) vertical particle velocity waveforms at the free surface. The calculated timing and amplitude of the first spall closure and second spall are in good agreement with the data.

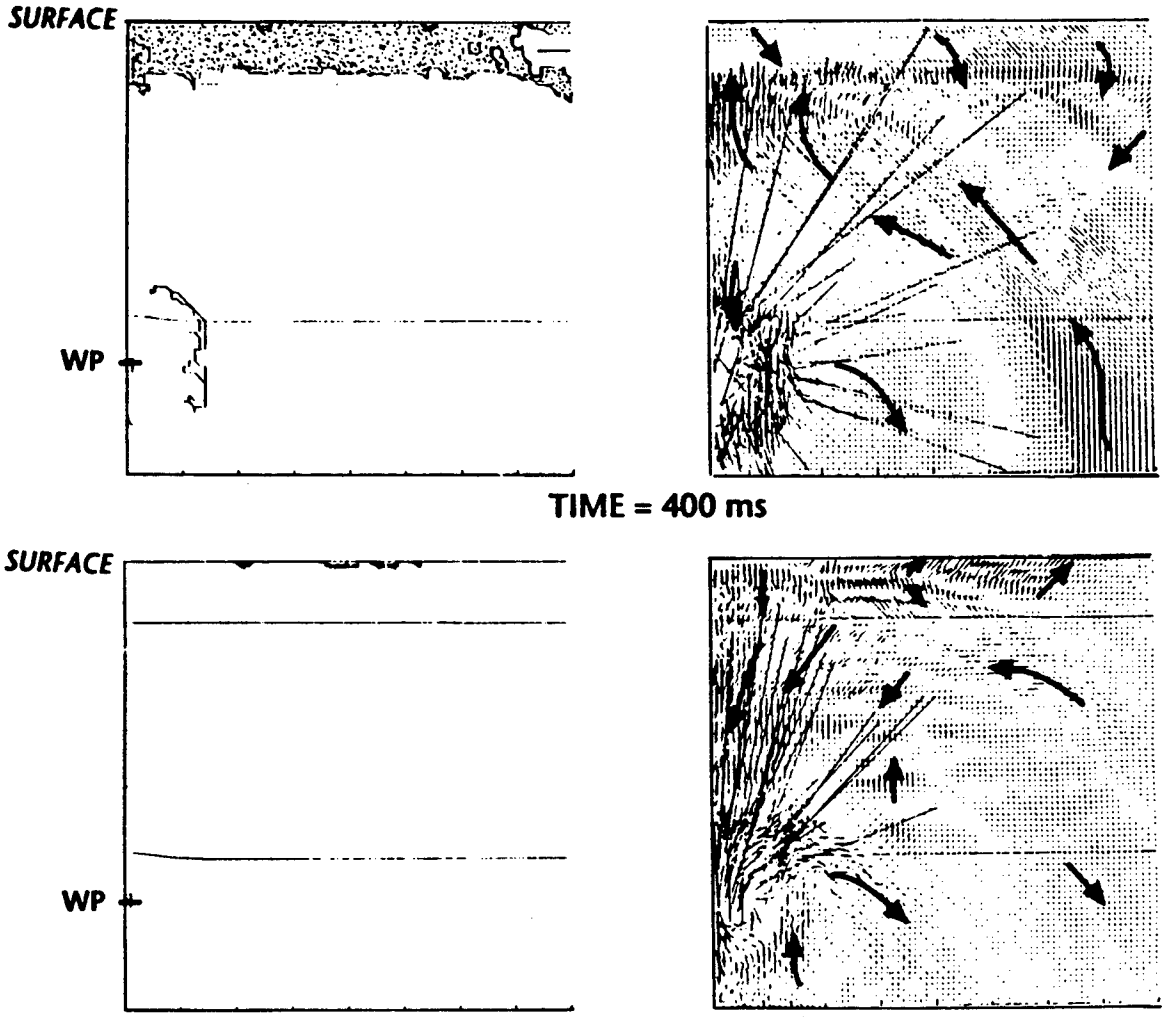


Figure 6. Calculated spall and velocity field plots at 400 and 520 ms. Stippled regions on the left are regions of zero stress (spall). Velocity vector plots on the right indicate the direction and magnitude of motion with lengths linearly proportional to the velocity. Heavy arrows indicate general sense of motion. Long, thin vectors originating from near the working point (WP) are associated with cavity gas, and should be ignored.

THIS PAGE INTENTIONALLY LEFT BLANK.

Modelling of Nuclear Explosions in Hard Rock Sites

Wendee M. Brunish and Fred N. App
Geophysics Group, Los Alamos National Laboratory
Los Alamos, NM 87545

This study represents part of a larger effort to systematically model the effects of differing source region properties on ground motion from underground nuclear explosions at the Nevada Test Site. In previous work by the authors the primary emphasis was on alluvium and both saturated and unsaturated tuff ([1], [2], [3]). We have attempted to model events on Pahute Mesa, where either the working point medium, or some of the layers above the working point, or both, are hard rock. The complex layering at these sites, however, has prevented us from drawing unambiguous conclusions about modelling hard rock.

In order to learn more about the response of hard rock to underground nuclear explosions, we have attempted to model the PILEDRIVER event. PILEDRIVER was fired on June 2, 1966 in the granite stock of Area 15 at the Nevada Test Site. The working point was at a depth of 462.7 m and the yield was determined to be 61 kt. Numerous surface, sub-surface and free-field measurements were made and analyzed by SRI [4]. An attempt was made to determine the contribution of spall to the teleseismic signal, but proved unsuccessful because most of the data from below-shot-level gauges was lost. Nonetheless, there is quite a bit of good quality data from a variety of locations.

Our previous modelling efforts have indicated that it is difficult to characterize how hard rock will respond to ground shock from the traditional methods of laboratory tests on core, and geophysical logging. Hard rock tends to have inhomogeneities in material properties on a fairly large scale, due mainly to fractures and faults. The core samples, therefore, tend not to be representative, particularly with regard to sound speed and shear strength. In order to obtain reasonable agreement with the waveform data obtained from a nuclear underground test, it is typically necessary to model the rock as being considerably weaker in shear than the core values indicate. Also, the sound speed, based on the times of arrival of accelerometer or velocity gauges, is often lower than the values obtained from core, presumably due to the influence of faults and

fractures. The rock may also undergo considerable damage from the strong shock, so that its response, after the passage of the outgoing shock wave, may indicate even further weakening of the rock mass. This study attempts to confirm and better quantify these effects. Our preliminary results indicate that the granodiorite at the PILEDRIVER site is not significantly stronger than the welded tuffs and rhyolites present on Pahute Mesa. In fact, the granodiorite may be more subject to fractures and joints, making it more easily damaged and weaker after damage. In particular, the near surface layers seem to be severely weathered, resulting in lower strength and greatly reduced sound speed.

A schematic diagram of the PILEDRIVER shot and most of the ground motion stations is shown in Figure 1. The data quality is, for the most part, very good. For several locations we have velocities both from integrated accelerometer traces and from velocity transducer gauges, and the agreement is generally excellent. The surface stations shown were all on a line bearing N58E from surface ground zero (SGZ). A few other gauges located at a bearing of S5E were situated across the Boundary Fault from SGZ to investigate possible motion along the fault. We have not included these gauges in our study at this time.

We have performed a series of calculations with different layering, physical properties and material properties in an attempt to determine which properties are most important in shaping the observed waveforms. Although this study of hard rock is far from exhaustive, and we have so far only looked at the PILEDRIVER waveforms, some conclusions are already apparent.

The treatment of damage is extremely important, i.e., the amount of shear the rock can support after the passage of the initial "shock" wave, as well as the strength of the shock required to damage the rock. Calculations were performed for HARDHAT, in a similar granodiorite to that found at PILEDRIVER, by Wagner and Louie [5]; they found that despite numerous variations in the way the equation of state of the rock was modeled, they were unable to match the slow drop of the trailing end of the velocity waveform. They concluded that "shock conditioning" was an important missing component of their model. More recent work by Rimer et al. [6] among others, has confirmed the importance of how damage is modeled on the resulting waveforms.

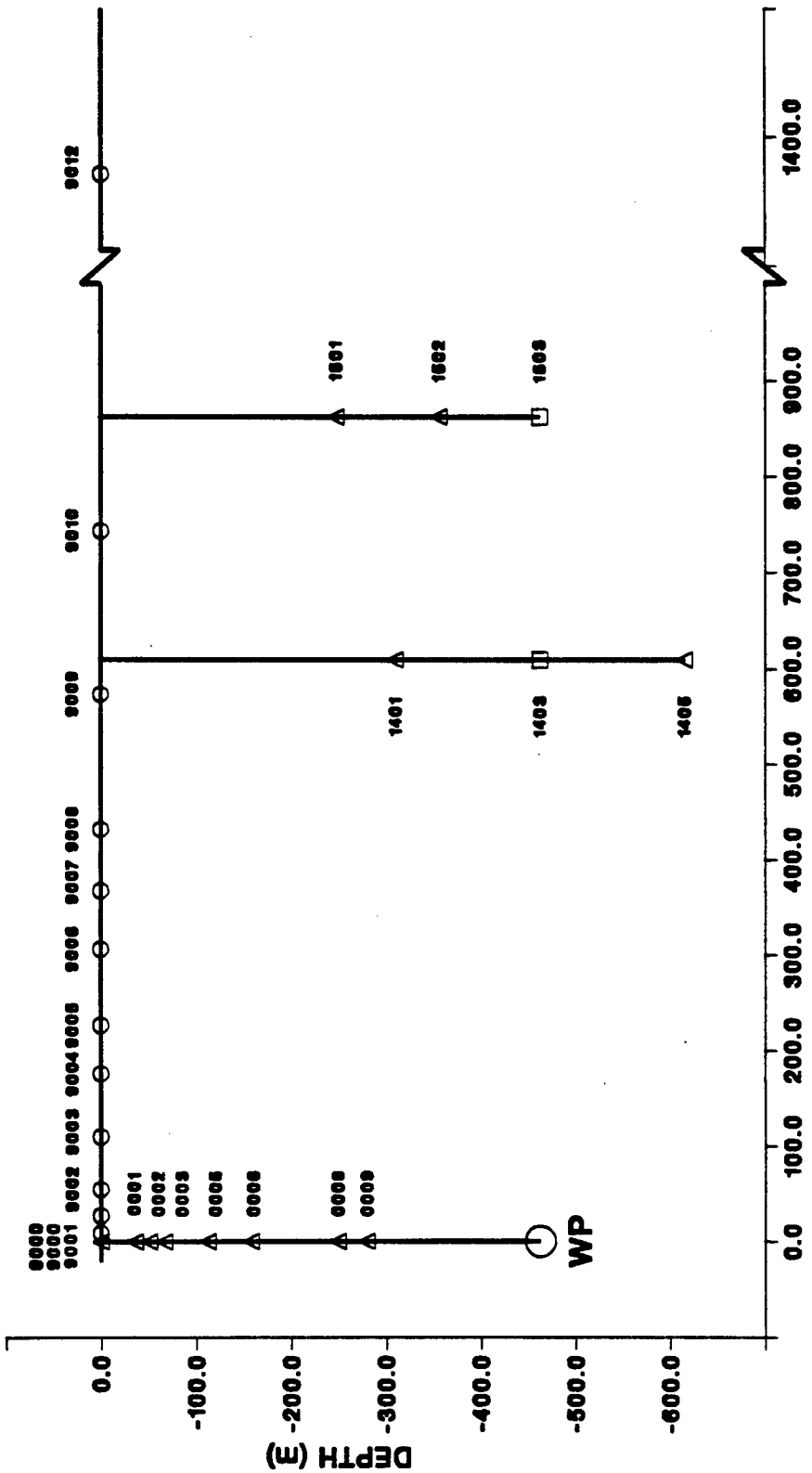


Figure 1. PILEDRIVER ground motion stations

Another important aspect is the presence of the near-surface weathered layers. Both the dispersion in the waveforms themselves and the arrival times at the near surface stations confirm the degraded condition of these layers. The arrival times for the stations in the "zero" hole indicate that while the sound speed at depth is near 6000 m/s, the sound speed within 50 m of the surface drops down to about 1600 m/s. An intermediate layer has an acoustic velocity, based on arrival times, of about 4500 m/s.

In the calculations we performed for the present study, we varied the strength, the amount of damage and the compressibility of the working point layer, and the thickness, the sound speed, the compressibility and the shear strength of the weathered layers. Some of the more important parameter variations are shown in Table I.

Some of the results for the aforementioned calculations are shown in Figures 2 through 5. In all of the plots, the solid lines are the calculational result and the dashed lines (or symbols in Figure 3) represent the experimental data.

Figure 2 shows best vertical velocity waveform matches achieved so far (for calculation PD12 as shown in Table I). In Figure 3, we show a comparison of peak vertical velocity versus range for this calculation and the PILEDRIVER data.

Figure 4 shows the waveforms obtained when we use "good quality" granite, as described by Hoek and Brown [7], for the working point material (calculation PD11). This is the same material response model used by App [8] in his 1-D study of material property effects on the seismic source function. The calculated waveforms are much more impulsive and lack the broad tail seen in the experimental data. The granodiorite at PILEDRIVER, based on the characteristics of the recorded waveforms, is considerably weaker than the type of rock that is usually characterized as granite. Apparently the PILEDRIVER medium is not "good quality" granite.

Figure 5 shows some of the surface ground motion for the PD12 "baseline" calculation and for a calculation (PD18) where the weathered layers were modeled as significantly slower and weaker than the working point material. The weak near surface layers spread out the waveform. Also, we see in the data that the overall slope of the velocity decrease is not

Table I.
PILEDRIVER calculation material properties

	Calculation		
	PD11	PD12	PD18
Weathered layer:			
thickness (m)	35	150	50/150
initial crush pressure (kb)	0.10	0.10	0.10/0.05
sound speed (m/s)	2100	2100	1600/4700
Working point layer:			
max. unconf. strength* (kb)	2.52	0.945	0.945
initial crush pressure (kb)	0.10	0.40	0.40
sound speed (m/s)	4000	5500	5500

PD11 = "good quality" granite
PD12 = weaker, easily damaged granite
PD18 = like PD12 but thicker, weaker surface layers

* maximum stress difference material can support in triaxial loading

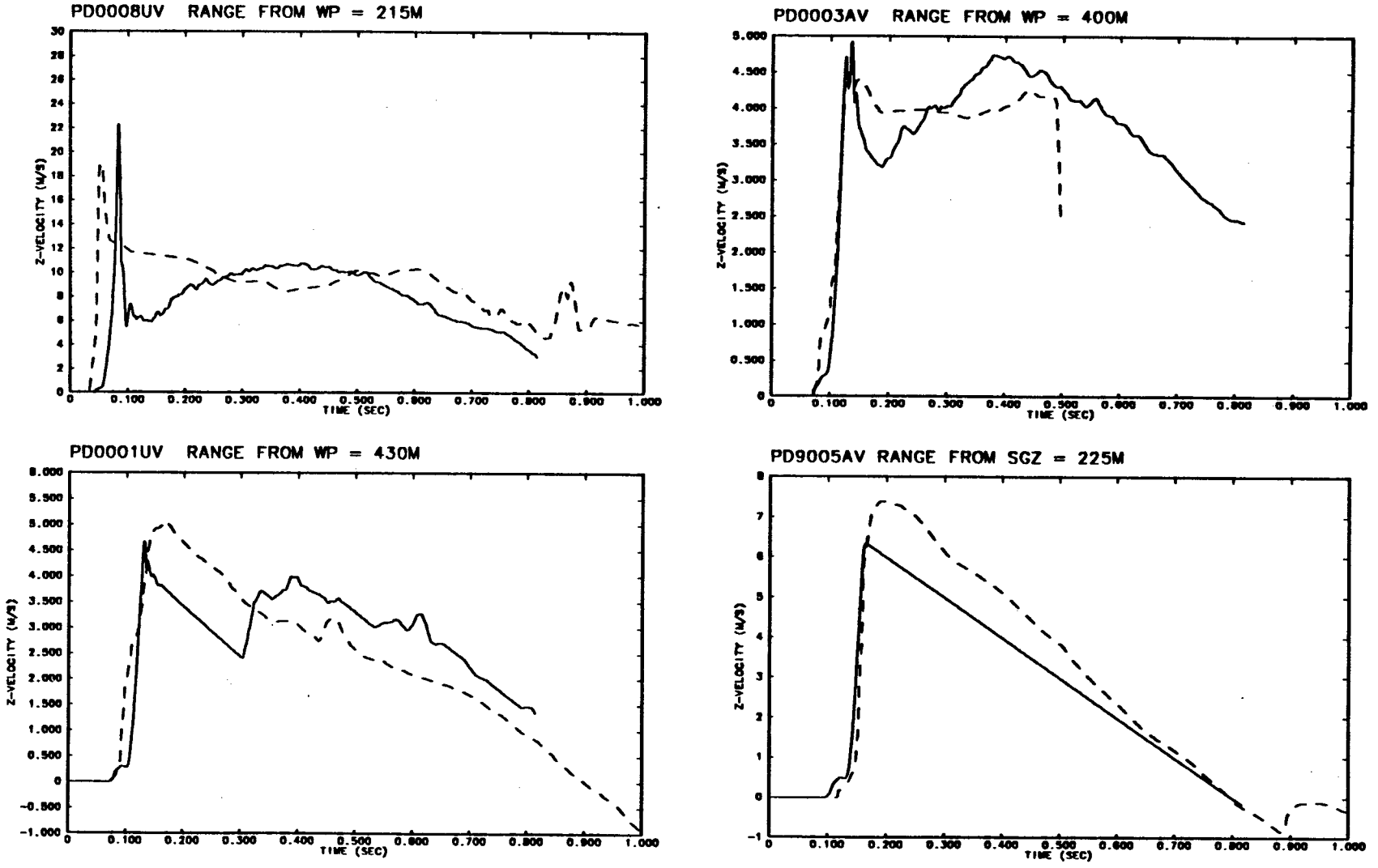
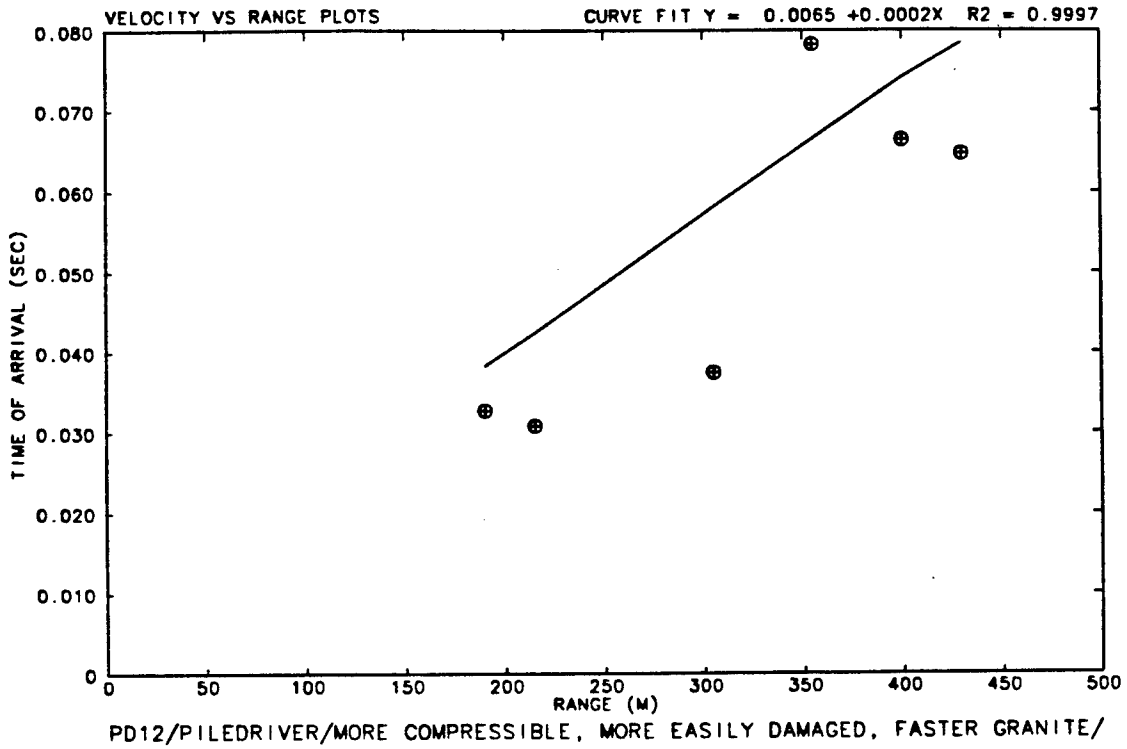


FIGURE 2. BEST MODEL (PD12)


VELOCITY VS RANGE PLOTS
CURVE FIT Y = 0.0065 +0.0002X R2 = 0.9997
TIME OF ARRIVAL (SEC)
0.080
0.070
0.060
0.050
0.040
0.030
0.020
0.010
0
0
50
100
150
200
250
300
350
400
450
500
RANGE (M)
PD12/PILEDRIVER/MORE COMPRESSIBLE, MORE EASILY DAMAGED, FASTER GRANITE/

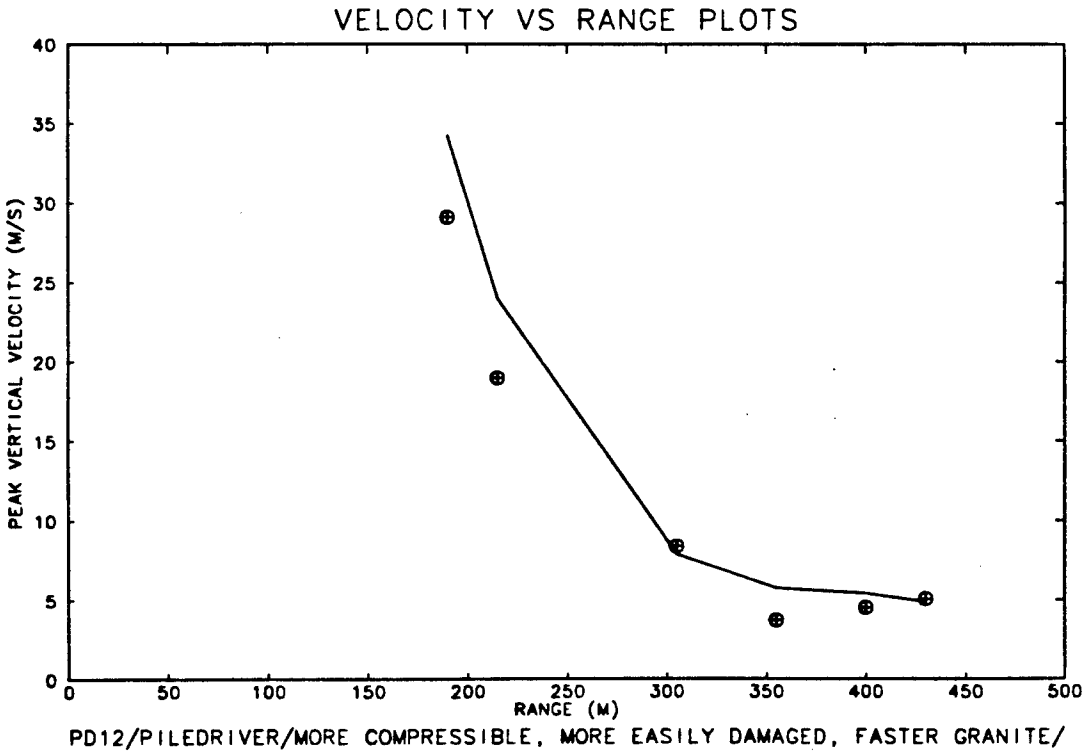

VELOCITY VS RANGE PLOTS
PEAK VERTICAL VELOCITY (M/S)
40
35
30
25
20
15
10
5
0
0
50
100
150
200
250
300
350
400
450
500
RANGE (M)
PD12/PILEDRIVER/MORE COMPRESSIBLE, MORE EASILY DAMAGED, FASTER GRANITE/

Figure 3

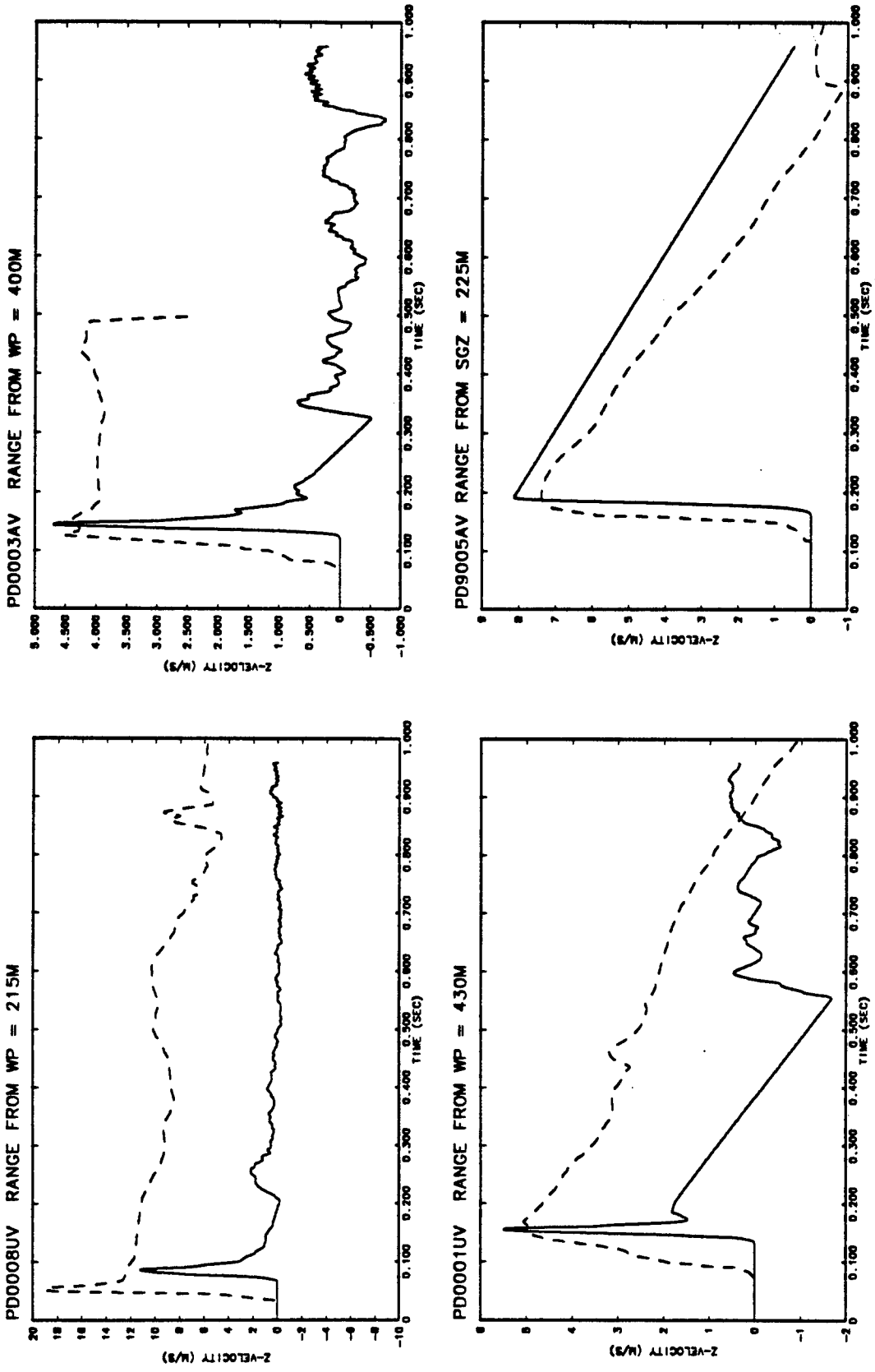


FIGURE 4. GOOD QUALITY GRANITE MODEL (PD11).

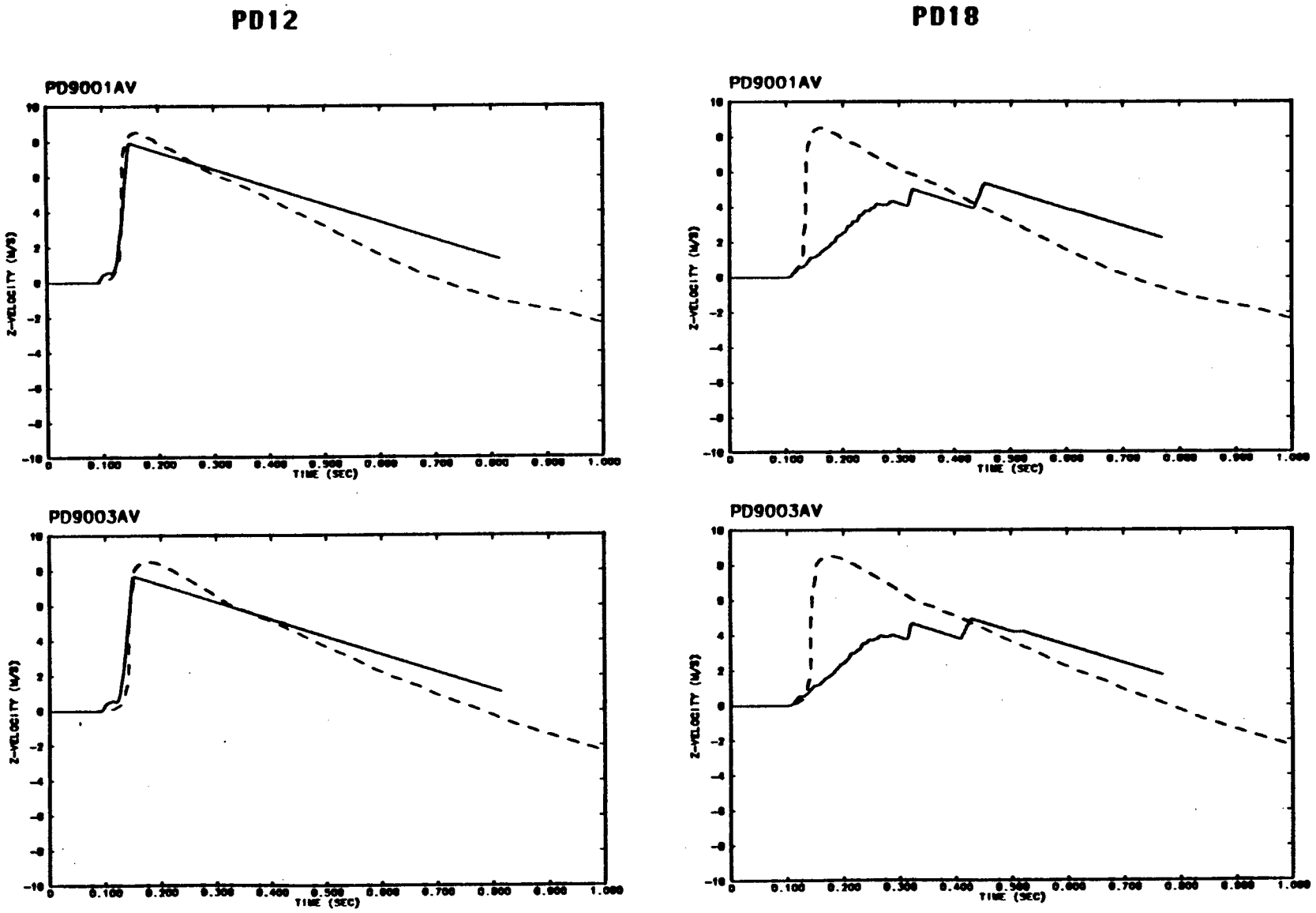


FIGURE 5. PILEDRIVER SURFACE MOTION: PD12 AND PD18 COMPARISON

consistent with a -1 g spall, but closer to -1.2 g. Heuze et al. [10] successfully captured the greater than -1 g spall observed for the SHOAL granite event using a discrete element code. Our finite difference code apparently lacks some of the physics necessary to capture a greater than -1 g surface acceleration observed at some hard rock sites, including PILEDRIVER. In fact, the calculated behavior when we use a very weak near-surface layer (PD18) is more similar to our earlier calculations of the MERLIN event in alluvium ([1], [2], [9]), where we found that observed spall closure accelerations of less than -1 g were due to shear failure, associated with the initial surface rarefaction, in very weak near-surface materials. While the surface layers at PILEDRIVER appear to be weak, they are not so weak as to allow a less than -1 g acceleration.

In summary, we have been able to obtain relatively good agreement with the experimental PILEDRIVER waveforms. In order to do so, we had to model the granodiorite as being considerably weaker than "good quality" granite, and it had to undergo considerable weakening due to shock damage as well. In addition, the near-surface layers had to be modeled as being weak and compressible and as have a much lower sound speed than the material at depth. This is consistent with a fractured and jointed material at depth, and a weathered material near the surface.

The authors would like to thank Tom Tunnel and Albert Martinez of EG&G for the rapid and excellent digitization of the PILEDRIVER waveforms. We would also like to extend thanks to Charles Snell for providing us with copies of many reports on ground motion in hard rock. Thanks are due to Norton Rimer for supplying us with information about some of his calculations and for helpful discussions. We are grateful to Jack House and the Nuclear Test Containment Program and to Tom Weaver and the Source Region Program for supporting this work. And thanks to Marie Kaye for her help in preparing this paper. This work was performed under the auspices of the U. S. Department of Energy by Los Alamos National Laboratory which is administered by the University of California under contract W-7405-Eng-36.

References:

1. W. M. Brunish and F. N. App, Modelling of MERLIN Alluvium, Fifth Symposium on Containment of Underground Nuclear Explosions, CONF-8909163, Vol. 2, pp. 96-132 (1989).

2. F. N. App and W. M. Brunish, Stress Wave Calculations of Four Selected Underground Nuclear Tests: MERLIN, HEARTS, PRESIDIO, MISTY ECHO, Los Alamos National Laboratory EES-NTC-91-03 (1991).

3. W. M. Brunish and F. N. App, Modelling and Comparison of Two Tunnel Events at the Nevada Test Site, Los Alamos National Laboratory LAUR-92-518, (1992).

4. H. V. Hoffman and F. M. Sauer, Operation FLINT LOCK Shot PILEDRIVER Project Officers Report - Project 1.1 Free-Field and Surface Motions, Poulter Laboratory for High Pressure Research POR-4000 (1969).

5. M. H. Wagner and N. A. Louie, HARD HAT/PILEDRIVER Ground Motion Calculations, Shock Hydrodynamics Incorporated SAMSO-TR-69-47 (1969).

6. Norton Rimer, Jeff Stevens and Don Halda, Modeling of the Ground Motion from Events in Granitic Rocks, presented at the Modeling and Material Properties Working Group of the CAT on 13 June 1990, SAIC/PacTech SSS-DVR-90-11661 (1990).

7. E. Hoek and E. T. Brown, Underground Excavations in Rock, Institute of Mining and Metallurgy, p. 176 (1980).

8. Frederick N. App, Sensitivity of the Close-in Seismic source Function to Rock Properties, Numerical Modeling for Underground Nuclear Test Monitoring Symposium, Durango, CO (1993).

9. F. N. App and W. M. Brunish, Modelling Surface Motion and Spall at the Nevada Test Site, Los Alamos National Laboratory LAUR-92-500 (1992).

10. F. E. Heuze, O. R. Walton, D. M. Maddix, R. J. Shaffer, and T. R. Butkovich, Effects of Explosions in Hard Rocks, Numerical Modeling for Underground Nuclear Test Monitoring Symposium, Durango, CO (1993).

THIS PAGE INTENTIONALLY LEFT BLANK.

EFFECTS OF EXPLOSIONS IN HARD ROCKS*

F. E. Heuze, O. R. Walton, D. M. Maddix, R. J. Shaffer, and T. R. Butkovich
Lawrence Livermore National Laboratory

1. Introduction – Dynamics of Rock Masses

This work relates to explosions in hard rocks (ex: basalt, granite, limestone...). Hard rock masses typically have a blocky structure created by the existence of geologic discontinuities such as bedding contacts, faults, and joints. At very high pressure—hundreds of kilobars and above—these discontinuities do not act separately, and the rock appears to be an equivalent continuous medium.

At stress of a few tens of kilobars and below, the geologic discontinuities control the kinematics of the rock masses. Hence, the simulation of rock dynamics, anywhere but in the very-near source region, should account for those kinematics.

2. Options for Analysis

In the very high pressure range continuum-based analysis is appropriate. In the discrete motion range one could consider:

- an equivalent continuum approach with anisotropy and plasticity. However, this is unlikely to provide the right kinematics
- embedding discontinuities in continuum models, such as using joint elements and slip surfaces in finite elements. Typically, these are limited in terms of the separation of elements which may reconnect arbitrarily to new elements
- complete discrete methods; ex: discrete elements, discontinuous displacement analysis (DDA). Discrete elements have progressed further than DDA

We have chosen to develop and apply discrete elements models to explosion phenomenology in rocks.

3. What is a Discrete Element (DE)

It is a mechanical model which can accommodate the interaction of a multitude of independent particles undergoing large motions, and which may separate from or collide with each other. DE models are characterized by the ability to search for and update contacts between the many elements, and to perform appropriate momentum exchanges. DE models originated in molecular dynamics, with linear

*Worked performed by the Lawrence Livermore National Laboratory under contract W-7405-ENG-48 with the U.S. Department of Energy.

momentum exchanges. In geomechanics, block interactions may involve highly nonlinear and hysteretic block contacts, and particle breakage.

4. The LLNL DIBS Model

DIBS (Discrete Interactive Block System) is a 2-dimensional discrete element model developed at LLNL for solid flow modeling, and extended to the analysis of explosion effects in blocky or particulate media. DIBS uses explicit time integration. Its main features are:

- Voronoi grid generation
- polygonal blocks with rounded corners
- multi-material capability
- silent boundaries
- non-linear and hysteretic block contacts
- gravity loading, and arbitrary stress or kinematic boundary loading
- excavation capability

DIBS is currently being enhanced by adding deformability and fracturing inside the blocks.

5. Applications

The four applications presented below all relate to chemical or nuclear explosions in basalt or granite. The salient results from these simulations are:

5.1 SHOAL (1963)

The SHOAL event was a 12.5 kt explosion, 350-m deep in granite in Nevada. We simulated a SHOAL-like event, with an approximation of the blocky granite geology as shown in Figure 1. We loaded a 22-m radius cavity with a pulse of total duration 150 ms to give a peak surface velocity of 5.66 m/sec.

This calculation had two highlights:

- as shown in Figure 2, return spall acceleration was calculated well in excess of -1g at surface ground zero (SGZ). This is precisely the phenomenology that was observed in granite tests in the 1960's but never satisfactorily modeled
- we also showed how the blocky rock mass creates a very strong anisotropy of energy propagation (Figure 3). The granite tests of the 1960's in Nevada also were noted for strong azimuthal differences in observed motions.

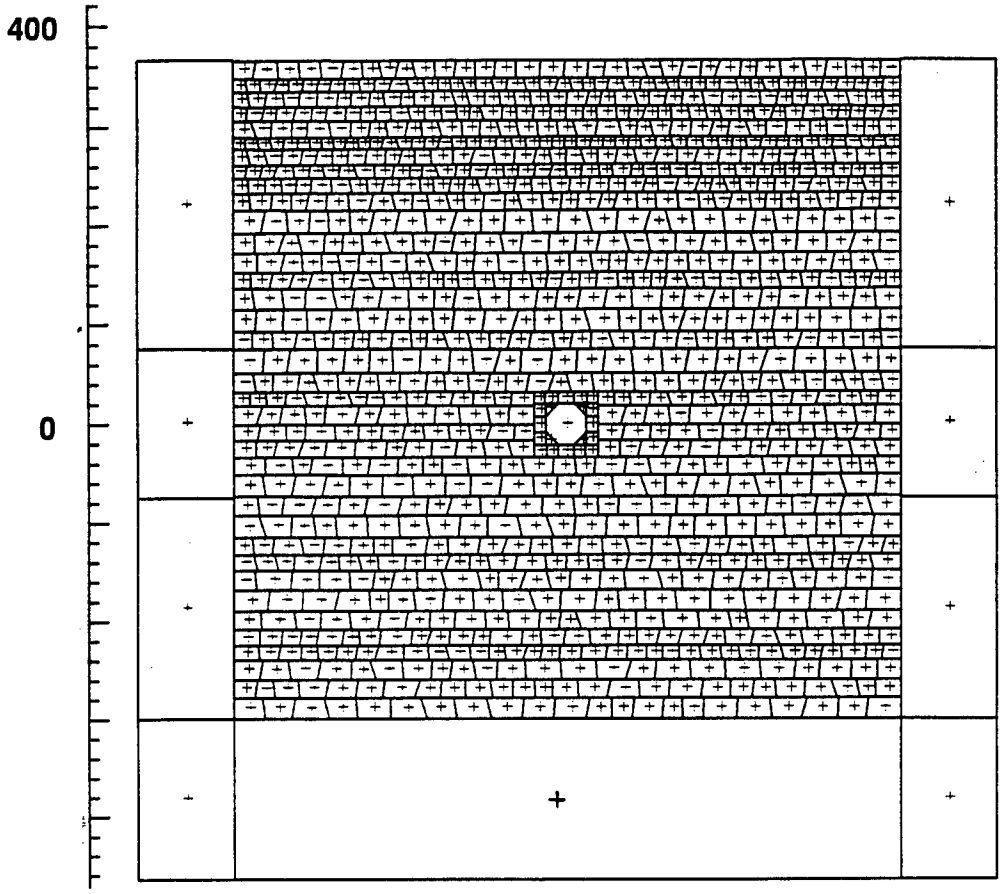


Figure 1: Model for the SHOAL-Like Calculation with DIBS.

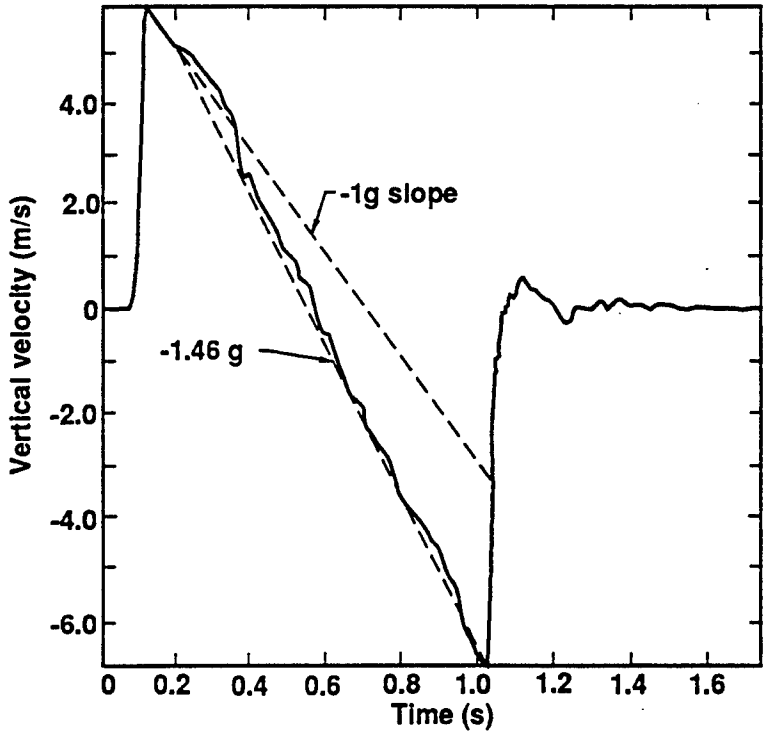


Figure 2: Vertical Velocity History at SGZ for SHOAL-Like Event.

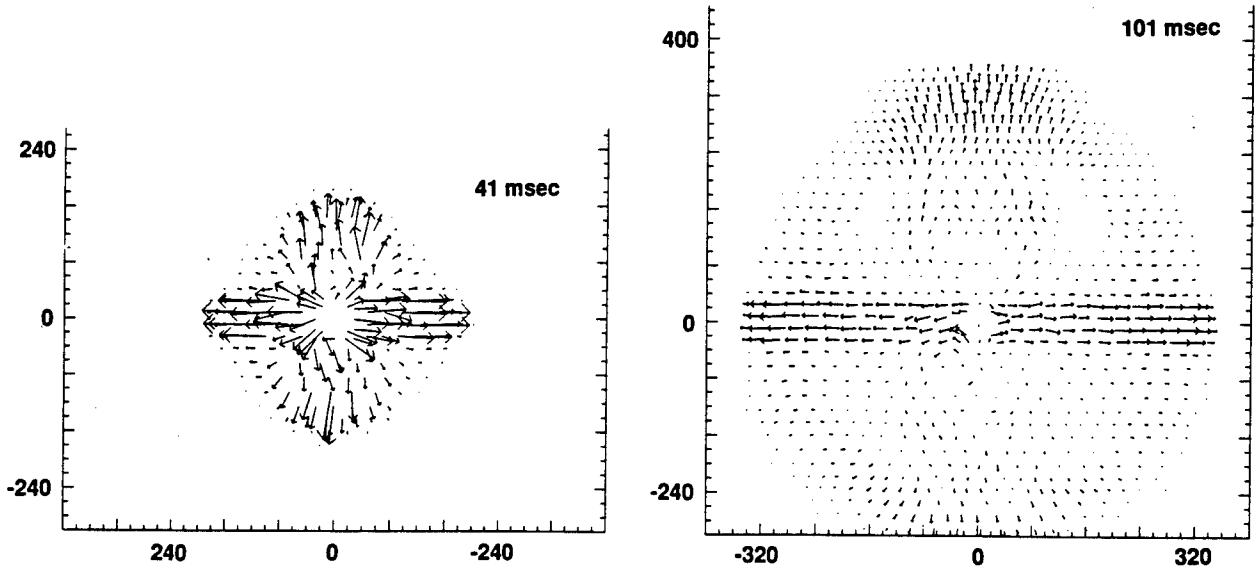


Figure 3: Velocity Vectors at Two Different Times in the Vicinity of a SHOAL-Like Event.

5.2 SULKY (1964)

SULKY consisted of 90 tons of nuclear explosive detonated at a depth of 27m in dry basalt at the Nevada Test Site (NTS). Peak spall velocity was measured at 26m/sec. We estimated cavity size at 9 to 11m diameter from hydrocode calculations and chose 10-m for this analyses. We heuristically adopted a cavity loading function, that matched spall velocity. Basalt properties and contact friction were estimated from published values for basalt. The simulation is shown in Figure 4. It captured the main features of the SULKY retarc including matching its height and central depression. It also showed a very large reorientation of surface velocity vectors towards a vertical throw out, as seen on films of the event.

5.3 PILEDRIVER (1965)

PILEDRIVER was a 61kt structural effects test in granite at NTS. For DIBS simulation, we selected a particular tunnel section (DL 0+70) which had seen significant roof fall and floor heave. The 735-block grid was loaded under in-situ stresses, the tunnel was excavated, and the dynamic impulse was applied to the left boundary. The calculated tunnel response is shown in Figure 5. The nature and extent of the damage is consistent with that observed in the actual tunnel section.

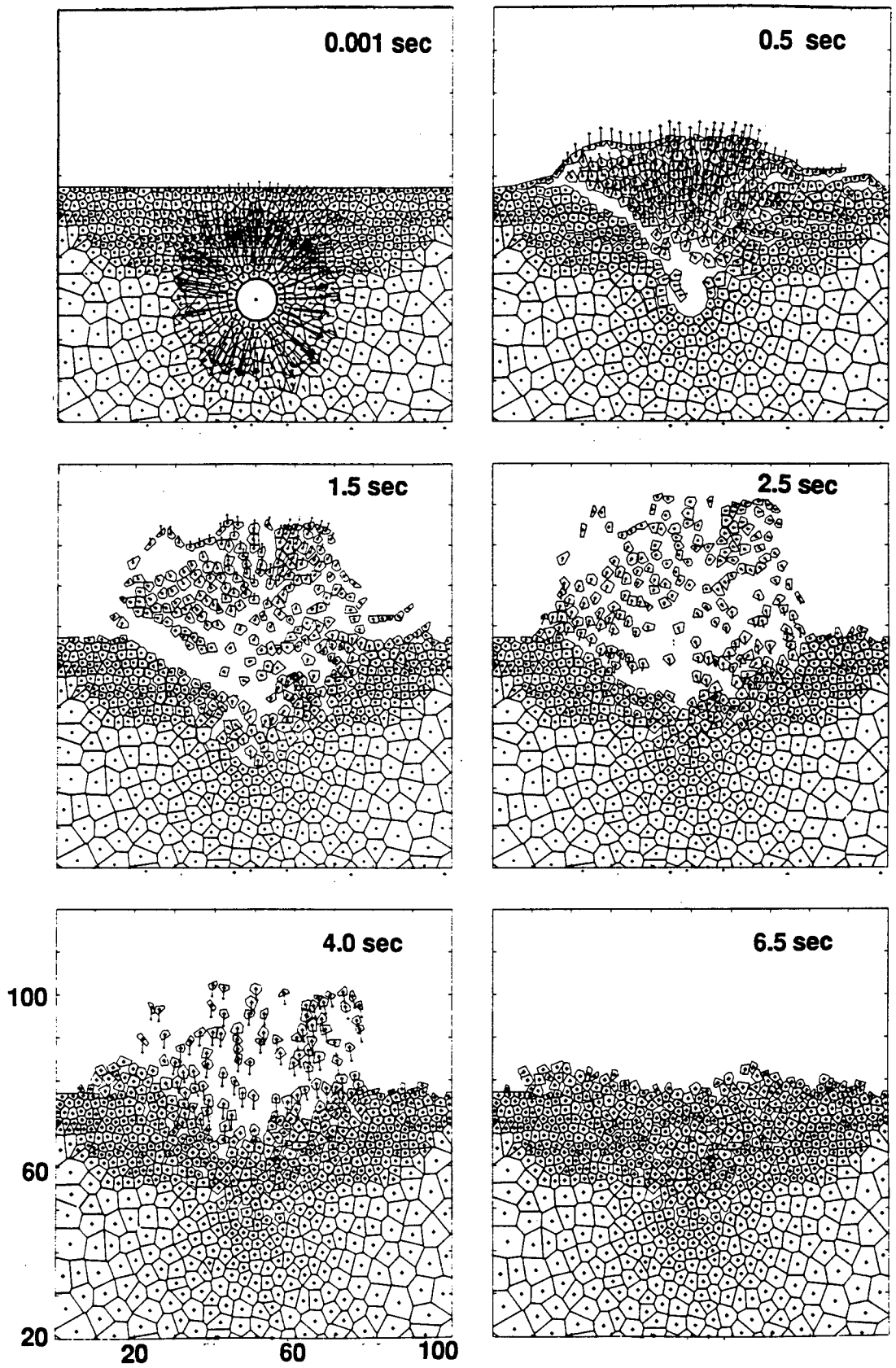


Figure 4: DIBS Simulation of the SULKY Event.

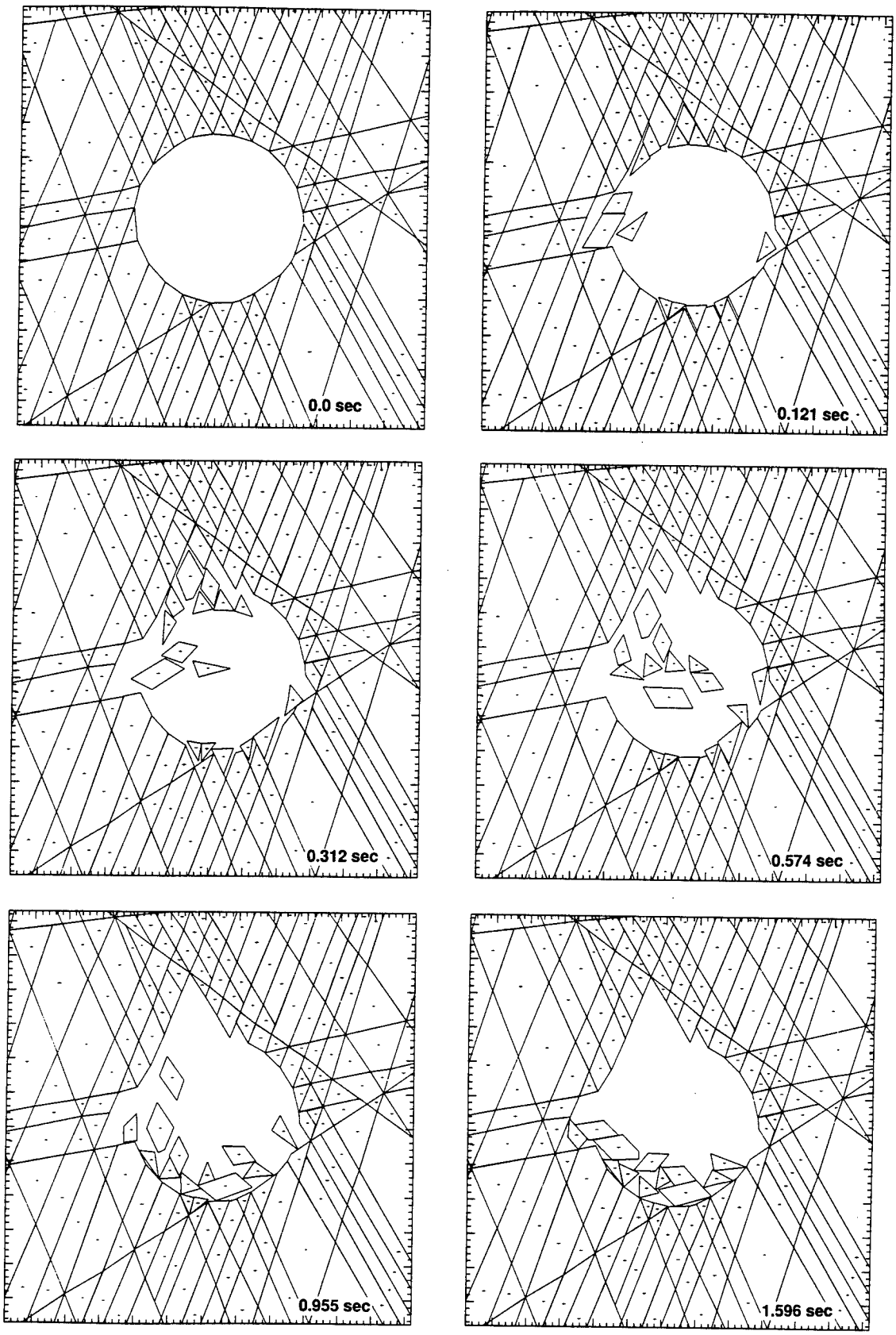


Figure 5: DIBS Simulation of the Response of Tunnel Section DL 0+70 in the PILEDRIVER Event.

5.4 STARMET (1970)

STARMET consisted of the detonation of 1980 kgs of high-explosives in a planar array of 11 boreholes (Figure 6). The event took place in granite about 100 km SE of Albuquerque, NM. The surface was transected by a shear plane with a strike nearly parallel to the array, and dipping toward it. Ground motion instrumentation was placed on either side of the array. We illustrate the results of the DIBS simulation by looking at the motion of a point (C) close to the trace of the shear (Figure 7). The DIBS results for the vertical displacement history of point C fall within the range of values measured in the field for points along the trace of a vertical plane parallel to the array and going through C. (The UDEC calculations were performed outside of LLNL, with another discrete element code). A very detailed comparison of the calculated and test results is provided in reference [1], which also expands on the SHOAL, SULKY, and PILEDRIVER simulations.

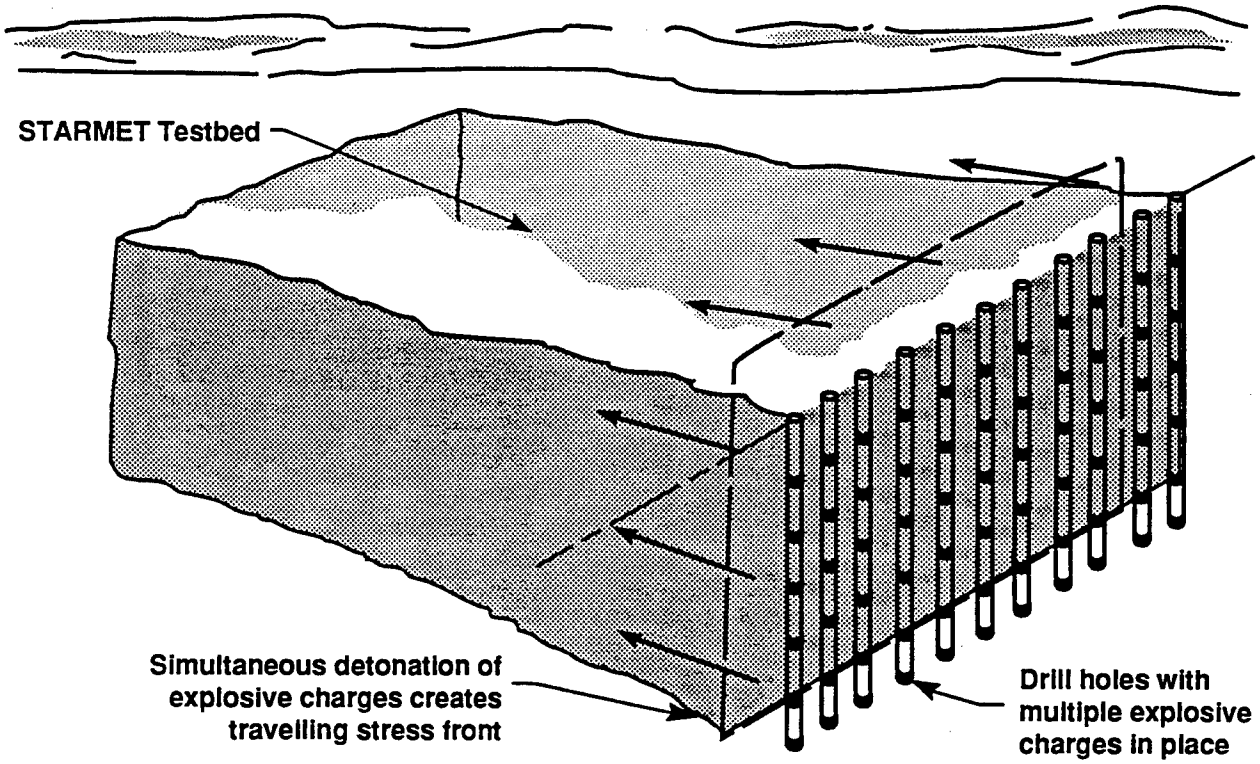


Figure 6: Lay-Out of STARMET Test

[1] Heuze, F.E., et al (1990) "Analysis of Explosions in Hard Rocks: The Power of Discrete Element Modeling", Lawrence Livermore National Laboratory, UCRL-JC-103498, 68 p.

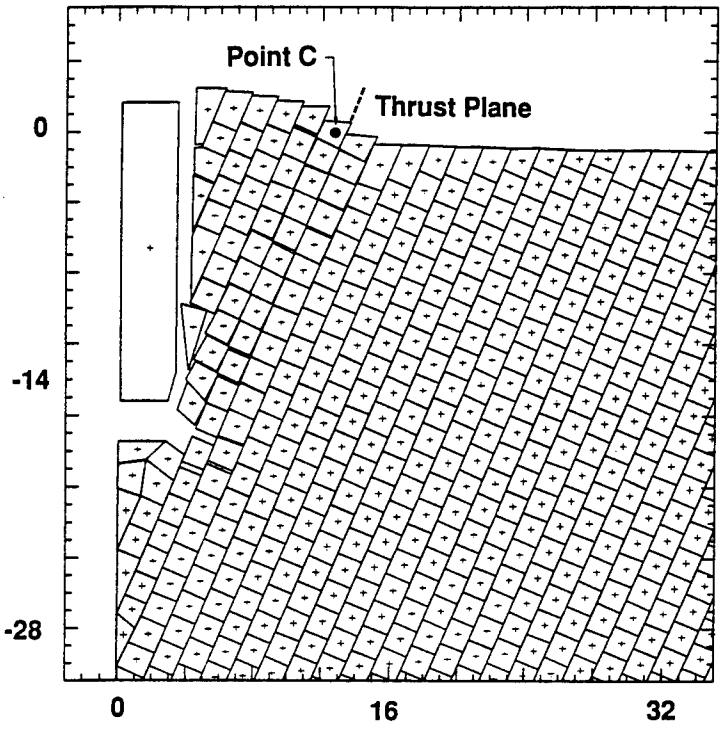


Figure 7: Blocky Structure of the STARMET Site, As Displaced by the Explosion in the DIBS Simulation.

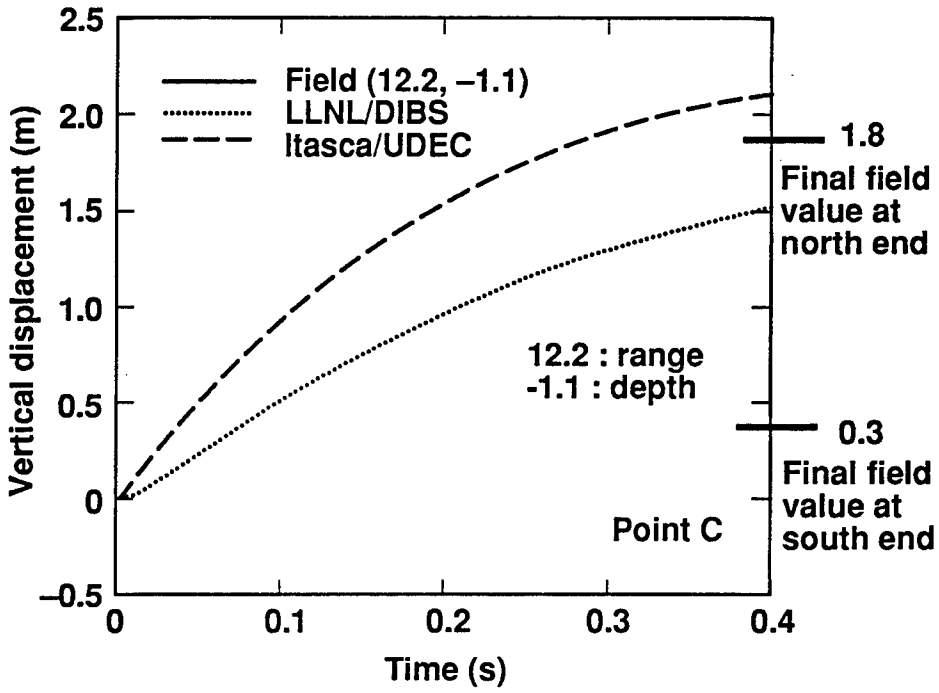


Figure 8: Vertical Motion Time-History of Points C (Figure 7): Comparison of DIBS and UDEC Results With Field Data.

MODELING UNDERGROUND EXPLOSIONS IN POROUS LIMESTONE[a)]

John W. White
March, 1993

Introduction

This study consists of two parts. In the first part , we describe our simulation of the small scale dynamic experiments performed by SRI[1], and how these simulations produced the parameters that were used in our computer model for 16% porous limestone. The second part describes the simulation of an underground nuclear explosion in which the limestone model is used to examine the sensitivity of yield estimation to the uncertainties in the computer model.

SECTION I: Simulation of Small Scale Experiments

Characterization of the SRI Tests

For the computer simulation, the SRI experiment was considered to be perfectly spherical. At the center of the rock sphere was a 1 cm diameter ball of decompressed PETN explosive. The PETN was ignited at its center, and a detonation wave proceeded outward driving a shock into the rock. Detectors were placed at 9 radial locations in the rock, and the computer model was required to simulate their measurements of particle velocity as a function of time. The radii employed were: 10, 15, 20, 25, 30, 40, 50, 65, & 80 mm.

The limestone was tested in four different configurations: dry (air filled pores at room temperature), saturated (water filled pores at room temperature) and frozen (both dry and saturated). The samples had 16% porosity; and the four configurations gave three different results. Both dry configurations (frozen or room temperature) gave similar results. Limestone is composed almost solely of calcium carbonate. If no water is in the pores, there is no reason for freezing temperatures to significantly affect the mechanical properties. The results from the SRI research on Indiana limestone are summarized in their most recent report[1].

A Limestone Material Model Description

The KDYNA[2] computer code was used to model the SRI experiments using EOS # 11 and material model #23 in our simulations. EOS #11 describes the volumetric portion of the material response, relating the pressure (P) to the compression (μ); with μ defined as $\rho/\rho_0 - 1$. Here ρ is the density and ρ_0 is the density at 1 bar. The model allows for the loading and unloading history of any rock element to be different after failure occurs. This can happen when porosity is squeezed out of the dry limestone material used in SRI tests. Material model #23 describes the rock's elastic properties and the manner by which it fails. This particular model assumes that the Poisson's ratio is a constant. For more material model details such as shear or tensile failure, stress relaxation etc. see the KDYNA manual.

The above approach is not unique; it is one of several possible choices. It was chosen because it is simple, fairly general and because the limestone data dealt with pores that contained either air or water (but not both). For example, when dealing with rock having a mixture of air and water in the pores, an effective stress model might have proven advantageous.

a) Work performed under the auspices of the U. S. Department of Energy by Lawrence Livermore National Laboratory under contract #W-7405-Eng-48

Model Parameter Constraints and Sensitivity

There is a wealth of experimental data for limestone that constrain the input parameters for the above model. A good example is given by the limestone compressibility and failure data[3] gathered by Heard, Abey and Bonner. The SRI experimenters were also able to determine many of the material properties for their specific limestone samples.

The type of data described above has been synthesized by Butkovich[4] in a computer program that will generate P-μ curves and strength curves for silicate and carbonate rocks having a wide variety of porosity and water content. The initial selection of parameters for simulations of the SRI limestone experiments came from the Butkovich program or directly from the SRI measurements. Many calculations were run to test the sensitivity of parameters in matching the SRI experiments. Most parameter variations produced little change. On the other hand, both the determination of the onset of failure associated with pore crush and the shape of the shear strength curve required a departure from the Butkovich program.

Calculational Set-up and Results

The PETN explosive had a 0.45 cm radius and was divided into 13 equally spaced zones. Lighting times were input to produce the appropriate detonation speed. A plastic shell was just outside the PETN; it was 0.05 cm thick and was split into two zones of equal thickness. The limestone extended to a radius of 13.5 cm, and it was divided into 444 uniformly spaced zones. Numerical controls (such as artificial viscosity) were used to damp numerical noise and to insure numerical stability. Convergence of the numerical scheme was successfully verified.

Both the experimental data and the computer model have limitations. Thus, it makes no sense to have a computer model match the experimental data perfectly. Still, as seen below, the calculational results are in surprisingly good agreement with the data.

Figure 1 shows the experimental velocity time histories of the middle detector location (at a 30 mm radius) with our modeling study results; the key output are the modeling parameters that were required to produce the match. The model parameters were all in good agreement (within 15 %) with the values produced by the Butkovich program, the data of Heard et. al. or the measurements provided by SRI except for the two previously mentioned strength parameters. See figure 2 for the shear strength curves used by the model. *The surprise is that the saturated limestone retains significant strength until the 10 kb pressure level is reached.*

The frozen wet limestone is stronger than wet limestone at room temperature by a factor of two; and at low pressure its shear strength is higher than that of dry limestone. Ice appears to add some strength, but both wet limestones lose their strength near 10 kb, and little difference remains between them at higher pressures. Beyond a pressure of 10 kb, both saturated limestone strength curves diminish to coincide with the quasi-static data of Heard. One hypothesis is that the water acts as a lubricant in a way that depends on the strain rate. The stress wave acts on the rock in the small scale experiment so briefly that the water (at low pressure) may not penetrate the cracks quickly enough to eliminate the strength. As the pressure reaches a sufficiently high value (10 kb); the water penetration of the cracks is expedited. If this hypothesis is true, *we must be concerned with matters of scale* because field experiments will involve longer time scales and and slower strain rates.

The comparison of calculated results with experimental data shown in figure 1 is typical of the comparisons at all detector radii. Agreement is improved slightly at smaller radii and degraded slightly at larger radii. Note that a small change in the strength curve occurs when the wet rock is frozen, but this produces a sizeable change in the wave shape.

Also interesting is the effect produced in the particle velocity time history when the shear strength "hump" (below 10 kb) is removed. For pressures less than ten kb, let the strength vanish as is the case for the quasi-static experiments with limestone. The result shown in figure 3 is different from that of figure 1. The rock now behaves more like a fluid. The wave propagation properties of the material are very sensitive to the strength at low pressure.

SECTION II: The Effect of EOS on Yield Estimation

Set-up and Results of Yield Estimation Sensitivity Study

We want to determine the effect of EOS parameters on yield estimation for experiments of 10 kt or less. This means that we must now examine the sensitivity of yield estimates to EOS variations in the pressure range of 100 kb to 10 kb and below. For pressures above 100 kb, the effect of EOS variations on yield estimation is dominated by the need to obtain an accurate determination of the Hugoniot plus the release adiabat. These are most strongly affected by porosity and water content. Strength effects contribute only in a minor way to the yield estimation process at pressures above 100 kb.

In this study, we isolate the mid-to-low pressure regime (below 100 kb) by running calculations with three regions, and the inner two regions are only used to produce the desired boundary conditions for the limestone. The inner region is an iron gas of 1.0 m radius, and a 1 kt energy source is deposited within it. For the second region we arbitrarily chose a tuff similar to that used in the Bristol[5] analysis. The radius of the tuff extends to 4.6 m, and the limestone extends beyond to a radius of 50 m. With this arrangement, the peak pressure reached at the inside of the limestone is 100 kb for every one of the limestone calculations; and a peak pressure of 10 kb is reached at a radius of about 10 meters. Figure 4 shows the calculational layout.

Figure 5 shows the calculated peak velocity (and peak pressure) attenuations for the different forms of limestone. The two saturated curves are similar, but the frozen one displays faster attenuation because its failure curve is stronger and more energy is dissipated in shear failure. Our dry calculations show strong velocity attenuation in the mid-to-low pressure regime. This is because our P-μ and strength curves provide severe dissipation as the pores are crushed.

Scaling does not apply rigorously for layered geologies. Layer thicknesses would have to scale as the cube root of the yield for scaling to be fully appropriate. Still, scaling provides a crude way of calculating how the EOS uncertainties affect the yield estimation process. We used cube-root scaling to examine the effect of freezing on the saturated rock as portrayed in figure 5. For example, suppose we mistakenly used the EOS for wet rock at room temperature instead of the EOS for frozen wet rock. This would result in a significant error in yield estimation[6].

On-Site Yield Estimation

Although this study has not presented any new calculations on the effects of layering, reference 5 pertains directly. The Bristol experiment was fired in a heavily layered medium (tuff) with the amount of air filled porosity varying from layer to layer. Its CORRTEX cable was located to sample the diverging stress wave in the regime of peak pressures from 100 kb to 10 kb. Five rock layers were required to model the outgoing shock wave so that the calculated yield estimate was within 15%. A variety of single layer calculations were unable to match the yield to within 50%. Layering must be included for experiments that are meant to simulate tests that work in the mid-to-low pressure range.

As detectors are placed further from the device, they experience weaker signals. Different errors in the EOS are encountered that must be considered in addition to the previous errors.

This leads to a compounding of error accumulation as signal interpretation is removed farther from the explosion site; although there is the advantage of avoiding aspherical source spoofing at large distances. CORRTEX is usually assessed as having a yield uncertainty of 30% (two sigma at 90% confidence level) with a standard canister. But the combination of difficult geology (lots of air filled porosity with partial saturation) that is poorly characterized (particularly with respect to layering) might result in worse yield estimation accuracy (a factor of 2 or 3 ?). On the other hand, the Russian site at Novaya Zemlya may be geologically friendly for verification procedures because most of the NZ rock has no more than 1% or 2% porosity; and those pores are filled with frozen water. The water table is near the surface and the soil and rock are in the permafrost state to a considerable depth. Both the P-μ curve and the strength curves are relatively simple for saturated rock, and they can be estimated reasonably well .

SUMMARY

We examined the effect of limestone's EOS on the yield estimation process for waves with peak pressures below 100 kb. This is important in extending the verification program to yields below 10 kt. We have found that porosity and water content continue to be major factors, but strength is now also important. Strength can be affected significantly by the degree of saturation and temperature. Furthermore, we have seen that saturated limestone may retain significant strength until moderate pressure is attained. The low pressure regime is also more sensitive to the effects of layering because the limitations of scaling become pronounced.

Acknowledgements

L. Glenn originally suggested this research topic, and has provided continuing support. Thanks are also due A. Attia. D. Clarke, W. Moss and J. Rambo for constructive reviews of the project; and to A. Florence for helpful discussions regarding the SRI experiments.

References

1 S. A. Miller and A. L. Florence, Laboratory Particle Velocity Measurements on Indiana Limestone and Sierra White Granite, GL-TR-91-000, January 1992

2 J. L. Levatin, A. Attia and J. O. Halquist, KDYNA Users Manual, UCRL-ID-106104, September 1990

3 H. C. Heard, A. E. Abey and B. P. Bonner, High Pressure Mechanical Properties of Indiana Limestone, UCID-16501, June 1974

4 T. R. Butkovich, A Technique for Generating Pressure-Volume Relationships and Failure Envelopes for Rocks, UCRL 51441, November 1973

5 R. A. Heinle and J. W. White, Hydroyield Diagnostics for the Bristol Event UCRL-ID-109437 February 1992

6 John W. White, Computer Modeling of Low Pressure Laboratory Experiments on Indiana Limestone and Sierra White Granite and the Implications for Yield Estimation, UCRL-ID-112449 January 1993

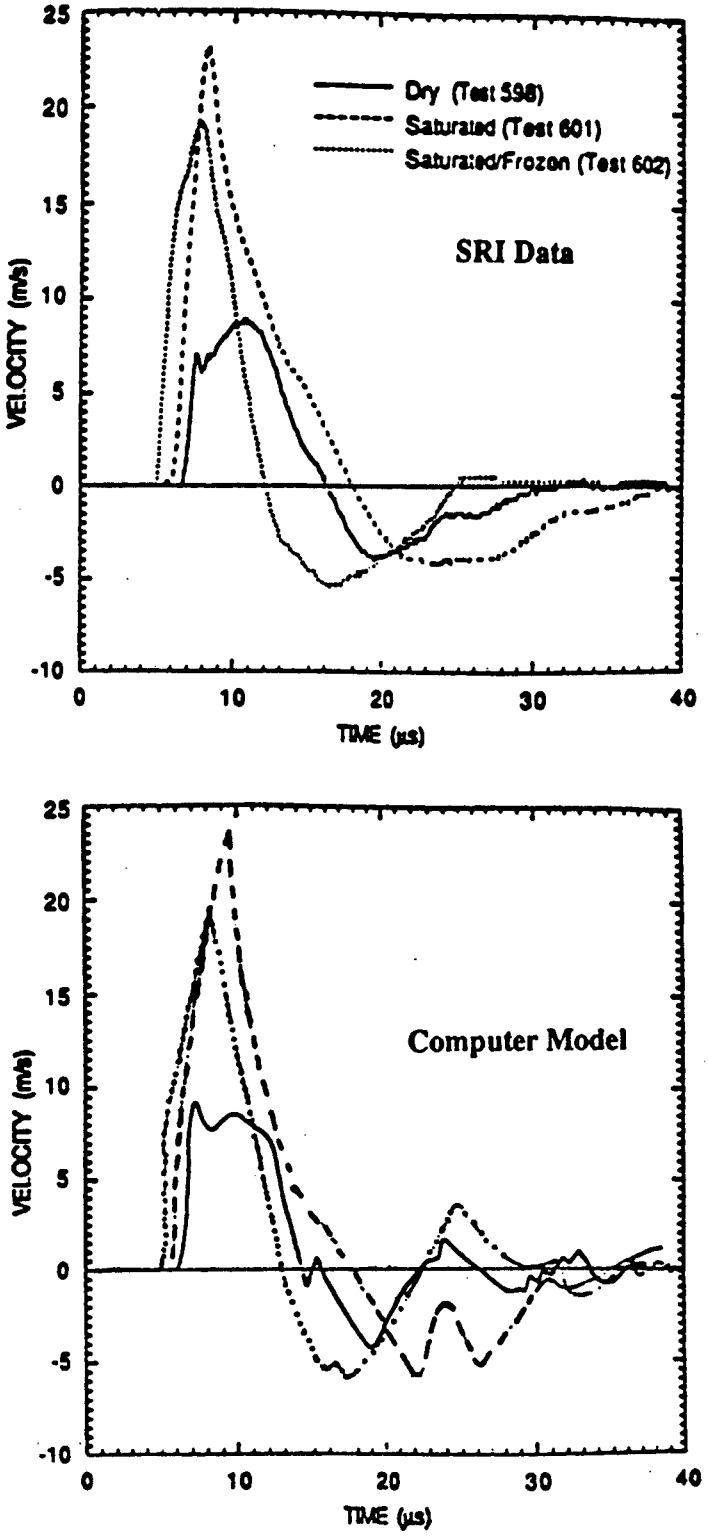


Figure 1. The upper portion of the figure shows the particle velocity time-histories (from SRI data) of three limestone states for the detector located at a radius of 30 mm. The lower portion shows the calculational results for the same configurations.

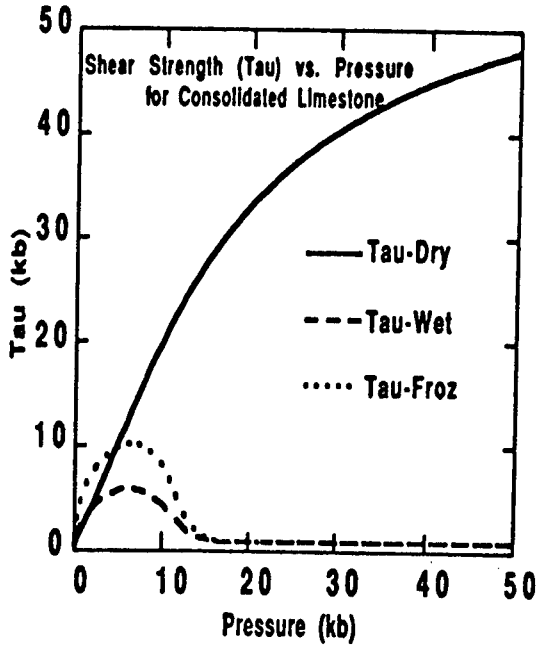


Figure 2. The above shear strength curves were required in the computer to obtain the agreement between calculation and experiment of figure 1. The particle velocity time histories are very sensitive to the above strength model details. Note that at very low pressures, the strength of the wet and frozen limestone is even greater than that of dry limestone.

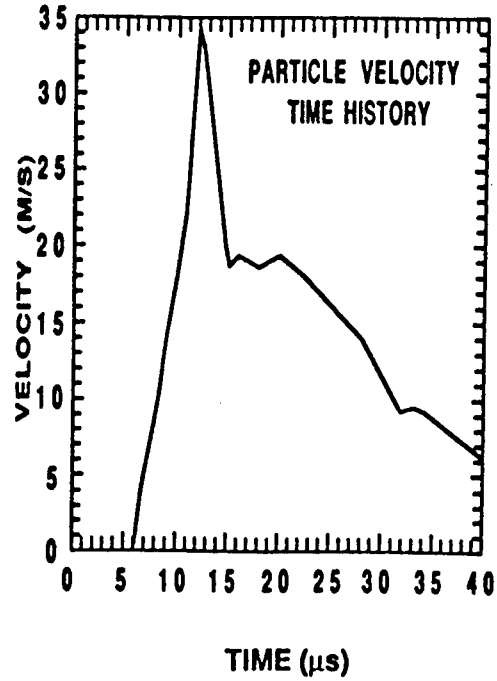


Figure 3. This shows the calculated particle velocity time history when virtually no shear strength is present in the saturated limestone. It is useful to compare it to the room temperature saturated limestone curve in figure 1 that has only a small strength "hump" as shown in figure 2.

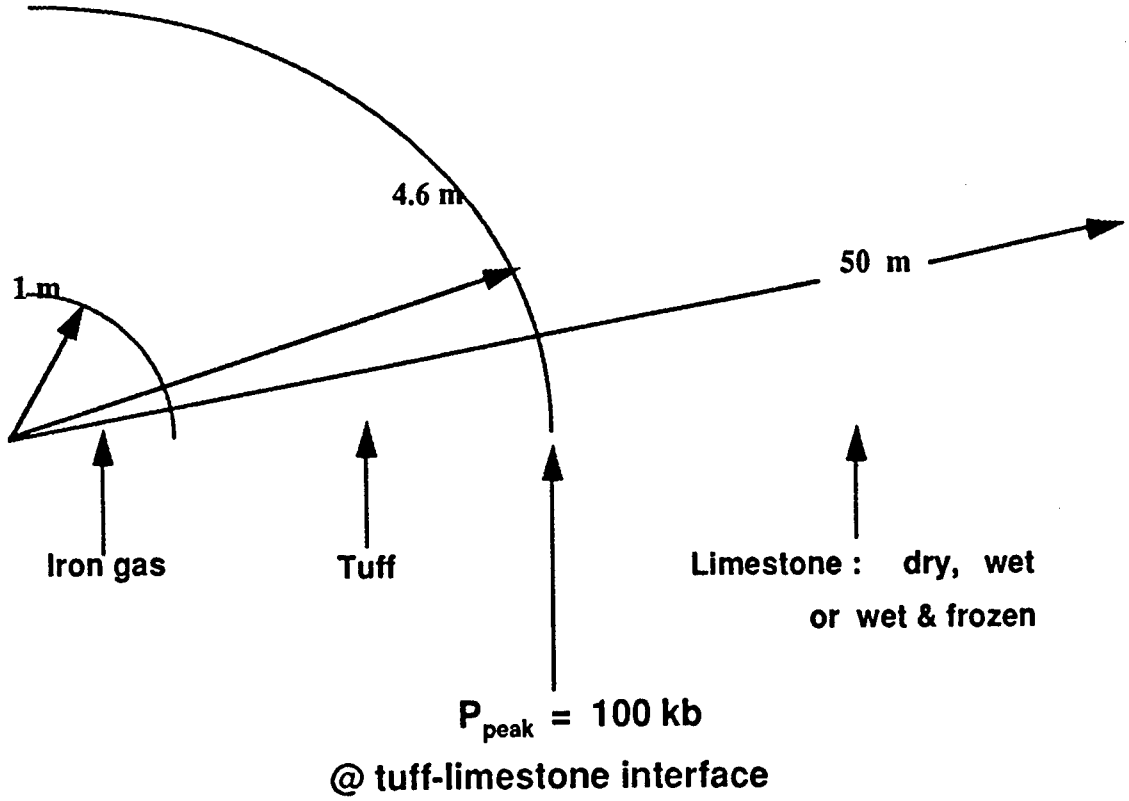


Figure 4. The above diagram shows schematically the (spherical) geology used in the calculations for the study of yield estimation sensitivity to uncertainties in our material models. The peak pressure reached at the interface between the tuff and the limestone is 100 kb. The limestone experiences peak pressures of 100 to 10 kilobars and below; and this is the regime in which we are interested.

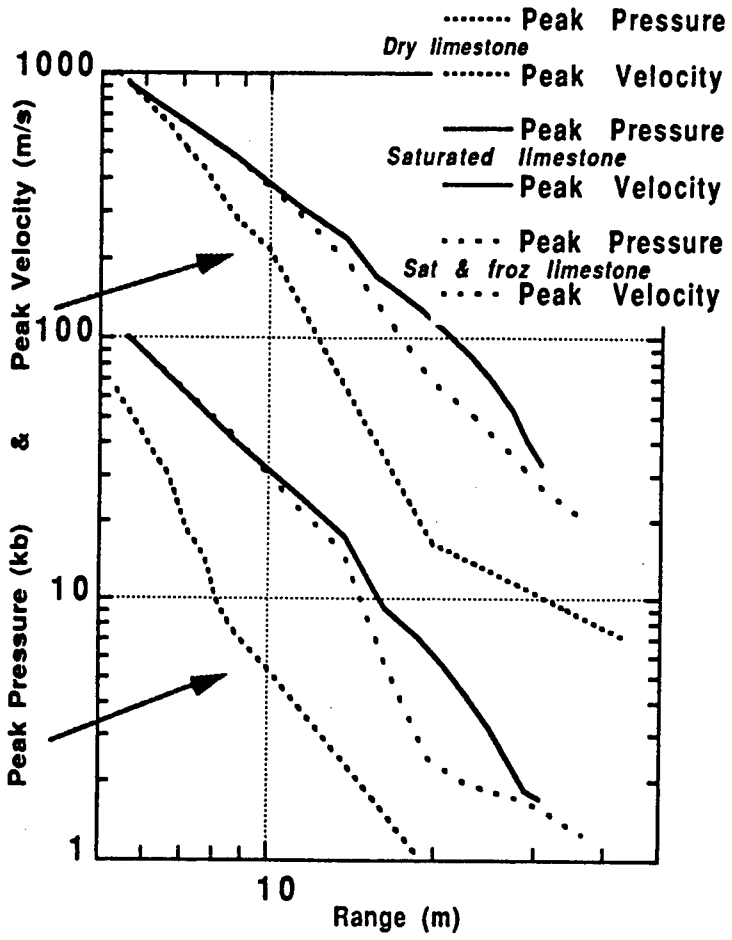


Figure 5. The above graph demonstrates how the attenuation effect changes as the 16% porosity limestone changes its pore content and temperature. The two saturated limestone models provide substantially different answers after the wave has passed the 10 m radius. By that point, the peak pressure in the wave has dropped to 10 kb.

Using neural networks to infer the Hydrodynamic yield of aspherical sources

B. Moran and L. Glenn

Abstract:

We distinguish two kinds of difficulties with yield determination from aspherical sources. The first kind, the spoofing difficulty, occurs when a fraction of the energy of the explosion is channeled in such a way that it is not detected by the CORRTEX(1) cable. In this case, neither neural networks nor any expert system can be expected to accurately estimate the yield without detailed information about device emplacement within the canister. Numerical simulations however, can provide an upper bound on the undetected fraction of the explosive energy. In the second instance, the interpretation difficulty, the data appear abnormal when analyzed using similar-explosion-scaling and the assumption of a spherical front. The inferred yield varies with time and the confidence in the yield estimate decreases. It is this kind of problem we address in this paper and for which neural networks can make a contribution.

We used a back propagation neural network to infer the hydrodynamic yield of simulated aspherical sources. We trained the network using a subset of simulations from 3 different aspherical sources, with 3 different yields, and 3 satellite offset separations. The trained network was able to predict the yield within 15% in all cases and to identify the correct type of aspherical source in most cases. The predictive capability of the network increased with a larger training set. The neural network approach can easily incorporate information from new calculations or experiments and is therefore flexible and easy to maintain. We describe the potential capabilities and limitations in using such networks for yield estimations.

Introduction:

The use of artificial neural network methods in hydrodynamic yield estimation methods has been discussed by Dowla *et al*(2). In that report, 24 explosions in tuff for which there are experimental CORRTEX data, were analyzed. The events ranged in yield from approximately 71 to 1150 kt, and were all well tamped. Here, we extend the analysis to include simulated explosions inside canisters which are permitted within the standard geometry constraints imposed by the protocol of the TTBT(3).

The current US methodology is based on a piece-wise point source analysis. This rule-based methodology however, cannot easily incorporate information from new calculations or experiments and is therefore somewhat rigid. In this paper we explore the use of a neural network to address the

problem of yield determination from aspherical sources and describe our experience with the data sets calculated by Hill *et al*[4].

Difficulties with aspherical sources:

There are 2 kinds of difficulties with yield determination from aspherical sources. The first kind, the spoofing difficulty, means that there exists a center of energy (COE) for which the inferred yield is invariant with time but that the magnitude of that yield is incorrect. This happens when a portion of the energy of the explosion is channeled in such a way that it is not detected by the CORRTEX cable. Obviously, neither neural networks nor any expert system can be expected to detect this kind of difficulty without some knowledge about the canister.

As an example of a spoofing configuration, consider the case where the device is at the top of the canister and a baffle is placed below the device. Figure 1 shows that such a configuration can produce widely different shock fronts depending on the areal density of the baffle. Although the top portion of the shock front for these calculations are all spherical, the speed of propagation of the front and hence the time it takes to reach the satellite cable depends on the areal density. A qualitative explanation of how a plate below the device reduces the speed of the shock front, and hence the inferred yield, is as follows: During the energy production from the source and deposition in the ambient material, the plate acts as a tamper which confines the energy of the device. A spherical shock front centered around the device, then begins to develop. Impulse on the tamper however, imparts a velocity to it which uses up some of the device energy and decreases the driving pressure behind the main shock. Since for a given impulse imparted to the plate, its velocity and its kinetic energy are both inversely proportional to its mass, we can expect that a decrease in the plate areal density will increase the energy preferentially channeled down the empty canister. The fraction of the total energy which remains around the device to drive the main shock thus decreases with a decrease in the areal density of the plate. This qualitative explanation is not valid in the limit of zero plate areal density. In that case, the early transport of energy down the empty canister generates a nearly cylindrical wave front which can be analyzed at late time to produce a good estimate of the correct yield. Figure 2 shows the fraction of energy detected using the US methodology.

The second kind of difficulty, the interpretation difficulty, means that regardless of the chosen COE , the inferred yield varies with time. This indicates that either the standard curve used in explosion scaling does not represent the in situ rock or that the source is aspherical. It is this latter scenario which we address in this paper and for which neural networks can make a contribution. The important determination of the "best" standard curve through the use of artificial neural networks or other techniques will not be discussed here.

Simulated configurations:

We considered the three aspherical configurations suggested by the Soviet white paper(5) and shown in Figure 3: the first is LC1, a device located at one end of an air filled, 12 m-long canister whose outside diameter is 2.5 m. The second is LC6, a similar configuration to LC1 except that a partition, with an areal density of 52.5 g/cm^2, is placed so as to confine the initial hohlraum to a length of 1.7 m. The final configuration is LP1, a 1.7 m long and 2.24 m diameter device connected to an air filled LOS pipe 7.65 m long and 0.508 m diameter. Each of the three configurations was simulated by Hill *et al*(4) with an input yield of 105, 150, and 195 kt and three different horizontal offsets for the satellite CORRTEX cable: 8, 10, and 14 m. The device in each of these 27 data sets was at the bottom of the canister, thus ensuring that all the explosion energy would be detected by the CORRTEX cable.

Building the neural network:

We used a commercially available(6) back propagation software package to build a network that can predict the correct yield and recognize canister configurations. The input to the net consists only of data that would be available in a verification scenario: The standard curve, the surveyed horizontal offset of the CORRTEX cable, and the cable crush length-versus-time data. A major difference between this network and the one discussed by Dowla *et al*(2) is that this network was designed to "see" the whole yield- versus-time curve thus considerably enhancing its ability to predict the yield of an aspherical source.

Preparation of the input consisted of the following steps:

1) For each configuration, calculate the explosion horizon (i.e. vertical offset) as the location of the first cable-crush. For the simulated explosions, that location is the lowest vertical coordinate which indicates crushing, it makes no assumptions about the location of the device within the canister.
2) Use the surveyed horizontal offset and the vertical offset to calculate a radius-versus-time curve for each configuration, yield, and horizontal offset. We used the exact horizontal offset for the simulated calculations and discuss the effects of uncertainties in the offset in the next section.
3) For each radius-versus-time curve, use explosion scaling and the standard curve to calculate a yield-versus-time curve.
4) For each yield-versus-time curve, make a coordinate transformation to a yield versus vertical distance above first crush and interpolate that curve to find the yield at vertical distances of 0, 3, 6, 9, 12, 15, 18, 40, and 50 m above first crush. These locations, although arbitrary, were chosen to provide representative data from the early and the late time portions of the curve.

The input to the net consisted of the horizontal offset, the yield at the first crush, and the differential yield at the other 8 locations described above. The differential

yield is the difference between the yield and the yield at the first crush. Using differential quantities for input improves the accuracy of the network.

We used one hidden layer with 10 nodes. We found that using 2 hidden layers produces a faster training but poor generalization. The output consisted of the simulated yield and 3 variables, each between 0 and 1, that describe the probability of a given configuration.

Yield estimation results:

We trained the network using a subset of the 27 simulated data sets and tested its predictive capability on the remaining sets. We found that choosing a representative subset for training enhances the predictive capability and that increasing the training subset from 18 to 26 decreased the maximum error in the estimated yield from about 25% to 15%. All the results reported henceforth are from training using 26 data sets and predicting the yield of the 27th set.

Training was stopped when the estimated yields from all the training set were within 10% of the exact values and typically took about 15 minutes on a Mac IIfx. We found that training to a smaller error did not improve the predicted results. This is due to the relatively small number of training sets and the tendency of the net to "memorize" rather than "generalize" in such cases.

Figure 4 shows the predicted yield as a function of problem number. On the same graph we show the results of the US methodology. Note that the maximum error using the neural net is about half that of the US methodology and whereas the US methodology results show a distinct bias, the neural network results do not.

We have tested the stability of the net by slightly changing the horizontal offsets and found that the predicted yields change only slightly.

Summary and conclusions:

We have built and tested an artificial neural network that was capable of predicting the yield from a limited number of aspherical sources. Although the network was trained using a limited number of examples, it has demonstrated improved accuracy with increasing size of the training set. Such a network is useful when it is suspected that the source is aspherical.

There are two issues that need to be addressed when using such a network: The first is how well does one know the standard curve and the second is a question of uniqueness of the solution.

In all our calculations, the standard curve and the simulated aspherical explosions were modeled using the same equation of state for the rock. In a treaty mode, the standard curve needs to be constructed from various measurements of the rock and thus has some uncertainty. An important question that remains to be answered is how well can a neural network be trained to choose the "best" standard curve.

The uniqueness issue addresses the question of whether it is possible for two different configurations of different yields to produce CORRTEX data that appear very similar to the neural net. Our experience with the 27 data sets indicates that this can only happen when the source is at the top of the canister.

Acknowledgments:

Work performed under the auspices of the US Department of Energy by Lawrence Livermore National Laboratory under contract number W-7405-ENG-48.

References:

1- R. G. Deupree, D. D. Eilers, T. McKown, and W. H. Storey, "CORRTEX: A Compact and Versatile System for Time Domain Reflectometry," Los Alamos National Laboratory Report No. LA-UR-80-3382 (1981).

2- F. Dowla, R. Leach, L. Glenn, B. Moran, R. Heinle "Neural network methods in hydrodynamic yield estimation," To appear in Pure and Applied Geophysics 1993, also Lawrence Livermore National Laboratory report UCRL-JC-112369, December 1992.

3- Delegations to the Nuclear Testing Talks. "Protocol to the Treaty Between the United States of America and the Union of Soviet Socialist Republics on the Limitation of Underground Nuclear Weapon Tests," Section I, item 17 and section V, paragraphs 2 and 3. Geneva, Switzerland, 1990.

4- R. Hill, private communications, 1992.

5- "Concerning Errors of Hydrodynamic Yield Measurement Method for Testing in a Standard Configuration," Paper WD-031 #2761 (June 21, 1989), Official Translation of Document of the Soviet Delegation - handed over at HOD Mtg., August 4 1989.

6- BrainMaker for the Macintosh version 1.0. California Scientific Software, 10024 Newtown Road, Nevada City, CA 95959 (1991)

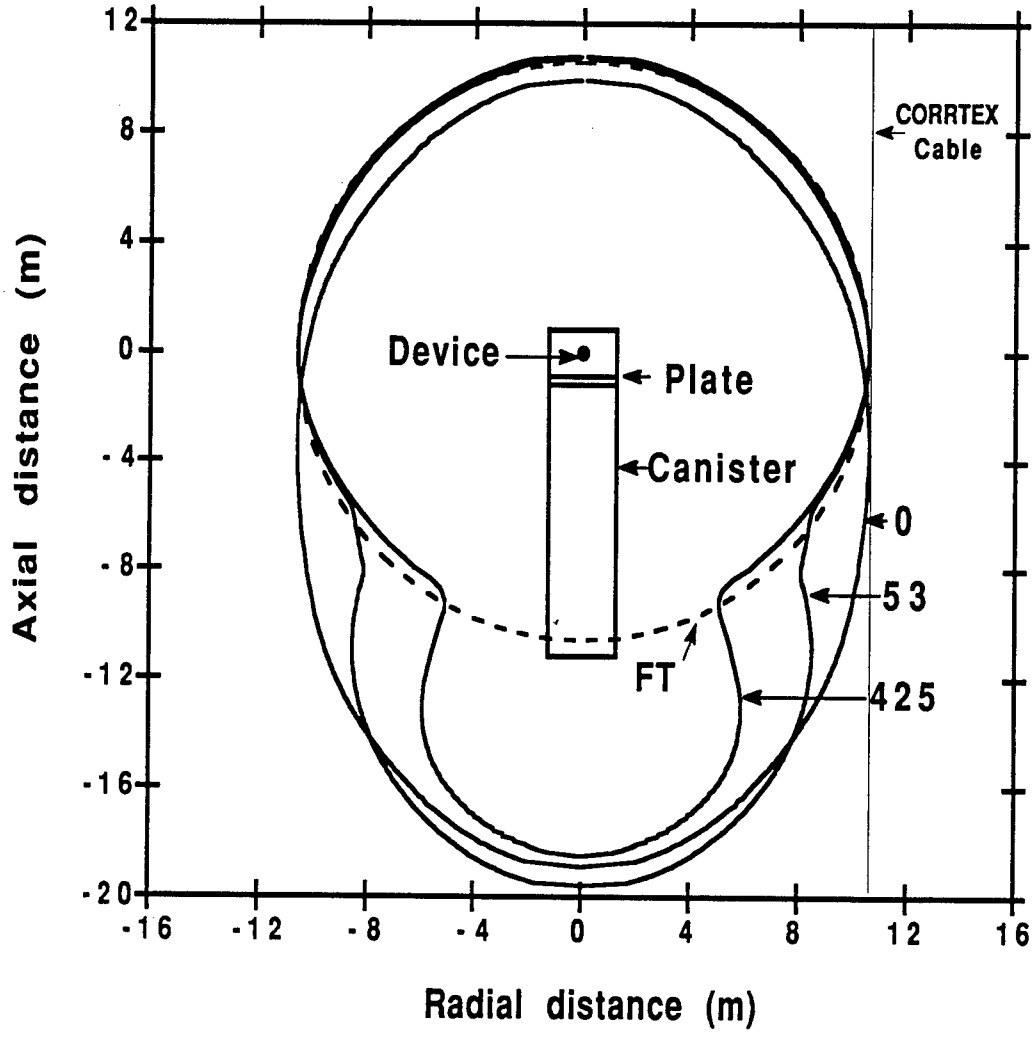


Fig. 1. Shock front contours for 4 calculations (150 kt) at the time corresponding to first arrival at the CORRTEX cable 10.5 m away from the device. The dashed line is a fully tamped explosion (FT); the numbers near the other contours are the areal densities of the plate in units of g/cm^2

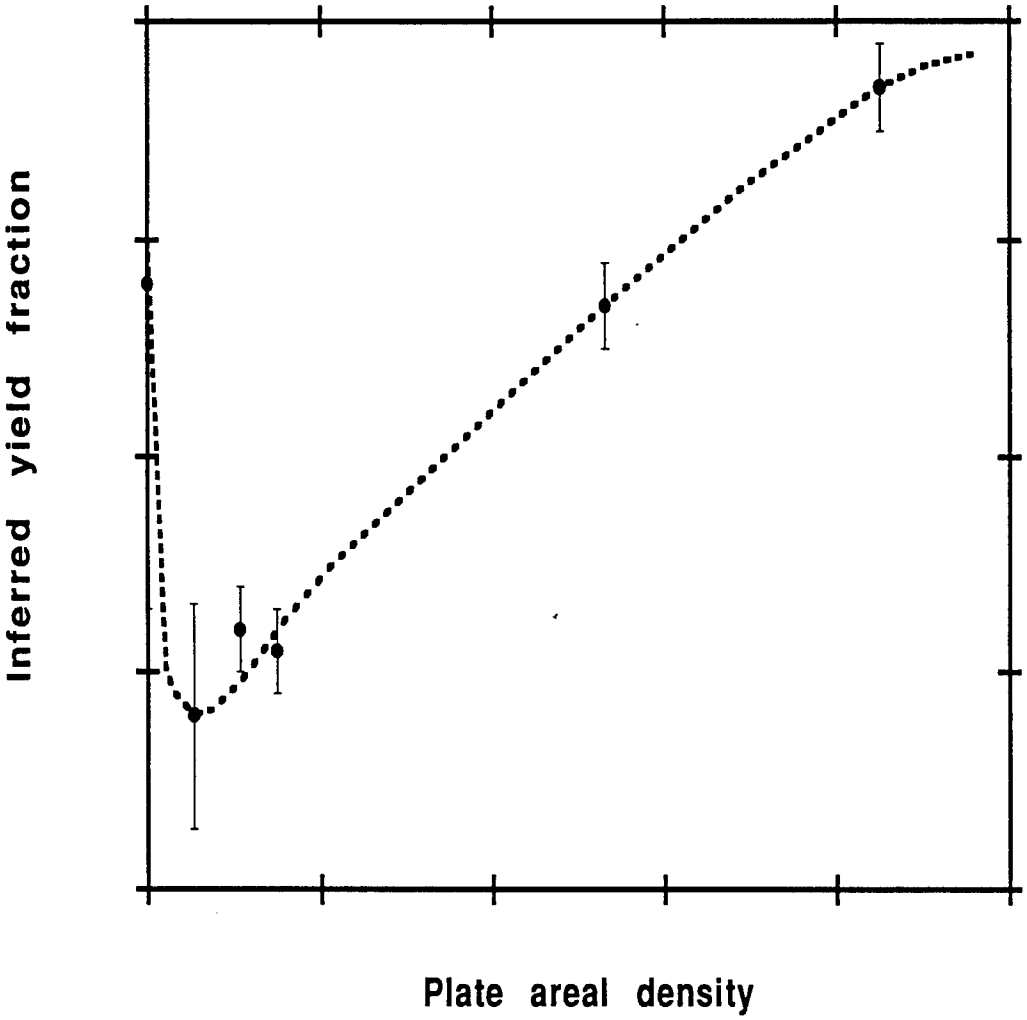


Fig. 2. Schematic of the inferred yield fraction as a function of the plate areal density.

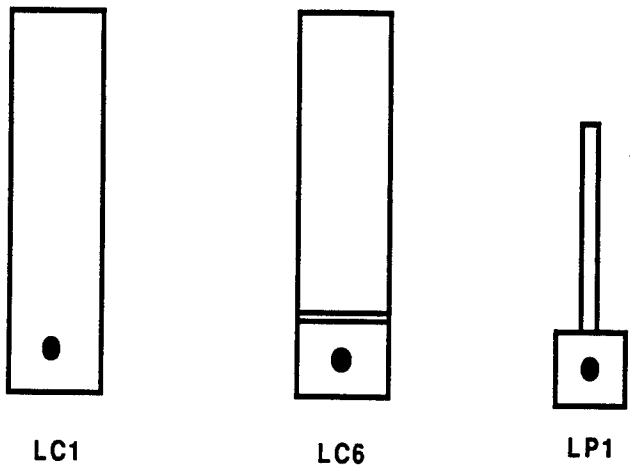


Fig. 3. Aspherical configurations modeled in this paper.

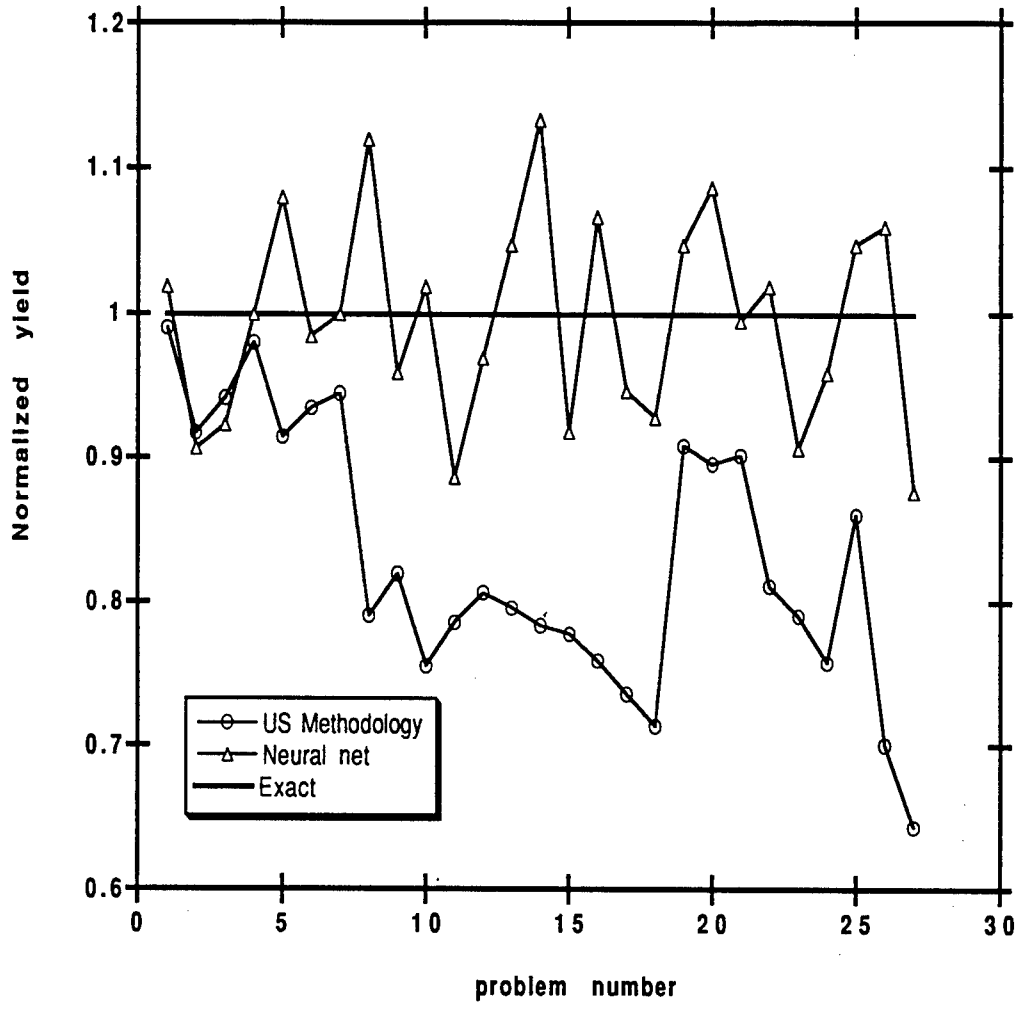


Fig. 4. Normalized yield for the 27 simulated calculations

THIS PAGE INTENTIONALLY LEFT BLANK.

Comments on Statistical Issues in Numerical Modeling for Underground Nuclear Test Monitoring

WL Nicholson and KK Anderson
Pacific Northwest Laboratory, Richland, WA 99352

The Symposium concluded with prepared summaries by four experts in the involved disciplines. These experts made no mention of statistics and/or the statistical content of issues. The first author contributed an extemporaneous statement at the Symposium because there are important issues associated with conducting and evaluating numerical modeling that are familiar to statisticians and often treated successfully by them. This note expands upon these extemporaneous remarks.

Statistical ideas may be helpful in resolving some numerical modeling issues. Specifically, we comment first on the role of statistical design/analysis in the quantification process to answer the question "what do we know about the numerical modeling of underground nuclear tests?" and second on the peculiar nature of uncertainty analysis for situations involving numerical modeling.

The simulations described in the workshop, though associated with topic areas, were basically sets of examples. Each simulation was tuned towards agreeing with either empirical evidence or an expert's opinion of what empirical evidence would be. If agreement was not reached, that is, if the tuning was not successful, a discussion was provided of what was lacking and how the model should be embellished in order to reach agreement. While the discussions were reasonable, whether the embellishments were correct or a forced fitting of reality is unclear and illustrates that "simulation is easy." We also suggest that these examples of simulation are typical and the questions concerning the legitimacy and the role of knowing the reality are fair, in general, with respect to simulation. The answers will help us understand why "prediction is difficult."

Successful prediction demands comprehensive understanding of the relationship between the situation used to develop the model and the situation to be predicted so that in some sense prediction is interpolation (or not-too-gross extrapolation). This brings us now to the first issue with statistical content: with respect to a specific area from numerical modeling, how do we determine what we know? Some sort of a systematical evaluation is in order. Statistical design/analysis offers a tool for such an evaluation. Consider for example a relatively simple and hopefully reasonably well-understood area, that of one-dimensional hydrodynamic modeling, what we must accomplish for simulated yield estimation within a spherical geometry. We think conceptually of the set of simulations that could be done to encompass the reality of 1-D hydrodynamic experimentation. Each point in that space, here called a parameter space, is defined by a set of material properties and modeled using well-established mechanisms. The systematic evaluation begins with a check-off in that parameter space. Where have simulations been done? Where have such simulations been validated by being compared to experimental data? Looking across the simulations that have been done, to what degree is there compatibility? Where in the parameter space are there simulations that in some sense are anomalous and do we have explanations? For example, an interesting and important fact is that in some cases, simulations do not agree with reality, because input parameters, such as material properties, are determined by tests conducted in the laboratory. Glenn [Ref. 1] showed laboratory mechanical behavior that was distinct from the behavior of the same material in a field exercise. Thus in some sense the simulation was placed at the wrong point in the parameter space.

Once this systematic description of what simulations have been done and the level of agreement is established a plan can be formulated for "filling in the holes", that is, for increasing what we know. At that point, because budgets are finite and ever shrinking, we must be economical in our attack in filling in the holes. We need a buy in from the modelers and so that the increased level of knowledge is attained in an efficient, timely, and economical fashion.

A possible interesting application of empirical or statistical modeling here would be to develop a model that would predict the results of a numerical model based on a fit of the numerical model's outputs on the input points in the parameter space [Ref. 2]. Such "modeling the model" approaches have been successful in complex reactor melt down catastrophe situations [Ref. 3] where each simulation of a catastrophe is very computer intensive so that it is really impossible to cover the parameter space in a timely and economical fashion.

The second statistical issue we wish to discuss is uncertainty in the context of numerical modeling. Uncertainties are usually measured by the degree of agreement with an experiment or other description of reality. Uncertainties are either random or systematic. In the context of numerical modeling, random uncertainty, usually thought of as measurement error, is an explanation for why empirical measurements do not exactly agree with a correct model. Random uncertainty is the more familiar, being the one that is usually treated in the statistical literature. Random uncertainty is reduced by doing more of the same. The simplest example is independent repetitions of a simple experiment to estimate a single unknown quantity. That quantity is estimated with the mean over all the repetitions of the experiment. Quadrupling the number of repetitions of the experiment halves the uncertainty as measured by the root mean squared error. In more complicated situations, say where the random uncertainties are correlated from repetition to repetition, the reduction in root mean squared error is not as dramatic. However, in general, with enough repetition, a pre-specified root mean squared error can be attained.

Systematic uncertainty is much more complicated. Here the same error is present in all repetitions, averaging over more does not reduce such error. In the context of numerical modeling, systematic uncertainty as a problem is some fundamental difference between data and model. Systematic uncertainty indicates that deeper thought is necessary, possibly more physics, in order to construct and/or improve the model to include an explanation for the systematic effect. The critical point is that in comparing numerical modeling to reality most of the uncertainties appear to be

systematic. The solution is either to improve the models so that the systematic uncertainties are eliminated, or to understand/bound the maximum size of systematic uncertainty and, hence, the maximum disagreement that is possible between model and reality.

Hydrodynamic yield estimation provides an excellent example of the uncertainties that appear to be present in the results of numerical modeling. Figure 1 is such an example of yield estimation as a function of time, determined by yield scaling a hydrodynamic standard to a CORRTEX radius-verses-time curve at each time point. The random uncertainty in the raw CORRTEX crush length data is only several centimeters on a mean squared basis. The several familiar characteristics of the curve are systematics. The short term oscillating pattern is unexplained, but conjectured to be the result of ill-understood dynamics in the cable crushing process. The shape and amplitude of the pattern seems to be dependent on the type of cable. The steep initial rise in yield and low frequency oscillation are systematic discrepancies between reality, the CORRTEX radius-versus-time, and simulation, the hydrodynamic modeled radius-versus-time. Thus, yield appears to be a moving target. The final yield value, usually attained as an average over the analysis window and here illustrated as the horizontal line, clearly depends upon where the window is located.

A critical issue here is, what do we do if we do not know the yield and truly have to depend upon the CORRTEX experiment and the modeling of that experiment with an appropriate hydrodynamic calculation. One might argue that if there is a monotone trend across the time window, then whatever the discrepancy is between experiment and hydrodynamic model, it changes sensibly in the same direction as the shock front moved out to the satellite hole. Hence, the time with the least systematics is the early time. Of course one can argue just as logically for other time windows. The reality is that we do not know which time window gives the best yield estimate. In particular, selection of a time window because the yield-versus-time curve is flat over that window is no more logical than other selections.

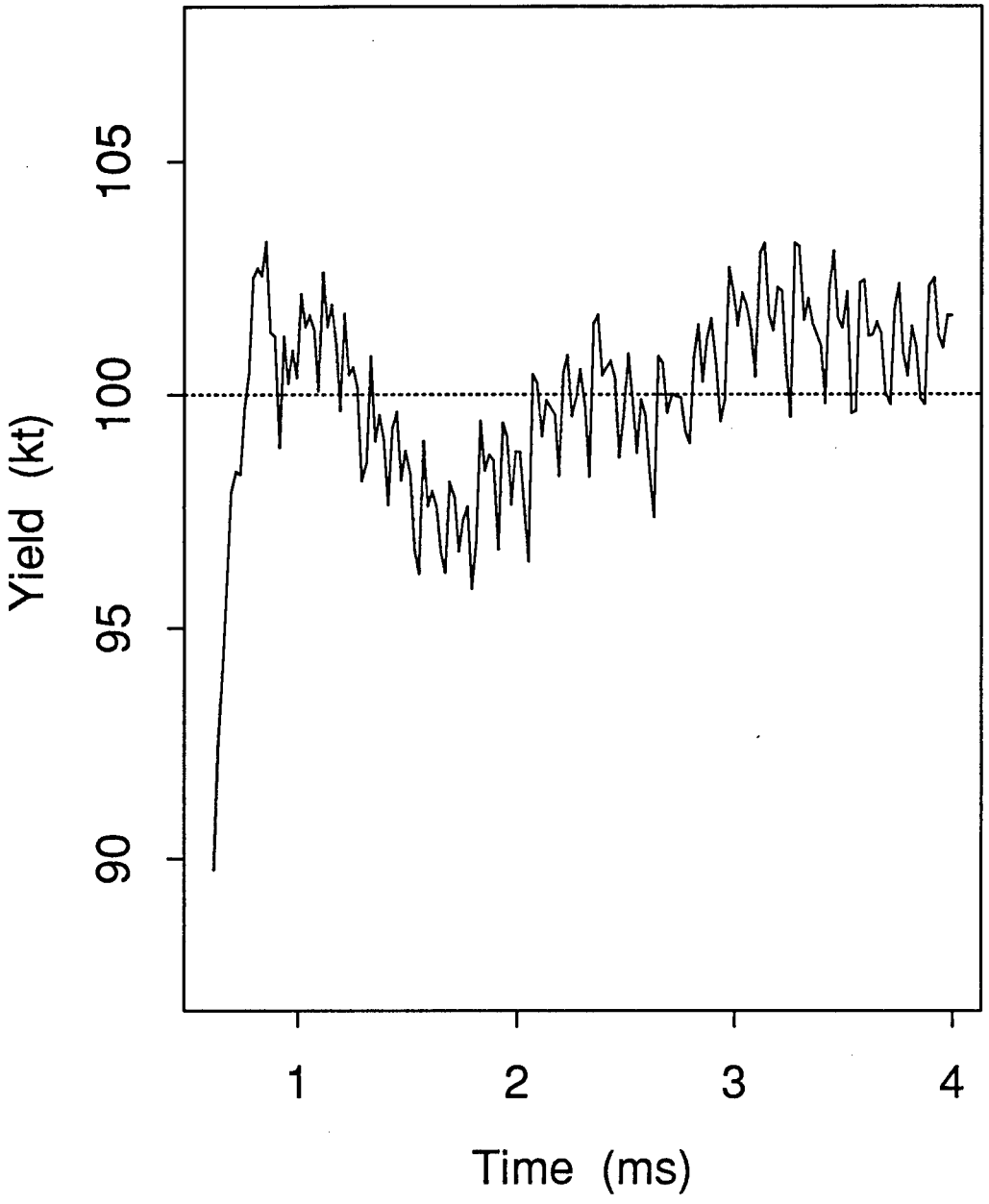


Figure 1. A typical yield-versus-time curve from a single CORRTEX cable. The average yield was set arbitrarily at 100 kt.

Acknowledgement

This research sponsored by the U. S. Department of Energy under Contract DE-AC06-76RLO 1830.

References

1. Glenn, L. A., *Modeling the Explosion-Source Region: An Overview,* in Numerical Modeling for Underground Nuclear Test Monitoring Symposium, Durango, CO, March 23-25, 1993.

2. Sack, J., W. J. Welch, T. J. Mitchell, and H. P. Wynn, *Computer Experiments,* Statistical Science, Vol. 4, pp. 409-423, 1989.

3. Tukey, J. W., *Useable Resistant/Robust Techniques of Analysis,* in Proceedings of the First ERDA Statistical Symposium, Los Alamos, NM, November 3-5, 1975, published as BNWL-1986 UC-32, Pacific Northwest Laboratory, Richland, WA, 1976.

CONSTRAINTS ON EQUIVALENT ELASTIC SOURCE MODELS FROM NEAR-SOURCE DATA

Brian Stump
Dept. of Geological Sciences, Southern Methodist University
Dallas, TX 75275-0395

Abstract

A phenomenological based seismic source model is important in quantifying the important physical processes that affect the observed seismic radiation in the linear-elastic regime. Representations such as these were used to assess yield effects on seismic waves under a Threshold Test Ban Treaty and to help transport seismic coupling experience at one test site to another. These same characterizations in a non-proliferation environment find application in understanding the generation of the different types of body and surface waves from nuclear explosions, single chemical explosions, arrays of chemical explosions used in mining, rock bursts and earthquakes. Seismologists typical begin with an equivalent elastic representation of the source which when convolved with the propagation path effects produces a seismogram. The Representation Theorem replaces the true source with an equivalent set of body forces, boundary conditions or initial conditions. An extension of this representation shows the equivalence of the body forces, boundary conditions and initial conditions and replaces the source with a set of force moments, the first degree moment tensor for a point source representation. The difficulty with this formulation, which can completely describe the observed waveforms when the propagation path effects are known, is in the physical interpretation of the actual physical processes acting in the source volume. Observational data from within the source region, where processes are often nonlinear, linked to numerical models of the important physical processes in this region are critical to a unique physical understanding of the equivalent elastic source function.

The focus of our seismic source studies has been placed on the utilization of near-source seismograms for the constraint of the equivalent elastic source function in the form of the first degree moment tensor. Such studies minimize trade-offs that can develop between source and propagation path effects since the problem is linear in both terms. Data from within the source region can be used in the interpretation of the equivalent elastic source function, thus improving its physical understanding. The Coalora explosion (11 Feb. 83) in Yucca Flats at the Nevada Test Site is used as an example of such a near-source data analysis designed to quantify the equivalent elastic source function in terms of moment tensors. The isotropic, deviatoric and spall contributions from the source are separated and quantified with the inverse modeling of the near-source data. Moment tensor inversion produces an isotropic source strength of 8×10^{20} dynes, which is 5–10 times larger than the deviatoric component. A secondary, longer period arrival is found on the diagonal elements of the moment tensor with the largest contribution on the vertical dipole. This contribution can be interpreted in terms of the tensile failure of near surface layers or spall. Spall source strength from the waveform inversion is within a factor of two of forward spall models developed from acceleration data within the spall zone.

In order to better interpret these equivalent elastic source representations in terms of the important physical processes in the source region, results of numerical experiments and data from within the nonlinear zone must be interfaced with the elastic zone data and interpretations. The quantification of processes such as spall, source asymmetries and material failure mechanisms can only be taken into account with such interdisciplinary studies.

Overview

This paper is a general discussion of the equivalent elastic source representation that seismologists typically utilize with particular application to seismic waveforms generated by underground nuclear explosions. It follows closely the theme of several other presentations in particular that of Steven Day. The theoretical aspects of the representation will be further illustrated with an empirical study of a Nevada Test Site (NTS) explosion. The key point to emphasize is that the representation will be *linear* in both the *source* and *propagation* effects thus providing for trade-offs between these two. In our case we are particularly interested in the explosion source function but are forced by nature to observe this phenomenon through many different propagation paths.

Past motivation of these studies has been the quantification of seismic coupling under a Threshold Test Ban Treaty monitoring scenario. Today, we find increasing interest in nonproliferation monitoring, which means that we must understand differences between nuclear explosions (possibly decoupled), single chemical explosions, mining explosions, mine induced events, and earthquakes. Our source representation must provide the opportunity to identify such differences—possibly the relative excitation of P and S waves—and use these results in development of discriminants. In a nonproliferation environment our community may be called upon to monitor and discriminate as many as a thousand events per day. The key for completing this task and where I see the contribution of the calculators is relating the equivalent elastic source function of seismology and the resulting discriminants (often empirically developed) to the physical processes in the source region.

Source Representation

First set aside a source volume, V_o, in which an equivalent set of body forces, initial conditions or boundary conditions can be used to represent the displacement field given the propagation path effects or Green's functions for the medium. All the nonlinear source processes are included within this volume. One form of the general representation theorem that relates the observed seismogram (u_n) to the source and propagation path effects can be expressed as:

$$
\begin{aligned}
u_n(\mathbf{x}',t') = & \int_{V_o} \int_{-\infty}^{\infty} G_{ni}(\mathbf{x}',t';\mathbf{x},t)\, \rho(\mathbf{x})\, f_i(\mathbf{x},t)\, dt\, dV + \\
& \int_{V_o} \begin{bmatrix} G_{ni}(\mathbf{x}',t';\mathbf{x},0)\, \rho(\mathbf{x})\, \dot{u}^{\circ}_i(\mathbf{x}) - \\ \dot{G}_{ni}(\mathbf{x}',t';\mathbf{x},0)\, \rho(\mathbf{x})\, u^{\circ}_i(\mathbf{x}) \end{bmatrix} dV + \\
& \int_{\partial V_o} \int_{-\infty}^{\infty} \begin{bmatrix} G_{ni}(\mathbf{x}',t';\mathbf{x},t)\, T_i(\mathbf{x},t) - \\ G_{ni,j}(\mathbf{x}',t';\mathbf{x},t)\, C_{ijkl}(\mathbf{x})\, U_k(\mathbf{x},t)\, n_l \end{bmatrix} dt\, dV
\end{aligned}
\qquad (1)
$$

The first source term includes the body forces (f_i), the second term the initial conditions ($\dot{u}^{\circ}_i$ and u°_i) and the third term the boundary conditions (T_i and U_k) that make up the equivalent source representation. The propagation path effects between the source and receiver are accounted for by the Green's functions (G_{ni}). The initial and boundary conditions can be cast into a form that

resembles body forces and thus a body force representation is taken as the most general source model.

$$u_n(\mathbf{x}',t') = \int_{V_o} \int_{-\infty}^{\infty} G_{ni}(\mathbf{x}',t';\mathbf{x},t)\, \rho(\mathbf{x})\, f_i(\mathbf{x},t)\, dt\, dV \qquad (2)$$

The source volume, V_o, is where the real and equivalent sets of body forces that make up our source are localized. Our goal is to determine the set of forces from the observed motions in the linear-elastic region. The unique physical interpretation of these forces that represent the source can only be developed with some understanding of the linear and nonlinear processes inside the volume V_o. It is in this region that additional observations and numerical simulations can be used to aid in the interpretation.

In order to simplify the representation, particularly when the radiated wavelengths are long compared to the source dimensions (point source assumption), the body forces are used to create force couples and dipoles. Force moments are defined as follows:

$$M_{ij}(\mathbf{O},t) = \int_{V_o} x_j\, f_i\, (\mathbf{x},t)\, dx^3 \qquad (3)$$

The resulting moment tensor (six components since it is symmetric) simplifies the source representation in Equation 2 representing the displacement field as a convolution of Green's functions with the six elements of the second degree moment tensor—a linear representation. This simplification assumes a point source representation where the wavelengths of the observed motion field are long compared to the source dimension:

$$u_n(\mathbf{x}',t') = G_{ni,j}\, (\mathbf{x}',t';\mathbf{O},0) \otimes M_{ij}\, (\mathbf{O},t') \qquad (4)$$

In this paper the above equation will be applied to a set of observations (u_n) with a set of Green's functions or propagation path effects ($G_{ni,j}$) to determine the equivalent elastic source function or moment tensor (M_{ij}). The equation will be applied in the frequency domain since convolution in the time domain is equivalent to multiplication in the frequency domain:

$$u_n(\mathbf{x}',f) = G_{ni,j}\, (\mathbf{x}',f;\mathbf{O},0) \cdot M_{ij}\, (\mathbf{O},f) \qquad (5)$$

Moment Interpretation

Before proceeding some simple interpretations of the moment tensor will be given. It can always be divided into an isotropic and deviatoric component (Figure 1). The isotropic contribution ($M_{ii}/3$) is the part of the source that is independent of coordinate transformation and is diagrammed in Figure 1 (M_I) as 3 orthogonal dipoles. It is linearly related to the commonly used reduced displacement potential, $\psi(t)$. The deviatoric component of the source (M_{ij}^D) in many instances can be related to a simple system of force couples, representative of a shear dislocation. A third source, possible important for contained explosions, is the opening of a tensile crack. If the crack surface is normal to the vertical direction then this model might account for near surface spall (M_T).

These source models may be useful in interpreting our seismic source function particularly if one can interpret these representations *physically*. Inside our source volume, V_o, many processes are ongoing—some of which are nonlinear. The interpretation of the moment tensor in terms of these processes may be quite nonunique—which is where the interface of this meeting resides. These processes within the source volume can include the hydrodynamic response, radiation coupling, pore crush, shear failure, tensile failure, driven motions on planes of weakness, tectonic strain release, cavity rebound, cavity asymmetries and free surface interactions.

COALORA Data

The focus is on seismic data and the resolution of the moment tensor or source representation using the equations developed. One can observe seismic radiation from the explosion in the nonlinear zone, at near-source (few km), regional (within a country) or teleseismic distances. We will focus on the near-source data since it provides the simplest propagation path effects (Green's functions) and the opportunity to heavily instrument explosions in an experimental fashion.

The Coalora nuclear explosion was detonated on 11 Feb. 83 in area 3 of the Nevada Test Site. Its announced yield is less than 20 kt. The near-source array designed to measure three component motions at a number of azimuths and distances is diagrammed in Figure 2. This instrumentation array was specifically designed for recovery of the six elements of the moment tensor.

Our ultimate goal is to compare the equivalent elastic source function with the physical processes inside V_o. One such process is spall or the tensile failure of near surface layers. In the case of Coalora a number of gauges were placed in the spall zone so that the depth and range of the process were constrained, spall mass and momentum estimated, and an equivalent spall moment rate determined which can be compared later to the moment tensor determinations using the near-source, linear elastic data. The spall zone data from Coalora are reproduced in Figure 3. Using this data from within the failure zone, the mass of the spall zone is estimated to be $1.2–4.4\times10^{10}$ kg. The peak velocities within the spall zone, the duration of spall, and its spatial extent are used to constrain the spall moment rate to $0.9–3.4\times10^{21}$ dyne-cm/s.

A portion of the near-source observational data that will be used in the inversion for the moment tensor components is reproduced in Figure 4. In this example the radial (R), vertical (Z) and transverse (T) displacements at three of the near-source recording sites illustrate the simple waveforms and thus validate the application of layered Green's functions for the purposes of moment tensor retrieval. The vertical and radial components of displacement show significant azimuthal symmetry reflective of the isotropic part of the source function (M_I). The transverse displacements show changes in polarity with azimuth as a result of the deviatoric source component (M_{ij}^D).

In order to complete the moment tensor inversions, a set of Green's functions or propagation path effects must be calculated for the near-source region around the Coalora explosion. Using downhole acoustic logs in Yucca Flats, geological models of the region, and reflection surveys in the source area a plane layered velocity-density model was developed and Green's functions calculated. These numerical propagation path effects in combination with the observational data were substituted into Equation 5, which was solved frequency by frequency for the six elements of the moment tensor. The resulting moment tensor can be multiplied by the Green's function to produce a synthetic displacement that can be compared to the observational data. This comparison can be used to judge the adequacy of both the source and propagation model. Comparison between the observed and calculated near-source ground motions for the Coalora

explosion are reproduced in Figure 5. The fit to the data is excellent. Since the original representation (Equation 5) is linear in both the source and the propagation, trade-offs between the two can exist while the good quality of the fits to the data is retained. For this reason it is important to constrain the Green's functions or propagation path effects as tightly as possible with supplementary information as was done in this case. It is also important to explore the physical interpretation of the source model for consistency with additional observations from within the source volume or nonlinear region.

COALORA Source Representation

The moment rate tensor (time derivative) and moment tensor for Coalora as determined by the inversion of the near-source data are reproduced in Figure 6. The diagonal elements of the source or isotropic components (M_{xx}, M_{yy}, M_{zz}) are found to dominate—its peak strength is 8×10^{20} dyne-cm. In order to use this isotropic moment characterization of the explosion seismic source in coupling studies, inversions of data from many different explosions would have to be conducted.

The force couples (M_{xy}, M_{xz}, M_{yz}) are at least an order of magnitude smaller—not much earthquake-like motions (driven motions/tectonic release). It is this part of the source representation that is used to model the transverse motions that were observed from the explosion.

The moment tensor displays a secondary, longer period arrival that is largest on the M_{33} component. The size of this secondary source falls right in the middle of our estimate of moment from the spall zone data. Its time delay relative to the initially spherically symmetric component of the moment tensor is also consistent with the spall secondary source model. This comparison of the moment tensor with source information within the nonlinear region illustrates how the seismic data and data/models from within the nonlinear region can improve one's confidence in the interpretation of the moment tensor resulting from data inversion.

Conclusion

The analysis of near-source data from the Coalora explosion has been used to illustrate how seismologists produce their equivalent elastic source representation, its relationship to propagation path effects, and its *physical interpretation.* It is really this last point that I see as the focus of the Durango meeting. We seismologists sit outside the source region, V_o, making ground motion measurements. Inside V_o are many nonlinear, dynamic processes that must be taken into account when interpreting the source model.

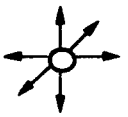
The moment tensor representation provides a linear relation between the source and propagation path effects. With a set of numerical Green's functions, observational data from the elastic region can be used to constrain the source model. The importance of secondary source processes such as spall can be quantified by such a procedure, particularly when data and calculations from within the nonlinear zone are available to aid interpretation.

SIMPLE MOMENT TENSOR INTERPRETATIONS

$$M_{ij} = \frac{M_{ii}}{3} + M_{ij}^{D}$$

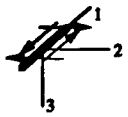
SEPARATION INTO ISOTROPIC AND DEVIATORIC COMPONENTS

$$M_I = \frac{M_{ii}}{3} = 4\pi\rho\alpha^2\Psi(t)$$



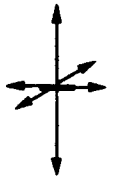
ISOTROPIC

$$M_{ij}^{D} = \mu A\bar{u}\begin{bmatrix} 0 & 1 & 0 \\ 1 & 0 & 0 \\ 0 & 0 & 0 \end{bmatrix}$$



DEVIATORIC FORCE COUPLE

$$M_T = \delta\bar{u}_3 A\begin{bmatrix} \lambda & 0 & 0 \\ 0 & \lambda & 0 \\ 0 & 0 & \lambda+2\mu \end{bmatrix}$$



SPALL/TENSILE FAILURE

Figure 1. Simple decompositions of the moment tensor are pictorially illustrated. Any moment tensor can be decomposed into an isotropic (M_{ii}) and deviatoric component (M_{ij}^{D}). The isotropic component is proportional to a purely volumetric source while a shear dislocation can be represented in terms of the deviatoric component. In the case of explosions, the secondary spall source can be represented as the opening of a tensile crack (M_T).

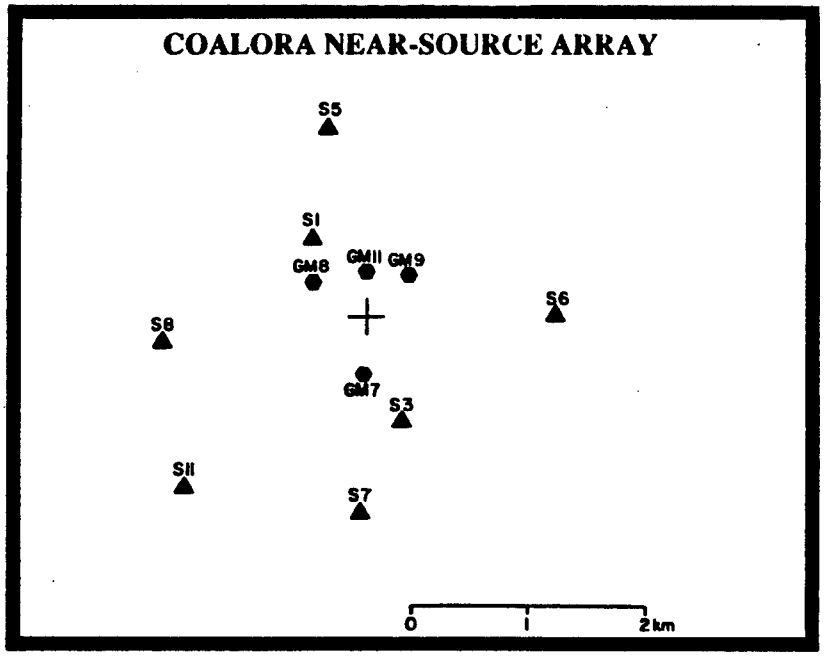
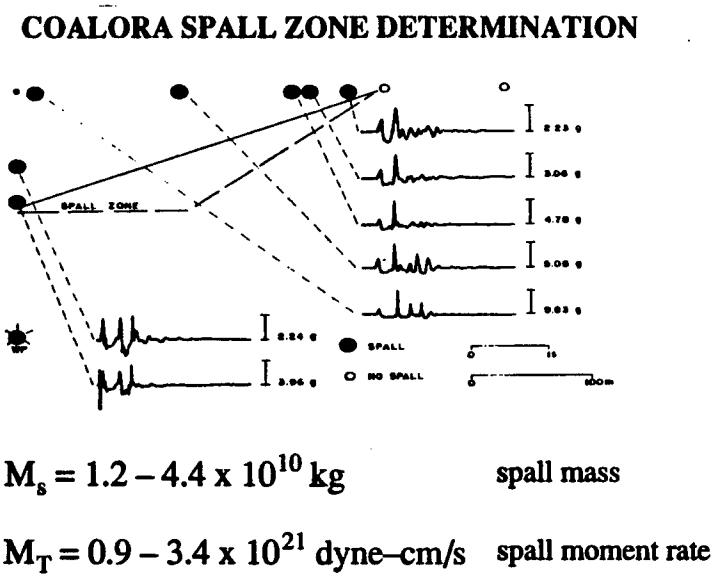


Figure 2. Plan view of an array of three-component accelerometers deployed at the free surface around the nuclear explosion, COALORA.



$M_s = 1.2 - 4.4 \times 10^{10}$ kg spall mass

$M_T = 0.9 - 3.4 \times 10^{21}$ dyne–cm/s spall moment rate

Figure 3. Vertical section displaying accelerograms from downhole and surface circles represent vertical accelerometer records that showed the characteristic -1 g dwell indicative of spall. Solid and heavy dashed lines are assumed boundaries for the depth of the spall zone.

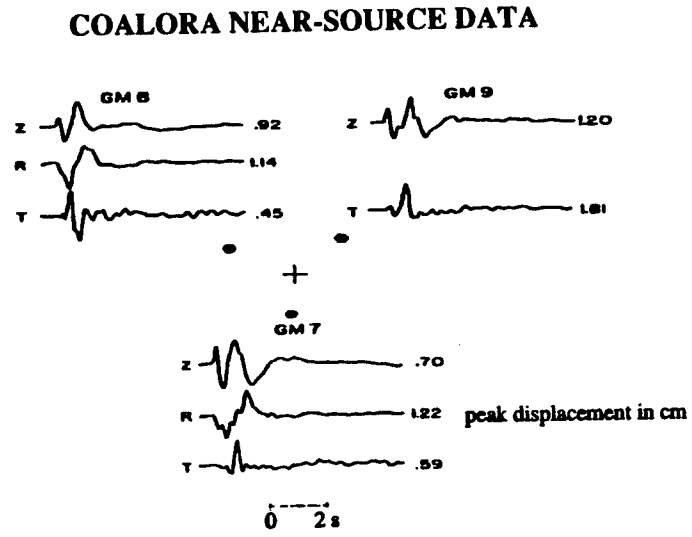


Figure 4. Displacement waveforms (accelerations integrated twice) at three azimuths from the source and at a range of 549 m. Vertical (Z), radial (R) and transverse (T) displacements are given.

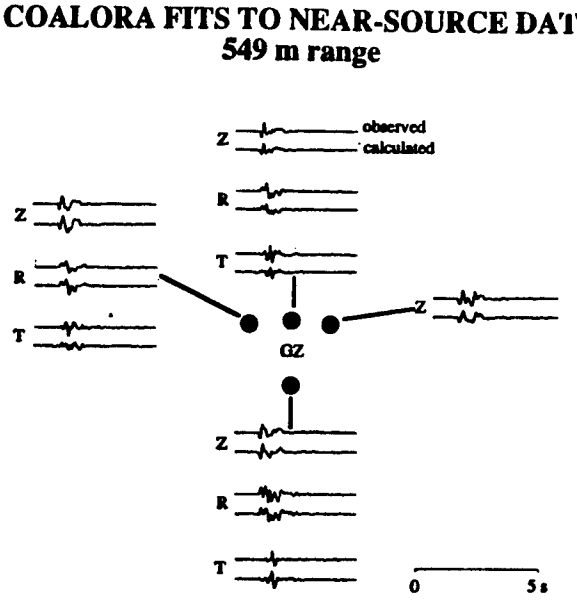


Figure 5. Observed and calculated seismograms from moment tensor inversion of the COALORA data.

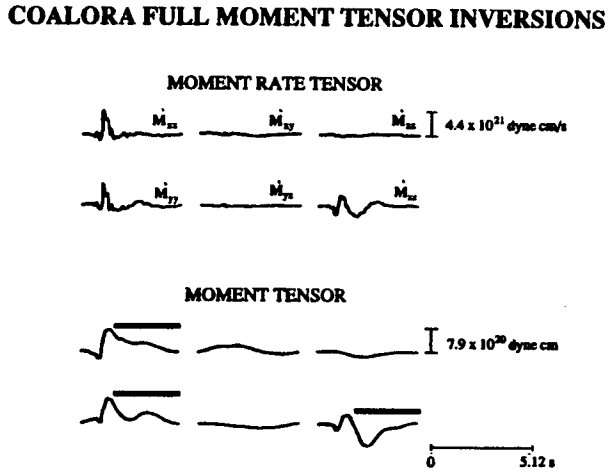


Figure 6. The moment rate ($\dot{M}_{ij}$) and moment (M_{ij}) tensors from an inversion of the moment tensor is highlighted with a bar.

2D and 3D Numerical Modeling of Seismic Waves from Explosion Sources

K. L. McLaughlin, J. L. Stevens, T. G. Barker, S. M. Day*, and B. Shkoller

S-CUBED, P.O. Box 1620, La Jolla, CA 92038.

*Department of Geological Sciences, SDSU, San Diego, CA 92182

Introduction

Over the last decade, nonlinear and linear 2D axisymmetric finite difference codes have been used in conjunction with far-field seismic Green's functions to simulate seismic waves from a variety of sources. In this paper we briefly review some of the results and conclusions that have resulted from numerical simulations and explosion modeling in support of treaty verification research at S-CUBED in the last decade. We then describe in more detail the results from two recent projects. Our goal is to provide a flavor for the kinds of problems that can be examined with numerical methods for modeling excitation of seismic waves from explosions. Two classes of problems have been addressed; nonlinear and linear near-source interactions. In both classes of problems displacements and tractions are saved on a closed surface in the linear region and the representation theorem is used to propagate the seismic waves to the far-field.

Nonlinear Source Modeling

In one class of problems, nonlinear near-source physics has been modeled using 2D axisymmetric nonlinear finite difference codes such as CRAM and STELLAR. These codes include the effects of geologic layering, the free surface, nonlinear yielding, pore crushing, tensile failure, and gravitational acceleration. This class of problems has focussed upon the nonlinear sources of seismic waves. The motion is propagated outward from the nonlinear source region by finite differences to a region of linear elastic motion. The displacements and tractions are monitored in this linear region on a closed surface and then the representation theorem (Aki and Richards, 1980) is used to propagate seismic waves to regional or teleseismic distances. Some of the work conducted on these problems is reviewed in Stevens et al. (1991). Issues of interest that have been examined using these methods include:

explosion triggered tectonic strain release

nonlinear free-surface interaction (spall) and dependence upon depth of burial

effects of depth of burial including cratering upon seismic radiation

effects of topography above the explosion and dependence upon depth of burial

decoupling in ellipsoidal cavities and

complex hydrodynamic sources.

Both teleseismic and regional waves have been simulated from these sources using far-field body wave propagator, modal summation, and reflectivity Green's functions. A few of the results from these numerical investigations include:

a model was developed for tectonic release as a mechanism for long-period Rayleigh phase shifts and Love excitation from explosions (Day et al., 1987),

tectonic release was found to be insignificant for short-periods (McLaughlin et al., 1988),

spall was found to be an insignificant source of long-period radiation (Day et al., 1983),

a detailed seismic model for spall was developed and applied to P waves and Lg (Barker et al., 1990a, 1990b, and McLaughlin et al. 1990),

the effects of cratering on P waves was quantified (McLaughlin et al., 1988),

seismic radiation was found to be insensitive to hydrodynamic source complexity (Davis et al., 1993), and

Lg excitation from nonlinear free-surface interaction was found to be insensitive to scale depth of burial, and topography above the source.

In each of these investigations, nonlinear source models have been propagated to the far-field using the representation theorem. We now briefly describe some results of nonlinear numerical simulations to examine the sensitivity of Lg excitation to scaled depth of burial.

Lg Excitation As A Function Of Scaled Depth

Based on empirical observations RMS Lg has been recognized as a stable and reliable yield indicator (Hansen et al., 1990; and Patton, 1990). Several nonlinear simulations in granite were used to examine the theoretical basis for mb(Lg):yield stability against variations in near surface topography above the source and in variations in scaled depth of burial. Figure 1 illustrates the numerical problem. Three calculations were conducted at yields of 14 Kt and depths of 144 and 261 m. One calculation was conducted at a yield of 28 Kt and a depth of 144 m. Three of the calculations were performed with a 6.7 degree sloping free surface. One of the calculations (14 Kt and depth of 144 m) was performed with a flat free-surface.

Figure 2 illustrates the volumes of nonlinear yielding that were predicted by each calculation. Dark regions illustrate the volumes that initially yielded under compression. Hashed regions illustrate volumes of rock that failed in tension. Note the rings of tensile failure parallel to the free surface. These rings of tensile failure are related to the spall of material as the compressive wave reflects off the free-surface as a tension wave.

Displacements and tractions were monitored on a cylindrical surface surrounding the region of failure and the representation theorem was used to compute synthetic seismograms at a distance of 400 km. Modal summation was used to compute the P-SV Lg signals in the 0 to 1 Hz bandwidth. Modes 2 through 15 are shown in Figure 3.

The RMS Lg signal strength was then computed for each synthetic seismogram. The results indicate a remarkable insensitivity of the RMS Lg amplitude to scaled depth of burial. The three 14 Kt simulations differ in RMS Lg amplitude by less than 11% or less than 0.05 magnitude units. The RMS Lg amplitude from the 28 Kt simulation is 2.05 times larger than the 14 Kt simulation. These results show remarkable stability of RMS Lg to variations in scaled depth of burial and/or a sloping free-surface. These numerical simulations show that the observed RMS mb(Lg):yield

stability has a theoretical justification.

It is believed that much of the Lg excitation is from the non-linear free-surface interaction. Detailed modeling of the nonlinear free-surface interaction in these calculations and others have shown that spall momentum is proportional to yield over a wide range of scaled depths of burial. The combined results from these and other numerical simulations in granite and tuff spanning the range from 1 to 125 Kt and scaled depths of burial from 47 to 260 m/$Kt^{1/3}$ indicate that spall momentum is generally between 2 and 4 x 10^{10} Nt-s/Kt. These numerical experiments indicate that scaled depths of burial in excess of 260 m/$Kt^{1/3}$ are required to significantly reduce spall from contained nuclear explosions.

Linear Elastic Near-Source Modeling

In a second class of problems, linear finite difference codes are used to model elastic wave propagation near the source. In these linear-elastic scattering calculations lateral heterogeneity near the source introduces complexity into the seismic radiation that is observed in the far-field. For several applications, the representation theorem has been used to propagate modes and body waves to regional and teleseismic distances. Both 2D axisymmetric and 3D scattering problems have been considered. In two applications, a Fresnel-Kirchoff integral method is used to propagate surface waves from 3D calculations (see McLaughlin et al. 1992a). A few of these problems include:

2D axisymmetric long period surface waves from explosion sources within mountains and within islands (Stevens et al. 1991),

2D axisymmetric long period surface waves from explosions in low velocity basins surrounded by high velocity country rock (Stevens et al. 1991),

2D axisymmetric high frequency waves from explosions in high velocity salt domes surrounded by low velocity sediments,

3D long period surface waves from explosions located in a subduction zone (McLaughlin et al. 1992a),

3D long period surface wave propagation across the Barents Sea (McLaughlin et al. 1991),

3D strong motion shaking in low velocity basins surrounded by high velocity country rock (McLaughlin et al. 1992b), and

3D seismic radiation from an explosion source located behind a quarry face.

Although 3D finite difference modeling was conducted as early as the late 1970's (see Day 1980), 2D finite differences have remained the standard modeling tool for over a decade because of limited memory and speed of computers. However, as computer speed and memory has increased, 3D modeling has increasingly become feasible. 3D modeling was initially limited to long-period seismic waves but with recent advances in recursive grid refinement (RGR) we find that we can perform useful 3D calculations with about the same amount of memory and computer time that are required for a conventional 2D calculation. The usable bandwidth of 3D calculations has therefore been significantly increased in the last year. In the following section we

describe a recent calculation that explores seismic radiation from behind a quarry face.

An Explosion Behind A 3D Quarry Bench

As seismic verification interests turn to the problems of monitoring small events it has become clear that large industrial blasts are an important part of the detection and discrimination problem. Large quarry blasts must be identified and separated from the background of earthquakes. Besides the problem of identifying these events by seismic means, large quarry blasts could be used to hide small clandestine tests. It is unlikely that these clandestine tests will occur in areas where we have extensive experience in discrimination of explosions and earthquakes. Therefore it is necessary to understand the physics behind seismic characteristics of large quarry blasts, explosions, and earthquakes in order to formulate a rational approach to identify these sources by seismic means.

Some recent work at S-CUBED has focussed on the importance of rock movement (spall) from quarry blasts as a seismic source as well as the nature of the explosion behind the quarry face. We have found that in standard quarry practices the spall of material from the quarry face should an important a source of seismic radiation (Barker, et al. 1993a). In addition, it was found that the presence of a steep free-surface interface adjacent to the explosion can have profound effects upon the radiation from a point explosion (Barker et al., 1993b). Barker et al. (1993b) show that the presence of a quarry bench adjacent to the point explosion results in an apparent reduction of the horizontal couple perpendicular to the quarry bench. This results in enhanced SV radiation over that of an explosion in a half-space and the P waves are reduced in directions perpendicular to the quarry face. This previous work was based on 2D finite differences and could not address 3D aspects of the problem. To this end we have conducted 3D finite difference simulations of elastic waves scattered from an explosion located immediately behind a quarry face.

Several 3D linear elastodynamic calculations were performed using TRES-3D with recursive grid refinement (RGR). TRES-3D is a full elastic-plastic 3D finite difference code modeling the complete elastic field including all orders of reflection, refraction, and scattering. TRES-3D has recently been updated to function with RGR. Calculations are designed to investigate the effects of an explosion behind a quarry face compared to an explosion in a half-space. Figure 4 shows the geometry of the explosion source behind a quarry face. The explosive source is introduced as a pressure excess with a specified time history in a zone behind the quarry face. The quarry face is 80 m tall and the quarry is 800 m square. The plane through the source perpendicular to the quarry face is considered a plane of reflection symmetry for the purposes of the calculation.

Three levels of RGR were used (see Figure 5). With RGR, finer grids are placed within coarser grids to refine the regions of interest. This is a useful strategy for this problem because the model velocities increase with depth (increasing Z) and because we wish to describe the quarry face with finer detail than is required to propagate waves at depth in the model. Accuracy of the finite difference equations require that we maintain a minimum number of zones per wavelength at the upper frequency of

interest. Therefore we choose a coarse gridding that is sufficient to support undispersed waves at depth and we choose finer zoning near the surface where the wavelengths are short. The velocity model chosen has a P wave velocity of 2500 m/s at the surface and 4000 m/s at depth. For this calculation the coarsest grid (level 1) has a zoning of 160 m spacing. Grids on levels 2 and 3 have zonings of 80m and 40m respectively. The finite difference calculations are therefore accurate to about 3.6 Hz at the surface and 1.5 Hz at depth. Each grid was the same logical dimension of 60 by 40 by 40 zones. We used 1 grid at level 1, 2 grids at level 2, and 6 grids at level 3, for a total of 9 grids. In this manner, a total of only 0.864 million zones were required instead of 6.144 million zones that would have been required with conventional uniform gridding of 40 m throughout the volume. Because we wish to avoid reflections from the outer grid boundaries, we use a volume large enough that reflections from the outer boundaries can be ignored. By using RGR we save computer memory (0.864 vs 6.144 million zones) and the total number of zone-cycles is reduced by two orders of magnitude (27 million vs 2.5 billion zone-cycles). Each calculation required about 8 hours of wall clock time on an SGI Indigo R4000 workstation. Comparison benchmarks on the fully vectorized TRES-3D (with RGR) indicate that these computations would require about 15 to 20 minutes of CPU time on a Cray YM-P. Consequently, not only has 3D modeling become economical, 3D modeling has become feasible on workstation class computers with reasonable turn-around times.

Figure 6 shows the free-surface vertical velocity at time = 0.8 sec during the calculation for a region 4960 m by 3360 m corresponding to the top of the level 2 grids surrounding the quarry. The rectangular region of the quarry is clearly visible in the plot since it has no motion at this level in the grid. The motion near the source has been clipped to make the motion further away from the source more apparent. Note the asymmetry in the radiation. Radiation across the quarry is substantially reduced. Figure 7. shows seismograms illustrating the differences in the P-wave radiation from the quarry. Although preliminary, analysis suggests that the presence of the quarry face introduces an apparent radiation pattern to the explosion and SH radiation is generated. The apparent explosion couple perpendicular to the quarry face is reduced and the explosion acts like a compensated linear vector dipole (CLVD) source. Our plans are to compute far-field motion from the source using the representation theorem. Using these calculations as a guide we can formulate simple models for the seismic excitation from quarries.

References

Aki, K. and P. G. Richards (1980). **Quantitative Seismology - Theory and Methods,** W. H. Freeman and Co., San Francisco.

Barker, T. G., and S. M. Day (1990). A Simple Physical Model for Spall From Nuclear Explosions Based Upon Two-Dimensional Nonlinear Numerical Simulations, **Geophysics Laboratory Report GL-TR-90-0189.**

Barker, T. G., S. M. Day, K. L. McLaughlin, B. Shkoller, and J. L. Stevens (1990). An Analysis of the Effects of Spall on Regional and Teleseismic Waveforms Using Two-Dimensional Numerical Modeling of Underground Explosions, **Geophysics Laboratory Report GL-TR-90-0126.**

Barker, T. G., K. L. McLaughlin, and J. L. Stevens (1993a). Numerical Simulation of Quarry Blast Sources, **S-CUBED Report SSS-TR-93-13859,** Submitted to Phillips Laboratory.

Barker, T. G., K. L. McLaughlin, J. L. Stevens, and S. M. Day (1993b). Numerical Simulations of Quarry Blast Sources: The Effects of the Bench, **S-CUBED Report SSS-TR-93-13915,** Submitted to Phillips Laboratory.

Davis, C. G., W. E. Johnson, J. L. Stevens, N. Rimer, T. G. Barker, E. J. Halda, E. Bailey, and W. J. Proffer (1993). Seismic Signals from Axisymmetric Radiation - Hydrodynamic Source Calculations, **Los Alamos National Laboratory Report LA-12506-MS.**

Day, S. M. (1980). Three-Dimensional Finite Difference Simulation of Fault Dynamics, **S-CUBED Report SSS-R-80-4295.**

Day, S. M., J. T. Cherry, N. Rimer, and J. L. Stevens (1987). Nonlinear Model of Tectonic Release From Underground Explosions, **Bull. Seism. Soc. Am., 77,** pp 996-1016.

Day, S. M., N. Rimer, and J. T. Cherry (1983). Surface Waves From Underground Explosions With Spall: Analysis of Elastic and Nonlinear Source Models, **Bull. Seism. Soc. Am., 73,** pp 247-264.

Hansen, R. A., F. Ringdal, and P. G. Richards (1990). The Stability of RMS Lg Measurements and Their Potential for Accurate Estimation of the Yields of Soviet Underground Explosions, **Geophysics Laboratory Report AFGL-TR-90-0061.**

McLaughlin, K. L., T. G. Barker, S. M. Day, B. Shkoller and J. L. Stevens (1988). Effects of Depth of Burial and Tectonic Release on Regional and Teleseismic Explosions Waveforms, **Geophysics Laboratory Report AFGL-TR-88-0314.**

McLaughlin, K. L., T. G. Barker, and S. M. Day (1990). Implications of Explosion Generated Spall Models: Regional Seismic Signals, **Geophysics Laboratory Report GL-TR-90-8133.**

McLaughlin, K. L., T. G. Barker, S. M. Day, B. Shkoller, and J. L. Stevens (1992a). Effects of Subduction Zone Structure on Explosion-Generated Rayleigh Waves: 3-D Numerical Simulation, **Geophys. J. Int. 111,** pp 291-308.

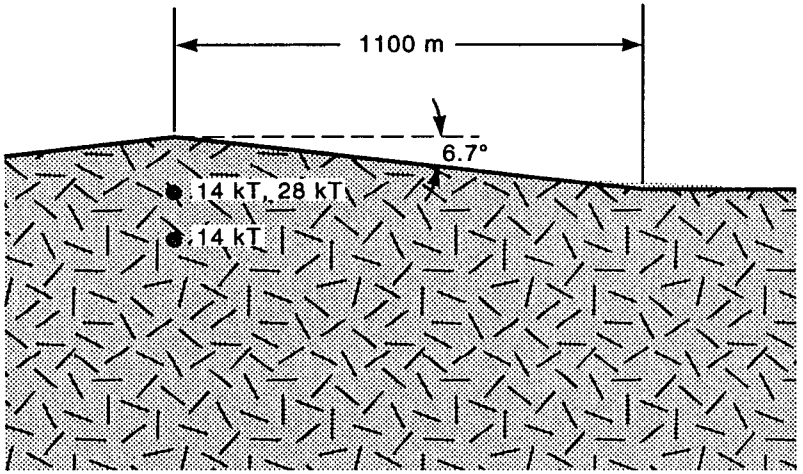
McLaughlin, K. L., T. G. Barker, J. L. Stevens, B. Shkoller, and S. M. Day (1991). Three-Dimensional Finite Difference Modeling of Surface Wave Propagation Across the Barents Shelf, **S-CUBED Report SSS-TR-91-12828,** submitted to Geophys. J. Int.

McLaughlin, K., J. Stevens, and B. Shkoller (1992b). Recursive Grid Refinement For Finite Difference Algorithms, **EOS 73 #43,** p 340.

Patton H. J. (1988). Application of Nuttli's Method to Estimate Yield of Nevada Test Site Explosions Recorded on Lawrence Livermore National Laboratories Digital Seismic System, **Bull. Seism. Soc. Am. 78,** 1759-1772.

Stevens, J. L., T. G. Barker, S. M. Day, K. L. McLaughlin, N. Rimer, and B. Shkoller (1991). Simulation of Teleseismic Body Waves, Regional Seismograms, and Rayleigh Wave Phase Shifts Using Two-Dimensional Nonlinear Models of Explosion Sources, **Explosion Source Phenomenology, Geophysical Monograph 65, American Geophysical Union,** pp 239-252.

Stevens, J. L., K. L. McLaughlin, S. M. Day, and B. Shkoller (1991). Two-Dimensional Axisymmetric Calculations of Surface Waves Generated by an Explosion in and Island, Mountain, and Sedimentary Basin, **S-CUBED Report SSS-TR-91-12833,** in press Geophys. J. Int.



Slope 1, 2, 3, & 4 Calculations

	Y(KT)	DOB(m)	SDOB(m/KT$^{1/3.4}$)	Slope
SLOPE 1	14	144	66	6.7
SLOPE 2	14	261	120	6.7
SLOPE 3	28	144	54	6.7
SLOPE 4	14	144	66	0.0

Figure 1. Four nonlinear 2D axisymmetric simulations of explosions in granite were conducted at 14 KT and 28 KT, depths of 144 or 261 m, and free-surface slopes of 6.7 or 0.0 degrees.

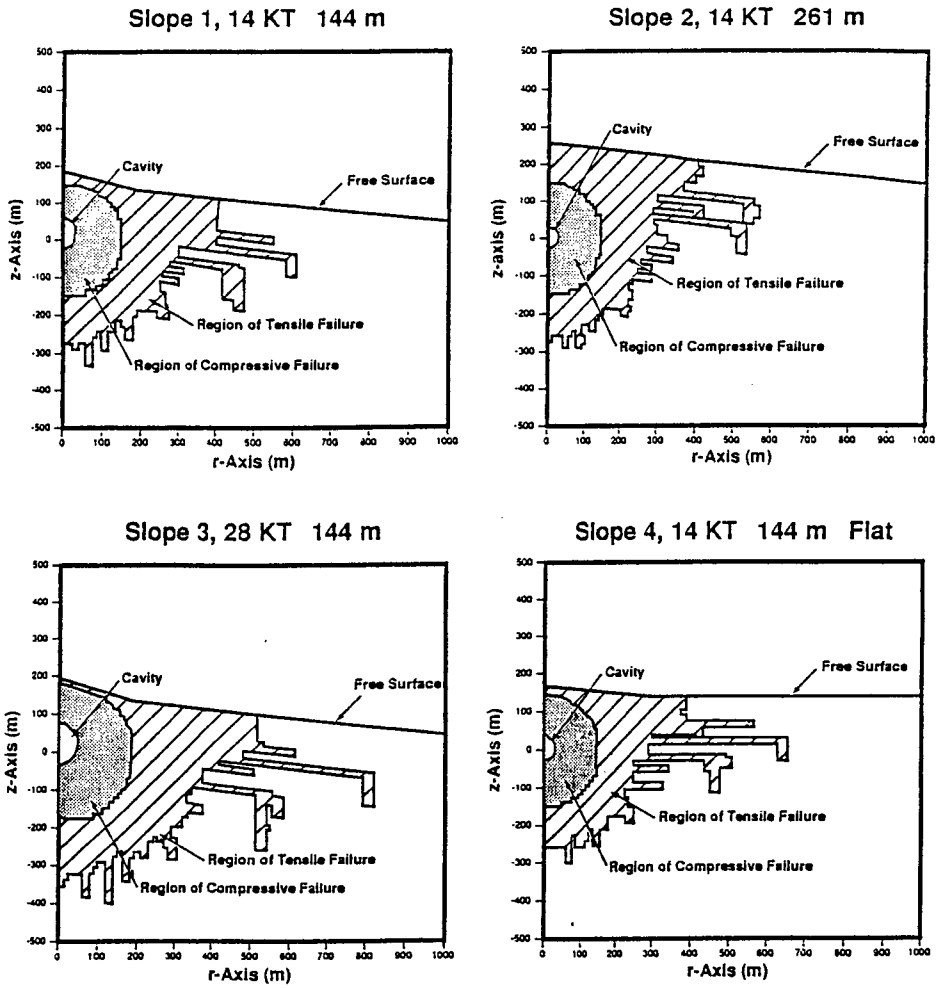


Figure 2. The regions of failure are shown around each cavity. Regions that failed mainly in tension and compression are highlighted. In all four cases. there was significant spall at the free-surface.

HIGHER MODES (Lg)

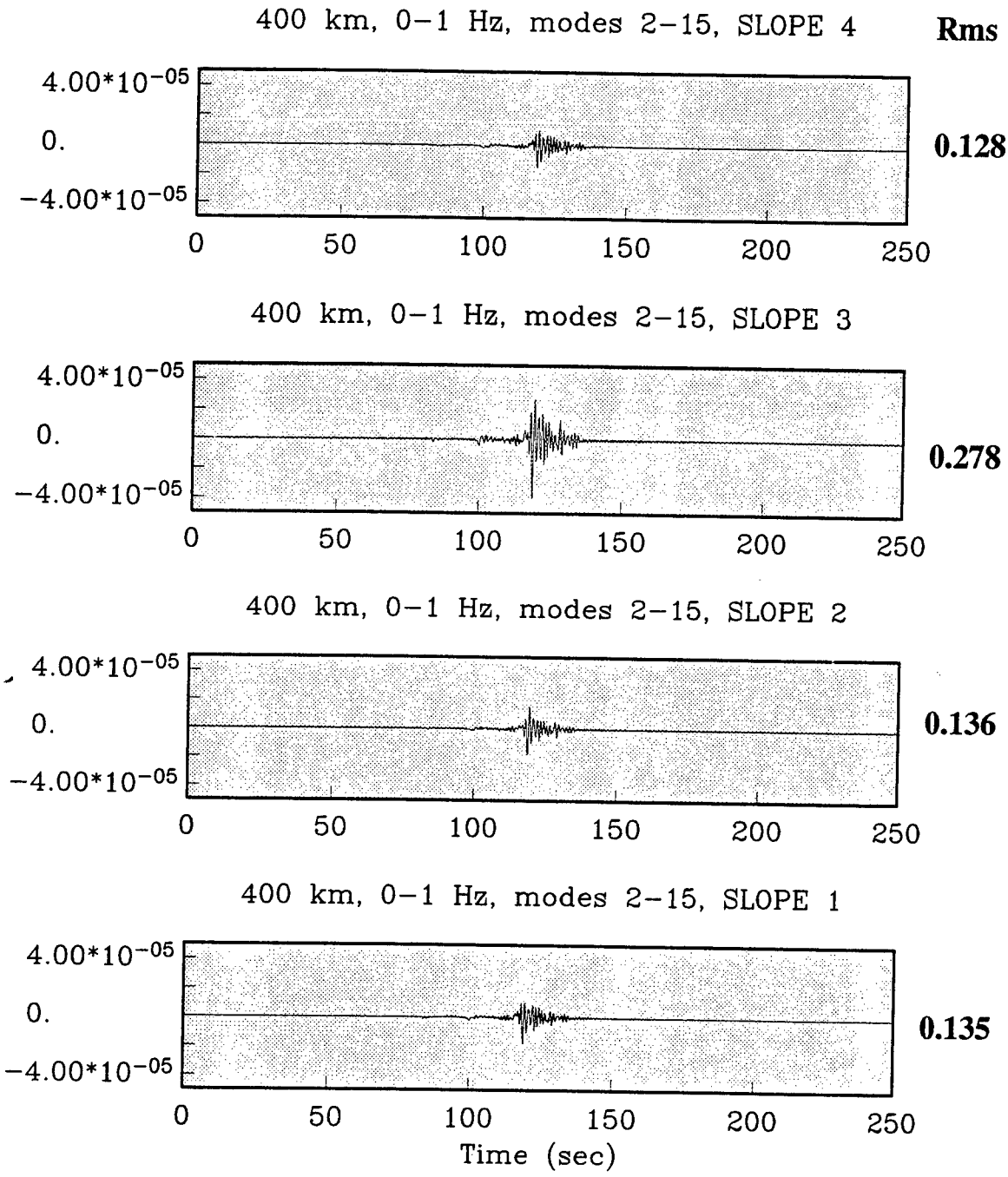


Figure 3. Vertical component 0 to 1 Hz synthetic Lg waveforms at a distance of 400 km are shown for the four simulations. Lg was synthesized by modal summation using modes 2 through 15. The fundamental Rayleigh (mode 1) was not included to emphasize Lg. The RMS Lg amplitudes vary by less than 11% for cases Slope 1, 2, and 4. The RMS Lg amplitude of Slope 3 (28 KT) is 2.05 times larger than Slope 1 (14 KT).

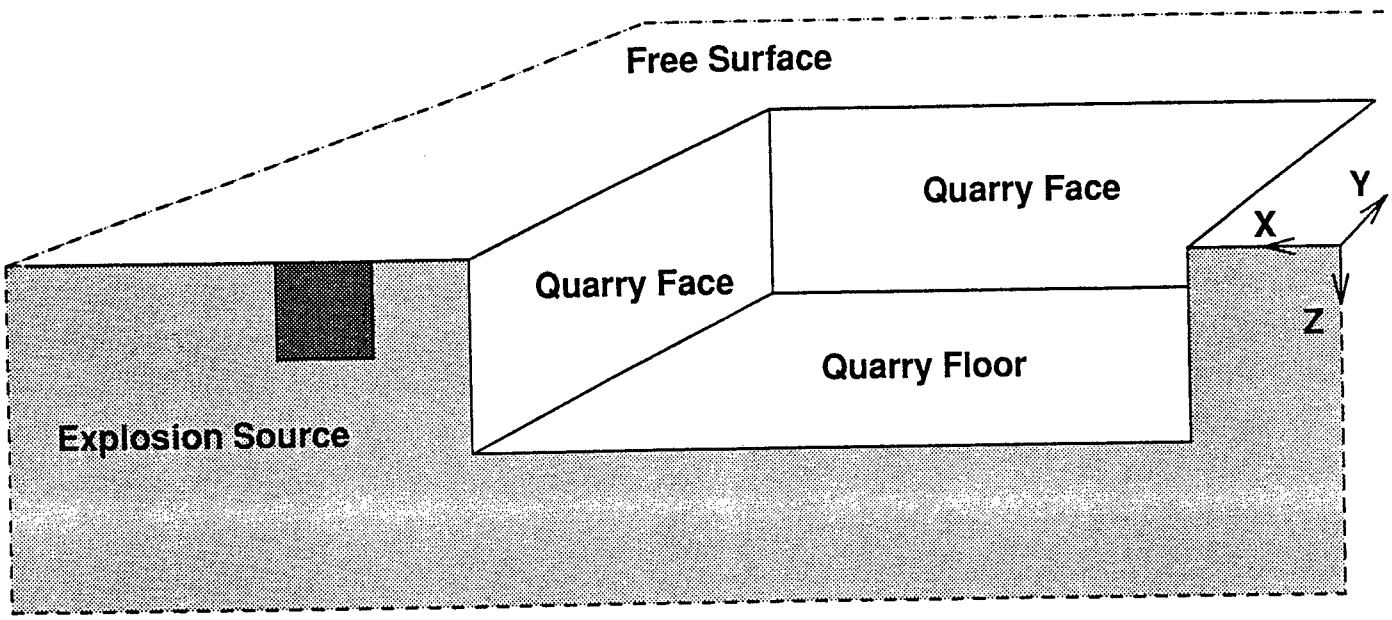


Figure 4. Geometry of the explosive source behind the quarry face. The quarry face is 80 m high, and the quarry is 800 m square.

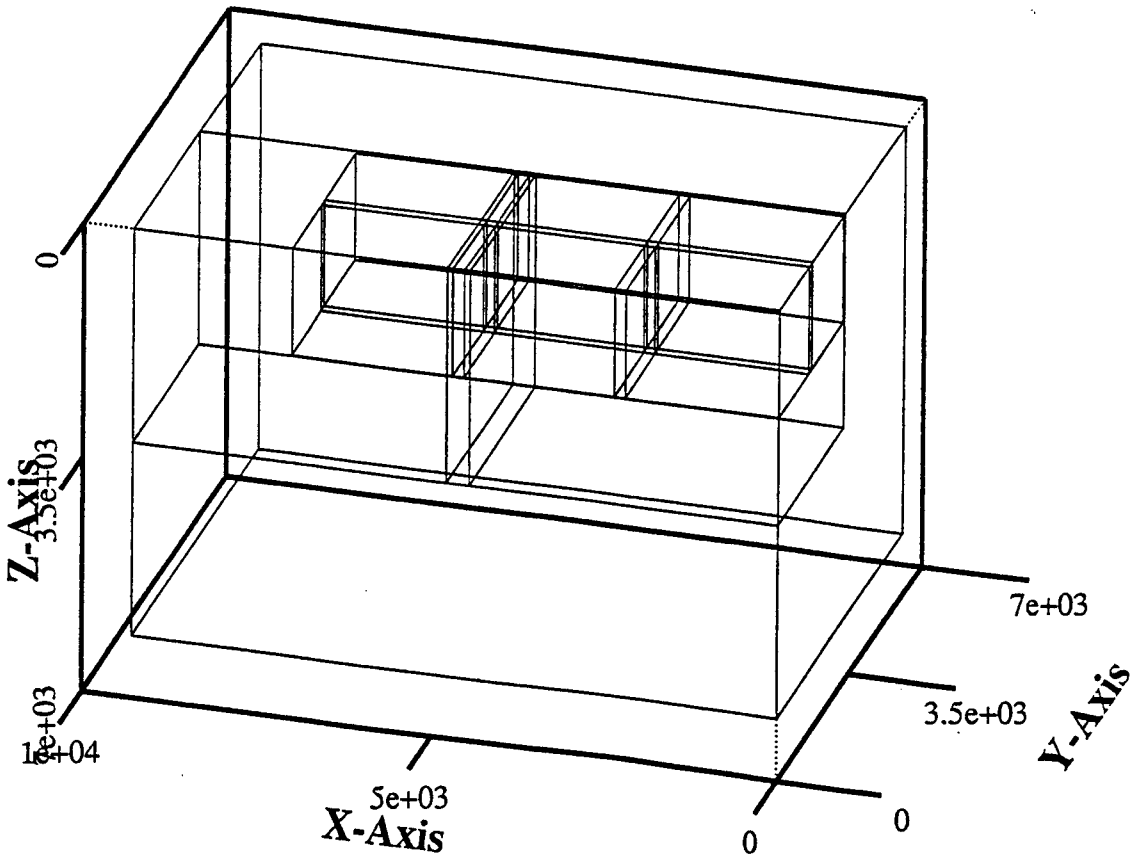


Figure 5. Three levels of nested grids are shown in 3D. The coarsest grid (level 1) is zoned at 160 m, level 2 is zoned at 80 m, and the finest level is zoned at 40 m. Each level has a refinement of a factor 2. The source and the quarry are located at the top of the model in one of the finest zoned grids.

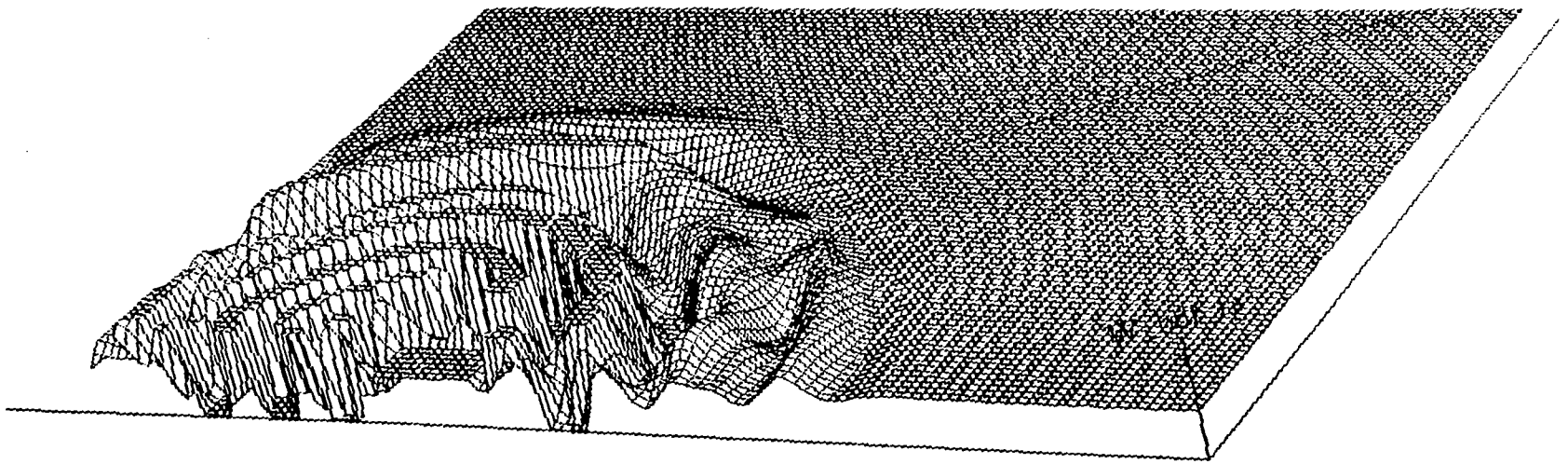


Figure 6. Vertical free-surface velocity from a grid immediately surrounding the quarry. The region displayed is 4960 m by 3360 m. The motion near the source has been clipped to make the wavefront further from the source more visible. Attenuated propagation across the quarry is readily apparent.

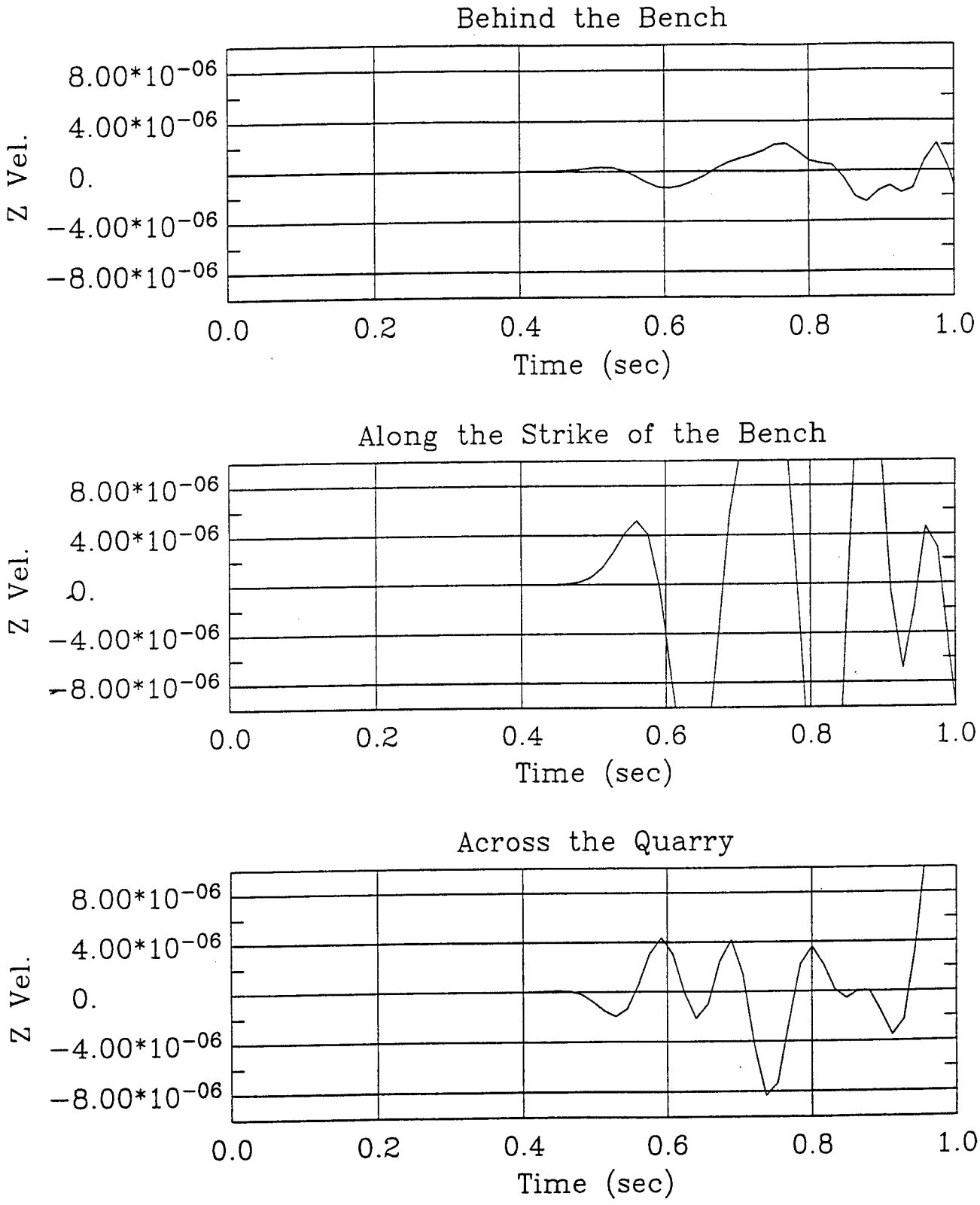


Figure 7. Three vertical component seismograms are shown at the same scale and the same range. At the top is a receiver behind the bench of the quarry, in the middle is a direction along the quarry face, and at the bottom is a receiver across the quarry. The initial P wave is severely attenuated for directions perpendicular to the face of the quarry consistent with the theory that the quarry face reduces the effective explosion couple perpendicular to the free-surface.

THIS PAGE INTENTIONALLY LEFT BLANK.

DIRECTIONAL EXCITATION OF Rg DUE TO RIPPLE-FIRED EXPLOSIONS: 2-DIMENSIONAL FINITE-DIFFERENCE SIMULATIONS[1]

Rong-Song Jih (Teledyne Geotech Alexandria Laboratories, 314 Montgomery Street, Alexandria, VA 22314-1581)

INTRODUCTION

A major issue for the Non-Proliferation Treaty is the discrimination of large chemical explosions from possible clandestine or small nuclear tests. Unless discrimination is possible, the numerous mining blasts could give ample opportunity for concealing clandestine tests. Rippled-fired explosions are commonly used to fragment rocks during quarry and open-pit mining. The periodicity inherent in the ripple firing could produce a seismic reinforcement at the frequency of the delay between shots or rows. It has been suggested that the convolution of a single explosion with a comb function of variable spacing and variable amplitude can be used to model the distinctive signature of ripple firing (Stump, 1988; Anderson and Stump, 1989; Smith, 1989; Hedlin *et al.*, 1990; Chapman *et al.*, 1992; Reamer *et al.*, 1992; and many others). Baumgardt and Ziegler (1988) delicately demonstrated that the incoherent array-stack spectra can be used to identify some multiple shots recorded at NORSAR. By superpositioning the waveform due to a single shot with proper time delay, they were able to model the source multiplicity under the assumption that the spatial spreading of the shots is negligible with respect to the distance to the receiver. The work by Stump *et al.* successfully characterized the major features of the wavefield due to ripple firings at near-source ranges.

There are, however, some other wave excitation characteristics of ripple-fired explosions which are not predicted by such spectral or waveform superposition approaches. In this study, the linear finite-difference (LFD) method is utilized to seek some insights into the ripple-fired explosions using various possible combinations of the experimental set-up. The LFD method has the advantage that the solution contains all conversions and all orders of multiple scattering. It permits examinations of fairly general models with arbitrary complex variations in material properties and free-surface geometry. Furthermore, it doesn't require many assumptions commonly invoked in other theoretical approaches. The basic limitations to the LFD method or the finite-element method are the computational cost and memory requirements. These constrain the size of the grid and the number of time steps that can be calculated over a reasonable time frame. Several non-standard features have been incorporated into the 2-D LFD code used in this study: [1] explicit boundary conditions for the polygonal free-surface topography (Jih *et al.*, 1988), [2] a pure Rayleigh-wave packet as yet another initial condition (McLaughlin and Jih, 1986,1987; Jih *et al.*, 1988), [3] the marching grid technique for extending the propagation distance in the lateral direction (Jih *et al.*, 1989), and [4] the strain filter for far-field body wave synthetics (Stead and Helmberger, 1989; Jih *et al.*, 1989).

SIMULATION RESULTS

Several previous theoretical studies with spectral superposition approach (*e.g.*, Smith, 1989; Greenhalgh, 1980) suggest that for ripple firings with simple configurations and precise delay, the spectrum will be reinforced at every $1/\Delta t$ Hz, where the Δt is the delay time between the shots. However, our numerical experiments indicate that even with a very simple, linearly distributed shot array in the half space, the frequencies at which the amplitude reinforcement could occur also depend on the relative azimuth angle and take-off angle with respect to the rupture direction. Figure 1 gives the spectral ratios of *P*-wave synthetics to that due to a single explosion. It is clear that the reinforcement does occur at exactly every 50 Hz along the orthogonal direction, consistent with Smith's prediction (1987, 1989). For

[1]Work supported under Phillips Laboratory contract F29601-91-C-DB23.

other directions, however, the frequency at which the enhancement would occur is affected due to the *Doppler Effect.* Suteau-Henson and Bache (1988) and Smith (1989) reported that the spectral scalloping from mine blasts may not always be observed. Kim *et al.* (1991) also found that seismograms from the same quarry recorded at the same station could have distinct spectral characteristics. This phenomenon has been generally attributed to the considerable fluctuation in delay times and sub-charge sizes. Alternatively, Anderson and Stump (1989) suggest that different Green's functions must be utilized for each of the sources in an explosive array. Such spatial effects can lead to significant azimuthal variation in the radiated wavefield, as illustrated in Stump and Reamer (1990). Results shown in Figure 1 appear to be in agreement with Stump's observations.

Figure 2 gives the vertical component of the displacement field of 7 ripple-fired explosions. Of interest is that both R_g and S* are strongly enhanced in the forward direction. In fact, one of the standard industrial practices in reducing potential damage caused by ground vibration is to detonate ripple shots in a direction away from the structures of concern (Dick *et al.*, 1983). An immediate implication of this exercise on the discrimination problem is that the lack of R_g is not necessarily indicative of deep sources. The R_g could be weak simply because the blast was set off in a direction away from the receiver. Furthermore, although path effects such as the anelastic attenuation and the scattering by shallow heterogeneity and topography in the upper crust can reduce R_g significantly, as demonstrated by Jih *et al.* (1988) and McLaughlin and Jih (1986, 1987), the reported lack of R_g in many seismograms from known quarry blasts could also be due to an intrinsic source effect (such as the shooting pattern) rather than the path effects alone.

For the 7 ripple-fired explosions shown in Figure 2, the peak amplitude of the fundamental Rayleigh wave packet in the forward direction is typically three times as large as that of the backward direction, as indicated by Figure 3a. If the ripple shots were embedded in a model with moderate topography (Figure 4), the topography would behave just like secondary sources to radiate the scattered energy. The peak amplitude of Rayleigh wave is then reduced by a factor of 3 and 10 in the backward and forward directions, respectively. However, the surface wave in the forward direction still has a larger peak amplitude (Figure 3b).

PRELIMINARY CONCLUSIONS

The analysis of these simulation results is still in progress, so all conclusions given at this time must be considered preliminary. It seems that the ratio of seismic phases (*e.g.*, L_g-to-P) could vary significantly due to different configurations of the shot array, which could explain the observed different degrading and enhancing pattern of various seismic phases of different blasts from the same location. Also, the frequency of spectral enhancement due to ripple firing could be shifted even when the delay between shots/rows is precise.

Ripple firing could excite directionally dependent R_g and S*. Thus the lack of R_g may not be always indicative of a deep source. Rather, it could also be due to the shot pattern. However, the enhanced R_g in the forward direction of ripple firing can be strongly attenuated by lateral heterogeneity and surface topography. The scattered R_g energy could then couple into the crustal waveguide as L_g and other phases (McLaughlin and Jih, 1986, 1987; Jih and McLaughlin, 1988). Since such scattering mechanisms are commonly present in many quarry sites or mines, it is not surprising that the directional enhancement of R_g may not be always observable. The spall could obscure the azimuthal dependency of R_g as well. Previous LFD modeling studies (McLaughlin and Jih, 1986, 1987) suggest that the near-source R_g-to-S scattering is usually stronger than that of R_g-to-P, which could provide a plausible explanation as why quarry blasts and mining blasts should discriminate less well from earthquakes than would contained nuclear explosions. Further quantitative analysis along this line could be very useful.

REFERENCES

Anderson, D. and B. Stump (1989). Seismic wave generation by mine blasts, in *Report GL-TR-89-0194,* Geophysics Laboratory, Hanscom AFB, MA.

Baumgardt, D. R. and K. A. Ziegler (1988). Spectral evidence for source multiplicity in explosions: application to regional discrimination of earthquakes and explosions, *Bull. Seism. Soc. Am.,* **78,** 1773-1795.

Chapman, N. C., G. A. Bollinger, and M. S. Sibol (1992). Modeling delay-fired explosion spectra and source function deconvolution at regional distances, *Report PL-TR-92-2250,* Phillips Laboratory, Hanscom AFB, MA.

Dick, R. A., L. R. Fletcher, and D. V. D'Andrea (1983). Explosives and Blasting Procedures Manual, *Information Circulation 8925,* Bureau of Mines, United States Department of the Interior.

Greenhalgh, S. A. (1980). Effects of delay shooting on the nature of P-wave seismograms, *Bull. Seism. Soc. Am.,* **70,** 2037-2050.

Hedlin, M. A. H., J. B. Minster, and J. A. Orcutt (1990). An automatic means to discriminate between earthquakes and quarry blasts, *Bull. Seism. Soc. Am.,* **80,** 2143-2160.

Jih, R.-S., K. L. McLaughlin, and Z. A. Der (1988). Free boundary conditions of arbitrary polygonal topography in a 2-D explicit elastic finite-difference scheme, *Geophysics,* **53,** 1045-1056.

Jih, R.-S., C. S. Lynnes, D. W. Rivers, and I. N. Gupta (1989). Simultaneous modeling of teleseismic and near regional phases with linear finite-difference method (abstract), *EOS, Trans. Am. Geophys. Union,* **70-43,** 1189.

Jih, R.-S., and K. L. McLaughlin (1988). Investigation of explosion generated SV Lg waves in 2-D heterogeneous crustal models by finite-difference method, *Report AFGL-TR-88-0025,* Geophysics Laboratory, Hanscom AFB, MA.

Kim, W. Y., D. W. Simpson, and P. G. Richards (1992). High-frequency spectra of regional phases from earthquakes and chemical explosions, in *Report PL-TR-91-2285,* Phillips Laboratory, Hanscom AFB, MA.

McLaughlin, K. L., and R.-S. Jih (1986). Finite-difference simulations of Rayleigh wave scattering by 2-D rough topography, *Report AFGL-TR-86-0269,* Geophysics Laboratory, Hanscom AFB, MA.

McLaughlin, K. L., and R.-S. Jih (1987). Finite-difference simulations of Rayleigh wave scattering by 2-D shallow heterogeneity, *Report AFGL-TR-87-0322,* Geophysics Laboratory, Hanscom AFB, MA.

Reamer, S. K., K.-G. Hinzen, and B. W. Stump (1992). Near-source characterization of the seismic wavefield radiated from quarry blasts, *Geophys. J. Int.,* **110,** 435-450.

Smith, A. (1989). High-frequency seismic observations and models of chemical explosions: implications for the discrimination of ripple-fired mining blasts, *Bull. Seism. Soc. Am.,* **79,** 1089-1110.

Smith, A. and R. D. Grose (1987). High-frequency seismic observations of signals and noise near RSON: implications for the discrimination of ripple-fired mining blasts, *Report UCID-20945,* Lawrence Livermore National Laboratory.

Stead, R. and D. Helmberger (1988). Numerical-analytical interfacing in two-dimensions with applications to modeling NTS seismograms, in *Scattering and Attenuation of Seismic Waves, Vol. 1,* Special issue of *Pure and Applied Geophysics,* **128,** 157-193.

Stump, B. (1988). Wave propagation issues associated with explosive sources, *10th Annual DARPA/AFGL Seismic Research Symposium, (Addendum 27-43),* Fallbrook, CA.

Stump, B. and S. K. Reamer (1990). Physical constraints on seismic waves from chemical and nuclear explosions, *12th Annual DARPA/GL Seismic Research Symposium, 159-165,* Key West, FL.

Stump, B., S. K. Reamer, and R. E. Reinke (1988). Temporal and spatial source effects from near-surface explosions, *10th Annual DARPA/AFGL Seismic Research Symposium, 95-113,* Fallbrook, CA.

Suteau-Henson, A., and T. C. Bache (1988). Spectral characteristics of regional phases recorded at NORESS, *Bull. Seism. Soc. Am.,* **78-2**, 708-725.

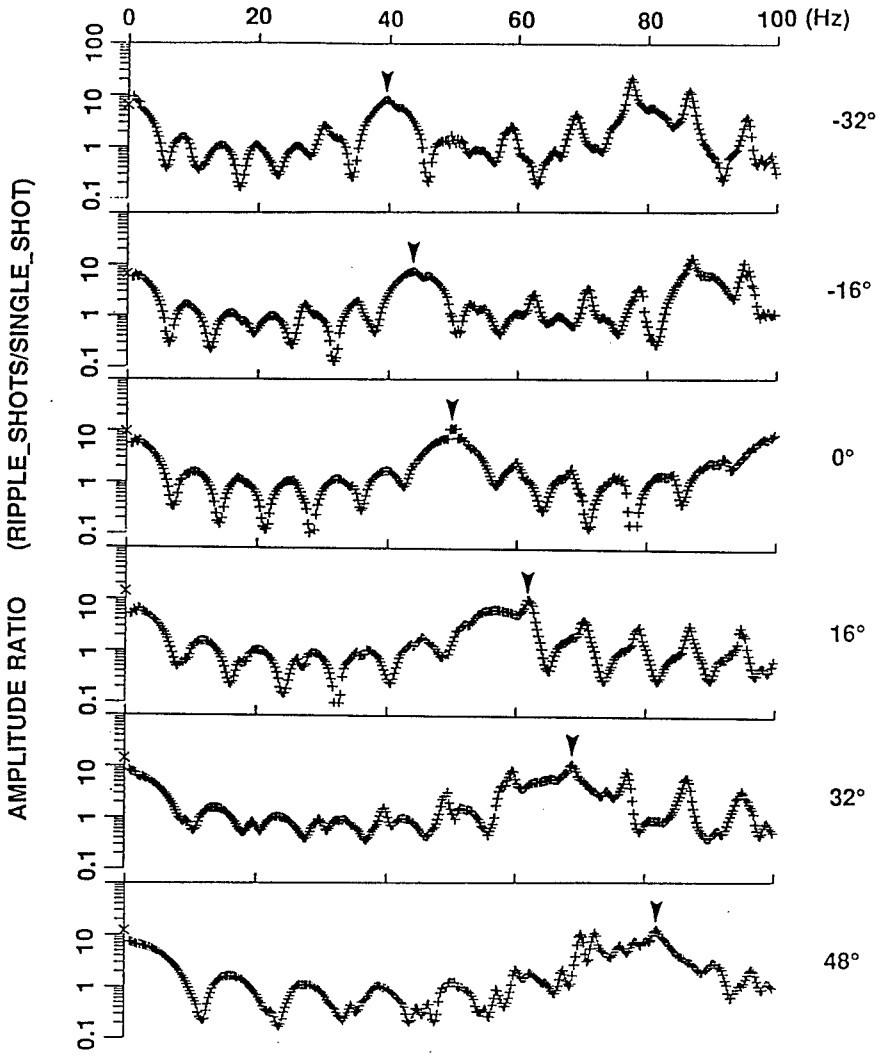
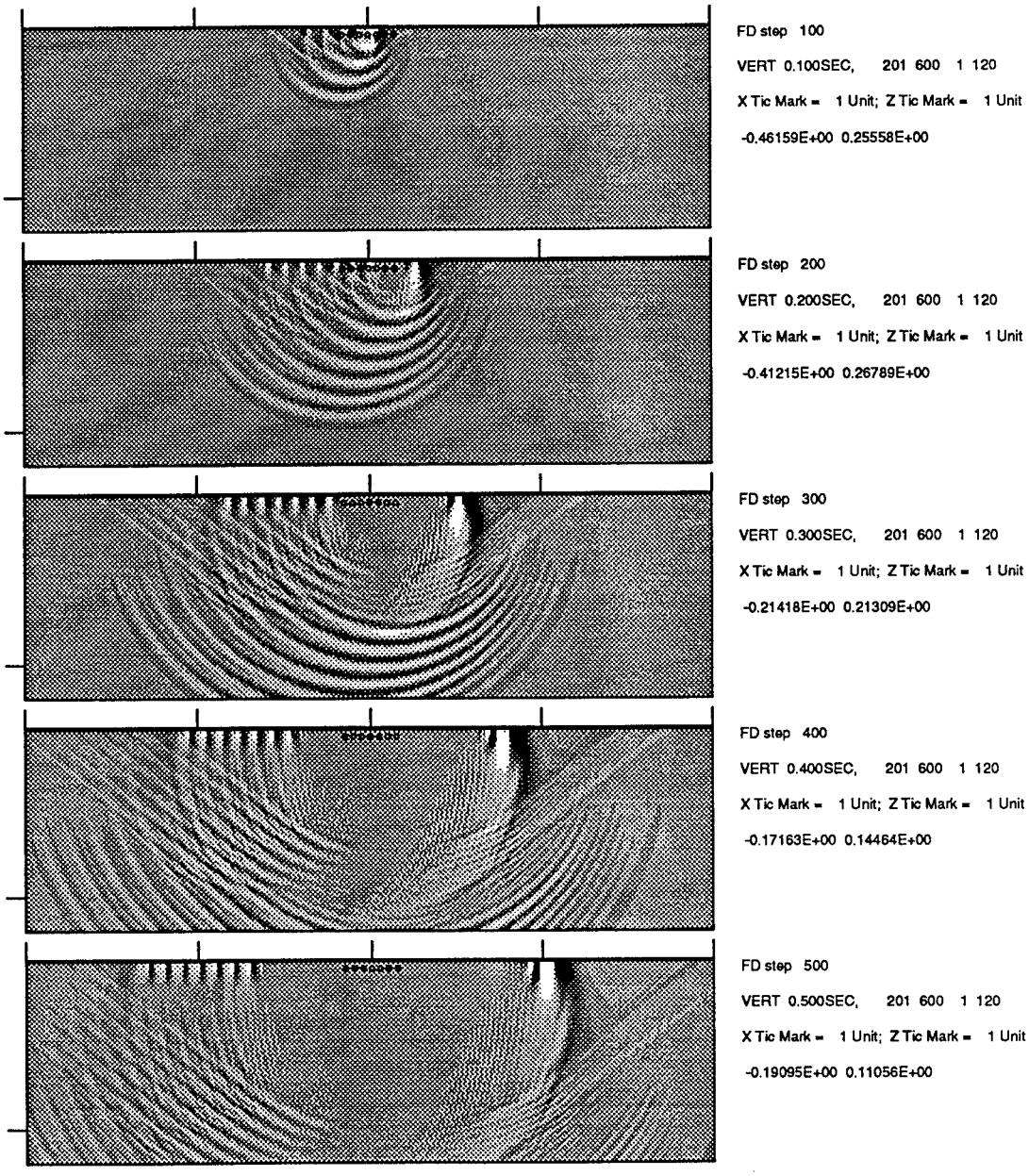


Figure 1. The spectral ratios of P-wave synthetics due to 7 ripple-fired explosions (with a delay of 20 ms) to that due to a single explosion. The take-off angles are shown on the right. The spectral reinforcement (ϒ) does occur at exactly every 50 Hz along 0° take-off angle, *i.e.*, the ray perpendicular to the rupture direction. For other directions, however, the frequency at which the enhancement occurs is affected due to the *Doppler Effect.*



7 shallow ripple-fired blasts

DT=20ms, H=30m

Vp=5.02km/s, Vs=2.898km/s

Figure 2. Snapshots of the vertical displacement field with temporal spacing of 0.1 second. Note that the fundamental Rayleigh wave and S* are strongly enhanced in the forward direction.

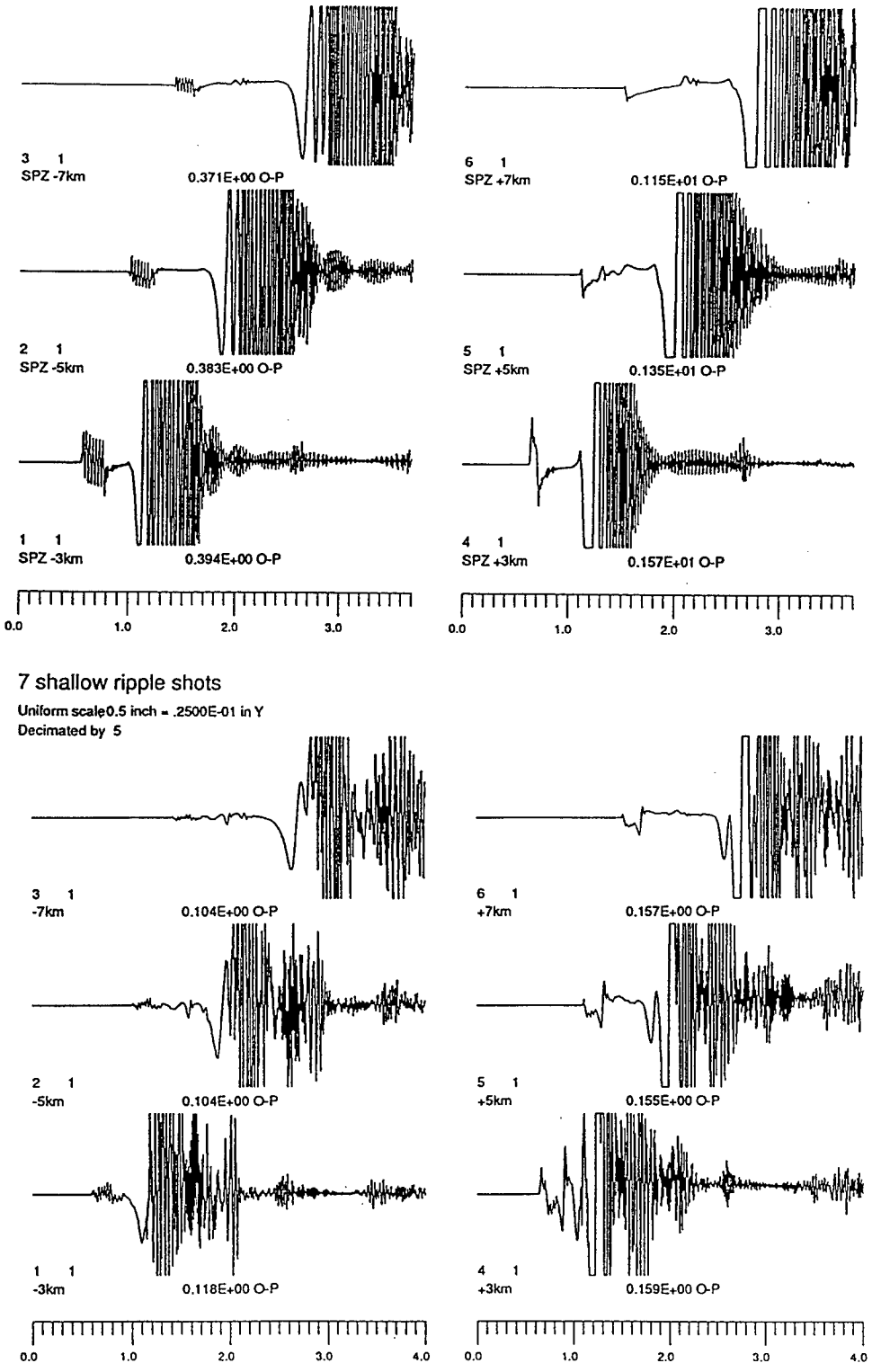
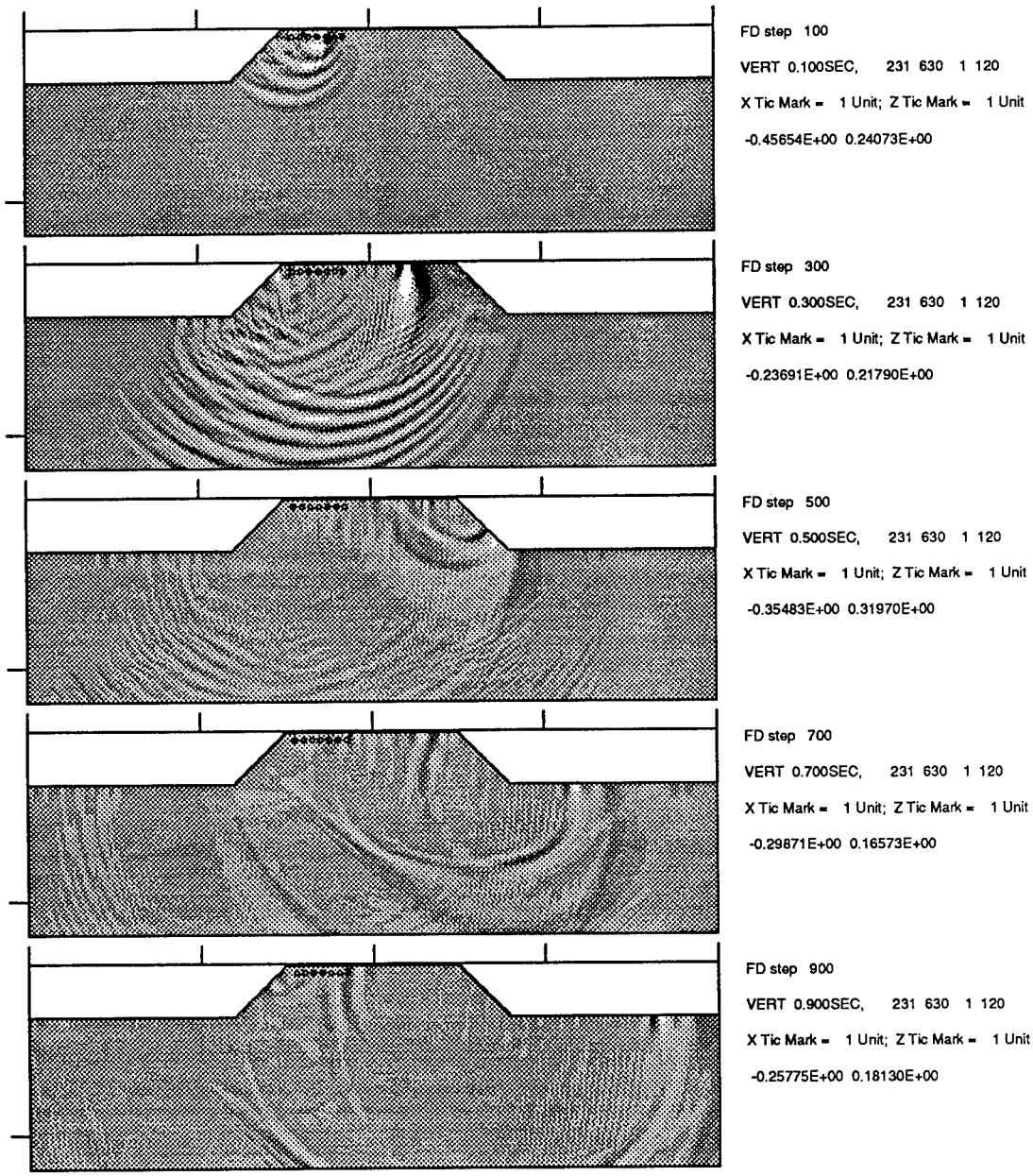


Figure 3. The full-wave synthetics computed at various local distances at forward (right) and backward (left) directions, respectively, for 7 ripple shots in a model with or without the topography. In the half-space model (top), the peak amplitude in the forward direction is about three times larger than that of the backward direction. The topography attenuates the Rayleigh wave in both directions dramatically and produces a more complex waveform.



7 shallow ripple-fired shots
Trapezoidal topography
Vp=5.02km/s, Vs=2.898km/s

Figure 4. Same as Figure 2 except for the model with a moderate topography. Note that the topography radiates the fundamental Rayleigh wave energy into body waves of much lower frequency as shown at 0.5 and 0.7 sec. Part of the Rayleigh wave energy is trapped between the two ramps (*cf.* 0.6 and 0.7 sec) and eventually scattered into the coda waves.

THIS PAGE INTENTIONALLY LEFT BLANK.

Equivalent Elastic Treatment of Near Source Propagation

Lane R. Johnson

Center for Computational Seismology, Lawrence Berkeley Laboratory,
and Seismographic Station, University of California,
Berkeley, California 94720

Introduction

The relationship between the energy of an explosive source and the amplitude of the seismic waves which are radiated into the far field has been a primary interest of the verification program since its beginning (Latter et al., 1959). The problem is made difficult by the fact that the seismic energy represents only a small fraction of the total energy. Most of the energy of the explosion is deposited within the elastic radius by a series of complicated non-linear processes. Given that the wave propagation problem beyond the elastic radius is essentially solved, the primary difficulty concerns the treatment of the non-linear region surrounding the source. A number of computer codes have been developed for modeling this region, but they are fairly complicated, involving hydrodynamic effects, shock waves, and non-linear equations of state. Because of the basic numerical approach which is followed in these codes, they do not readily provide insight into questions about which parameters are playing the critical role in determining the radiated elastic waves. This has motivated the investigation of an alternative method of modeling this region immediately surrounding an explosive source.

The basic approach being investigated is to use an equivalent elastic treatment for the region between the original cavity radius and the elastic radius. This concept of an equivalent elastic medium has been used quite successfully by earthquake engineers to model the non-linear behavior of soils that occurs during strong ground motion. The present attempt uses constraints on the energy flux as an aid in selecting the relevant elastic parameters. The complete solution for the case where the density and elastic constants vary in an arbitrary manner as a function of radius has been derived. Thus it is possible to make the material properties a function of the stresses and strains in the outward propagating pressure pulse and obtain the results in the form of a simple numerical propagation of the analytical solutions. The present formulation relates density and bulk elastic properties to the peak over-pressure in the pressure pulse and shear and anelastic properties to the maximum shear stress. The material properties are adjusted in an iterative process so that the appropriate properties are present in the vicinity of the propagating pressure pulse. While this approach is only an approximation to calculations with hydrodynamic equation-of-state codes, it has the advantage of providing simple analytic results in which the role of various model parameters are easily investigated. This is important when one wants to conduct a sensitivity analysis over a wide range of explosion sizes and material parameters.

Equivalent Elastic Treatment for Compression

Let ρ_u be the ultimate or maximum density and P be the peak overpressure. Then, following Majtenyi and Foster (1992) one can approximate the density

dependence upon pressure as

$$\rho(P) = \rho_u - (\rho_u - \rho_o)\, e^{AP}$$

where

$$A \equiv \frac{1}{V_{po}^2}\frac{1}{\rho_u - \rho_o}$$

and ρ_o and V_{po} are zero pressure values. The compressional velocity as a function of pressure is

$$V_p(P) = \left[V_{po}^2 + \frac{2}{\rho_u}[P + \frac{1}{A} ln(\frac{\rho(P)}{\rho_o}]\right]^{1/2}$$

Equivalent Elastic Treatment for Shear

Let μ_{max} be the small strain shear modulus. It can be obtained from the small strain shear velocity by

$$u_{max} = \rho\beta^2$$

Then let τ_{max} be the maximum shear stress that the material will sustain. Define the reference strain by

$$e_r = \frac{\tau_{max}}{\mu_{max}}$$

Then the simple hyperbolic stress-strain relationship (Hardin and Drnevich, 1972) yields the effective shear modulus

$$\mu(e) = \mu_{max}\frac{1}{1 + e/e_r}$$

Similarly, the effective damping is

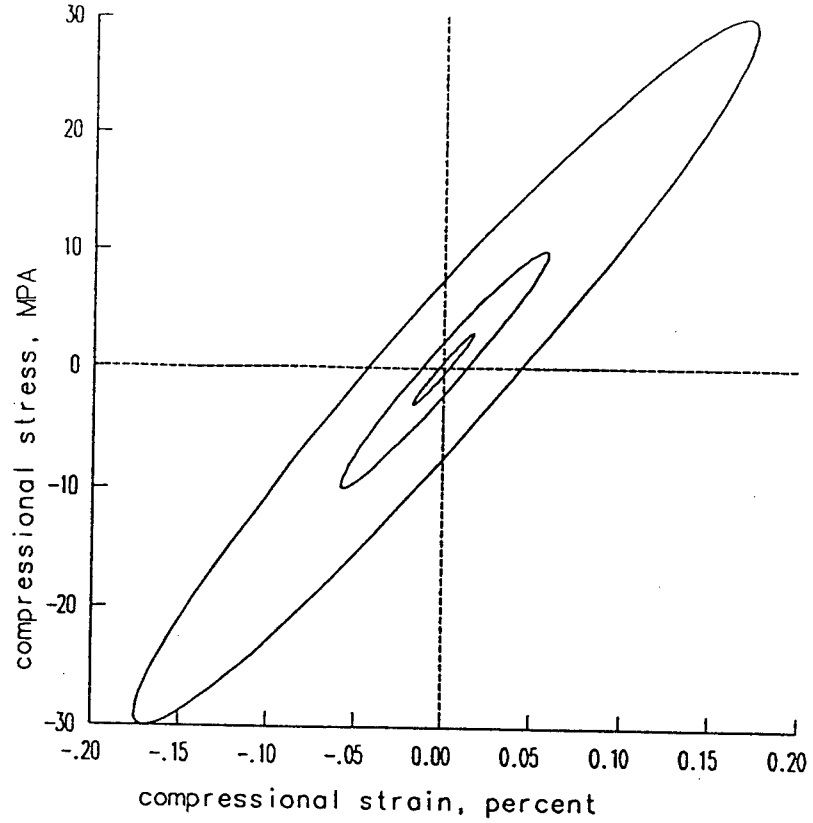
$$\delta(e) = \delta_{max}\frac{e/e_r}{1 + e/e_r}$$

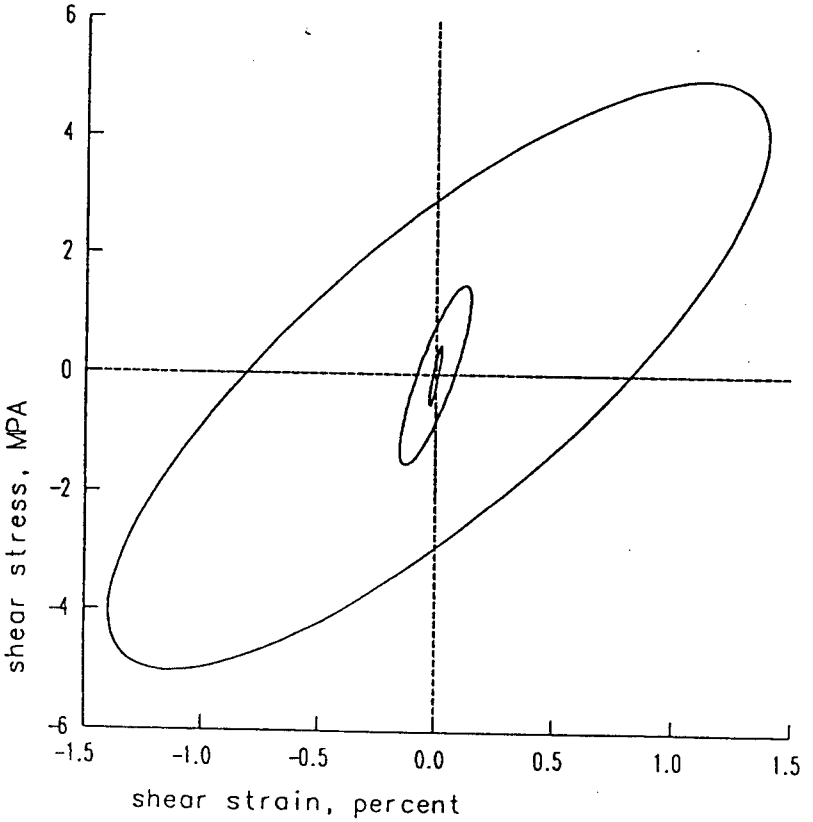
The damping ratio is related to the attenuation by

$$Q_s^{-1} = \frac{2\,\delta}{\sqrt{1 - 4\delta^2}}$$

Hysteresis Curves

The equivalent elastic treatment can be characterized in terms of hysteresis curves that change as a function of stress. The first figure shows such hysteresis curves for an equivalent elastic treatment of wet tuff. In the case of compressional stress, there is a slight increase in the real part of the modulus as the stress increases and the imaginary part also increases. In the case of shear stress, there is a marked decrease in the real part of the modulus and an increase in the imaginary part as the level of the stress increases.





Hysteresis loops for both compression and shear at three different levels of strain in wet tuff. The equivalent elastic treatment was used for both the real and imaginary parts of the elastic moduli.

Elastic Wave Propagator Solution

The use of the equivalent elastic method requires that the elastodynamic equations of motion be solved for an explosive source in an inhomogeneous medium. Standard propagator methods can be used to solve this problem.

Assuming a series of spherically symmetric homogeneous shells, the displacement and radial traction in any shell can be written as

$$\begin{bmatrix} u \\ t_r \end{bmatrix} = \mathbf{A}_n \begin{bmatrix} a_n^{(1)} \\ a_n^{(2)} \end{bmatrix}$$

where the shell matrix $\mathbf{A}_n$ involves spherical Hankel functions and the material constants of layer n, and the coefficients $a^{(1)}$ and $a^{(2)}$ represent the amplitudes of inward and outward propagating waves, respectively. The requirement of continuity of displacement and stress between shells leads to

$$\begin{bmatrix} a_n^{(1)} \\ a_n^{(2)} \end{bmatrix} = \mathbf{B}_n(\omega)\, \mathbf{B}_{n-1}(\omega) \cdots \mathbf{B}_2(\omega) \begin{bmatrix} a_1^{(1)} \\ a_1^{(2)} \end{bmatrix}$$

where

$$\mathbf{B}_n(\omega) \equiv \mathbf{A}_n^{-1}(r_n, \omega)\ \mathbf{A}_{n-1}(r_n, \omega)$$

Then, by specifying the boundary condition at the inner shell (pressure history) and the outer shell (outward propagating waves only) it is possible to obtain the complete solution to the problem.

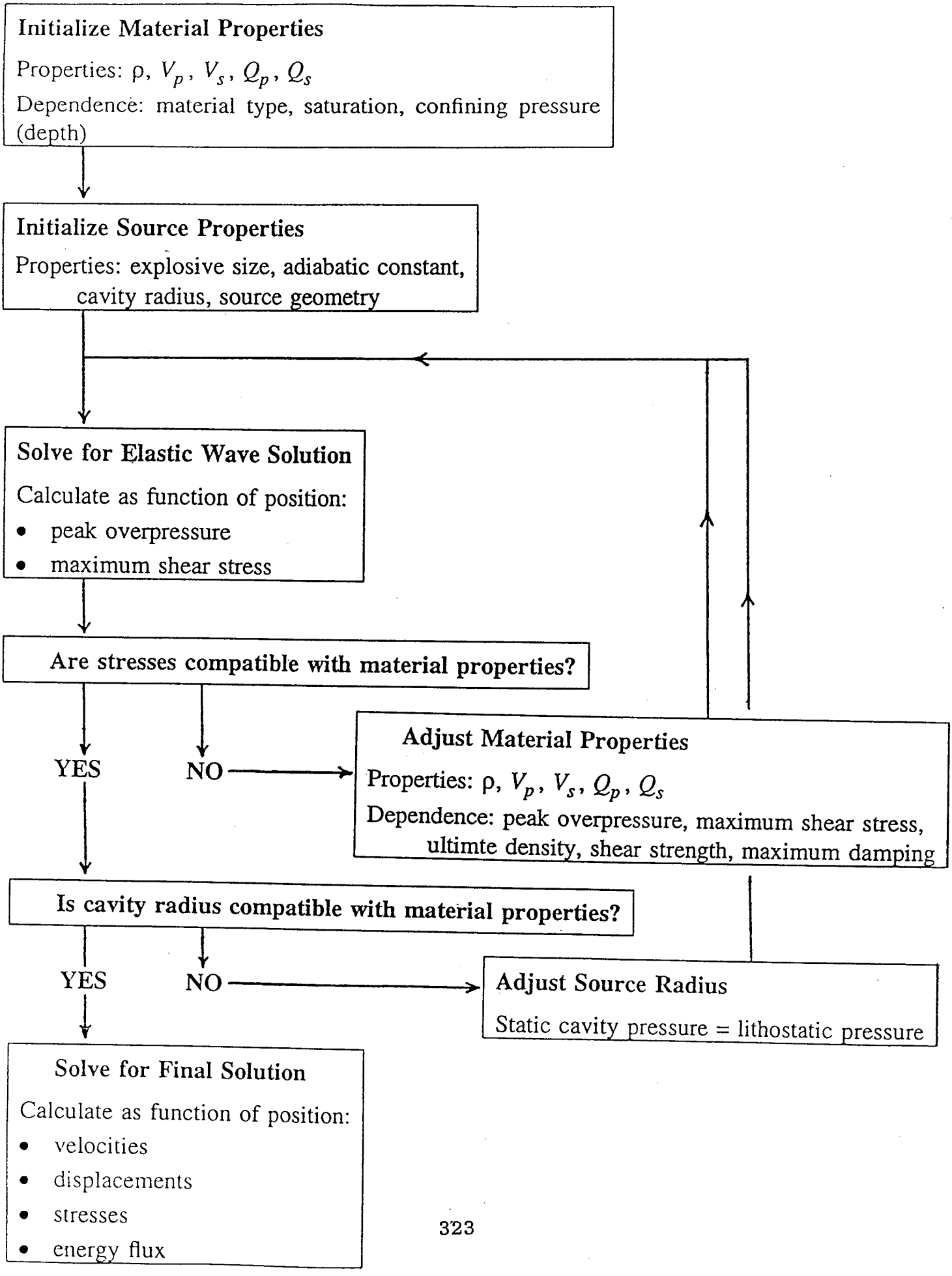
Method of Calculation

The flow chart in the second figure outlines the basic steps of the computational scheme. After initializing the parameters of both the material properties and the explosive source, the elastic wave solution is obtained in the surrounding material. In general the stresses associated with this solution will be large enough so that the initial material properties are not appropriate. Thus the material properties are adjusted on the basis of the calculated stresses and the entire process completed. After convergence of the process of adjusting the material properties, the source radius is also adjusted to allow for the inelastic growth of the cavity. Then, after a final iteration on the material properties, the final solution is obtained.

Experimental Check of the Method

This method of calculating fields of an explosive source is illustrated by some initial calculations in the third figure. The upper panel shows the first 10 msec of measured particle velocity within a few meters of a buried chemical explosion, while the lower panel shows the results of simulating these measurements with an analytical code that employs equivalent elastic material properties. The data were obtained during the OSSY2 experiments of 1991.

Starting with the material properties obtained from the OSSY2 experiments as initial values, the elastic wave solutions were obtained out to a distance of 40 meters


Initialize Material Properties
Properties: ρ, V_p, V_s, Q_p, Q_s
Dependence: material type, saturation, confining pressure (depth)
Initialize Source Properties
Properties: explosive size, adiabatic constant, cavity radius, source geometry
Solve for Elastic Wave Solution
Calculate as function of position:
• peak overpressure
• maximum shear stress
Are stresses compatible with material properties?
YES
NO
Adjust Material Properties
Properties: ρ, V_p, V_s, Q_p, Q_s
Dependence: peak overpressure, maximum shear stress, ultimte density, shear strength, maximum damping
Is cavity radius compatible with material properties?
YES
NO
Adjust Source Radius
Static cavity pressure = lithostatic pressure
Solve for Final Solution
Calculate as function of position:
• velocities
• displacements
• stresses
• energy flux

from the source point. Using the stresses that resulted from this solution, the material properties were adjusted according to the method described under the equivalent elastic treatment. Then a new wave solution was obtained using the modified material properties. This process was repeated until there was essentially no change in material properties between iterations.

The equivalent elastic modification of the material properties was most pronounced in a region that extended out to about 2 meters from the shot point. In this region the density and compressional velocity were increased by up to 5% while the shear velocity and shear quality factor were decreased by over 90%. At larger distances there was little modification in the density and compressional velocity, although there were significant but decreasing effects upon the shear velocity and shear quality factor out to distances of about 10 meters.

The next step was to calculate a new effective cavity radius for the source. The criterion used was that the static cavity pressure should equal the lithostatic pressure. This resulted in the cavity radius increasing from 9 cm to 20 cm.

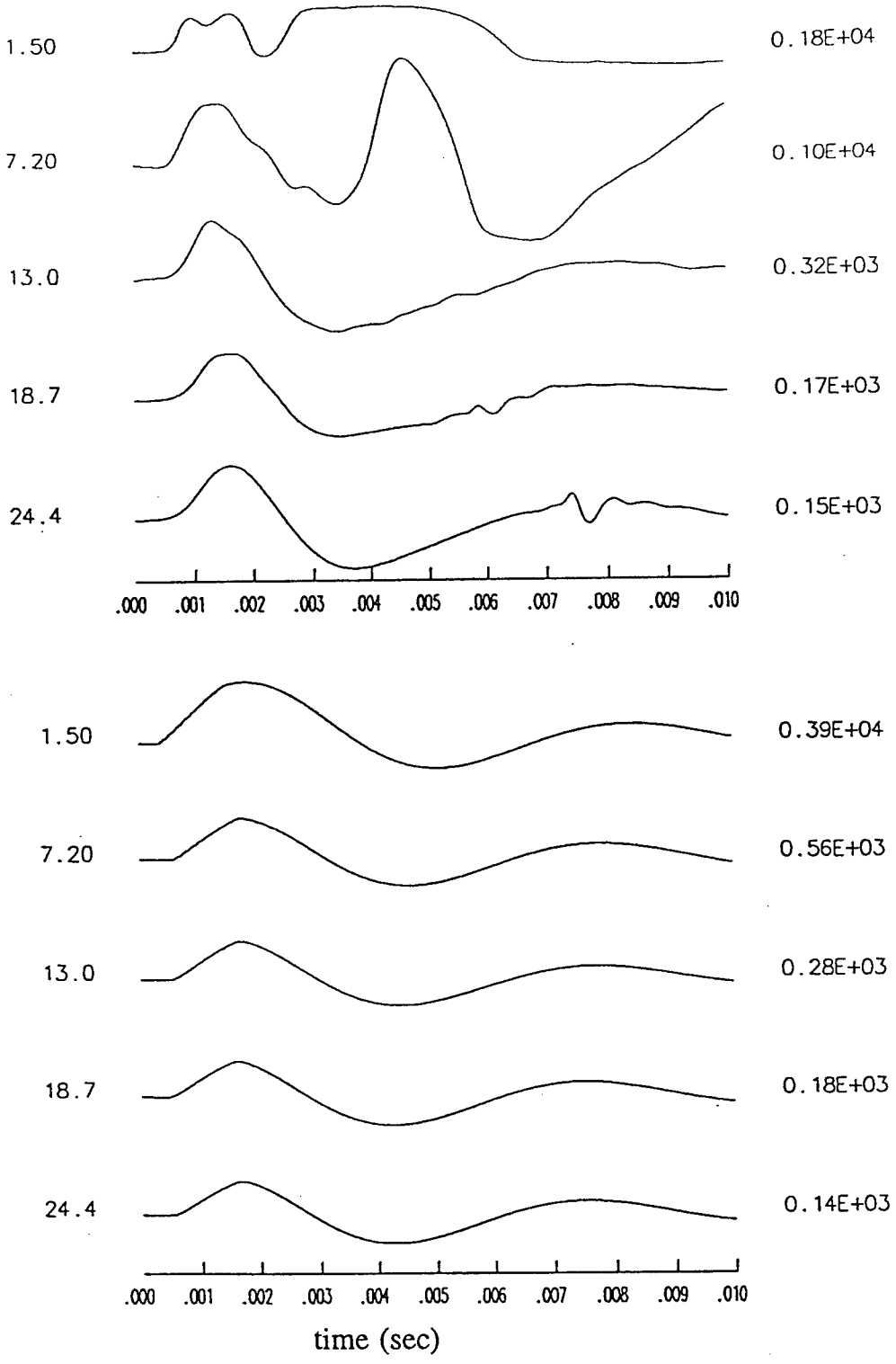
Using the effective material properties and the effective cavity radius, a final wave solution was obtained to yield the results shown in the figure.

The agreement between the observed and calculated velocities in the figure indicates some promise for this type of an approach. The recordings at the two closest distances of 1.5 and 7.2 meters are somewhat suspect, so the comparison here may not be valid. The accelerations at the first gage was in excess of 8000 g and there is a suggestion on the acceleration record that the gage may have broken loose and gone into ballistic motion. The acceleration at the second gage was greater than 2500 g and the maximum acceleration occurs during the second pulse that is delayed by about 4 msec, which is very difficult to explain in terms of an outgoing pressure wave. At the three outer gages the observed records seem more reasonable, indicating an outward propagating wave that changes slowly with distance. The simulated records agree quite well in amplitude and period in this range, although the asymmetry in the waveforms in somewhat different for the observed and calculated results. One possible explanation for this difference is that the dispersion associated with the anelastic properties of the medium has not been properly modeled in the simulations. This, along with many other aspects of the simulation calculations, need considerably more investigation.

Conclusions

The approach described here is not a substitute for complete equation-of-state codes, but it does provide an effective method of investigating some of the basic elements of wave propagation near an explosive source. The computer codes are quite efficient, so that it is possible to run extensive simulation studies in which the role of various parameters is investigated.

One characteristic of the equivalent elastic method is that it requires a relationship between material properties and the level of strain. Further development and use of this method we require the assembly of a data base of empirical relationships for equivalent elastic treatments that covers all of the different types of materials which might serve as source media for explosions. The literature contains considerable data



Recorded and calculated free field measurements for a chemical explosion. The explosion consisted of 100 pounds of C4 explosive which was detonated at a depth of 534 meters in Yucca Valley. The upper panel shows velocities that were recorded by a linear array of gages directly above the explosion. The number on the left of each trace is the radial distance of the gage from the center of the explosion in meters and the number on the right is the maximum velocity in cm/sec. The traces have been multiplied by distance from the explosion for the purposes of plotting.

of this type for various soils, but comparable data pertaining to hard rocks has not yet been located.

References

Hardin, B. O., and V. P. Drnevich, Shear modulus and damping in soils: design equations and curves, J. Soil Mech. and Found. Div., Proc. Am. Soc. Civil Eng., 98, 667-692, 1972.

Latter, A. L., E. A. Martinelli, and E. Teller, Seismic scaling law for underground explosions, Phys. of Fluids, 2, 280-282, 1959.

Majtenyi, S. I., and E. L. Foster, Propagation velocity of shock waves and presure waves in soil and rock, Geophys. Res. Let., 19, 865-868, 1992.

SEISMIC WAVEFORM MODELING OF EXPLOSIONS AT DISTANCES OF 10 - 100 KM

Robert B. Herrmann
Ghassan Al-Eqabi
Kevin Hutchensen

Department of Earth and Atmospheric Sciences
Saint Louis University
3507 Laclede Avenue
St. Louis, MO 63103

ABSTRACT

The classification of shallow seismic sources in terms of size and mechanism is not trivial when the sources are small in size and recorded at distances less than 1000 km. Current operational techniques serve to distinguish between spatially distributed industrial chemical explosions with intershot delays and point sources on the basis of spectral scalloping. Data sets used for algorithm validation are not robust enough to contain both shallow (< 2 km) and deeper (> 2 km) crustal earthquakes, large point chemical explosions, as well as arealy distributed chemical explosions. Wave propagation theory may make up for these knowledge gaps.

Perfect event discrimination is not presently possible. The suite of all recorded seismic events can be, and is being, culled on the basis of depth, spectral characteristics indicative of delayed shots and spectral ratios between different phases in different frequency bands, leaving a subset of events requiring further examination, if possible. The application of wave propagation theory can assist in the analysis of some of the remaining events to do the following:

1) add more information to the procedure by estimating the absolute source spectrum; 2) use the absence of short period surface waves together with source spectrum to constrain depth; 3) use the shape of the spectrum near 1 Hz to distinguish between events of large spatial extent from point sources (e.g., industrial explosions which do not exhibit spectral modulation) from point explosions and small earthquakes; 4) quantify the equivalent yield of sources.

The need for further research ultimately depends on the level of interest. If the magnitude of a 1 kT explosion is approximately 4.0, then the application of current waveform modeling techniques to broadband recordings may be very useful, even out to 1000 km, to assist discrimination. The challenge is to be able to classify events of smaller magnitude / yield over the same distances.

INTRODUCTION

The purpose of this paper is to review the results of processing some explosion and earthquake data in the 10-100 km distance range, to highlight observations that may be of use in the identification/discrimination problem and to indicate problem areas. This presentation is not all inclusive of research efforts, but serves to indicate some aspects of the problem.

SHORT PERIOD SURFACE WAVE STUDIES

We have looked at some short period surface waves generated by 1 ton chemical explosions in the state of Maine as part of a USGS sponsored refractions study. Figure 1 shows the various shot points and lines. At short distances the vertical component time histories are dominated by the fundamental mode surface wave. The interesting feature of this data set was the appearance of lateral variations in the surface wavetrain. Figure 2 shows one such data set. This data set is characterized by a well defined shear-wave arrival as well as the surface wave.

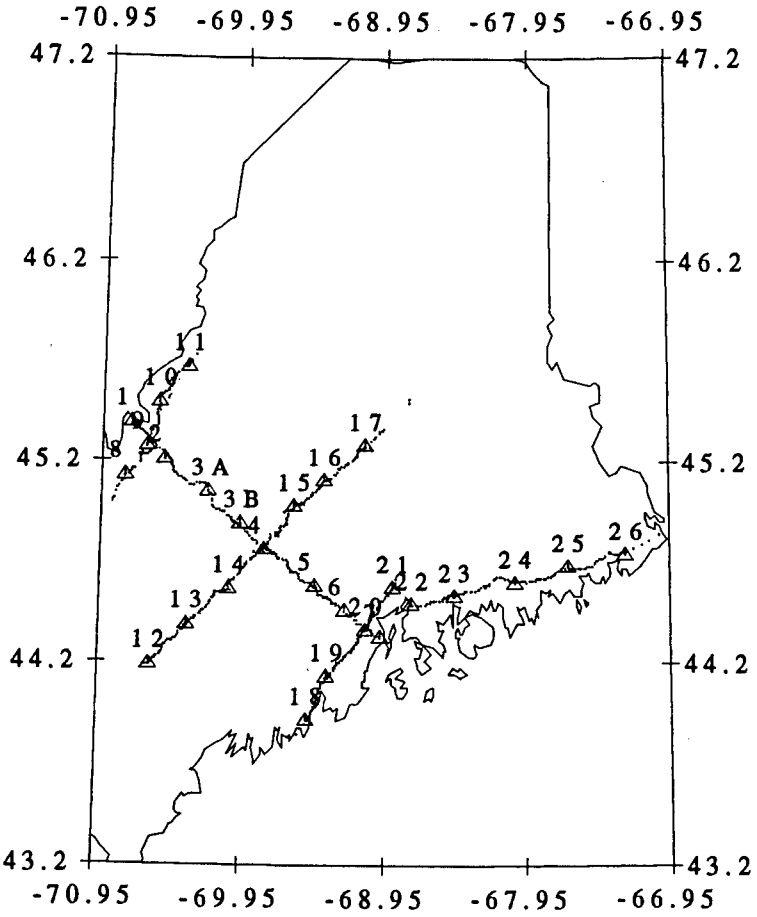


Fig. 1. Map showing USGS shot points and refraction lines in Maine. The shot points are indicated by the numbered triangles. The sensor locations are indicated by the small dots emanating from the shot points.

The surface wave data show good dispersion, but closer examination shows that the dispersion changes laterally. Distance segments indicating uniform dispersion were used to define inter-station dispersion from which a shear-wave velocity depth profile was derived for the segment. The results for all segments were used to define a laterally varying model. To emphasize the

lateral variation, the percentage deviation about a spatially uniform model is plotted in Figure 3. The large changes and their spatial locations correlate well with changes in surface geology.

A test of this model and its depth resolution is made by making forward synthetics by tracing rays through the two dimensional velocity structure (Figure 4). The predicted S-wave arrival times are indicated in Figure 2 by the near horizontal curve that lines up with the shear-wave arrivals. The agreement is excellent, considering the fact that only the surface-wave, and not the S-wave data were used to define the model. The ray tracing gives confidence in the inverted model to depths of 2 km. The isotropic source model cannnot account for the excitation of these S waves, although it is interesting that they become very apparent at about 8 km, where the model undergoes a significant lateral change.

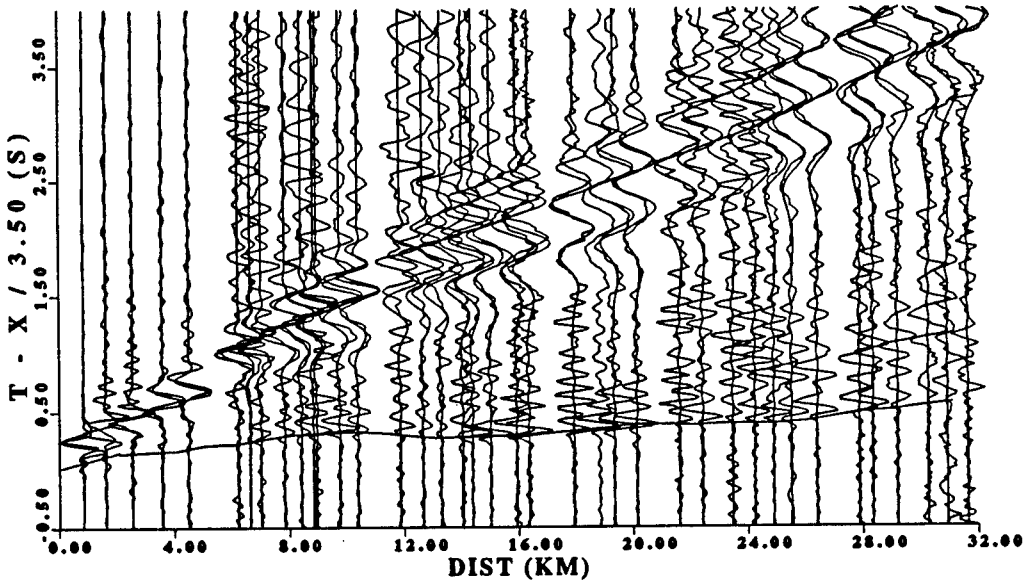


Fig. 2. One data set from USGS line. Shot Point 1 - NW. The observed trace and the predicted traces are shown. In addition the model predicted S-wave arrivals are shown. Both observed and synthetic time histories are lowpass filtered at 5.0 Hz to emphasize the fundamental mode surface wave.

Besides obtaining the shear-wave velocity model, shallow shear-wave Q can be estimated, as well as the isotropic source moment. Figure 5 shows a data set from Shot Point 6 to the southeast. Figure 6 shows the inferred lateral model variation; the predicted traces are also shown in Figure 5. Figure 7 shows the observed and predicted falloff surface-wave amplitude with distance in different frequency bands. The agreement indicates that the derived shear-wave Q model is acceptable.

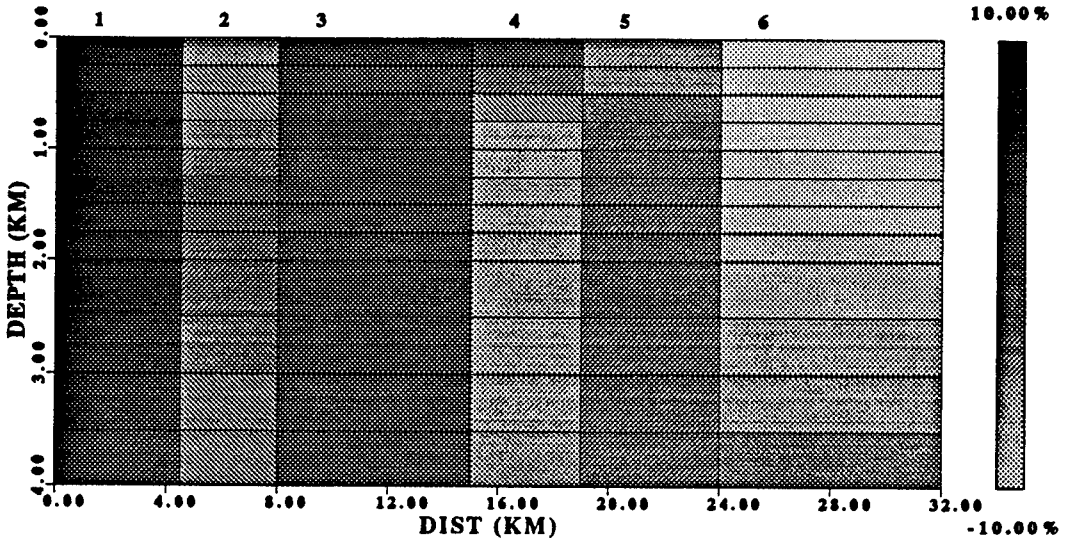


Fig. 3. Lateral variation of the earth model derived for the Shot Point 1 - NW profile. The shading indicates the percentage lateral variation in the shear-wave velocity for each layer. with respect to a base model.

The data of Figure 7 are also used to estimate the seismic moment in different frequency bands, with the conclusion that a simple step source pressure time function would describe the observations in the 0.5 - 5.0 Hz band. Thus an isotopic moment can be estimated from the data set.

Figures 8 and 9 present the yield normalized isotropic moment and Ψ_∞ estimates for the Maine data set together with other estimates available in the general literature. The surface-wave inferences fit well, and also indicate the scatter possible different estimates of isotropic moment for nominal one ton shots, when the porosity of the host material, degree of tamping and depth of burial are not well constrained.

SHORT PERIOD EARTHQUAKE AND EXPLOSION SIGNALS

We recently recorded local earthquakes and mining explosions at two stations of the regional seismic network run by Saint Louis University. The earthquakes and explosions were at approximately the same location in southwestern Indiana. The traces are shown in Figure 10. The P-wave amplitude spectra at the two stations are given in Figures 11 - 12. The 920616 blast P-wave spectra at WDIN shows spectral modulation in the 1 - 10 Hz band that may be indicative of ripple fired shots.

The interesting feature is that the two source signatures, blast and earthquake are significantly different. This is obvious at short distances at

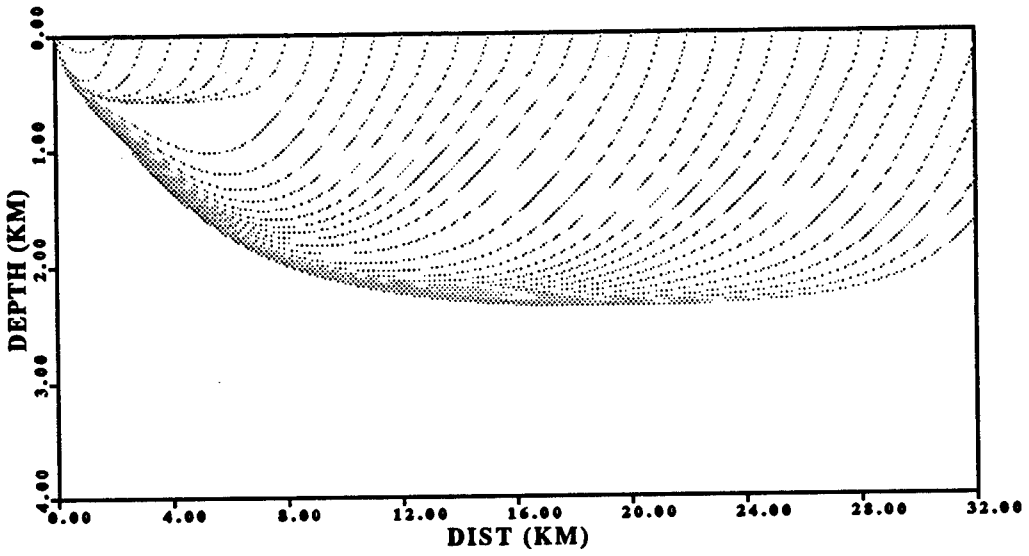


Fig. 4. S-wave rays traced through the laterally varying earth model.

WDIN but is also apparent at larger distances at WDIN. The earthquakes have a flat spectrum in the 1-10 Hz range while the blast spectra falls off as f^{-2} in roughly the same band. Similar differences are seen in the spectra obtained from the S-wave window. Since the high frequency levels (~ 10 Hz) are approximately the same for all events, this could be interpreted by saying that the blast has a lower corner frequency and higher seismic moment than the earthquakes. When interpreting earthquakes, the inverse of corner frequency is taken to be proportional to source dimension.

The implication is that it may be easy to distinguish between spatially large and small sources if one can adjust for source seismic moment. Typical large mining explosions are spatially large and have significant time delays between the first and last charge fired. The *caveat* is that there must be some absolute source measure so that the corner frequency could be interpreted in terms of source dimension.

CONCLUSIONS

This presentation shows the ability to define the source spectrum from array data by analyzing the fundamental mode Rayleigh surface wave. The use of array data was very important because this permitted the definition of the velocity and attenuation characteristics of the transmission medium independent of knowledge of source spectrum level or shape, since these were in turn subsequently derived from the data set. The derived isotropic moment -

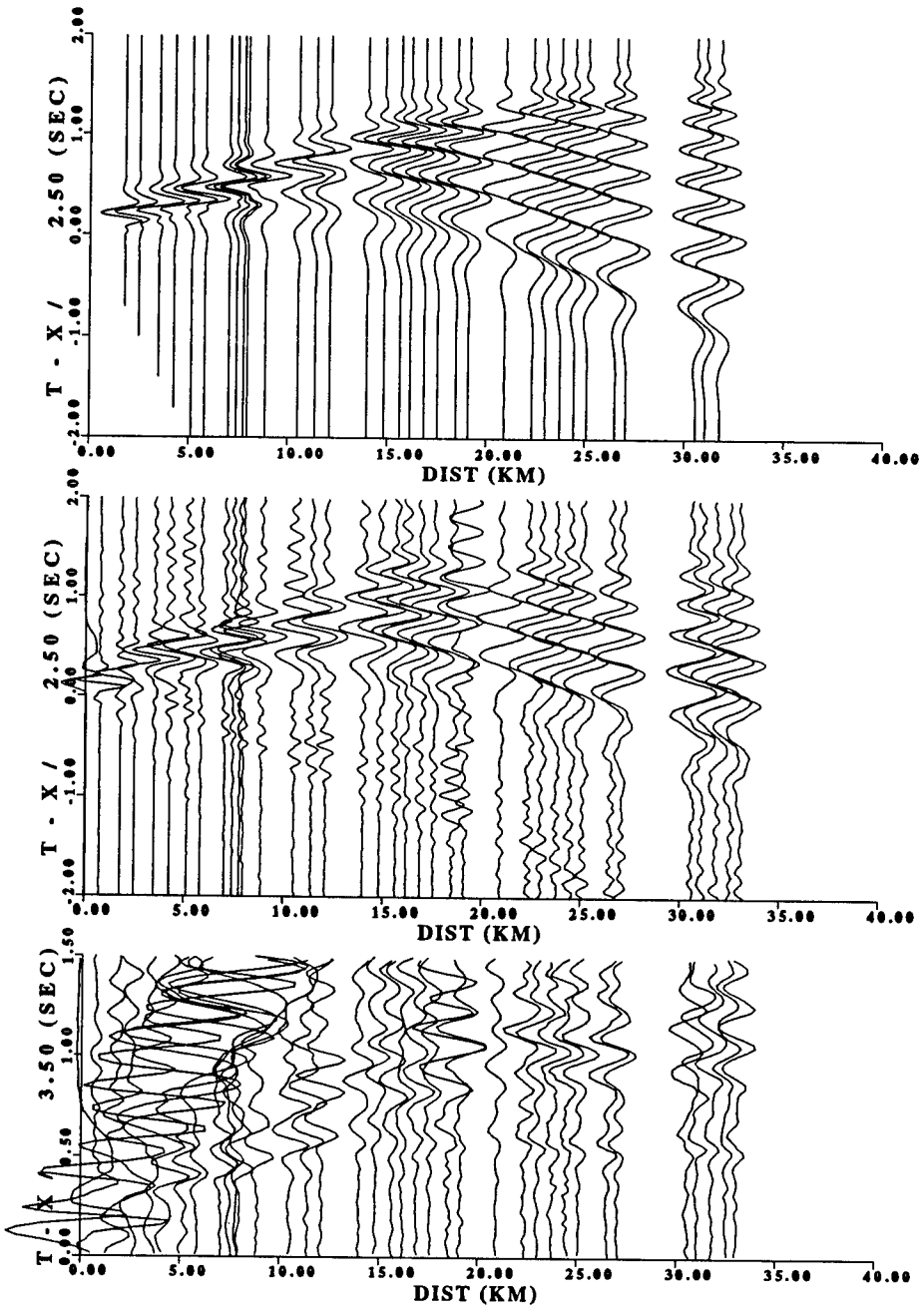


Fig. 5. Comparison of observed and synthetic seismograms for the Shot Point 6 - SE profile. Top) predicted surface wave arrivals for the laterally varying model. Center) observed data low pass filtered at 5.0 Hz and displayed to feature the surface-wave arrivals. Bottom) the same data set displayed to emphasize the shear-wave arrivals. Both the S-wave and surface-wave data indicate that the medium is faster at distances beyond 10 - 15 km.

yield relation for these point chemical explosions agreed with other estimates. No attempt was made to model the P-wave amplitudes at higher

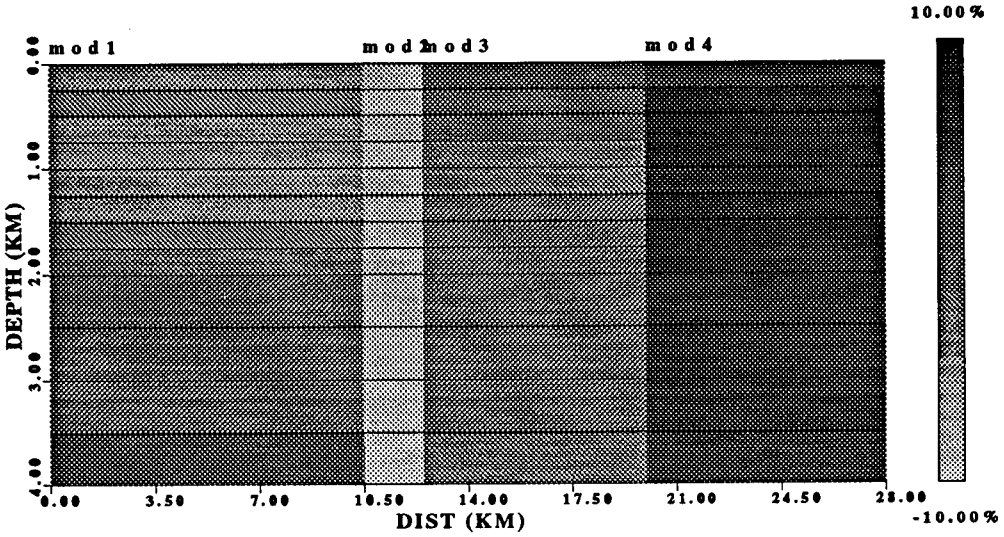


Fig. 6. Derived lateral variation in earth model. The percentage lateral variation about the horizontal average for each layer is shown.

frequencies and the mechanism of the SV-wave generation by the explosion.

Theoretical and numerical work on the equivalent seismic source representation for a chemical explosion in a cylindrical borehole would assist in understanding the SV-wave generation and might help distinguish between spherical point explosions and the explosive deployments typical of mining operations.

If three component data had been available, then inferences on non-symmetrical aspects of the source process could also have been inferred from the relative generation of SH and SV waves. This might also be useful in distinguishing mining explosions from point explosions.

The examination of the limited P-wave spectra data set showed differences between the mining blasts and the earthquakes, which could be interpreted in terms of source dimensions. A point explosion would be similar to an earthquake in that both would have smaller source dimensions than a spatially distributed mining explosion for the same seismic moment. This this observation may be relevent only in its ability to definitely classify some events as mining explosions and hence to remove them from further analysis.

This presentation reflects only the interests of the senior author, and is not inclusive of past and present research going on. In line with this *caveat*, he would like to ask for information and also to propose an experiment to

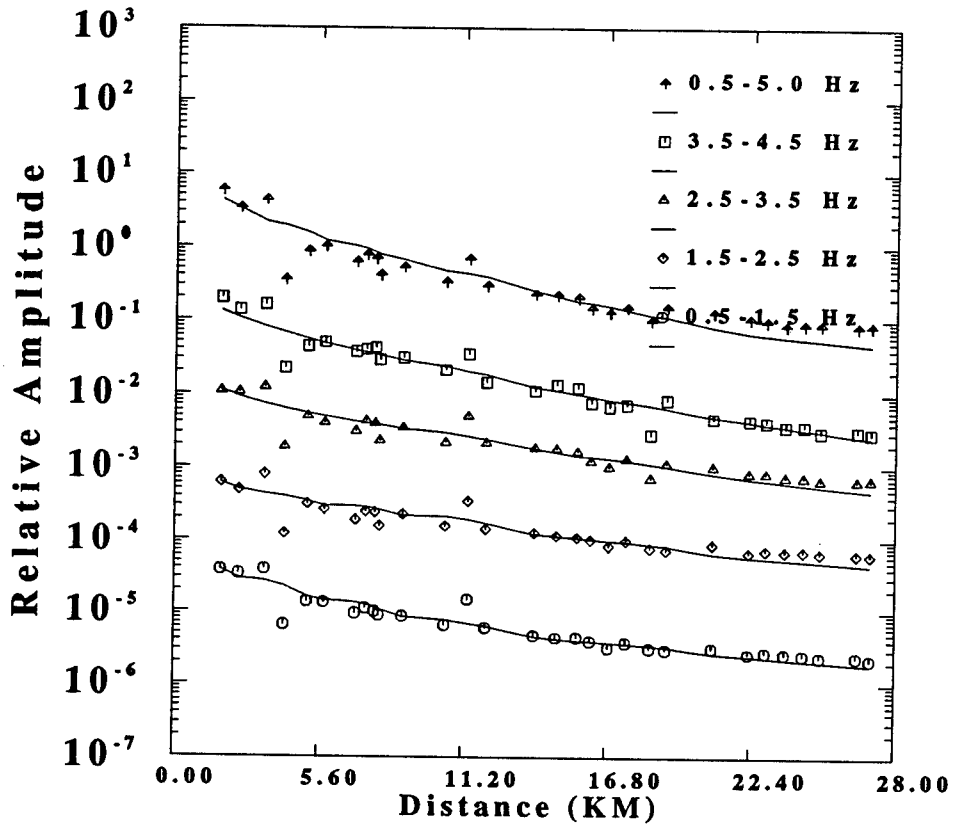


Fig. 7. Comparison of observed and predicted amplitudes with distance in different frequency bands. To do this, both observed and synthetic data were bandpass filtered, and the peak amplitude was read off.

provide data for analysis.

Basic Information Required

- In order to properly focus seismological studies, it is necessary to have guidance on the minimum size of nuclear explosion to be identified. Is it to be a 1kT decouple event or a 0.1kT coupled event (coupling refers to the ability of the explosion energy to be detected seismically)?
- If decoupling is a significant concern, what is the minimum size of a decoupled event that is of interest, and what are the characteristics of the event in the elastic range in terms of equivalent seismic forces in the frequency range of 0.02 - 100 Hz?
- Although the decoupling factor is usually described in terms of low frequency levels, a more fundamental question concerns the spectral corner frequencies of coupled and decoupled events of the same size. If the corner frequency is not affected by decoupling, then this may be a

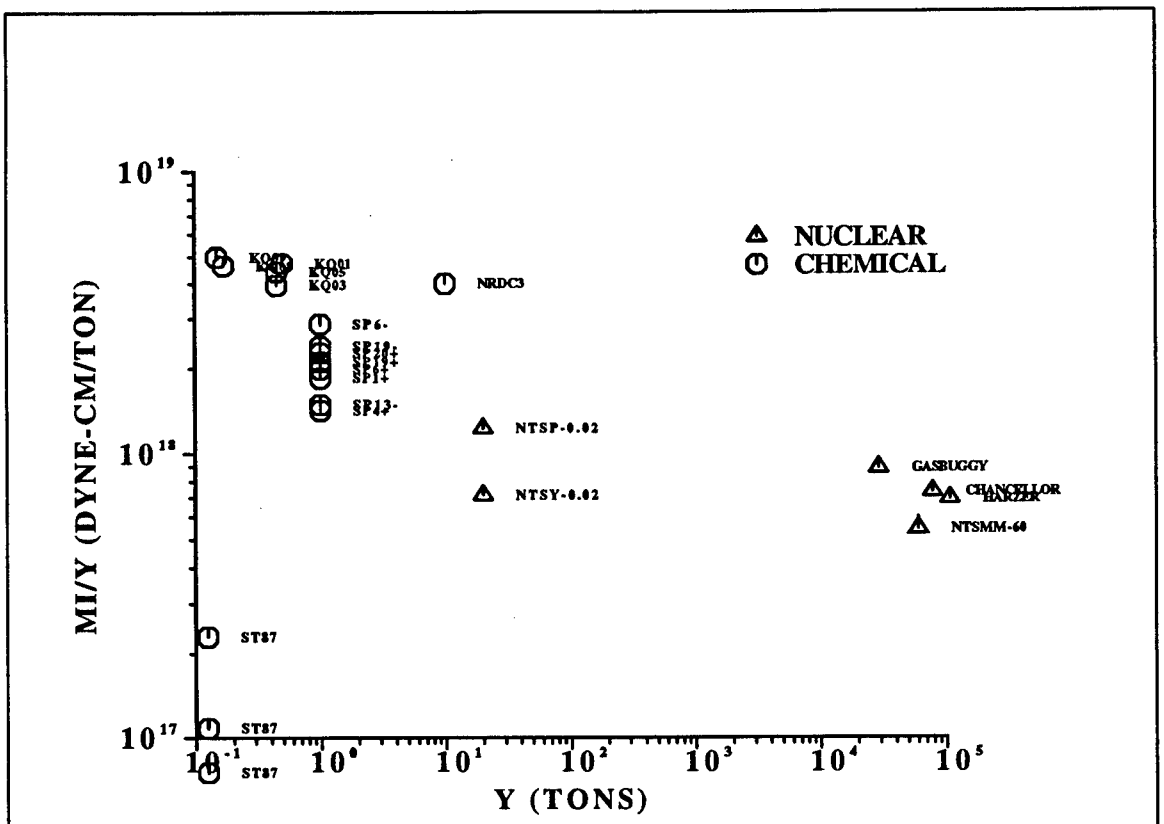


Fig. 8. Comparison of yield normalized isotropic moment estimates. The Maine results are indicated by the SP symbol and the Kaiser Quarry results of Johnson are indicated by the KQ symbol.

discriminant between coupled and decoupled events.

- Can any differences in the physics of chemical and nuclear explosions be discerned in the zone of elastic wave propagation?
- For completeness, what would be the seismic signature of a large point explosion is set off in a soil instead of rock?
- What is an allowable mis-identification rate?

These address the problem of detecting the seismic signal in the presence of earth noise and the proper interpretation of that signal. Under suitable continuity of the upper crust, broadband seismic signal analysis should be very simple out to 1000 km for a nominal 1kT coupled explosion since the signal would be well recorded. Smaller effective source sizes will require other analysis techniques and perhaps especially designed seismic data acquisition arrays. They certainly require an understanding of the process of seismic wave generation by the source and structural heterogeneities between the source and receiver.

A Fun Data Acquisition Experiment

Significant work has been done by B. Stump, L. Johnson and others on instrumenting explosions in the distance range of 0 - 10 km for the purpose of

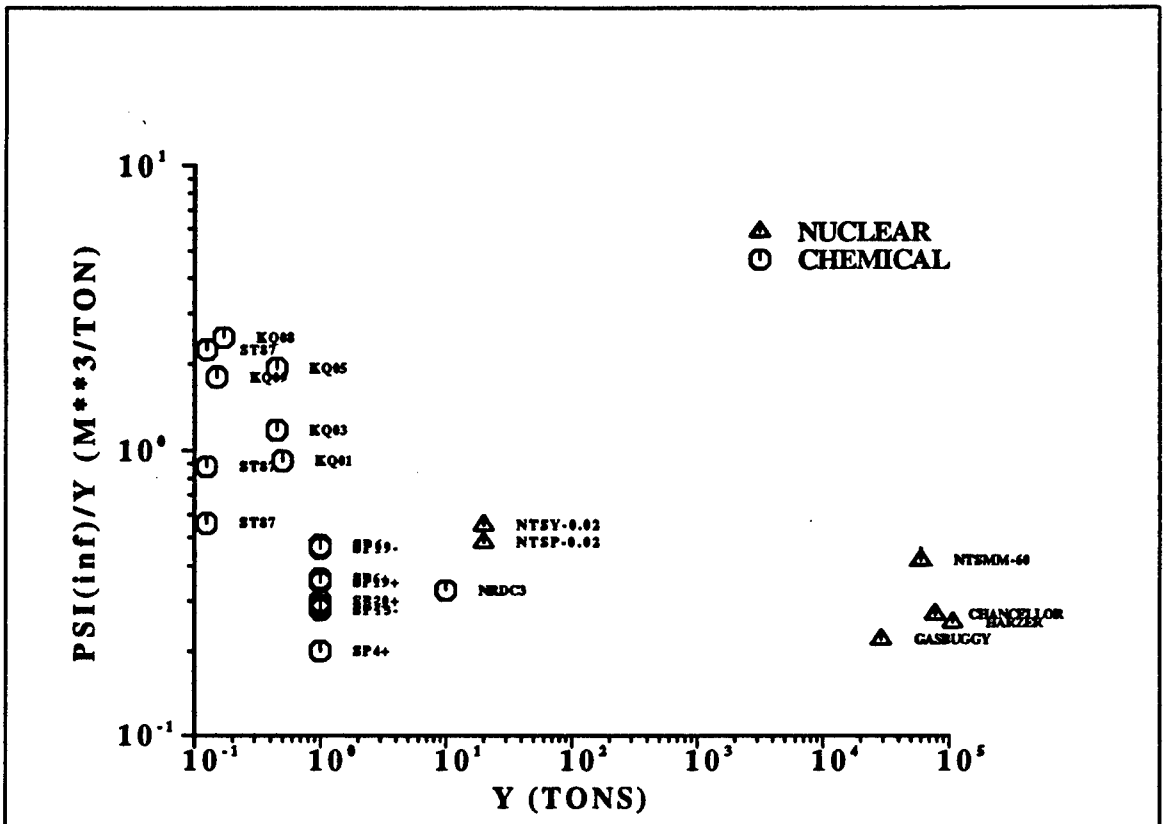


Fig. 9. Comparison of yield normalized Ψ_∞ estimates.

understanding the equivalent seismic source. They seek to define the non-isotropic components of the source as well as secondary source phenomena, such as spall.

In addition, as described above, the deployment of arrays in the 10-100 km range permits recovery of source spectrum from surface waves since the shallow shear-wave vvelocity and Q models are easily derived. The data sets analyzed here were from vertical instruments, and hence questions of non-isotropic source radiation could not be addressed.

Finally, arrays and broadband instruments at 1000 km may be able to discern source characteristics, but not with the same detail as from short distances.

The experiment, Figure 13, would be to deploy three types of data acquisition to monitor the wavefields in the 0-10, 10-100 and 1000 km ranges for a large point and a large distributed, delayed shot. Each data set would be analyzed to define the source process. The result would be a test of what near-field phenomena can be discerned at short distances. The effects of wavefield scattering on observations would be able to be quantified, and the mechanisms of S-wave and Lg-wave generation might be better understood.

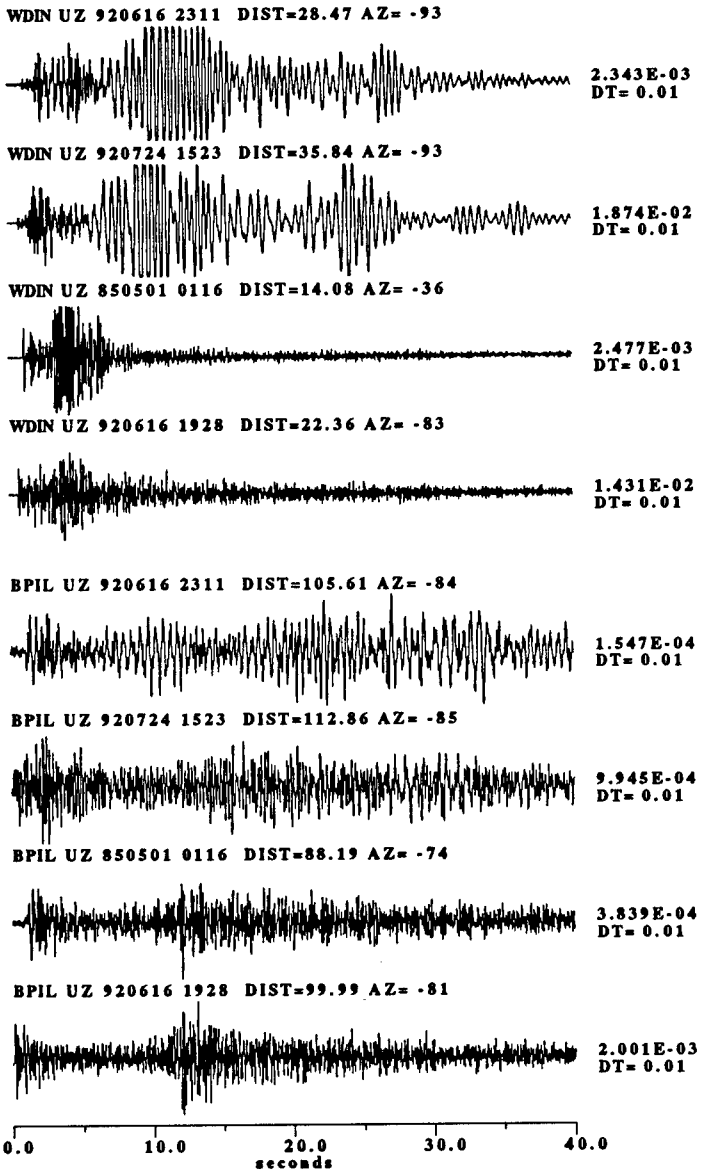


Fig. 10. A sequence of four vertical component time histories recorded at stations BPIL and WDIN. For each station, the upper two traces correspond to two different blast, and the lower two traces to two different earthquake recordings. Annotation shows distance (DIST), azimuth (AZ), maximum ground motion (in cm/sec) and sample rate (DT in sec). The low frequency Rg coda is very pronounced in the blasts at WDIN. The Rg coda is not as pronounced at BPIL for the two blasts, but the S phase arrivals on the two earthquakes are more distinct.

Herrmann, R. B., G. Al-Eqabi, and K. Hutchensen (1992). Quantification of m_{Lg} for small explosions, *Scientific Report No. 1,* Phillips Laboratory, Air Force Systems Command, PL-TR-92-2109, 47 pp.

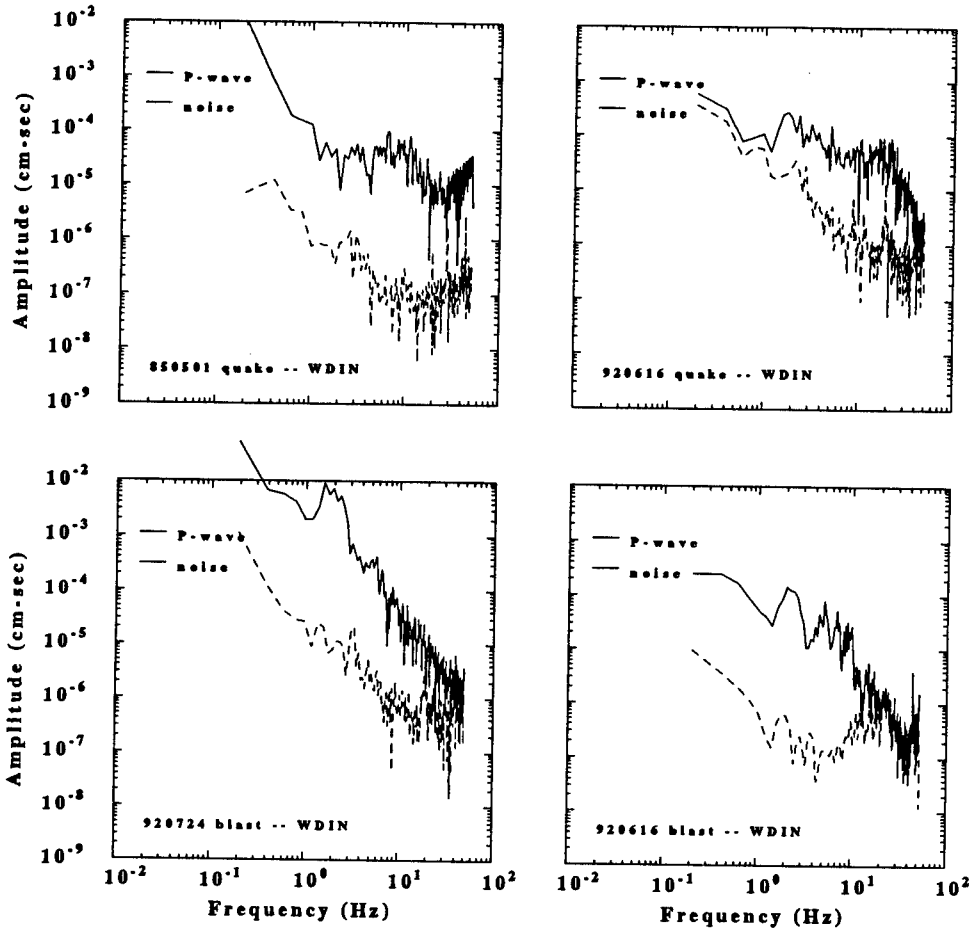


Fig. 11. P-wave spectra for the station WDIN traces shown in Figure 10. The spectra of the two earthquakes is given at top, and of the two blasts at the bottom. The spectra of the background noise preceding the P-wave arrival is given by the dashed lines in each figure.

Herrmann, R. B., G. Al-Eqabi, and K. Hutchensen (1993). Quantification of m_{Lg} for small explosions, *Final Scientific Report No. 1,* Phillips Laboratory, Air Force Systems Command, (submitted).

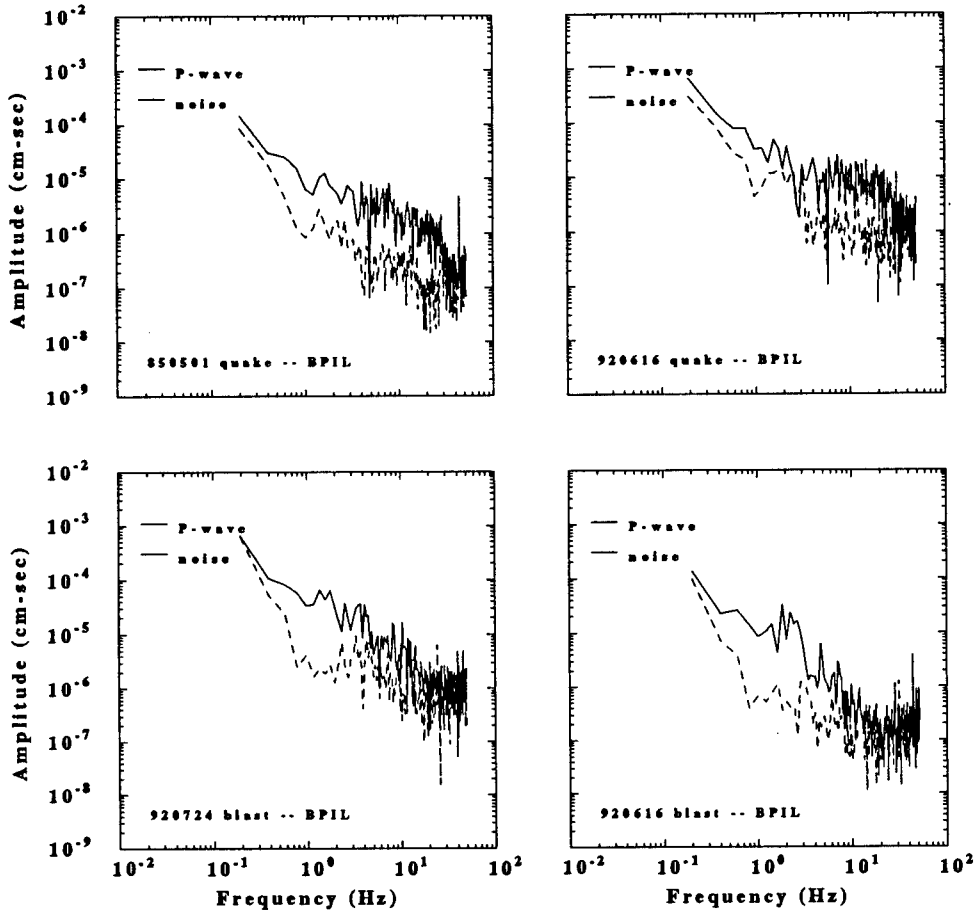


Fig. 12. P-wave spectra for the station BPIL traces shown in Figure 10. The spectra of the two earthquakes is given at top, and of the two blasts at the bottom. The spectra of the background noise preceding the P-wave arrival is given by the dashed lines in each figure.

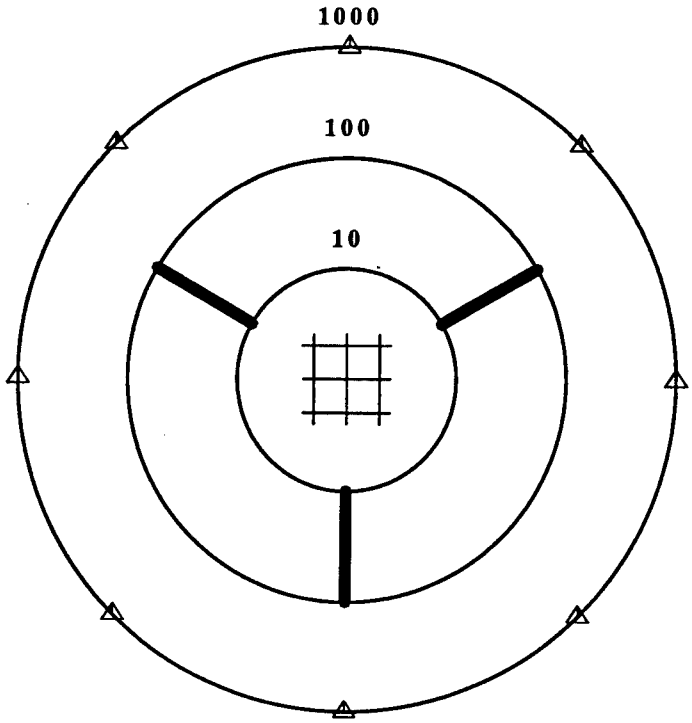


Fig. 13. A schematic data acquisition experiment to test the ability of different data sets to discern the complexity of the explosion source process. The experiment monitors a point or delayed explosion with a dense array within 10 km of the shot point. A second experiment consists of three-component instruments deployed in three arrays from 10 -100. The last set of instruments monitors the explosion at the regional distance of 1000 km.

Modeling of Tamped and Decoupled Explosions in Salt (Simulation Is Easy. Prediction Is Difficult!)

P. Goldstein and L.A. Glenn

Lawrence Livermore National Laboratory

Abstract

We compare predictions of the strain hardening model of Glenn (1990), with and without damage, to free field and seismic observations of SALMON, STERLING, and 64 kt (tamped) and 8 kt (decoupled) explosions in an Azgir salt dome in the former Soviet Union (FSU). We find good agreement between the model (without damage) and observations of both SALMON and STERLING. In contrast, the average spectral ratio of the tamped to decoupled Azgir explosions is systematically smaller than predicted by the strain hardening model without damage. Much better agreement is obtained when damage is included in the model of the decoupled Azgir explosion.

Introduction

Recent papers by Adushkin et al., (1992), Sykes (1992) and Glenn (1993) have pointed out significant differences between the decoupling factors found from the SALMON/STERLING experiment and a tamped/decoupled explosion experiment performed in an Azgir salt dome in the former Soviet Union (FSU). In this paper, we explain this discrepancy in terms of differences in strength of the medium for the *decoupled* explosions. The explanation of discrepancies such as this are important because they help improve our understanding of explosion sources and increase confidence in our predictive capabilities.

We compare both freefield and seismic recordings of nuclear explosions in salt with those predicted by Glenn's (1990) strain hardening model for salt. This model was developed in two steps. First, laboratory strength data and elastic properties measured in the field were combined with thermodynamic properties of salt to obtain a first order model. In this first order model, yield strength was assumed to be pressure and strain independent. In this case it was not possible to simultaneously match the observed and predicted cavity radii, peak displacements, and particle velocity waveforms of SALMON. Glenn (1990) obtained much better agreement by implementing a linear strain hardening model, the motivation for which was the fact that the observed plastic wave speed in SALMON significantly exceeded the bulk wave speed. Hopkins (1960) showed that when the yield strength takes the form $Y = Y_o + H' \varepsilon_p$, where ε_p is the equivalent plastic strain and H' the hardening modulus, the ratio of the plastic-to-bulk wave speeds is a unique function of the ratio of hardening to bulk moduli. The hardening modulus thereby derived was employed only for plastic strains below those measured in the laboratory; for $\varepsilon_p > 1.45 \times 10^{-3}$, extrapolated experimental data were used.

For gauges within 600 m of SALMON, predictions of Glenn's model are comparable to those predicted by the model of Rimer and Cherry (1982), which assumes that strength is a function of plastic work. However, at ranges beyond 600 m, the Rimer-Cherry model had plastic wave speeds equal to the bulk wave speed, in disagreement with the observations.

Following Wells (1969), damage was included in this model by modifying the stress field in the vicinity of the cavity to account for plastic unloading. Yield strength at the cavity wall was constrained by the Wells (1969) solution and was varied sigmoidally from this value to the dynamic hardening value at the edge of the microfracture zone (Glenn, 1993).

SALMON and STERLING

SALMON and STERLING were a pair of explosions, conducted in salt, that were designed to study the potential for evading detection of a nuclear test by cavity decoupling. SALMON was a 5.3 kt nuclear explosion conducted in the Tatum salt dome near Hattiesburg, Mississippi (Figure 1). STERLING was a 0.38 kt nuclear explosion detonated in the 17 m radius cavity generated by SALMON (Table 1). Free field recordings of both explosions were obtained at distances ranging from 160 to 660 m (Figure 1). SALMON and STERLING were also recorded at a variety of surface locations (Figure 1). More detailed descriptions of these experiments can be found in Springer, et. al. (1968), and Denny and Goodman (1990).

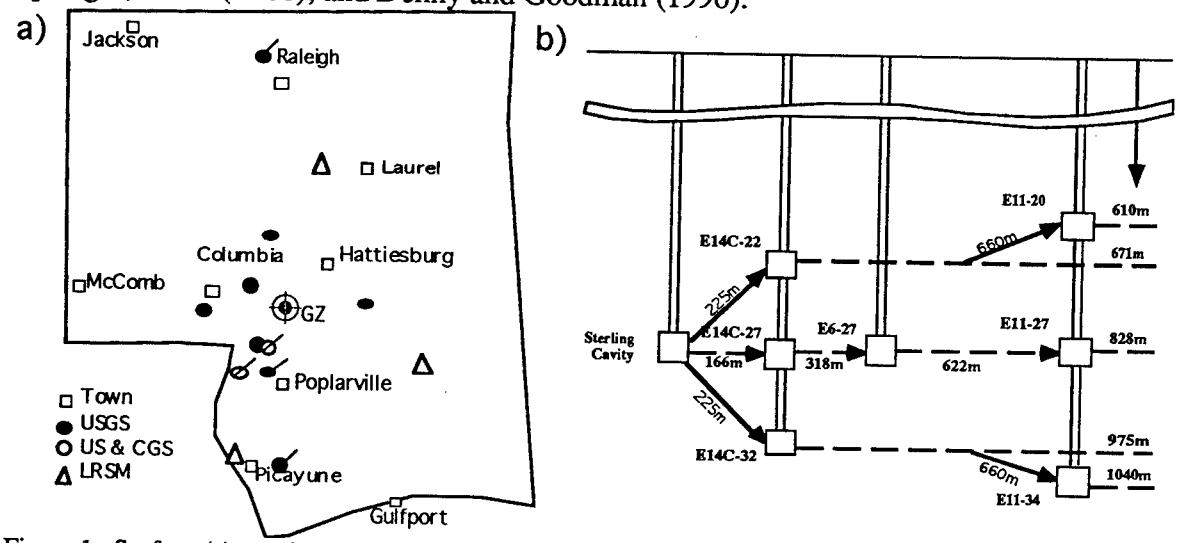


Figure 1. Surface (a) and freefield (b) instrumentation locations for SALMON and STERLING. Flagged surface locations recorded both SALMON and STERLING. Freefield instrumentation boreholes were at a variety of azimuths but are shown in the same vertical cross-section. Freefield stations are labeled by their slant range and name.

Table 1. Source Parameters of SALMON, STERLING, and the Azgir explosions.

Event	Date	Depth (m)	Yield (kt)	$R_0W^{-1/3}$(m/kt$^{1/3}$)*
SALMON	10/22/64	828	5.3	~0.2
STERLING	12/3/66	828	0.38	23.7
A-III (Azgir)	12/22/71	987	64	~0.2
A-III/2 (Azgir)	3/29/76	987	8	18.1

R_0= the initial cavity radius and W is the yield.

We compare both free field and seismic observations of SALMON and STERLING with predictions of Glenn's (1990) strain hardening model. We begin by comparing calculated and observed, free-field reduced-velocity-potential spectra of SALMON at two stations at distances of approximately 660 m (Figure 2). Agreement between the model and data is reasonably good, given the scatter in the data.

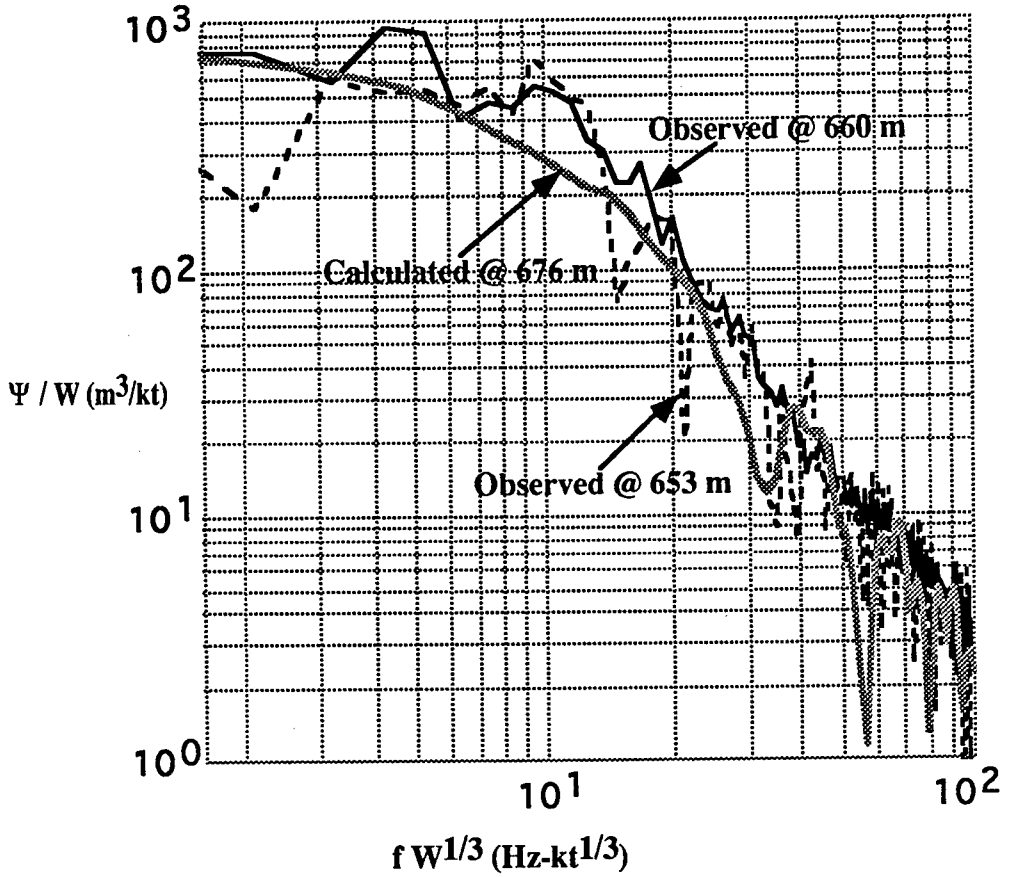


Figure 2. Comparison of calculated yield-scaled reduced velocity potential spectrum for SALMON with observed free-field data in the nonlinear zone.

In contrast to SALMON, all the free field data from STERLING are in the linear elastic zone (e.g., Glenn 1990). Since all the gauges are in the elastic zone, reduced-displacement-potentials, their derivatives, and corresponding spectra should be independent of distance. Although there is some scatter, this appears to be a good first approximation. Based on this approximation, we computed a mean reduced velocity potential spectrum from all the gauges in the free field and found good agreement with the prediction of the model (Figure 3).

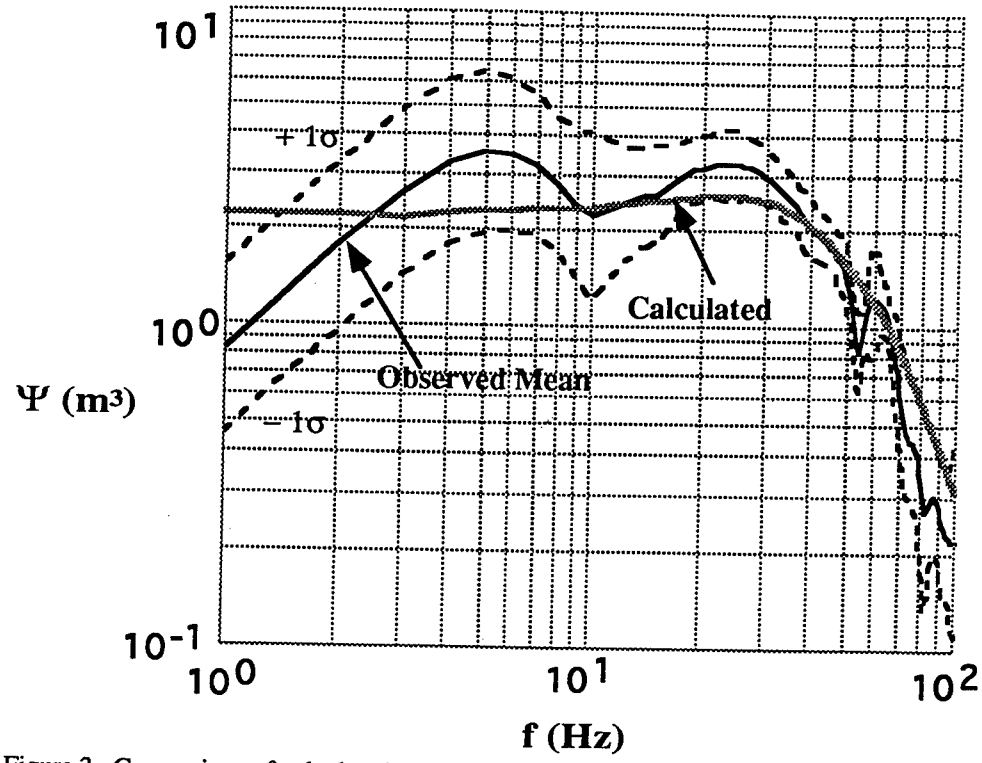


Figure 3. Comparison of calculated reduced velocity potential spectrum for STERLING with the mean of free-field data in the range: 160m<R< 660m. The dashed lines represent ± 1 standard deviation from the observed mean.

SALMON and STERLING were also recorded by the U. S. Geological Survey and U.S. Coast and Geodetic Survey at a number of surface sensors, at distances ranging from 10 to 110 km (Figure 1). We used spectral ratios to assess the agreement between the strain hardening model and the data recorded in the far field. Spectral ratios were used because, in principle, they are insensitive to geologic heterogeneities between the source and receiver; once the signals have reached the linear elastic regime. The seismic displacement amplitude spectrum $U(\omega)$ can be written as $U(\omega) = S(\omega)H(\omega)$ where, $S(\omega)$ is the source spectrum and $H(\omega)$ describes path effects. Then the spectral ratio $SR(\omega)$ is,

$$SR(\omega) = \frac{U_T(\omega)}{U_D(\omega)} = \frac{S_T(\omega)}{S_D(\omega)} \frac{H(\omega)}{H(\omega)} \qquad (1)$$

where the subscript T is for tamped and D is for decoupled.

As indicated in Equation 1, the contribution to the far field spectral ratio due to the path cancels out of the numerator and denominator. Effects of recording system responses can also be eliminated in a similar way provided the instrument responses were identical in the frequency band of interest.

Comparison of the calculated spectral ratio with those from far field recordings of SALMON and STERLING are shown in Figure 4 There is excellent agreement between the observed and predicted spectral ratio from 0 to 20 HZ. Spectral ratios for SALMON and STERLING are not accurate above 20 HZ because of low signal to noise levels in the SALMON data (Blandford and Woolson, 1979).

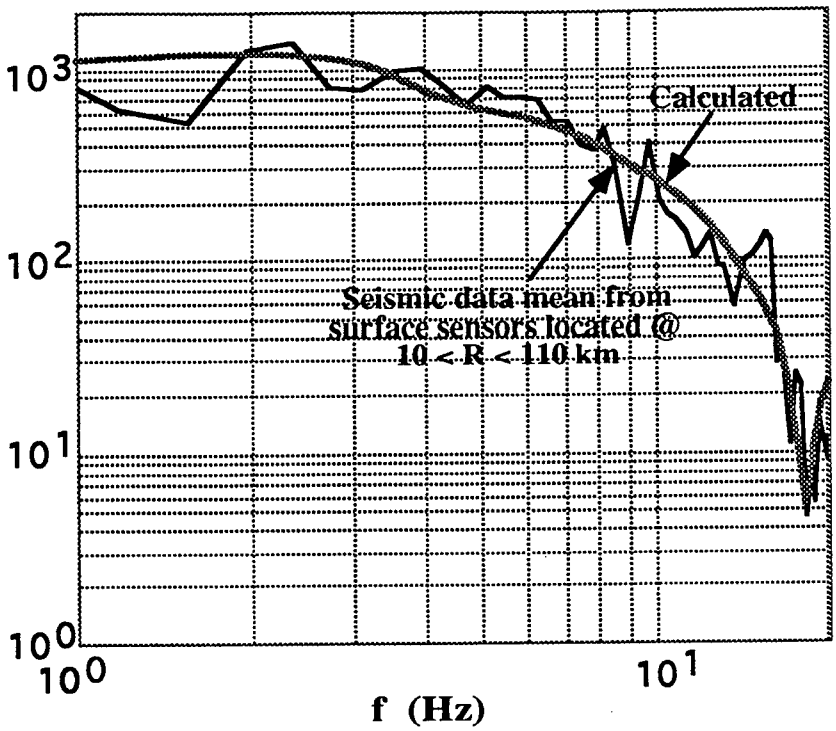


Figure 4. Comparison of the calculated spectral ratio with the average obtained from seismic observations of SALMON/STERLING in the range: 10<R<110 km.

Spectral ratios are also of interest because they are directly proportional to the amplitude decoupling factor,

$$f(\omega) \equiv \frac{\Psi_T(\omega)/W_T}{\Psi_D(\omega)/W_D} = \frac{SR(\omega)}{W_T/W_D}, \qquad (2)$$

where Ψ is the spectral representation of the reduced displacement potential and W is the yield. The static value ($\omega = 0$) is the conventional seismic decoupling factor, and is approximately 70; in good agreement with previous studies (e.g., Denny and Goodman,1991, and Springer et al., 1968).

Tamped and Decoupled Azgir Explosions

In this section we compare predictions of the strain hardening model of Glenn (1990), with and without damage, to seismic observations of a tamped and decoupled explosion pair that was detonated in an Azgir salt dome (Adushkin, et al. 1992). A-III had a yield of 64 kt, was detonated on December 22, 1971 (Sykes, 1992), and created a cavity with equivalent radius of 36.2m. Approximately five years later an 8 kt device (A-III/2) was detonated inside the cavity generated by A-III. Additional source parameters are listed in Table 1. Digitized 3-component seismic recordings of these explosions, at distances ranging between 1 and 154 km were made available to us by Ivan Kitov of the Russian Academy of Sciences.

As in the previous section, we focus on spectral ratios of recordings at approximately co-located stations because they are fairly insensitive to path and site effects. In Figure 5 we

compare the spectral ratios predicted by the strain hardening model, with and without damage, to the average spectral ratio observed at 7 of the 10 co-located seismic stations.

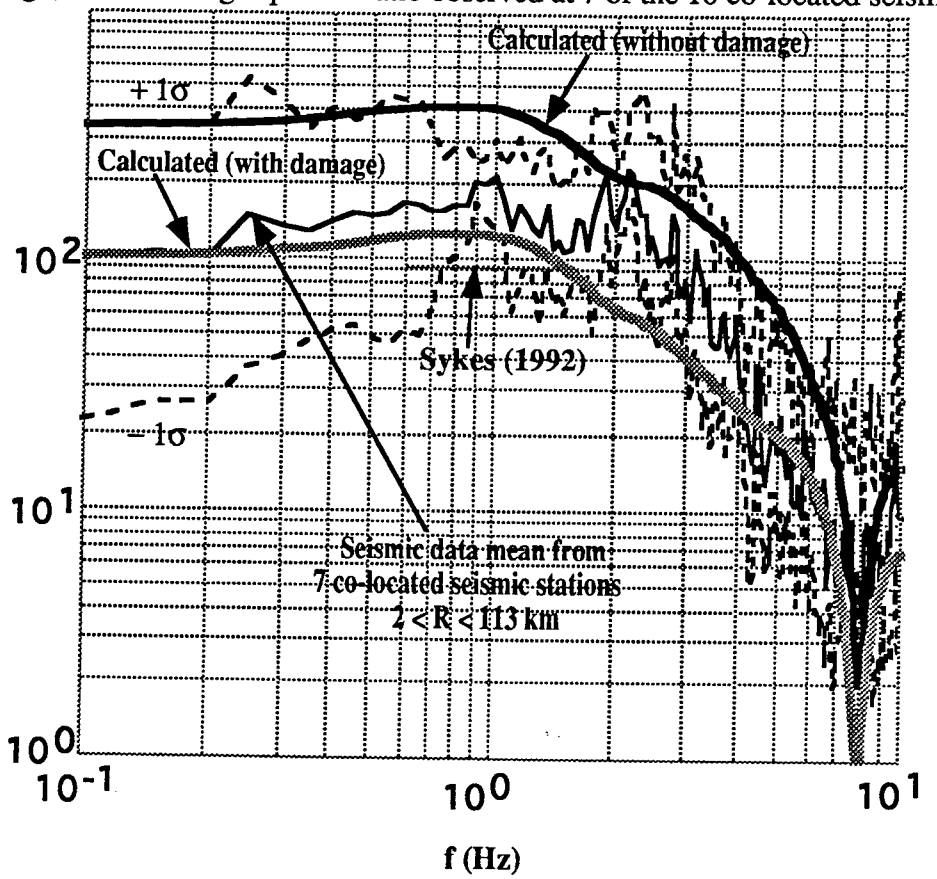


Figure 5 Amplitude spectral ratio for Azgir explosions A-III and A-III/2. The black solid line is the mean from 7 co-located seismic stations in the range 2 < R < 113 km. The dashed lines show ± 1 standard deviation. The heavy black line is the simulation (without damage) and the heavy gray line is the simulation (with damage). The horizontal line derives from Sykes' (1992) estimate based on teleseismic data.

Three stations were excluded from our spectral ratio estimates because of significant differences in the waveforms of the tamped and decoupled explosions below both of their corner frequencies. At these low frequencies, and at the distances in question (2, 18.2, and 40 km) it is unlikely that these differences are source related. Alternative explanations are that these stations were not really co-located and/or their instrumentation malfunctioned or differed between these events. Including the 3 stations in question in our analysis does not change the mean spectral ratio significantly, but it does increase the variance in the 1 to 5 Hz frequency band.

As indicated in Figure 5, the strain hardening model without damage predicts a greater low frequency spectral ratio (or equivalently decoupling factor) than is observed. Although there are significant uncertainties in this spectral ratio estimate, its mean value is consistent with the amplitude ratio obtained by Sykes (1992) who used time domain amplitude ratios ($m_b(P_n)$) and teleseismic data. When damage was included in the strain hardening model for A-III/2, much better agreement was obtained. The most notable discrepancy that remains is near 2 HZ close to the corner frequency of the larger shot.

Based on the mean low frequency spectral ratio and a yield ratio of 8 the conventional seismic decoupling factor is approximately 12, much lower than expected, based on the strain hardening model and our experience with SALMON and STERLING (Glenn, 1993).

Additional observations that are consistent with damage as an explanation for the smaller than expected spectral ratios and decoupling factor include: 1) first motion amplitudes of the decoupled explosion's waveforms that are much larger than predicted, 2) Yield-scaled final cavity radii of SALMON and A-III that are consistent with the strain hardening model without damage, and 3) thermal diffusion calculations that indicate that the temperature of A-III/2's cavity walls was high ($\geq 100^{\circ}C$) just prior to the explosion. Such high temperatures are expected to reduce the strength of the salt (Glenn, 1993). Glenn (1993) also points out that decoupling factors estimated from the COWBOY chemical explosion experiments are consistent with the Russian datum from A-III/A-III/2.

Conclusions

Based on comparisons of observed and predicted, free-field and seismic waveforms and spectra, Glenn's (1990) strain hardening model, without damage, provides good estimates of the ground motions and decoupling factor corresponding to SALMON and STERLING. However, the average spectral ratio (or decoupling factor) of a tamped/decoupled explosion pair in an Azgir salt dome is systematically lower than predicted by this model. Much better agreement is obtained when the model is modified to account for damage (induced by the tamped explosion) to the walls of the decoupled explosion's cavity.

Acknowledgements We thank Marv Denny for providing data from the SALMON and STERLING experiments and Ivan Kitov for making data from the Azgir explosions available to us. This work has been performed under the auspices of the U.S. Department of Energy by Lawrence Livermore National Laboratory under Contract No. W-7405-Eng-48.

References

Adushkin, V. V., D.D. Sultanov, I.O. Kitov, O.P. Kuznetsov, (1992), "Overview of the experimental data and theoretical simulations of underground nuclear explosions decoupled by large air filled cavities," Reports of the (Russian) Academy of Sciences, 327, No. 1.

Blandford, R. R. and J. R. Woolson, (1979), "Experimental spectral analysis of SALMON/STERLING decoupling,"SDACTR-79-3, Teledyne Geotech, Alexandria, VA,

Denny, M. D., and D. M. Goodman (1990),"A Case Study of the Seismic Source Function: SALMON and STERLING Reevaluated," *J. Geophys. Res.* **95**, 19705–19723.

Glenn, L. A. (1993), "Comparing U.S. and Russian Experience with Cavity Decoupling in Salt," accepted for publication in*Geophys. Res. Lett.* see also Lawrence Livermore National Laboratory, Livermore, CA, UCRL-JC-112466.

Glenn, L. A. (1990), "*Strain Hardening in Salt---Results of the SALMON Experiment*" *J. Energy Resources Technology,*. **112**, 145-148.

Hopkins, H.G., (1960), "Dynamic Expansion of Spherical Cavities in Metals," Progress in Solid Mechanics, Vol. 1 eds., I.N. Sneddon and R. Hill, North Holland Publishing Co., Amsterdam, Chap. III.

Rimer, N., and J. T. Cherry (1982), "Ground Motion Predictions for the Grand Saline Experiment," Report No. VSC-TR-82-25, S-CUBED Corporation, La Jolla, Calif., July.

Springer, D., M. Denny, J. Healy, W. Mickey, (1968), "The STERLING Experiment: Decoupling of seismic waves by a shot-generated Cavity," *J. Geophys. Res.* **73**, 5995-6011.

Sykes, L.R., (1992), Magnitude and decoupling factor for 9-kiloton decoupled Russian explosion: Implications for monitoring test ban treaties," EOS supplement, October 27, 359.

Wells, W.M., (1969), Calculation of Shrinkage of the SALMON Cavity, *J. Geophys. Res.* **74**, 2791-2794.

Addendum

On April 27, 1993 we learned from V. B. Adamskii of the All Union Scientific Research Institute of Experimental Physics (Arzamas-16) that the yield of the decoupled explosion (AIII-2) may have been 11.5 kt, not 8 kt as reported by Adushkin et al., (1992). This is being investigated.

Coupling of an Overdriven Cavity

H. Douglas Garbin

Seismic and Ground Motion Div.9311
Sandia National Laboratories

Introduction:

It is well known that when a nuclear test is conducted in a sufficiently large cavity, the resulting seismic signal is sharply reduced when compared to a normal tamped event. Cavity explosions are of interest in the seismic verification community because of this possibility of reducing the seismic energy generated which can lower signal amplitudes and make detection difficult. Reduced amplitudes would also lower seismic yield estimates which has implications in a Threshold Test Ban Treaty (TTBT). In the past several years, there have been a number of nuclear tests at NTS (Nevada Test Site) inside hemispherical cavities. Two such tests were MILL YARD and MISTY ECHO which had instrumentation at the surface and in the free-field. These two tests differ in one important aspect. MILL YARD was completely decoupled. i.e. the cavity wall behaved in an elastic manner. It was estimated that MILL YARD's ground motion was reduced by a factor of at least 70. In contrast, MISTY ECHO was detonated in a hemispherical cavity with the same dimensions as MILL YARD, but with a much larger device yield. This caused an inelastic behavior on the wall and the explosion was not fully decoupled.

The question of whether partial decoupling exists has not yet been resolved. Early calculations by Rodean[1] suggest a slight signal enhancement may occur in an overdriven cavity above an equivalent tamped explosion. His decoupling curve also present a sharp increase in coupling near 10 m/kt$^{1/3}$ cavity radius. Thus it appears that an explosion is either completely decoupled or completely coupling radius (radius at which the explosion becomes fully decoupled) is 10 m/kt$^{1/3}$, to completely evading a TTBT at large yields because of the volume required. If it is assumed that the scaled coupling radius (radius at which explosion becomes fully coupled) is 10 m/kt$^{1/3}$, to completely decouple a 150 kt explosion requires a spherical cavity with a radius of 53 m. This would demand a very expensive mining operation if not carried out in salt. Even a 10 kt shot would require a 22 m cavity radius.

Recently, a paper by King et. al.[2] suggests that partial decoupling may be a viable option. The calculations were carried out to a scale radius of 3.4 m/kt$^{1/3}$ which gave a 40% decrease in coupling. Thus, if full decoupling is not necessary, but a reduction of the seismic output is desired, cavity explosions become a feasible option. An estimate on the cavity size can be made by a straight line extrapolation of King et. al. curve. This is represented approximately by equation (1):

$$W/W_0 = 1 - R/10 \quad (1)$$

where W_0 = the actual yield
W = the seismically measured yield
R = the scaled cavity radius (m/kt$^{1/3}$).

This expression indicates that a scaled cavity radius of 5 m/kt$^{1/3}$ would suffice in reducing the seismic estimate by a half. Under these conditions, a 150 kt explosion in a cavity with a 27 m radius would appear to have a yield of 75 kt. This is still a rather large volume to mine. For a 200 kt test to behave as is it were at the present 150 kt treaty limit, a cavity of only 14.6 m is required. Figure 1 is a plot of the cavity radius as a function of yield if one wanted all explosions above 150 kt to appear to be at the present limit. Because of the possibility of partial decoupling, a closer look at the data in overdriven cavities is warranted.

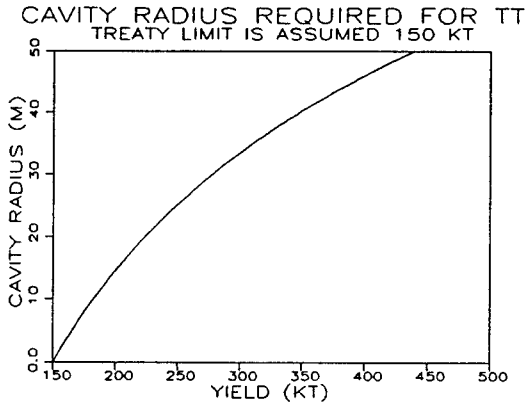


Figure 1 Required cavity radius for presumed nuclear yield to be within TTBT 150 kt limit.

Although the calculations that produced the above estimates assume the existence of partial decoupling, data have not confirmed this result at seismic ranges. In previous experiments at NTS, decoupling was measured using surface accelerometers for both the reference and cavity explosions. The analysis of this data indicated that MILL YARD was completely decoupled and the overdriven cavity of MISTY ECHO produced no measurable decoupling. Both events used DIAMOND BEECH as the reference explosion. DIAMOND BEECH has several significant advantages as a reference explosion for its use with MILL YARD. First it was detonated only a couple of hours after MILL YARD and the same surface gauges were used to measure the ground motion of both explosions. This utilization of the same gauges insured that the signals of both explosions traveled through similar structure and propagation path differences are minimized. In contrast, MISTY ECHO is located about 1 km from DIAMOND BEECH and measured ground motion at different gauge locations. This spatial separation can accentuate signal differences not associated with the source. If the path of the cavity and reference events are substantially different, then variations that occur in the signal may be the result of the path properties, not the source properties.

EXPERIMENT DESCRIPTION

To avoid extensive layering along the signal paths, free-field data obtained in the MINERAL QUARRY experiment is used for comparison with free-field MISTY ECHO ground motion. Both MINERAL QUARRY and MISTY ECHO had accelerometers located in the free-field near the same level of their respective working points. MINERAL QUARRY had only two sites instrumented in this experiment. These were located at ranges near enough to be considered in the free-field and far enough for the medium to respond linearly. The experiment consisted of two triaxial acceleration packages. Each were placed in 10 m deep bore holes located in the right rib of the bypass drift. They were at ranges of 700 ft (215 m) and 1000 ft (306 m) from the working point. The packages were aligned in a manner to produce radial, vertical and tangential signals with respect to the working point (WP). The accelerometers are designed to work in environments as high as 200 g which is well above the expected amplitudes.

The free-field gauges in MISTY ECHO were located at similar ranges. Their ranges are 170, 350 and 363 m. The gauge located at 170 m may lie in the non-elastic regime. I am assuming a non-linear behavior for stresses above 0.25 kb and the 170 m station has a stress estimated at about .5 kb. The other two are situated on the opposite sides of a fault which is thought to have moved vertically. The radial signals did not exhibit differences in ground motion that the vertical components displayed.

RESULTS

Three component acceleration data were obtained from two locations on the MINERAL QUARRY event. Plots of the radial channels are shown in Figure 2. A total of about 0.8 seconds were recorded but only 0.4 seconds are shown on the plots. The radial components gave the largest amplitudes. The peak acceleration at 215 m is about 36 g and 15 g at 306 m. The data have very good signal to noise levels. Spectral calculations indicate the frequency content is good out to about 250 hz. Above that frequency, the signal amplitude resolution is too insensitive.

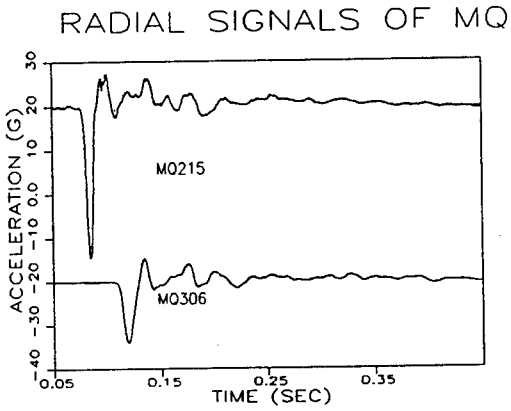


Figure 2: MINERAL QUARRY Radial Signals at 215 and 306 m

Both the vertical and tangential signals were predictably much smaller than the radial amplitudes. This is an indication that the gauges were aligned fairly well. The initial vertical peak at 215 m is about 4 g and only .3 g at 306 m. Similarly, the tangential signals are also smaller than the radial data.

MISTY ECHO recorded signals from gauges located at ranges of 170, 350, and 363 m. Figure 3 is a comparison of 350 m radial data to the acceleration record of MINERAL QUARRY at 306 m. Both of these signals are used in the decoupling analysis and the wave forms are quite similar to each other.

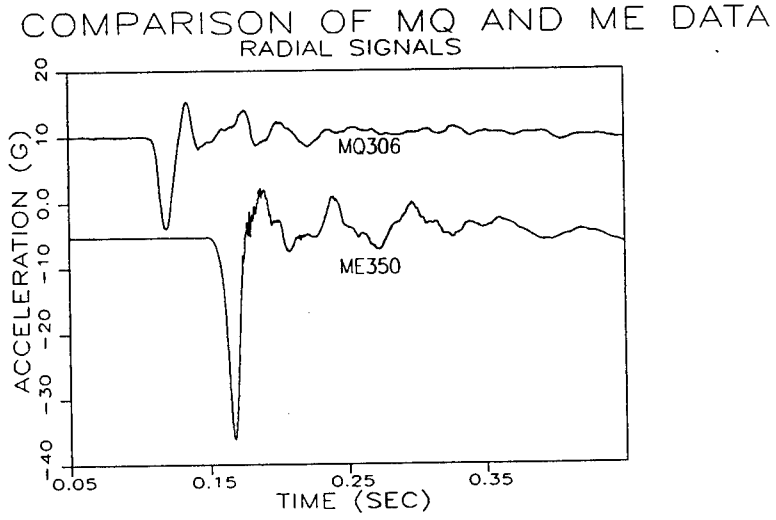


Figure 3: Radial Acceleration Comparison

ANALYSIS

Before the decoupling analysis can begin, some operational definition of the phenomenon should be made. This is done by imagining an idealized experiment. Suppose we measure the ground motion due to a tamped device of a known yield with gauges located at various ranges. Let us now excavate a cavity about the working point of the tamped explosion and perform the same experiment. Ignoring the changes in the medium due to the first explosion, decoupling is defined as the spectral ratio of the ground motion due to a reference event to that of a cavity event with the same yield detonated at the same location with instruments at the same ranges. Obviously, this idealized state is never realized since tests are not dedicated to decoupling. In general, the tests differ in all three aspects of yield, location and range. Thus, to make an estimate, the reference data (MINERAL QUARRY) is cube root scaled to the yield of the cavity explosion; i.e., MISTY ECHO. The general relationship for scaling acceleration is:

$$u_s\left(r_{mq}/s, t/s\right) = s * u\left(r_{mq}, t\right) \quad (2)$$

where: u = measured MINERAL QUARRY acceleration,
u_s = MINERAL QUARRY acceleration scaled to MISTY ECHO,
r_{mq} = range of gauges with respect to the WP,
t = time,
and the scaling factor s is given as:

$$s = \left(W_{mq} / W_{me}\right)^{1/3} \quad (3)$$

W_{mq} = MINERAL QUARRY yield,
W_{me} = MISTY ECHO yield.

The procedure requires scaling not only the acceleration, but also the time and ranges. In additional to cube root scaling, a geometric spreading factor is done so the ranges of MINERAL QUARRY and MISTY ECHO are the same. The final scaling expression is:

$$u_s\left(r_{me}, \omega\right) = u\left(r_{mq}/s, \omega\right) * r_{mq}/s/r_{me} \quad (4)$$

where: r_{me} = MISTY ECHO range,
r_{mq} = MINERAL QUARRY range,
ω = circular frequency.

The ratio of $\left|u_s / u_{me}\right|$ gives the decoupling as a function of frequency. This technique is applied only to acceleration data and avoids difficulties with the permanent displacement or any linear trends in the signals.

The value of the scaling factor s is determined from the yields as given by the sponsoring lab. This produced a scaling factor near one. The calculated decoupling curve is given in Figure 4. This particular plot is an average over four possible pairs of ratios (2 MISTY ECHO, 2 MINERAL QUARRY signals). The data at 170 m in MISTY ECHO is not included because it may be in the nonlinear range. The two outer curves are the 1 standard deviations of the four pair averages at each frequency. The straight line is the average decoupling over the total frequency range shown. Note that this curve's average is less than 1 which implies coupling enhancement.

The decoupling is given in Figure 4 exhibits a constant ratio over the large frequency range. Previous experimental analysis has shown low frequency decoupling to be significantly higher than at the lower frequencies. MILL YARD was decoupled by a factor of 70 near 3 Hz and only 10 at 30 Hz.

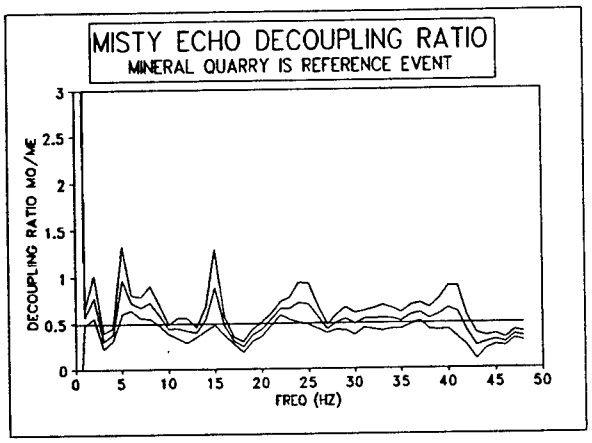


Figure 4 MISTY ECHO Decoupling, MINERAL QUARRY Reference Case

In addition to the above analysis on the acceleration, calculations were also done using the Reduced Displacement Potential (RDP). This quantity is defined by the relation:

$$d(r,t) = \frac{\partial}{\partial t}\left[\frac{\phi(\tau)}{r}\right] \quad (5)$$

where ϕ is the Reduced Scalar Potential
d = radial displacement
t = time, $\tau = t - r/c$
r = range
c = p-wave velocity

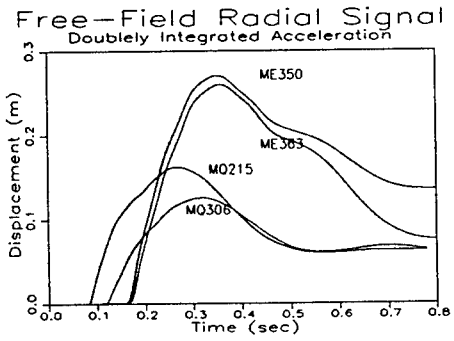


Figure 5 Displacements in MISTY ECHO and MINERAL QUARRY

The form of the RDP plots are similar to the displacement result. The displacement curves are shown in figure 5 and the RDP curves are shown in Figure 6. Because of the permanent offsets at late times, the Fourier Transforms are not calculated directly. Instead, curves are fit to the RDP shown in Figure 6 using the Haskell expression. This is given as:

$$\Phi(\omega) = \Phi(\infty)[1 - \exp(-\kappa\tau)f(\kappa\tau)] \quad (6)$$

$\Phi(\infty)$ is related to the permanent radial displacement $u(\infty)$ by:

$$\Phi(\infty) = r^2\, u(\infty) \quad (7)$$

The function f(x) is given as:

$$f(x) = 1 + x + x^2/2 + x^3/6 + Bx^4 \quad (8)$$

For these relations to be useful, three constants need to be determined, $\Phi(\infty)$, κ and B. $\Phi(\infty)$ can be found either by the late time value of $\Phi(\tau)$ or through the expression (7). κ and B are determined from the RDP curves. The Fourier Transform of equation 6 can be written as:

$$(i\omega)\Phi(\omega) = \Phi(\infty)\frac{\{i(1+B)\omega/\kappa + 1\}}{(i\omega/\kappa + 1)^5} \quad (9)$$

An average spectral function is found for both MISTY ECHO and MINERAL QUARRY. MINERAL QUARRY is scaled and the ratio taken. Figure 7 is the RDP spectral ratio of the two events. The high frequencies have decoupling values near the acceleration analysis. The low frequencies are higher but still less than 1, indicating coupling enhancement. This analysis is subject to the same low frequency criticisms expressed with acceleration.

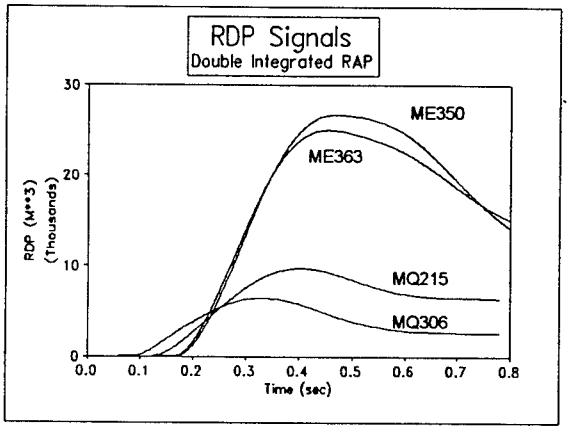


Figure 6 Reduced Displacement Potential in MISTY ECHO and MINERAL QUARRY

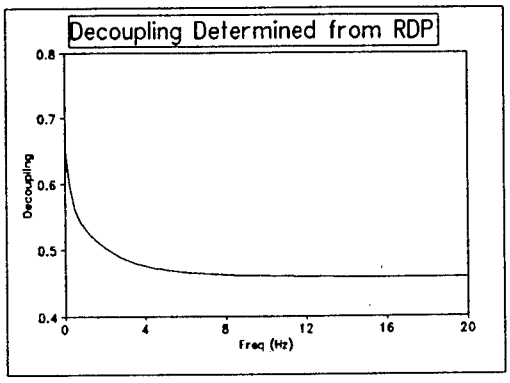


Figure 7 MISTY ECHO RDP Decoupling, MINERAL QUARRY Reference Case

Explosive coupling is not just a function of whether it occurred in a cavity. Granite is a better coupler than tuff. However, the material properties of MINERAL QUARRY and MISTY ECHO are quite similar. Table I is a list of some of these properties with the corresponding values. One important property that is missing in this table is the material strength. However, the properties that are listed are almost identical although the two explosions occurred about 1 km apart. This gives added weight that signal enhancement is due to the cavity.

Table I

Physical Properties of MISTY ECHO and MINERAL QUARRY

	MINERAL QUARRY	MISTY ECHO
Tunnel	U12n.22	U12n.23.
Depth	389.4 m	400.2 m
Medium	Tuff	Tuff
Lithologic Unit	Tunnel Bed 4	Tunnel Bed 4
Density (Grain)	2.46 Mg/m^3	2.45 Mg/m^3
Density (Bulk)	1.88 Mg/m^3	1.91 Mg/m^3
Water Content Vol.%	20.1%	19.1%
Porosity Vol.%	39.0%	36.7%
Saturation Vol.%	97.0%	99.4%
Sonic Velocity	2920 m/sec	2860 m/sec

CONCLUSION:

One of the prime objectives of the MINERAL QUARRY seismic experiment was to obtain ground motion data in the free-field to investigate the possibility of partial decoupling in previous cavity events. This part of the experiment has been a success. Using spectral ratios of the cube root scaled reference event (MINERAL QUARRY) and MISTY ECHO indicate a coupling enhancement of 2. The RDP calculated for each event was fit to a Haskell type source function yielded similar results. Whether this is due to the cavity or material properties is unclear, but most of the media properties of the two events are almost identical. The low frequency data does not reveal the expected higher decoupling which may be attributed to the window length and offset or trends in the records.

1. E. S. Husebye and S. Mykkeltveit (Eds.), " Identification of Seismic Sources - Earthquake or Underground Explosion ", Rodean, H. C., "Inelastic Processes in Seismic Wave Generation by Underground Explosions", D. Reidel
Publishing Co., 1981, Boston.

2. King, D. S., B.E. Freeman, D.D. Eilers and J.D. Johnson," The Effective Yield of a Nuclear Explosion in a Small Cavity in Geological Material: Enhanced Coupling Revisited", J. Geophys. Res., 94, 12375-12385, 1989.

Simulating High-Frequency Seismograms in Complicated Media: A Spectral Approach

J. L. Orrey and C. B. Archambeau
Department of Physics
University of Colorado
Campus Box 583
Boulder, CO 80309-0583

August 26, 1993

1 Summary

The main attraction of using a spectral method instead of a conventional finite difference or finite element technique for full-wavefield forward modeling in elastic media is the increased accuracy of a spectral approximation. While a finite difference method accurate to second order typically requires 8 to 10 computational grid points to resolve the smallest wavelengths on a 1-D grid, a spectral method that approximates the wavefield by trigonometric functions theoretically requires only 2 grid points per minimum wavelenth and produces no numerical dispersion from the spatial discretization. The resultant savings in computer memory, which is very significant in 2 and 3 dimensions, allows for larger scale and/or higher frequency simulations.

The spectral methods we are investigating solve the elastodynamic equations of motion by approximating the spatial dependencies as truncated series of orthogonal functions and by integrating the expansion coefficients in time as in a finite difference method. Such a formulation maintains a continuous spatial representation, in contrast to a collocation method. In collocation, also referred to as a pseudospectral method, the equations of motion are solved in a discrete spatial domain. We derive the spectral method from a variational formulation of momentum conservation and compare its accuracy to a collocation method in approximating wavefields in strongly heterogeneous media.

By treating the governing equations in the wavenumber domain, products in the spatial domain are replaced by convolutions, and the spatial solution is synthesized via a Fast Fourier Transform (FFT). However, if the density and/or moduli wavenumber spectra are broad, the finite bandwidth of the orthogonal basis set can result in aliasing. As an illustration, consider the contributiions from single-wavenumber trigonometric functions to the spatial product of modulus and strain. The spectrum of the stress field contains contributions at the sum and difference of the wavenumbers of the modulus and strain fields. Aliasing occurs if the stress field's spectrum lies outside the bandwidth of the basis functions. We show how such aliasing affects surface and body wave synthetics, and we demonstrate how bandlimiting a structural model to avoid aliasing improves the accuracy of spectral computations with strong structural heterogeneities.

Aliasing errors due to material structure are particularly severe when representing a traction-free surface condition. Whereas a conventional trigonometric basis is continuous, the free surface condition introduces a field discontinuity between the top and bottom of the spatial grid. Introducing a discontinuous basis set mitigates this well-known problem. We compare the accuracy of

surface waves produced using a discontinuous basis to those with a trigonometric basis and an explicit free surface condition.

2 Spectral Methods

In the equations that follow, Greek subscripts denote spatial coordinate directions, and $\mathbf{n}_\beta$ is a unit vector in the β direction. Boldface subscripts and superscripts on summations and integrals represent a three-dimensional set of integers, e.g. $\mathbf{k} = (k_1, k_2, k_3)$, so that $\sum_{\mathbf{k}}$ represents a triple sum. Summation over repeated indices is assumed, and the symbol i in an exponent represents $\sqrt{-1}$.

For a spectral solution to the elastodynamic equations of motion, we expand each component of the displacement field in a truncated series of trigonometric functions over the volume $V_X = \prod_{\beta=1}^{3} X_\beta$ of the spatial domain:

$$u_\alpha(\mathbf{x},t) \;=\; \sum_{\mathbf{k}=-\mathbf{K}/2}^{\mathbf{K}/2} \hat{U}_\alpha(\mathbf{k},t)\, e^{i2\pi\mathbf{k}\cdot\mathbf{x}}. \tag{1}$$

The position $\mathbf{x}$ and hence the wavenumber $2\pi\mathbf{k}$ are made unitless by normalizing each coordinate with respect to the corresponding domain length X_β. The expansion coefficients are then

$$\hat{U}_\alpha(\mathbf{k},t) \;=\; \int_0^1 e^{-i2\pi\mathbf{k}\cdot\mathbf{x}} u_\alpha(\mathbf{x},t)\, d^3x. \tag{2}$$

We obtain the governing equation for these coefficients by substituting the expansion of equation (1) into the variational statement of momentum conservation:

$$\begin{aligned}&\int_0^1 [\,\rho(\mathbf{x})\ddot{\mathbf{u}}(\mathbf{x},t)\cdot\delta\mathbf{u}^*(\mathbf{x}) + \underline{\sigma}(\mathbf{x},t)\cdot\delta\underline{\epsilon}^*(\mathbf{x}) - \mathbf{f}(\mathbf{x},t)\cdot\delta\mathbf{u}^*(\mathbf{x})\,]\, d^3x \\ &- \oint_{S_\sigma} \mathbf{t}(\mathbf{x},t)\cdot\delta\mathbf{u}^*(\mathbf{x})\, dS \;=\; 0,\end{aligned} \tag{3}$$

where dots indicate time derivatives, $\delta\mathbf{u}(\mathbf{x})$ is a virtual displacement, $\delta\epsilon(\mathbf{x})$ is a virtual strain, and a * indicates a complex conjugate. $f_\alpha(\mathbf{x},t)$ is a body force density and the surface integral is taken over that part of the surface on which the tractions $t_\alpha(\mathbf{x},t)$ are applied.

As a special case, consider an isotropic medium whose modulus is given by

$$E_{\alpha\delta\beta\gamma}(\mathbf{x}) \;=\; \lambda(\mathbf{x})\,\delta_{\alpha\delta}\delta_{\beta\gamma} + \mu(\mathbf{x})\,(\delta_{\alpha\beta}\delta_{\delta\gamma} + \delta_{\alpha\gamma}\delta_{\beta\delta}). \tag{4}$$

By expanding the Lamé coefficients and density in the chosen basis, e.g.

$$\lambda(\mathbf{x}) \;=\; \sum_{\mathbf{k}=-\mathbf{K}/2}^{\mathbf{K}/2} \hat{\lambda}(\mathbf{k})\, e^{i2\pi\mathbf{k}\cdot\mathbf{x}}, \tag{5}$$

the equation to be solved for the wavenumber coefficients is

$$\begin{aligned}\sum_{\acute{\mathbf{k}}} \hat{\rho}(\mathbf{k}-\acute{\mathbf{k}})\,\ddot{\hat{U}}_\alpha(\acute{\mathbf{k}},t) \;+\; &\sum_{\acute{\mathbf{k}}} [\,(2\pi)^2 k_\alpha k_\beta(\hat{\lambda}(\mathbf{k}-\acute{\mathbf{k}}) + \hat{\mu}(\mathbf{k}-\acute{\mathbf{k}})) \\ &+ \delta_{\alpha\beta}\sum_{\gamma=1}^{3}(2\pi k_\gamma)^2\hat{\mu}(\mathbf{k}-\acute{\mathbf{k}})\,]\,\hat{U}_\beta(\acute{\mathbf{k}},t) - \hat{F}_\alpha(\mathbf{k},t) \;=\; 0\end{aligned} \tag{6}$$

where the limits on the 3-D sums are implied by the bandwidth of the chosen basis. Notice that products in the spatial domain have become convolutions in the wavenumber domain. Their general form is

$$\hat{T}(\mathrm{k}) = \sum_{\acute{\mathrm{k}}} \hat{E}(\mathrm{k}-\acute{\mathrm{k}})\,\hat{\epsilon}(\acute{\mathrm{k}}) \tag{7}$$

and they can be computed with FFTs.

3 The Collocation or Pseudospectral Method

If we solve the governing equations in the spatial domain instead of in the wavenumber domain, both domains are discretized. The two domains are related by a discrete Fourier series. Such a treatment is called a collocation method, but it is also referred to as a pseudospectral method for reasons described below.

Let the continuous space $\mathbf{x} = x_\beta \mathbf{n}_\beta$ be discretized into the positions $j_\beta \Delta x_\beta \mathbf{n}_\beta$, with N_β collocation points evenly spaced by a distance Δx_β along the direction β. The wavenumbers are then discretized as $\frac{2\pi m_\beta}{X_\beta}\mathbf{n}_\beta$ for $m_\beta = -N_\beta/2+1, ..., N_\beta/2$, and $X_\beta = N_\beta \Delta x_\beta$. The spatially discretized displacement is

$$u_\alpha(j_\beta \Delta x_\beta \mathbf{n}_\beta, t) \equiv U_\alpha(\mathbf{j},t) = \sum_{\mathbf{m}=-\mathbf{N}/2+1}^{\mathbf{N}/2} \tilde{U}_\alpha(\mathbf{m},t)\, e^{i2\pi m_\beta j_\beta / N_\beta} \quad ; \quad j_\beta = 0, ..., N_\beta - 1. \tag{8}$$

The index $m_\beta = N_\beta/2$ corresponds to the Nyquist frequency for the direction β. Due to the discrete orthogonality relation

$$\frac{1}{N}\sum_{m=0}^{N-1} e^{i2\pi m j/N} = \begin{cases} 1 & \text{if } j = nN; n = 0, \pm 1, \pm 2, ... \\ 0 & \text{otherwise} \end{cases} \tag{9}$$

the expansion coefficients are

$$\tilde{U}_\alpha(\mathbf{k},t) = \frac{1}{V_N}\sum_{\mathbf{j}=0}^{\mathbf{N}-1} U_\alpha(\mathbf{j},t)\, e^{-i2\pi m_\beta j_\beta / N_\beta} \quad ; \quad V_N \equiv \prod_{\gamma=1}^{3} N_\gamma \tag{10}$$

and the continuum field is represented by the N/2-degree trigonometric interpolation of the nodal quantities of equation (8) :

$$u_\alpha(\mathbf{x},t) \simeq \sum_{\mathbf{m}=-\mathbf{N}/2+1}^{\mathbf{N}/2} \tilde{U}_\alpha(\mathbf{m},t)\, e^{i2\pi \mathbf{m}\cdot\mathbf{x}}. \tag{11}$$

Field derivatives in the discrete space are defined in terms of this continuous field:

$$\partial_\beta u_\alpha(\mathbf{x},t) \simeq \sum_{\mathbf{m}} \tilde{U}_\alpha(\mathbf{m},t)(i2\pi m_\beta)\, e^{i2\pi \mathbf{m}\cdot\mathbf{x}} \tag{12}$$

so that

$$\partial_\beta U_\alpha(\mathbf{j},t) \simeq \sum_{\mathbf{m}} \tilde{U}_\alpha(\mathbf{m},t)(i2\pi m_\beta)\, e^{i2\pi m_\beta j_\beta / N_\beta}. \tag{13}$$

The discrete Fourier expansion coefficients $\tilde{U}_\alpha(\mathbf{m},t)$ can be regarded as approximations to the continuum field coefficients $\hat{U}_\alpha(\mathbf{k},t)$ of the previous section, where the trapezoidal rule is used to evaluate the integral in equation (2). Provided that the continuous Fourier series representation of the field converges to the value of the field at the nodal positions $j_\beta \Delta x_\beta$, then the discrete space and continuous space coefficients are related as

$$\tilde{U}_\alpha(\mathbf{m}) = \hat{U}_\alpha(\mathbf{m}) + \sum_{\mathbf{j}=-\infty}^{\infty} \hat{U}_\alpha(\mathbf{m} + \mathbf{N}\cdot\mathbf{j}) \quad ; \quad \begin{cases} m_\beta = -N_\beta/2+1, ..., N_\beta/2 \\ j_\beta \neq 0 \qquad \beta = 1,2,3 \end{cases} \tag{14}$$

since the higher mode coefficients $\hat{U}_\alpha(\mathbf{m} + \mathbf{N}\cdot\mathbf{j})$ alias the $\mathbf{m}^{th}$ mode at the node positions $j_\beta \Delta x_\beta \mathbf{n}_\beta$. Evidently the representation of the continuum field of equation (11) involves two approximations: one due to truncation of the Fourier series, as in the spectral method, and one due to the interpolation. However, Canuto, et. al. [1] discuss how in spite of the difference in approximation error between the two methods, as suggested by (14), the interpolating polynomials and the truncated Fourier series have similar convergence properties and share the same asymptotoic behavior as $\mathbf{N} \rightarrow \infty$. For a homogeneous full space the two solution methods are identical. To illustrate these similarities, we will discuss the accuracy of the two methods for approximating a traction-free boundary.

Instead of using the formulation of equation (6) for computation, we solve two first-order equations for stress and velocity, respectively. Solving for the stress tensor components simplifies the computational scheme at some cost to core memory storage, but it allows for the inclusion of anelastic attenuation by the method of Emmerich and Korn [3]. We solve for velocity values instead of displacements in order to simulate absorbing computational grid boundaries by the method suggested by Cerjan, et. al. [2]. The velocity field is attenuated within a zone of grid points near the boundaries, and the amount of attenuation increases as the wavefield approaches the boundaries. In terms of velocity and stress, the collocation method involves numerically solving the equation of motion

$$\rho(\mathbf{j})\dot{V}_\alpha(\mathbf{j},t) + \sum_{\mathbf{m}} (-i2\pi m_\beta)\tilde{T}_{\alpha\beta}(\mathbf{k},t)\, e^{i2\pi m_\beta j_\beta/N_\beta} - f(\mathbf{j},t) = 0 \tag{15}$$

and the general constitutive relation

$$\dot{T}_{\alpha\beta}(\mathbf{j},t) = E_{\alpha\beta\delta\gamma}(\mathbf{j}) \sum_{\mathbf{m}} (i2\pi m_\gamma)\tilde{V}_\delta(\mathbf{m},t)\, e^{i2\pi m_\beta j_\beta/N_\beta} \tag{16}$$

by integrating the nodal quantities $\dot{V}_\alpha(\mathbf{j},t)$ and $\dot{T}_{\alpha\beta}(\mathbf{j},t)$ in time by a second-order finite difference discretization. The quantities $\rho(\mathbf{j})$ and $E_{\alpha\beta\delta\gamma}(\mathbf{j})$ are the material density and modulus values at the position $j_\beta \Delta x_\beta \mathbf{n}_\beta$. The velocity expansion coefficients $\tilde{V}_\delta(\mathbf{m},t)$ are obtained by an FFT as in equation (10).

Observe that the wavenumber representation of the constitutive relation (16) is

$$\dot{\tilde{T}}_{\alpha\beta}(\mathbf{m},t) = \sum_{\mathbf{j}} \tilde{E}_{\alpha\beta\delta\gamma}(\mathbf{m}-\mathbf{j})\,(i2\pi j_\gamma)\,\tilde{V}_\delta(\mathbf{j},t)\,, \tag{17}$$

which has the same form as equation (7).

4 Accuracy of Solutions

The stress field will be aliased if the resulting bandwidth of the convolution sum in (7) exceeds the bandwidth of the basis set used to synthesize the spatial domain stress and strain fields. Let the

spatial strain field be composed of a total of K_β nonzero wavenumbers in the direction β. Since we require that the stress and strain fields have the same bandwidth, the indices k and $\acute{\text{k}}$ in equation (7) have the same range. The range of the index difference $k_\beta - \acute{k}_\beta$ on the modulus is then $-K_\beta$ to K_β, and a stress field bandlimited to $\pm K_\beta/2$ wavenumbers samples the modulus spectrum up to $\pm K_\beta$ wavenumbers. If the bandwidth of the modulus exceeds $\pm K_\beta$, then the convolution in (7) will be aliased. For the collocation method, in which equation (16) is solved instead of (7), aliasing from the convolution cannot be avoided if the bandwidths of the material structure and the wavefield are the same. The term pseudospectral was used by Orszag [6] to describe such a method, since with aliasing the method is not a complete spectral method.

In our spectral-domain simulations, we initialize the material moduli and density with a wavenumber bandwidth of $\pm K_\beta$ for a wavefield bandlimited to $\pm K_\beta/2$, and we compute the convolutions in equation (6) using an FFT. The FFT array that contains the coefficients of the K_β positive and K_β negative moduli or density wavenumbers must include at least $K_\beta/2$ zeroes to avoid wraparound from the periodic nature of the FFT [7]. Hence an array of length $5K_\beta/2$ is required to compute the discrete convolutions in (6) with the given moduli and density sampling. If we truncate the sampled bandwidth of the material structure to only $\pm K_\beta/2$ wavenumbers, then the required FFT array length is only $3K_\beta/2$, and the wavefield and material wavenumber spectra have the same bandwidth. In a pseudospectral method, where the material parameters and the wavefield variables are defined at the same spatial locations, alias-free convolutions can be computed, but for N_β collocation points in the direction β the material structure must be bandlimited to within the wavenumber range of $\pm 2N_\beta/3$. (For computations on a staggered grid [9][8], the material parameters are defined at different locations than the wavefield variables but their bandwidth is either greater than or equal to the wavefield bandwidth). Therefore, comparing alias-free computations in the spectral domain to a collocation method for the same spatial wavefield bandwidth, the spatial resolution of the structure can be higher for spectral-domain computations than for a collocation method.

In order to avoid Gibbs oscillations in the structure's spatial representation from an abrupt truncation of its wavenumber spectrum , we apply a low-pass filter to smooth the chosen structure's spectrum. The vertically-layered structure in Figure 1a was bandlimited and smoothed to produce the structure in Figure 2a. Any structural variations "sharper" than those of Figure 2a will result in aliasing error for the given discrete spatial sampling, but accurate solutions may be obtained in the presence of some aliasing. Notice how the sharply discontinuous structure of Figure 1a results in gradual annihiliation of the body waves in the synthetic seismograms shown in 1b, which were produced by a pseudospectral method in 2-D and have a maximum frequency content of 1 Hz. The explosive source function was applied at a depth of 500 meters. In contrast, the smoother structure of Figure 2b results in good agreement between the pseudospectral solution and a Normal Mode calculation [4] for the same structure, even though some aliasing occurs due to moderately sharp structure features. The two solutions are compared in Figure 3 for a maximum frequency of 1 Hz.

Perhaps the greatest drawback to a spectral or pseudospectral method is the difficulty of including a traction-free surface condition. If a conventional trigonometric basis is used, the free surface condition is equivalent to a material discontinuity that causes aliasing as discussed above. Nevertheless, we have obtained the most accurate surface wave solutions using the pseudospectral method with an explicit zero-traction condition along a single line of spatial nodes. In contrast, an explicit zero-traction condition in the spectral-domain solution does not produce accurate surface waves. It therefore appears that the pseudospectral method's errors from truncation and interpolation that we discussed above cancel in the presence of an explicit free surface condition along a line of spatial nodes. The cancellation is such that the error due to aliasing is relatively small. Compar-

ing the Rayleigh waves in Figure 3 for the pseudospectral solution and the accurate Normal Mode solution, it appears that aliasing errors in the pseudospectral method cause delays in the Rayleigh wave arrival.

An alternative approach to satisfying the free surface condition is to choose a basis set in the variational formulation that provides rapid convergence to the governing equation's solution and to the boundary conditions, and to simply neglect the surface integral in equation (3). A discontinuous basis set is appropriate. A Chebychev basis is one example [5], but it requires the costly use of a fourth-order or higher time integration scheme. We have chosen as a basis set in 2-D the complex exponential of equation (1) for the horizontal direction and cosines for the vertical direction (a "mixed" set):

$$u_\alpha(\mathbf{x},t) = \sum_{\mathbf{k}=-\mathbf{K}/2}^{\mathbf{K}/2} \hat{U}_\alpha(\mathbf{k},t)\, e^{i2\pi k_1 x_1}\, cos(\pi k_2 x_2) \quad ; \quad 0 \le x_\beta \le 1 \quad \beta = 1,2. \tag{18}$$

The cosines above are the eigenfunctions of the 1D wave equation with stress-free endpoints. A spectral solution with this basis set produces the Lamb's problem solution of Figure 4 for vertical particle velocity recorded at the surface of a homogeneous half-space and for an impulsive line load at the surface. The analytic Rayleigh wave solution is symmetric about the positive velocity peak and does not change in time. The solution is not as good as one produced with the pseudospectral method with an explicit free surface, but it does emphasize the importance of the chosen basis set in approximating the boundary conditions. In this regard, we are investigating other discontinuous basis sets to improve the Rayleigh wave solution.

References

[1] C. Canuto, M. Y. Hussaini, A. Quarteroni, and T. A. Zang. *Spectral Methods in Fluid Dynamics.* Computational Physics. Springer Verlag, New York, 1988.

[2] C. Cerjan, D. Kosloff, R. Kosloff, and M. Reshef. A nonreflecting boundary condition for discrete acoustic and elastic wave equations. *Geophysics*, 50(4):705–708, April 1985.

[3] H. Emmerich and M. Korn. Incorporation of attenuation into time-domain computations of seismic wave fields. *Geophysics*, 52(9):1252–1264, September 1987.

[4] D. Harvey. Seismogram synthesis using normal mode superposition: the locked mode approximation. *Geophys. J. R. astr. Soc.*, 66:37–61, 1981.

[5] D. Kosloff, D. Kessler, A. Filho, E. Tessmer, A. Behle, and R. Strahilevitz. Solution of the equations of dynamic elasticity by a chebychev spectral method. *Geophysics*, 55:734–748, 1990.

[6] S. A. Orszag. Numerical simulation of incompressible flows within simple boundaries: I. galerkin (spectral) representations. *Stud. Appl. Math.*, 50:293–327, 1971.

[7] W. H. Press, B. P. Flannery, S. A. Teulosky, and W. T. Vetterling. *Numerical Recipes, the Art of Scientific Computing.* Cambridge University Press, Cambridge, 1986.

[8] Jean Virieux. P-sv wave propogation in heterogeneous media: Velocity-stress finite-difference method. *Geophysics*, 51(4):889–901, April 1986.

[9] D. C. Witte and P. G. Richards. The pseudospectral method for simulating wave propagation. *Computational Acoustics*, 3, 1990.

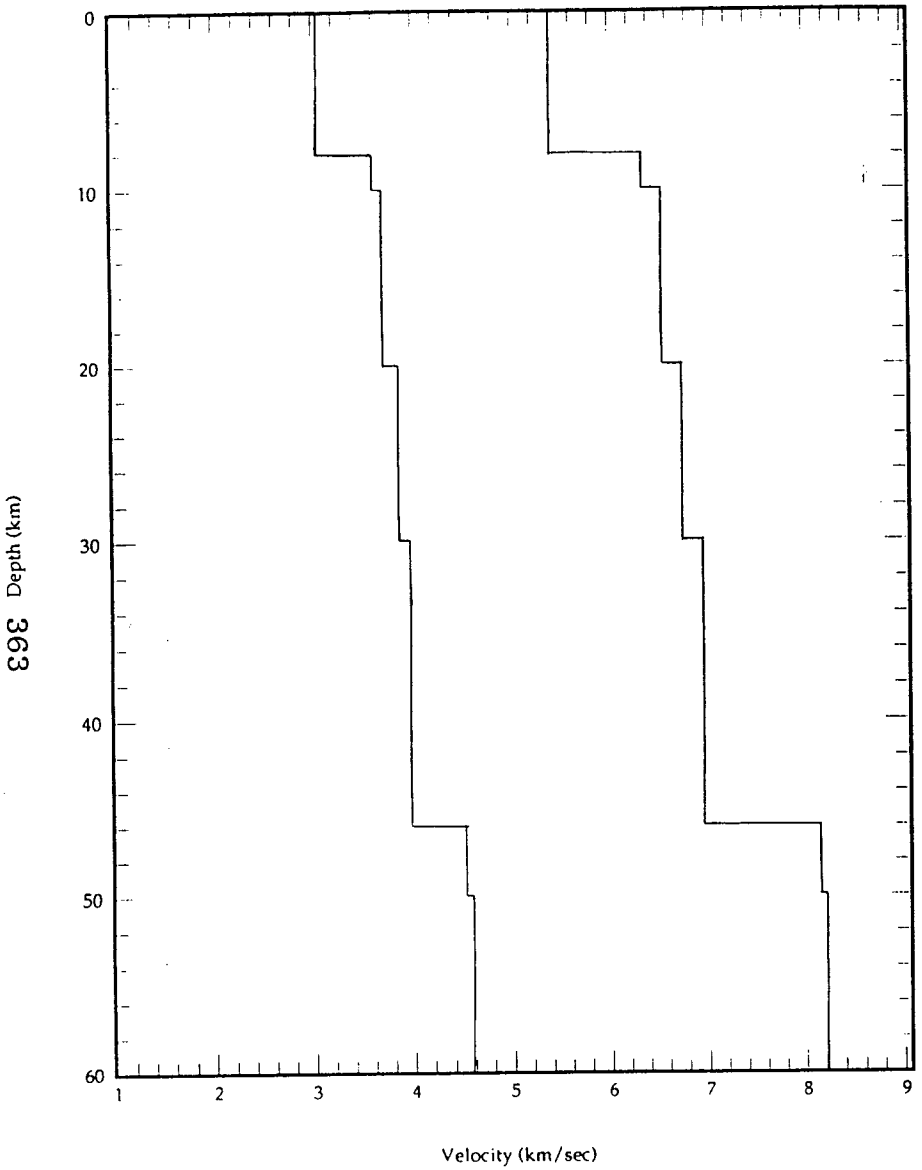


Figure 1a: Discontinuous layered earth structure used to produce the seismograms in figure 1b.

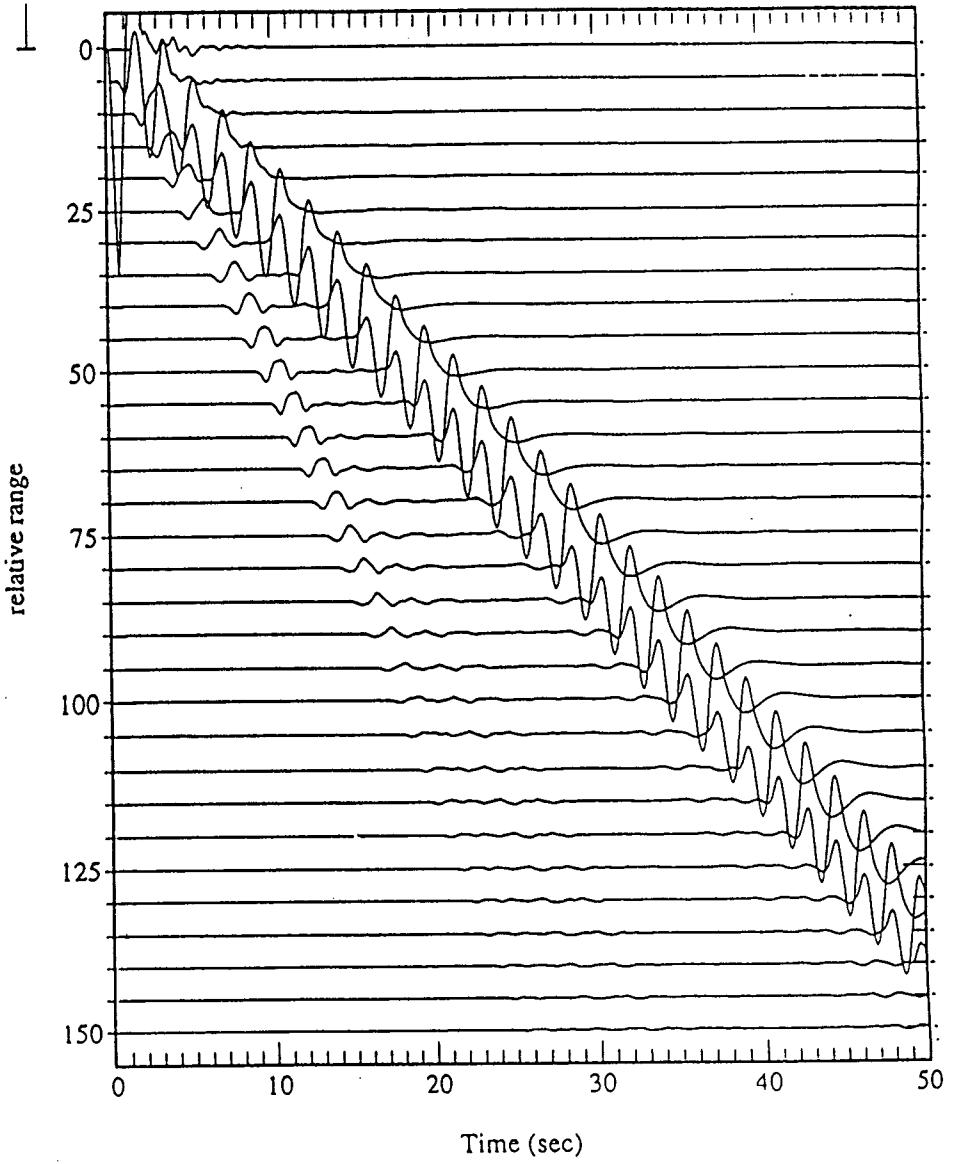


Figure 1b: Pseudospectral synthetic seismograms for the layered earth structure of figure 1a.

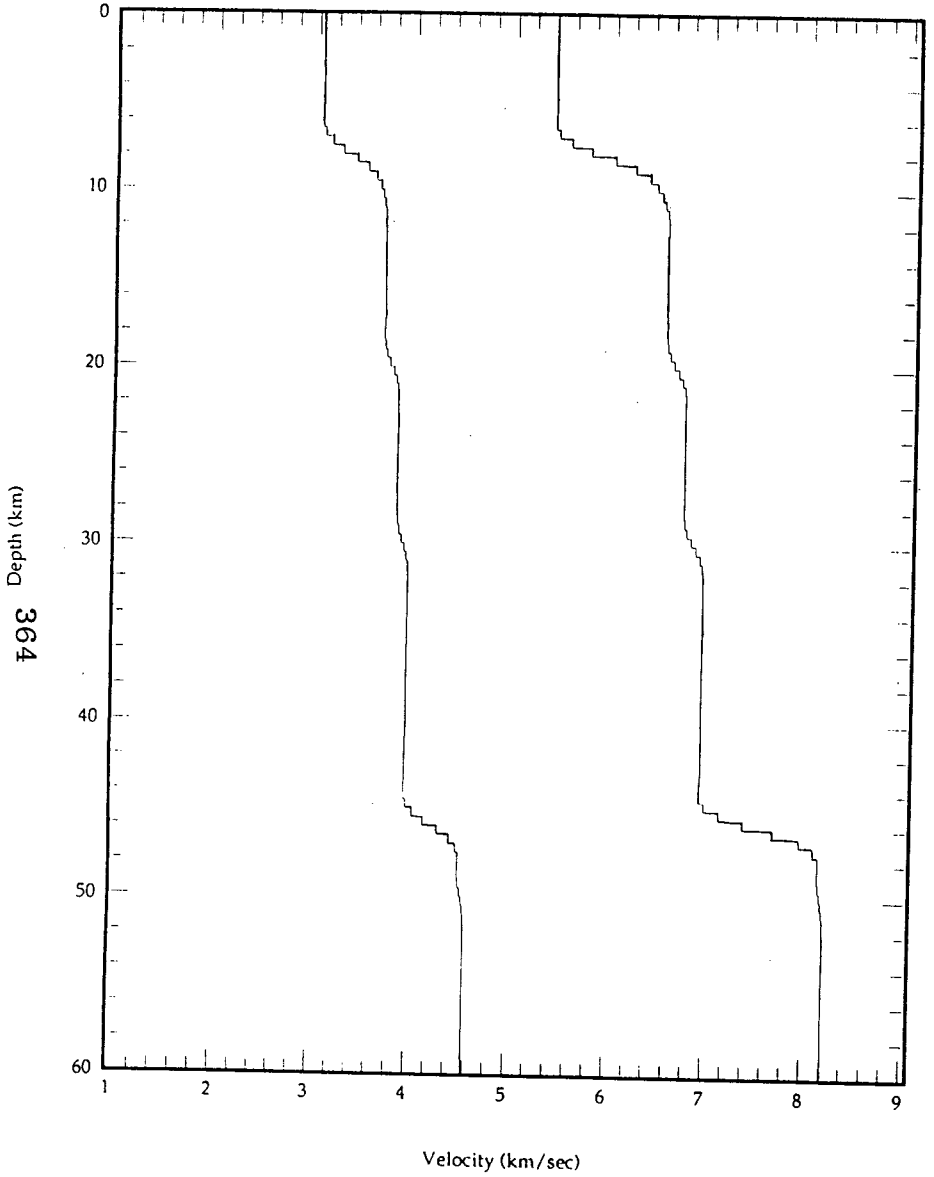


Figure 2a: Bandlimited version of the earth structure of figure 1a.

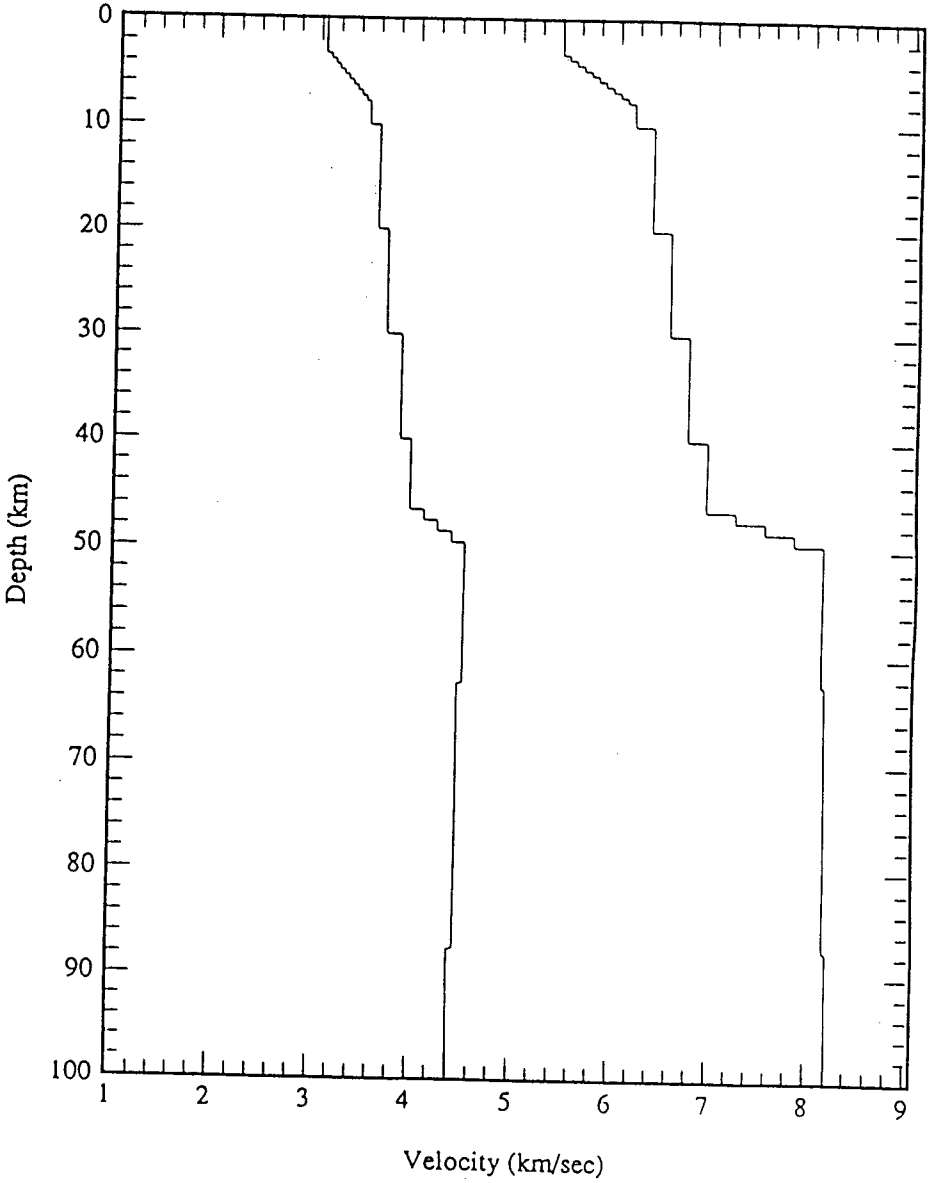


Figure 2b: Layered earth structure used for the seismograms in figure 3.

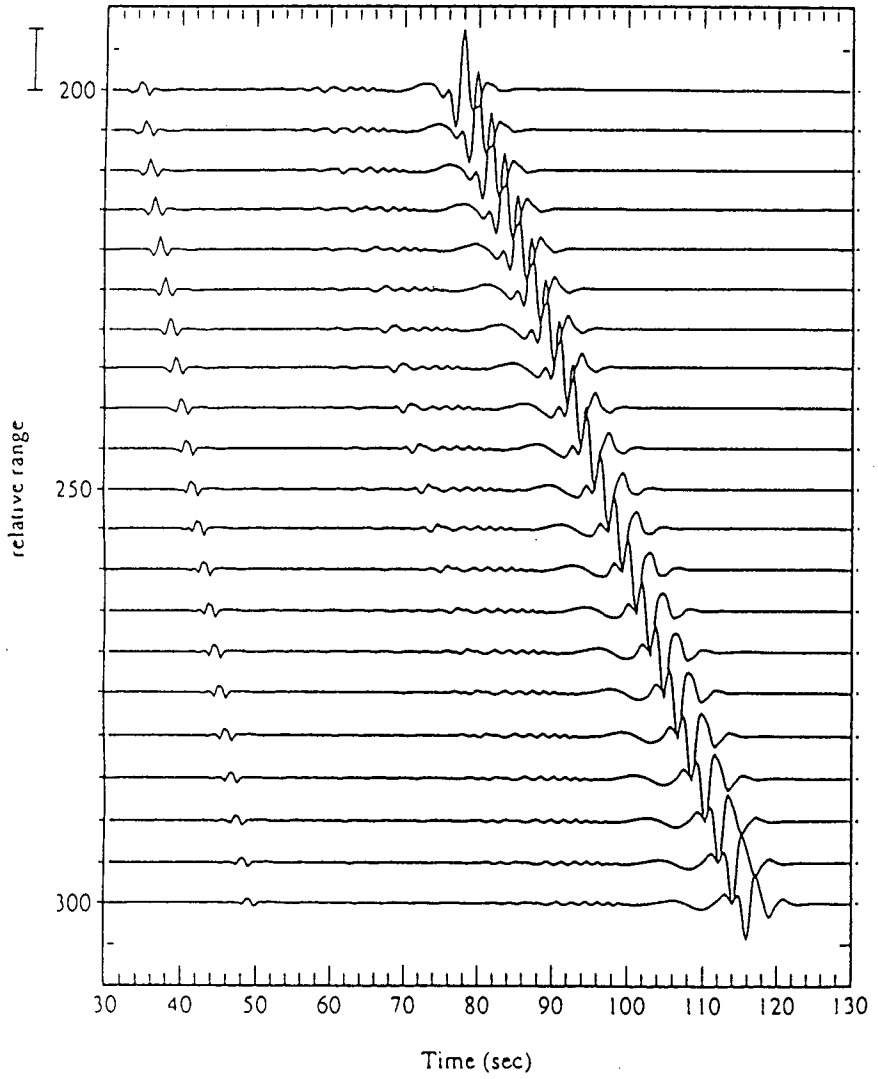


Figure 3a: Pseudospectral synthetic seismograms for the layered earth structure of figure 2b. The maximum frequency content is 1 Hz.

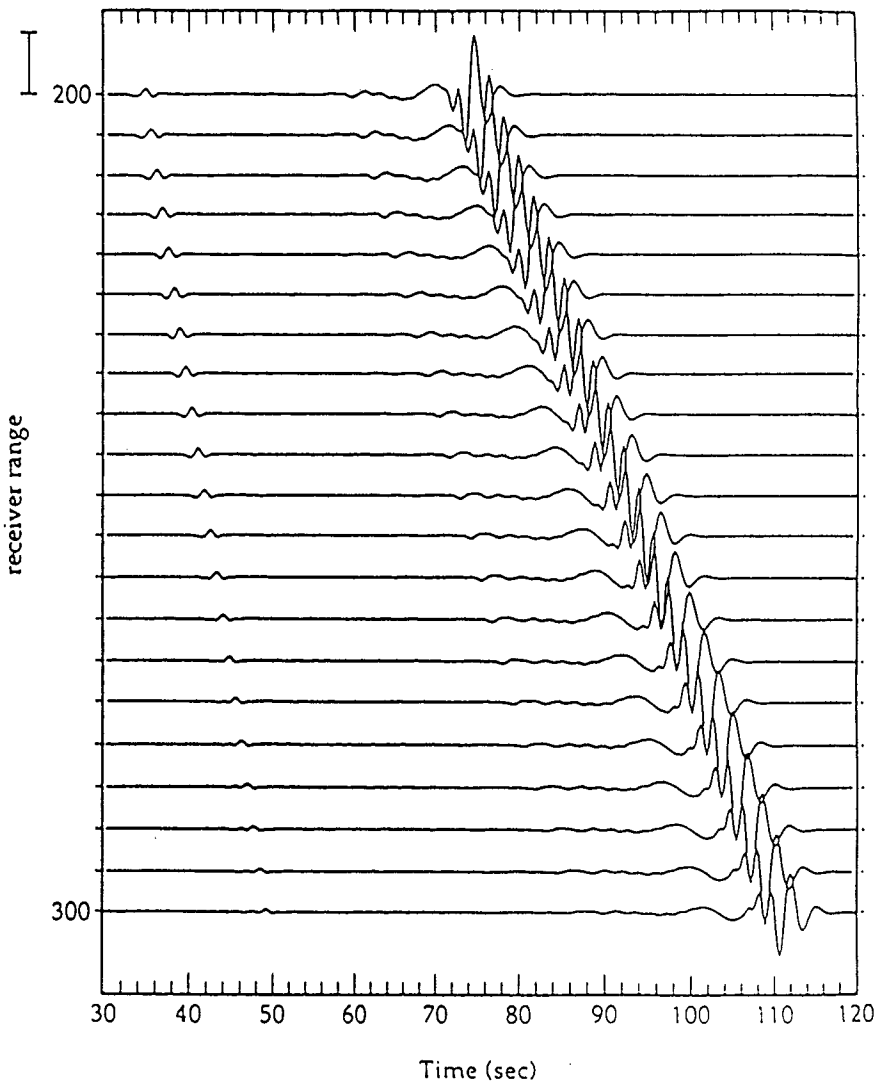


Figure 3b: Normal Mode synthetic seismograms for the layered earth structure of figure 2b. The maximum frequency content is 1 Hz.

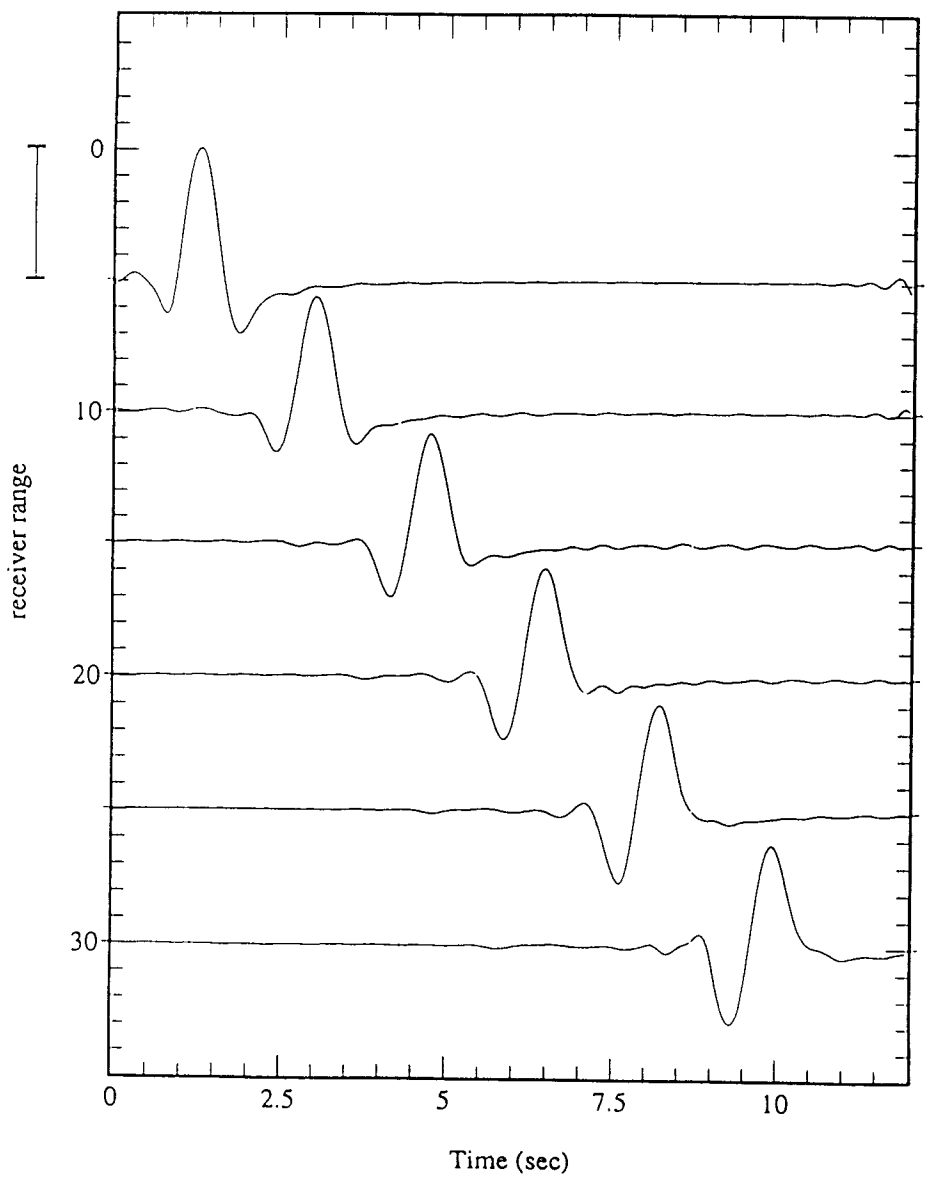


Figure 4: Vertical velocity from spectral solution to Lamb's problem using the basis set of equation 18.

Modeling Seismic and Atmospheric Wave Fields Generated by Near Surface Sources

Charles B. Archambeau
John B. Davies
Jeffrey L. Orrey

Theoretical and Applied Geophysics Group
University of Colorado
Campus Box 449
Boulder, CO 80309

Summary

This study is designed to develop both linear and nonlinear wave propagation methods that can model the excitation and propagation of atmospheric and seismic waves from explosion and earthquake sources in realistic, complex media models which include strong lateral variability, randomness and nonlinear response effects.

In modeling the excitation of the atmosphere and ionosphere we include the usual non-linear transport effects as well as ionization and electromagnetic interactions in order to infer secondary electromagnetic effects produced by large amplitude neutral waves propagating upward into the ionosphere from surface or near surface explosion sources. The overall objectives of the atmospheric-ionospheric modeling are (a.) to predict fluctuations in the electron densities and ionization layer positions in the ionisphere which can be correlated with active EM monitoring by ground stations and (b.) to predict secondary EM field emissions from ion and electron movements induced by the large amplitude atmospheric waves from below. Here the idea is to evaluate and design active and passive E-M sensing methods coupled with seismic methods to define a monitoring environment which will allow large industrial explosions to be easily identified based on the strengths and character of the seismic and atmospheric-ionospheric disturbances produced.

The objectives of the seismic wave propagation modeling are to take account of near source non-linear phenomena and topographic effects, medium randomness and strong lateral variability in the earth structure, particularly in the crust and upper mantle. We hope to obtain close fits to the complex seismic wave fields observed at regional and teleseismic distances and in so doing, to generate a basis for refined detection and discrimination of small seismic events.

Basic Concepts and Approach

If small nuclear tests are detonated in a decoupling cavity, then their signals, in the low frequency range below 5Hz, are reduced by nearly two orders of magnitude. In this case the decoupled nuclear explosion produces signals of the same size as common industrial explosions of which there are many thousands per year in industrial areas. Consequently, it will be necessary to be able to seismically distinguish between these numerous industrial explosions and possible decoupled nuclear tests if a treaty banning such tests were to rely principally on seismic methods for verification. At the present time there is no well documented method for such discrimination, although it is likely that seismic (spectral) methods employing new high frequency (.5 to 50 Hz) seismic detectors, operating with very low internal noise and deployed at depth or as "tight arrays" to reduce high frequency earth noise, will make it possible to distinguish between these types of explosions, as well as between small earthquakes and decoupled nuclear explosions. In this study we seek to build a firm understanding of the regional seismic wave fields produced by different types of seismic sources in order to properly define discrimination methods and procedures and be able to test and predict their variability and sensitivity in different regional structures.

In addition to seismic methods for event and identification there are other possibilities that are beginning to receive serious consideration. Clearly, sensing of acoustic signals from large industrial explosions is a possible means of identifying these events, since neither nuclear tests nor earthquakes will produce such a large signal in the atmosphere. However, because of signal attenuation and high acoustic noise levels at the earth's surface, even relatively large acoustic signals from most industrial explosions of interest may not be observable beyond a few hundred kilometers. Nevertheless, acoustic sensors located quite near active mining areas would be very useful in identifying the large near surface explosions that are of greatest importance. Since large scale mining areas are relatively rare, one would need to monitor only a few areas using this method to achieve nearly total monitoring coverage of the largest industrial explosions. Consequently locally distributed acoustic sensor arrays around major mining areas can provide critical data for monitoring, particularly when coupled with similar seismic monitoring arrays.

Even quite small industrial explosions at normal mining depths will produce a much larger signal in the atmosphere than a decoupled nuclear test. Further, while even the larger acoustic signals will be small relative to noise after propagation over a few hundred kilometers in the atmosphere near the earth's surface, this is not the case for the acoustic wave field propagated directly upward into the upper atmosphere and ionosphere. In this case the fact that the air density decreases rapidly with altitude causes the amplitude of an acoustic wave to increase rapidly with increasing height and to strongly perturb the ionosphere over an area of the order of 100 kilometers in radius around the source epicenter. Consequently, remote EM sensing of the ionosphere using radio frequency transmitter - receiver systems can detect ionospheric perturbations due to the acoustic waves from industrial explosions. Observationally the acoustic waves produce ionospheric boundary motions resulting in doppler shifts in the reflected EM signals recorded on the ground. By placing radio frequency receivers and transmitters in a distributed network, comparable to an in - country seismic monitoring network of about 30

stations, it appears possible to provide complete monitoring capability on a continental scale. In principal it should be possible to identify large industrial explosions with high probability due to the EM signal shifts observed. Coupled with seismic monitoring then, the occurrence of an event that had an explosive seismic signature but that produced no ionospheric EM effect would indicate a probable decoupled nuclear test.

Besides the possibility of active monitoring of the strong perturbations in the reflecting layers of the ionosphere by radio frequency sounding, it is possible to detect secondary EM emissions from the source region and the ionosphere. Thus, passive electromagnetic monitoring of the electromagnetic environment, particularly at low radio frequencies, offers yet another opportunity to address source identification and discrimination issues.

In this study we focus on modeling the atmospheric and ionospheric disturbances produced by near.surface explosions of various types in order to provide an understanding and quantitative prediction of the magnitude and character of these effects. Based at least partly on such results, we can then hope to define and test particular methods of acoustic and EM monitoring that can be effective.

Atmospheric and Ionospheric Modeling

Because of the exponential decrease of atmospheric density with height, buoyant pulsed gravity waves generated by surface or subsurface seismic sources can be of appreciable amplitude throughout the atmosphere. Furthermore, above 100km in height, these flow transients affect the ionospheric E-M fields through changes in the distribution of the charged particles. The basic equations governing motions of the neutral atmosphere are the conservation laws of mass, momentum and energy together with the ideal gas equation of state. The specific nonlinear continuum equations incorporate nonlinear advective terms as well as the gravitational field, gas compressibility, viscosity effects and thermal conductivity. For electron motions in the ionosphere a first-order continuity equation is used which assumes that electrons move with the neutral atmosphere.

The set of partial differential equations for the atmosphere are converted to a corresponding set of finite difference equations in order to effect numerical integration in time and space. The non-linear terms are treated non-locally on the lattice for stability, effectively controlling, internally, the instabilities. In addition, random velocities and pressures are attributed to the inherent fine scale turbulence in the atmosphere and are incorporated in the modeling as are mean drift particle velocities. In particular, in order to account for the inherent turbulence in the atmosphere, the flow variables at a point are decomposed into a mean flow, governing winds, and a perturbed flow that incorporated the turbulence. A new approach designed to include turbulence has been developed using random perturbations, obtained from a random number generator which are input directly into the finite difference equations. Turbulence is also produced by a random distribution of temperature at the surface which produce thermal structures with upward and downward flows. Horizontal winds, impacting on a variable and random topography, also produce upward and downward motions which have a random stochastic character.

The set of non-linear partial differential equations are converted to a corresponding set of finite difference equations for numerical integration in time and space. Upwind

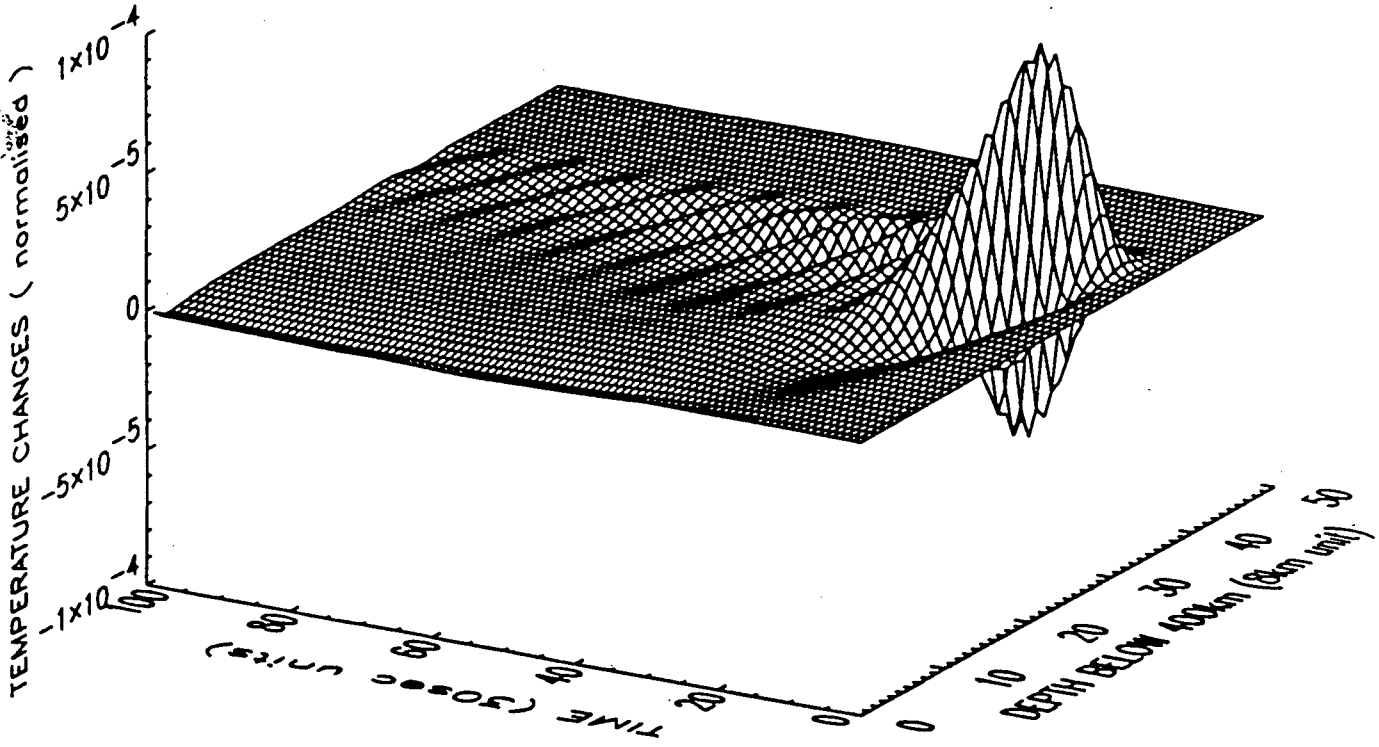
differencing is used for first order spatial gradients with the advection velocity terms acting at the upwind print. However, if the velocity operates on its own velocity gradient, such non-linear terms are treated non-locally on the lattice for stability, effectively controlling internally any unstable growth.

There are at least three types of boundary important to the modeling of fluid flows. The air-ground surface is topographically complex with a turbulent boundary layer of the order of a few meters at the interface. At this boundary, vertical velocities are random both in time and at spatial locations. Because of the presence of the lower boundary layer above a complex topography, horizontal velocities are not taken as zero but incorporate winds and turbulence effects. The top atmospheric boundary is open with decreasing density. The topmost boundary should mimic the conditions for an open atmosphere with specific considerations for buoyancy and field gradients. We have examined various options including fixing velocities and densities and their gradients. However, we have adopted the general open flow boundary such as we also use for the artificial side boundaries. The side boundaries are artificial, due to grid restrictions, and must mimic open boundaries that allow free flow in either direction. We have adopted the more usual approach wherein the dependent variables are constrained to stay constant at these open boundaries.

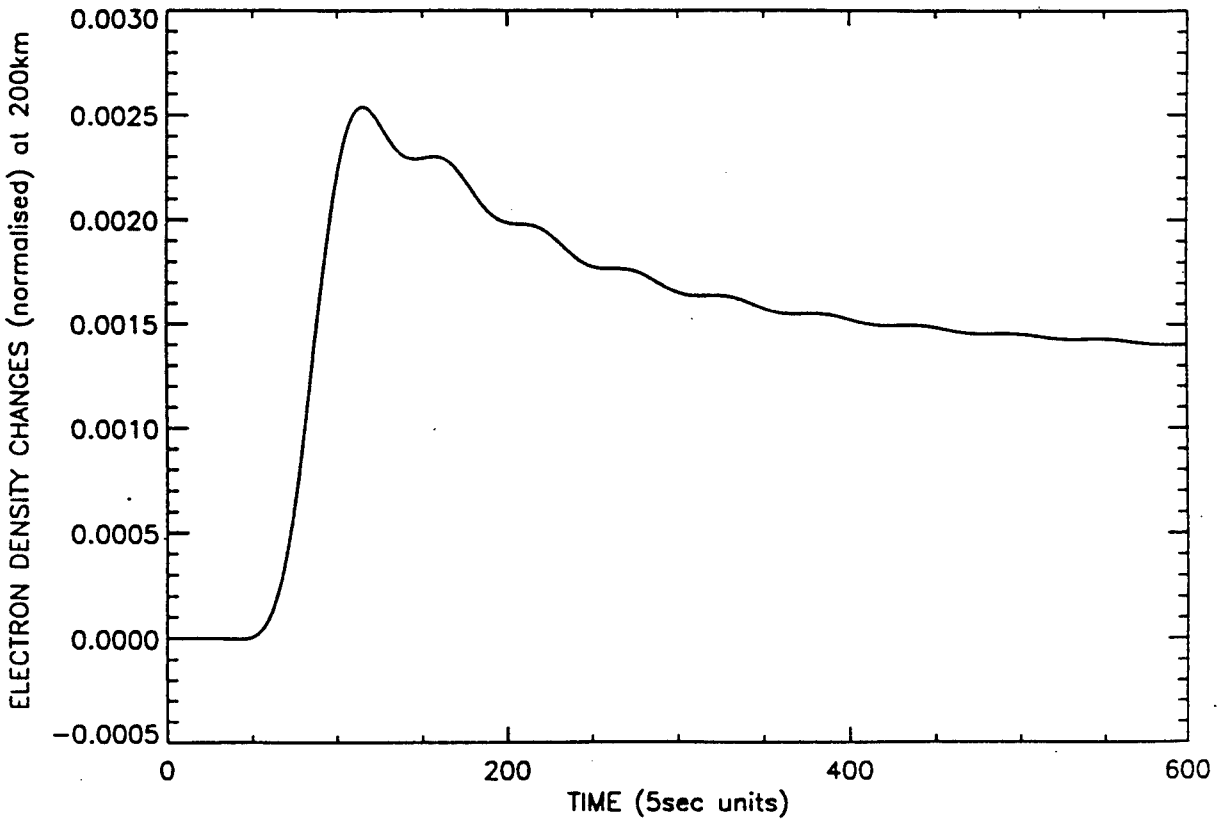
Explosive sources at and below the ground are simulated and their resultant effects on the atmosphere are integrated upward and outward. Various velocity sources are used at the lower boundary with differing time, amplitude and radial dependences. The standard input is a source, comprised of the first differential of a gaussian in time, that approximates the initial pulse from an underground explosion. Cartesian coordinates are used to model the 3-dimensional system with the source at the center of the bottom plane. The results of the atmospheric modeling for effects of a surface explosion can be summarized as follows:

(1.) A time dependent transient pulse propagates upward with increasing amplitude relative to the ambient pressure. This produces asymmetric flows which control the flow development and the upward propagation of the transient. The initial positive density pulse is propagated upward more slowly than the following negative density pulse which has increased buoyancy. This initiates a sequence of circulation patterns that develops through what appears to be asymmetric triangular modes across the horizontal cross-section. The circulation patterns for the phenomena are characterized by upward central motions of the lighter matter, which, at the neutral buoyancy level, push outward to the side. The centroid of the transient pulse initially moves upward rapidly, but slows down to the group velocity speed of sound in the atmosphere. The advected air mass tries to remain in its horizontal stratification in order to minimize changes in its gravitational potential. However, it appears that energy and momenta are transported through traveling waves in the circulation pattern. Similar effects have been observed in the real atmosphere when thermals propagate upward from the Earth's surface with similar circulation patterns.

(2.) After a model dependent characteristic time a bifurcation of the flow occurs with the eventual reversal of the velocity directions. The bifurction phenomena occurs, in this model, every 100 seconds, so that it has a period of just over 3 minutes. A drag force is input in order to model the effect of the inherent background turbulence of the atmosphere. A drag force, which removes 2% of the



(a.) Time and spatial variation of the temperature change expressed as a fractional change in the temperature.



(b.) Time variation of the electron density change expressed as a fractional change in the electron density at 200 km. altitude.

Figure (1.) - Fluctuations in the ionospheric temperature and electron density due to a transient pressure pulse at the earth's surface from a near surface explosion.

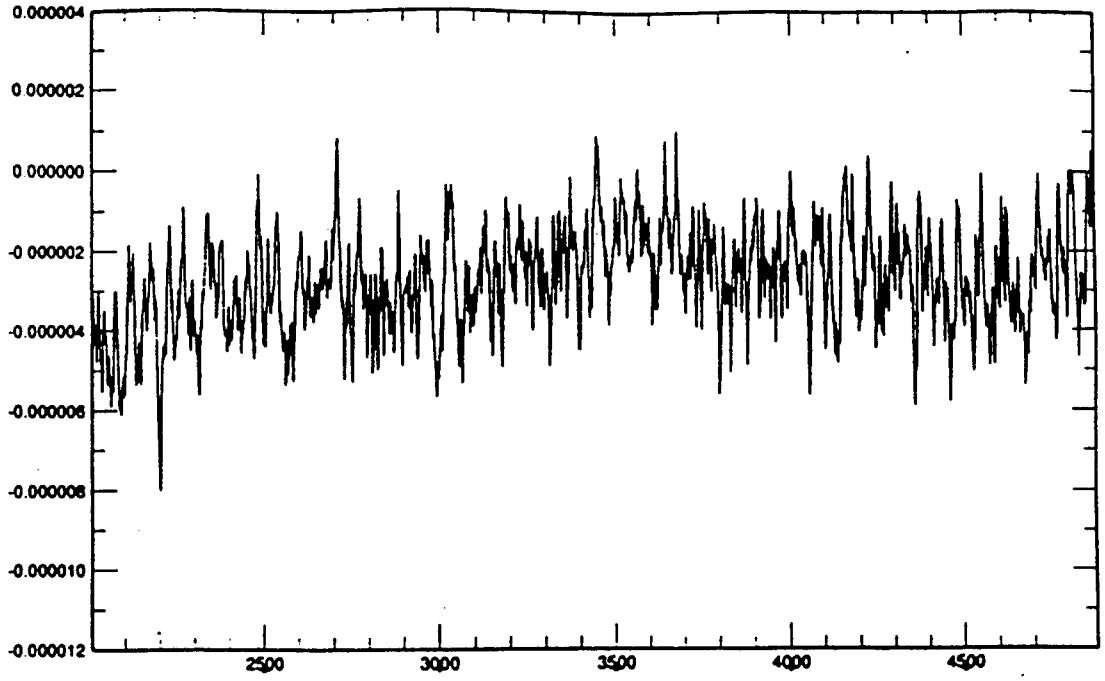
component velocities at each computational grid point at each time step, removes the periodic bifurcation and a standing wave is formed in the atmosphere with constant field patterns. However, with a 1% removal rate, the patterns are periodic with similar bifurcations as in the zero drag case. Because existing atmospheric turbulence acts on the transient gravity wave as a perturbation, we have also modeled its effect by imposing a random component on each field at each time step and grid point. The usual bifurcations are obtained but with differing patterns from the zero turbulence case. However, the appearance of the pressure and density fields is more realistic due to added diffusion and random components.

As the transient pulse moves upward in the atmosphere, it magnifies in amplitude relative to the exponentially decreasing ambient pressure. Thus, the level at which a specific pressure is located will oscillate as the transient pressure pulse moves through. To the first order, the electrons in the ionosphere are assumed to move with the flow of the dominant neutrals. Thus the change in the electron density can be calculated from a conservation law, whose integration in time gives the total electron density variation. The ambient electron density is approximated by the Chapman function which has a maximum electron density at 350km and effectively zero electron density below about 90km. For reasonable synthetic velocity sources at the ground surface, we find that changes in electron density from 100km up are of the same order as those observed by E-M experiments conducted over surface and subsurface explosions. In this regard, Figure (1) shows an example of the predicted fluctuations in temperature and electron density in the ionosphere due to a near surface underground explosion. In this case the explosion was taken to be a tamped underground nuclear test at a depth of 300 meters with a seismic body wave magnitude near 5. (Much smaller industrial explosions very near or at the earth's surface would typically produce comparable or even larger signals.)

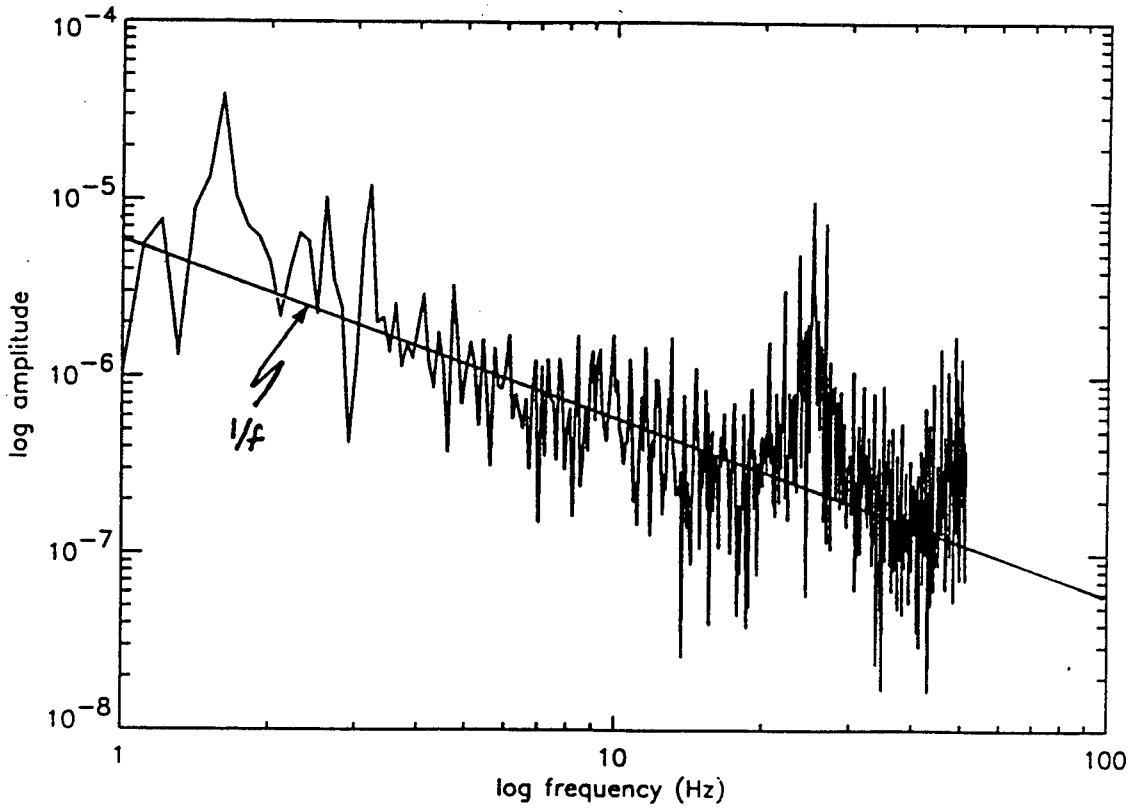
Coupled Atmospheric-Seismic Modeling: Atmospheric Generated Seismic Noise.

In order to investigate the production of seismic noise by atmospheric processes, the atmospheric codes were linked with the linear elastic seismic codes. The lower atmosphere, composed of a daytime turbulent boundary layer with a height of 2 km, is simulated with a random surface topography. Winds, blowing on this topography, induce upward and downward flow velocities. Random temperature changes in space on the ground surface also produce flows that self-organize into plumes that coalesce above the boundary layer into larger scale thermals. Together with random turbulence in the boundary layer, these flows induce pressure and velocity effects on the ground surface. These effects are the input into the seismic modeling code which integrates in time from the topmost surface boundary.

Preliminary results indicate that the seismic noise that is produced decreases in amplitude with depth and, as shown in Figure (2), produces a spectrum that has a trend that decreases as 1/f with increasing frequency, in the range from about 1 to 50 Hz. Below about 40 meters the seismic noise appears to interact in such manner that much smoother variations in spatial distributions are obtained than at the surface and with associated decreasing fluctuations in time. Both topography and winds are found to be of major importance in terms of amplitude and character of the noise. From preliminary results, it can be expected that time of day will also be important due to the change of the turbulent boundary layer with the heating of the Sun and its temporal dependence.



(a.) Seismic noise (velocity versus time) near the free surface due to the atmospheric turbulence.



(b.) Fourier spectrum of the seismic (velocity) noise in (a.). The trend of the mean spectrum is as f^{-1}, which is what is commonly observed.

Figure (2) Theoretically predicted seismic noise due to models of atmospheric turbulence at the earths free surface.

THIS PAGE INTENTIONALLY LEFT BLANK.

ANALYSIS OF NEAR-FIELD DATA FROM A SOVIET DECOUPLING EXPERIMENT

By

Chandan K. Saikia[1], James P. McLaren[1] and Donald V Helmberger[2]

[1]Woodward-Clyde Consultants, 566 El Dorado Street, Pasadena, CA 91101

[2]Seismological Laboratory, California Institute of Technology, Pasadena, CA 91125

ABSTRACT

Recently Adushkin *et al.* (1992a) presented some results on a decoupling experiment performed in a salt dome in Azghir near the Caspian Sea. A large coupled shot (64 kT) was followed five years later by a decoupled shot (8 kT) fired in the cavity formed by the earlier event. Both events were recorded locally and this data has been provided by the Soviet scientists in a cooperative effort to better understand the seismic coupling problem. This data, in conjunction with WWSSN observations, is analyzed in an effort to determine the RDP's and an estimate of t^*. Our preliminary results suggest that RDP appropriate for the large event is quite similar to that of LONGSHOT (80 kT event). Their teleseismic observations are difficult to distinguish in waveshape. The M_S for LONGSHOT is 3.9 while that for the coupled Russian event is 3.3. The m_b for the LONGSHOT (5.8) is slightly smaller than for the Russian event (m_b=6.0, ISC). This comparison of m_b:M_S appears to be common to most Azghir events as compared to the US experience. The t^* appropriate for Amchitka (t^*=0.9) was established by near-field and teleseismic modeling of waveform data similar to this study where we obtain a t^*=0.5 to 0.6. The RDP for the small event is less well resolved but appears to be only partially decoupled. Prior estimates of decoupling factors range from 30 (based on this data by Adushkin) to 70 (for the Sterling/Salmon experiment). Our analysis produces a decoupling factor of about 15 using near-field data which is similar to the teleseismic modeling result.

INTRODUCTION

The open exchange of seismic data between the US and the Soviet Union marks the beginning of a new era in the field of nuclear seismology and monitoring (Adushkin, 1992). In the past, all empirical studies of nuclear seismic data were restricted to the US and French test sites. Although the comparative studies of US and Soviet sites were limited to analysis of teleseismic data, some of the most revealing studies have been based on near field and regional data. In many ways, the less that the seismic energy propagates through the laterally varying earth, the more can be determined about the initial source. For example, Figure 1 displays a set of synthetic waveforms for a spherical and aspherical cavity explosion (labeled explosion, prolate and oblate) with the data at near-in distances for the CANNIKIN event. The prolate and oblate cavity synthetics were produced with quadrupole correction for asphericity, both fixed at 40%

contributions (Stead and Helmberger, 1988). The modeling of these waveforms can be used in conjunction with teleseismic P-waves and long-period body waves and surface waves to establish appropriate RDP's and the effective attenuation operator t^* (Figures 2 and 3). Figure 2 shows a set of short-period WWSSN records for the Amchitka event LONGSHOT (Lay *et al.*, 1984a). In Figure 3, we present four representative types of short-period MILROW waveforms in the four columns. At the bottom is shown the synthetic seismograms computed using varying t^* and a near-field source model (K=9, B=1, Helmberger and Hadley, 1981) given by

$$\psi(t) = \psi_\infty \{ 1 - e^{-Kt} [1 + Kt + (Kt)^2/2 - B(Kt)^3] \}$$

where the corner frequency parameter, K, scales as predicted by the Mueller-Murphy model (1971), B is a parameter related to the amount of overshoot in the reduced displacement potential, and ψ_∞ is the measure of the long-period estimate. Figure 4 shows the scaling of parameter B with yield, i.e., for increasing yield (ψ_∞ for LONGSHOT is 0.137×10^{11} cm^3, for MILROW is 1.4×10^{11} cm^3, and for CANNIKIN is 5.69×10^{11} cm^3) and depth of burial, the broadband estimate of B is inversely proportional (Lay *et al.*, 1984b). But, what is important in Figure 3 is that as the value of t^* increases, the interference of the second upswing, which is pP, becomes less apparent and the dominant period of the signal increases.

Our long term objective is to repeat this type of analysis at some of the former Soviet (i.e., CIS) test sites. The initial data set comes from a decoupling experiment performed in a salt dome in Azghir just north of the Caspian Sea (Adushkin *et al.*, 1992). Figure 5 shows the locations of many CIS peaceful nuclear explosions (PNE) as well as the Azghir test site. The yield of the coupled event (Dec 22, 1972) is 64 kT and the depth was 1 km. Figure 6 shows the cross-section and physical properties of the borehole where the testing of this event was carried on. A decoupled shot of 8 kt (March 29, 1976) was fired in the same cavity which was roughly 38 m in radius. This decoupled event was mislocated to the North by about 350 km and identified as an earthquake by the ISC.

DATA

Our study is based both on the analysis of waveforms recorded at near-field stations from the above two explosions and teleseismic data recorded on WWSSN stations. However, additional near-field data are expected to be available from eight other CIS explosions (Dr. Jerry Carter, Center for Seismic Studies, CSS, personnel communication). The data that have been analyzed so far were obtained from Adushkin via CSS and were digitized by the Soviets using the recently developed scanner technology at the California Institute of Technology. Both vertical and radial component data of these two events are shown in Figures 7 and were recorded on the standard recording channel consisting of a short-period pendulum seismometer with an

electromagnetically damped coil transducer (VBPP-seismometer of strong motion, USF, SM-3, S5S) with a natural period in the range of 1 to 4 seconds and galvanometer with natural period in the range 5-20 Hz. This produces a flat instrument response in the range 0.5-20 Hz. Following personal communication with Dr. Ivan Kitov from the Institute for Dynamics of the Geospheres, Moscow (IDG), the peak amplitude of the original data was multiplied by a factor of 4/3 to account for an inconsistency between the resolution of the scanner and the amplitude measurements of the digitizing program.

There were 17 portable seismic stations recording the decoupled explosions in the distance range of 1 to 154 km. The locations of these stations represented two profiles, one oriented to the north-east from 1 to about 84 km and other to the north-north west from 26 to 154 km.

The information on the in-country geology and technical conditions were made available to us by Dr. Ivan Kitov (personal communication). The depth of the sediment above the shot location is approximately 275 m with 210 m of shale and sand (Vp=1800 to 2000 m/sec) and 75 m of gypsum and anhydrite with standard properties. The salt layer is approximately 2-3 km thick (average Vp=4400 m/sec). Beneath this salt layer, there is a limestone layer of about 15 to 20 km thickness with a Vp of 5 km/sec. The total thickness of the crust is approximately 40 km and the apparent velocity of Pg is 6.2 km/sec. This estimate of Pg velocity was obtained from the seismic measurements obtained during the explosions inside the salt dome.

MODELING OF SOURCE RDP FROM NEAR-FIELD DATA

The objective of this section is to model the RDP for the two events by keeping the complexity, possibly caused by the variation in the crustal structure, at a minimum. The data appears to have some limitations as described below. For example, by inter-correlating the source of the coupled event with the records of stations 8 and 9 from the decoupled event and by inter-correlating the source of the decoupled event with records of station 8 and 9 from the coupled event, we produce two similar appearing seismograms at station 8 but two different-looking seismograms at station 9 (Figure 8). If the paths are the same, the resulting waveforms should look similar. This suggests that the seismograph at Station 9 may not have been replaced at exactly the same site when recording the decoupled event.

To minimize the path effect and to calibrate source RDP's, we have initially used the waveforms recorded at station 1 and 6 for both coupled and decoupled events. We modeled the waveforms from the coupled event recorded at station 6, even though the station is 4.6 km away from the source and not the closest station, because the decoupled event is sufficiently large for the initial P signal to have long periods, and close enough not to be affected strongly by the structure. To demonstrate the consistency of the derived source model, we have then modeled the data recorded at stations 2, 3 and 5 for the decoupled event.

We used the frequency-wavenumber algorithm (Saikia, 1993) to compute the medium

response which was convolved with the Helmberger-Hadley source as discussed above to synthesize the near-field seismograms. Two crustal models (IVAN.0 and IVAN.5, Figure 9) were used in this investigation. The model IVAN.0 was developed based on the geophysical parameters provided by Ivan Kitov. The IVAN.5 model is a slight modification of the IVAN.0 model, especially in the top layer. These two models produce synthetic seismograms which are similar in both shape and amplitude. However, we feel that IVAN.5 produces a better fit in the frequency content, although the improvement may be only marginal. The strategy to model the source RDP was to construct a set of synthetic seismograms for a suite of source models by varying the parameters K and B.

Figure 10 shows a suite of synthetic seismograms from the above two models at several distances. Clearly, the surface waves are poorly developed. The largest discrepancy appears to be the strong surface waves at stations 8 and 9 (18 km) relative to the direct P arrivals at the near-in station 1 and 8. This effect is apparently caused by 2D structure where the sediments thicken away from the dome and traps energy (Stead and Helmberger, 1988). Ivan Kitov is presently working on some possible 2D structures appropriate for these more distant stations. Figure 11 shows the preliminary agreement between the data and synthetic seismograms computed for the two events along with the map view diagram of the stations relative to the shot location. The source RDP's are also listed. At this stage, we have used B=1 and the Amchitka scaling law to derive ψ_{∞}. The coupled event is similar to the LONGSHOT explosion (80 kT; B=1, K=16.7 and ψ_{∞}=0.137x10^{11} cm^3, Lay *et al.*, 1984) at Amchitka and so the source RDP's of the two events appear consistent. The synthetic for the IVAN.0 and the preferred models are displayed. While the agreement at station 6 is reasonable, there is a clear mismatch at station 1 for both the events in the duration of the signal following the initial P wave. This station is located at a distance of 1.03 km from the shot point and it is possible that the station is within an inelastic limit.

Figure 12 shows the comparison between data and synthetics for the decoupled event at the other three stations using the same source RDP. The amplitude and waveshape at these additional three stations have also been modeled.

To estimate the RDP of the coupled event we held the value of B at 1.0 simplify our assumptions. By modeling the waveform shapes of the coupled event we established that the optimal fit in near-field waveform for that event was obtained with a K of 26.43 and a ψ_{∞} of 0.66x10^{11} cm^3. This RDP was used as described in the next section to establish the t^* for the source region.

MODELING OF TELESEISMIC WAVEFORMS

While the short-period P waves for the coupled event could be observed at several teleseismic WWSSN stations, the decoupled event was too weak to be recorded at these stations.

Although we did not have an exhaustive collection of WWSSN waveforms available for the coupled event, we were able to retrieve and digitize data from 12 stations, namely BAG, BUL, ESK, KTG, MAL, MAT, OXF, PRE, PTO, SDP, SHK and WIN. These WWSSN waveforms in conjunction with the derived source model given in the previous section for the decoupled event was analyzed in an effort to estimate the appropriate value of t^* for the Azghir area. With the source parameters of the coupled event established by near-field modeling, we were able to vary the t^* until we produced a suite of synthetics whose m_b was identical to that measured by the ISC.

Several seconds of short-period P waves were digitized and were modeled using the generalized ray theory (Langston and Helmberger, 1975). The m_b of this event is 6.0 (ISC bulletin) and to match this m_b, we needed a t^* of 0.53 seconds to map the source RDP of the coupled event. Figure 13 shows a comparison between data at several WWSSN stations and synthetics computed at the teleseismic station WIN located at 75.5° away from the shot. This t^* estimate is significantly lower than the t^* estimate obtained of 0.9 seconds obtained by Burdick *et al.* (1984) for the Amchitka site. The m_b for LONGSHOT(5.8) is slightly smaller than that of the coupled event. On the other hand, LONGSHOT has a large M_s of 3.9 as compared to 3.3 for the CIS event.

DECOUPLING FACTOR

The event of March 29, 1976 was detonated in the cavity formed by the explosion of the December 21, 1971. It is expected that the seismic waves from the 1976 event is affected by the air-filled cavity, the decoupling being directly dependent on the cavity radius and the media properties (Latter *et al.*, 1961). For example, Latter *et al.*, have estimated a decoupling factor as large as 200 or 300 in very hard rock and 150 in salt. Similarly, for the Sterling event, a decoupling factor of about 70±20 was estimated by Springer *et al.*, (1968). In a recent study, Adushkin *et al.* (1992b) estimated a decoupling factor of 30 for this decoupled event based on the energy calculation consistent with a decoupling factor of 20 based on the amplitude measurements. The energy decoupling factor was calculated as the ratio of actual yield of the decoupled explosion to that of the effective yield estimated on the basis of statistical relationships established for the tamped explosions.

In this study, we have used two independent time-domain analyses for both near-field and teleseismic data separately to estimate the decoupling factor. To determine the decoupling factor from the near-field data, the announced yield (64 kT) of the coupled event is scaled to account for any amplitude differences, possibly caused by the inadequacies in the chosen one-dimensional velocity model IVAN.5. This is done by adjusting the yield by the ratios of the vector sum of initial P displacements in the vertical and radial seismograms of the data to the synthetic waveforms. We determined this ratio using station at 1.03 and 4.6 km. The values of $(Z^2+R^2)^{1/2}$

for the initial displacements recorded at these two stations are 3.33 cm and 1.10 cm, respectively, and their corresponding synthetic values from IVAN.5 at the two stations are 9.67 cm and 1.48 cm, respectively. The mean of the two ratios, which is 0.547, is used to rescale the announced yield when computing the synthetics, thus reducing 64 kT to 35 kT. To determine the apparent yield of the decoupled event, we use the near-field surface waves recorded at station 8 and 9. The ratios of the surface wave amplitude of the decoupled event to the coupled event at station 8 are 0.007244 and 0.01903 and at station 9 are 0.01787 and 0.01912 for the vertical and radial components, respectively. If the yield is directly proportional to the amplitude, then the effective yield 35 kT multiplied by the mean value of the surface-wave amplitude ratios at each station would measure the apparent yield for the decoupled event, which is 0.46 kT estimated at station 8 and 0.646 kT estimated at station 9. Since the announced yield for the decoupled event is 8 kT, the average decoupling factor from this analysis is about 15.

For the teleseismic analysis, we made an adjustment to the Amchitka scaling law to account for the difference in t^*, i.e., 0.9 for the Amchitka event and 0.53 for the Azghir event, same as the t* estimated for the Shagan River test site by Murphy *et al.*, (1992). The regional m_b for the decoupled blast is 4.0 (Sykes and Lyiubomirskiy, 1992), which consequently results in an estimate of 0.55 kT as the apparent yield for the decoupled event when the modified scaling law is used. This is equivalent to a decoupling factor of 15.

CONCLUSIONS

One of the important conclusions of this study is that the decoupling factors obtained in this study based on both teleseismic and near-field data are smaller than the value estimated by the Russians (Adushkin *et al.*, 1992b). Thus, the coupling is quite strong compared to the coupling estimated for the United States experiments. The near-field seismograms show variation of the waveform and a complex crustal structure is needed to model the waveforms. Nonetheless, we could use the waveforms recorded very close to the shot point to minimize the propagation effect and determine the source RDP of the two events.

The t^* measurement which we determined from modeling 12 stations is 0.53 seconds, which is significantly lower than the t^* previously established at Amchitka. The t^* measurement is based on a limited set of observations and more teleseismic observations from other events need to be analyzed to reduce uncertainty in this estimate.

ACKNOWLEDGEMENTS

The authors acknowledge the support provided by Los Alamos National Laboratory, University of California under contract no. 9-XQ2-3977D-1.

REFERENCES

Adushkin, V. V., I. O. Kitov, and O. D. Sultanov (1992a). Experimental results of USSR nuclear explosion decoupling measurements, Presented at the 14th annual PL/DARPA Seism. Res. Symp. (Published as visiting scientist report C92-04 by CSS) 12p.

Adushkin, V. V., I. O. Kitov, O. P. Kuznetsov, and D. D. Sultanov (1992b). Seismic efficiency of decoupled nuclear explosions, (manuscript in preparation),.

Burdick, L. J., T. Wallace and T. Lay (1984). Modeling near-field and teleseismic observations from the Amchitka test site, J. Geophys. Res., 89, 4373-4388.

Helmberger, D. V. and D. M. Hadley (1981). Seismic source functions and attenuation from local and teleseismic observations of the NTS events JORUM and HANDLEY, Bull. Seism. Soc. Am., 71, 51-67.

Langston, C. A. and D. V. Helmberger (1975). A procedure for modeling shallow dislocation sources, Geophys. J. R. Astr. Soc., 42, 117-130.

Latter, A. L., R. E. LeLevier, E. A. Martinelly, and W. G. McMillan (1961). A method of concealing underground nuclear explosions, J. Geophys. Res., 66, 943-946.

Lay, T., L. J. Burdick, and D. V. Helmberger (1984a). Estimating the yields of the Amchitka tests by waveform intercorrelation, Geophys. J. R. Astr. Soc., 78, 181-208.

Lay, T., D. V. Helmberger and D. G. Harkrider (1984b). Source models and yield-scaling relations for underground nuclear explosions at Amchitka Island, Bull. Seism. Soc. Am., 74, 843-862.

Murphy, J. R., B. W. Barker, J. N. Jenab and M. E. Marshall (1992). Yield estimate research, Presented at the 14th annual PL/DARPA Seism. Res. Symp. 304-310.

Mueller, R. A., and J. R. Murphy (1971). Seismic Characteristics of underground nuclear detonations, Part I. Seismic spectrum scaling, Bull Seism. Soc. Am., 67, 1675-1692.

Saikia, C. K., D. V. Helmberger and L. J. Burdick (1992). Regional wave propagation and high-frequency/low-frequency energy level discriminant, Presented at the 14th annual PL/DARPA Seism. Res. Symp. 351-360.

Saikia, C. K. (1993) Modified frequency-wavenumber algorithm for regional seismograms using the Filon's quadrature - Modeling of Lg waves in eastern North America, Geophys. J. International (Accepted).

Springer, D., M. Denny, J. Healy, and W. Mickey (1968). The Sterling experiment: decoupling of seismic waves by a shot generated cavity, J. Geophys. Res., 73, 5995-6011.

Stead, R. J. (1989). Finite differences and a coupled analytic technique with applications to explosions and earthquakes, Ph.D. Thesis, California Institute of Technology, 337p.

Stead, R. J. and D. V. Helmberger (1988). Numerical-analytical interfacing in two dimensions with applications to modeling NTS seismograms, Pageoph, 128, 157-193.

Sykes, L. R. and P. Lyubomirskiy (1992). Analysis of small seismic events near azghir,

Kazakhstan; Implications for identifying chemical and decoupled nuclear explosions in major salt-dome province, Presented at the 14th annual PL/DARPA Seism. Res. Symp. 415-421.

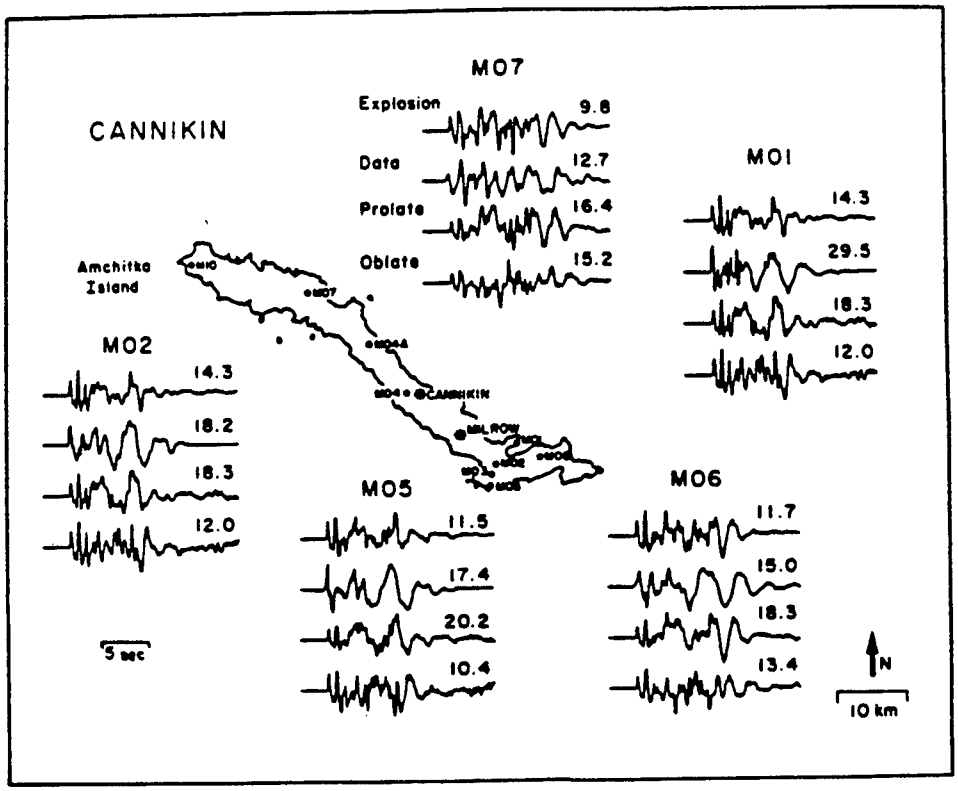


Figure 1. Comparison of synthetics for a spherical and aspherical cavity explosions (labeled Explosion, Prolate and Oblate) to data from CANNIKIN. The prolate and oblate cavity synthetics are computed with a quadruple correction for asphericity, both fixed at a 40% contribution. Peak amplitudes are in cm/s as displayed above each trace. The synthetics have been filtered with a t^{*}=0.05 operator and detrended to remove an exponential with time artifact of the higher order terms of the asymptotic source expansion (Stead, 1989). The crustal model is 2D constructed from local geologic maps. The source parameters are based on 1D model (Lay *et al.* 1984) .

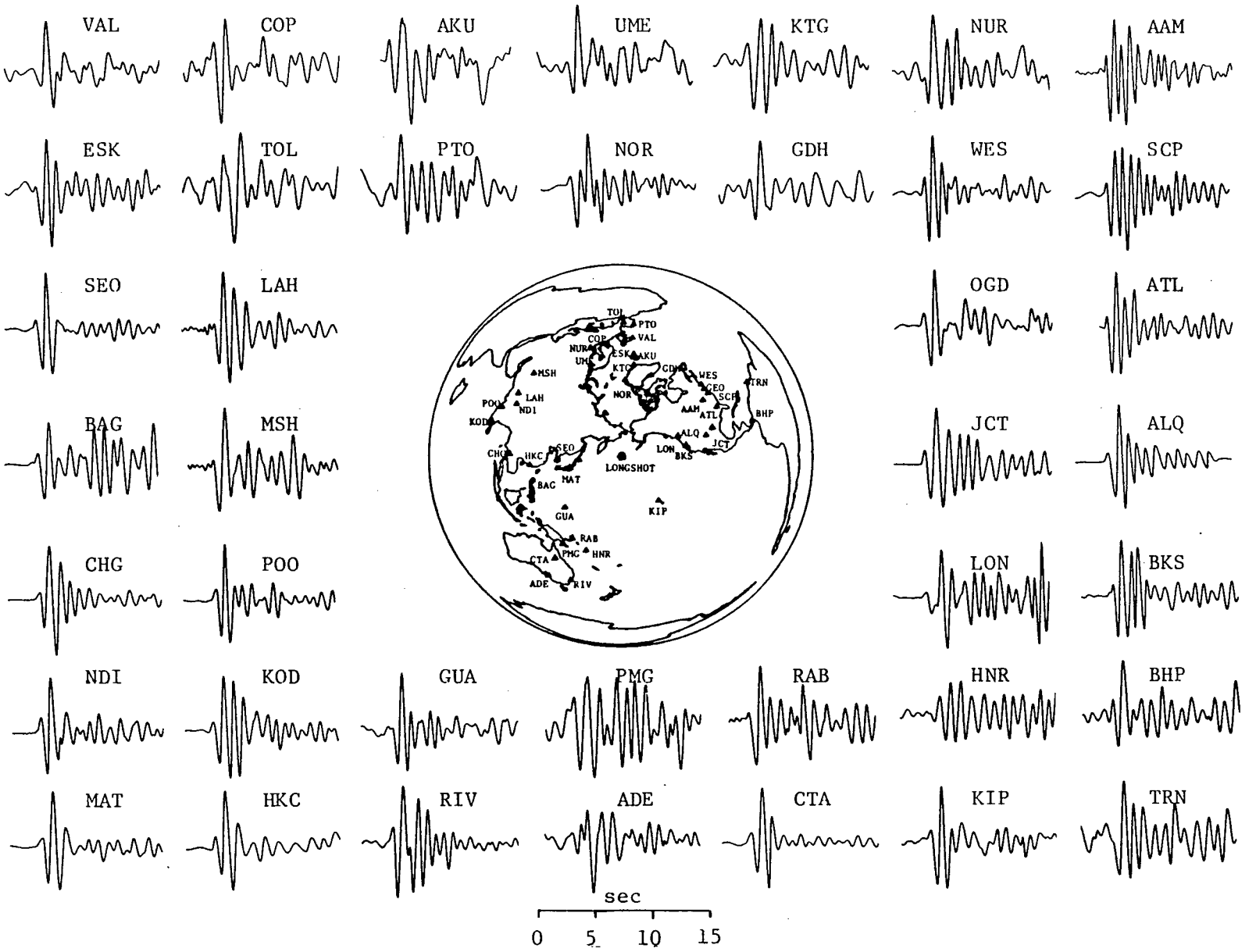


Figure 2. Short-period WWSSN records from the Amchitka event LONGSHOT. These records plus similar records from MILROW & CANNIKIN were used to determine (t^*=0.9) which yields the proper (m_b) given the prospective source descriptions from the near-field data.

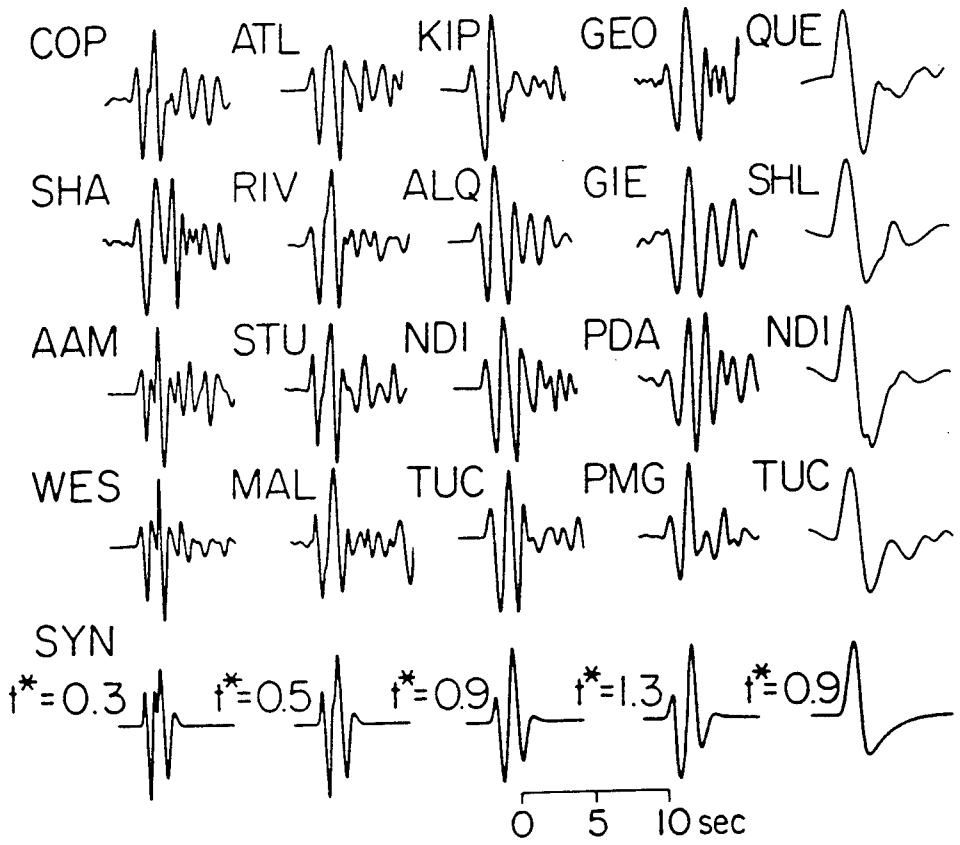


Figure 3. Example set of MILROW observations and synthetics showing the effects of t^* on waveshape but only the m_b measurements were used in estimating t^*, after Burdick, *et al.* (1984).

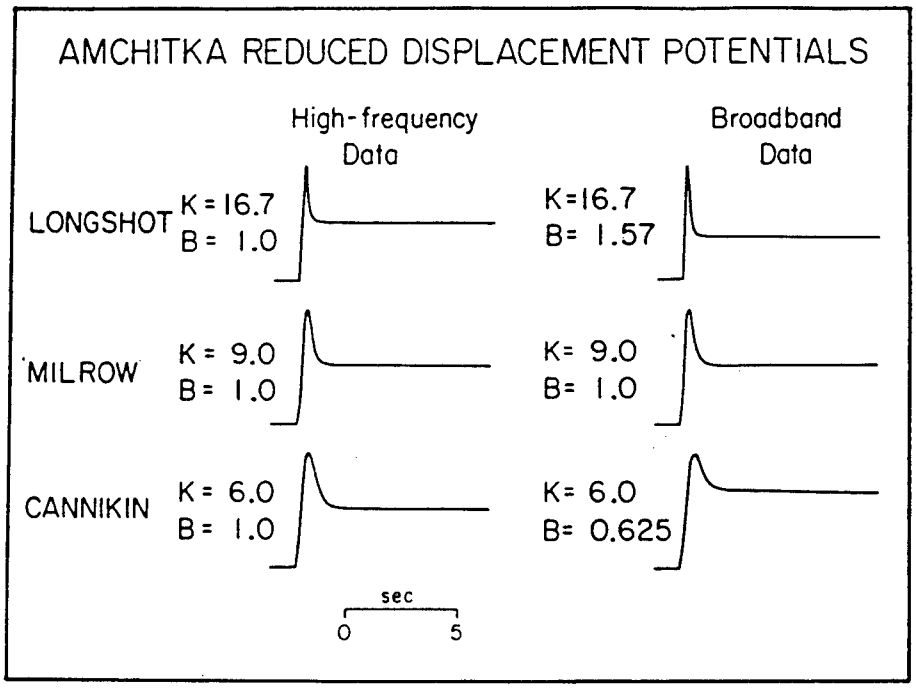


Figure 4. Reduced displacement potentials corresponding to source models of LONGSHOT, MILROW and CANNIKIN derived from both high-frequency and broadband data.

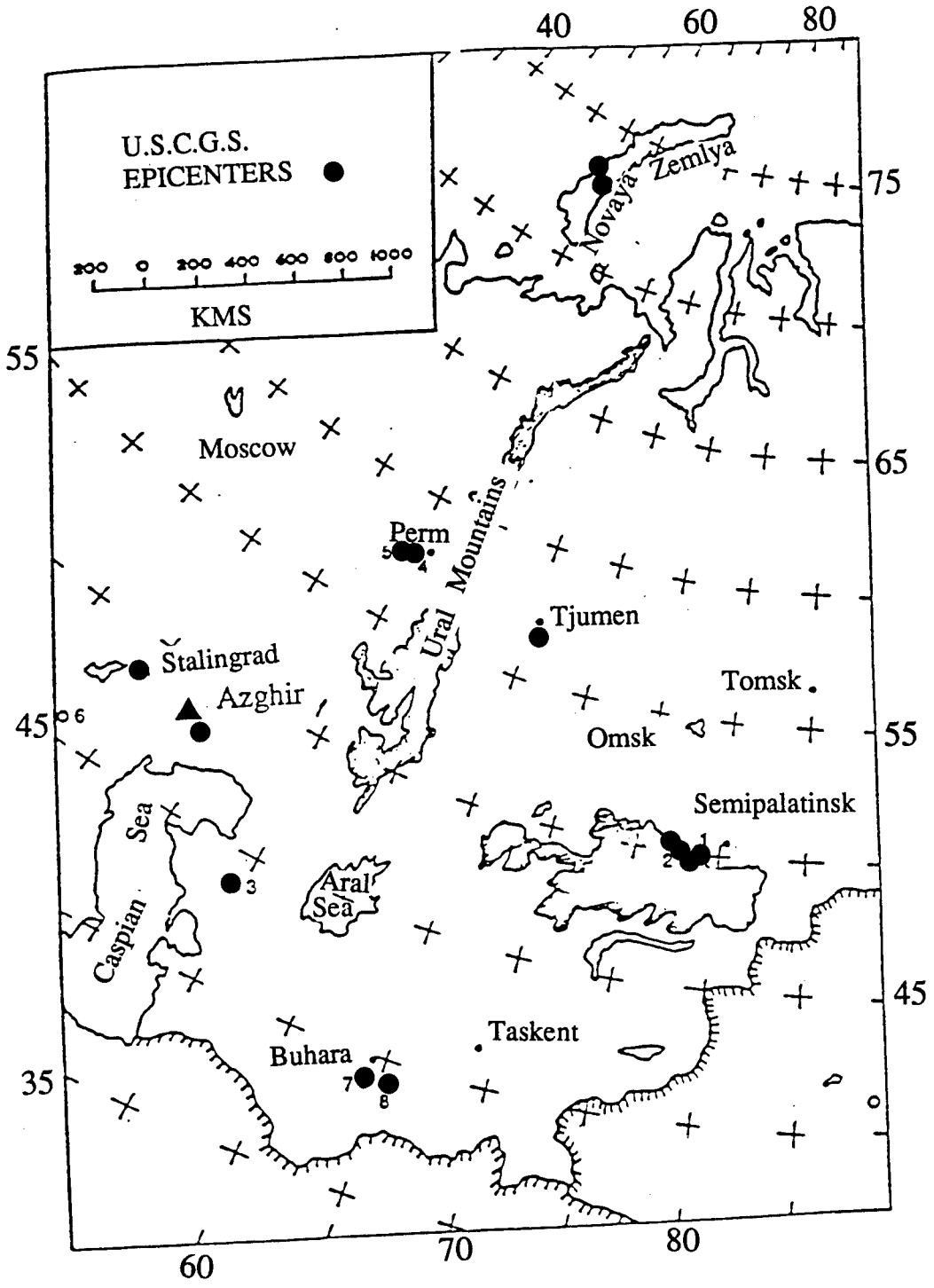


Figure 5. Map showing the location of Azghir north of the Caspian Sea. Also shown are the locations of other PNE (Peaceful Nuclear Explosions) from the former Soviet Union.

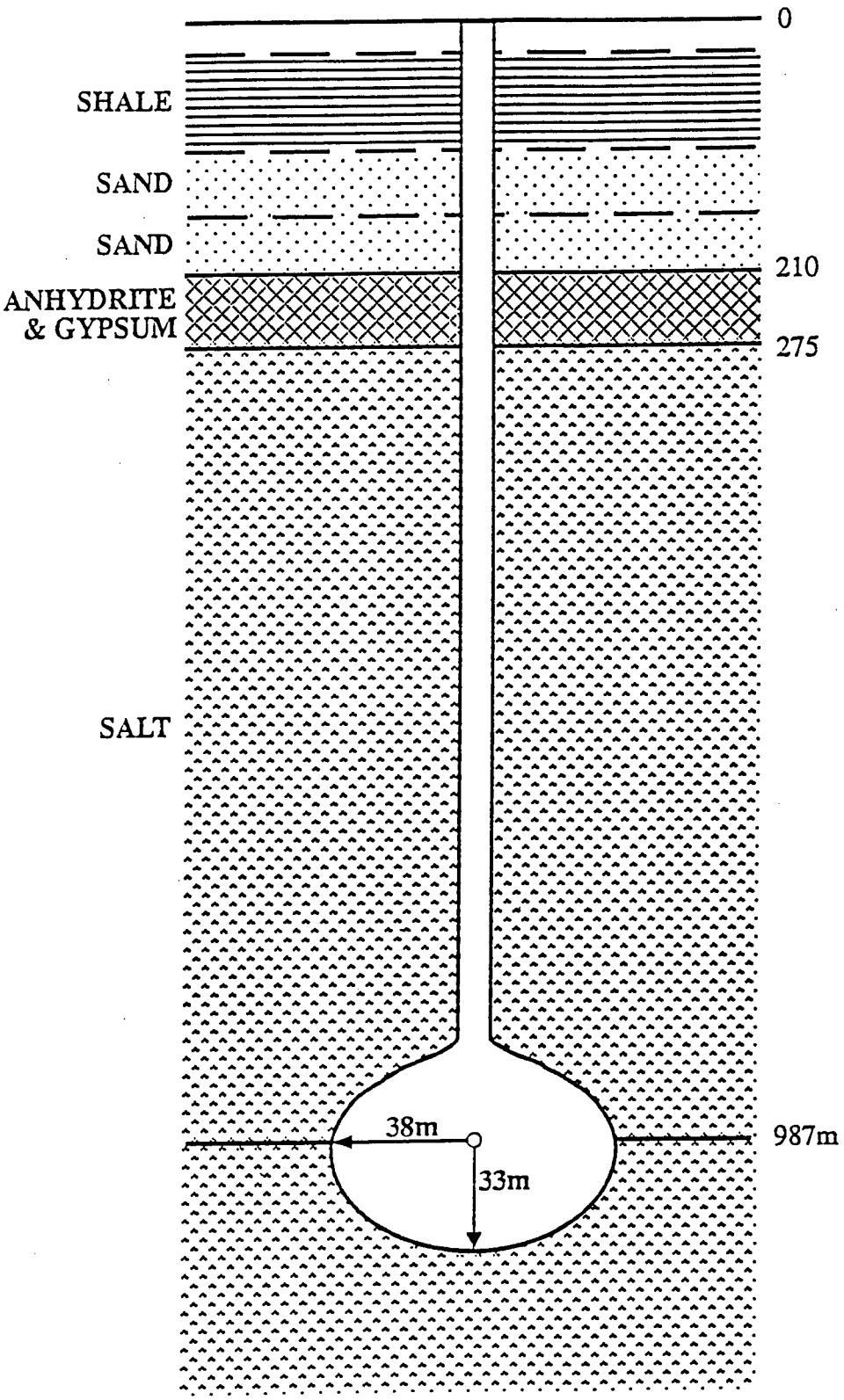


Figure 6. Cross section of borehole for the coupled explosion with yield of 64 kT. The air-filled cavity was created by this explosion and was used for the decoupled event.

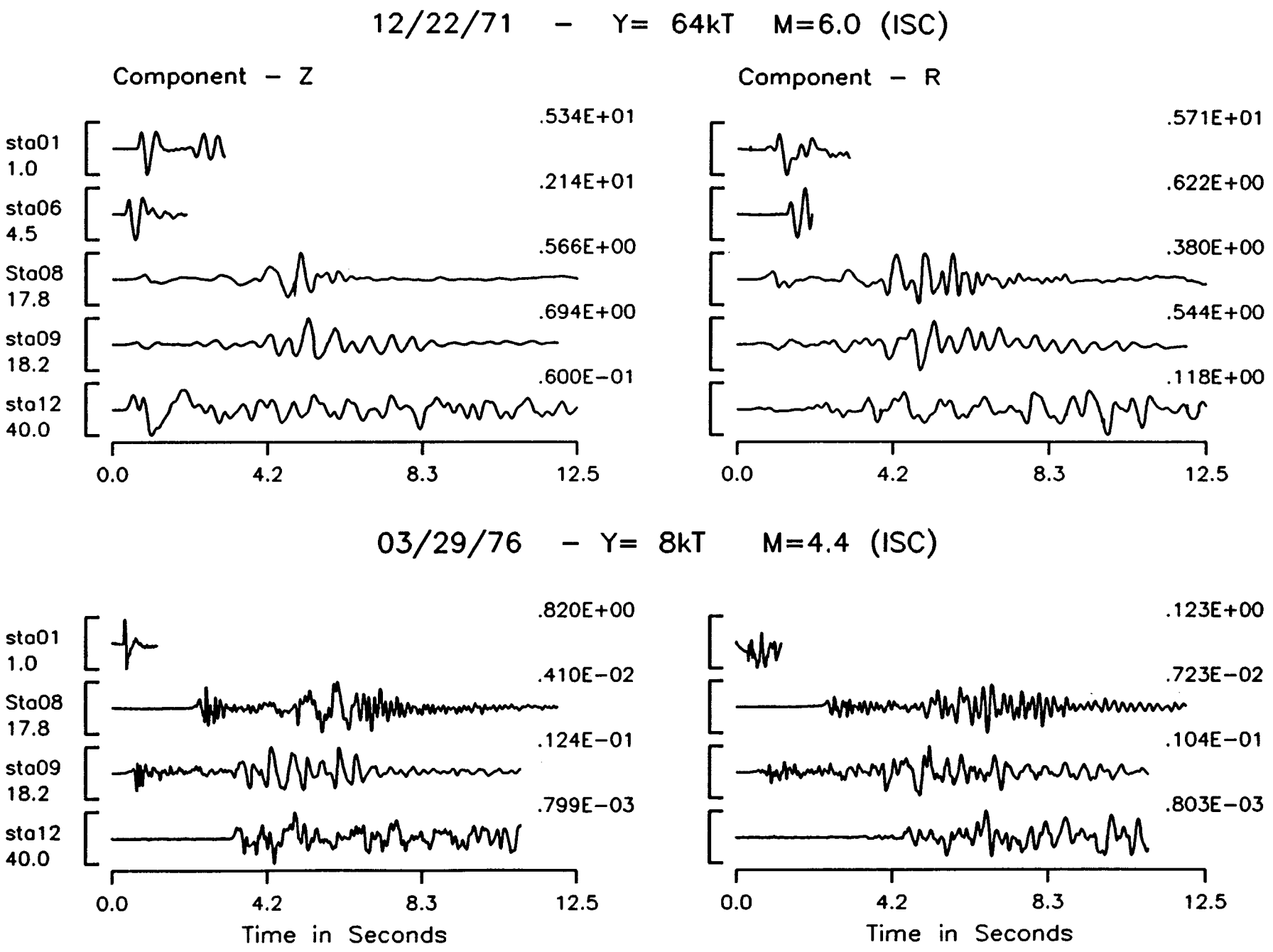


Figure 7. Display of near-field vertical and radial component seismograms recorded at selected stations from the December 22, 1971 coupled (64 kT) and from the March 29, 1976 decoupled explosion (8 kt).

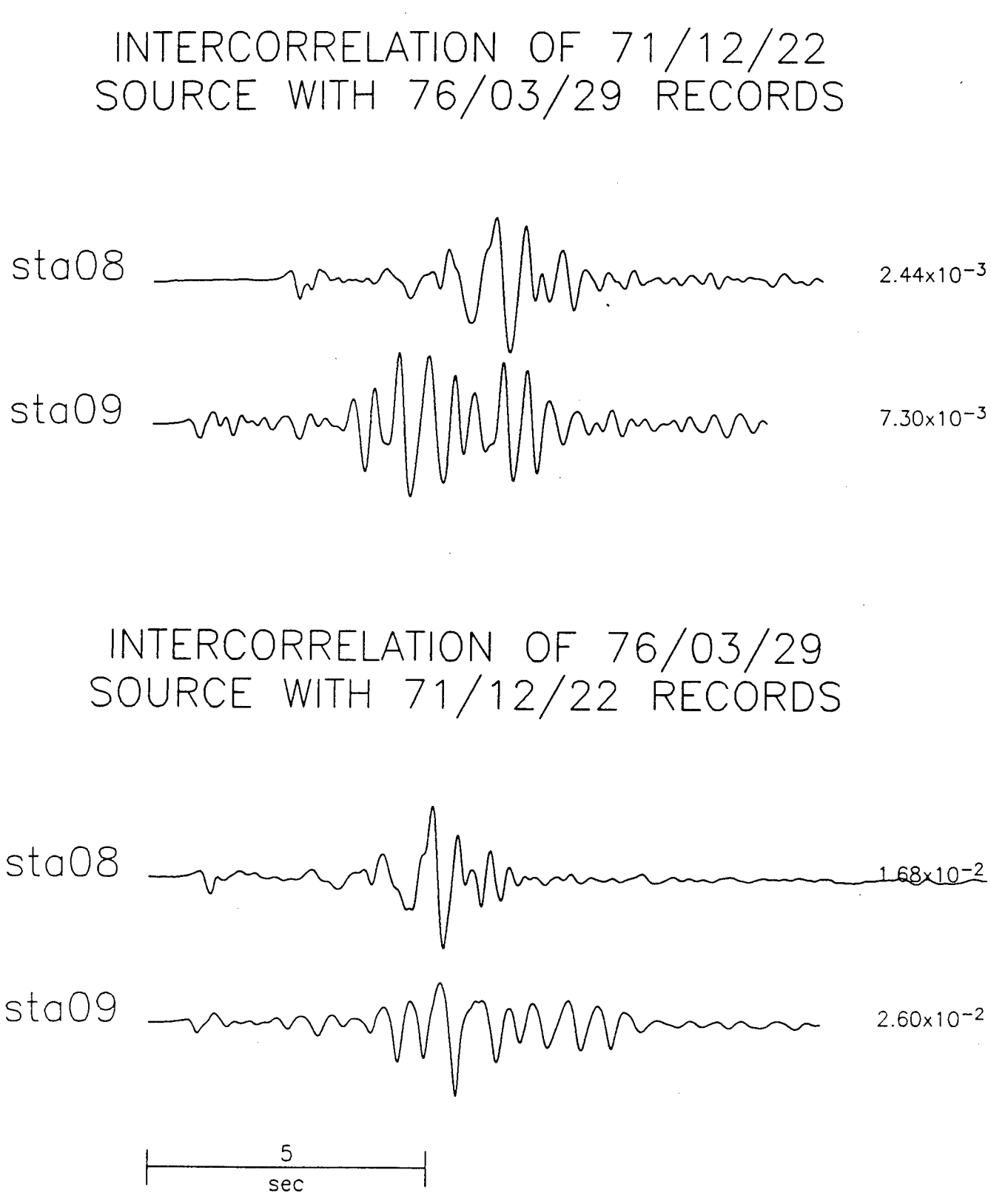


Figure 8. Results of an intercorrelation experiment where the assumed RDP's from the near-field seismogram at station 1 is convolved with the observations at Δ=17.8 km (sta08) and 18.2 km (sta09). Note the mismatch in timing and amplitude.

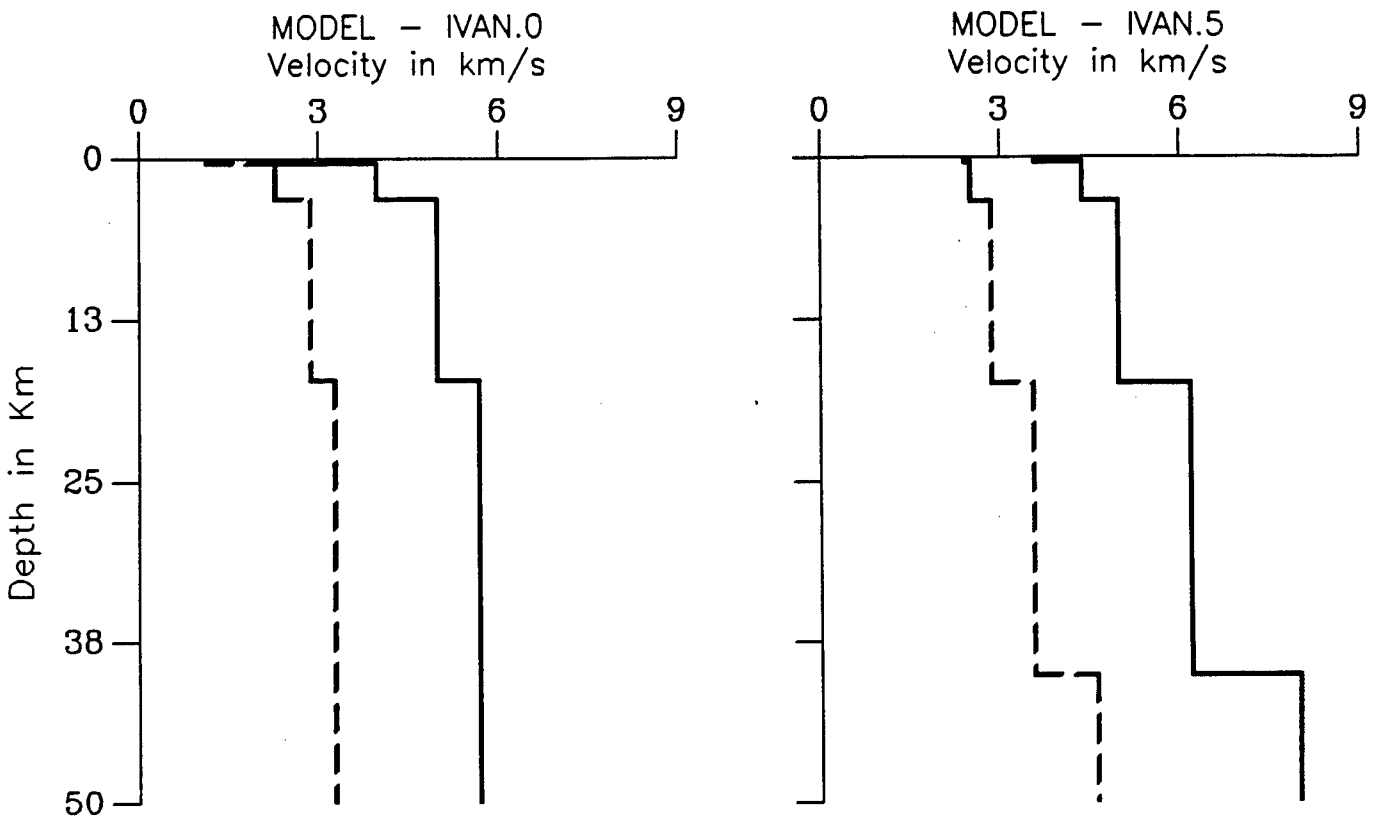


Figure 9. Crustal models of the source region. Model IVAN.0 is based on the in-country geology provided by Ivan Kitov and IVAN.5 is modified version of IVAN.0 where the near-surface low-velocity material is removed.

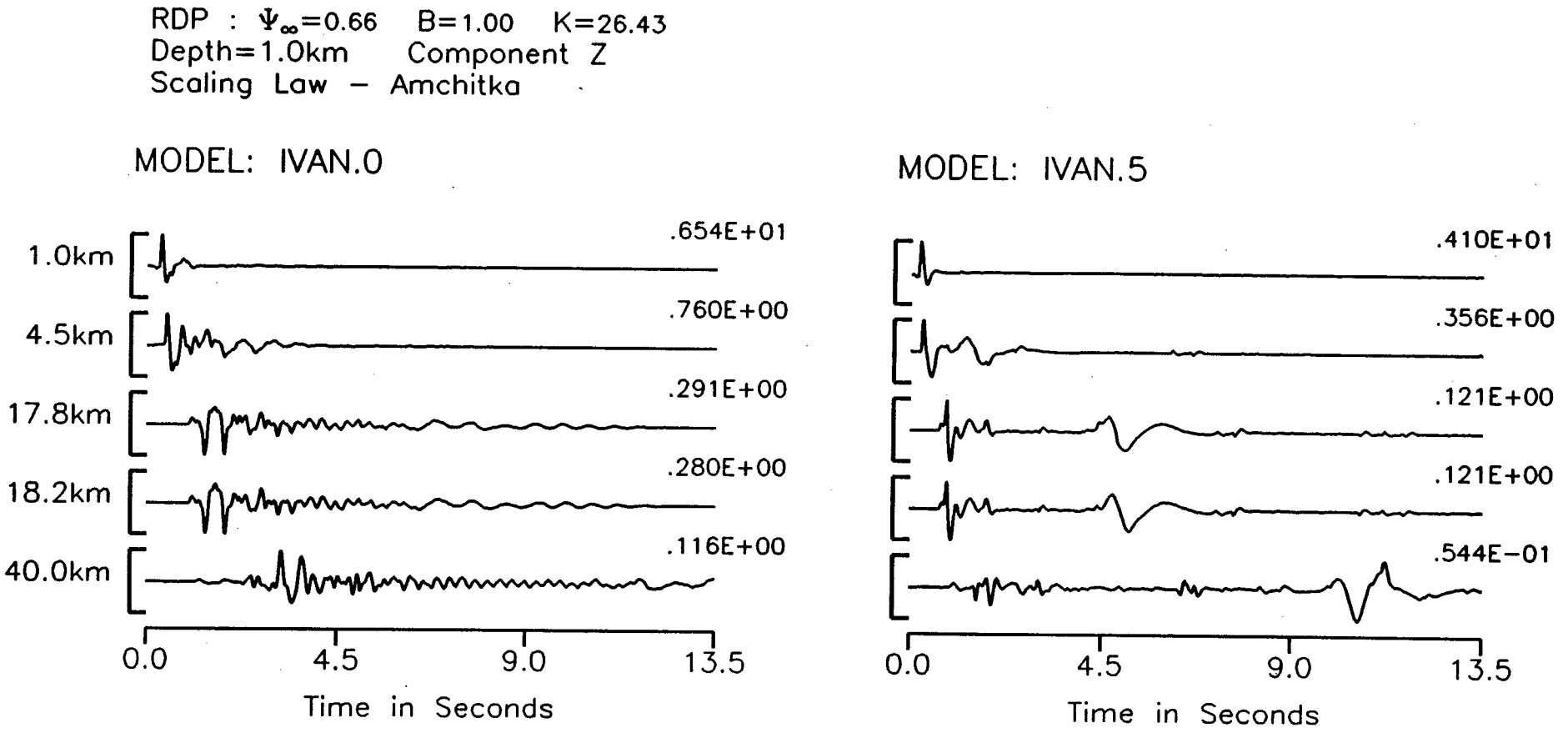
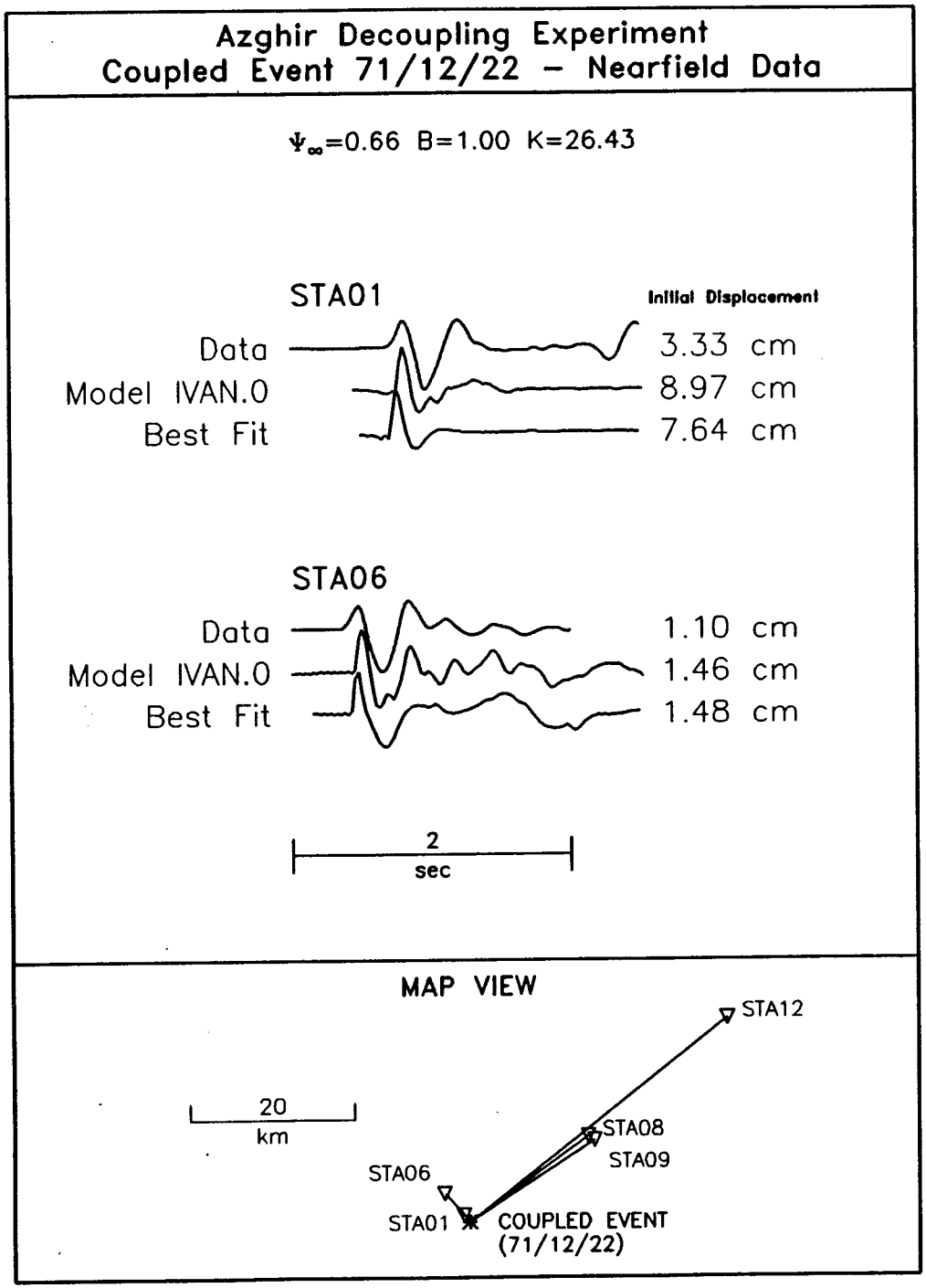


Figure 10. Example sets of synthetic seismograms computed using Helmberger and Hadley source type from the Amchitka scaling law using the crustal models IVAN.0 and IVAN.5. Although the models are only slightly different, the resulting synthetics differ significantly.



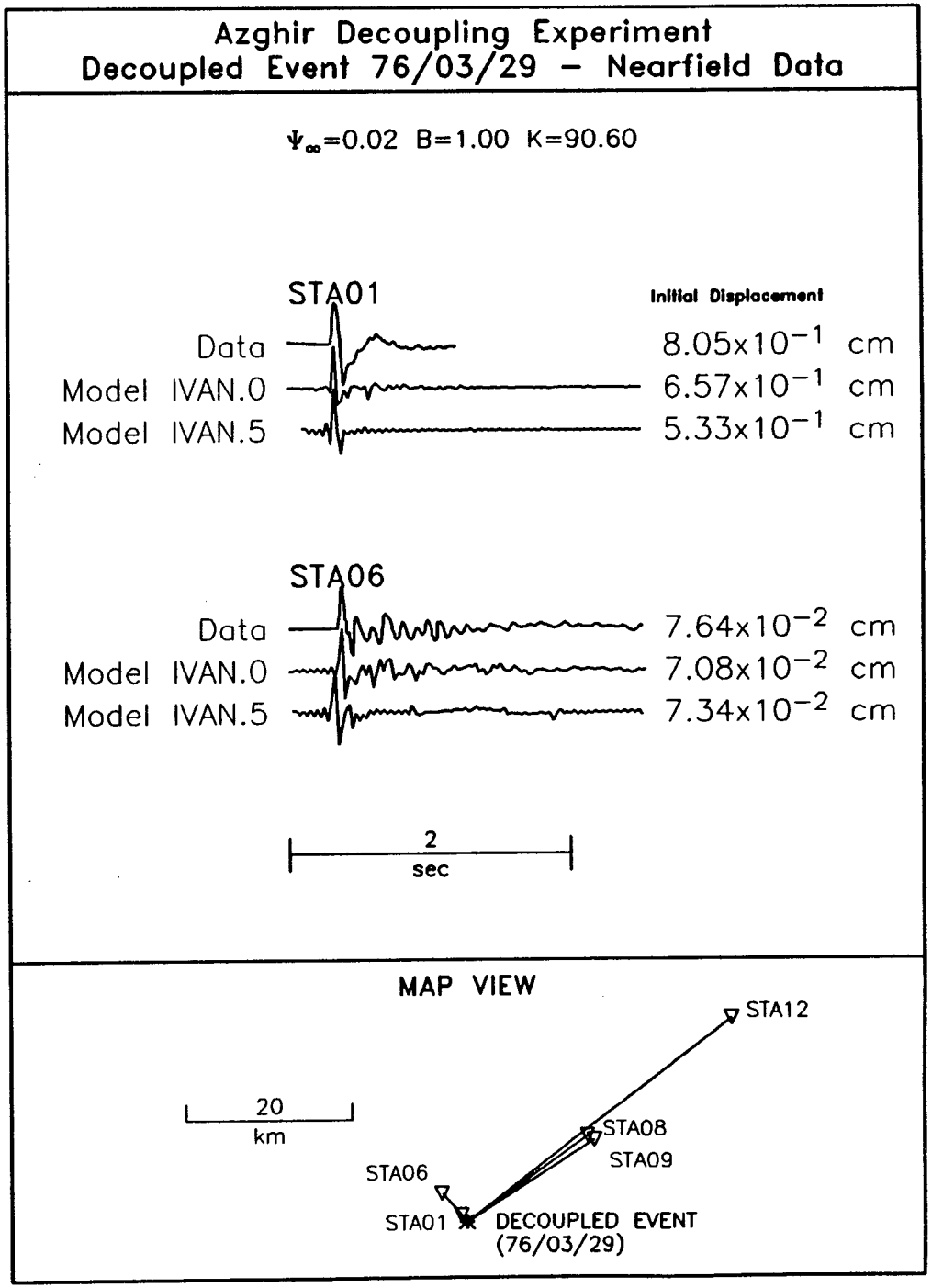


Figure 11. Comparison between data and synthetic seismograms at station 1 and 6 for both the events along with the map view. The source RDP of the two events are determined based on the agreement in the amplitude and the frequency content.

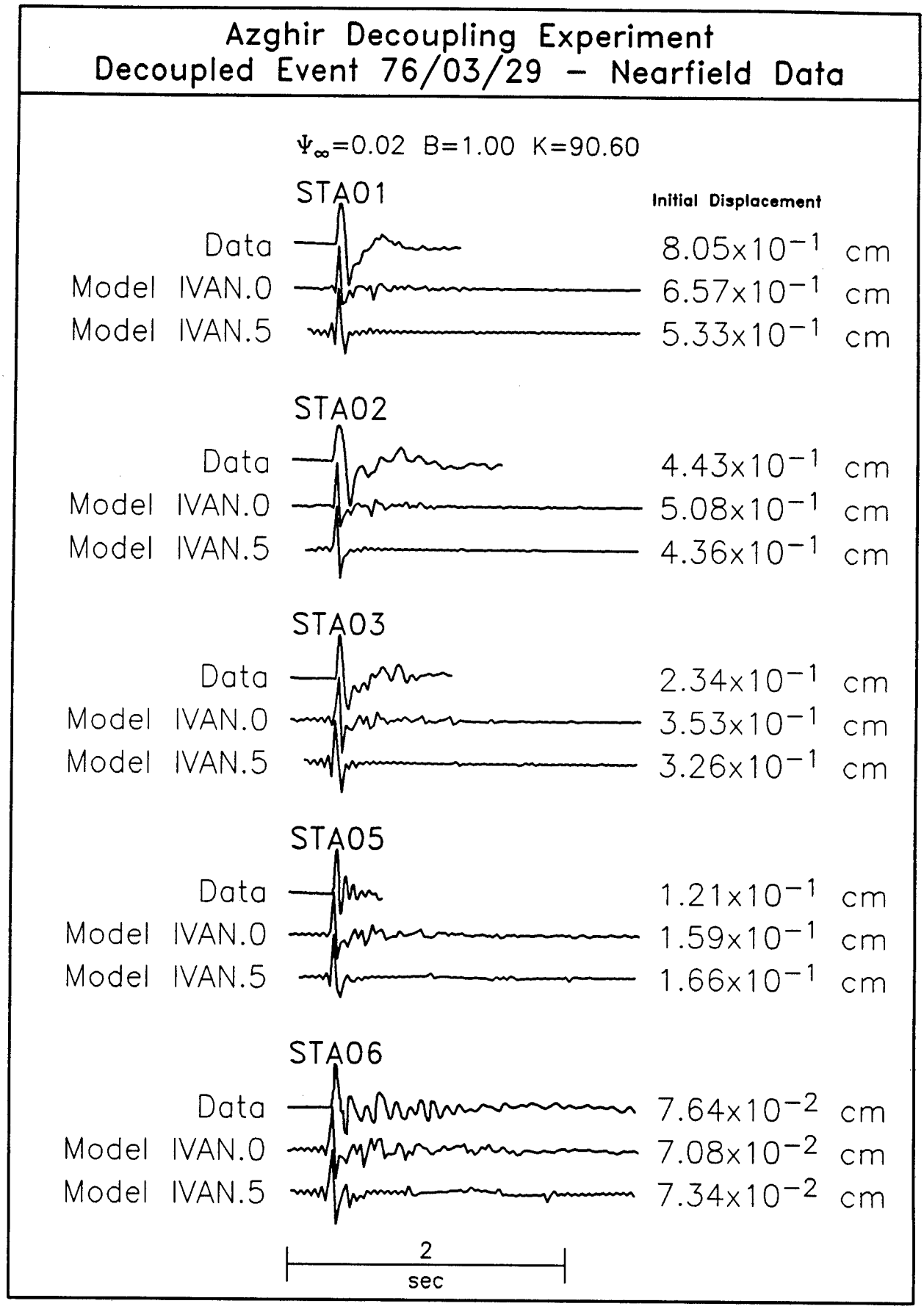


Figure 12. Using the source RDP of the decoupled event, the synthetic seismograms at other stations are compared with the data. The agreement between the data and the synthetics is reasonable.

TELESEISMIC SHORT-PERIOD DATA & REPRESENTATIVE SYNTHETIC COUPLED EVENT

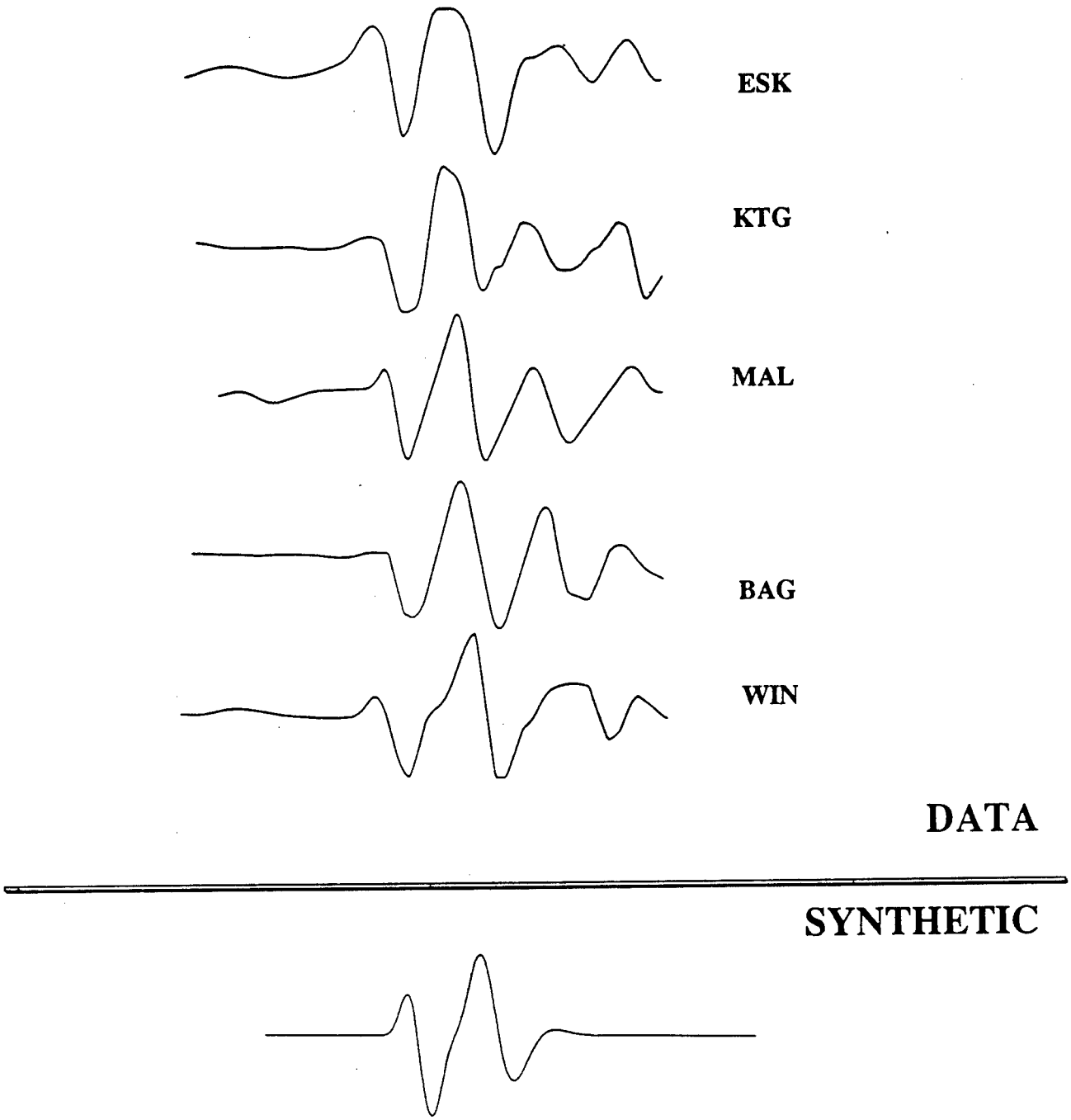


Figure 13. Comparison of an example set of teleseismic short-period waveforms for the Dec. 22, 1972 event and synthetics that match that ISC (m_b=6). A t^*=0.5 is required to map the RDP from Figure 10 into this m_b.

THIS PAGE INTENTIONALLY LEFT BLANK.

FREE-FIELD GROUND MOTION MEASUREMENTS IN THE NONLINEAR–TO–ELASTIC TRANSITION REGION

Kenneth H. Olsen and *Anthony L. Peratt*

On–Site Hydrodynamic Yield Program, Group P-15, MS-D406
Los Alamos National Laboratory, Los Alamos, NM 87545

Equivalent elastic seismic source functions experimentally determined from close-in free-field observations have been made on fewer than about 20 U.S. underground nuclear explosions—and most of these were done prior to 1970. Yet there are several fundamental aspects of explosion source phenomenology of importance to current seismic verification problems that remain incompletely understood. To help obtain a more detailed understanding of several basic source mechanism questions, we are conducting a series of experiments in the N-tunnel complex at Rainier Mesa (NTS) in which stress gauges and triaxial accelerometer arrays are deployed simultaneously in free-field geological environments at shot level as well as on the mesa surface above the explosion. Long-term scientific objectives are:

- To improve detailed understanding of basic physical processes involved in shaping and attenuating stress waves as they propagate in the free-field from a hydrodynamic region very close to the explosion, through a zone where solid–state material failure (crush and shear) is highly non-linear, and finally into a region of purely elastic behavior. These types of data also have great utility for containment diagnostic assessment as well as for nuclear test-ban verification applications.
- To simultaneously compare details of free-field waveforms with near-field, strong-motion (but still ~elastic domain) seismograms obtained at the ground surface within a few depths-of-burial (but mainly outside the spall radius). The goal is to test whether near-field surface ground motion observations are adequate to constrain explosion source functions for regional and teleseismic verification purposes without requiring detailed knowledge of nonlinear processes in the free-field.

In this presentation, we report preliminary analyses and comparisons of *free-field* seismograms obtained on three low-yield nuclear events in wet tuff (MISTY ECHO, 1988; MINERAL QUARRY, 1990; and HUNTERS TROPHY, 1992—we also will make similar measurements on the nearby CHEMICAL KILOTON experiment). We deal here almost exclusively with our free-field observations at ranges covering the transition from the distal portion of the nonlinear zone into elastic response, *i.e.*, peak radial stresses from about 1 kilobar (kb) down to less than 100 bars. (The coordinated mesa-surface observations are discussed separately elsewhere by Brian Stump and his collaborators.) Although an important component of our study is the interpretation and modeling of the free-field waveforms by means of two-dimensional, finite difference calculations which follow partitioning of energy and evolution of stress waves through non-homogeneous geologic structures characterized by non-linear material response, we here want to focus mainly on an overview of the experimental accelerometer data themselves and to suggest only general interpretations which later must be tested by detailed calculational modeling. Preliminary interpretations of some of these data based on 2-D modeling will be made elsewhere by F. App, W. Brunish, and co-workers.

Although several detailed waveform analysis procedures are underway, including frequency spectra and estimates of reduced displacement potential (RDP) for each free-field station and component, most comparisons to date are based on *peak transient values* of acceleration, particle velocity (integrated acceleration) and displacement (doubly integrated acceleration). On initial inspection of the data, the most striking aspect is the great departure from the dominantly radial motions commonly assumed in analytical treatments of source function theory. Even within the non-linear zone less than 100 m from the working points, vertical components of acceleration and velocity are between 10 and 30 % of corresponding radial components. R and Z components become nearly equal at the most distant stations (~1 km range) and each follows a rather well defined power-law amplitude decay with slant range (tangential components are usually < 10% of R but are poorly predictable). This strong R-Z component correlation is easily explained by the presence of a strong velocity gradient in the wet tuff immediately beneath tunnel level which causes strong upward refraction of initially down-going rays near the source. Although all three shots are within 1 km of each other in the same tunnel complex, significant differences seem to exist in peak amplitude decay rates from shot to shot which may suggest a high sensitivity to apparently subtle variations in material properties and/or to tamping conditions near the working points (*e.g.*, MISTY ECHO was detonated in a hemispherical cavity).

Peak transient free-field data (Figs. 1 - 6)

Three previous nuclear events in N-tunnel complex during 1988-1992 have been subjects for our coordinated free-field and mesa-top ground motion experiments. For each of these, from 6 to 8 new tri-axial *free-field accelerometer packages* were grouted into special boreholes at depths about 6 m below tunnel floor-level (in order to minimize perturbations from tunnel wall motions). For each new installation, the majority of accelerometer packages were positioned primarily to span the transition zone between the non-linear (crush and shear) material failure regime of wet tuff and the more distant ranges expected to exhibit nearly-linear, elastic response for that particular shot. An additional consideration in laying out each array was to achieve as wide an azimuthal distribution as possible. Because these free-field instruments and associated cabling were never subjected to shot-time stresses greater than 100 kilobars (kb), most survived and could be reactivated for the next shot. (They were then usually well outside the elastic radius for the new working-point.) Thus, the number and range-interval of free-field observations has grown with each succeeding event until we will be recording about 25 free-field sites for the CHEMICAL KILOTON event.

Figure 1 compares the *directly measured* first peak accelerations for each R, Z, T gauge component from a single event, MINERAL QUARRY. Power-law fits have been made for each component. Even though we expect the peak radial stresses in the wet tuff medium (not shown) to exhibit a change in amplitude decay rate as a function of range (r) from approximately r^{-2} in the crush/shear region to r^{-1} in the elastic range in the range interval between 100 and 300 m (the "elastic radius"), such a decay-rate "kink" is not apparent for either acceleration, particle velocity, or peak transient displacement data sets shown here.

Figure 2 displays the companion set of peak velocities and peak transient displacements for MINERAL QUARRY. These are derived by time integration of the accelerograms from which the data points in Fig. 1 were obtained.

Figure 3 compares observed *radial-component peak acceleration* values for the three different nuclear events. Significant differences are apparent between the three shots. For classification reasons, only directly observed data can be shown here instead of yield-scaled values. Nevertheless, when the data are scaled by the respective yields, significant differences in fitted slopes and scaled amplitudes remain. The reasons for these differences are being explored by non-linear 2-D numerical modeling programs and by conventional seismic ray-tracing and synthetic seismogram calculations. Preliminary results suggest that observed variations may be due to a variety of effects, including emplacement cavity geometry differences and/or apparently subtle small variations in wet tuff material properties in different parts of the tunnel complex.

Figure 4 presents the vertical-component accelerations for the three events. The strong relationship between radial and vertical components for all three parameters (acceleration, velocity, and displacement) of these data sets are chiefly due to the strong upward refraction caused by the steep velocity gradient in the tuff just below tunnel level in this part of the N-tunnel complex.

Figure 5 compares the *peak radial velocity* values for the three nuclear events

Figure 6 displays the corresponding peak *vertical velocity* data and fits for the three events.

PEAK FREE-FIELD ACCELERATIONS
Radial (R), Vertical (Z), & Transverse (T)
As MEASURED on MINERAL QUARRY event

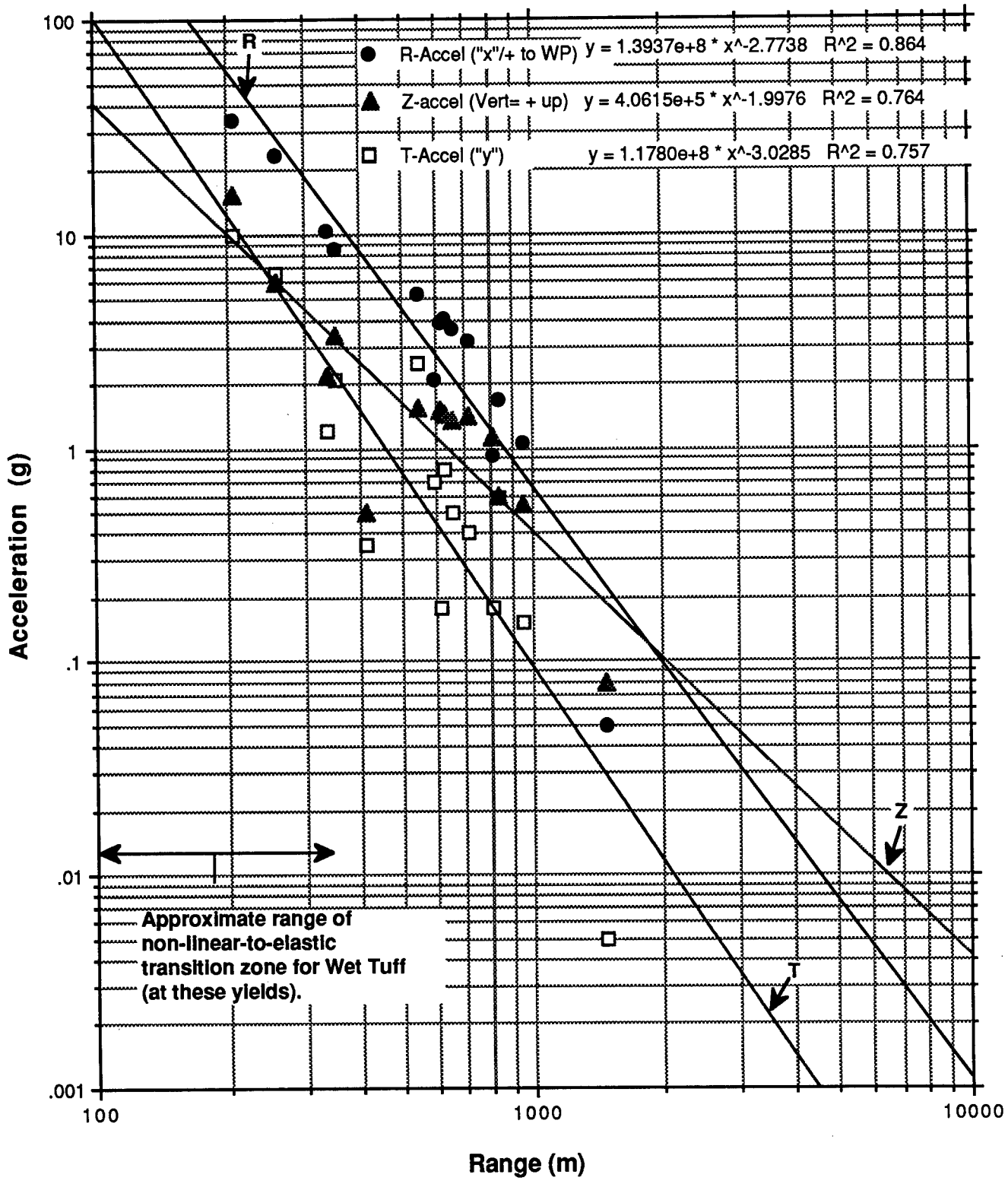


Fig. 1

PEAK TRANSIENT FREE-FIELD DISPLACEMENTS & F-F VELOCITIES (R, Z, & T) integrated from OBSERVED MINERAL QUARRY accelerations.

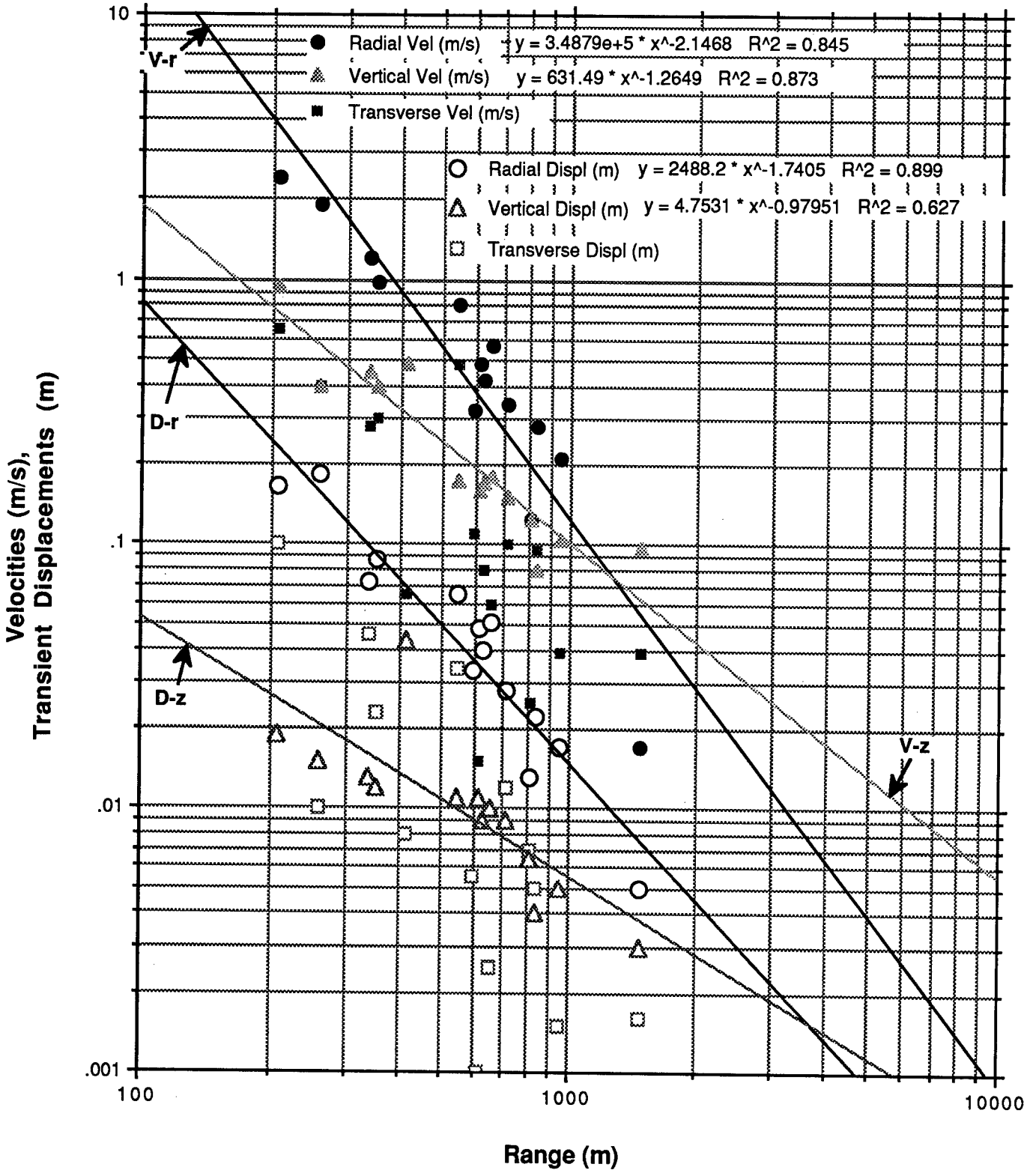


Fig. 2

FREE-FIELD ACCELERATIONS
Peak RADIAL Component:
Misty Echo, Mineral Quarry, Hunters Trophy

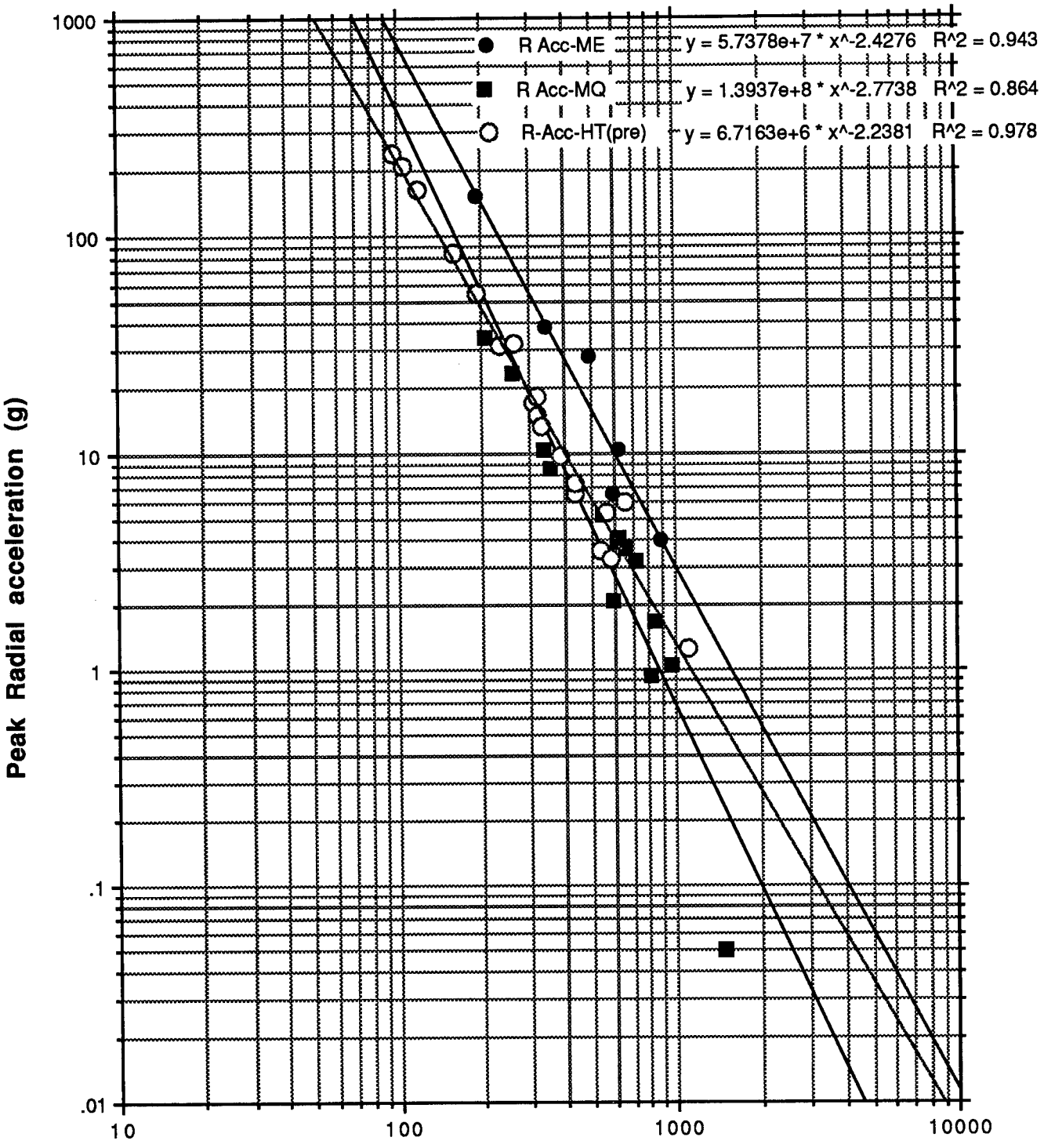


Fig. 3

FREE-FIELD ACCELERATIONS
Peak VERTICAL Accelerations:
Misty Echo, Mineral Quarry, Hunters Trophy

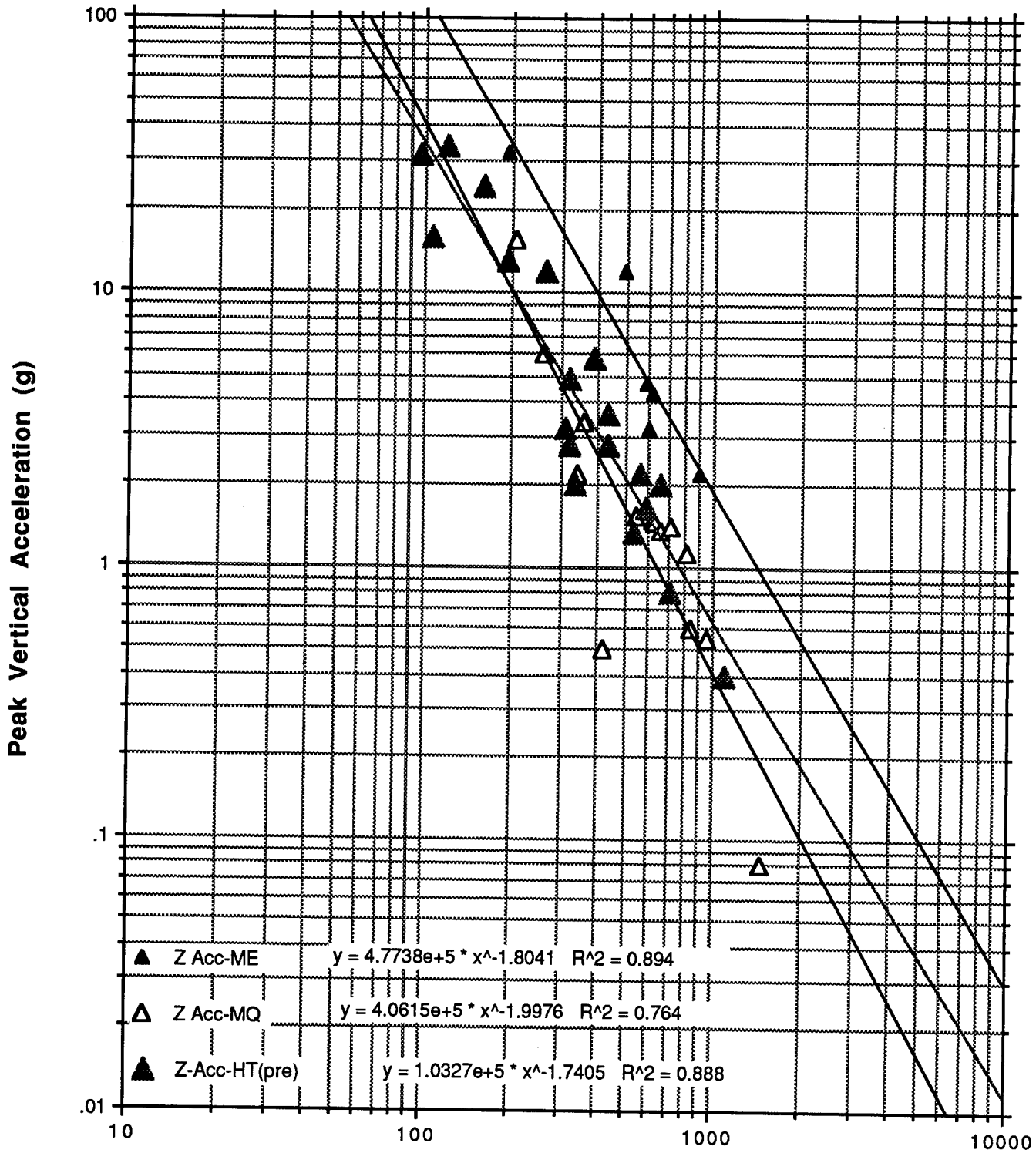


Fig. 4

FREE-FIELD VELOCITIES
Peak RADIAL Particle Velocities:
Misty Echo, Mineral Quarry, Hunters Trophy

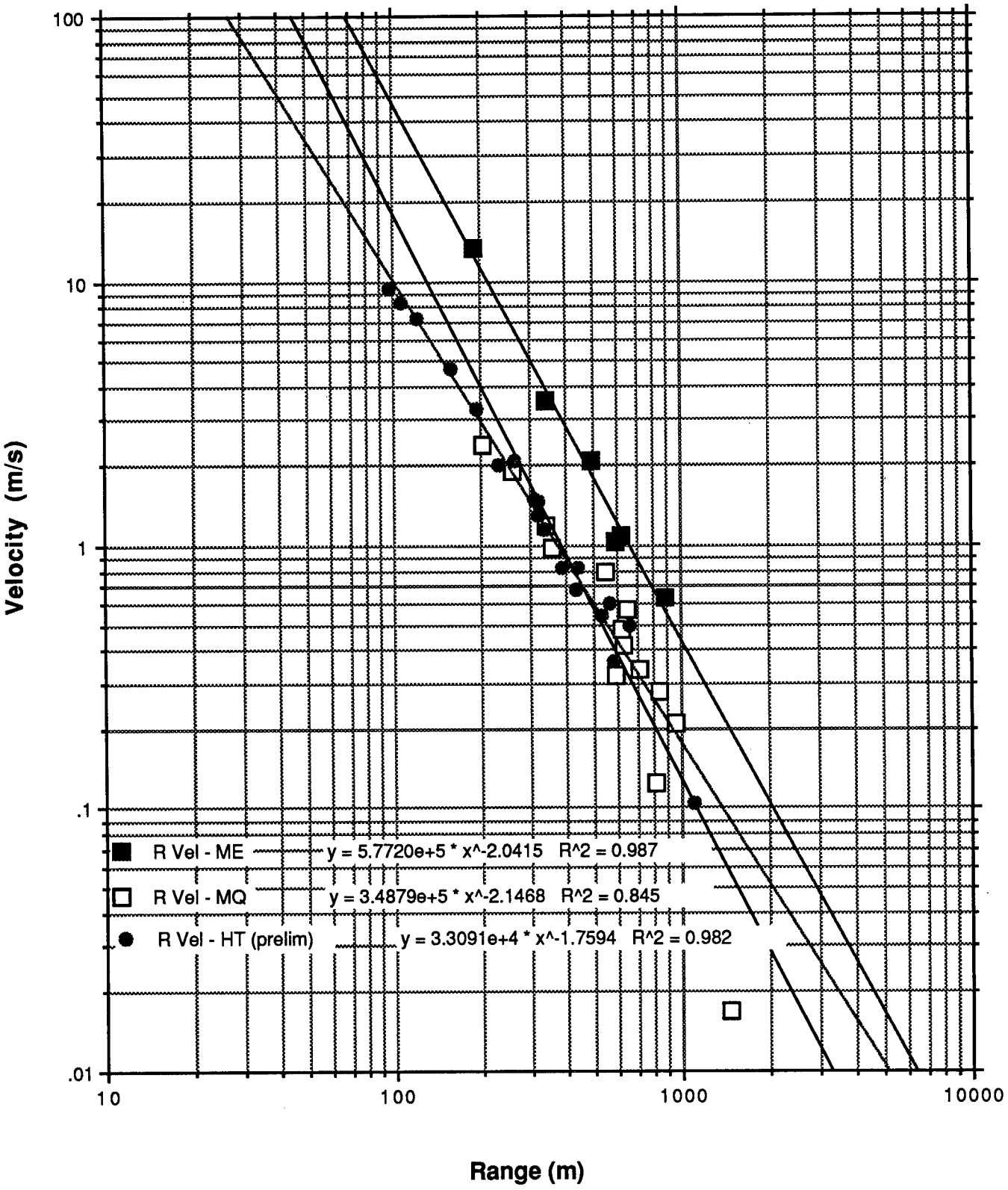


Fig. 5

Fig. 6

FREE-FIELD VELOCITIES
Peak VERTICAL Particle Velocities:
Misty Echo, Mineral Quarry, Hunters Trophy

